University of Sussex

SNO+ supernova sensitivity during pure scintillator phase

Michal Rigan

Declaration

I hereby declare that this thesis has not been and will not be, submitted in whole or in part to another University for the award of any other degree.

Signature:

Michal Rigan

UNIVERSITY OF SUSSEX

Michal Rigan, Doctor of Philosophy

SNO+ supernova sensitivity during pure scintillator phase

Abstract

SNO+ is a liquid scintillator experiment looking for a neutrinoless double beta decay in ^{130}Te. Observing this decay would mean that neutrinos are Majorana particles, one of the possible extensions to the Standard Model. Additionally, this decay allows one to measure the effective mass of the neutrino, something that is still unknown. To observe this very rare decay mode new stringent cleanliness requirements are necessary. Because of this, a new calibration system (TELLIE) was commissioned for SNO+ that does not require a deployment inside the detector. TELLIE is based on an array of LEDs delivering light via optical fibres. The calibration procedure using this system, its performance, and a comparison to a deployed calibration source is presented. TELLIE was found capable of providing calibration to the required precision.

SNO+ also has unique sensitivity to core-collapse supernova neutrinos from our galaxy. A burst trigger with the aim to detect and alert on a supernova burst was developed, built, and commissioned for SNO+. The detection mechanism is outlined. A complementary monitoring platform was produced to provide an initial analysis of the detected bursts. The trigger was tested on a supernova Monte Carlo. Additionally, it was proven to be sensitive to the sudden changes in the activity of the detector, detecting an earthquake and issues with the electronics. A procedure to analyse a neutrino burst once detected is also suggested. It consists of a tagging method to distinguish the inverse beta decay events, an energy correction for energetic positrons, and an analysis of cuts to clean the burst from the backgrounds. This method is used to extract basic observables from a supernova explosion and evaluate the sensitivity of SNO+ during the scintillator phase.
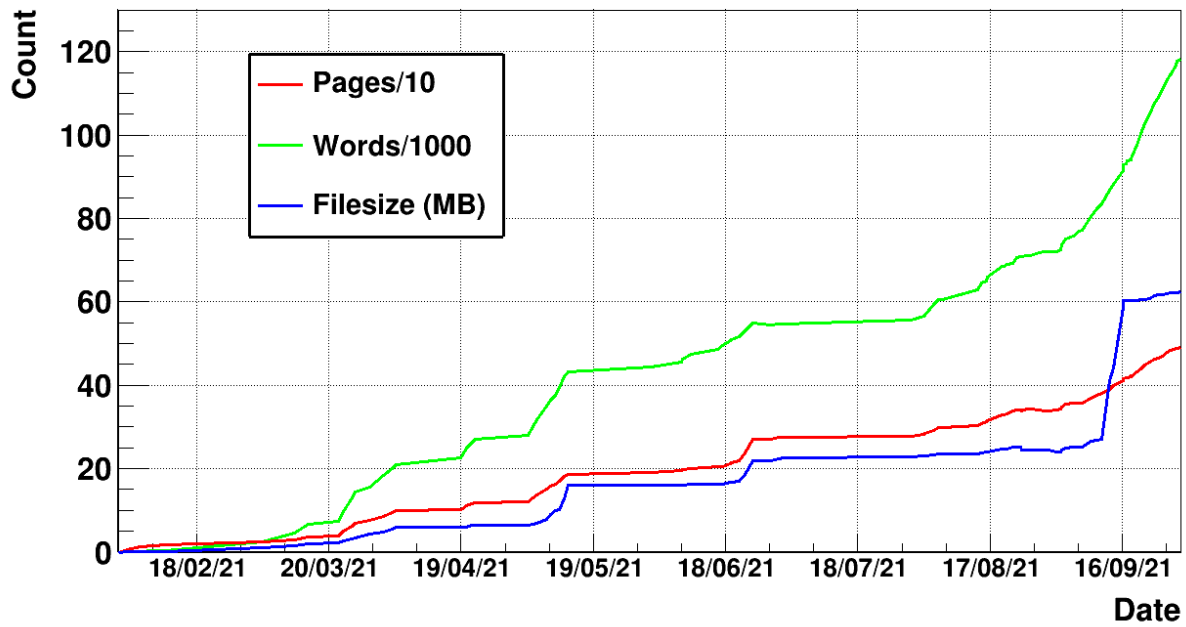
Figure 1: The timeline of writing of this thesis. The counting takes into account every single page and word and as such should not be used for any official reporting.

Acknowledgements

I would firstly like to thank my supervisor Simon Peeters for his patience, advice and support. His guidance was invaluable, and he has always gone above and beyond what was necessary.

A big thank you to Martti Nirkko, who has willingly became my mentor and pointed out all the flaws in my otherwise flawless reports. Equally, to Mark Stringer, for introducing me to most of what had become my life for several years.

Thanks also to SNO+ and SNOLab members Elisabeth Falk, Jeff Tseng, Javier Caravaca, Janet Rumleskie, Logan Lebanowski, Mark Ward, Erica Caden, Tanner Kaptanoglu, Ryan Bayes, and Christine Kraus for providing help in several aspects of my research.

Very special thanks go to people who made extremely early mornings in absolutely freezing cold actually enjoyable: Tereza Kroupova, Iwan Morton-Blake, Josh Wang, and Vincent Albanese. Additionally, to people who made a year in Canada went by too fast: Cindy Lin, Benjamin Tam, Rhea Gaur, Stefan Nae, and Lorna Nolan. It was well worth it.

Thanks also go to my fellow Sussex EPP students and technicians Charlie Mills, Tony Earle, Sammy Valder, Alex Booth, Iker de Icaza and Nicolo Tuccori for making Brighton an unforgettable place.

Lastly, but most importantly, I would like to thank my family and my girlfriend. Without the unconditional support of my parents, this would not have been possible.

Contents

List of Tables

List of Figures

Author's contributions

The second chapter of this thesis provides an introduction and background required for the complete understanding of the work presented in other parts of the thesis. This chapter is comprised of material from textbooks, articles, and lecture notes.

The overview of the experiment, its parts, and goals described in chapter three are based on publications, technical reports, and internal documents. However, the author was involved in the process of loading of the scintillator as well as part of the processing group, maintaining the data flow, data processing, and the production of simulation data. The remote control room commissioned at the University of Sussex was also set up by the author.

Regarding the calibration sources, the author was involved in the preparation and cleaning of the laserball (in collaboration with Martti Nirkko), and performed the profiling of the UFO. The content presented at the latter part of the chapter, including the maintenance of TELLIE hardware, several performance tests, and software development, is all author's work.

Chapters 4 through 6 contain mostly work performed by the author, with the exception of initial portions of the chapters that serve as a more detailed introduction.

For the PMT calibration, the corrections to the hit times were developed by other members of the SNO+ collaboration but were adapted by the author, as was the analysis procedure of TELLIE data. The author was heavily involved in the data taking, and performed the analysis, and benchmarking of TELLIE data, as well as developed parts of the software, monitoring, and scripts required for the overall functioning of the calibration system. This includes remeasurements of delays, updating fitting procedures, improving monitoring plots, and creating database tools. The evaluation of the performance of the calibration system and its comparison to laserball (the deployable calibration system) are all author's work.

The supernova burst trigger was built on the base of unused (and obsolete) L2 system developed by Kevin Labe. Only minimum functionality was kept and majority of the new burst trigger platform was designed and built anew. The content presented in chapter 6, including burst logic, processors, infrastructure, links to databases, alarms, monitoring, and connection to SNEWS, was done by the author.

Regarding chapter seven, the initial theory portion is based on the material from textbooks. A credit should be given to Mark Stringer for the knowledge on the kinematics, and to Belina von Krosigk, for exceptional review of all relevant supernova interaction channels as well as co-developing the supernova neutrino signal generator that is used for the analyses in this thesis, SNUGen. Additional thanks goes to the Garching supernova group for providing the supernova models. The rest of the chapter - SNUGen studies, the analysis of external water events, reconstruction of supernova Monte Carlo, the signal to background analysis, and most importantly, the SNO+ sensitivity analysis (including the IBD tagging method, the energy corrections, and cuts) - is all author's work.

Chapter 1

Introduction

All truths are easy to understand once they are discovered;
the point is to discover them.

GALILEO GALILEI

Neutrino oscillations are only possible if neutrinos are not massless. The observation of the oscillations meant that the Standard Model (SM) of particle physics is not complete. One potential solution is that neutrinos are Majorana particles. This is possible for neutrinos, being the only neutral fermions. The most promising way of confirming this is to observe a neutrinoless double beta decay ($0\nu\beta\beta$). This process is forbidden by the SM due to the lepton number violation, and is only possible if neutrinos are Majorana particles. In addition, it also allows one to measure the effective neutrinos mass. This extremely rare decay is therefore being searched for by several neutrino experiments, including SNO+. Details about neutrinos, neutrino oscillations, and the neutrinoless double beta decay are presented in Chapter 2.

SNO+ is a multi-purpose liquid scintillator detector for studying neutrinos with the main physics goal of observing the $0\nu\beta\beta$ decay. It reuses the equipment from the original Sudbury Neutrino Observatory (SNO) experiment. The light yield is estimated to be 50 times higher for SNO+. There have been several upgrades to the detector, including a completely new external calibration system. This addressed the new strict cleanliness requirements of the liquid scintillator, as the calibration system does not require deployment inside the detector, thus minimising any potential contamination. The detector is described in Chapter 3 of this thesis, alongside the details of the upgrades.

The new calibration system consists of 95 optical fibres distributed uniformly inside the SNO+ cavity to provide full coverage of the photo-multiplier tubes (PMTs). It is named ELLIE, and it uses LEDs to produce light. The primary purpose is the calibration of the timing response of the PMTs, however, the system is also capable of monitoring the attenuation and scattering in the scintillator. The exact method of calibration using ELLIE (specifically using the timing module TELLIE) is explained in Chapter 4. Additionally, the same system was also used to stress test the SNO+ electronics in a study simulating a supernova (SN) signal.

A SN explosion marks the end of a life of a massive star. It is solely responsible for the creation of heavy elements in the Universe. In addition to creating extremely beautiful pictures by the emission of photons, supernovae (SNe) also emit a significant number of neutrinos (almost all of the energy is carried away by the neutrinos, in fact). Therefore, SNe are the ultimate source of neutrinos, which are still quite unexplored. These neutrino are, in turn, a window inside the core of a dying star. The physics of SN, and the neutrino generation and emission are outlined in Chapter 2.

In addition to the $0\nu\beta\beta$ decay search, SNO+ is also sensitive to solar, atmospheric, reactor and geo (anti)neutrinos. Most importantly for this thesis, SNO+ can detect neutrinos released by a SN, if it occurs in our galaxy.

The detection of SN neutrinos is important for several reasons. It allows us to learn about the neutrinos themselves, it points to the effects taking place inside the core of the star, it makes it possible to study oscillation effects in regions of high density and over long distances, and it serves as an early warning, given the neutrino emission from the SN happens up to few hours before the optical signal reaches the Earth. Therefore, a prompt detection is crucial. A trigger developed to detect such bursts and alert when they were observed was designed for SNO+ and is detailed in Chapter 5. Its performance is also evaluated in the same chapter.

Chapter 6 analyses the sensitivity of SNO+ during the scintillator phase to a range of SN models using a custom Monte Carlo generator. It starts by describing the interactions used to detect SN neutrinos, followed by an overview of available models. The effect of various parameters, such as the neutrino mass ordering, or the choice of equation of state, is assessed. Additionally, the chapter suggests a possible reconstruction procedure to reconstruct a SN signal once detected. This includes a specific tagging method and a cor-

rection of the reconstructed energies. The efficiency of this procedure is finally determined by the analysis of a default model and a model leading to a black hole remnant.

My conclusions are summarized in the final chapter, Chapter 7. It briefly indicates the results of various studies, and the efficiencies of the applied methods. My personal suggestions are included.

A list of abbreviations is available just after the list of bibliography.

The thesis also contains several appendices. These are not essential, but add information that is helpful and can be used as a point of reference in the future. These are:

- Appendix A: This appendix describes the method to extract the relative time offsets between TELLIE LEDs. This is necessary for the calibration of the PMTs;

- Appendix B: A table listing the runs used for all TELLIE datasets is presented in this appendix. If the method is ever changed, the datasets can be reprocessed using these numbers;

- Appendix C: This appendix contains additional plots and tables presenting data from the remeasurement of TELLIE fibre delays. It mostly serves as a documentation;

- Appendix D: Additional comparison plots for TELLIE and other calibration system are stored here;

- Appendix E: A detailed overview of the Supernova Burst Trigger is available in this appendix;

- Appendix F: This appendix lists all available SN Monte Carlo models via the custom generator. It firstly presents the models by the input parameters. Secondly, it displays the data from the models using a specific visualisation. The purpose of this appendix is to highlight the variety of the SN models or ease the process of picking a model to study. It is a sort of an encyclopedia. It also looks rather nice.

Chapter 2

Supernova Physics

It is no good to try to stop knowledge from going forward.
Ignorance is never better than knowledge.

Enrico Fermi

2.1 Introduction

This chapter introduces the SN physics with the focus on neutrinos. Firstly, neutrinos are briefly introduced, with the focus on neutrino mixing and oscillations. The evolution of a star is described after that, from the point of the creation of the star creation until the end of the life cycle. The possible endpoints are outlined, with the conditions required for each. The SN explosion, being the source of the neutrinos, is detailed. This includes the classification of the SN types, the physical process of the collapse and the explosion, and the associated neutrino emission throughout the various phases. The resulting neutrino signal is described afterwards, highlighting the features of the signal, the observables, and the method of detection. Additionally, the observed neutrino signal from the last nearby SN is summarized, alongside the predicted frequency and distribution of SN explosions in the galaxy. Finally, the chapter briefly mentions the effect of the neutrino-matter interactions on the burst signal.

2.2 Neutrinos - Standard Model

2.2.1 Brief history

A neutrino was first proposed by W. Pauli in 1930 as a prospective solution for the missing energy as well as spin statistics in the β decay [1]. He suggested that a neutral

weakly interacting fermion emitted in the β decay could solve the problem, calling it a *neutron*. The 'real' neutron as we know it today was discovered in 1932 by J. Chadwick, so E. Fermi renamed Pauli's particle to *neutrino* [1]. It was believed to be massless.

Following the three generations of leptons: an electron e^-, a muon μ^-, and a tau τ^-, there neutrino flavours were predicted: an electron neutrino ν_e, a muon neutrino ν_μ, and a tau neutrino ν_τ. Each lepton has a corresponding antiparticle with positive charge. For neutrinos, these are $\bar{\nu}_e$, $\bar{\nu}_\mu$, and $\bar{\nu}_\tau$, respectively.

In 1962, the first serious accelerator neutrino experiment took place at BNL[1], providing evidence for the existence of second neutrino, ν_μ. Few years later the Standard Model was formulated, and in 1973 neutral current neutrino interactions were discovered [1]. The third neutrino type - ν_τ - was implied by the discovery of the tau particle in 1975 at SLAC[2] [2], and directly observed in 2000 by the DONUT collaboration [3].

The experimental confirmation of neutrino oscillations [4] meant that neutrinos are massive, since the oscillations are only possible if there is a mass discrepancy between the neutrino flavour states. This is the first conclusive experimental deviation from the SM. There are two consequences: the SM is only an effective theory of a greater theory beyond the SM, and neutrinos are the first messengers of this new physics [1].

In addition to oscillations, there are many questions that can be answered by studying neutrinos. Firstly, there is the question of neutrino antiparticles. The matter-antimatter asymmetry could be resolved by a different mechanism of mass generation for neutrinos. Neutrinos could also help give insight into phenomena that are otherwise inaccessible, such as SN explosions or the Big Bang. Furthermore, some form of heavier neutrino could possibly solve the puzzle of the dark matter.
All in all, there are many reasons to look for neutrinos and study their properties and interactions. Neutrinos are the spotlight of this thesis.

Neutrino sources   Neutrinos are labelled depending on their origin. There are several sources of neutrinos. Generally, they can be grouped into natural sources and man-made sources. The neutrinos that are produced naturally are solar neutrinos, atmospheric neutrinos, geo neutrinos, and supernova neutrinos.

---

[1]Brookhaven National Laboratory.

[2]SLAC National Accelerator Laboratory, originally named Stanford Linear Accelerator Center.
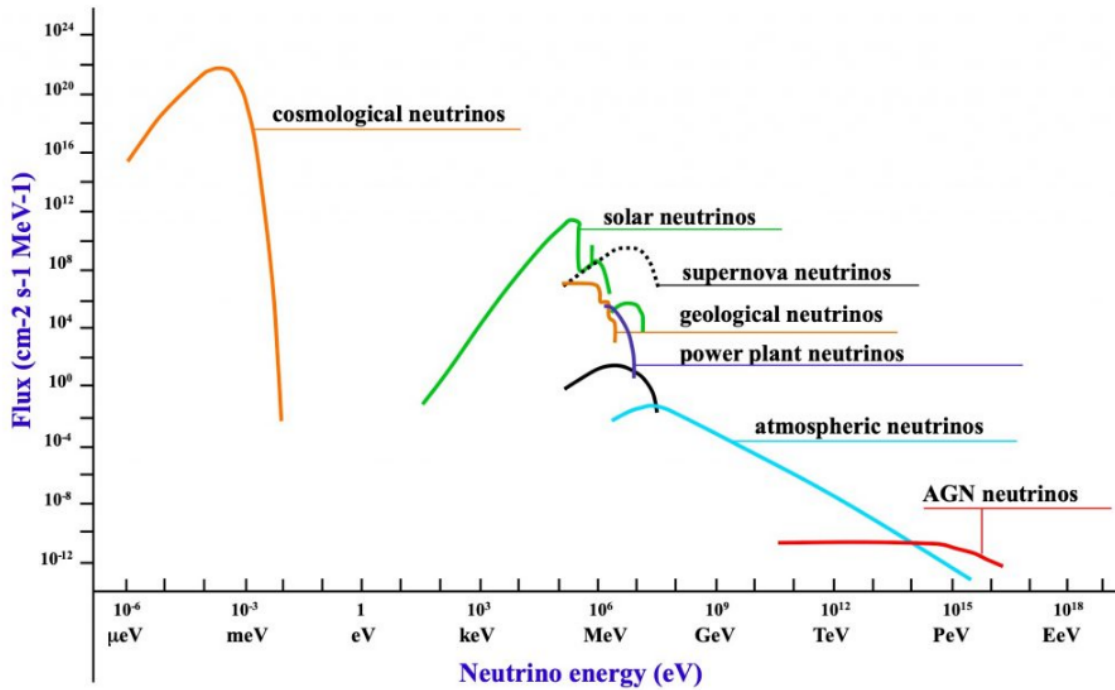
Figure 2.1: The neutrino flux versus neutrino energy, by the neutrino source. Also called the Grand Unified Neutrino Spectrum. Figure from [5].

Neutrinos can also be man-made. These include accelerator neutrinos and reactor neutrinos.

The flux and the energy of the neutrinos generated by various sources are shown in Figure 2.1.

Supernova neutrinos

Neutrinos of a wide range of energies are also produced during SNe. These are extensively described later in this chapter and in Chapter 6.

Diffuse supernova neutrino background   It is also predicted that a weak glow of MeV neutrinos and antineutrinos from distant core-collapse SNe exists and could be detected on the Earth [6]. This is called the diffuse supernova neutrino background (DSNB). It has not yet been detected, but it is believed that the current upper limit on the $\bar{\nu}_e$ flux is close to the prediction based on the astrophysical data. The next generation experiments with increased sensitivities are expected to detect few DSNB events per year [6].

Relic neutrinos

Relic neutrinos are the product of the standard Big Bang. They are also referred to as the Cosmic Neutrino Background (CNB). It is theorised that neutrinos were present

during the early Universe filled with hot plasma, later decoupling due to cooling and expansion [7]. They are believed to still be present in free space, but due to their extremely small temperature they also experience extremely small weak interaction cross section with matter [7]

$$\sigma \sim G_{\mathrm{F}}^2 m_\nu^2 \sim 10^{-56} \left(\frac{m_\nu}{1eV}\right)^2 \mathrm{cm}^2,$$

where σ is the interaction cross-section with matter, G_F is the Fermi constant, and m_ν is the mass of the relic neutrino.

This extremely small cross-section is the reason why the relic neutrinos are still present today but it also makes it impossible to detect them with current technology. However, there is indirect evidence from Big Bang cosmology [8].

2.3   Neutrinos - beyond Standard Model

This section will briefly address neutrino mixing and the derived flavour changing effects.

2.3.1   Neutrino mixing

Neutrino mixing describes the relation between the neutrino flavour (the weak eigenstate [3]) and the mass eigenstates [9]. These eigenstates are not identical - similar to what is present in the quark sector.

If we assume there are n flavour eigenstates $|\nu_\alpha\rangle$ with $\langle\nu_\beta|\nu_\alpha\rangle = \delta_{\alpha\beta}$ and n mass eigenstates $|\nu_i\rangle$ with $\langle\nu_i|\nu_j\rangle = \delta_{ij}$, these are connected via a (unitary) mixing matrix U as

$$|\nu_\alpha\rangle = \sum_i U_{\alpha i} |\nu_i\rangle, \qquad |\nu_i\rangle = \sum_\alpha \left(U^\dagger\right)_{i\alpha} |\nu_\alpha\rangle = \sum_\alpha U_{\alpha i}^* |\nu_\alpha\rangle . \tag{2.1}$$

The properties of the matrix are

$$U^\dagger U = 1, \qquad \sum_i U_{\alpha i} U_{\beta i}^* = \delta_{\alpha\beta}, \qquad \sum_\alpha U_{\alpha i} U_{\alpha j}^* = \delta_{ij}. \tag{2.2}$$

For antineutrinos, the $U_{\alpha i}$ is replaced with $U_{\alpha i}^*$.

If we assume the flavours of the three detected neutrino flavours ν_{e}, ν_μ, ν_τ; these do not coincide with the mass states ν_1, ν_2, ν_3 due to neutrino mixing. Instead, the flavour states are a combination (a superposition) of the mass states and vice versa. This is shown in Figure 2.2.

---

[3] Weak eigenstates participate in weak interactions.
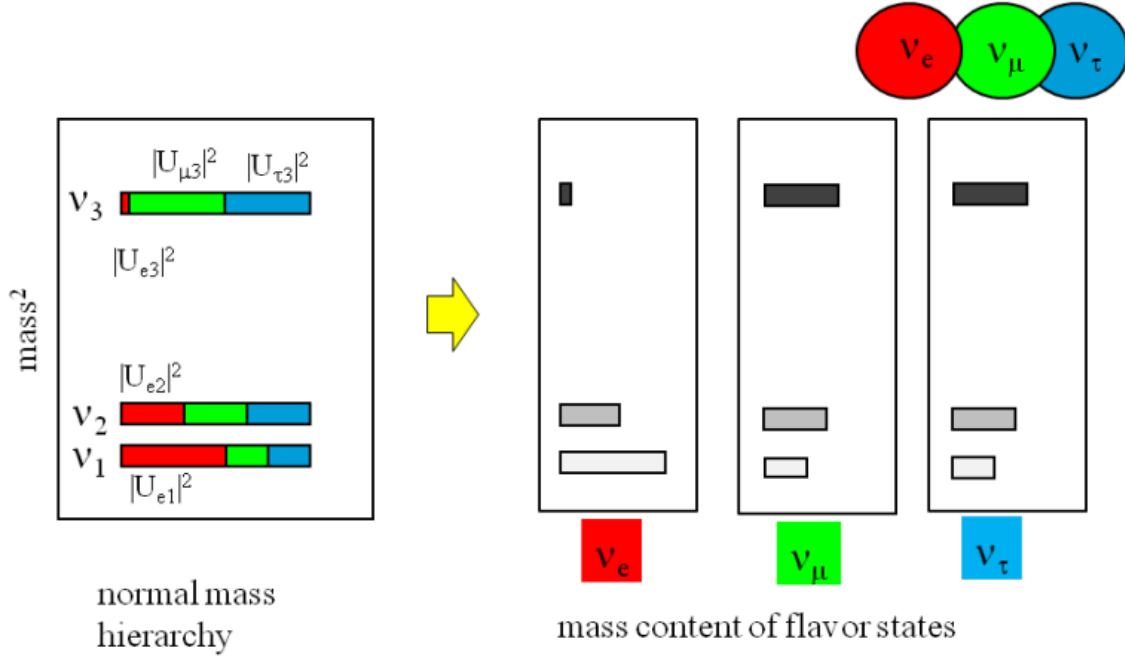
Figure 2.2: The representation of neutrino mixing. Left: flavour composition of the mass eigenstates. The mass is represented by a box, colours correspond to different flavours. The proportions represent the probabilities of finding particular mass state in the given flavour state. Right: The neutrino flavour states represented by their composition of mass eigenstates. Figure from [9].

The practical consequence of mixing is that, for example, ν_3 would interact with probability of (approximately) 48% as ν_μ, 50% as ν_τ and 2% as ν_e. It also follows that the flavour states are composed - more specifically are a coherent combination - of mass states.

2.3.2   Neutrino oscillations in vacuum

The neutrino oscillations are the consequence of neutrino mixing. The oscillations can be detected if the coherent superposition of states is present. Even though the individual lepton numbers are not conserved, the total lepton number is [10].

The mass eigenstates are stationary and change with time as

$$|\nu_i(x,t)\rangle = e^{-iE_i t} |\nu_i(x,0)\rangle. \tag{2.3}$$

Neutrinos are produced as flavour states. The flavour state is a superposition of mass states. These mass states propagate according to Eq. 2.3. This means that neutrino generated as $|\nu_\alpha\rangle$ will, in time, change as

$$|\nu(x,t)\rangle = \sum_i U_{\alpha i} e^{-iE_i t} |\nu_i\rangle = \sum_{i,\beta} U_{\alpha i} U_{\beta i}^* e^{ipx} e^{-iE_i t} |\nu_\beta\rangle. \tag{2.4}$$

This means that the flavour content of the final state differs from the initial content. This is the basis of neutrino oscillations, based on neutrino mixing.

The flavour conversion is then given by the transition amplitude A as

$$A(\alpha \to \beta)(t) = \langle \nu_\beta | \nu(x,t) \rangle = \sum_i U_{\beta i}^* U_{\alpha i} e^{ipx} e^{-iE_i t}. \tag{2.5}$$

And the probability of transition P can be obtained from the transition amplitude as

$$P(\alpha \to \beta)(t) = |A(\alpha \to \beta)|^2 = \sum_i \sum_j U_{\alpha i} U_{\alpha j}^* U_{\beta i}^* U_{\beta j} e^{-i(E_i - E_j)t}; \tag{2.6}$$

if we assume relativistic neutrinos, this can be rewritten as

$$P(\alpha \to \beta)(t) = \sum_i |U_{\alpha i} U_{\beta i}^*|^2 + 2\mathrm{Re} \sum_{j>i} U_{\alpha i} U_{\alpha j}^* U_{\beta i}^* U_{\beta j} \exp\left(-i\frac{\Delta m_{ij}^2}{2}\right) \frac{L}{E}, \tag{2.7}$$

with $\Delta m_{ij}^2 = m_i^2 - m_j^2$ being the mass difference, E being the energy and L being the distance.

The oscillatory behaviour is only present if at least one neutrino mass eigenstate is different from zero and if mixing of flavours exists [10]. As can be seen in Eq. 2.7, oscillations are only sensitive to mass difference and dependent on the L/E factor.

2.3.3 Mass ordering

As shown, the transition probabilities contain mass difference parameters. However, the order of these values relative to each other is unknown, as this is impossible to obtain from the mass difference alone. This is known as the neutrino hierarchy, or ordering. The two possible options for the ordering of the mass differences are shown in Figure 2.3.

The normal ordering (NO, NH) is the case where the smaller mass splitting is below the bigger splitting value. The inverted ordering (IO, IH) is then the second case. The ordering is still not determined (but only these two options are possible for the three detected neutrinos). There are next generation neutrino experiments planned with the goal of determining the exact ordering [12].

2.3.4 Neutrino oscillations in matter

The Mikheyev-Smirnov-Wolfenstein (MSW) effect, also called the matter effect, describes how neutrino oscillations in matter differ to the vacuum case. The cause is the presence of electrons in matter, changing the mass eigenstates due to charged current coherent scattering of electron neutrinos [13].
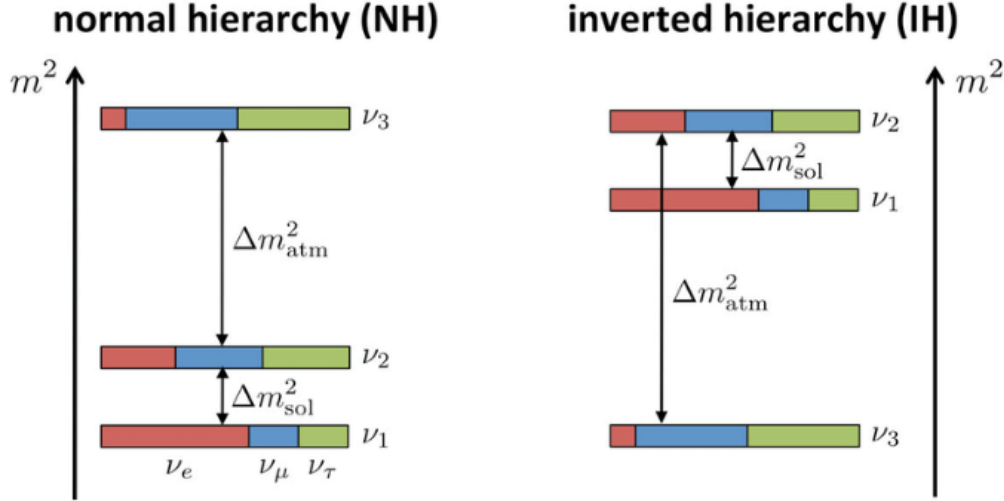
Figure 2.3: A visual representation of the two possible neutrino mass hierarchies. Additionally, the relative flavour composition of each mass eigenstate is shown (as colours). Figure from [11].

For simplicity, two neutrino mixing will be considered here. For the example of solar neutrinos, the mixing between ν_e and ν_α[4] is present. The normal mixing equation gives

$$\nu_e = \cos\theta_{12}\nu_1 + \sin\theta_{12}\nu_2, \tag{2.8}$$

$$\nu_\alpha = -\sin\theta_{12}\nu_1 + \cos\theta_{12}\nu_2. \tag{2.9}$$

In this case the θ_{12} is the vacuum mixing angle, as described in Subsection 2.3.2. The mass states are the eigenstates of the Hamiltonian H_0 of the system.

In matter, however, the total Hamiltonian changes to $H = H_0 + V$, where V represents the matrix of potentials of the matter that is present. The eigenstates of H are now different

$$\nu_e = \cos\theta_{12}^m\nu_{1m} + \sin\theta_{12}^m\nu_{2m}, \tag{2.10}$$

$$\nu_\alpha = -\sin\theta_{12}^m\nu_{1m} + \cos\theta_{12}^m\nu_{2m}. \tag{2.11}$$

In this case we see different mixing angles θ^m and different mass eigenstates ν_m. Both (angles and eigenstates) are different to the vacuum counterparts [9]. Note that the flavour states are the same. This difference is highlighted in Figure 2.4.

---

[4]α in this case represents certain combination of the muon and tau neutrinos [9].
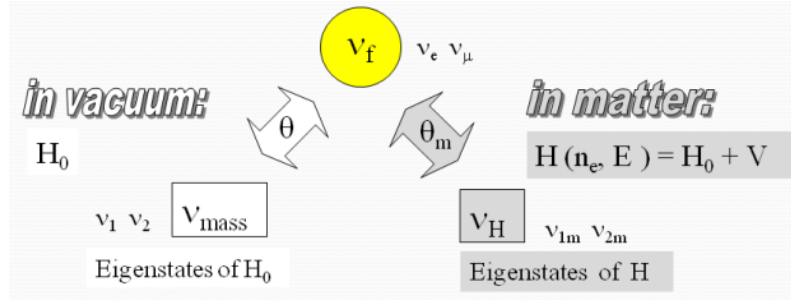
Figure 2.4: Comparison of the neutrino mixing in vacuum and in matter. Figure from [9].

The equations for states can be inverted to give the mass states - the eigenstates to Hamiltonian in matter - as

$$\nu_{1m} = \cos\theta_{12}^m \nu_e - \sin\theta_{12}^m \nu_\alpha, \tag{2.12}$$

$$\nu_{2m} = \sin\theta_{12}^m \nu_e + \cos\theta_{12}^m \nu_\alpha. \tag{2.13}$$

It can be seen that the angles uniquely fix the flavour contributions of the eigenstates. The mixing is a function of density [5] - when the density changes, the flavour proportions of the eigenstates change [9]. The mixing angle is therefore a dynamic variable

$$\theta_m = \theta_m(n(t), E),$$

where n is the density and E is the energy.

Additionally, there are new resonance conditions possible, allowing for complete flavour evolution. These are detailed in Subsection 2.10.2.

Neutrino mass implications

There are significant implications of neutrinos having mass. These implications are either:

1. The neutrino is a Dirac particle and there exits a right-handed neutrino, which does not interact via the weak force, i.e. the sterile neutrino;

2. The neutrino is a Majorana particle. The mass term couples left-handed neutrino and right-handed antineutrino, implying it must have mass. Lepton number violation is present;

3. The neutrino is Majorana and the see-saw mechanism is present. A very heavy neutrino either still exists, or existed and decayed, possibly explaining the baryon asymmetry.

---

[5]In this case, the matter density of the environment.

2.4 Neutrinoless double beta decay

The neutrinoless double beta decay ($0\nu\beta\beta$) is a rare decay forbidden in the SM due to the lepton number violation. It is only possible if neutrinos are Majorana particles. Additionally, it also makes it feasible to determine the effective neutrino mass. Due to these two quite significant implications, several neutrino experiments are looking for the neutrinoless double beta decay as the most promising way to prove the Majorana nature of neutrinos.

The standard double beta decay ($2\nu\beta\beta$) has been observed (although it is also quite rare). The reason why some isotopes decay through $2\nu\beta\beta$ instead of the common single beta decay is due to the mass of the isotope being less than the daughter isotope after the beta decay

$$m(Z, A) < m(Z + 1, A). \tag{2.14}$$

In that case the beta decay is forbidden and $2\nu\beta\beta$ is energetically allowed. This decay generally proceeds as

$$(A, Z) \rightarrow (A, Z + 2) + 2e^- + 2\bar{\nu}_e. \tag{2.15}$$

Here, the nuclear charge changes by 2 units and the atomic mass is unchanged. There are only few isotopes that decay through this process and the half-lives are generally very long ($\mathcal{O}(10^{24})$ years [14]).

The $0\nu\beta\beta$ violates the lepton number conservations by 2 as no neutrinos are present as the daughter particles

$$(A, Z) \rightarrow (A, Z + 2) + 2e^-. \tag{2.16}$$

This process is driven by light Majorana neutrino exchange as shown in Figure 2.5. This requires a neutron to decay, emitting a right-handed $\bar{\nu}_e$ that is absorbed by a second neutron as a left-handed ν_e. Clearly, this is only possible for a Majorana ν. Additionally, the chiral right-handed ν must be able to evolve a left-handed chiral component - a process only possible if the ν has a mass. Moreover, if there are no νs emitted, all energy of the decay has to be carried away by the electrons. If there is a peak present at the very edge of the predicted energy spectrum, a neutrinoless double beta decay took place. This is also shown in Figure 2.5. Due to isotopes also exhibiting $2\nu\beta\beta$, there is an intrinsic irreducible background. Excellent energy resolution is therefore required [15].
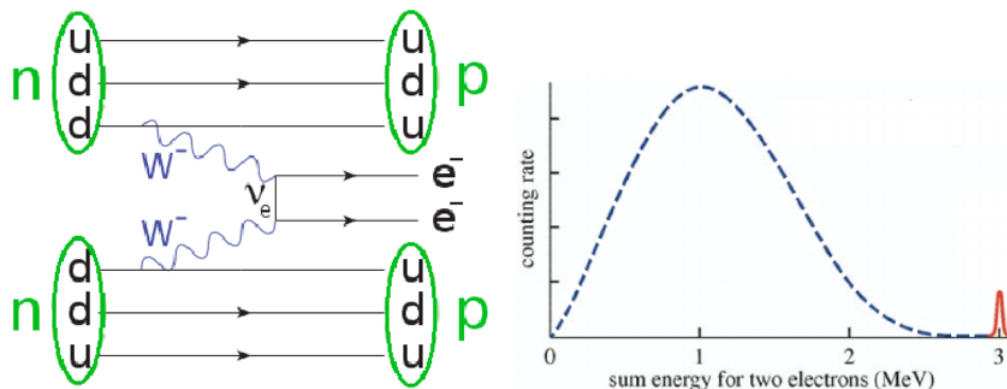
Figure 2.5: Left: the Feynman diagram of the neutrinoless double decay process. Right: the expected energy spectrum of the two daughter electrons. The red peak represents the $0\nu\beta\beta$ peak. Figure from [16].

The predicted $0\nu\beta\beta$ rate is significantly smaller than that of $2\nu\beta\beta$. This creates two requirements for any experiment searching for $0\nu\beta\beta$: excellent energy resolution to distinguish this events from $2\nu\beta\beta$, and significant amount of the isotope.

The search for neutrinoless double beta decay is the main physics goal of the SNO+ experiment. Details about the choice of isotope, loading, and sensitivity are available in Subsection 3.2.3.

2.4.1 Measuring mass using $0\nu\beta\beta$ decay

It is possible to express the half-life of $0\nu\beta\beta$ decay as

$$T_{0\nu}^{-1} = G^{0\nu} g_A^4 |M^{0\nu}|^2 \frac{\langle m_{\beta\beta} \rangle^2}{m_{ee}^2}, \tag{2.17}$$

where:

- The $G^{0\nu}$ is a known phase-space factor: it determines how many electrons have sufficient energies and momenta to participate accounting for the Coulomb effects of the nucleus. It's a function of the nuclei;

- The g_A^4 is the axial vector coupling constant (often quenched for heavy nuclei [15]);

- The $M^{0\nu}$ is a nuclear matrix element: it describes the nuclear structure effects of the parent, daughter, and intermediate nuclei - in short, the probability of the parent nucleus to emit two virtual W bosons [17]. It is the source of the biggest uncertainty in this calculation;

- The $m_{\beta\beta}$ is the effective neutrino mass.
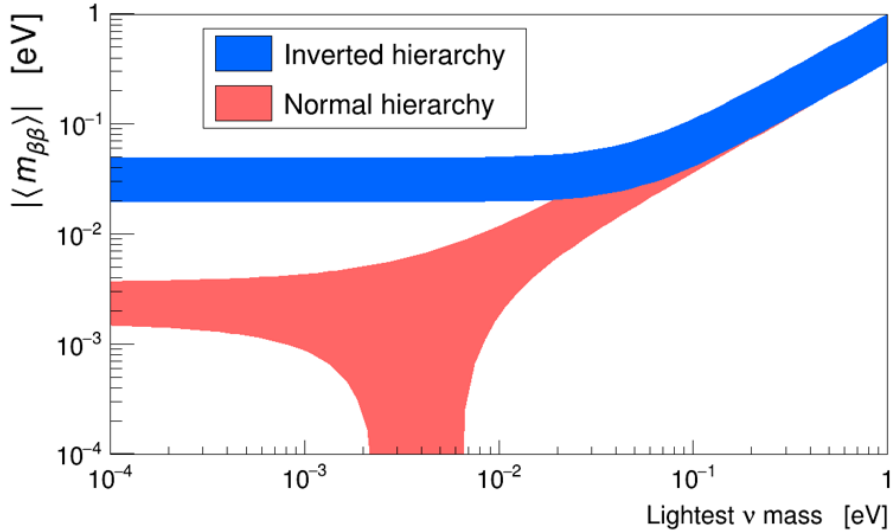
Figure 2.6: A plot of the effective mass $m_{\beta\beta}$ that can be measured using $0\nu\beta\beta$ decay as a function of the lightest neutrino mass. This plot assumes the current best limits for the mixing angles.

The effective mass in this case relates to the coherent sum of the neutrino masses

$$m_{\beta\beta} = \left| \sum_{i=1}^{3} |U_{ei}|^2 m_i e^{i\alpha_i} \right|, \tag{2.18}$$

where U corresponds to the mixing matrix elements and $e^{i\alpha_i}$ represent the complex phases (CP violating terms in the mixing matrix). This means that the measurement of the $0\nu\beta\beta$ decay provides a handle on the scale of the neutrino mass. The mass sum is the only neutrino physics observable to which this process is sensitive. This can be combined with the oscillation experiments results to obtain the mass of the lightest eigenstate [14].

2.4.2 The lobster plot

The effective mass involves the mixing angles which are known, the CP violating phases that are unconstrained, and the neutrino masses where the squared differences are known from oscillation experiments, but the absolute mass scales are currently unknown [17]. The knowledge of the mixing angles and mass squared differences can be used to put restrictions on the possible value of the mass of the lightest neutrino. This is often referred to as 'the lobster plot' and is shown in Figure 2.6.

It can be seen that the $0\nu\beta\beta$ decay can also hint towards the mass ordering. If the effective mass is found to be < 0.01 eV, only normal hierarchy would be allowed.

2.4.3 $0\nu\beta\beta$ decay experiments

As described, the sign of a $0\nu\beta\beta$ decay is a spike in the spectrum of the sum of the emitted electrons at a specific energy (Q-value of the transition). The $2\nu\beta\beta$ spectrum is instead continuous up to the Q-value.

The sensitivity to $m_{\beta\beta}$ scales with the square root of the half-life [14]

$$T_{1/2}^{0\nu} \propto a\sqrt{\frac{Mt}{B\Delta E}}, \tag{2.19}$$

where a is the abundance of the isotope, M is the source mass, t is the measurement time, B is the number of background counts, and ΔE is the energy resolution of the detector. Therefore, experiments aim to: use isotopes with high natural abundance (enriching is possible but expensive), have plenty of the isotope, run the measurement for longer time periods with low backgrounds and great energy resolution.

In general, there are two basic types of $0\nu\beta\beta$ decay experiments:

- The counting experiment: the source is typically the detector - this allows for high mass and great energy resolution but tends to measure the sum only, i.e. the energy of both electrons at once;

- The tracking experiment: the two electrons are detected independently using tracking and calorimetry which is great for background mitigation but this type of experiment is often constrained by the amount of source mass.

SNO+ will also look for the $0\nu\beta\beta$ decay in ^{130}Te. This is described in Subsection 3.2.3 and Subsection 3.2.4.

2.5 Star evolution

A star is a huge celestial body made mostly of hydrogen and helium. It is extremely hot and dense sphere of gas producing heat and light via nuclear fusion reactions. There are billions of stars in our galaxy alone and they offer great variety in size, mass, luminosity and temperature. In addition to the beautiful scene they provide for us to look at, stars are essentially responsible for life since all heavier elements are created via nucleosynthesis[6] in stars.

---

[6]The **nucleosynthesis** is the process of creating new atomic nuclei from pre-existing nucleons by the nuclear fusion reaction.

2.5.1 Star creation

Stars are born in hydrogen-based dust clouds called stellar nebulae by the gravitational collapse forming a protostar [18]. The protostar continues to accrete mass until it transforms to the pre-main-sequence stage, blowing away its envelope and becoming optically visible [19]. After contraction, which increases the density and temperate, hydrogen burning begins, and the star enters the main-sequence stage [19].

The simplest fusion reaction combines two protons and two neutrons to form an α particle (^{4}He). The electromagnetic repulsion would normally keep the protons apart, however, due to the extreme conditions the strong nuclear force can bind the protons together via quantum tunnelling [20]. There is an associated mass deficit due to the nuclear binding energy that is released by this process. This energy creates hydrostatic equilibrium, pushing against the force of gravity. This is the life of a star in a nutshell, a constant fight between gravity and nuclear burning. The range of the binding energy as a function of the atomic mass number is shown in Figure 2.7. The energy is especially high for the transition between hydrogen and helium.

2.5.2 Life of a star

Most stars will continue burning H as part of the main-sequence (MS) until its depleted. The duration of their MS depends both on the mass (available energy) and the rate of the energy consumption (luminosity). Eventually, there is no more hydrogen available in the core. It is, therefore, converted to helium, the star expands due to the increased burning in outer layers and luminosity increases rapidly. The star transforms into a giant or a supergiant, depending on the mass [18].

The core continues to shrink in size, increasing the density and temperature. At some point the temperature is high enough to allow for helium fusion, forming beryllium. Beryllium can, in turn, capture another helium and form carbon nucleus. The process can repeat, burning and forming heavier and heavier elements.

2.5.3 How it all ends

Lower mass stars do not have mass high enough to squeeze the core and develop heavier elements. These stars can reach up to the step of fusing carbon, eventually expand and cool down, forming a white dwarf star, and thin shell of matter spread over huge distances
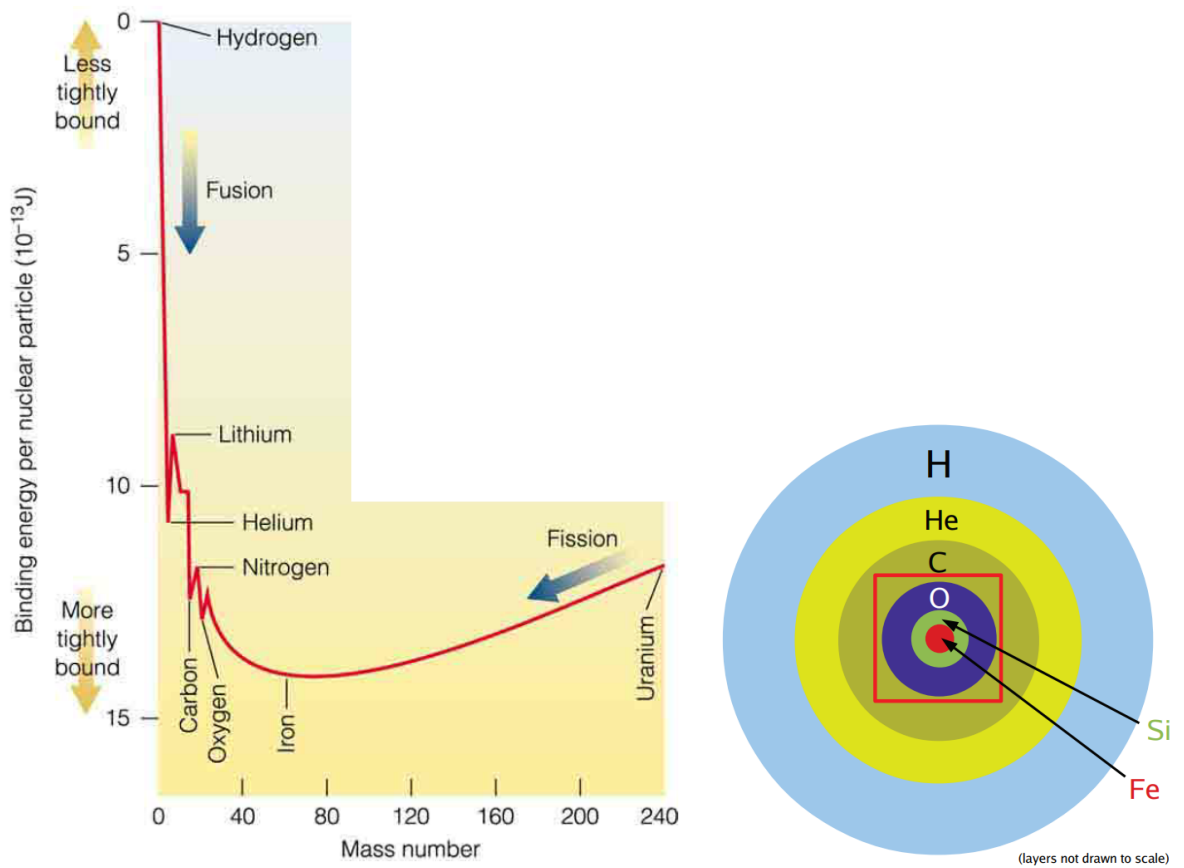
Figure 2.7: Left: The binding energy released by fusion reactions as a function of the atomic mass. This is the basis of nucleosynthesis in stars. Figure from [20]. Right: A schematic onion-shell structure of a SN progenitor star. Not to scale. Plot from [21].
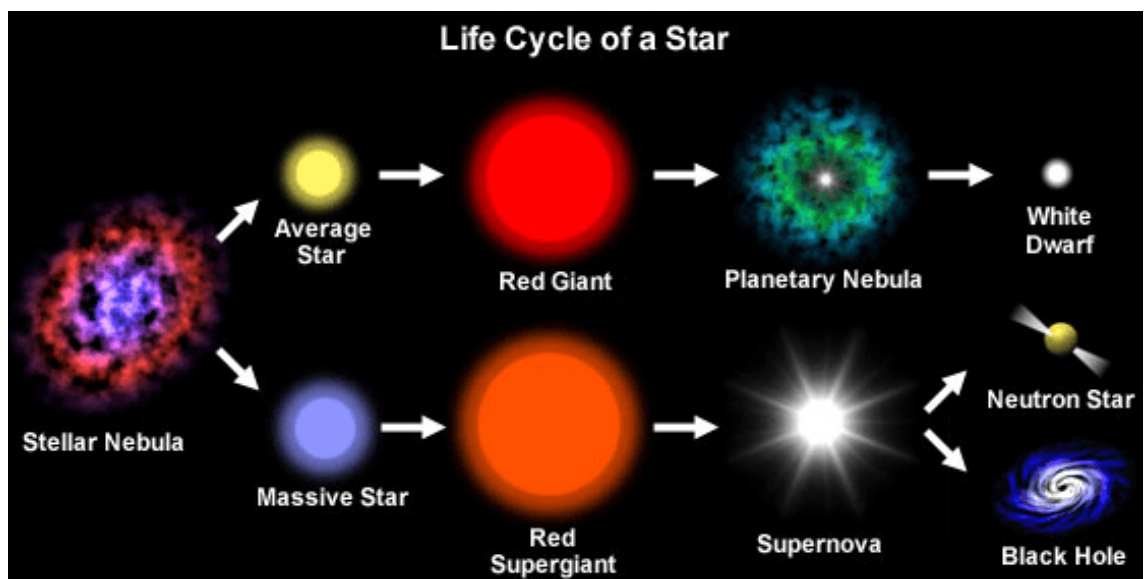
Figure 2.8: The possible life cycle options for stars. Figure from [22].

called planetary nebulas. The core does not collapse completely due to the pressure of electrons (Pauli exclusion principle).

High mass stars continue the fusion process, up to iron. The fusion of iron is endothermic, causing rapid collapse of the core. This is how SN is formed. SNe are described in more detail in the next section, Section 2.5.5.

The core that remains will either become a neutron star or a black hole, depending on the mass. The life cycle of a star is depicted in Figure 2.8.

2.5.4   Mass limits

It is currently estimated that stars below $\sim$9 $M_\odot$ do not collapse to form white dwarfs [23]. The stars with the mass between 9 and 10 $M_\odot$, where degenerate neon-oxygen cores are formed, can either collapse due to the electron capture and form a neutron star, or lose envelopes and become white dwarfs [23]. All stars above 10 $M_\odot$ end their lives due to the core collapse.

The final end point of very massive stars is strongly dependent on the metallicity - the abundance of heavier nuclei in the star. For stars above 40 $M_\odot$, low metallicity stars form black holes directly, while high metallicity stars form fallback[7] black holes [23]. At very high metallicity only neutron stars are made [23].

There are also some stars with extremely low metallicity that do not leave any remnant - these are the pair instability SNe described later. An overview of the possible remnant based on metallicity is shown in Figure 2.9.

White dwarf

A white dwarf is the remnant of a small mass star after it expelled most of its outer material. Unless the core is accreting mass, it will cool down over long period of time. It has very high density. Stars with the core mass at death below the Chandrasekhar limit[8] will always end as white dwarf stars [20].

---

[7]A **fallback** black hole can occur due to the rapid accretion - fallback - of material that pushes the neutron star above its maximum mass, usually accompanied by the ejection of the envelope, as opposed to the direct black hole formation [24].

[8]The **Chandrasekhar limit** is accepted as 1.4 times the mass of the Sun.
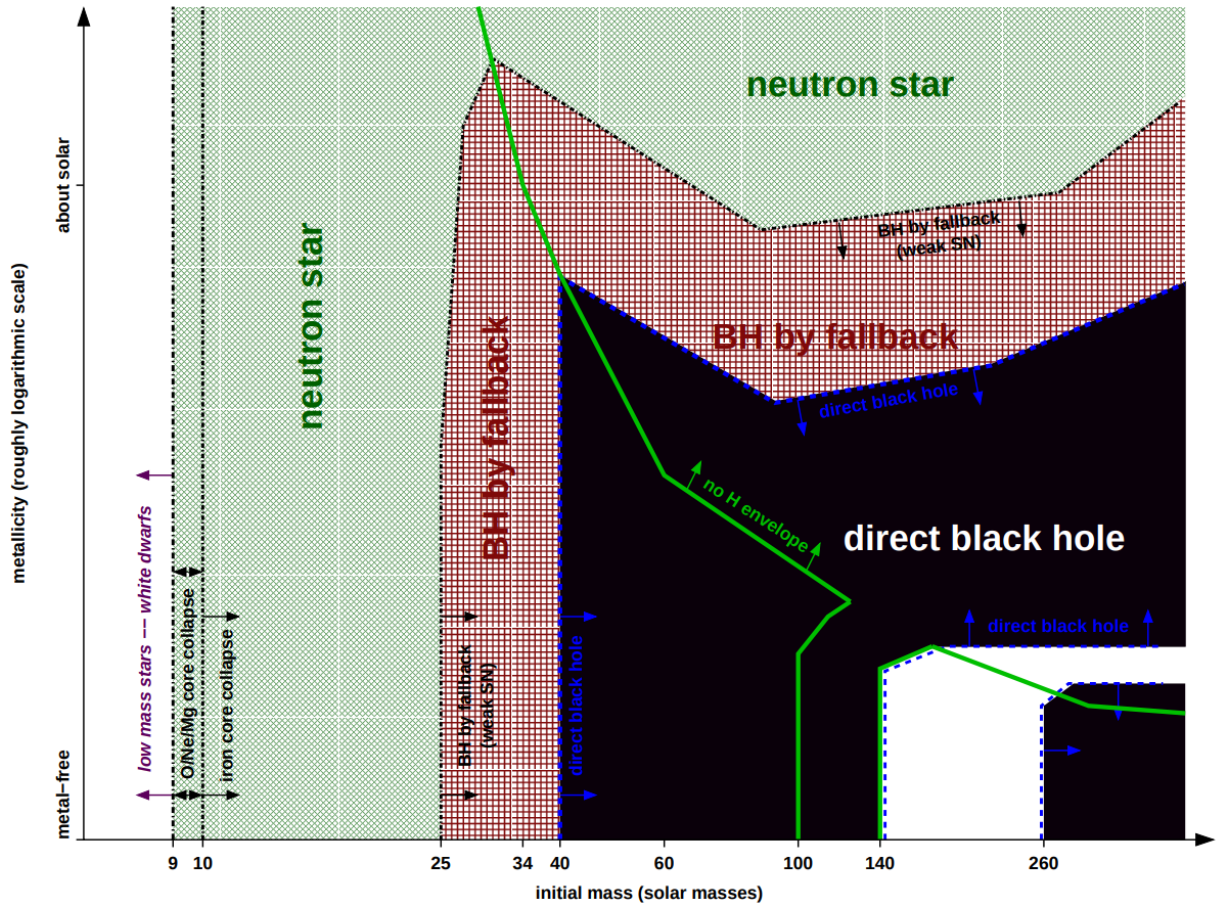
Figure 2.9: The remnants of massive single stars as a function of the initial metallicity. The green line separates regions where the star keeps the hydrogen envelope. The blue line borders the region of the direct black hole formation. The white region represents the region of the pair-instability SN leaving no remnant. Figure from [23].

Neutron star

The stars with core mass at death of approximately 1.4 to 3 $M_\odot$ form neutron stars (NS). These are the most dense observable objects. They are small and typically have low intrinsic luminosities, however, some non-quiet types of neutron stars have also been observed.

Black hole

A black hole (BH) is a body that is all contained within its Schwarzschild radius - a critical radius where the escape velocity equals the speed of light [20]. The black holes are usually observed by their impact on the neighbouring bodies.

2.5.5   Supernova explosion

A SN is extremely luminous, extremely energetic explosion of a star, associated with the end of the star's MS period. Most SNe[9] release 99% of the binding energy in the form of neutrinos over a short period of the order of 10 seconds. The remaining energy is associated with the optical light (the beautiful pictures we all think about) and the kinetic energy of the ejected matter. Neutrinos are also believed to play a crucial role in the explosion mechanism, scattering the layers of the star.

There are several SN types, and these are described below. It should be mentioned that the exact cause and process of the explosion is not fully understood yet. What is evident though is that SNe are not only the biggest explosions in the Universe and the furnaces to create heavy metals but they are also an absolute physics playground. The electromagnetic forces affect the behaviour of the plasma and are responsible for the optical signal. The driving force behind the collapse and release of energy is the gravity. The weak force controls the interaction of the neutrinos with matter and the strong force plays crucial role in the formation of the super-dense core [25].

2.6   Supernova classification

The SN classification was developed based on the absorption lines in the emitted optical spectra. Additional features in the shape of the light intensity profiles as observed on

---

[9]SNe is the abbreviation for supernovae.
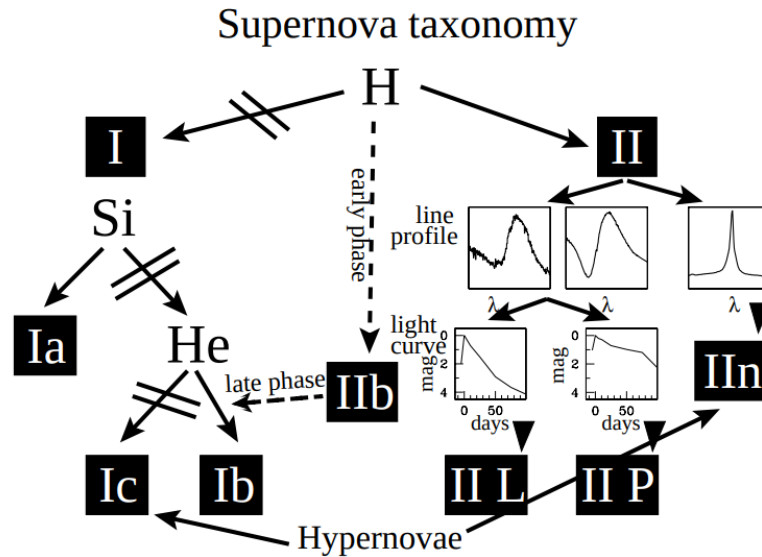
Figure 2.10: The SN classification based on the spectral features of the signal. Figure from [26].

the Earth are used for further subdivision of the types. This classification is shown in Figure 2.10.

The basic division is based on the presence of the H lines in the observed spectrum. Type I SNe do not show any H presence while SNe Type II do. The presence of the lines corresponds to the burning process and the composition of the progenitor. Type I is further subdivided into Ia, Ib, and Ic, based on the presence of Si and He lines, as shown in the classification figure.

Type II SNe are divided based on the line profiles and the shape of the light curves[10]. The end types include: Type IIn - represented by the narrow peak in the line profile, Type IIL - showing linear decrease in the light curve profile, and Type IIP - where light curve reaches a plateau. Again, this is shown in Figure 2.10. More details can be found in [26].

This type of classification, however, does not describe the underlying cause of the SN. This is more relevant for neutrino physics as the cause determines whether there is an observable neutrino signal. Therefore, the division into thermal runaway and gravitational core-collapse SNe is more relevant and will be used here. Thermal runaway SNe arise from the explosive thermonuclear burning - called the runaway fusion - ignited on the degenerate white dwarfs in a binary system [27]. These SNe convert most of the energy into the synthesis of heavy elements and into the kinetic energy of the ejected matter [28]. The neutrino signature is therefore minimal (if any). These are not considered further

---

[10]The **light curve** is the light intensity profile over time, as observed without the influence of the atmosphere.

throughout this thesis. The SNe caused by the core-collapse typically convert most of the energy into neutrinos. These are described below.

2.6.1 Core-collapse origin

There are several mechanisms that can conclude in the core collapse, each of them potentially resulting in different explosion and remnant. The type of the collapse is mostly defined by the mass of the progenitor at birth and its metallicity, which also directly affect the mass loss rate and the overall life evolution of given star.

The main focus is given to stars undergoing the iron core-collapse (mass of 10-40 $M_\odot$ in Figure 2.9). Quite similar in terms of the neutrino emission is also the region of stars forming O-Ne-Mg core (mass of 9-10 $M_\odot$ in the same figure). These are both Type II SNe, estimated to contribute about 90% of all CC SNe [23] and are therefore understood the best.
These are briefly described below. The process of neutrino emission for iron CC specifically is then detailed in Section 2.7.

2.6.2 Iron core-collapse SN

In iron core-collapse (Fe CC) SN, as the name suggest, the Fe core collapses after it exceeds the Chandrasekhar mass limit [29]

$$M_{\mathrm{Ch}} \approx 1.457 \left(\frac{2}{\mu_e} \right)^2 M_\odot, \tag{2.20}$$

where μ_e corresponds to the mean molecular weight per electron, defined as $\mu_e = A/Z$, with A and Z being the atomic mass and atomic number, respectively [28]. At this point, the electron degeneracy pressure is no longer sufficient to counter the gravitational collapse. An implosion proceeds within seconds, the outer layers fall inwards and the explosion is imminent.

This collapse results in Type II or Type Ib/c SN, leaving a NS or BH remnant. Type II SNe caused by the iron core progenitor represent approximately 60% of all CC SNe [28]. These are often referred to as the standard CC SN and are therefore the ones examined in this thesis. The details of the process are discussed in Section 2.7.

2.6.3 Electron-Capture SN

The progenitors of the electron-capture (EC) SN typically develop oxygen-neon-magnesium (O-Ne-Mg) cores through C burning but reach electron degeneracy before the Ne burning can be ignited [30]. The increasing electron Fermi energy enables electron capture due to the low reaction thresholds of Ne and Mg [30]. This inevitably triggers the gravitational collapse.

It is estimated that stars of 9 - 9.25 $M_\odot$ will eventually end via EC SN, however, this is strongly metallicity dependent. Some estimates report between 20-30% of all SNe could be EC SNe [30].

The explosions of the EC SNe are relatively faint, ejecting little C, O and Ni. There are several remnants associated with this type of explosion.

2.6.4 Pair-Instability SN

The cause of the pair-instability (PI) SN is the formation of e^+e^- pairs from high-energy photons. These convert the thermal energy to the rest-mass energy, reducing the adiabatic index[11] and causing the gravitational instability [30]. The stars between $\sim$100 and $\sim$140 $M_\odot$ and above $\sim$260 $M_\odot$ typically collapse to form a BH. However, stars with intermediate masses can develop violent explosion due to the ignition of the thermonuclear fuel, which is still available. This causes complete disruption of the star, with the explosion energies reaching $> 10^{53}$ erg[12] [30]. Due to these high energies, this type of SN was previously labelled hypernova.

In the case of BH formation, depending on the rotation and the angular momentum, huge amounts of energy are released in neutrinos [30].

2.6.5 Photo-disintegration SN

The very heaviest progenitors (above 260 $M_\odot$) have cores hot enough to generate gamma rays that cause photo-disintegration [23]. In photo-disintegration the iron in the core breaks down due to interaction with the high energy gamma rays as

$$^{56}\text{Fe} + \gamma \rightarrow 13 \ ^4\text{He} + 4n, \tag{2.21}$$

$$^4\text{He} + \gamma \rightarrow 2 \ ^1\text{H} + 2n. \tag{2.22}$$

---

[11]The **adiabatic index**, also known as the heat capacity ratio, is the ratio of the heat capacity at constant pressure to heat capacity at constant volume.

[12]**Erg** is a unit of energy equal to 10^{-7} joules.

This is sped up by the electron capture on protons, requiring even more energy, speeding up the collapse. Because this process is endothermic, no explosion is present and a massive BH is formed directly.

2.7 Neutrino emission

The core-collapse, or more specifically the iron core-collapse SN, is the most typical SN and will be discussed in greater detail here.

The core of a star consists of the final products of its nuclear burning history in the form of the concentric shells, containing heavier and heavier ashes of previous stages [31]. This is often referred to as the onion structure, and is shown on the right side of Figure 2.7. Just before the collapse, the core is similar to a hot white dwarf with typical diameter of 3000 km, central temperature of 10^{10} K, and central density of 10^9 g cm^{-3} [31].

2.7.1 Onset of collapse

The instability of the core is initiated by high energy photons producing α particles and free nucleons. The binding energy of the heavier nuclei is endothermic, partially disintegrating the iron group. This causes a reduction of the effective adiabatic index, rising the Fermi energy[13] of the degenerate electrons, and finally allowing the electrons to capture on nuclei. Electron neutrinos are produced and these escape, causing the loss of lepton number, softening the pressure increase with density, and speeding up the collapse [31]. This can be seen in the top left plot of Figure 2.11.

2.7.2 Neutrino trapping

At very high density ($\sim 10^{12}$ g cm^{-3}), the neutrino diffusion timescale is longer than the timescale of the freefall of the gas and the neutrinos cannot freely escape anymore. This is referred to as the neutrino trapping, and it is a consequence of low energy ν_e scattering on the heavy nuclei [32]. This, however, cannot stop the collapse. The ν_e produced by electron capture are being swept inwards. It finally decelerates when the nuclear matter density is reached and repulsive contributions to the nucleon interaction potential increase.

---

[13]The **Fermi energy** is the energy difference between the lowest and highest occupied state in a quantum system.
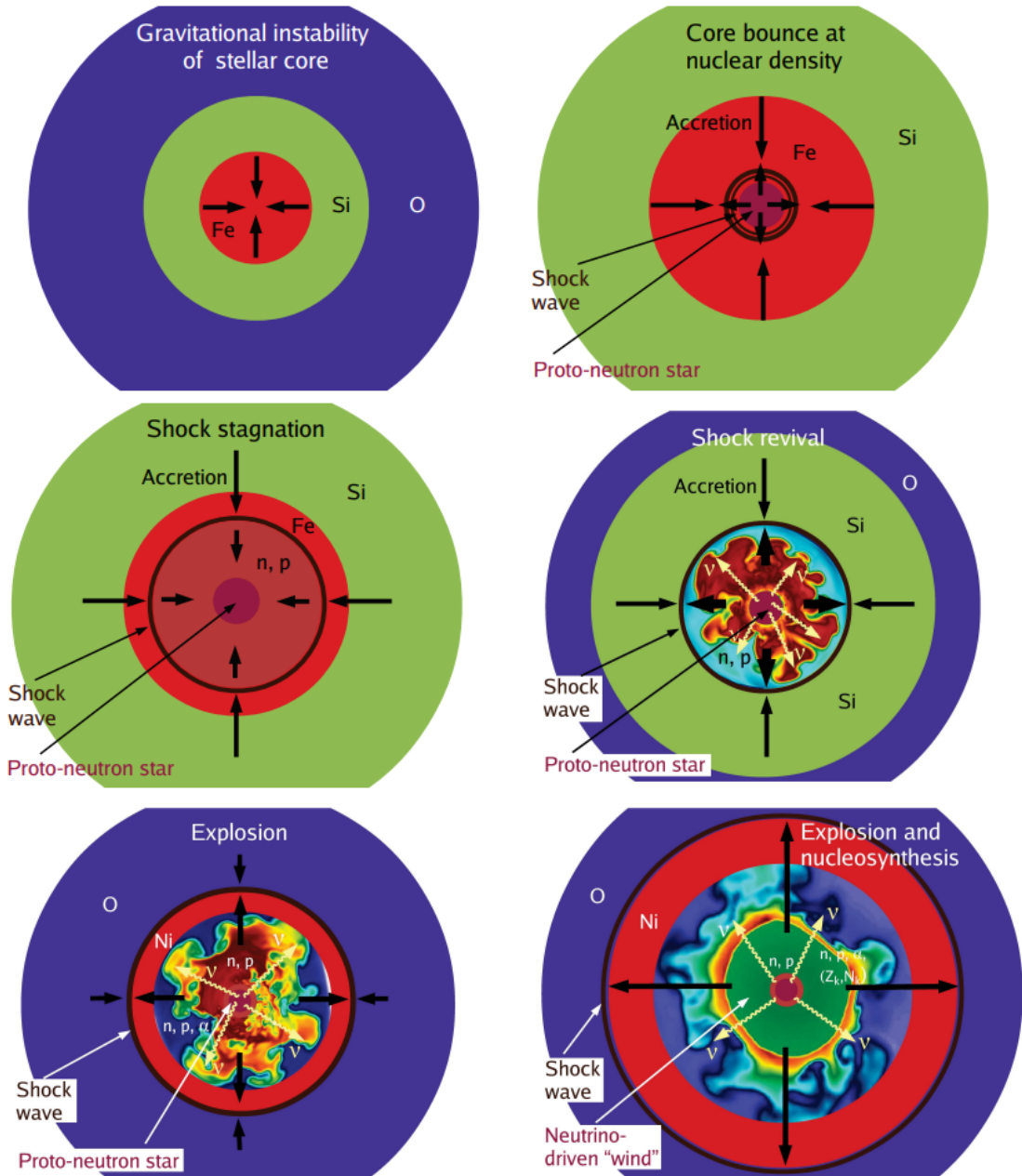
Figure 2.11: A schematic representation of the evolution stages of the core-collapse SN explosion. Top: the onset of the stellar core-collapse (left), the core bounce and shock formation (right). Middle: the shock stagnation (left) and the shock revival (right). Bottom: the explosion and nucleosynthesis. Plot from [21].

2.7.3 Core bounce and shock formation

At this point, the collapsing inner core decelerates and rebounds. This is due to the heavy nuclei dissolving, causing a sharp rise in the incompressibility, and the nuclear force between the nucleons providing resistance [32]. This creates a shock front (top right of Figure 2.11). This shock travels outward against the still ongoing collapse of the iron-core [32].

2.7.4 Burst at shock breakout

Behind the shock front, the electron capture process is creating huge amount of electron neutrinos at this point. These are still trapped until the shock reaches lower densities. At that exact moment, the breakout burst[14] is emitted - a luminous flash of ν_e.
The loss of ν_e causes a drop in the electron lepton number and an abundance of positrons [32]. This, combined with the heating of the forming proto-neutron star (PNS) make pair-production processes (such as $e^- e^+$) efficient, forming heavier neutrinos and antineutrinos. The ν_e production also still proceeds via $e+$ captures.

2.7.5 Shock stagnation and revival

Due to the exceptional loss of energy (both kinetic and thermal) the shock decelerates. Meanwhile, the pressure, temperature, and density behind the shock increase [32]. This causes Fe dissociation, requiring additional energy. A thick layer of dense matter accumulates and the mass accretion rate slows down. The PNS shrinks due to the energy loss (to about 150 km radius, well inside the iron core [32]), the shock is halted, and a stagnant accretion shock is formed (middle left plot, Figure 2.11). This prompt bounce-shock fails to initiate the SN explosion on its own.

The shock needs to be revived to generate the explosion. The exact mechanism is still being researched. One of the possible causes for the revival is the *delayed neutrino-driven explosion mechanism*[15]. The basis of the process is the exchange of energy (heating) of the matter with neutrinos that are produced in the hot interior of the nascent NS as

$$\nu_e + n \rightarrow p + e^-, \tag{2.23}$$

$$\bar{\nu}_e + p \rightarrow n + e^+. \tag{2.24}$$

---

[14]Often referred to as: ν_e burst, neutrino burst, deleptonisation burst, neutronisation burst and more.

[15]This mechanism appears as the most promising explanation for CC SNe and was successfully proven by numerical simulations [32].

If there is enough deposited energy by the heating process (which has much slower fall off rate than cooling [31]) the SN explosion can be revived. This is dependent on the luminosity of the neutrinos, which is a function of the accretion rate of the shock. It is predicted that the explosion will happen if the neutrino luminosity achieves the critical value [31]

$$L_{\nu,c}(\dot{M}) \propto \beta^{-2/5} \dot{M}^{2/5} M_{ns}^{4/5}, \qquad (2.25)$$

where $L_{\nu,c}(\dot{M})$ is the critical luminosity, β is the parameter defined by the ratio of post-shock to pre-shock density, $\dot{M}$ is the mass accretion rate of the shock, and M_{ns} is the mass accretion rate of the NS. This is shown on the middle right plot of the Figure 2.11. The accretion on the NS radiates ν_e and $\bar{\nu}_e$, which carry away the released binding energy.

If the explosion is successful a blast wave takes off. ^{56}Ni and other radioactive isotopes are being created in the shock heated core due to burning - as can be seen in the bottom left of Figure 2.11. In addition to that, α particles and Fe nuclei are being recombined, and neutrino wind is being produced. The neutrino wind is the baryonic outflow, shed off the surface of the NS by the neutrino heating [21]. It fills the surrounding of the remnant. At this time, the accretion has ended (bottom right of Figure 2.11).

2.7.6 PNS cooling

When the accretion ends, the PNS enters the cooling phase, emitting (anti)neutrinos of all flavours sustained by the remaining gravitational binding energy. This is comparably the longest period of the process, on the time scale of neutrino diffusion [21]. It is estimated that the neutrinos formed around the newly formed NS can reach > 100 MeV, but due to several absorption, re-emissions, and scatters, leave the star with the final mean energies of 10-20 MeV [32].

Note on energy

The total energy of the explosion is built up on a timescale of several 100 ms instead of being determined at the instant of the explosion [21]. There are several contributing factors, such as: neutrino heating, convection, recombination of free nucleons to form α particles, photo-disintegration, and a little contribution comes from the nuclear burning in outer layers [31]. If the energy is not sufficient to unbind the overlying layers and provide enough kinetic energy for the explosion, the shock may partially or fully fall back onto the remnant. This means, the explosion can be faint or completely unsuccessful in which case

it won't create any effects that could be observed at long distance.

The impact of neutrinos

Nevertheless, it is obvious that neutrinos are heavily involved in the process of SN explosion. Even if the neutrino heating was not the main mechanism behind the shock revival, neutrinos would still contribute massively. The neutrinos generated in the extreme environment of the proto-neutron star[16] experience constants re-absorption, re-emission and scattering, participating in billions of interactions on average over several seconds, before reaching lower density layers [32]. In the end, neutrinos of all types and flavours carry away most of the energy and drive the evolution, from the hot star until the cold end. The whole process, including the neutrino contribution, is presented one more time in the Figure 2.12.

2.8 Neutrino signal

The neutrino signal is linked to the neutrino emission process described above. This section describes the phases of neutrino emission.

2.8.1 Signal description

The neutrino signal from a SN explosion can be divided into three main phases: the ν_e burst (the burst phase), the accretion (the accretion phase), and PNS cooling (the cooling phase). Each of these has significant features. In addition to that, there is an increase in neutrino emission for a longer period before the collapse. These four epoch are described below.

The pre-supernova epoch

All stars emit neutrinos, with the rate and the amount being affected by the mass, the evolutionary state, and the current burning fuel of the star. At the point of carbon burning, the energy carried away by neutrinos is higher than that being carried away by photons [33]. This is slowly increasing and is dependent on the progenitor, with more neutrinos being emitted by Fe-core stars [33].
The dominant thermal processes emit (anti)neutrinos of approximately 1 MeV, while the

---

[16]The **proto-neutron star** is the hot, mass-accreting, proton- and lepton-rich predecessor object of the neutron star [32].
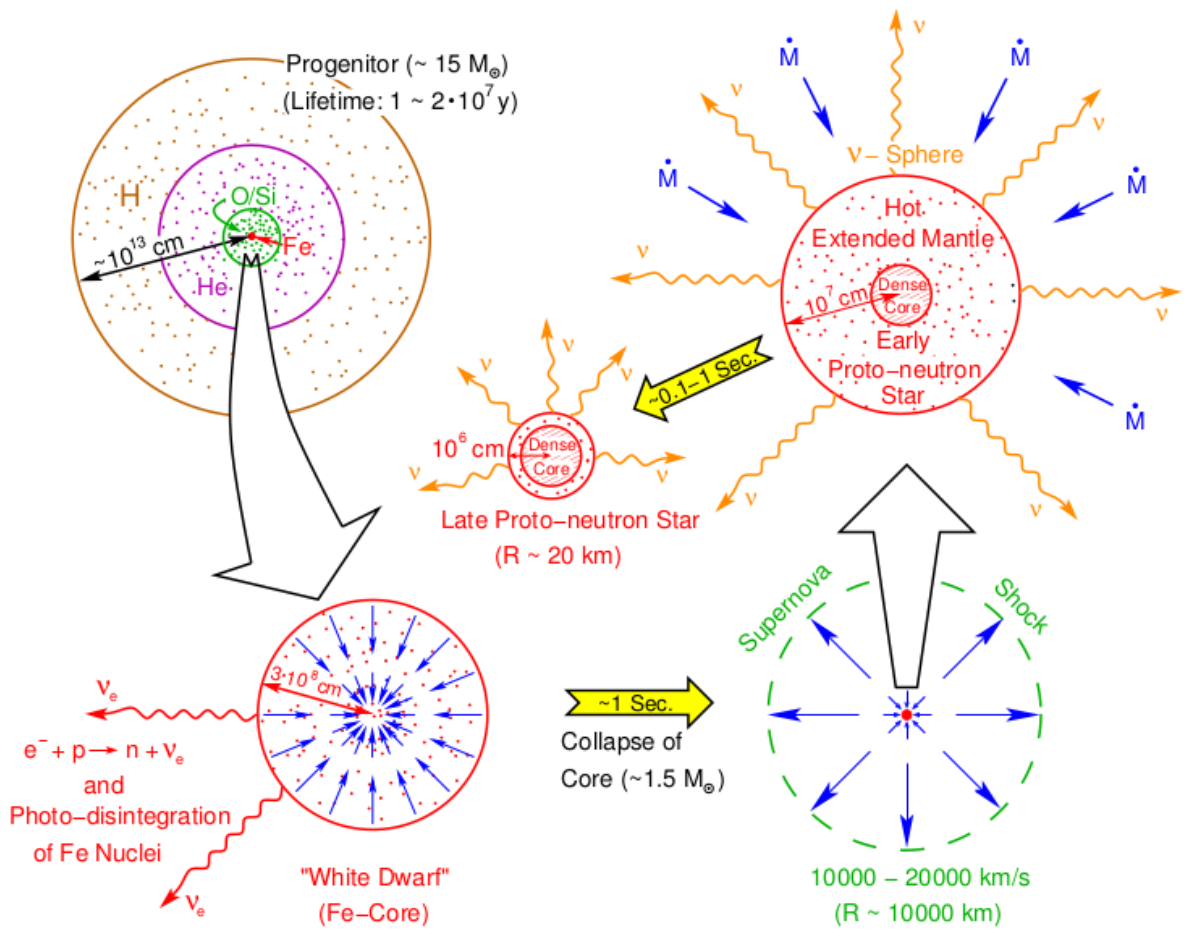
Figure 2.12: The evolution of a massive star from the onset of the collapse to the formation of the neutron star, with the focus on the neutrino contribution. The process starts at top left, with the onion-like structure formed around the massive star. The iron core itself is zoomed at the bottom left. Similarly to the white dwarf, the core is maintained by the fermion pressure of electrons. Once the temperature is high enough to allow for the photo-disintegration, the contraction accelerates via the electron capture, releasing ν_e, which are free to escape. Immediately after that the collapse is stopped, PNS begins to form and the nuclear density is reached. The bottom right represents the strong shock wave that forms afterwards, travelling outward, causing the SN explosion. The NS that forms is shown in the top right. It is extended early on, accreting more matter as it contracts. The whole process, including the collapse, heating, explosion, and cooling, are all driven by the emission of (anti)neutrinos of all flavours over a time period of tens of seconds. Plot from [32].

subordinate weak processes create energies up to ∼10 MeV. Depending on the energy threshold, the detectors on the Earth could possibly detect these pre-supernova neutrinos.

Burst phase

As described, as the shock becomes transparent to neutrinos when it reaches lower density layers of the outer core a luminous flash of neutronisation neutrinos is released. This is where the neutrino luminosity of the SN explosion is often the highest (in most cases by several factors). The burst usually peaks few milliseconds after the core bounce [32].

The ν_e emissions is continuously increasing well before the bounce because of the electron capture becoming possible in bigger and bigger fractions of the core due to the compression. There is a dip in the ν_e luminosity shortly after the core bounce as a consequence of the strong compression and the redshift effect of the region where ν_e are generated.

Regarding the heavy-lepton neutrinos, these are being produced shortly thereafter due to the high pair processes that are possible in the heated matter. This is visible by the increase in their luminosity. The $\bar{\nu}_e$ follow shortly. It should be noted that the presence of high ν_e peak and the following increase in the luminosities of other flavours is a generic behaviour that is not strongly dependent on the progenitor star [34].

The peak of the burst (in this example) reaches 10^{53} erg s^{-1} in luminosity and releases 10^{51} erg of energy within 20 ms [32]. The peak in luminosity also coincides with the peak of the mean energy of ν_e . The heavy-lepton neutrinos reach higher mean energies, however, at considerably lower luminosities. This can be seen in the left portion of Figure 2.13.

Accretion phase

The accretion phase is marked by the decline of the ν_e luminosity, reaching a plateau. The ν_e and $\bar{\nu}_e$ are at similar level of luminosity, being generated by the charge-current interactions. The ν_e luminosity is slightly higher due to the still ongoing deleptonisation. The luminosities of the higher-lepton neutrinos are visibly lower since they require even more extreme conditions, thus only being produced from the dense regions inside the core.

In this phase, both the luminosity and the energy distributions are very different for various progenitor stars. This is due to the dependence of the neutrino quantities on the mass accretion rate and the mass of the progenitor star, both of which are a function of the compactness of the core [32]. Additionally, there are several unique processes that can

affect the hydrodynamical stability, causing non-radial flow in the core. This can manifest as quasi-periodic fluctuations of luminosities and mean energies.

It can be seen in the middle portion of Figure 2.13 that all luminosities show slow decrease over the accretion phase. The luminosities for the ν_x[17] are generally very similar. The luminosities of neutrino (anti)neutrinos are enhanced by the accretion and are thus slightly higher [32].
Regarding mean energies, there is an overall increase during this phase for all neutrino flavours. This increase is steeper for ν_e and $\bar{\nu}_e$, due to the local temperature maximum caused by the compressional heating of the accretion layer [32]. Generally, ν_e show the lowest mean energy in this phase. The mean energy of ν_x and $\bar{\nu}_x$ are high throughout, with $\bar{\nu}_e$ reaching the highest mean energy for a short period.

Cooling phase

The PNS continues to emit neutrinos for several seconds after the explosion. During the cooling phase, the luminosities of all neutrino species are almost identical (within ten percent [32]) and all display continuous decline. The cooling also affects the mean energies, which turnover at around one second and begin to decrease. This is available in the right portion of Figure 2.13.

Due to the weakly interacting properties of neutrinos, they are extremely efficient in carrying away the energy of the exploding star. It is estimated that 99% of the total energy is emitted by neutrinos, while only 1% is used by the shock wave, and only 0.01% is converted to the electromagnetic radiation [28]. The relative length of each phase, along with the dominant neutrino flavour per phase, is shown in Table 2.1.

A summary of interactions producing neutrinos during SN is available in Table 2.2. The following sections will focus on the detection of the signal instead.

2.8.2 Features of the signal

It was previously mentioned that there are unique processes affecting the neutrino spectra specifically during the accretion phase. These can also contribute to the explosion

---

[17]ν_x represents neutrino flavours other than electron, i.e. ν_μ and ν_τ. The same grouping is also used for the antiparticles, $\bar{\nu}_x$.
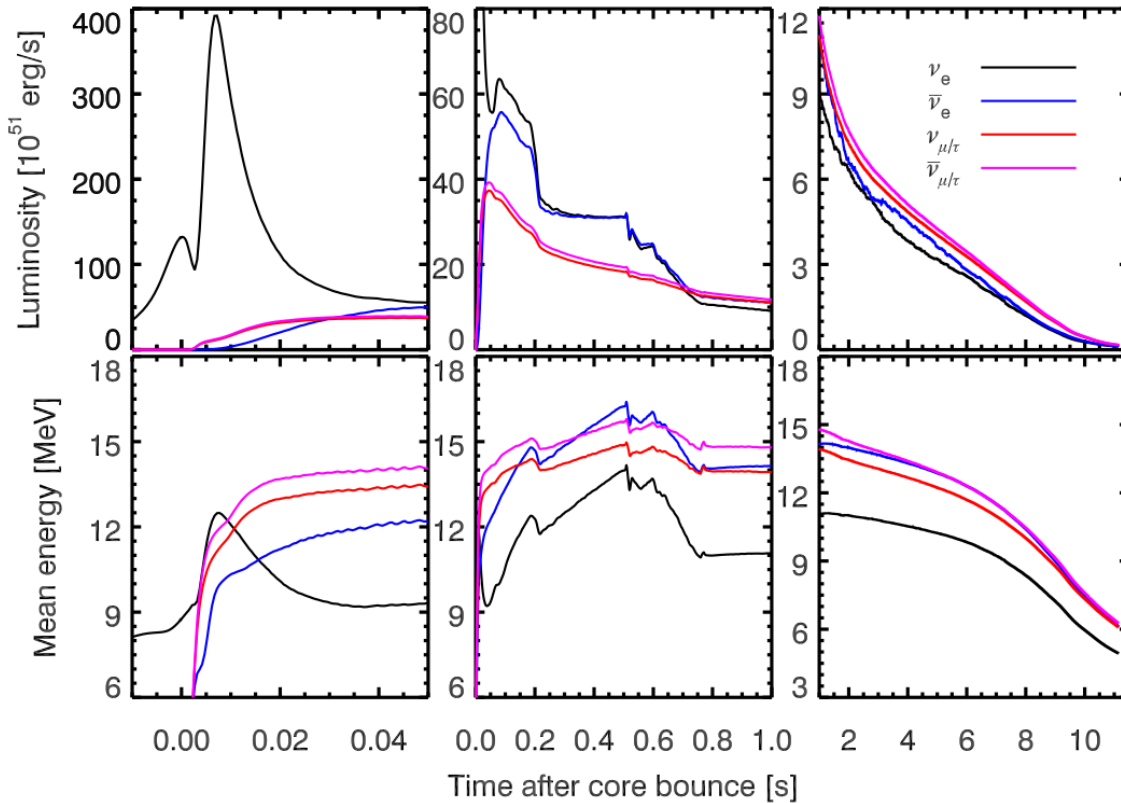
Figure 2.13: The luminosity and mean energy distribution of the neutrino signal from a SN explosion simulation. The left portion represents the burst phase, middle part is the accretion phase, and the right section corresponds to the cooling phase. In this case of 27 $M_\odot$ progenitor, the explosion sets in at 0.5 s after the core bounce, the accretion ends at approximately 0.75 s, after which the cooling phase proceeds. The weak-magnetism corrections of neutrino-nucleon scattering are included (as opposed to later models from the Garching group). Plot from [32].

Phase	Duration	Dominant neutrino
Pre-supernova	$\sim$days	ν_e and $\bar{\nu}_e$
Collapse	$\lesssim$50 ms	initially largely ν_e, later all
Accretion	$\sim$100 ms for O-Ne-Mg core	$\nu_x < \bar{\nu}_e < \nu_e$
	$\sim$200 - 700 ms for Fe core	$\nu_x < \bar{\nu}_e < \nu_e$
Cooling	$\sim$10 s	$\nu_x \sim \bar{\nu}_e \sim \nu_e$

Table 2.1: Table summarising the phases of the SN burst with focus on the length and the dominant neutrino type. Data from [35].

mechanism. The most notable are [35]:

- **The convection**: The basis of convection is to transport heat outwards. The current understanding is that there are two regions of convection: inside the PNS and in the gain region below the shock. The inner convection boost the luminosity of neutrinos but reduces the mean energies. The outer convection brings heat close to the stalled shock and changes accretion rate;

- **The standing accretion shock instability (SASI)**: This phenomenon is caused by the small perturbations of a spherical accretion shock. This happens when the forward propagating shock wave is stalled. The consequence of this is a periodic 'slosh' movement (back and forth) of the accretion shock. In addition to helping the explosion, SASI also affects the neutrino luminosity, where clear periodic fluctuations can be seen;

- **The turbulence**: The effect of turbulence is to stiffen the equation of state[18] (EOS) of the matter behind the shock. This results in the material exhibiting greater pressure at a given density;

- **The lepton-emission self-sustained asymmetry (LESA)**: LESA results in a significant, quasi-stable dipole moment that affects electron (anti)neutrinos only. It is a consequence of a large scale asymmetry of the PNS system during the accretion phase. There is no associated asphericity of the heavy-lepton flavours or the luminosity overall.

It should be mentioned that these effects can be seen in simulations.

2.8.3   Signal detection

There are several ways to detect the neutrinos emitted by the SN explosion. The specific techniques depend on the target medium. However, the general approach is the same - to collect as many events as possible, for all available flavours, preferably with event-by-event time resolution and great energy resolution [36]. Additionally, lot of the signal is carried by heavy-lepton flavours which requires sensitivity to neutral current (NC). The event rate scales strongly with distance as $1/R^2$, where R is the distance to SN. The expected energy is relatively high ($\sim$10 MeV) for the burst and accretion phase, making it possible

---

[18]The **equation of state** is an equation relating variables describing the state of the system under the given set of physical conditions.

to detect. The detector backgrounds may affect the later stages of the burst, where both luminosity and energy continue to decrease.

One of the backgrounds is the energetic cosmic-ray muons that can cause spallation events[19], produce nuclear fragments, and create fake bursts of similar length to the SN burst. This can be distinguished by identifying the parent muon and requiring spatial uniformity [36]. The underground experiments naturally suppress this source of the backgrounds. Other backgrounds are mostly other sources of neutrinos in this expected energy range, such as reactor, solar, and atmospheric neutrinos. However, given the scale of the SN burst, both energetic, time and the shape of the distribution, these should be easily distinguishable. The detector types and their detection technique are briefly described below.

Scintillator detector and water Cherenkov detector

The SN interaction channels available to scintillator and water Cherenkov detectors are explained in detail in Subsection 6.2 as these are the channels that SNO+ is sensitive to.

Liquid argon time projection chamber

The liquid argon detectors detect electron (anti)neutrinos via the charged current interactions as

$$\nu_e + {}^{40}\mathrm{Ar} \rightarrow e^- + {}^{40}\mathrm{K}^*, \tag{2.26}$$

$$\bar{\nu}_e + {}^{40}\mathrm{Ar} \rightarrow e^- + {}^{40}\mathrm{Cl}^*. \tag{2.27}$$

Both of these can be tagged via the de-excitation γs. The elastic scattering of neutrinos on electrons is also possible. The large argon detectors are suitable for SN detection given the possible particle identification by the rate of the energy loss, fast timing and good energy resolution, unaffected by the Cherenkov threshold [36].

Heavy nuclei detector

The detectors employing heavy nuclei (iron, lead) may yield high rates of interactions with SN neutrinos. These can be observed via leptons and ejected nucleons. The ejection multiplicity is a function of the neutrino energy, adding to the knowledge of the burst. In

---

[19]Spallation events are nuclear reactions in which a heavy nucleus emits a large number of nucleons as a result of being hit by a high-energy particle.

lead the relevant interactions are

$$\nu_e + {}^{208}\text{Pb} \rightarrow e^- + {}^{208}\text{Bi}^*, \tag{2.28}$$

$$\nu_x + {}^{208}\text{Pb} \rightarrow \nu_x + {}^{208}\text{Pb}^*. \tag{2.29}$$

In both cases the excited nuclei de-excite via nucleon emission.

Low threshold detector

Nuclear recoils from the coherent elastic neutrino-nucleus scattering can be detected by very clean detectors with low radioactive backgrounds. The rejection of electronic recoil is mandatory. The noble liquid detectors (with xenon, neon, or argon) in particular - having very small recoil energy threshold - are promising candidates. These are sensitive to all NC coherent interactions [36].

2.8.4 Signal observables

In addition to observing the neutrino signal, there are several other observables that can point to completely new physics. For most of these, the SN signal is the only way to learn anything about it.

These include: measuring the energy of explosion, observing the black hole formation, observing the progenitor structure, observing LESA, determining whether SASI occurred and its frequency, and more. For more complete list, with details on each observable, please refer to [35]. The estimation of the energy of the explosion is detailed in 6.8.8 and signatures of the black hole formation are discussed in 6.9.

2.8.5 SN1987A

On the 24$^{\text{th}}$ February 1987 a very bright Type II SN was discovered in the Large Magellanic Cloud (LMC) [1]. LMC is a satellite galaxy of the Milky Way, approximately 50 kpc from the Sun. This SN was named SN1987A and was the first SN visible to naked eye since 1604. The progenitor was found to be a blue supergiant Sanduleak [1]. The SN1987A was studied over radio, infrared, optical, ultraviolet, and x-rays, but no compact remnant has been identified [1].

Four neutrino experiments were actively taking data on that day: Kamiokande II [37], Irvine-Michigan-Brookhaven (IMB [38]), Baksan [39], and Mont Blanc liquid scintillator detector (LSD [40]) [1]. While Kamiokande II and IMB are water Cherenkov detectors,

Baksan and LSD use liquid scintillator. All of these experiments have recorded neutrino events above their corresponding background rates several hours before the optical signal. 11, 8, and 5 neutrino events were detected by Kamiokande II, IMB, and Baksan, respectively. There is one additional event detected by Kamiokande II, but it is attributed to background. The signal detected by LSD was later dismissed due to energetic requirements and strange time offset [41].

The detected neutrino events from SN1987A by the aforementioned detectors are shown in Figure 2.14. The Kamiokande II had a fiducial volume of 2.14 ktonne and the energies of the events ranged from 6.3 to 35.4 MeV. The IMB experiment had a fiducial volume of 3.3 ktonne and increased energy threshold levels due to issues with power [43]. It has reported 8 events, however, it is estimated that the total number of events was 22, but some events were not properly recorded due to significant dead time of the electronics [44]. The much smaller Baksan experiment with the fiducial volume of 0.2 ktonne had much higher backgrounds due to the detection medium and only provided the events details after the time range was provided by other experiments.

These neutrino events were found to be compatible with the general features of the standard core-collapse SN scenario [7]. Additionally, a new limit was set on neutrino masses by the spectrum and the spread of these detected neutrinos [45].

2.9 Supernovae distribution

2.9.1 Predicted frequency

Because there is much to gain by detecting a SN signal, it is important to understand that these events are relatively rare in our galaxy. There are several studies available that estimate the frequency of core-collapse SN in the Milky Way by different approaches.
The historical rate of iron CC SNe in our galaxy is estimated to be $3.2^{+7.3}_{-2.6}$ per century [35] based on the model for distance, magnitude probability distribution, and extinction. Another approach using scaling from the rates in other galaxies estimates 2.8±0.6 per century, while method based on the massive stellar birthrate gives 1-2 per century [35]. Finally, radioactive aluminium emission measurements yield 1.9 ± 1.1, and 2.8 ± 0.1 per century is estimated by the study based on the birthrate of pulsars[20].

---

[20]A **pulsar** is a highly magnetized rotating compact star emitting beams of electromagnetic radiation out of its magnetic poles.
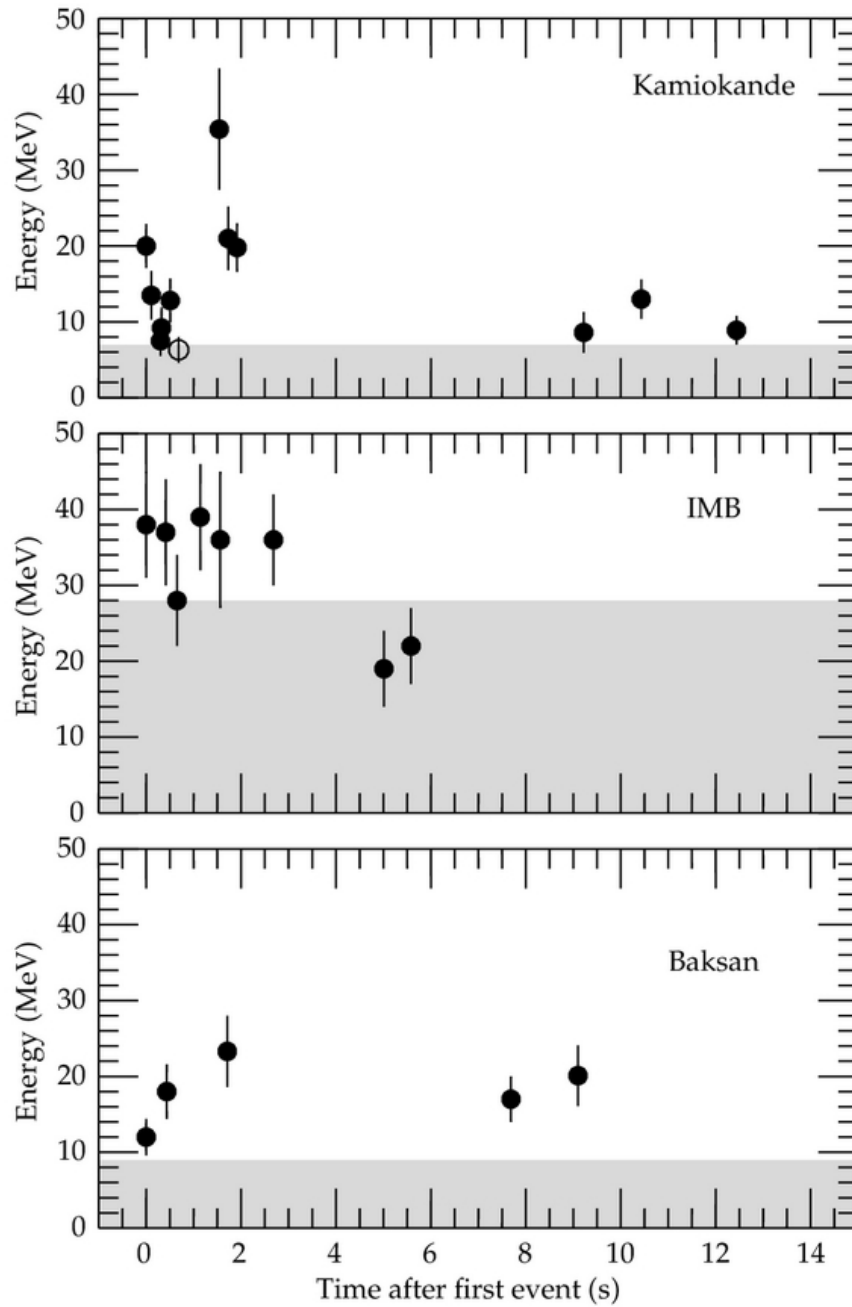
Figure 2.14: The neutrino events observed by Kamiokande II, IMB, and Baksan detectors associated with the SN1987A. The energies shown are the energies of the secondary positron from the inverse beta decay process. The grey areas of the plots represent the trigger efficiency below 30%. In this case, the first observed event from each experiment is recorded at t=0, however, there are unknown relative time offsets between these bursts. The single open circle event from Kamiokande II is attributed to background. Plot from [42].

Type of process	Interaction
Beta process	$e^- + p \rightleftharpoons n + \nu_e$
	$e^+ + n \rightleftharpoons p + \bar{\nu}_e$
	$e^- + A \rightleftharpoons \nu_e + A^*$
Neutrino scattering	$\nu + n, p \rightleftharpoons \nu + n, p$
	$\nu + A \rightleftharpoons \nu + A$
	$\nu + e^\pm \rightleftharpoons \nu + e^\pm$
Thermal pair process	$N + N \rightleftharpoons N + N + \nu + \bar{\nu}$
	$e^+ + e^- \rightleftharpoons \nu + \bar{\nu}$
Neutrino-neutrino reaction	$\nu_x + \nu_e, \bar{\nu}_e \rightleftharpoons \nu_x + \nu_e, \bar{\nu}_e$
	$\nu_e + \bar{\nu}_e \rightleftharpoons \nu_{\mu,\tau} + \bar{\nu}_{\mu,\tau}$

Table 2.2: Table summarizing the production of neutrinos in the SN core and the nascent neutron star. ν represents any neutrino type, ν_x can be $\nu_\mu, \bar{\nu}_\mu, \nu_\tau, \bar{\nu}_\tau$, A is the atomic nucleus, N corresponds to any nucleon. Data from [21].

The predicted SN probability as a function of SN distance is shown in Figure 5.45. It can be seen that the most probable distance to the CC SN in the Milky Way is around 10 kpc. The SNO+ SN trigger efficiency as a function of SN distance is described in Section 5.6. Additionally, there is a small chance that the SN will be at a distance smaller than 2 kpc. This would result in a significant burst of high energy neutrinos that can potentially overwhelm the detectors at the Earth. Study analysing how close a SN can be to still be detected without any data loss for SNO+ is presented in Subsection 5.11.1.

2.10   Neutrino-matter interactions

2.10.1   During SN

There is a huge variety of neutrino interactions pre, during and post SN explosion. Some of these are mentioned in previous sections (Section 2.7 and Section 2.8). The basic groups include beta processes, neutrino scattering, thermal pair processes, and neutrino-neutrino interactions. A summary is available in Table 2.2.

The interaction channels used to detect SN neutrinos by neutrino detectors are detailed in Subsection 6.2.

2.10.2 Influence of oscillations

It should be noted that due to the high densities inside the core and the outer layers, neutrinos do interact with matter frequently which enables oscillations via the MSW effect (Subsection 2.3.4). In these extreme conditions, resonances can occur. This affects the burst and the neutrino profile.

Neutrinos interact with matter (protons, neutrons, and electrons) via the exchange of Z and W bosons. The interactions via Z boson are available to all neutrinos regardless of the flavour, while the W boson interactions with electrons are only available to ν_e. This causes a shift to the effective mass, adding a potential V to the Schrödinger equation

$$V = \pm\sqrt{2}G_F N_e, \tag{2.30}$$

with G_F being the Fermi constant and N_e being the density of electrons [46]. The Hamiltonian for the vacuum (two flavour approximation) is then

$$H_{\text{vac}} = \frac{\Delta m^2}{4E} \begin{pmatrix} -\cos2\theta & \sin2\theta \\ \sin2\theta & \cos2\theta \end{pmatrix}, \tag{2.31}$$

while the modified Hamiltonian for matter is [12]

$$H_{\text{mat}} = \frac{\Delta m^2_{\text{mat}}}{4E} \begin{pmatrix} -\cos2\theta_{\text{mat}} & \sin2\theta_{\text{mat}} \\ \sin2\theta_{\text{mat}} & \cos2\theta_{\text{mat}} \end{pmatrix}, \tag{2.32}$$

$$= H_{\text{vac}} + \frac{V}{2} \begin{pmatrix} 1 & 0 \\ 0 & -1 \end{pmatrix}, \tag{2.33}$$

where the last line represents the matter Hamiltonian rearranged into the form of vacuum plus the additional potential. θ is the mixing angle, as explained in Subsection 2.3.1.

After additional rearranging, one can obtain [12]

$$\Delta m^2_{\text{mat}} = \Delta m^2 \sqrt{\sin^2 2\theta + (\cos2\theta - \frac{2V}{\frac{\Delta m^2}{E}})^2}, \tag{2.34}$$

$$\sin^2 2\theta_{\text{mat}} = \frac{\sin^2 2\theta}{\sin^2 2\theta + (\cos2\theta - \frac{2V}{\frac{\Delta m^2}{E}})^2}. \tag{2.35}$$

It can be seen that a special resonance condition can happen [47] when $\cos2\theta = \frac{2V}{\frac{\Delta m^2}{E}}$, at which point $\sin^2 2\theta_{\text{mat}}$ is equal to unity. Therefore, it is entirely possible for neutrinos of one flavour to evolve into entirely different flavour [48].
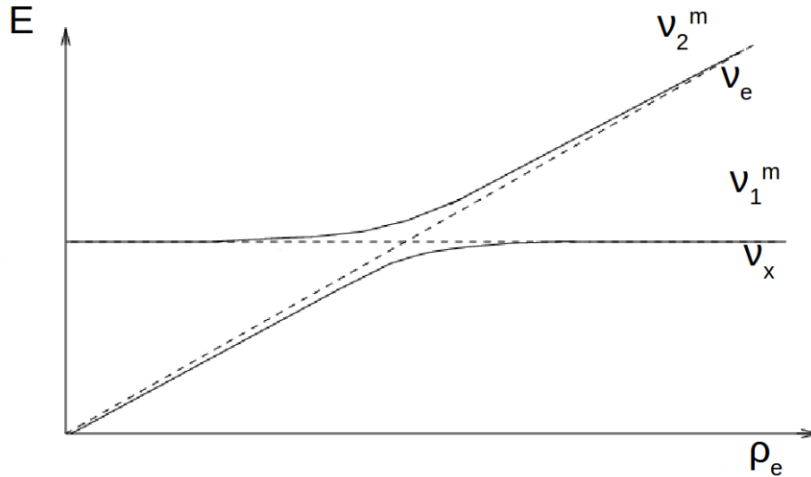
Figure 2.15: An illustration of the MSW effect. E corresponds to the total energy of the neutrino and ρ_e represents the density of surrounding matter. The flavour eigenstates are represented by the dashed lines while the mass eigenstates are indicated by solid lines. Figure adapted from [43] and modified.

This effect is shown in Figure 2.15. The resonance condition[21] is expressed by the crossing of flavour eigenstate (dashed) lines. It can be seen that the matter effect becomes more dominant at high densities of matter, causing the production of ν_e in the heaviest mass eigenstate. This is not the case for ν_x, unaffected by the additional potential. Since neutrinos are produced inside a SN in regions if immense density of matter, this effect dominates. As they travel away, they travel through media with almost monotonically decreasing density towards vacuum [49]. It should be noted that the neutrinos leave the SN in mass eigenstates and therefore vacuum oscillation does not occur as they travel towards the Earth (for the majority of predicted mixing angles [49]).

The effect of neutrino conversion can be observed through several features, such as: the Earth matter effects, the (partial) disappearance of the neutronization peak, or the distortion of the ν_e energy spectra. Additionally, there have been studies suggesting that the neutrino mass spectrum can be obtained from the SN neutrino burst [49].

Effect on burst phase

At the dense core with very high electron density, ν_e neutrinos are in the highest energy mass eigenstate. For the case of the normal hierarchy this corresponds to ν_3, while in the inverted ordering, this is ν_2. Due to the neutrino mixing (Subsection 2.3.1), and the heavy contribution of ν_3 to ν_μ and ν_τ flavour eigenstates, the burst would be detected at

---

[21]This resonance condition is also referred to as the level crossing.
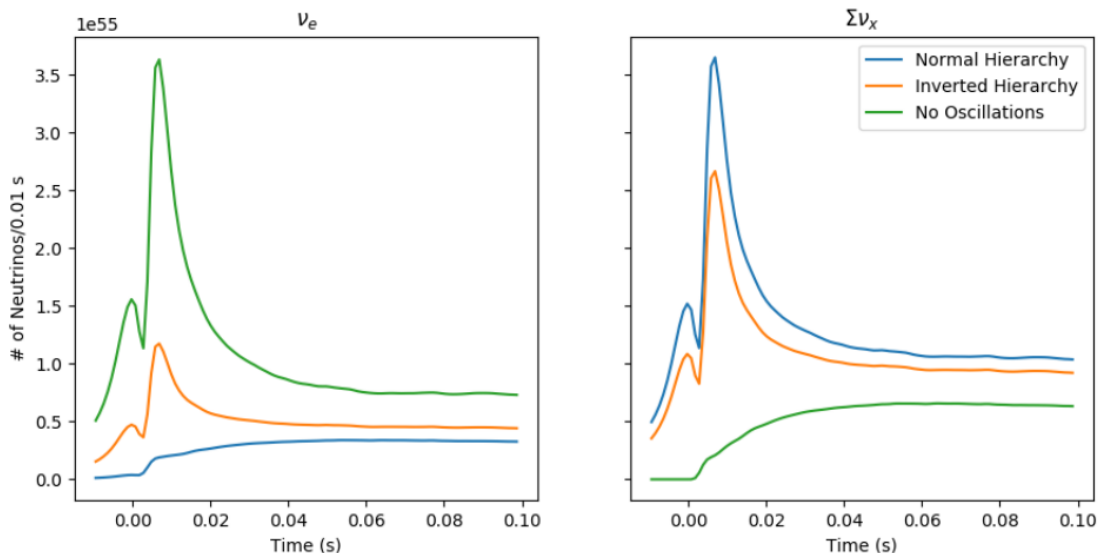
Figure 2.16: The effect of neutrino oscillations on the neutrino burst. The left plot represents the luminosity profiles of the ν_e, while the right plot highlights the effect on $\sum \nu_x$. The dataset for both hierarchies as well as no oscillation case is shown. Figure from [43].

the Earth mostly as these heavier-lepton neutrinos, with suppressed ν_e signal due to the small component of ν_3, given the normal hierarchy case. Alternatively, in the case of the inverted hierarchy, the suppression of the ν_e burst is smaller, due to higher ν_2 component in the ν_e flavour eigenstate. This is highlighter in Figure 2.16.

Additionally, the neutrino burst signal can also be affected - if it passes through the Earth before being detected - by the MSW matter effect. It is expected that A Fourier analysis can be performed on the detected spectrum to look for oscillatory effects. However, recent simulations suggest that this would not be possible even for the next generation detectors [43].

2.10.3 Self interactions

SNe are extremely rich in neutrinos and at extreme densities $\nu - \nu$ interactions are not negligible. These are called the neutrino self-interactions (SI). They are non-linear and induce instabilities in the flavour space, strongly dependent on the angle between the momenta of the colliding particles [50].

These interactions were modelled using the *neutrino bulb model* [51]. The model is based on the uniform and isotropic neutrino emission of all flavours. The signature of the SI is the spectral split - a swap of neutrino energy spectra for certain energy range. This
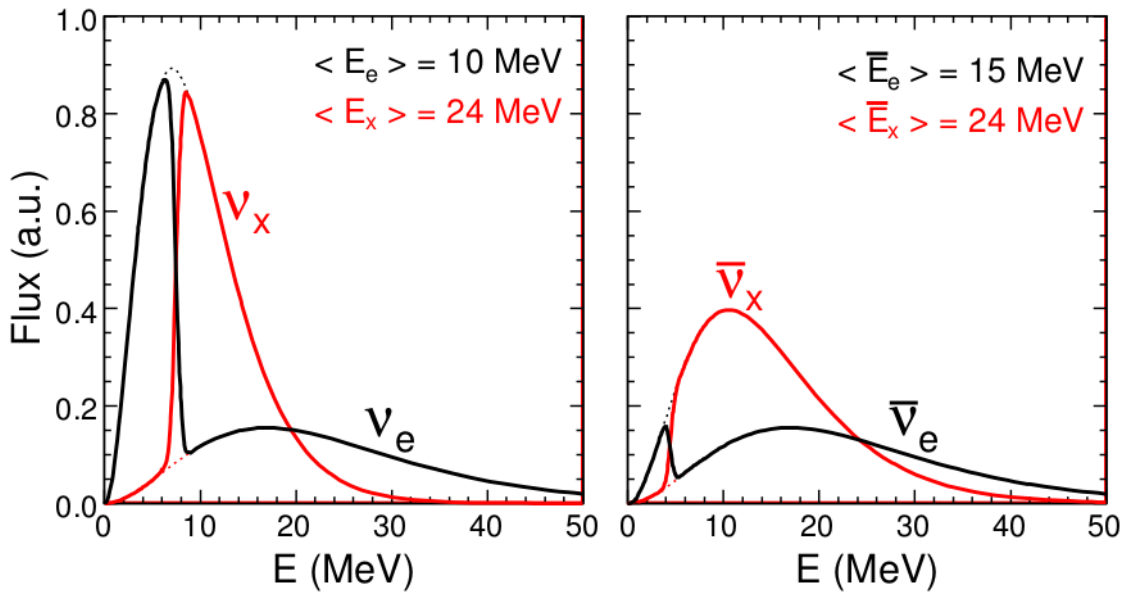
Figure 2.17: The effect of the neutrino self-interactions causing the spectral swap, based on the neutrino bulb model. The left plot represents the fluxes for neutrinos, the right plot shows the antineutrino fluxes. The original fluxes are shown as dotted lines. Figure from [50].

is shown in Figure 2.17. These effects are strongly dependent on the spherical symmetry and require further research [50].

Chapter 3

The SNO+ experiment

It doesn't matter how beautiful your theory is, it doesn't matter how smart you are. If it doesn't agree with experiment, it's wrong.

<div align="right">RICHARD P. FEYNMAN</div>

3.1 Introduction

This chapter introduces the SNO+ experiment. It starts by describing the SNO detector and outlining the changes made in transition to SNO+. The phases of SNO+ experiment with their corresponding physics goals are presented. The electronics at its current state and the software used by the collaboration is outlined. The calibration sources are listed. A more detailed description of optical calibration sources, with a summary of hardware changes and stability studies, finalises the chapter.

3.2 The SNO+ detector

The SNO+ experiment reuses the original Sudbury Neutrino Observatory (SNO) detector with several additions and upgrades. This detector was built between 1990 and 1999, and is located near the city of Sudbury, Northern Ontario, Canada[1]. The detector resides in the SNOLAB underground facility - a class 2000 clean room - to prevent radioactive contamination of the experiment(s)[2] by the mine dust [52]. The centre of the detector is at a depth of 2092 ± 5 m (5890 ± 94 meter-water-equivalent) underground [53]. This overburden provides effective shielding from cosmic muons - only about three muons

---

[1] The coordinates are $46°28'30''$ N and $81°12'4''$ W.

[2] There are several experiments hosted in SNOLAB.

pass through the detector per hour on average - this is important as muons may produce neutrons or unstable isotopes [54]. The detector is shown in Figure 3.1. The target medium for the SNO experiment was approximately one ktonne of heavy water[3]. It was operating between 1999 and 2006 and was awarded the Nobel prize in 2015 for demonstration that neutrinos change identities, a process that requires that neutrinos have mass [9]. A brief overview of the detector is given in this section, more details can be found in [53].

3.2.1 Parameters of the detector

The detector consists of [53]:

- The 600.5 cm radius hollow acrylic sphere - called the acrylic vessel (AV) - made of 5.6 cm thick acrylic;

- The 17.8 m diameter stainless steel geodesic sphere, known as the photo-multiplier tubes support structure (PSUP);

- Approximately 9500 20 cm diameter photo-multiplier tubes (PMTs);

- A non-imaging light concentrator, mounted on each PMT.

The AV is loaded with the detector medium, and is mounted within the PSUP. PMTs are, in turn, mounted on the PSUP. The PSUP is held in place by cables connected to bolts on the ceiling and the walls. There is an acrylic cylinder (the neck) at the top of the sphere which leads up to the deck of the detector. The neck is usually sealed but allows for deployment of sources. The deck holds the detector electronics. Considering the light concentrators, the total effective photo-cathode coverage was 54% - this is the highest photo-cathode coverage of any ktonne scale water Cherenkov or liquid scintillator detector [56]. The whole system is suspended inside an excavated 30 m deep and 22 m wide barrel-shaped cavity [43]. The cavity walls and floor consist of shotcrete[4] lined with 8 mm thick urylon[5] as a radon barrier. The cavity itself is filled with approximately 7000 tonnes of ultra pure water (UPW) that provides further shielding from the intrinsic radioactivity of the PMTs and surrounding rocks for the inner detector. It is often referred to as the external water - or external region - of the detector. Additionally, the deck area at the top of the detector is surrounded by a tent to prevent radon contamination [43].

---

[3]**Heavy water**: deuterium oxide (^{2}H$_2$O, D$_2$O), is a form of water that contains only deuterium [53].
[4]Sprayed concrete.
[5]**Urylon** is a polynonamethlene urea fibre [57].
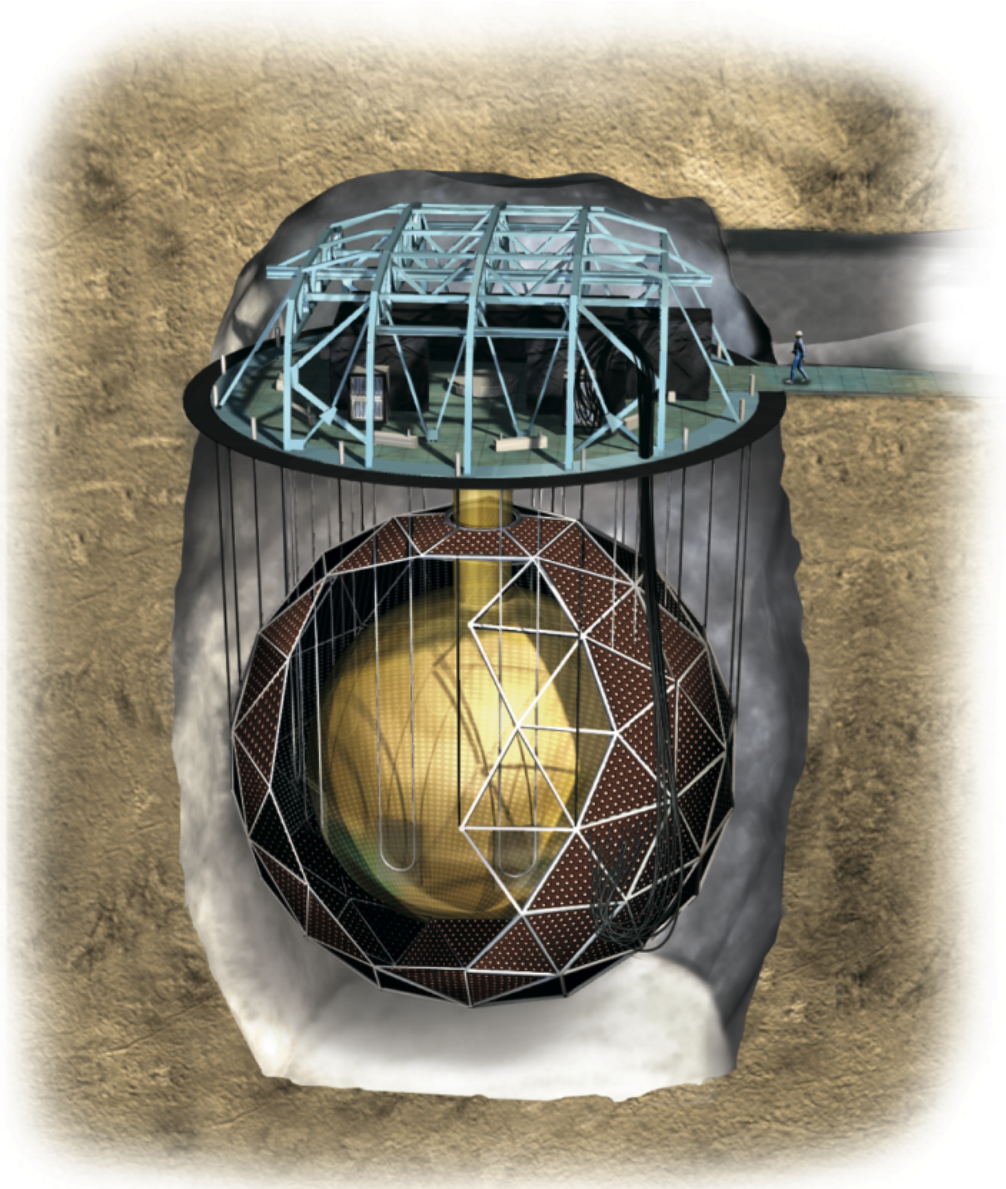
Figure 3.1: Artist impression of the Sudbury Neutrino Observatory (National Geographic). The acrylic vessel is the centre volume in yellow, containing the target medium, and is surrounded by the (partially omitted to allow a view of the acrylic vessel) PMT support structure. The layered shielding approach can be seen. Figure from [55].
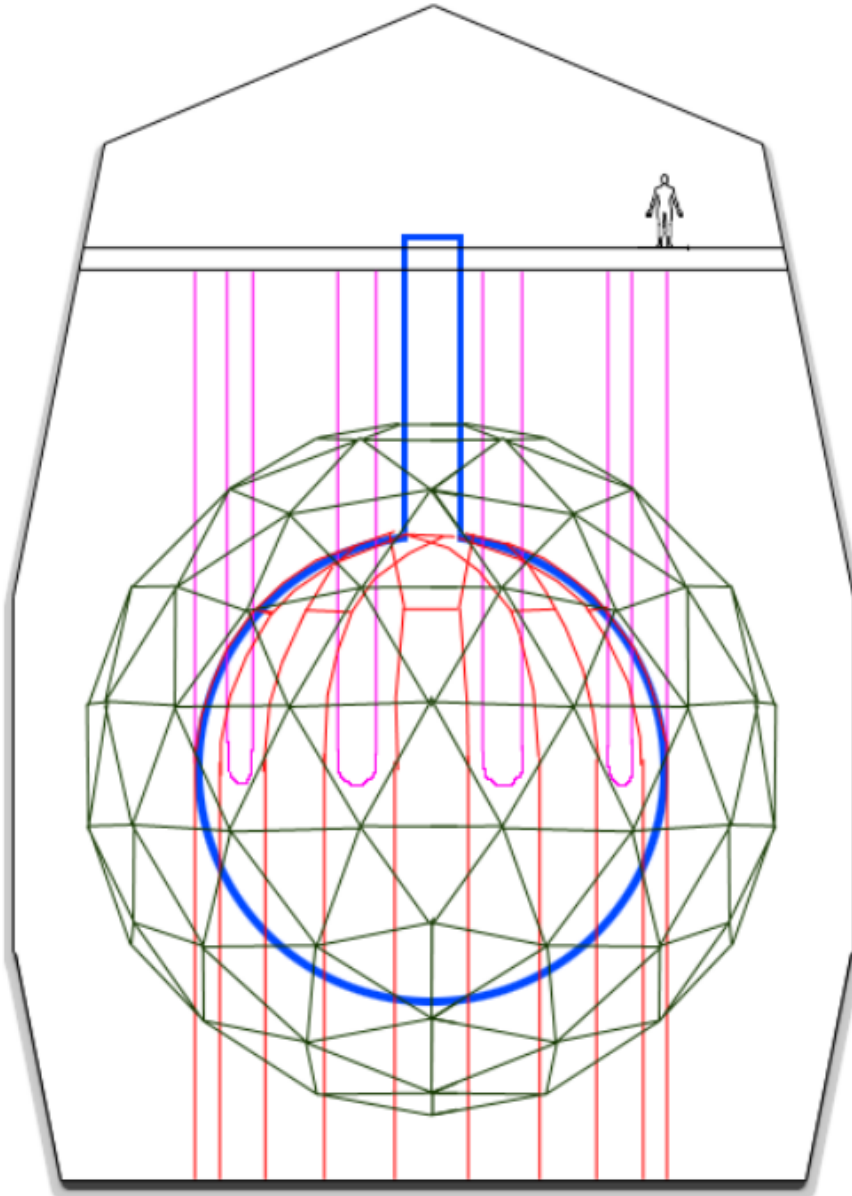
Figure 3.2: Stylised schematic of the SNO+ detector, roughly to scale. The geodesic PSUP is shown in dark green, PMTs are removed for visibility. The hold-up and hold-down ropes are shown in pink and red respectively. The AV is in bold blue. The cavity and the deck are shown in black. Plot from [58].

The AV is supported by a set of 10 loops of 30.48 m long rope made of Vectran[6] - see Figure 3.2. Each loop is connected to the AV via belly-plates - slabs of 11.4 cm thick acrylic [43] bonded to the AV - at equidistant intervals around the equator. The ends of the loops are supported by whippletrees[7] that are mounted on the deck, above the cavity. Bearings that are used allow the ropes to rotate freely, preventing additional tension. Tension can also be altered by the position of the locknuts on the threaded bars. The exact position of the AV can be controlled using this system. The tension of each rope is being monitored through the use of load cells.

There were several changes to the rope system for SNO+ - the major being the addition of hold-down ropes - these are outlined in the following subsection.

3.2.2 Upgrading SNO detector

SNO+ is a graded-shield type detector, where the centre of the detector - inside the AV - has the least background, with rates increasing as the distance outwards increases [59]. Because SNO+ is designed to look for rare events, low background rates are required. The change is focused around modifying previous water Cherenkov detector (SNO) to liquid scintillator detector (SNO+) while keeping the backgrounds as low as possible.

Several changes to the detector were needed to transition to liquid scintillator detector. Some of these required the development, construction, and deployment of completely new systems - such as the scintillator processing and purification systems - other necessitated improvements of the trigger system and DAQ electronics. Additionally, new calibration systems were developed as well. These are discussed in Section 3.6.

The scintillator and the radioactive isotope that is to be loaded inside the detector at later stage are to be purified underground in purpose built chemical plants. These are briefly outlined in Subsection 3.2.3.

The higher data rates caused by the lower energy thresholds have consequently demanded refurbishing of existing electronics as well as the replacement of significant parts of the trigger and front-end DAQ electronics. Furthermore, faulty PMTs have been repaired or replaced. All changes were made to provide additional functionality and improved stability. These are described in more detail in Section 3.3.

---

[6]**Vectran** is a liquid crystal polymer.

[7]**A whippletree** is effectively a bar balanced on a pivot, the bar is loaded at each end and the pivot balances the load [55].

Another addition during the upgrade process was the deployment of hold-down ropes. Because the density of the scintillator of choice is 0.86 g cm^{-3} [55], the buoyant force on the AV is now compensated for by means of a rope net anchored to the floor of the detector cavity, as shown in Figure 3.2. The hold-down rope net was designed using finite element analysis to spread the load evenly, minimising the possibility of AV deformation. The selected material is Tensylon - an ultra-high molecular weight polyethylene, previously used in Borexino [60]. Load cell are also used to monitor the tension for these ropes. Some PMTs had to be removed allowing the rope to pass through the PSUP, lowering the PMT coverage to 51% [55].

A cover gas system using high purity nitrogen atmosphere was also upgraded to serve as a seal from radon gas as well as to balance the pressure swings in the mine. The design is such that a radon reduction by a factor of 10^5 is aimed to be reached [61].

Likewise, a system of six cameras was installed onto the PSUP. These can provide high resolution images that can be used for monitoring of the position of the AV and deployed sources [62]. An example pictures using these cameras are shown in Figure 3.3.

3.2.3 Active target materials

SNO+ experiment includes three phases based on the medium that is loaded inside the AV. The first phase had UPW inside the AV - this is referred to as the water phase. For the second phase, the medium was changed to liquid scintillator via the process of scintillator filling. This process has been completed by the SNO+ collaboration on 29$^{\text{th}}$ April 2022, marking the start of the pure scintillator phase. For the final phase, ^{130}Te will be loaded inside the AV to allow the search for neutrinoless double-beta decay. This stage is upcoming. These phases are briefly discussed below.

Water phase

SNO+ water phase - where the detector was effectively a low-threshold water Cherenkov detector - collected data from September 2017 to July 2019 [63]. The main physics goal was the search for the invisible modes of nucleon decay in ^{16}O. This process is predicted by theories that link the electroweak and strong forces [64]. It is generally detected via de-excitation gamma ray, produced after a nucleon decays in ^{16}O, leaving the atom in

excited state. An example of the 'invisible' decay channel in ^{16}O is

$$^{16}\text{O} \rightarrow {}^{15}\text{O}^* \rightarrow \bar{\nu}\bar{\nu}\nu. \tag{3.1}$$

Generally, after the invisible nucleon decay the ^{16}O can decay to:

- The ^{15}O*, if the decaying nucleon was a neutron;

- The ^{15}N*, if the decaying nucleon was a proton.

Scintillator phase

This phase of SNO+ (also referred to as the pure scintillator phase) uses liquid scintillator. This enables lower energy threshold of approximately 200 keV [55]. The scintillator was loaded straight into the water to prevent exposure to air and contamination. The water was being removed in parallel to the filling process. This is helped by the difference in the density between the water and the scintillator. The two media are clearly separated with visible interface between them (this can be seen in Figure 3.3). The scintillator was filled from the top part while water was extracted from the bottom.
This phase is expected to last until the spring of 2023.

The main focus of this phase is the study of solar neutrinos and reactor antineutrinos. Furthermore, the detector is sensitive to supernova neutrinos during this phase. Additionally, this phase is used to determine the optical model of the scintillator and to confirm backgrounds are at the expected levels.

The detection of particles in scintillator proceeds via excitation of scintillator molecules by charged particles interacting with it. A prompt de-excitation follows - in few ns - releasing a photon. This is the process of luminescence of which there are three types: fluorescence, phosphorescence, and delayed fluorescence[8]. In SNO+, the ionizing radiation is mainly caused by muons and decaying isotopes - the backgrounds and the isotopes of study. These particles deposit their energy in the scintillator while passing through it. The broad range of expected energies is between 0.1 and 10 MeV, except for supernova neutrinos that reach much higher energies. These are studied in Chapter 6.

Scintillator System The scintillator selected for SNO+ is Linear Alkyl-Benzene (LAB) with chemical formula $C_6H_5C_{12}H_{25}$. The light emissions peaks in the UV range and is

---

[8]More details on these processed regarding SNO+ are available in [65].
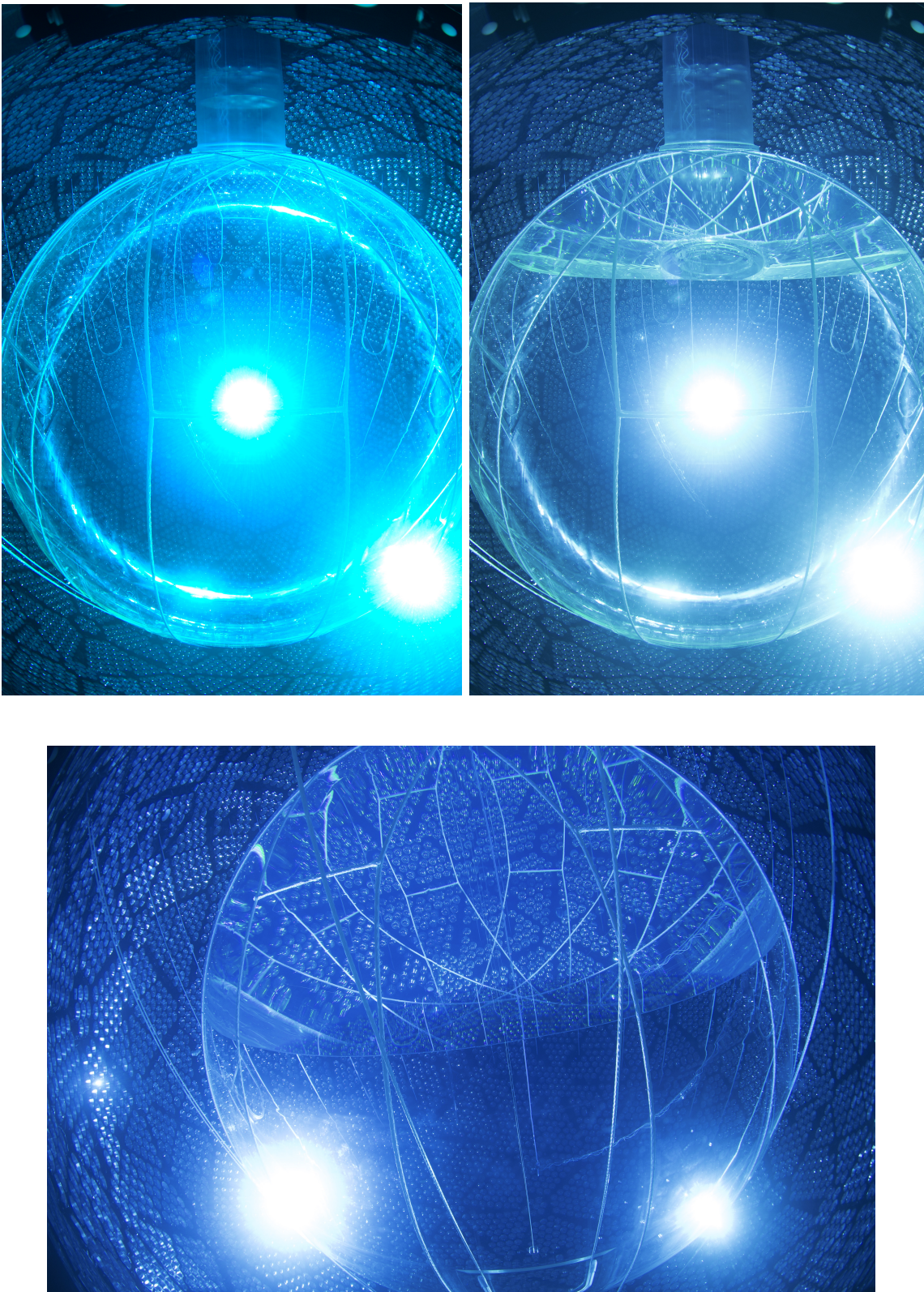
Figure 3.3: Photos of the SNO+ AV using new system of cameras. These pictures are taken at different points during the process of filling of the AV with scintillator. The scintillator-water interface can be clearly seen.

also in the region of highest absorption, thus, it often gets re-absorbed. Therefore, the wavelength shifters that are commonly used with liquid scintillators are utilised by SNO+. The wavelength shifter in use is PPO[9] that emits photons between 350-450 nm. The intended loading concentration is 2 g/l. In addition, secondary wavelength shifters will be used moving the emitted wavelength closer to the region of high quantum efficiency for SNO+ PMTs. There are several reasons for this choice of scintillator and wavelength shifters. Some of the reasons are:

- The intrinsic light yield of approximately 10^4 optical photons per MeV energy deposited by charged particles;

- The low scattering of this scintillator.

- The fast decay time;

- The chemical compatibility of the scintillator with the AV;

- The low toxicity of the scintillator;

- The relatively high flash and boiling points (170 °C and 278 to 314 °C, respectively [59]).

Regardless of the type, a general advantage of the organic scintillator is that it is non-polar and therefore purifiable to 1000 times smaller concentrations of radio-impurities than water [53].

It should be mentioned that even though the light yield is much higher for scintillator compared to water, the directionality obtained from the Cherenkov light is lost - the Cherenkov light is still produced, however the emission of the light coincides with the de-excitation of the scintillator which produces much higher number of photons. The resolution is not high enough to resolve the two different signals and the Cherenkov light gets overwhelmed by the scintillator light. Additionally, the visible energy is also affected in scintillator by a process of scintillator quenching. This is described in Subsection 6.2.2.

The LAB is treated so that the cosmogenic activation is minimized. Once it is transferred underground the scintillator is purified in the purpose built plant via multistage distillation (to remove heavy metals and improve the UV transparency with dual-stream distillation of the PPO wavelength shifter). Additionally, larger impurities (dust) are

---

[9]**PPO** - 2,5-Diphenyloxazole is an organic scintillator used as a wavelength shifter with spectrum peak at 385 ns.
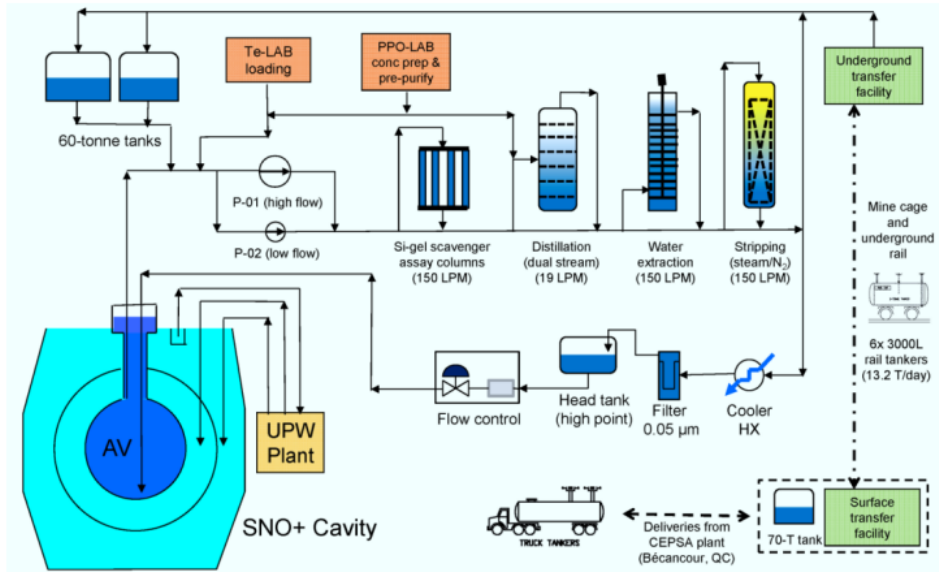
Figure 3.4: Simplified process flow diagram for the SNO+ distillation system. Plot from [66].

removed via the use of filters, and metallic pollutants are removed by the use of metal scavengers. The overview of the SNO+ distillation system is presented in Figure 3.4. Additional details about the purification plant are available in [66]. Details about the scintillation medium and its deployment can be found in [67].

The physics goals are different for the scintillator phase. The main aim is to measure low energy solar neutrinos and to study reactor and geo-(anti)neutrinos.

For the study of solar neutrinos, SNO+ hopes to examine the transition region between vacuum oscillations dominated neutrinos (low energy pep[10] and pp[11] neutrinos) and matter effects dominated neutrinos (higher energy pep and CNO[12] neutrinos) [61].

For reactor neutrinos, SNO+ is in the vicinity of three nuclear reactors which allows for the measurement of Δm_{12}^2 [61].

Finally, it's also possible to study geo-antineutrinos produced in Earth's crust and mantle. This could provide information on heat production mechanism of the Earth [61].

The expected energies of neutrinos SNO+ is sensitive to are:

- For solar neutrinos: $E_\nu = 1.44$ MeV (pep-chain), $E_\nu \sim 0.7 - 1.7$ MeV (CNO-cycle);

- For geo-neutrinos: $E_\nu \sim 1.8 - 3.5$ MeV;

- For reactor antineutrinos: $E_{\bar\nu} \geq 1.8$ MeV;

---

[10]The **proton-electron-proton reaction**, a rare electron capture reaction producing deuterium.

[11]The **proton-proton chain** nuclear fusion reaction.

[12]The **CNO cycle** is a catalytic fusion reaction.

- For supernova neutrinos: $E_\nu \geq 0.2$ MeV.

Scintillator quality assurance The quality of the scintillator to be filled inside the AV was strictly controlled during the fill phase. The quality assurance (QA) procedures are briefly described here. The author was a member of the QA team and was involved in the scintillator fill process.

The LAB arrives to the surface facility by trucks and is transferred to the storage tank via a pump system. The quality of the LAB in the truck is reported by the supplier and confirmed when receiving. LAB is then transferred underground by six 2 tonne rail carts (shown in Figure 3.5), these are filled from the storage tank. Underground, the rail carts are emptied into two 60 tonnes storage tanks.

Before the LAB is put inside the AV, several checks are performed. Some of the properties that are tested include [68]:

- **Physical properties that are checked**:

    - The density of the LAB;

    - The turbidity: a measurement of the suspended solid concentration;

    - The PPO concentration: measured using UV-Vis spectroscopy and densito-metry;

    - The temperature of the LAB sample.

- **The Radiopurity**: estimated using the BiPo counting: measured using Scout[13], an α/β coincidence counter;

- **Optical properties that are checked**:

    - The transparency and optical clarity: measured using UV-Vis spectroscopy;

    - The light yield: measured using Scout.

These checks are performed periodically before and while the scintillator is being filled inside the detector. If any result from the checks is outside of the acceptable range, the fill is postponed.

^{130}Te loaded phase

The main goal of SNO+ is to search for neutrinoless double beta decay in ^{130}Te. This isotope decays through $2\nu2\beta$ with half-life of $(7.0 \pm 0.9(\text{stat}) \pm 1.1(\text{syst})) \times 10^{20}$ years [70]

---

[13]**SCOUT** stands for Scintillator Counter of Uranium and Thorium [69].

Figure 3.5: A photo of the two tonne rail cart used for scintillator transfers.

and $Q_{2\beta} = 2527.518 \pm 0.013$ keV [71]. Tellurium addition will proceed by dissolving the Te acid in water and then using a surfactant to mix it into the scintillator. The purification is done both above-ground: $Te(OH)_6$ is dissolved in UPW and re-crystallised using nitric acid, then rinsed with ethanol; and underground: crystals are dissolved in water at 80 °C, then thermally re-crystallised [66]. In addition to that, to reduce the radioactive activation, the isotope is transferred by ship (lower altitude, lower exposure to cosmogenic particles) and is stored underground for several years to allow for the decay of activated isotopes. Loading of 0.5% by mass is planned with further loading being investigated.

SNO+ was originally planning to use neodymium (^{150}Nd) as radioactive isotope. The change to tellurium was made later on, due to several reasons, such as:

- The **compatibility** with the choice of the scintillator cocktail;

- Tellurium has **high natural abundance** - 34.08% [65] - so no enrichment is needed;

- The $2\nu\beta\beta$ background is reduced by approximately a factor of 90, due to longer $2\nu\beta\beta$ half-life [43].

The expected signal, alongside the backgrounds, for five years of running assuming m_β of 200 MeV is shown in Figure 3.6. Details about the calculations and backgrounds are available in [61].

3.2.4   Physics goals

To summarize, the main physics goal is to address the question of whether neutrinos are Dirac or Majorana particles, through the search of neutrinoless double-beta decay of ^{130}Te. Additionally, SNO+ is sensitive to reactor, geo, solar and supernova (anti)neutrinos.
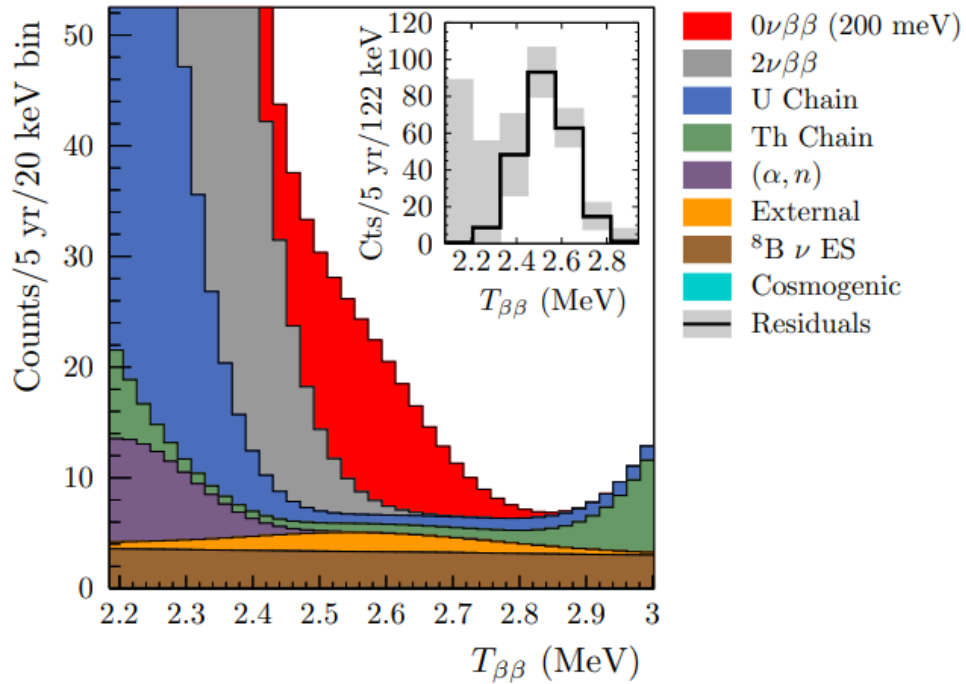
Figure 3.6: Summary stacked plot of all backgrounds and a hypothetical $0\nu\beta\beta$ signal corresponding to a mass $m_\beta = 200$ MeV for five years of data taking. 3.5 m fiducial volume cut is applied. 0.3% natural tellurium loading and 200 NHits/MeV light yield are considered. $T_{\beta\beta}$ is the effective kinetic energy. Plot from [61].

Supernova neutrinos are one of the focal points of this thesis.

More details about the physics goals and background mitigation for SNO+ are available in [72].

3.3   Electronics and DAQ

This sections aims to describe the process of collecting data via the electronics and DAQ and converting it into physics events as well as storing it into the digital format. The process, in general, starts by detection of a signal via PMTs, propagation of the signal through electronics follows, and finally, the data is digitized, converted, and transferred online. These steps are outlined in this section.

The expectation is that at least 200 and possibly up to 350 (depending on the loading and concentration of the double-beta decay isotope) photo-electrons per MeV from scintillation will be detected by the detector. At energies higher than 10 MeV - above the main physics goal range - there will be a significant fraction of multi-photon electron (MPE) hits, although, the majority of hits in an event will still be single-photon electron (SPE) [73].

3.3.1 Electronics

The observables in SNO+ are the charge and timing information of each PMT. The time is stored as a single value by the 'Time to Amplitude Converted (TAC)'. For charge, there are three values stored. These are:

- The **high-gain short integration charge** (QHS): it describes the size of the pulse causing the trigger on a PMT, over 60 ns;

- The **high-gain long integration charge** (QHL): it additionally includes late and scattered light, over 400 ns;

- The **low-gain long integration charge** (QLL): a low gain copy of the PMT pulse, used to monitor in-window pileup[14].

3.3.2 PMTs

The PMTs in use by SNO+ (and SNO as well) are eight inches Hamamatsu R1408 photo-multiplier tubes. These can be grouped into categories as:

- The **inward looking PMTs**: grouped together into panels, pointing at the centre of the AV. There are approximately 9400 PMTs of this type [61]. The average quantum efficiency[15] is around 20% [74];

- The **uutward looking PTMs** (OWL): 100 PMTs looking into the cavity, away from the AV. These are used as muon veto;

- The **Neck PMTs**: Few PMTs are installed in the neck region. These look for any possible light leaks and to veto events in the neck;

- Other types of PMTs: there are additional PMTs that are not generally used for physics data collection. Examples would be low gain channels, underwater test channels and spare channels.

All PMTs are connected with the electronics on the deck via a waterproof BNC cable providing both power and data lanes. The length of each cable is the same to minimize any times offsets. In addition to that, magnetic compensation coils are installed in the cavity walls to cancel out the effects of the Earth's magnetic field.

---

[14]**A pileup event** is a single reconstructed event caused by multiple (physics) events occurring in the same trigger window [65].

[15]In this case the efficiency is a combination of quantum efficiency and collection efficiency.
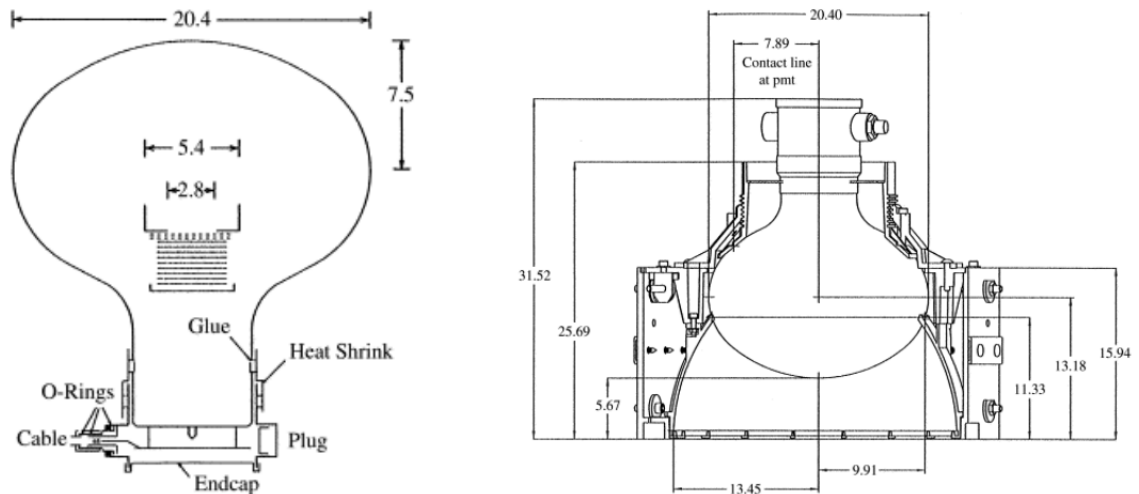
Figure 3.7: Left: cross section of the R1408 PMT. The dynodes are shown as solid horizontal lines, above the U shaped anode. The dashed lines above are the focussing grid. Right: cross section of the same PMT type now also showing the concentrator. All measures are in cm. Plot from [53].

The quantum efficiency of these PMTs is shown in Figure 3.15 and in Figure 3.20. The first figure also highlights the spectrum of the LEDs used by the calibration system for these PMTs and the absorption probability of the doped scintillator as a function of the wavelength. Another important property of the PMTs in use is the transit time spread, which is 1.7 ns (standard deviation) [73]. These features affect the selection and design of the time calibration array, which is described in detail in Chapter 4.

Photons interact with the glass surface of the PMT that is coated with photosensitive compound. Photon is emitted. It then accelerates through series of dynodes held at decreasing potential. Colliding with each dynode creates a shower of electrons, multiplying the number with each dynode. For SNO+ PMTs, this process results in overall gain of 10^7 of the initial electron count [69].

Regarding charge, PMT produces current at their base even with no incident photons - this is the dark current. To distinguish this from real photo-electrons a total deposited charge is used. This required a threshold to be set - this is the discriminator threshold, which determines whether the PMT will report a hit.

3.3.3   Triggers

Once the light is detected by a PMT, an analogue pulse travels via 35 m coaxial cable from the PMT position to the deck above the detector. The same length cable is used

for all PMTs in order to minimize time offsets. This pulse is then received at a paddle card. A single paddle card reads the data and provides voltage for eight PMTs. The PMTs can be controlled (turned on or off) individually via paddle cards. Four such cards are installed on one PMT Interface card (PMTIC). This means that each PMTIC has 32 channels[16] associated to it. The signal then propagates to a Front-End Card (FEC), which mirrors the PMTIC card. FECs determine whether the channel crossed the discriminator threshold (approximately 0.25 photoelectron) via CMOS chips. If the discriminator fires, a TAC starts ramping up, increasing the voltage from zero. There are three voltage values to be measured, as described in Subsection 3.3.1.

Every PMT crossing the discriminator threshold generates this trigger signal. Once a PMT has triggered, it is locked out for 400 ns - this is the event window - and cannot generate another trigger pulse until the lock-out period has passed and charge values are reset [43].

The PMTICs, as well as the FECs, are grouped in crates. There are nineteen crates total, each containing sixteen PMTICs[17]. Additionally, the crates are arranged in eleven racks, each capable of holding up to two crates. The racks are distributed circularly on the deck, above the detector cavity.

Each crate contains a Crate Trigger Card (CTC). This card receives signals from all channels in the crate and sends the sum of the signal onto the Master Trigger Card Analog (MTCA+). The MTCA+, very similarly, sums the signals from all crates. Naturally, there is a propagation delay associated with these transfers. The FEC to MTCA+ takes between 60 to 120 ns. The MTCA+ therefore contains the logic to determine whether a global threshold for the number of hits within a given integration time - the NHit - was crossed. If it was, the MTCA+ informs the Master Trigger Card Digital (MTCD). This add another 2 to 3 ns of propagation time. MTCD generates a Global Trigger (GT) if it received such command from the MTCA+ or if an external trigger was issued.

The GT is latched onto the 50 MHz clock, meaning the GT will be associated with the next clock tick[18]. If the GT is issued, the FECs stop the TACs from ramping and collect data from their PMTs, incurring a propagation delay of 60 to 150 ns. The channels that are locked out are read out and used to construct an event. The GT can only be issued every 450 ns.

---

[16]PMTs are often referred to as channels.

[17]Therefore, each crate contains sixteen PMTICs and FEC cards, totalling 512 channels.

[18]This occurs every 20 ns for a 50 MHz clock.

Additionally, there is a CAEN board available that digitizes the ESUM signal. All trigger signals above the threshold within 10 s on either side of the trigger signal are masked into the trigger word.

For more details about the trigger system please refer to [75].

There are several signals generated by FECs that can be used to form a trigger sum and generate a GT. Some of the most commonly used are NHIT100, NHIT20 and ESUMHI/LO.

NHIT100 NHIT100 is a discrete pulse of uniform height for each hit PMT, nominally 100 ns wide. It can be delayed between channels to change the position of the in-time coincidence around the detector. Can be set to high, medium or low thresholds. The most commonly used trigger in SNO+: this is because the photon transit time across the entire detector is around 80 ns, allowing light from single event to propagate through the detector medium and contribute to the trigger signal.

NHIT20 NHIT20 is similar to NHIT100, nominally 20 ns wide. It is useful to study backgrounds within the centre of the detector.

ESUMHI/LO ESUMHI/LO is a copy of the PMT pulse at either high (HI) or low (LO) gain. It provides a diagnostic tool and can also be used to construct more complex triggers for (OWL) PMTs and external triggers linked to the GPS. OWL PMTs produce the same pulses as regular PMTs but are summed separately.

A special note should be said about External Asynchronous (EXTA) trigger. This trigger is not latched onto the clock, meaning that there is no delay waiting for a clock tick. This is mostly used with calibration sources.

To summarize, the NHIT100 trigger represents the number of hit PMTs within 100 ns while the ESUM signal is the sum of all PMT pulses. A schematics of the triggering system and signal propagation is presented in Figure 3.8.

Note on event times As mentioned, the 50 MHz clock is what the global trigger latches onto. It resets approximately every two days and calculates times between events. There is also a 10 MHz clock which resets every 28.5 years. This clock defines the time of the event relative to a fixed date - this is set to 1st of January 2010 [43]. The clock is kept in synch using a GPS, controlling offsets every hour.
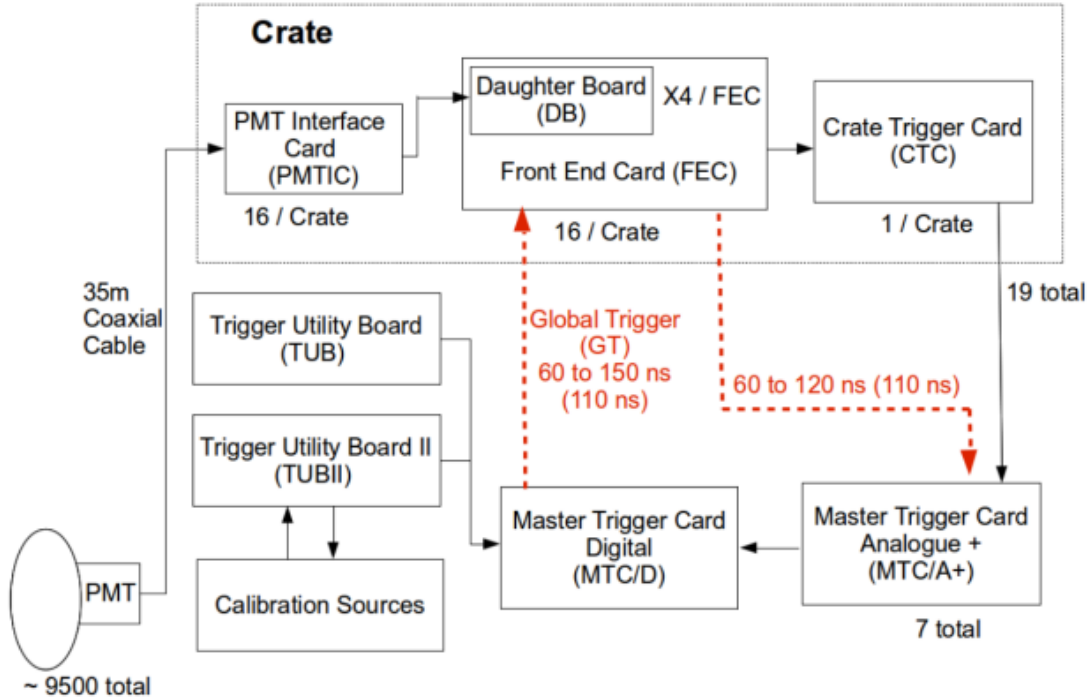
Figure 3.8: Representation of trigger signal propagation in SNO+. Plot from [76].

Electronic upgrades In SNO, there was a Trigger Utility Board (TUB) providing the master clock for the trigger systems as well as utilities and diagnostics to interface with the MTCD. For SNO+, there was an addition of Trigger Utility Board II (TUBII), providing additional clock and more options for external triggers. Furthermore, the CTCs have been modified to cope with higher currents. New control boards (XL3) have been developed for the CTCs to set trigger masks and charge pedestals. Likewise, the MTCA was upgraded to MTCA+. New features include: increase in the upper limit of the number of channels that could fire simultaneously, new logic to remove dead time, change of current sum to voltage sum, re-triggering capabilities and more.

The maximal manageable data rate was effectively increased from 2 Mbit/s to 250 Mbit/s, to accommodate for higher event rates and light yields [69].

3.3.4 Event data

Once a trigger is issued, the hits are stored in first-in first-out (FIFO) memory buffer. The digitised PMT hit consists of: PMT ID in a form of logical channel number, TAC (representing the hit time), charge values (QHS, QHL, QLX), global trigger ID (GTID), CMOS CELL number and few additional bits mostly used for status flags [77]. The hit information, alongside the trigger types, MTC clock time, GPS clock time, and CAEN trigger pulse form the digitised event.

As mentioned, each crate also contains an XL3 control board. XL3 scans data for a crate, collects it, and forwards it to `SNO+ Event Builder` - the builder is described in Subsection 5.2.1. The output of the builder is an event, a collection of data from XL3, CAEN and MTC by organizing PMTs into bundles and grouping them with corresponding trigger words and GTIDs. All events are then stored to ZDAB files. These files represent the raw data recorded by the detector.

3.4   Software and data processing

This section describes the software, processing and other data related topics for SNO+.

3.4.1   Reconstruction

The goal of reconstruction is to calculate the position, time and energy of a physics event. This is done via the use of processors and fitters[19].

The position is reconstructed using the coordinates of triggered PMTs and the times they report for the event by determining the vertex of the event that caused them. All triggered PMTs in the event window are assumed to belong to the same event and are used to reconstruct the vertex - i.e. only a single event (or single vertex) is reconstructed in one trigger window.

The vertex position is calculated using time residuals of all involved PMTs. This, naturally, requires precise calibration. This is the topic of Chapter 4.

The detector is expected to achieve position resolution of approximately 10 cm in scintillator and 25 cm in water, although, the directional information of the ionising particle is almost completely lost in scintillator - the Cherenkov component is present but extremely hard to detect.

3.4.2   RAT and ORCA

SNO+ Monte Carlo (MC) was originally developed for the Braidwood collaboration, called Reactor Analysis Tool (RAT) [56]. It was based on software which simulated a generic liquid scintillator experiment with a KamLAND like geometry [56]. It is written primarily in C++, using Geant4 [78] libraries to simulate physical processes and ROOT [79] libraries to store data.

There are several branches available in RAT. The most important are: the MC branch

---

[19]The **fitters** are technically a subgroup of processors aimed at the event reconstruction.

representing true Monte Carlo data; and the EV branch incorporating the detector response. Results of the reconstruction are also available in this branch.

RAT can analyse data by looping through them individually. Event properties can be updated via the use of processors. A processor has access to RAT branches, can read details of each event, and apply any desired logic. One such example is the `Burst Trigger` processor, described in Section 5.3.

ORCA is an object oriented DAQ, written in Obj-C using the Cocoa framework and the Apple developer tools. ORCA is the interface used by detector operators to interact with the detector. It controls the electronics, such as the value of thresholds and active triggers. This is usually done via different run types. A run is defined as a period of data-taking where the detector state and conditions remain constant. The nominal run length is one hour [74]. Runs are uniquely identified by an increasing integer number.

The data from ORCA can be used to update the database and is processed by RAT before being sent to the Grid for analysis.

3.4.3 XSNOED

XSNOED is the default event display used by SNO+. It was originally written for SNO in C++ using Motif as its graphical toolkit [80]. The user interface consists of the main detector display window - which displays the detector in 3D and allows for rotations - and a diverse range of additional windows that controls some aspect of the display with additional informations. Some of the features available in XSNOED are [80]:

- To display event-level information, such as GTID, NHit, run number, date and time;

- To display PMT-level information, such as time and charge, via many different views (3D, 2D, crate view, flat map[20], histogram and more);

- To display trigger sum waveforms from CAEN;

- To read events from ZDAB and ROOT files;

- To read events from dispatcher - this is used for live monitoring;

- To work with triggered events from the detector as well as Monte Carlo events;

---

[20]**A flat map** is a type of plot where SNO+ PMTs are shown in 2D view, with dots/markers representing individual PMTs. Because the shape of the structure holding the PMTs is spherical, the visualization is form of a map projection, where the sphere is 'sliced', similar to an orange peel. The positions on the flat map correspond to true positions, i.e. the top portion is the neck of the detector.

- To apply NHit and trigger masks;

- To sum PMT information;

- To read reconstructed vertices;

- To display MC tracks;

- To animate PMT hits to see evolution over time;

- To read PMT location and status information from the database.

Figure 3.9 shows two example plots from the XSNOED software, specifically the main view (showing PMTs around the AV in a 'real' like geometry) and the flat map view of the PMTs. Each dot represents a PMT. Multiple variables can be displayed. In this case, the data is summed for a single calibration run (real data) and the color represents the number of times each PMT triggered.

3.4.4   Storage

The data recorded by the detector is stored onto a data raid[21] underground. A suite of scripts then checks for new files and registers them to a CouchDB database[22] as well as submits transfer requests to a GRID file transfer scheduler (Grid-FTS). Once a replica of the data is available at the first Grid storage node, two further transfer requests are submitted. Current replica sites are SFU (Canada), FNAL (US) and RAL (UK) [81]. All in all, each raw data file recorded by SNO+ is stored in triplicate. Once the three copies are transferred and checked, the local copies are deleted.

3.4.5   Processing and production

There is multistage processing applied on the raw data.

Nearline   The very first stage happens directly on the servers underground. The raw runs are checked using 'nearline' system. This is a collection of processors that looks at the initial state of the data and extract some observables corresponding to the detector conditions. The output of the nearline process is a set of tables, which are used as an input to processing.

---

[21] A RAID stands for a redundant array of independent disks. It is a storage virtualization technology that combines multiple physical disks into logical units to improve redundancy, performance, or both.

[22] More details about CouchDB are available in Subsection 5.4.2.
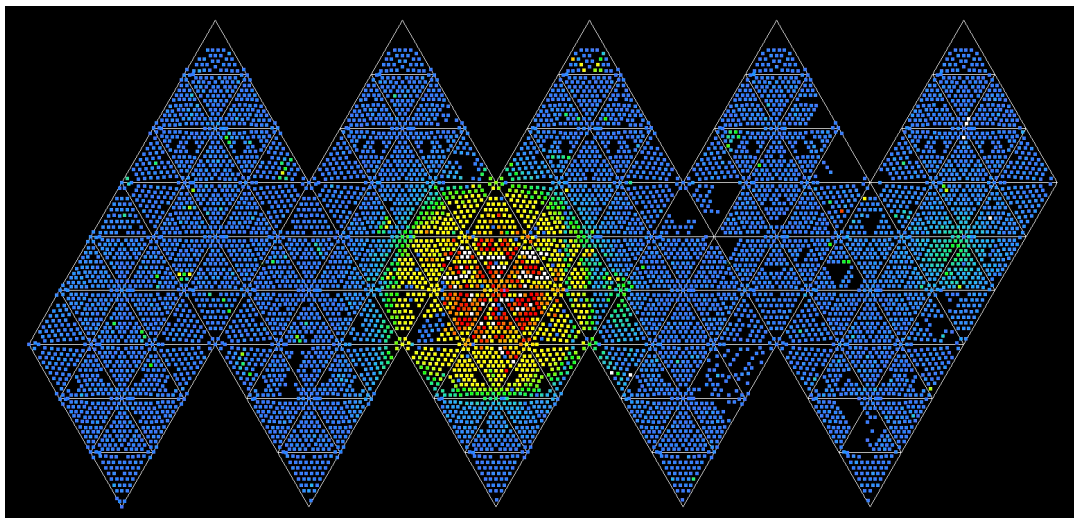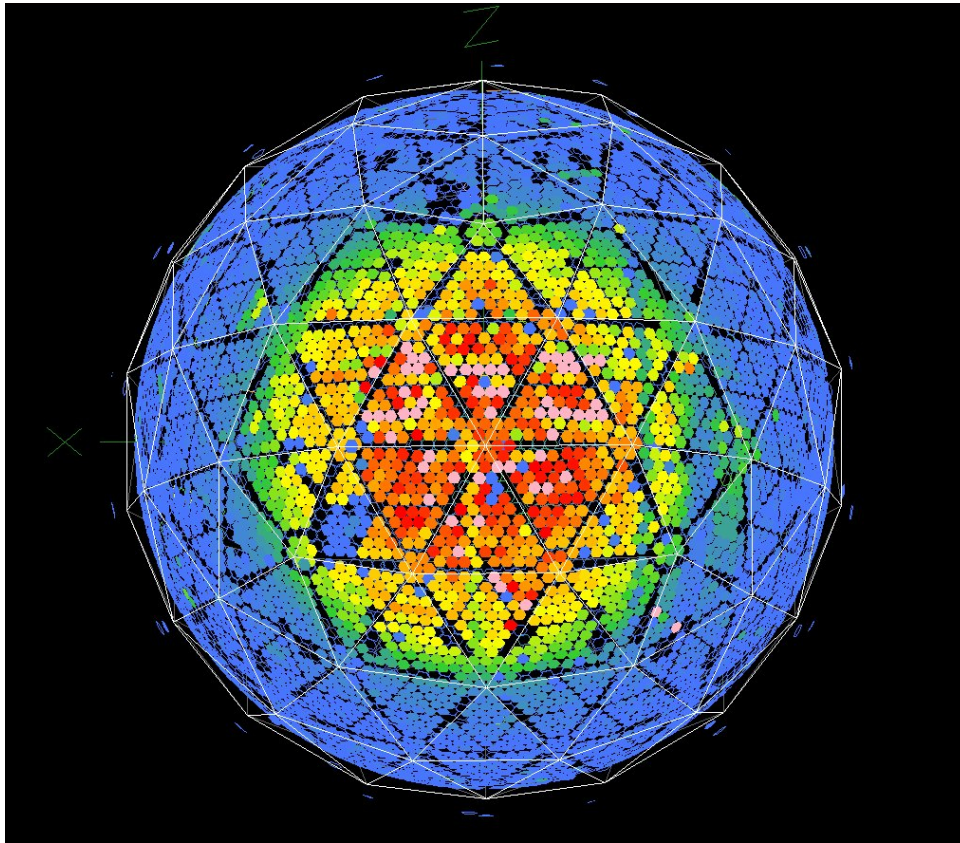
Figure 3.9: Two example windows from XSNOED software. In this case the plots are from a calibration run (TELLIE). Each coloured dot represents a PMT of the detector. The colour can show different variables, in this case the data is summed from a single TELLIE run with the colour representing the number of times each PMT was triggered. Top plot is the main window showing the 3D version of the detector. Bottom plot is a flat map view. A clear big beamspot can be seen for the direct light with a smaller secondary beamspot caused by the reflected light. For more details on TELLIE, please read Section 3.7. Figure 3.13 and Figure 4.15 show how the different beamspots visible in these plots are generated.

Processing   Once a run is transferred off-site and the nearline tables are available, the run can be processed. This includes running selection of RAT processors over the events. Firstly, data cleaning is applied to cut unwanted events. Then, different logic is applied depending on the run type - i.e. calibration runs and physics run require different treatment. Event reconstruction also takes place here. Processing (and sometimes reprocessing) takes place on the Grid network and a single output file is stored.

Production   Production is the use of RAT software to perform studies of the detector and its sensitivity. This usually involves generating events within the detector geometry via the use of event generators. These simulate events based on type and basic parameters and mimic the response of the detector. There are diverse uses for this, including prediction of backgrounds, simulation of calibration sources, research of optical properties and much more.

Database validation   The database hosts a document for every single data file, processing and production job. A comprehensive view, monitoring, and updating of the database is required. Several scripts are available to interface with the database. One of the contributions to the processing infrastructure by the author was the addition of the database validation scripts.

An example validation script is used to delete old data. The process is slightly different depending on the data to be deleted - processing, production or detector data - but the script can be used on all types. The script firstly collects the database documents that fulfil the arguments passed to it, loops through them to collect output files, updates these job documents, loops through the collected files, deletes physical files from all locations, and finally deletes the associated data documents.

In addition to content mentioned in this section, all relevant details of the detector and its status are stored in databases. There are several different databases used throughout and they, together, form a backbone of the software side of the experiment. Some are mentioned in the Chapter 5.

3.5   Control rooms

As mentioned before, the detector is mainly controlled via ORCA. There is also a suite of additional monitoring software that monitors specific subsystems. Detector is controlled

constantly, in shifts, by means of a control room. Control room is a set of computers that are capable to perform the monitoring, i.e. they have the hardware and software required to monitor the detector with appropriate connection to site.

3.5.1 Control room at Sussex

A remote control room for SNO+ was set-up at the University of Sussex in 2018 with author's involvement. The control room, with the abbreviation CRSU, was extensively tested, debugged, and successfully commissioned.

3.6 Calibration sources

The main goal of calibration is to ensure the the results of the detector are both accurate and precise. This requires understanding the detector and the electronics, investigating the scintillator properties, improving reconstruction methods and more. For SNO+, this means covering a wide range of energies: from 0.1 to several tens of MeV. There are several important parameters that require comprehensive understanding, such as scattering and absorption (in all materials: scintillator, acrylic, water), timing and charge response of the PMTs, and the angular response of the PMTs. Photons entering PMT at an angle (with respect to the normal) have lower chance of getting detected. This effect is reduced by the use of concentrators - devices consisting of 18 pieces of thin dielectric-coated aluminium sheets surrounding the PMT, curved in shape [69]. These have been found to be degrading over time [82]. The concentrators also increase the effective coverage by allowing photons from wide angles to deflect towards the PMT.

There are tight constraints on the calibration system enforced by the increased sensitivity and lower energy threshold.
Most of the energy and light yield calibration will be done using the radioactive sources. These are self-contained but require deployment.
The PMT timing, PMT gain, PMT response with varying event position as well as some scintillator properties will be calibrated using two complimentary optical sources. One is a diffuse light source called the laserball (LB). The other one is the External LED/Laser Light Injection Entity (ELLIE). The LB requires deployment while ELLIE is permanently mounted on the PSUP, in the external water region.
It should be repeated that the deployment process is more troublesome in liquid scintillator due to contamination. The deployment of the sources needs to be minimal.

Light yield and energy linearity calibration   As mentioned above, several radio-active calibration sources will be used for detector calibration. The aspects that can be calibrated are:

- The geometric uniformity;

- The energy linearity;

- The alpha-beta discrimination;

- The absolute light yield.

Some of these sources have been reused from SNO and modified, and new sources have also been developed for SNO+. These sources are:

- The ^{60}Co source: producing 2.5 MeV γ;

- The ^{48}Sc source: producing 3.3 MeV γ;

- The ^{24}Na source: producing 4.1 MeV γ;

- The ^{16}N source: producing tagged 6.1 MeV γ;

- The AmBe neutron source[23];

- The ^{90}Y β source[23];

- The ^{8}Li β source[23].

These sources are deployed within the AV, suspended from an umbilical cable. A source manipulator system is used, allowing the position to be controlled in three dimensions, as shown in Figure 3.10.

PMT calibration   In SNO, the PMT calibration was accomplished through the use of a deployed source, the laserball (LB). Modified version of LB is also used in SNO+. As mentioned, due to radiopurity requirements, the deployment of sources inside the AV has to be kept at minimum. For this reason a system complementary to the LB was developed. This is the External LED/Laser Light Injection Entity (ELLIE). These two, as well as few additional sources, are described below.

---

[23]In development.
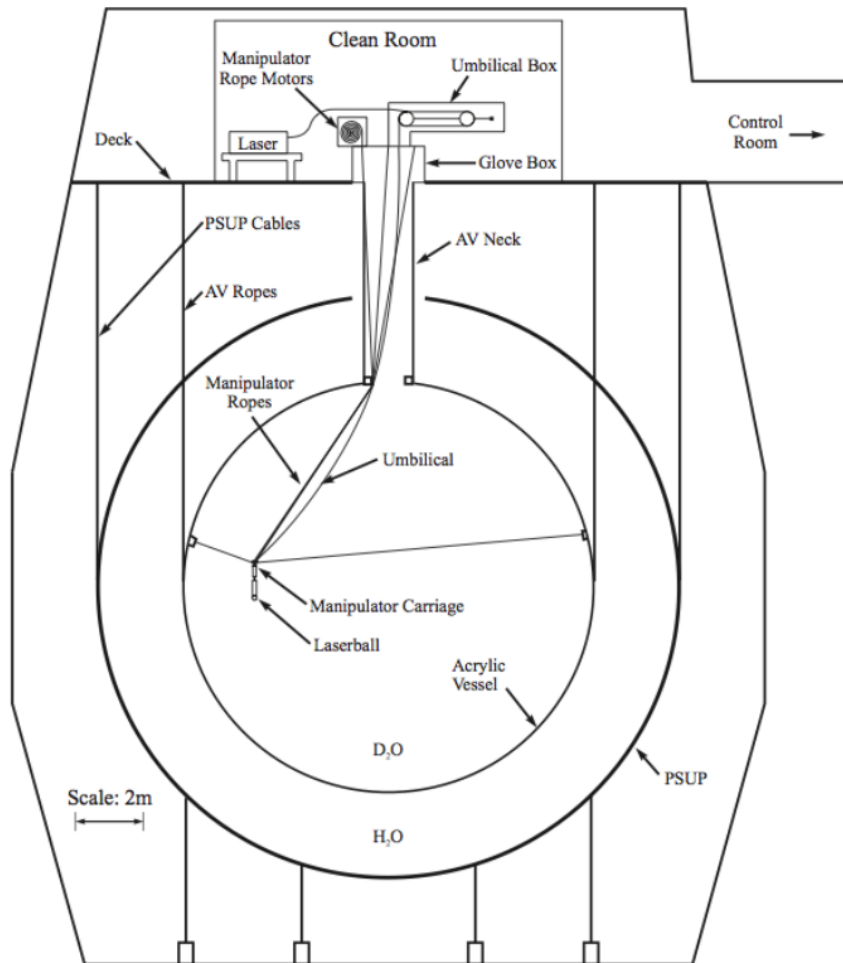
Figure 3.10: SNO source manipulator system, schematics. From [83].
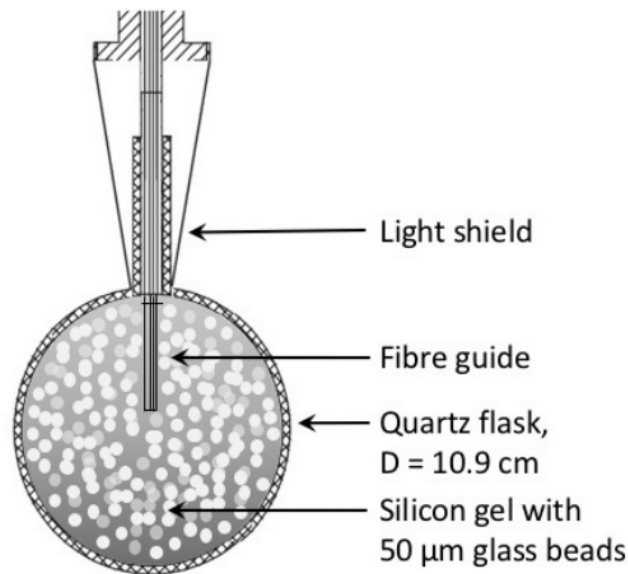
Figure 3.11: A schematic picture of the laserball calibration source. From [65].

3.6.1   Laserball

Laserball (LB) is a diffuse light source composed of a dye laser giving selectable wavelengths (between approximately 330 and 620 nm) and transmitting light via optical fibres to a spherical diffuser [83]. It's primarily used for PMT calibration (PCA) and optical calibration. Light is produced by nitrogen laser with width of 0.6 ns [53] located on the deck and transmitted via a quartz optical fibre into a quartz flask. The flask is deployed inside the AV using the manipulator system described before. The flask is a 109 mm sphere with 19 mm neck sheathed by a stainless steel casing to prevent reflected light to enter the AV. It is filled with silicone gel and uniformly distributed 50 μm glass bubbles. The bubbles scatter light from the laser resulting in production of isotropic light. The LB is visualized in Figure 3.11. Photo from the cleaning process is shown in Figure 3.12. The events are tagged through the use of EXTA trigger.

If the LB is positioned in the centre of the AV the light that is emitted arrives at the PMTs at approximately the same time. This allows for extraction of cable delays by comparing the relative time offsets of the PMTs. The whole procedure of PCA is, again, detailed in Chapter 4.

The optical calibration is performed by varying the position, which allows one to determine the attenuation and the angular response of the PMTs [84].

Figure 3.12: Cleaning of the laserball sphere and corresponding parts in the clean room at the University of Sussex.

3.6.2   ELLIE

The ELLIE system as a whole is described here. The calibration procedure using the TELLIE system is described in detail in separate chapter, Chapter 4.

ELLIE system is installed outside the active volume of the detector, mounted on the PSUP. ELLIE was designed to provide calibration of the PMT timing and gain, as well as the scintillator properties. It consists of three subsystems, these are:

- **AMELLIE**: the attenuation module;

- **SMELLIE**: the scattering module;

- **TELLIE**: the timing module.

Each subsystem use electronics mounted on the deck to generate optical pulses, which are transmitted into the AV via optical fibres terminating at the nodes of the PSUP. This is highlighted in Figure 3.13. While TELLIE and AMELLIE share the same control hardware, SMELLIE requires a tightly collimated beam produced by a coherent light source.

AMELLIE

AMELLIE uses LEDs at different wavelengths, injecting light at four different locations, in two different directions. Wide-angle quartz fibres are used to ensure plausible coverage, allowing in-situ monitoring of the stability of attenuation of the scintillator.

SMELLIE

SMELLIE uses four lasers at 375, 405, 440 and 550 nm wavelengths. These are connected via an optical fibre switch to twelve quartz fibres terminating at four different locations. Each fibre is connected to a collimator at the injection point, pointing in three different directions of 0°, 10°and 20° with respect to the center of the detector. The scattering of the scintillator can be measured analysing the position and time of PMT hits relative to the initial beam direction. Multiple injection points and directions serve as check against systematics.

TELLIE

TELLIE uses LEDs at a single wavelength of 505 nm which was chosen to be in the lowest opacity region of the Te-loaded scintillator absorption spectrum [85]. It injects light via 1 mm PMMA[24] fibres into each of the 91 PSUP nodes and one at the neck of the AV. These fibres have wide-angled opening and provide complete coverage of the PMTs.
The exact method of PMT calibration using TELLIE is described in Chapter 4. Due to how important TELLIE is for this thesis, it is described in its own section, Section 3.7.

3.6.3   Supernova source

A source to mimic a possible supernova signal is in development for SNO+. There are two goals for this source: simulate realistic SN neutrino burst to study the detector response, tagging and sensitivity, and to stress-test the DAQ and electronics in order to estimate how close a SN can be to be detected without issues.

The source itself needs to be a high rate, high occupancy optical source. To simplify deployment, the source is based on a laser diode and as such it can be deployed using the laserball. Some characteristics are [86]:

- A 405 nm laser diode;

- A 250 mW, 2 ns pulse;

- A dynamic frequency range of 0.75 Hz to 12.5 MHz;

- A variable energy pulse, up to 60 MeV event simulation;

---

[24]**PMMA** = polymethyl methacrylate, also know as acrylic glass or plexiglas.
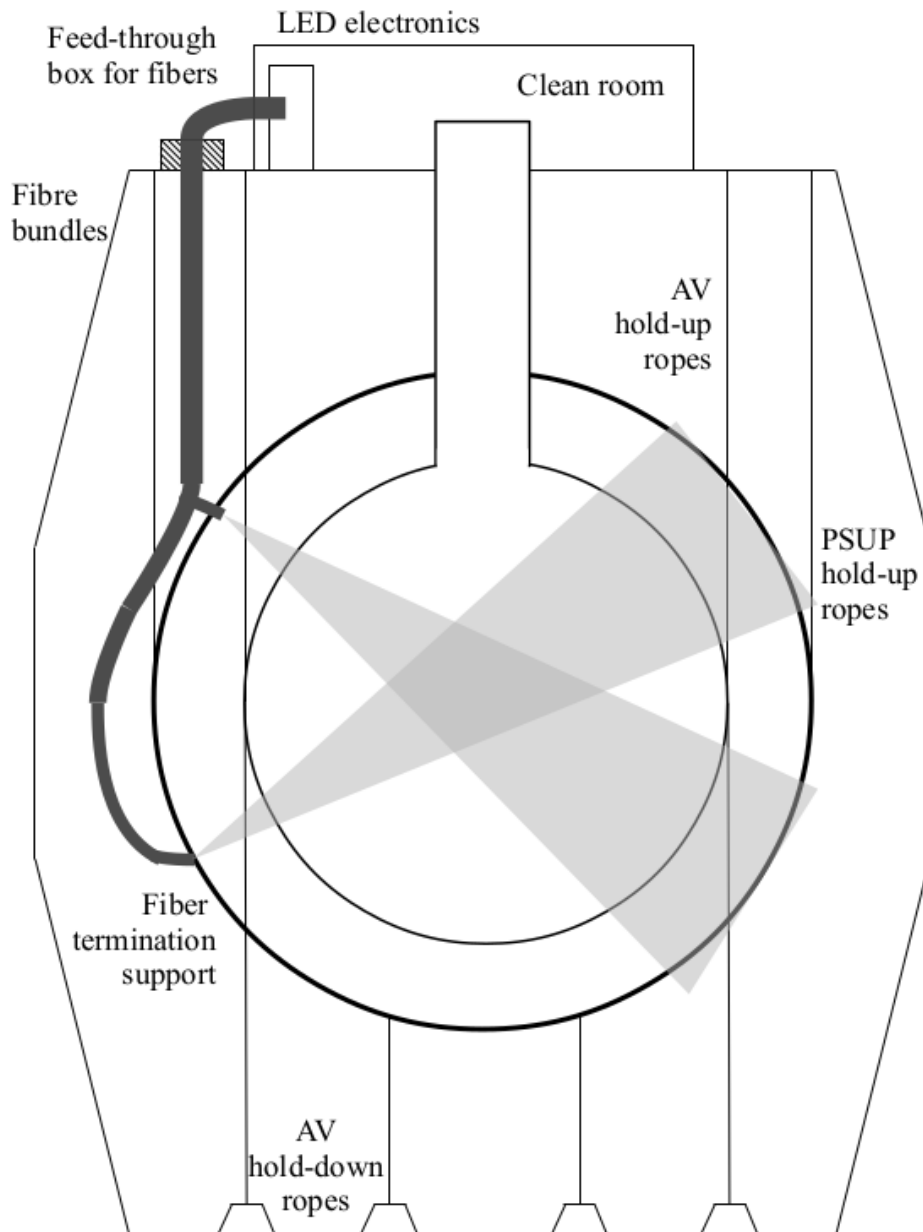
Figure 3.13: Sketch of the SNO+ detector showing the ELLIE calibration hardware on the top deck as well as example light injection points around the PSUP. From [55].
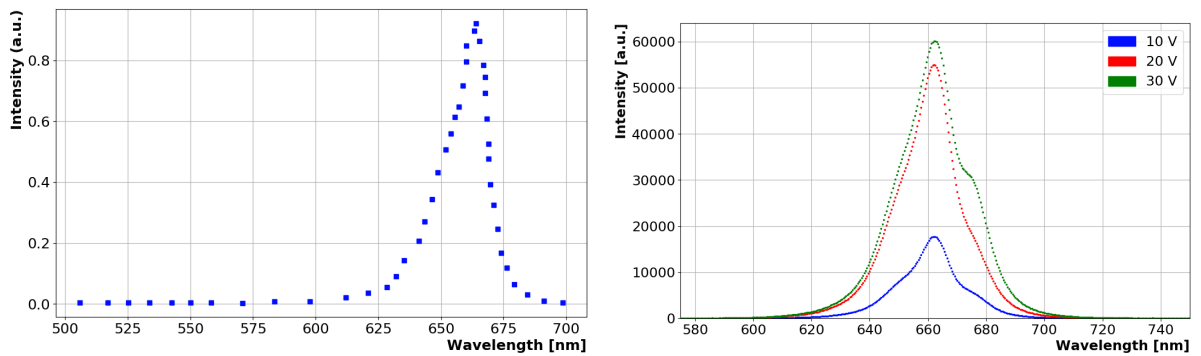
Figure 3.14: UFO wavelength profile: as given by manufacturer (left) and as measured (right).

- It is highly programmable to precisely resemble a SN signal in terms of length and intensity.

The source is nearing completion at this time and is planned to be deployed in near future.

3.6.4 Umbilical Flasher Object

The purpose of the Umbilical Flasher Object (UFO) is to allow for the determination of the position of any source once deployed inside the detector. It should reside at the top of the source connector that connects to the source. The UFO itself consists of eight LED contained within a cylindrical acrylic shell with outer diameter of 63.5 mm, wall thickness of 6.35 mm and length of 45.0 mm [87]. The LEDs will be connected to enclosed driver board that can pulse the LEDs sequentially using an external trigger.

The wavelength of the LEDs is quoted to be 655 ± 5 nm by the manufacturer. It was also measured by author and found to be approximately 661 ± 2 nm. The plots relating to the wavelength are shown in Figure 3.14. The quantum efficiency of SNO+ PMTs is rather low at this wavelength, $< 1\%$, shown in Figure 3.15. Other settings can be varied. The allowed input voltage is 7-30 V, pulse rate of 0.1-55 kHz can be selected, pulse length of 5-20 ns at FWHM can be obtained [87].

The procedure should be such that the cameras deployed on the PSUP can see the pulses emitted by the UFO without the light affecting the PMT data. Measurements of the expected radioactivity were done and the UFO is expected to emanate approximately one radon atom per day of deployment in LAB [87].
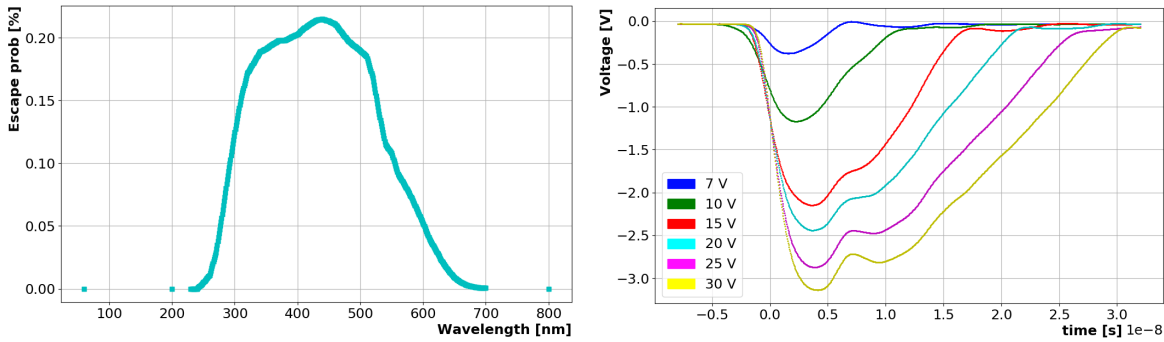
Figure 3.15: Left: The quantum efficiency of SNO+ PMT. The escape probability is very low at around 665 nm, the wavelength of the UFO. Right: The pulse shape of the UFO LED as a function of voltage.

UFO profiling

In addition to already mentioned spectroscopy measurement[25] (Figure 3.14), a pulse shape measurement[26] (Figure 3.15), and a profiling analysis of the UFO were performed by the author. The purpose was to evaluate the optical properties of the LED and gain understanding of the characteristics of the UFO device as the input parameters, such as frequency and voltage, change.

The set-up for the measurement is shown in Figure 3.16 while a photo from the measurement is shown in Figure 3.17.

The devices used for the measurement were:

- The UFO, specifically its LEDs: Brite-LED Optoelectronics part BL-LUDR5N15C-NB;

- The integrating sphere: Thorlabs IS126A;

- The photodiode: Thorlabs SM05PD1B;

- The photodiode amplifier (as power output measuring device): Thorlabs PDA200C;

- An external power supply;

- An external pulse generator;

- The corresponding cables.

---

[25]The LED spectroscopy was done using the Oceanoptics Maya 2000 spectrometer.

[26]The LED pulse shape was measured using a Thorlabs Photosensor H10720 series module.
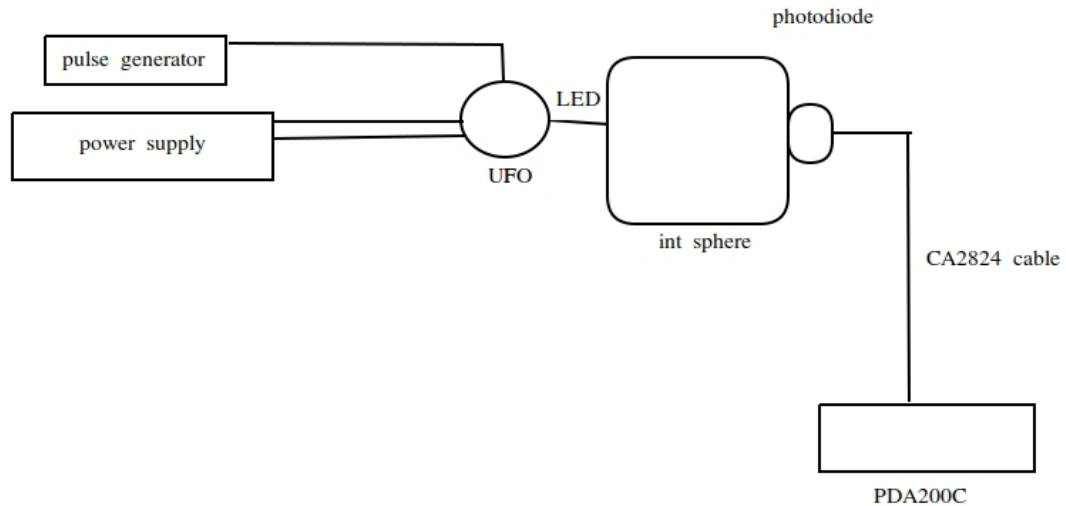
Figure 3.16: A sketch of the UFO profiling measurement set-up.

As can be seen in the sketch, the power supply and pulse generator were used to modify the input parameters. The LED was plugged into the integrating sphere. The measure of the light intensity was taken by the photodiode. The signal was amplified and a result given by the amplifier.

During the measurement, the pulse amplitude was alternated between 7 and 30 V, and wide range of frequencies was scanned, from 0.1 to 55 kHz. Other settings, such as the pulse width and the rotation speed, were kept constant.

To convert the measured value given by the amplifier to power output P, the current I was divided by the photodiode responsivity constant c. The result was divided by the frequency f to obtain the power per pulse. The equation used was [88]

$$P[\text{W}] = \frac{I[\text{A}]}{c[\text{A/W}]} * \frac{1}{f[\text{Hz}]}.$$

The photodiode responsivity constant was given by the manufacturer as 4.859×10^{-4} A/W at 655 nm.

Finally, to calculate the number of photons, the power obtained above had to be divided by the energy of each photon. The photon's energy is given by the usual Planck-Einstein relation

$$E = h * \frac{c}{\lambda},$$

where E is the energy of the photon, h is the Planck's constant, c is the speed of light, and λ is the wavelength of the photon. The resultant number of photons N is calculated by simple division: $N = \frac{P}{E}$.
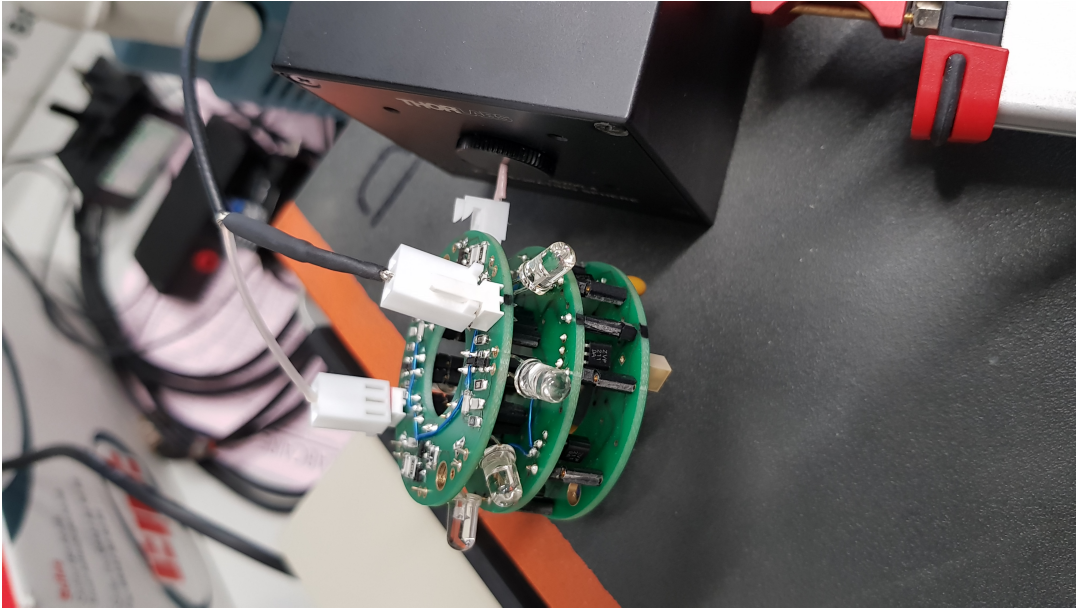
Figure 3.17: A picture of the umbilical flasher object connected to the integrating sphere during testing at the University of Sussex.

The important results of the study are shown in Figure 3.18 and Figure 3.19. The first figure focuses on the power output as a function of frequency, with higher sample rate at lower frequencies which represent the probable use case. The UFO was found to accurately follow a linear fit shown in the figure.

The second figure presents the measured number of photons generated by the UFO as a function of frequency for different voltage cases. The expected voltage setting for the UFO is 7 V. The number of photons generated by the UFO clearly increases with increased voltage, as is expected. There is a liner drop in the number of photons as the frequency increases. This trend seems to be generally quite stable and only changes slightly over the whole range of voltages.

More details of the measurements, more results, as well as results of the simulation testing can be found in [89].

3.7   TELLIE

This section describes the timing module for the ELLIE system, TELLIE. A brief overview of the system and its parts is followed by a small report on hardware maintenance and stability testing.
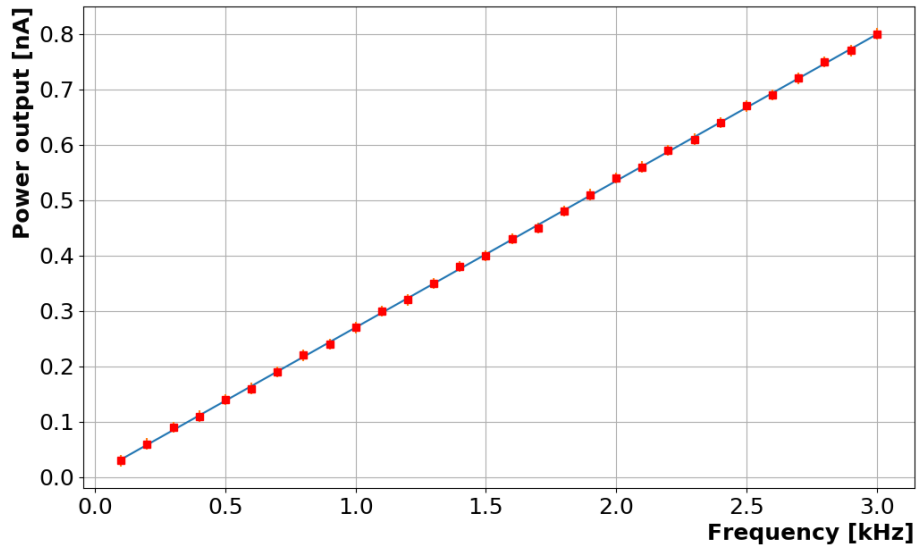
best fit: y= 0.136151320501 * x + 0.072342258529
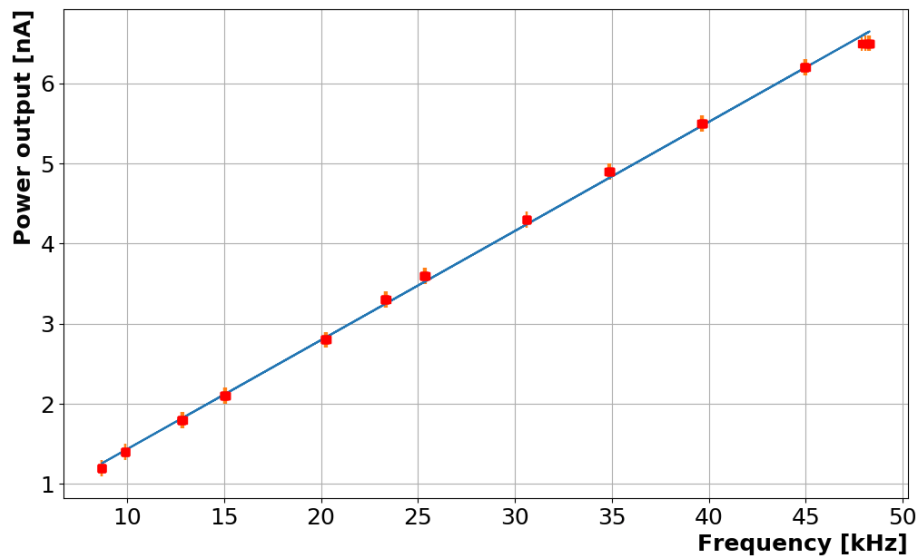
Figure 3.18: UFO profiling: power output as a function of frequency. Top plot focuses on small frequencies that are the expected frequencies to be used for UFO running.
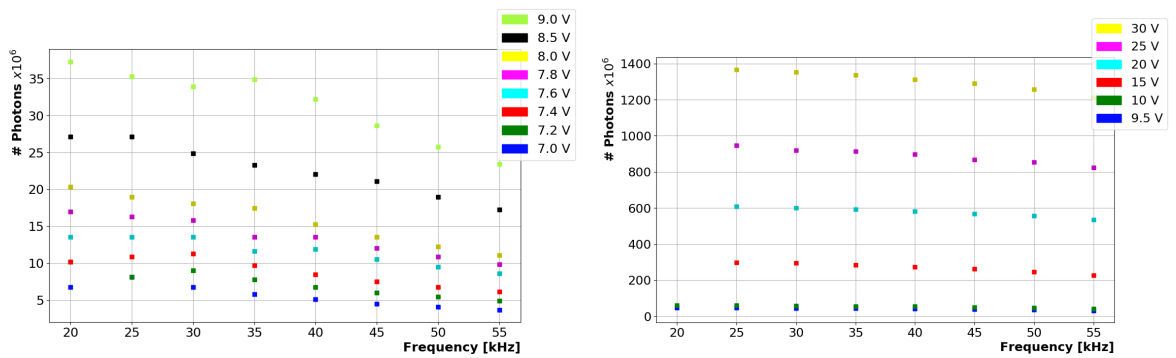
Figure 3.19: UFO profiling: Light intensity (expressed as the number of photons) as a function of frequency. Data for various voltage settings are shown.

3.7.1   Purpose and requirements

The TELLIE system was designed and built to allow one to obtain frequent timing and gain PMT calibration and monitoring of the data without the need to deploy a calibration source inside the detector. Two main time constraints for the light signal are the scintillator decay time - which for the LAB/PPO combination used in SNO+ is 4.6 ns [55] for the fast component - and the SPE PMT resolution - which is 1.7 ns [53] for SNO PMT, dominated by the transit time spread. Due to these constrains, the PMT time calibration accuracy goal was set at 1 ns such that it is insignificant compared to the other dominant factors.

Regarding technical parameters, the system was designed such that [55]:

- The light spectrum should be detectable in all operating phases;

- The produced pulses must be fast enough to ensure the measurement of the time offset of all PMTs can be done to a precision of 0.5 ns;

- The intensity should be able to provide SPE pulses in varying conditions of optical attenuation;

- The range of frequencies should be wide enough to allow for constant monitoring at a low rate (10 Hz) as well as during faster dedicated runs (up to 10 kHz);

- The angular emission profile must be such that all PMTs are sufficiently illuminated and there is plentiful overlap between different injection points (this is required to obtain offset between LEDs, a requirement for calibration, please see Chapter 4);

- Because the fibres - once installed in the cavity - won't be easily accessible, there should be redundancy allowing the system to be used for its purpose even if some fibres fail;

- The materials must be compatible with surroundings and other parts of the detector and the radioactivity must be negligible;

- The system must interface with existing SNO+ trigger and acquisition framework.

All of these requirements were met for the TELLIE system. 95 fibres are installed across 91 nodes spread around the PSUP plus additional neck node, shining light towards the centre of the detector. The fibres have wide aperture of $14.5°$ / $11°$ at 20% of the maximum intensity in air and water respectively [55]. Each fibre is a double cable to have enough spares in the case of breakage.

TELLIE and laserball It should be restated, that TELLIE and laserball are complimentary calibration sources for the timing response of the PMTs. TELLIE requires previous deployment of the laserball in close time proximity, so that the relative offsets between the different LEDs can be known precisely. After the PMTs are properly calibrated by the laserball, TELLIE can be used for recalibration of the PMTs. This was the original intend when designing TELLIE as to minimize the number of deployments of the laserball, as every deployment inside the AV increases the risk of contamination of the scintillator. TELLIE - being mounted externally - does not posses such risk. As such, TELLIE decreases the frequency required to deploy the timing calibration sources inside the AV, minimizing the risk of contamination, and maintaining the high cleanliness that is required for the SNO+ experiment. Both sources are used by the experiment.

Hardware The hardware used for TELLIE can be divided into in-situ (located inside the cavity) and ex-situ (on the deck) components.

3.7.2 Ex-situ hardware

The ex-situ hardware consists of 96 LED driver boards that produce the optical pulses arranged into boxes of 8 channels[27] (12 boxes total). 95 of these are used for calibration - shine light inside the detector - while the last one is used as a control. Additionally, there is a power box containing the custom power unit distributing DC power to the system and a control box. The control box is a the interface between TELLIE and it's control software, communicating with the individual drivers [90]. All of these parts are mounted on the ELLIE rack.

The light produced by the LED travels through three PMMA optical fibres. First connects the LED to a port on the output of the LED driver box (0.75 m, see Figure 3.23), second fibre connects this output to a patch panel (2 m) and the third connects the patch channel to the PSUP node (45 m) [90]. The patch channel serves as interface between in-situ and ex-situ components. A feed through box was added to minimize light leakage handling the 45 m fibres into the cavity.

Control box

The control box handles the control of the TELLIE hardware. At the heart is a Peripheral Interface Controller (PIC) chip compiled with instructions needed to operate TEL-

---

[27]Regarding the TELLIE system, channel and fibre are often used interchangeably.
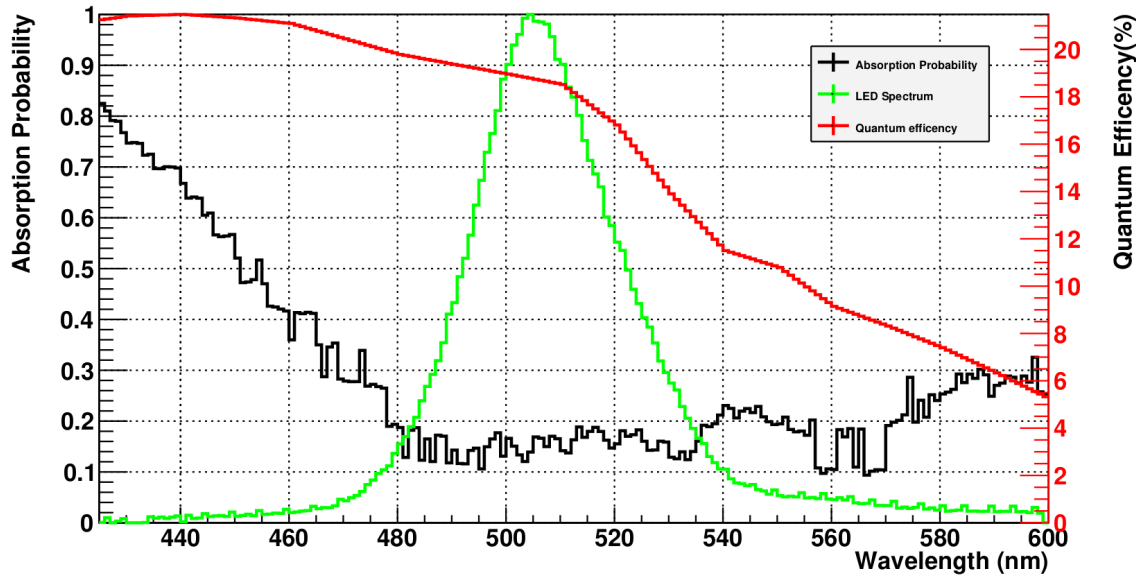
Figure 3.20: The probability spectrum of absorption of ^{130}Te doped LAB/PPO mixture (black), the average spectrum for all 96 LEDs as measured at Sussex (green), and the SNO+ PMT quantum efficiency (red). From [90].

LIE. There is an additional python wrapper that makes it more user friendly to send commands and receive responses from the control box. Ordinarily, the wrapper runs on a server underground that is accessible to ORCA, and therefore the control of TELLIE is available within the software controlling the detector. It is also possible to control TELLIE manually via a direct USB connection.

LEDs

Due to the requirements of the system, there are two important characteristics of the LED to be used. The time profile of the pulse needs to be as short as possible and the wavelength should be chosen to minimise scattering.

The wavelength was chosen to be 505 nm. This is a result of minimising the scattering in scintillator but still being in a range of high enough quantum efficiency of SNO+ PMTs. This is highlighted in Figure 3.20.

Regarding the speed of the pulse, considering both the rise time and fall time, the resistance of the LED is the most important parameter. The full description of this is available in [90]. The LEDs in use are BL-LUCY5N15C from Bright LED with differential resistance of only 10 Ω. The typical resistance of a LED is between 40 and 100 Ω [90].
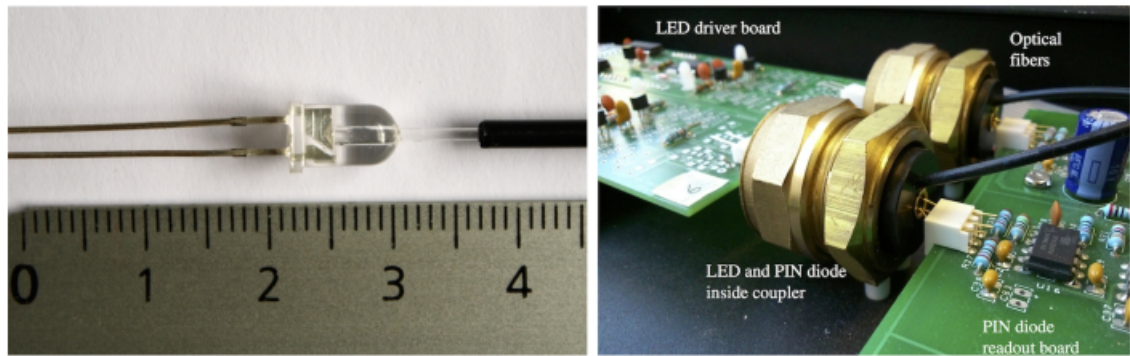
Figure 3.21: Left: Drilled LED with coupled optical fibre (rule in cm). Right: Brass cone coupling device containing the LED and the photodiode to monitor the light intensity per pulse. From [90].

To maximise optical transmittance each LED is hand drilled providing a socket into which an optical fibre of 1 mm is fixed. Optical glue as well as the brass cone[28] are used to provide a light tight environment and increase the mechanical stability. The coupling as well as the brass cone are shown in Figure 3.21.

LED drivers and PIN boards

The LED driver is capable of producing pulses with intensities between 10^3 and 10^6 photons per pulse, with pulse widths of 4.4 and 7.0 ns respectively, and has a maximum operating frequency of 136 kHz.

As mentioned, TELLIE channels are located in boxes. Each box hosts 8 channels. Channel, in this case, corresponds to a driver coupled to an LED, which itself couples directly into a 0.75 m optical fibre. These drivers are mounted on a motherboard that has a connection to the control box. Each LED is contained within a brass cone. A PIN diode[29] is mounted at the opposite end of the cone. The aim of the PIN diode is to monitor the light output of the LED at each pulse. Finally, there are two PIN boards inside the box, each connecting to four corresponding PIN diodes. A schematic of the set-up inside the driver box is shown in Figure 3.22. A photo of one TELLIE driver box is pictured in Figure 3.23.

---

[28]**The brass cone** used in TELLIE is not a perfect cone but has somewhat conical shape. The name is used throughout.

[29]**A PIN diode** is a diode with a wide, undoped intrinsic semiconductor region between a p-type semiconductor and an n-type semiconductor region.
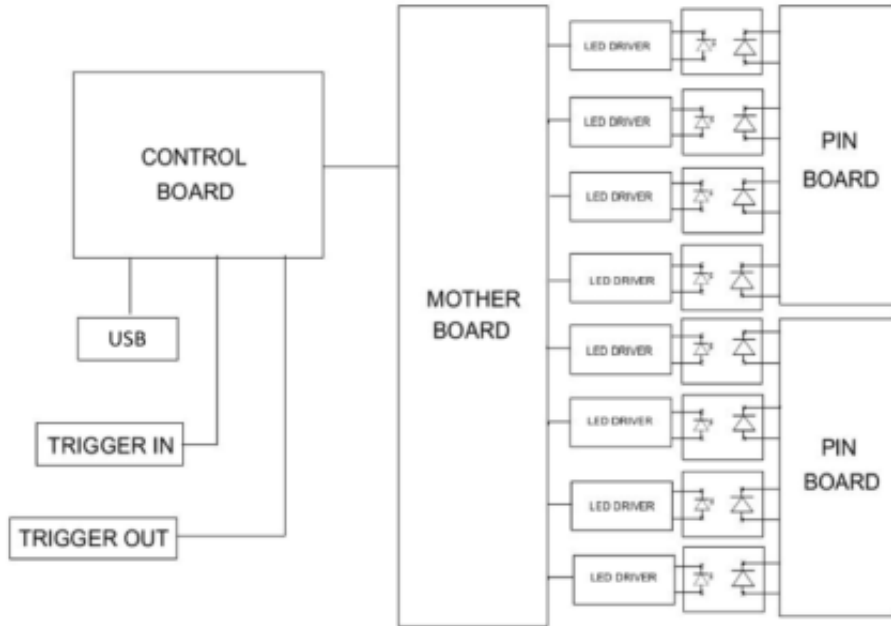
Figure 3.22: A schematics of the TELLIE driver box showing the basic connections to the control box and the position of the PIN diode boards monitoring LED output. Plot from [90].
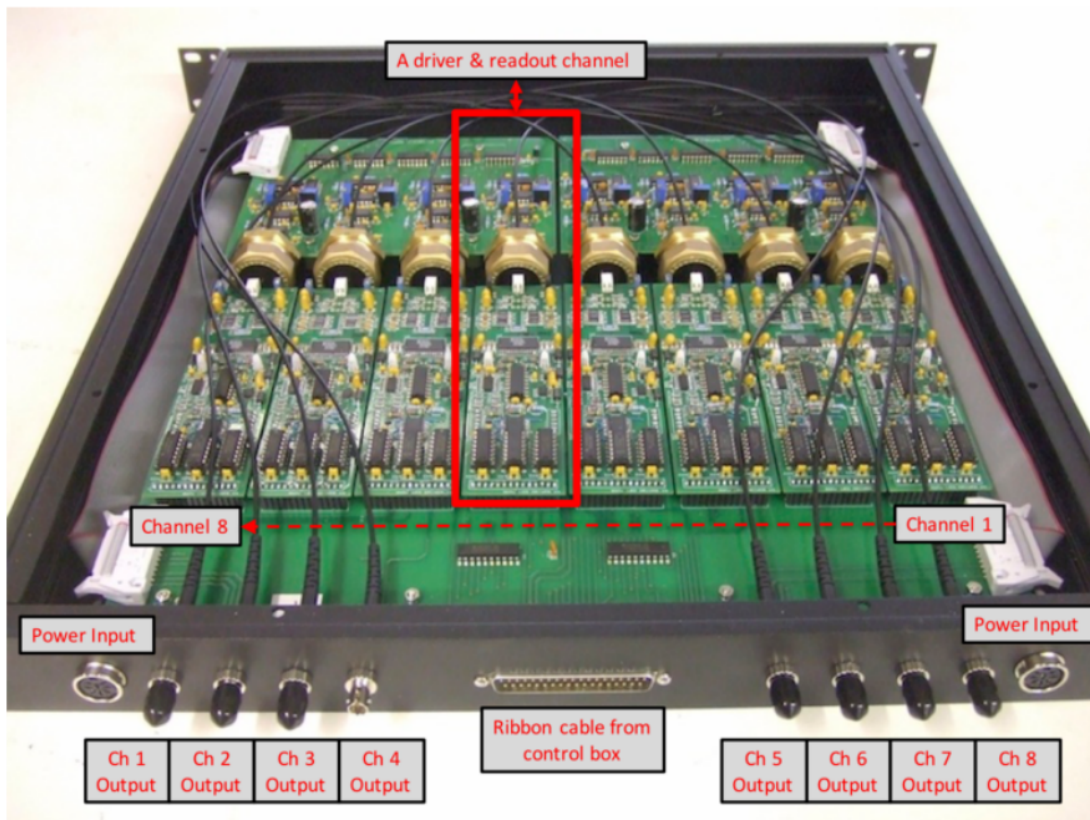
Figure 3.23: A photo of TELLIE LED driver box. A single TELLIE channel is highlighted in red. The internal 0.75 m long optical fibres can be seen connecting the LEDs to the output ports. Plot from [90].

The driver boxes are connected to the control box via a ribbon cable. Up to seven boxes can be daisy-chained onto single ribbon cable. The control box has two ports for ribbon cables, making it possible to connect up to 14 boxes. This also divides the set-up. The control box is in the middle of the rack, 7 driver boxes are connected via single ribbon to the bottom ribbon cable port and 5 more are connected to the top. A photo of the TELLIE rack is shown in Figure 3.24.

Each PIN diode contains two potentiometers. These allow oe to set the PIN's gain and sample point. In ideal scenario the gain would be set such that it is sensitive to low light levels without saturation at higher intensities. Because of the wide range of intensities, this is not possible. Therefore, the gain is optimized for sensitivity at low light output, which is the expected range for normal TELLIE operation.

3.7.3   In-situ hardware

As mentioned, the in-situ ELLIE hardware is any hardware that is inside the SNO+ cavity. This includes [90]:

- 110 45 m long duplex[30] PMMA optical fibres[31] that guide the light from the patch panel on the electronics deck to the fastening points on the PSUP;

- The feed-through-assembly which provides a light-tight seal for passing the optical fibres from the deck into the cavity;

- The mounting plates which the fibres couple into, mounted on the PSUP nodes.

The placement of the fibre system is determined by the requirement of providing a coverage of the PMTs as uniform as possible. To summarize, 95 fibres in total are installed onto 91 available nodes on the PSUP and one neck node. The positions of TELLIE channels on the PSUP are shown in Figure 3.25.

3.7.4   Operating modes

There are two modes of operation available for TELLIE [90]. These are:

- **The asynchronous mode** (master mode): the source of the signal that is used to trigger light generation is internal, within the control box;

---

[30]As mentioned, each fibre contains two strand fibres, it can be regarded as two cables.
[31]The additional fibres are spare.

Figure 3.24: A photo of the TELLIE rack. The control box is in the middle. Two ribbon cables are connected to the control box, one connects to 7 TELLIE driver boxes below it, other one connects to 5 TELLIE boxes and 1 AMELLIE box above it. A power box is at the very top, distributing power to all other boxes. Green tags are marking the optical fibres, with their corresponding ID number. The numbering ensures that the fibres are re-plugged to the correct channel output, if they need to be unplugged. Blue tags mark trigger-in and trigger-out cables. The USB interface cable is also visible connecting to the control box.
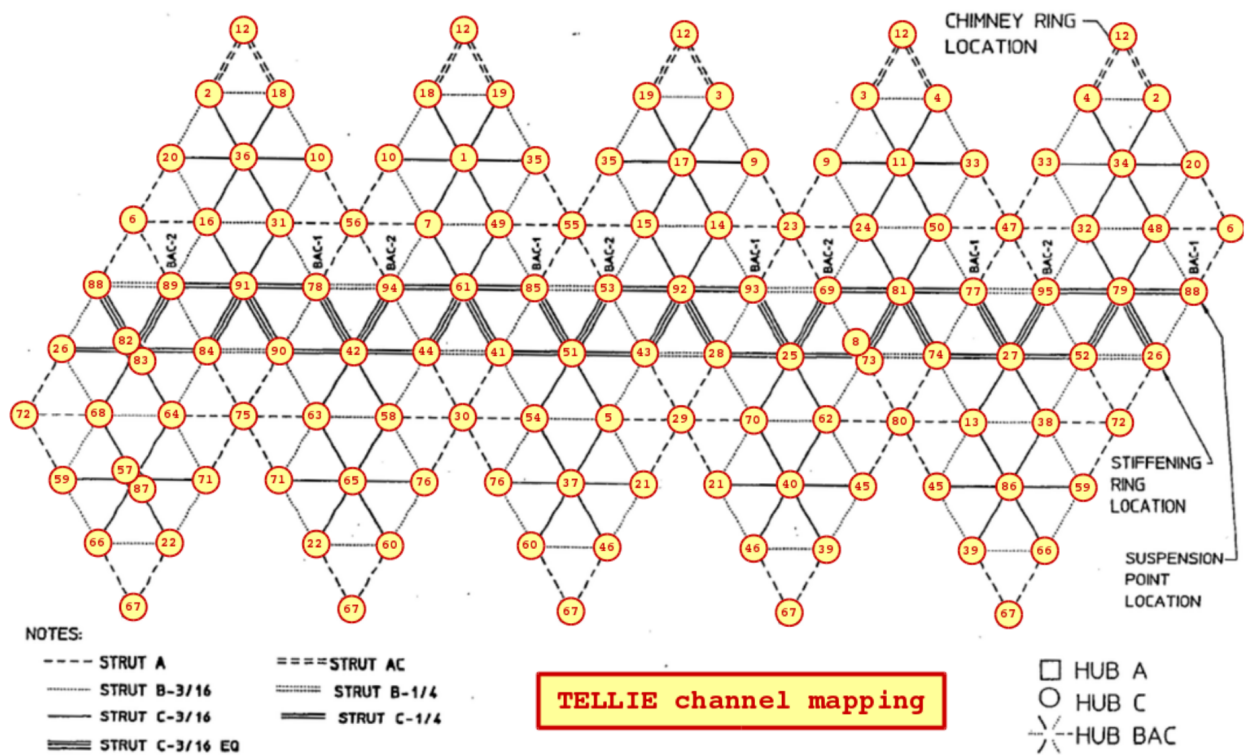
Figure 3.25: Schematics of the SNO+ PSUP structure, numbering TELLIE channels in relation to the PSUP nodes they are mounted on. Because there are 95 fibres connected to 92 nodes, three nodes have a second fibre installed for redundancy. Plot from [90].

- **The synchronous mode** (slave mode): the primary signal is generated by TUBii using dedicated trigger out channel. TUBii also distributes the 50 MHz lock to the rest of the detector. In this case, TELLIE's response can be synched with the detector system.

3.7.5   Run-level parameters

There are several I/O parameters that can be set. These are:

- The **number of pulses**: simply the number of light pulses to be generated by the LED;

- The **trigger delay**: a customizable time delay, used to centre the generated optical pulse in the SNO+ event window;

- The **delay between pulses** (master mode only): the temporal separation between subsequently generated signals;

- The **channel selection**: selection of the TELLIE LED driver channel to generate light;

- The **pulse height**: the amplitude of the pulse, always set to maximum due to inconsistencies between different boards;

- The **pulse width**: also called *the internal pulse width I_{PW}*, the only parameter that is varied to influence the light generation of the channel, inversely proportional to the light intensity;

- The **fibre delay**: channel dependent delay with the purpose to compensate for the board-to-board variations in time between a primary signal being received at the control box and light being produced at the requested channel (detailed in Subsection 4.4.1).

A XSNOED view of single TELLIE run is shown in Figure 3.9. More examples and details are presented in Chapter 4.

For more details on TELLIE hardware, please see [90]. For more details on TELLIE and how to run it, please see [85]. Report of the commissioning is available in [91]. Monitoring of the AV using TELLIE is available in [43] and [59].

The rest of this subsection will focus on changes and studies done on the system between 2018 and 2020 by the author. Most of the changes are general maintenance, some changes were attempted to improve the stability of the system, mostly to do with grounding and isolation.

3.7.6 Hardware maintenance

This subsection briefly describes the type of hardware maintenance performed with the system.

PIN board replacement

In some cases a channel can report zero PIN reading while still producing light. This is a sign of an issue with the PIN board reporting on the light intensity. In this case, the PIN board either needs a re-seat[32] or a complete swap for another functional board. This is quite rare and is easily fixable, the biggest issue being the access to the PIN board. The procedure requires accessing the DCR, disconnecting the board containing the PIN board in question, removing and opening the board, and finally either re-seating or swapping the board. Afterwards, the fixed board needs to be re-calibrated to optimize the PIN diode gain. Because there are four channels per PIN board, all connected channels require recalibration. The recalibration process is described in [92]. The report of one such process is available in [93].

Driver board replacement

Occasionally, there is a malfunctioning driver board for a TELLIE channel. This can usually be seen using monitoring software that reports on the status of TELLIE running (this monitoring is described in Subsection 4.7.1). A clear signature of the faulty driver is unstable light output over time. As is the case with the PIN boards, the driver boards usually need a simple re-seat, in rare cases a swap. It should be mentioned that the LEDs are always kept in place due to their coupling to the fibres, only the driver board for the channel is manipulated with. The modular design makes this quite a simple task. One such change is reported in [94]. A comparison of the stability of the light output of a single channel before and after such operation is shown in Figure 3.26.

---

[32]A reseat in this case represents brief unplugging and replugging of the hardware.
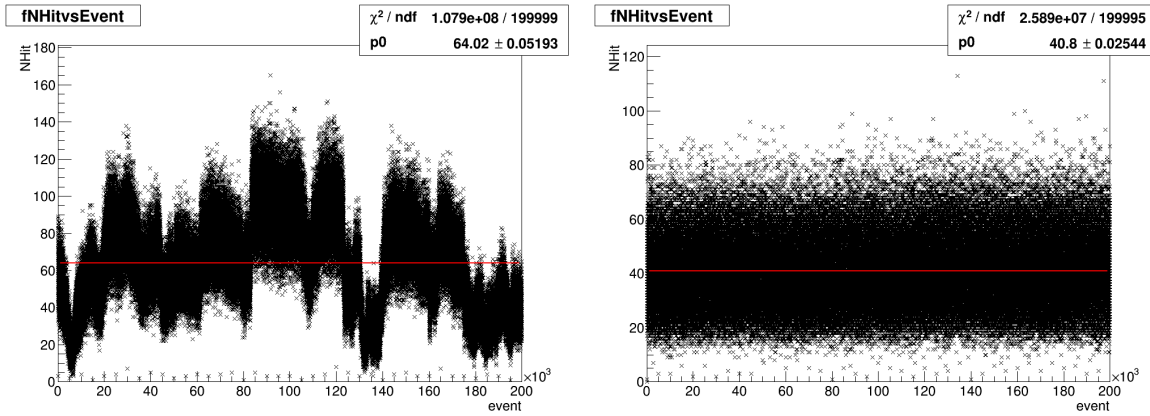
Figure 3.26: Comparison of the TELLIE driver light output stability before (left) and after (right) re-seating.

Figure 3.27: A picture of the isolated TELLIE ribbon cable, July 2019.

Ribbon cable isolation

In July 2019 the ribbon cable connecting the TELLIE driver boxes to the control box was isolated using electrical insulation shielding tape. The goal was to test the effect of isolating the ribbon cable on the amount of noise and the stability of the system. No significant change was found, leading to the idea of isolation board, detailed in Subsection 3.7.8. The report of this operation is in [95]. A photo of the isolated ribbon cable can be seen in the Figure 3.27.

Fuses isolation

There was an intensity drop found while collecting one of the PCA datasets with TEL-LIE (please see Chapter 4 for details). One of the fuses was found to be defective and

Figure 3.28: A picture of the TELLIE fuses after isolation work, March 2020.

was replaced. In addition to that, electrical tape was applied to isolate the contact points between the fuse holder and the fuse itself, for all fuses in the power box. This was done in order to prevent the fuses from shorting accidentally. This was not likely at all, but the addition of the tape makes it even less likely. This is reported in [95].

At later time, the fuses were routed outside of the power supply box via holes on the front panel of the box. These holes were previously intended for other type of fuses and were unused and covered by plastic plugs. The plugs were removed and fuses were fed through the holes. This serves two purposes. One, the fuses can be easily replaced if needed, without the need to work with an open power supply. Two, the fuses are to be replaced with smart fuses indicating whether they have blown. The new position of the fuses makes it very easy to spot this. The report of this work is in [96]. A picture of the remounted isolated fuses is in Figure 3.28.

3.7.7 Stability testing

There were few stability studies performed on the TELLIE system directly at the place of deployment, underground on the SNO+ deck.

Power cycle study

A simple study was performed to measure the effect of power cycling the TELLIE rack on the stability of light generation. The method of testing was to: power cycle the rack, run single channel at specific settings and monitor the PIN response, wait for 10 minutes, rerun the same channel at the same settings. Repeat the measurement.
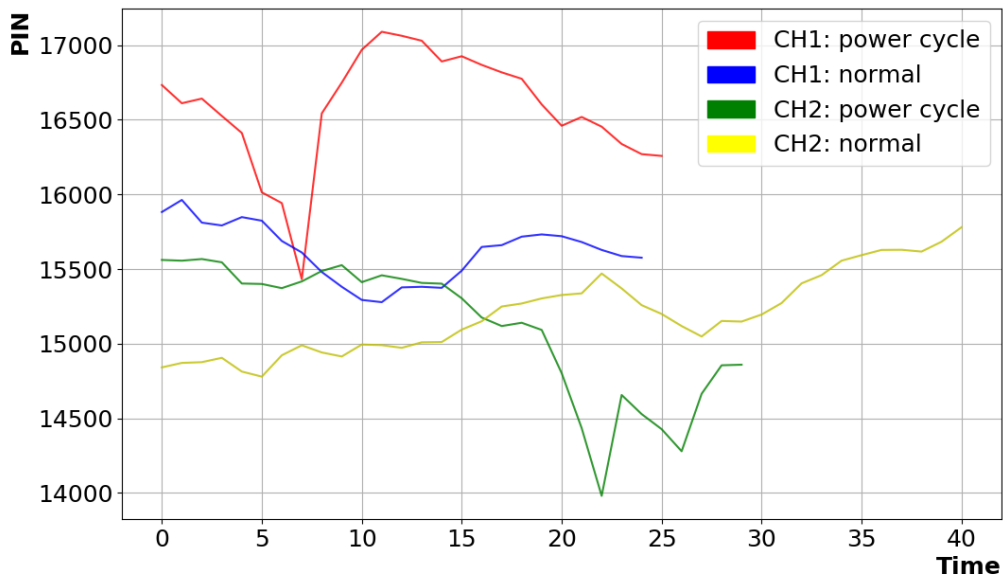
Figure 3.29: Result from the TELLIE power cycle study. The data is collected from a single channel immediately after power cycling and 10 minutes afterwards. The measurement was repeated one more time. The time is in arbitrary units, each unit roughly corresponding to two seconds.

The results of the study are shown in Figure 3.29. A visible difference was found for the two cases. The PIN response is a lot more stable after the waiting period. The study does not bear high statistical significance. Additionally, TELLIE is almost exclusively run after being powered on for a long time and it is suggested to continue to do so. The variation in the PIN response is expected to improve after the installation of grounding straps and isolation boards, Subsection 3.7.8.

Isolation study

The aim of the isolation study was to see whether TELLIE performs differently when only one driver box is connected to the control box and the power box when running. In normal conditions, all boxes are connected together via the ribbon cable, and all boxes are connected to the power box via individual power cables.

The method of testing was again quite simple: two channels were selected - one known stable and one recently found unstable - and run in the usual conditions with the whole rack connected up. Afterwards, each of the two channels was run in isolation - other boxes were disconnected both from the control box and from the power box. The PIN values were recorded.
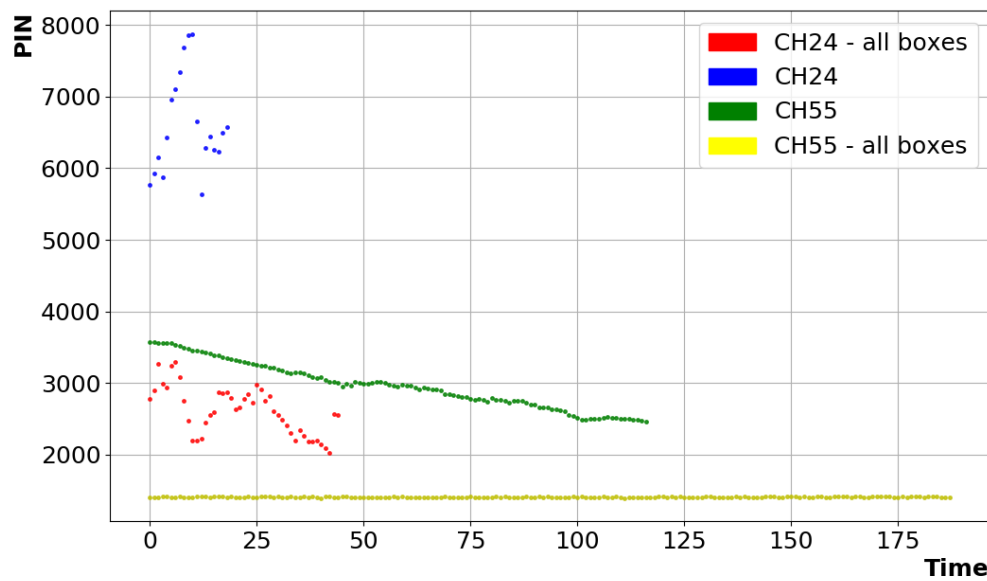
Figure 3.30: Result from the TELLIE isolation study. Two channels tested in two scenarios: isolated and in normal condition (marked as 'all boxes'). Time in arbitrary units.

The results of this study are presented in Figure 3.30. There is a clear difference between the isolated case and the normal case. For both channels, the PIN values were shifted to much higher values when isolated. On the other hand, the case where the channels where run in normal conditions, the variation of the PIN values seemed to be lower. In any case, this result was another motivation for development of the isolation boards and grounding straps.

Long term running study

Another study was performed to see the effect of running a single channel for prolonged period of time. This could point to mode effects, effects of warming or issues with discharging.

The method of testing was to disconnect a single TELLIE channel from the optical fibre connecting the channel to the patch panel. This way no light was going to leak inside the detector. Then, this channel was run continuously using constant settings for several hours. Again, the PIN values were recorded.

The results are shown in Figure 3.31. It is clear that the PIN values drift over time. This is believed to be a consequence of the changes in voltage. Since the PIN diode signal is amplified by two op-amps any small change in voltage can result in a shift of the PIN reading [43]. This should, again, improve with the installation of grounding straps and
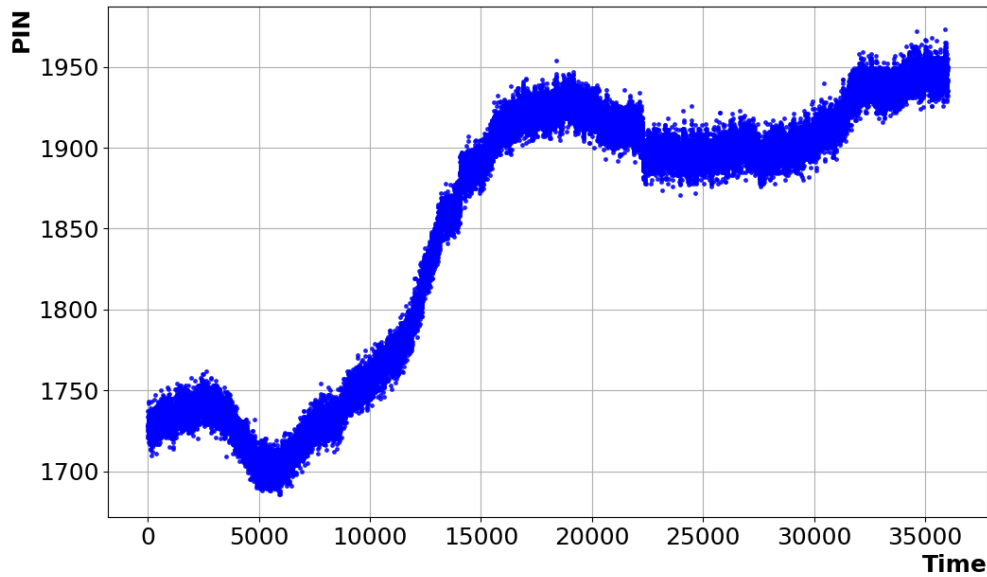
Figure 3.31: Result from the TELLIE long running study. Time is in arbitrary units, the whole range roughly representing approximately 30 hours. Visible shifts in the PIN readout can be observed over time.

isolation boards. It should also be mentioned that the normal data collection for dedicated PCA running requires single channel to run for few minutes only. On this scale, the shifts in PIN are slight. Additionally, the change in PIN value of 200 corresponds to quite small change in actual light intensity.

3.7.8   Isolation boards and grounding straps

Two improvements were researched, designed and built[33] for the TELLIE system: the grounding straps and isolation boards. The general goal of both is to improve the stability of the system and minimize any potential noise. These are described below.

Grounding straps

The aim of the grounding strap is to ground the bottom panel of the TELLIE driver box to a common ground. The panels on the boxes themselves are not shorted together due to non-conductive paint coating. This results in the box and the cones connected to it to potentially experience a floating potential that can negatively impact the PIN diode. The idea is to install a strap inside all TELLIE boxes, connecting the motherboard - which is grounded to the power supply - and the bottom panel of the box. This is shown in

---

[33]The idea and supervision by Simon Peeters, design and build by Antony Earle, testing by the author.

Figure 3.32.

Isolation boards

The isolation board is to be installed between the ribbon cable and the port for it on each TELLIE driver box as well as the control box (every single ribbon connector). The goal is to isolate these ribbon connections. It is believed that the ribbon cable, in its current deployment, creates a ground loop scenario between the boxes and the power supply, creating unwanted interference. A single isolation board is also shown in Figure 3.32.

Both grounding straps and isolation boards were already produced at the University of Sussex. Preliminary results of local testing can be found in [97]. More detailed description can be found in [98]. These were supposed to be installed underground in April 2020, however, due to the global pandemic, the deployment was delayed and has not been possible before the submission of this thesis.

3.7.9 Database tools

In addition to the hardware maintenance, a summary of the ELLIE inventory underground was made. A complete list is available at [99].
Each TELLIE part is assigned an ID. This includes LED drivers, LED cones, PIN boards and motherboards. A summary of the part IDs in the way they are currently installed was collected. The full list is available at [100].

The collected IDs as well as new calibration data for the channels were updated in the CouchDB database. Python scripts that can both load from and upload data to this database were created and made part of the common TELLIE repository. An example output using these database scripts for a single TELLIE channel is shown in Figure 3.33.

For future reference, a debugging guide was also made. It is available at [101].
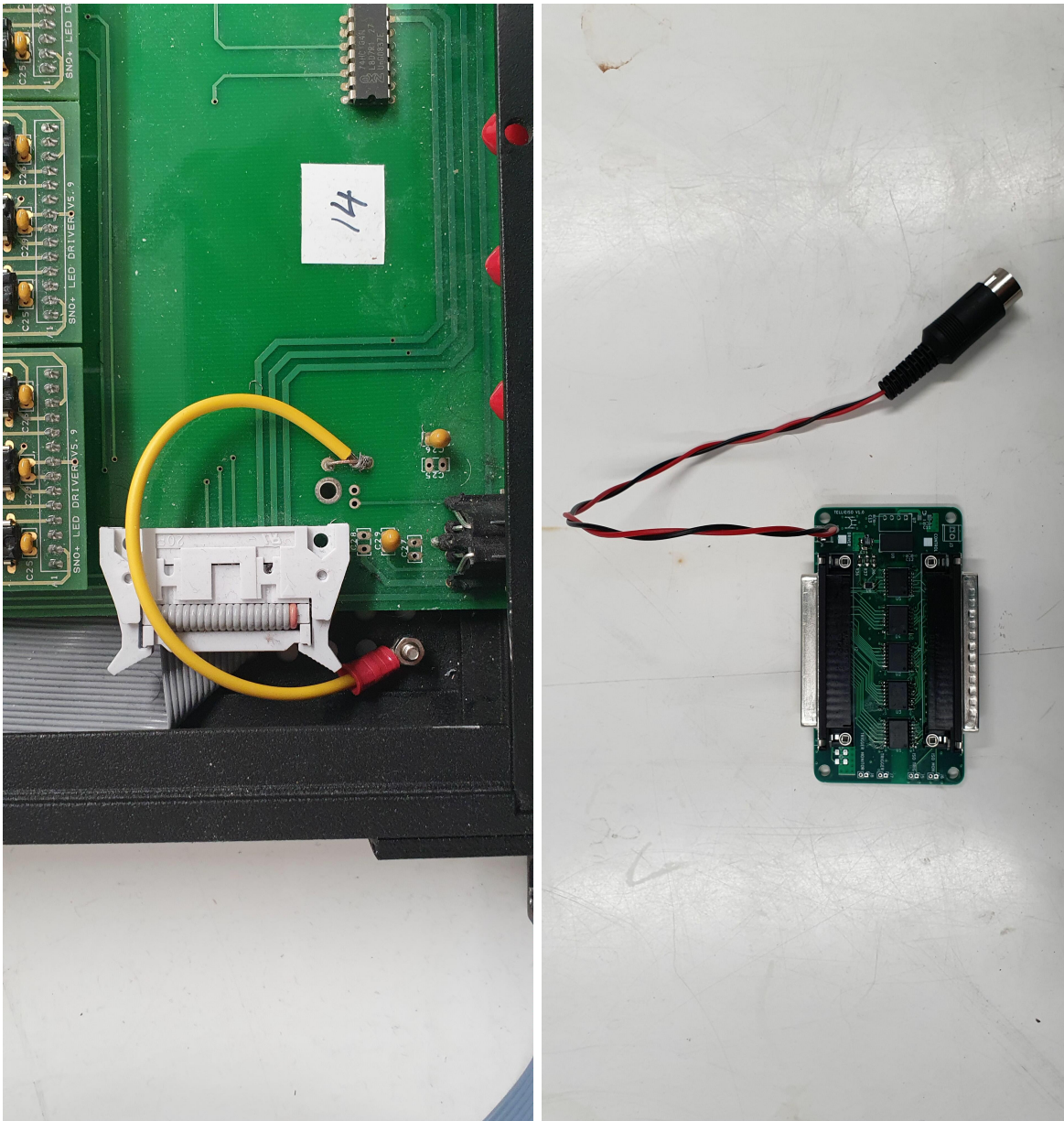
Figure 3.32: A picture of the TELLIE grounding strap (left) and TELLIE isolation board (right). Both are to be installed for the TELLIE system once possible. The goal is to improve the stability of the system and minimise interference.
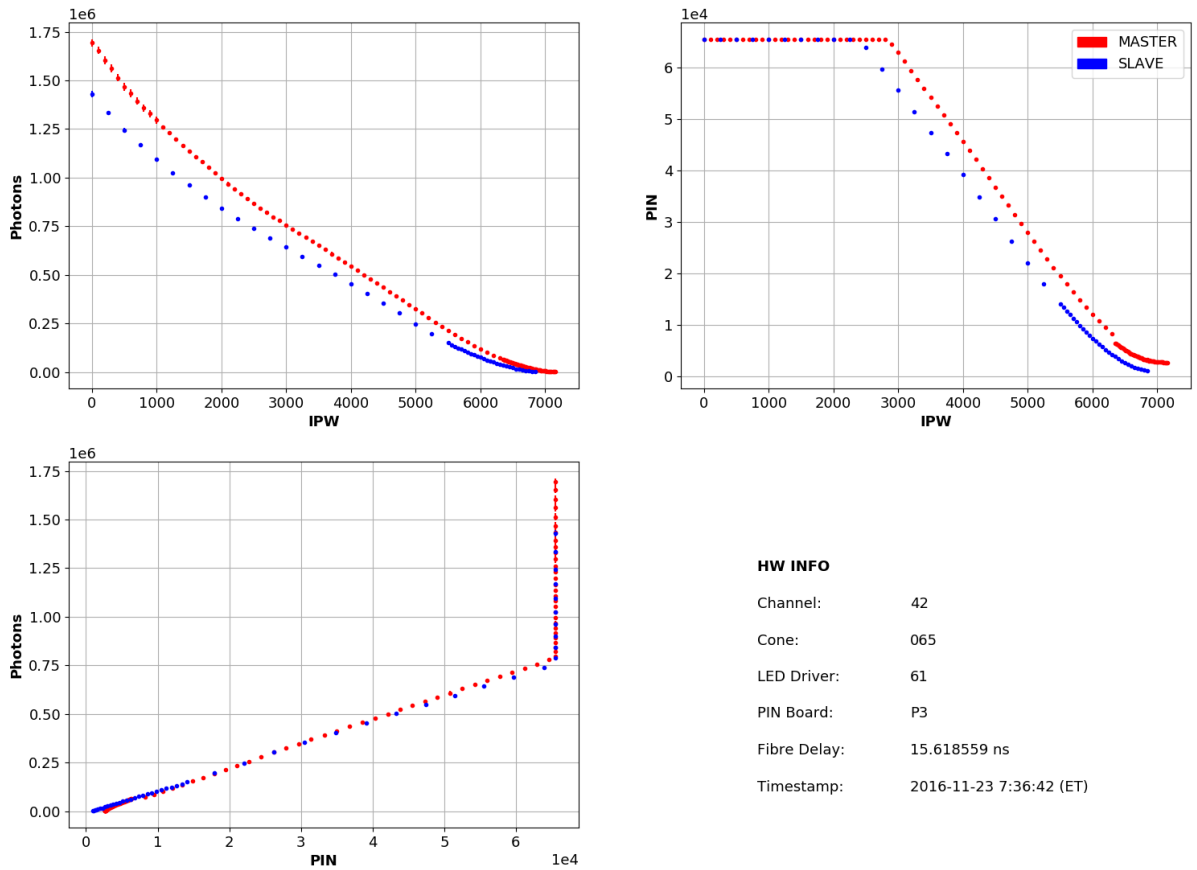
Figure 3.33: An example output using TELLIE database scripts. Everything known about selected channel is loaded from the database and presented. The data includes: basic description (such as the channel number, cone, driver and PIN board ID, the fibre delay) and profile data for this channel (this includes IPW to PIN, IPW to photons, and PIN to photons profiles).

Chapter 4

PMT Calibration

The most incomprehensible thing about the world is that it is comprehensible.

ALBERT EINSTEIN

4.1 Introduction

For a detector composed of a large array of PMTs - essentially being separate detectors - exact time calibration is fundamental to be able to compare the arrival times of photons across the system. Four values are measured for PMT hit that has crossed threshold: hit-time and three integrated charges [102]. The charge is used for energy reconstruction, while the time is essential to reconstruct position and time differences between events. These form the experimental observables. To obtain the reconstructed position from time measurement, it must be corrected for channel-dependent offsets. To retrieve the reconstructed energy from charge measurement, it must be corrected for any gain variations of the PMTs and for the dependence of the light collection efficiency as a function of the event position [102]. There are several offsets affecting the hit-time, the most pronounced being the cable delay and the discriminator effect (degraded PMT resolution by an effect arising from the combination of the fixed discriminator level and variations in the pulse sizes) [103]. The purpose of the PMT calibration is to account for the discriminator effect (often referred to as time-walk), to remove the time offsets, as well as to correctly measure and monitor the PMT gains.

There are several methods to calibrate SNO+ PMTs. Some require a calibration source to be deployed inside detector's vessel, other use calibration systems that are permanently

located inside the detector's cavity, mounted on the photo-multiplier tubes support structure (PSUP). This chapter will focus on the PMT calibration (PCA) using system of LED fibres called TELLIE. TELLIE stands for Timing module for Embedded LED/Laser Light Injection Entity. This particular source was added to SNO during upgrading to SNO+ to mitigate the need for source deployment [55].

The time response depends mainly on the decay time of the scintillator, on the single-photoelectron (SPE) resolution, on the overall synchronisation of the PMT array and on the correction of the time-walk effect. The main goal for the accuracy of the calibration is to make the uncertainty in PMT time delays and walk corrections to be subdominant to other effects. Given the decay time of the scintillator signal (4.6 ns) for the LAB/PPO mixture, and the SPE PMT resolution dominated by transit time spread (TTS = 1.7 ns) for the SNO PMTs, the PMT time calibration accuracy goal is set to 1 ns [102].
The charge values determine the gain of the PMTs, and are also essential for the energy reconstruction. If the gain of the PMT changes the photoelectron detection efficiency of the channel also changes. Therefore, the gain stability monitoring is additional goal of PMT calibration [102].

In this chapter, firstly, the PMT calibration is described, with associated requirements and goals. Effects that affect the recorded hit times are outlined, along with the time corrections and their implementation. There are several additional corrections and re-measurements that are necessary to improve the accuracy of the calibration - such as remeasurements of fibre delays and fits to fibre directions - these are also discussed. An overview of available TELLIE calibration datasets is presented with the accompanying benchmarking, assessing the performance of the calibration.
Additionally, this chapter briefly describes the progression of cable delays, trends in PCA tables, briefly outlines the plans for TELLIE automation as well as other PCA related topics, such as missing EXTA triggers and the monitoring of PMT charge response.

4.2 PCA

Each PMT has constant time delay independent of event position. This delay is a sum of the delay caused by the length of the cables for that PMT, the delay in the electronics, and transit time in the PMT itself. This value is referred to as the cable delay (sometimes also called the electronics delay [104]). Additionally there is correlation between time

and charge due to fixed discriminator threshold (time-walk effect) that is used in SNO+ causing loss of timing precision.

The data is recorded in ADC[1] counts. Then, the electronics calibration (ECA) is applied converting the time ADC counts to nanoseconds and charge ADC counts to ADC counts above pedestal (cap) [105]. Four values are extracted:

- **The time (ns)**: time PMT crossed the discriminator threshold, relative to constant offset (charge and channel dependent);

- **The QHS (cap)**: deposited charge over a short integration window;

- **The QHL (cap)**: deposited charge over a long integration window;

- **The QLX (cap)**: deposited charge over long integration window, low gain.

The ultimate goal of the PCA calibration is to determine (as accurately as possible) the hit-time and extract the charge spectrum parameters (detailed in Subsection 4.2.1). This is done primarily in two steps: **extracting** the PCA calibration constants (usually using dedicated calibration data obtained using a calibration source) and **applying** the PCA constants to data (this consists of testing, benchmarking and finally, calibration). As mentioned, in addition to the main goal of calibrating the PMTs to the accuracy of 1 ns, monitoring of the gain stability is a further intention [102].

4.2.1   PMT effects

This section aims to describe the timing effects: the electronics delay, the time-walk effect, and briefly touches on the charge spectrum characterization.

Electronics delay

The transit time from the cathode to the anode inside the PMT is about 30 ns [106]. Due to different trajectories from the cathode to first dynode there is a spread associated with the transit time (the time transition spread, TTS) of about 1.7 ns. In addition to this, up to 0.2 ns can also be introduced by different energies of the ejected electrons at the cathode. Therefore, there is an intrinsic variation to each PMT.

---

[1]**ADC** = analog-to-digital converter
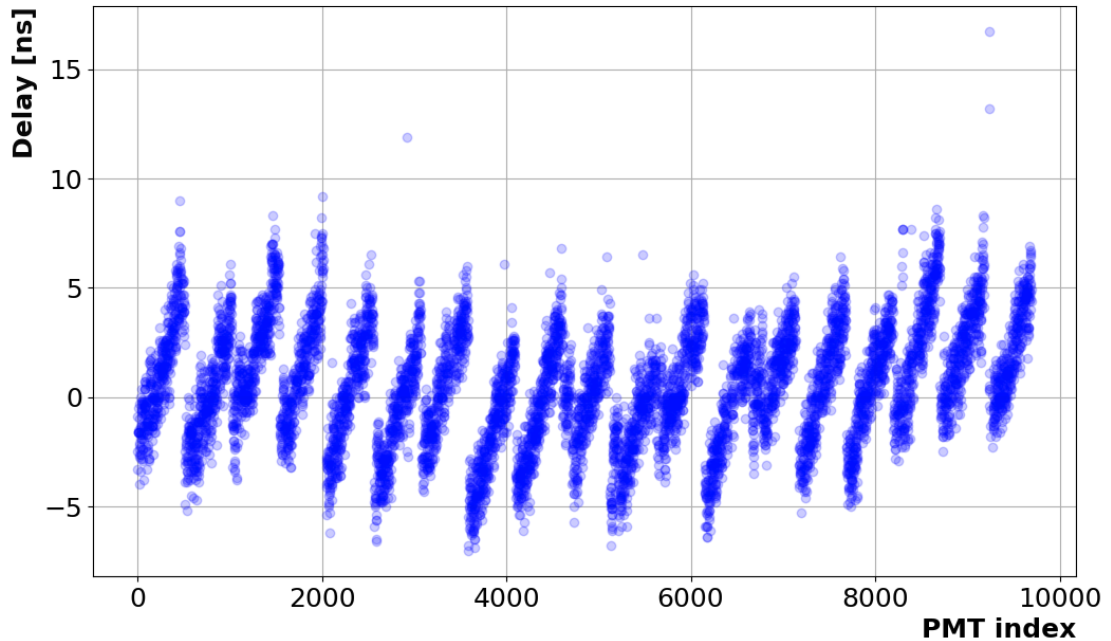
Figure 4.1: Visualization of the amount of variations in the electronics delay. The x-axis represents the PMT ID. Clear grouping of PMTs can be observed, this corresponds to separate crates, hosting the front-end electronics.

Even though the ECA gives the time at which the discriminator fires there are offsets between ECA times of different PMTs. These are introduced, as mentioned above, by different length of the cable and the length of traces in the electronics. Specifically the path-length from Crate-Trigger-Card (CTC) is different for each Front-End-Card (FEC) resulting in both the channel trigger delay and the Global-Trigger (GT) delay to be card dependent (the channel triggers delays are partially compensated for by the differences in path lengths of the electronics traces on the backplanes). Therefore, even after the ECA calibration the timing is still channel-dependent [103]. This can be seen in Figure 4.1. For more details about the detector's electronics please refer to the Subsection 3.3.1.

Time-Walk effect

Small pulses take longer to cross the discriminator threshold with respect to the center of the peak than large pulses. Therefore, the time at which the discriminator fires due to a PMT pulse depends on the size of the pulse. The size of the produced pulse by a single photo-electron (SPE) is subject to statistical fluctuations and as such is an effect that cannot be bypassed. This is referred to as the "time-walk" (TW) effect and is apparent when plotting ECA calibrated time against QHS, as shown in Figure 4.2.
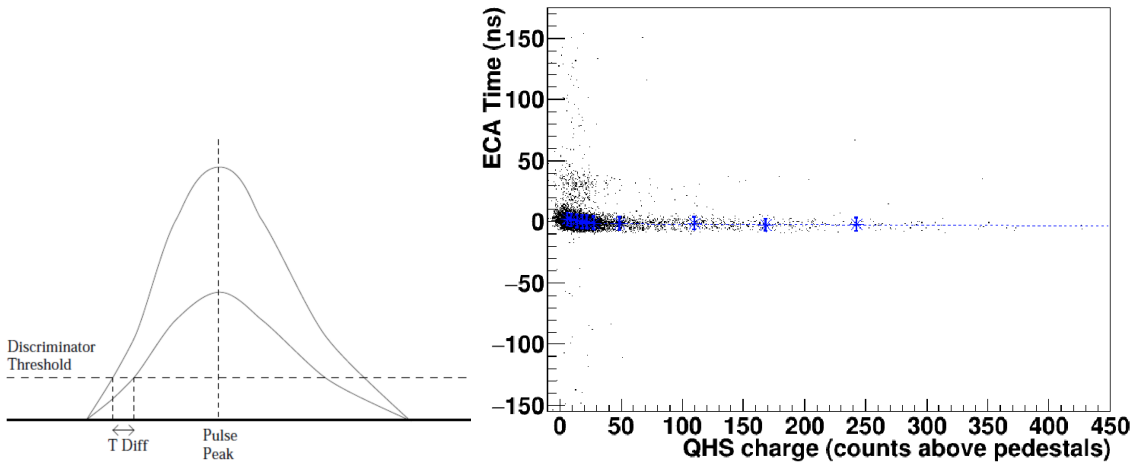
Figure 4.2: (Left) Example of the time-walk effect: two simultaneous pulses with different charge crossing the discriminator threshold at different times. (Right) ECA time against QHS charge collected from TELLIE run, PMT 4242. The blue crosses are a profile histogram of the data corresponding to the interpolation points.

Charges

The number of cap corresponding to one photo-electron (PE) ranges from PMT to PMT and has a significant spread. The aim of PCA is to characterize this single photo-electron charge spectrum thus allowing a charge to be converted into units proportional to the number of PEs. Additionally, because the discriminator level is fixed, the gain calibration can help estimate the relative PMT efficiency if the discriminator threshold is changed. The variation in the cap that corresponds to one PE is caused by two factors: variation in the true gains of the PMTs and variations in the components of the electronics (integrations and converters). The true gain can be affected by ageing effects (increase in the residual gas), voltage drifts, electronics card swaps and repairs [103].

To characterize the charge spectra, three characteristic parameters are extracted for each PMT (both QHS and QHL):

- **The threshold** (TH): this is the point where the spectrum drops significantly, at the position of the discriminator threshold;

- **The peak** (PK): this is the position of the maximum of the main region (containing most of the data);

- **The high-half point** (HHP): first point that falls to the half of the height of the peak, starting from the peak and searching to the right side (increasing charge).

These are shown in Figure 4.3.
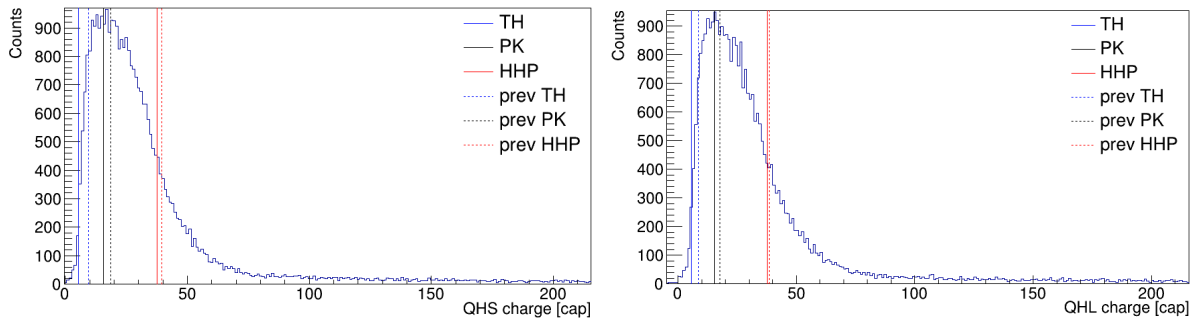
Figure 4.3: SNO+ PMT charge spectra. (a) A QHS charge spectrum for PMT 4242. (b) A QHL charge spectrum for the same PMT. The three characteristic points of each distribution (described in Subsection 4.2.1) are highlighted in the plot.

4.3 TELLIE PCA

TELLIE is one of the ELLIE subsystems designed to provide PCA calibration data while minimizing the risk of contamination since it's permanently deployed being attached to the PSUP (PMT Support) structure. It can potentially provide continuous PCA calibration data, however, until now the PCA data was obtained in dedicated PCA sessions. A full description of the ELLIE system is available in Subsection 3.6.2.

An important feature of the TELLIE LED pulse is the rise time. Because every fibre is connected to a dedicated driver board, the exact delays between the trigger and light emission can be different for each fibre. These have to be corrected for in order to find precise relative PMT times using TELLIE. It is possible to extract these times by looking at the difference in the position of the prompt peak for the corrected signals (corrected for the transit time, bucket time and angular systematic) from two LEDs seen by the same PMT. This is shown in Figure 4.4.

To obtain a full PCA dataset using TELLIE, all 95 TELLIE fibres across 92 nodes are used. These are run consecutively, with fixed frequency of 1 kHz, for 200 000 events. These settings are customizable, however, these values provide enough statistics to achieve a 0.5 ns error on the mean arrival time. The light intensity has to be tuned before taking the PCA run. This is done by running short runs consisting of few thousand event while varying the internal pulse width (IPW). The IPW is inversely proportional to the light intensity, therefore, lowering this value results in higher NHit - higher number of PMTs being hit by the light. The intensity is kept as constant as possible for the set of fibres and is kept in the single photo-electron (SPE) emission mode. SPE mode provides most accurate measurement of the time profile of a pulse whereas multi photo-electron (MPE)
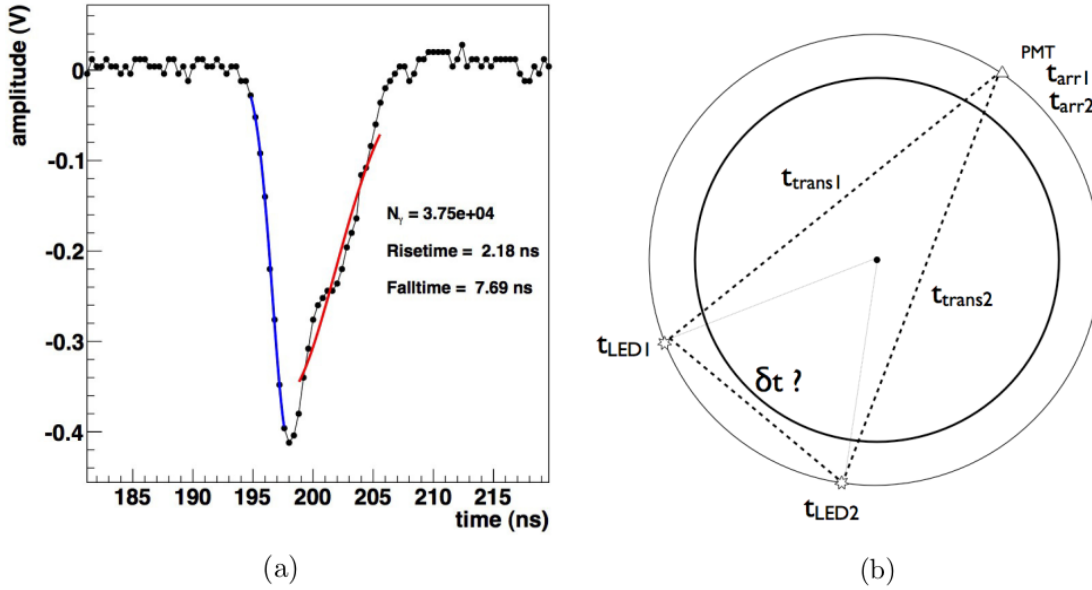
Figure 4.4: Characteristics of LED used in TELLIE system. (a) LED pulse averaged over many pulses after propagating through fibre. (b) Method to extract individual LED time offsets by comparing the position of the prompt time peak for two different LEDs at the same PMT. Figure from [103].

hits skew the time profile in the favour of the first detected photon [59].

It's important to note that the TELLIE system is a complementary system to another calibration source, the laserball. This is described in Subsection 3.6.1.

4.3.1   PCA constants: generation

The PCA constants extraction happens using the `PCAProc` processor in RAT. The processor loops over all events - in this case events for each run (one corresponding to each TELLIE fibre). For a full PCA dataset this equals to 200 000 (each run) × 95 (fibres) events. For each event, charge (QHS, QHL) and timing (t_{ECA}) information is collected for each PMT/LED combination. The data is later analysed to extract the constants which are, finally, checked against pre-defined limits (run-level, event-level and hit-level checks). The time value that is used is the injection time t, defined as

$$t = t_{\mathrm{ECA}} - t_{\mathrm{transit}},$$

where the transit time is the time it takes for the light to travel from the LED to the PMT.

Once the data is collected and validated throughout, the time-walk code calculates the interpolation points that describe the discriminator effect. For TELLIE, the offsets
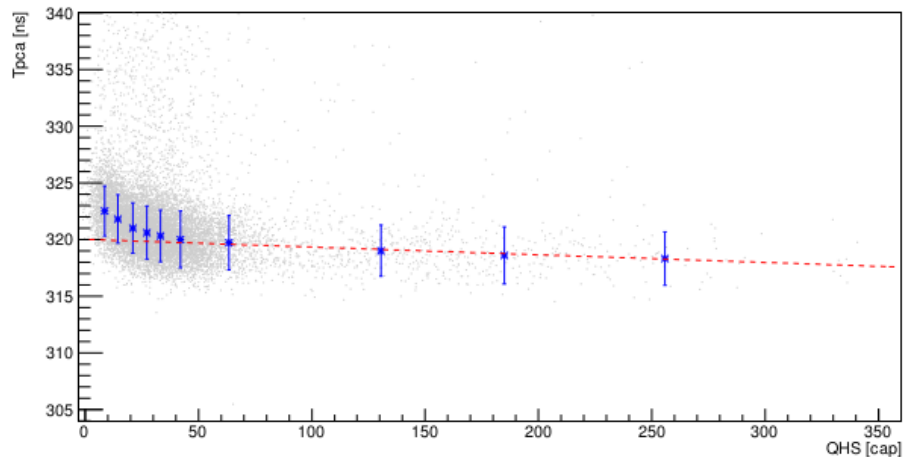
Figure 4.5: Example time-walk plot for PMT 1081. t_{ECA} vs QHS with fitted interpolation points. The read line is a straight line fit to the high charge tail.

between different LEDs are calculated as pointed out in Figure 4.4. Afterwards, for each PMT, the LED that has the most hits is picked as the 'best fibre[2]'. This PMT/LED combination is then used to extract the interpolation points - the final time-charge calibration constants for the PMT. This is quite wasteful way of calibration but was initially selected as it is easier to debug and allows for calibration even when one or more LEDs are not in perfect conditions (redundancy).

Interpolation points

As mentioned in Section 4.2.1, the walk calibration parametrizes the discriminator walk for all normal[3] PMTs. This is done using interpolation points (IPs). At SNO it was found that ten points described the shape of the walk function sufficiently [103]. The typical calibration dataset is dominated by SPE hits, most of them being of relatively small charge (the steepest part of the time-walk slope). The prompt time peak is found using a sliding window. The window finds a bin with most entries, with the length of 8.5 ns (this is to encompass the 5 ns walk and the width of the calibration source pulse) [103]. The typical time-walk plot for PMT 1081 is shown in Figure 4.5.

There is also a defined way to chose the charge bins. First, the shortest range containing 70% of the data is found. Any hits 50 counts above upper range of the shortest span are dropped so that the ratio of hits in peak to the number of hits in the tail is not biased.

---

[2]**Best fibre** corresponds to the TELLIE fibre that has the most hits for particular PMT after cuts are applied.

[3]A normal PMT refers to inward-facing PMT mounted on the PSUP, as opposed to, for example, outward-looking or low gain channels.

Then, the peak region is estimated as the shortest span containing 90% of the data. After the peak is found, the bins are allocated within three regions: pre-peak, drop and tail [103]. Once the bins are set, the processor stores:

- The charge of the interpolation point, this is the average charge of the bin;

- The time of the interpolation point, this is the median of the t_{ECA};

- The estimator of the RMS of t_{ECA} distribution.

The median is chosen because it is more reliable than the average since it is less susceptible to being affected by late hits from scattered light. In addition to this, the variance of the data around an average gradient for each bin is also stored, which is used to estimate the total variance of the channel. This is used for quality-control. If it is possible to calibrate the PMT, several values are stored:

- The number of interpolation points;

- The interpolation points (in packed format) followed by the fit parameters (to fit the high charge tail);

- The status word (indication errors, if any);

- The RMS for each point.

These represent the PCA constants and are, therefore, used by the PCA calibration code to correct all hits for the walk effect and the electronic delay.

Relative LED offsets

Each LED is attached to its own driver. These drivers are expected to have constant time-offset over time, however the offset is board-dependent. Therefore, the offset between the LEDs need to be corrected for. This is done by comparing overlapping PMTs between two LEDs (see Figure 4.4). A more detailed description is available as Appendix A.

Checks for bad channels

One of the functions of the PCA processor is to flag channels that behave badly at the time of data-taking. This is often caused by bad ADCs that experience discontinuities in the conversion of voltage to ADC counts. There are four parameters to identify bad channels:
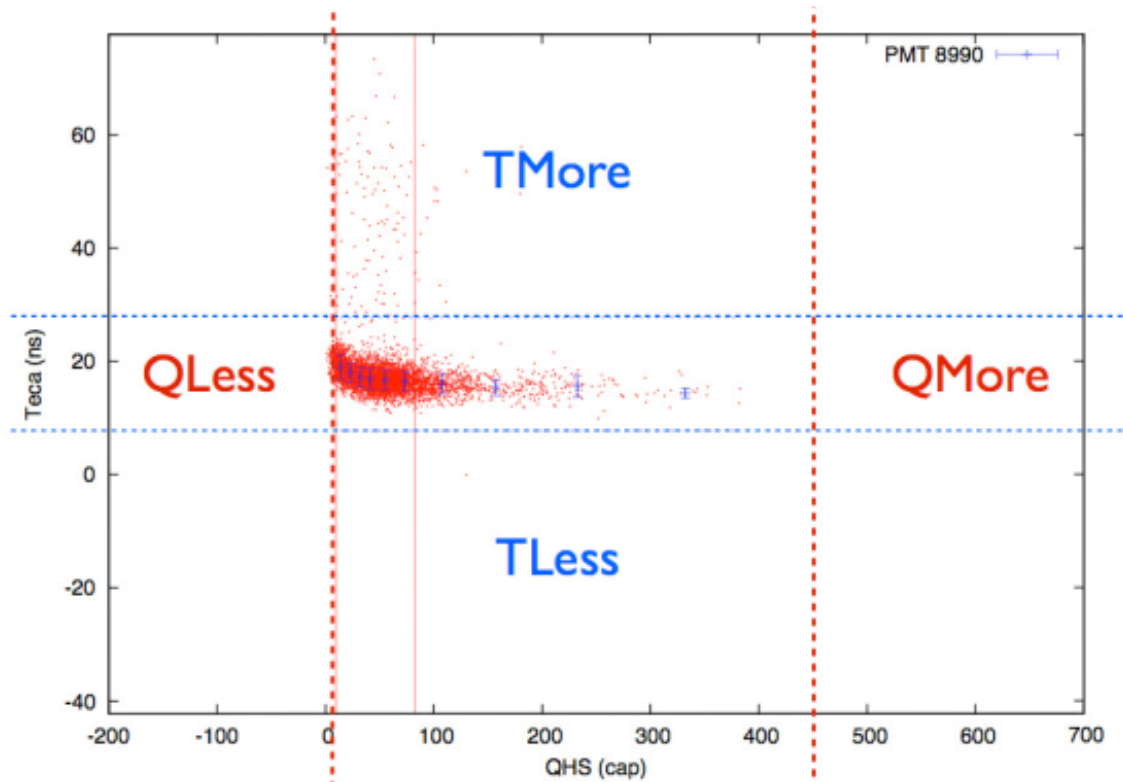
Figure 4.6: Example QHS versus t_{ECA} plot highlighting the QLess, QMore, TLess and TMore regions. The Fout and Flate parameters are calculated from these. Figure from [103].

1. The global **RMS** of the channel;

2. **Tstep**: normal walk interpolation points continuously decrease with increasing charge. Bad ADC channels often contain a step up instead of fall;

3. **Fout**: fraction of hits in regions TLESS and QLESS (these are described below);

4. **Flate**: fraction of the total number of hits which are in the TMORE region (described below).

The Fout and Flate are fraction tests checking the fraction of the hits contained within the fit. Regions TLess and TMore contain hits more than 10 ns from the time peak whereas QLess and QMore contain hits falling below the low edge of the lowest charge bin and above the high edge of the highest charge bin. These are highlighted in Figure 4.6.

4.3.2 PCA constants: application

Time

The ECA calibrated time (t_{ECA}) has to be corrected for the electronics delay and the discriminator walk (the time-walk effect) as described in 4.2.1. These two are corrected for

simultaneously using the extracted interpolation points. This is done via PCA calibrator and is called for each ECA calibrated hit. The TW points are obtained for the channel that was hit and the time correction is applied [103]. There are multiple cases that can arise:

- For a channel that has valid constants, the two IPs that straddle the charge of the hit are considered. Straight line interpolation between these two points gives the value of the walk at the charge in question;

- For charges below the first IP, the first two points are used to extrapolate back as long as the charge difference between the data and the first IP is smaller than the charge difference between the first and second IP (otherwise the time is set as -9999.0^4, invalid value (flag) for the data structure);

- For charges above the last IP, extrapolation between the last two points is used, however, only if the difference (between data and the last point) is half of the charge difference of the last two IPs.;

- If the difference is even higher than in the previous case, straight line fit is used instead;

- In the case no straight line fit is available, the value of the last IP is used;

- If there is no calibration available for the channel, the time is set to -9999.0.

These rules are highlighted in Figure 4.7.

Charge

Because the charges are currently unchanged by the PCA calibration (and are only used as input to RAT) these are not discussed in much detail in this thesis. A brief note on the monitoring of charges is outlined in Subsection 4.10.3.

4.3.3 PCA time corrections

As mentioned above, the hit time needs to be corrected for by the transit time (also called the time-of-flight). In addition to that, two other corrections are applied to the hit time to get more precise evaluation of the injection time. These are the bucket time and the angular systematic correction and are explained in this section.

---

[4]-9999.0 is used throughout as a mark for invalid value.
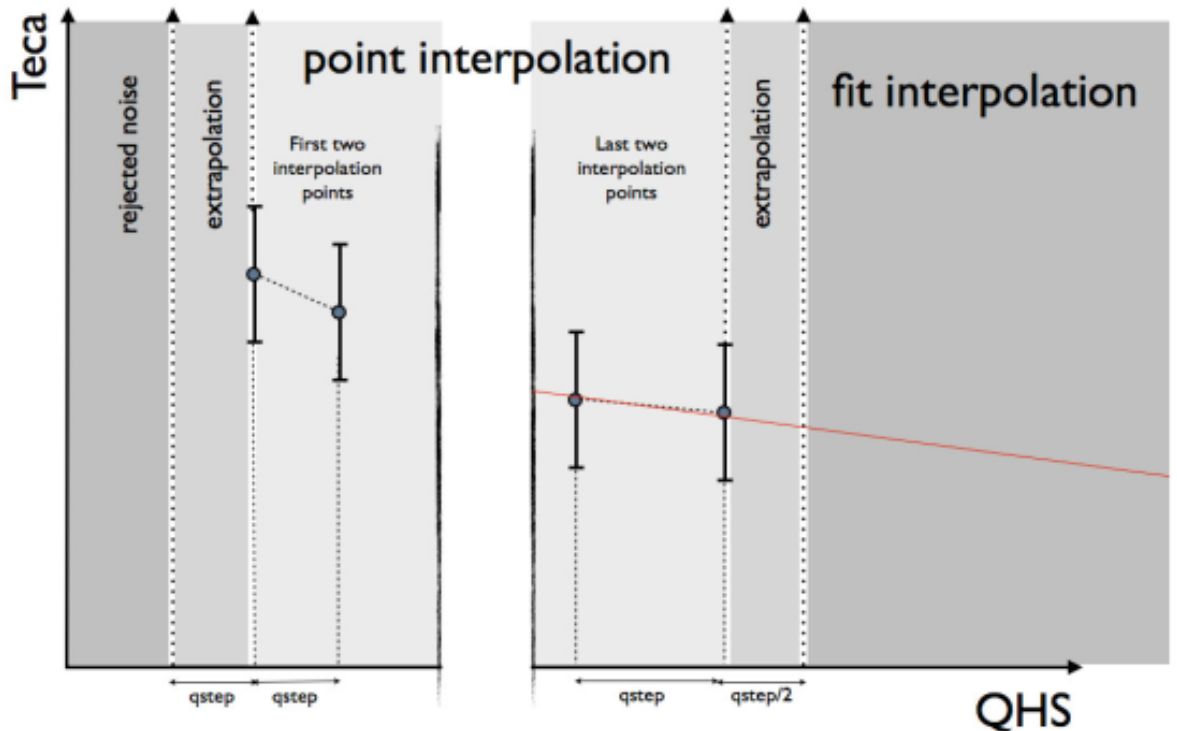
Figure 4.7: The application of the time-walk interpolation point constants to correct hit time depending on the hit charge value. Figure from [103].

Transit times

The transit time is the time it takes the light to travel from the point of origin to the finishing location. In the context of a physics event, these two locations would be a reconstructed event vertex and a PMT position. In the case of TELLIE, the point of origin is always the wet end of the TELLIE fibre located on the PSUP and the finishing point is the PMT. Generally, the path the light takes is not unique. There are multiple physically plausible paths between the two points and each will have different path length. These will be affected by different media the light can pass through, such as the AV, ropes, belly plates and similar. Additionally, there can be reflections and refractions along the way. This is highlighted in Figure 4.8.

The shortest path is the most probable (by likelihood) and best represents the (average) distance travelled by photons contributing to the prompt signal that is recorded by the PMT [107]. To ensure the shortest possible path is calculated, there is additional input parameter, the initial direction vector from the TELLIE fibre. The calculation is then executed by a software tool known as 'lightpath calculator' (LPC) [107]. LPC contains the detector geometry, including the physics parameters required for the calculation, such
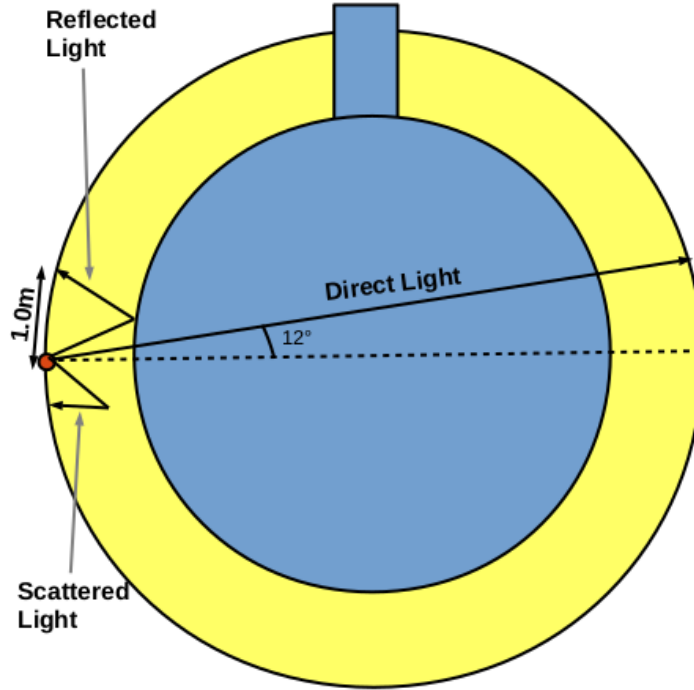
Figure 4.8: Examples of various path lengths TELLIE light can take through the detector. Additionally, some cut values used in PCA are also shown, such as the use of 12 degrees angular cut. Figure from [43].

as the refractive indexes. Combining this with the group velocities of the media and one can obtain the total Time-of-Flight as follows

$$t_{\text{ToF}} = \frac{d_{\text{InnerAV}}}{v_{\text{g-InnerAV}}} + \frac{d_{\text{AV}}}{v_{\text{g-AV}}} + \frac{d_{\text{Water}}}{v_{\text{f-Water}}}, \tag{4.1}$$

where d_* are the distances of the light path to the PMT through the inner-AV, AV and water regions and $v_{\text{g}-*}$ are the respective material group velocities of said regions [108]. The group velocity is related to the refractive index by

$$v_{\text{g}}(\lambda) = \frac{c}{n(\lambda) + \lambda \frac{\partial n}{\partial \lambda}}. \tag{4.2}$$

Bucket times

The light is detected by the inward facing PMTs located on the PSUP. A photon reaching a PMT has a probability of liberating an electron at the PMT photo-cathode. This electron then accelerates along the electric field lines across the PMT dynode stack. Additional electrons are emitted and the charge is collected at the PMT anode. If the threshold is reached, the PMT registers a hit. The PMT positions are defined to be the centre point of the plane which defines the entrance of the PMT bucket and concentrator assembly (as shown in Fig 4.9).
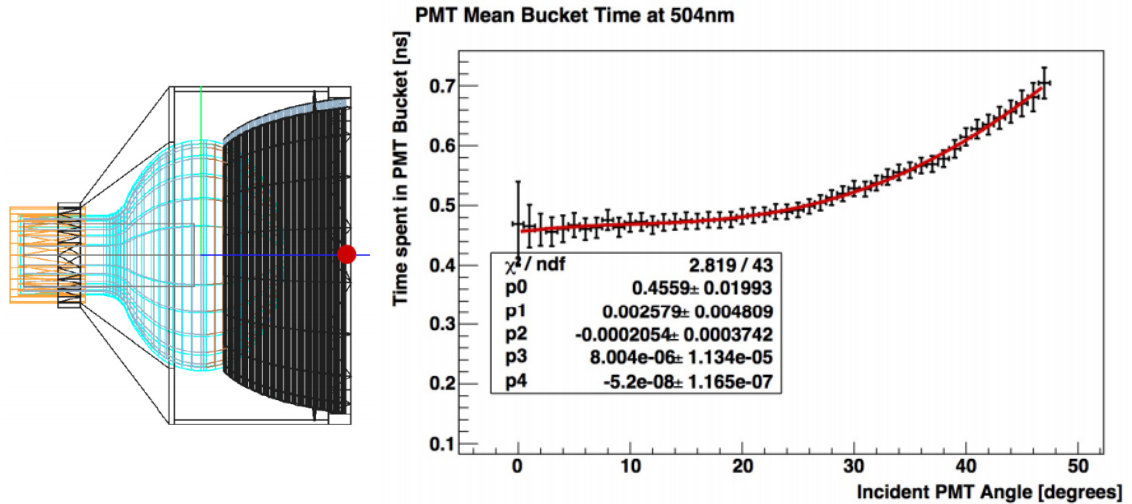
Figure 4.9: Left: Wireframe diagram of the PMT geometry as modelled in RAT. The PMT concentrator is in solid black, PMT is in blue and the black outline defines the perimeter of the PMT bucket. The red dot is the location of the PMT as returned by RAT. Right: The mean time light spends inside PMT bucket before hitting the cathode as a function of incident angle. Figure from [108].

In order to estimate a better transit time, it is useful to account for this time the light spends within the PMT bucket geometry once it enters. This is highly angle dependent and modifies the transit time (time-of-flight) as

$$t'_{\text{ToF}} = t_{\text{ToF}} + t_{\text{bucket}}. \tag{4.3}$$

The incident light vector on the PMT can be obtained from the LPC. This angle makes it possible to evaluate the angle of entry to the PMT face, thus obtaining the time the light spends propagating through the PMT bucket. More details on the method can be found in [108].

Angular systematic

There is one more effect affecting the hit time caused by the nature of TELLIE fibres. This effect occurs due to modal effects within the fibres: light injected at a $10°$ angle w.r.t. the fibre direction is injected into the detector up to 1 ns later than light injected at a $0°$ angle (or generally, the light coming out of a TELLIE fibre is delayed scaling with the angle at which it exits). This effect is generally known as the modal dispersion and is common for optical fibres. Throughout this thesis the effect is referred to as the 'angular systematic effect' and is shown in Figure 4.10.
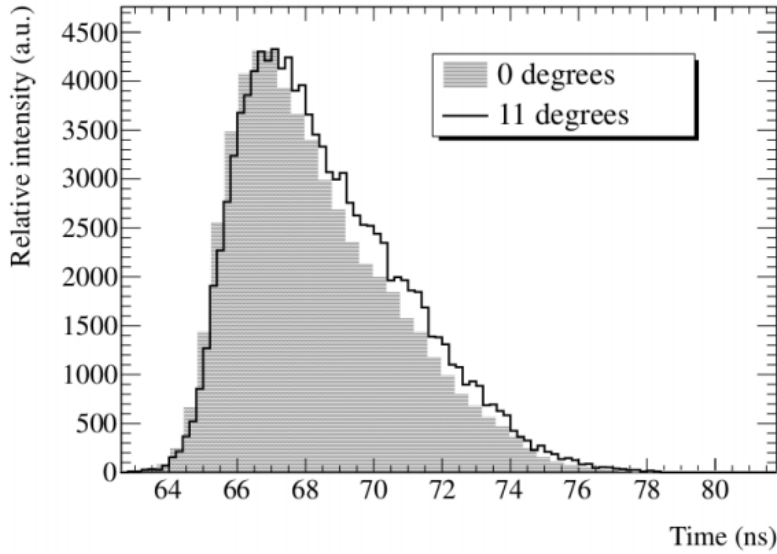
Figure 4.10: Normalised time distributions of TELLIE light pulses after going through the full length (45 m) optical fibre, at the central position (filled area) and at an angle of 11°in water (solid line). Figure from [109].

This systematic effect is parametrized using simple geometric assumptions (as seen in Figure 4.11) to express the time offset as a function of emission angle α with two free parameters t_0 and t_1

$$t(\alpha) = t_0 + t_1\left(\frac{1}{cos(\alpha) - 1}\right). \tag{4.4}$$

It can be seen that the t_0 is the global offset for $\alpha = 0$ and t_1 is a measure of how fast the fibre emission time rises at increasing angles. The parametrization is detailed in Figure 4.11 [109].

This is the method applied to a dataset in order to extract the angular systematic fits:

- Cuts are made on the PMT status to ensure good quality (channel status check, removed cross talk, PCA and ECA applied);

- Only the PMTs with $> 1\%$ occupancy are considered - this ensures high enough statistics;

- Only PMTs within 24° angle between the fibre and the PMT are considered;

- The injection time is calculated for each hit as: $t_{inj} = t_{hit} - t_{ToF} - t_{bucket}$;

- The time offsets for each PMT are filled into a histogram, the prompt time peak is fitted (direct light only) with a Gaussian function;
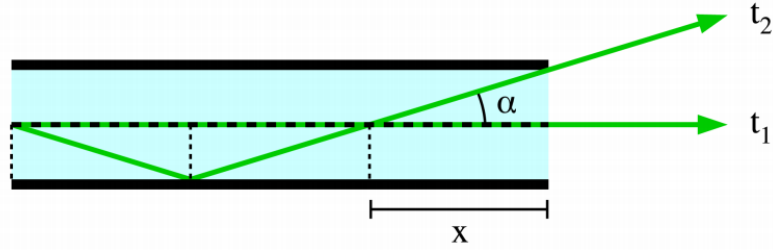
Figure 4.11: Simplified geometric model of a fibre (light blue) of length $L = N * x$. Assume that LED light (green) is injected into the fibre at $t = 0$. Light travelling along the optical axis will exit the fibre at injection time $t_1 = N * \frac{x}{c}$, while light travelling at an angle α will exit the fibre at $t_2 = \frac{N*c}{c*cos(\alpha)} = \frac{t_1}{cos(\alpha)}$. The difference in time for light travelling at an angle is $\Delta t = t_2 - t_1 = t_1 * (\frac{1}{cos(\alpha)-1})$. Assuming an arbitrary global offset t_0, the light is then emitted at $t(\alpha) = t_0 + \Delta t = t_0 + t_1 * (\frac{1}{cos(\alpha)-1})$. Figure from [109].

- Finally, the time offsets are plotted as a function of fibre emission angle;

- The geometric model described above is fitted to data, obtaining t_0 and t_1.

The fit to a single fibre is shown in Figure 4.12. Fit to full PCA dataset is displayed in Figure 4.13. The angular systematic study is done for each PCA dataset to get as precise injection times as possible, correcting for the modular effects affecting the time the light exists the fibre. Additional plots are in Section 4.9.

To conclude, these are the corrections that are applied to the PMT hit time to get the precise injection time $t_{\text{injection}}$ (also called residual time) for TELLIE PCA

$$t_{\text{injection}} = t_{\text{hit}} - t_{\text{ToF}} - t_{\text{bucket}} - t_{\text{angsys}}, \tag{4.5}$$

where:

- **The injection time**, $t_{\text{injection}}$: the time light leaves wet end of TELLIE fibre, being injected into the detector;

- **The hit time**, t_{hit}: the time of hit as recorded by PMT, whenever PMT registers charge above threshold;

- **The Time-of-Flight time**, t_{ToF}: the time it takes for light to propagate through the detector geometry, as explained in Subsection 4.3.3;

- **The bucket time**, t_{bucket}: the time spent in PMT's bucket geometry, as explained in Subsection 4.3.3;
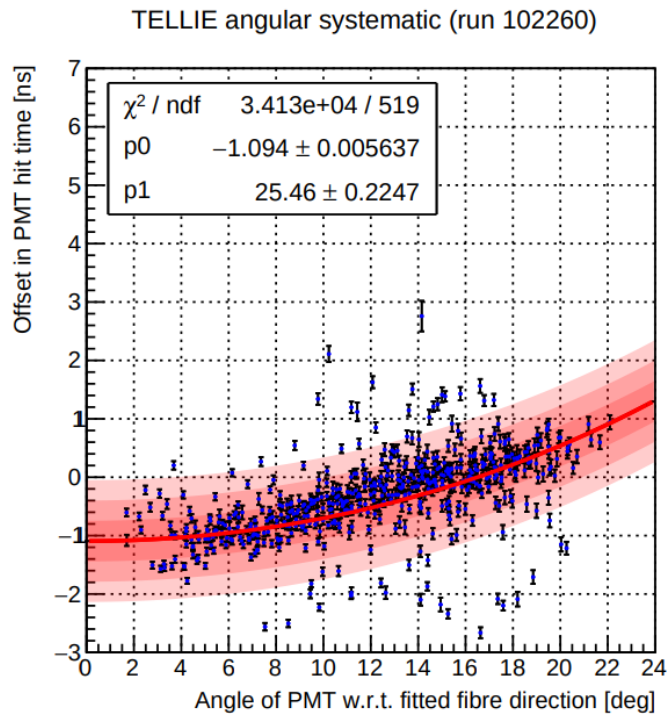
Figure 4.12: Fitting time residuals for all PMTs for single TELLIE fibre. The time residuals are fit with prescribed angular systematic fit. Figure from [109].
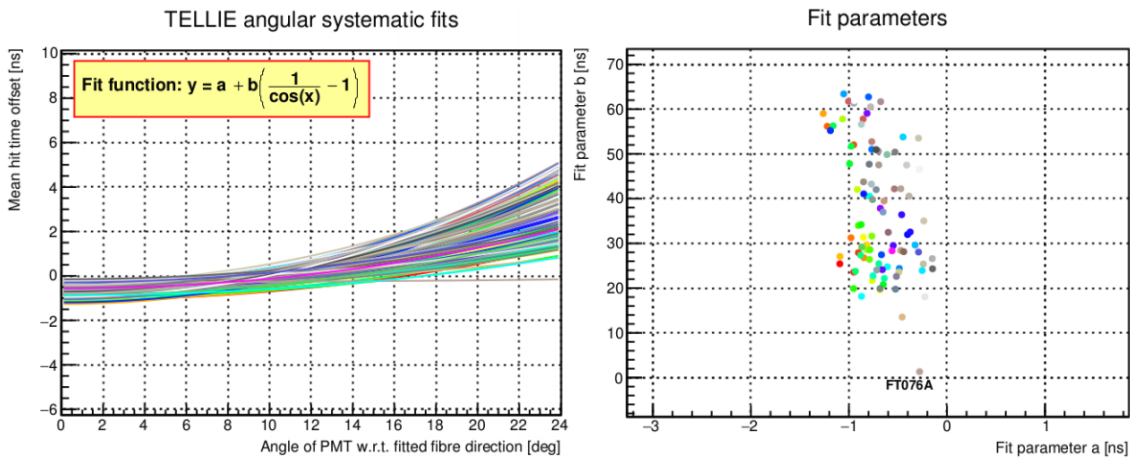
Figure 4.13: Summary plot of angular systematic fit for a full TELLIE dataset (95 fibres). Left: The mean hit time offset y plotted against the angle w.r.t. the fitted fibre direction x, with the fit function highlighted in the top left corner. The fit results for each fibre are shown as coloured line. Right: Fit parameters a and b plotted against each other, with each dot representing one fibre. The outlier FT076A is due to the large amount of scattering seen in this run. Figure from [109].

- **The angular systematic effect correction time**, t_{angsys}: the time correction for the modal effect the light experiences within the fibre, for light leaving the fibre at angle, as described in Subsection 4.3.3.

4.3.4   Analysis cuts

There are several cuts applied to TELLIE PCA data in order to improve the quality of the calibration. The most important cuts are:

- **Only one fibre per run**: this ensures there is just single injection point making it possible to apply transit corrections;

- **Occupancy check**: Occupancy is defined as $\frac{Hits_{\mathrm{seen}}}{Hits_{\mathrm{total}}}$. Only PMTs with occupancy between 1% and 5% are considered. The low cut ensures we are dealing with PMTs that have enough statistics (seen enough hits so that we can be sure this is not noise data) while the high cut ensures SPE mode (so that the hit times are not skewed): the multi-photoelectron hit contamination is below 1% at 5% occupancy [102];

- **PMT checks**: Only online, normal, enabled, high quantum efficiency PMTs are considered. Channel's status also needs to be satisfactory;

- **Light path checks**: it must be possible to calculate the path between the TEL-LIE fibre and the PMT. Additionally, total internal reflection cases are taken into account;

- **ECA check**: successful ECA calibration is mandatory;

- **The angular cut**: this cut ensures only the PMTs that are in the direct light beamspot (i.e. directly opposite the fibre) are calibrated by the given fibre. This is essential as only these PMTs will have valid (and physical) transits as well as reasonable angular systematic and bucket time corrections. Additionally, due to the angular emission profile of the fibres only the PMTs directly opposite the fibre will receive high enough light intensity. Essentially, only the PMTs that are hit directly (with no reflections) are being calibrated. Having multiple (and redundant) fibres around the detector ensures it is possible to calibrate all PMTs this way. The usual angular cut used in TELLIE PCA is 12 degrees;

- **The cross talk removal**: Electronics cross talk is also removed. Because of the capacitive coupling between adjacent channels a high-charge hit will cause the discriminators on adjacent channels to fire.

The angular emission profile of a TELLIE fibre is shown in Figure 4.14. This was measured in the laboratory at the University of Sussex for an example fibre. The light intensity is clearly the highest at the centre, close to zero degrees along both axis. The hit frequency then drops as the angle from the centre of the fibre increases (this is true for both axes). Even though the measurement was done ex-situ, this behaviour is also present when running TELLIE as installed in the SNO+ cavity, forming the aforementioned beamspots of light.

These resulting beamspots are also visible in real data after the cuts listed above are applied. This is shown in Figure 4.15 and Figure 4.16. These figures often make use of flat maps[5]. The beamspot shape is mainly due to angular and occupancy cuts. PMTs that are offline are not plotted. Other PMTs that do not pass cuts or other checks are set to 0 occupancy for better visual representation. PMTs in the center usually have the highest occupancy which then drops with distance from the center. However, if there are additional objects (ropes, belly plates, pipes) within the trajectory, the occupancy can be altered by shadowing, lensing, and other optical effects as highlighted in Figure 4.17. The beamspot represents what the direct light hits look like for a fibre in PCA dataset. Beamspots like this are created for each fibre, then, the best fibre is selected for each PMT before the calibration constants are obtained.

4.3.5 Evaluation of time corrections in TELLIE data

Following subsections will evaluate how significant the applied time corrections are, what ranges they cover and what form and shape they follow, if any.

Transit times

As mentioned in Subsection 4.3.3, the transit correction is the time the light travels within the detector, from the point of leaving the wet end of the fibre until it is detected at PMT. This is the most significant time correction. Since the PCA is focusing on PMTs that are directly on the opposite side of the detector, rejecting AV reflections, it is expected that the value of the transit time is going to be comparable to the time it takes light to travel approximately 18 meters (12 meters AV diameter plus approximately 3 meters of external water on each side), therefore, less than 80 nanoseconds. A spread

---

[5]**A flat map** is a type of plot where SNO+ PMTs are shown in 2D view, with dot markers representing individual PMTs. Because the shape of the structure holding the PMTs is spherical, the visualization is form of a map projection, where the sphere is 'sliced', similar to an orange peel. The positions on the flat map correspond to true positions, i.e. the top portion is near the neck of the detector.

Angular Distribution in Water
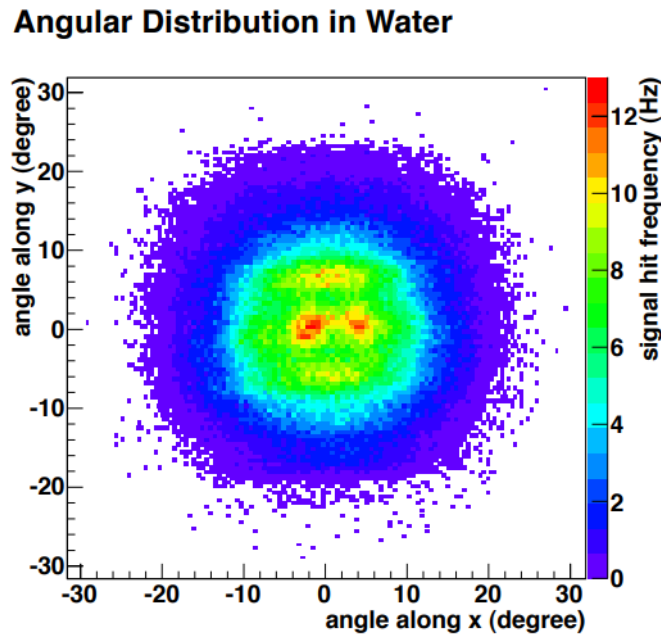
Figure 4.14: Two dimensional angular emission profile of TELLIE fibre. White areas correspond to zero intensity. Plot from [102].

of few nanoseconds is expected due to PMTs at different angles (and therefore distances) from the normal to the fibre. PMTs exactly opposite the fibre will likely have the highest transit time since the path is the longest. The number of PMTs giving higher transit time will increase due to to available PMTs within the given angular distance (there is more PMTs at higher angles in the 'beamspot' of selected PMTs). An example of the transit times for a single fibre from PCA dataset are displayed on the left in Figure 4.18. As expected, the transit times decrease with increasing angle, as the distance between the fibre and the PMT gets shorter. There is also more data points (PMTs) at higher angles as there is more available PMTs at higher angles within the beamspot. Considering the full dataset, only the best fibre is used to extract the PCA constants for specific PMT. Therefore we expect the transit times to be very close to the maximum value. This can be observed on the right plot in Figure 4.18.

Bucket times

Regarding the bucket time, only small time corrections that are affected by the incident angles of the photons being registered at the PMT, are expected. Because the PMTs in the middle of the beamspot are likely to be directly opposite the fibre, the angles will commonly be quite small (i.e. the light will often hit the PMTs quite directly). Therefore, considering the distribution from Figure 4.9 most of the bucket times should be below 0.5
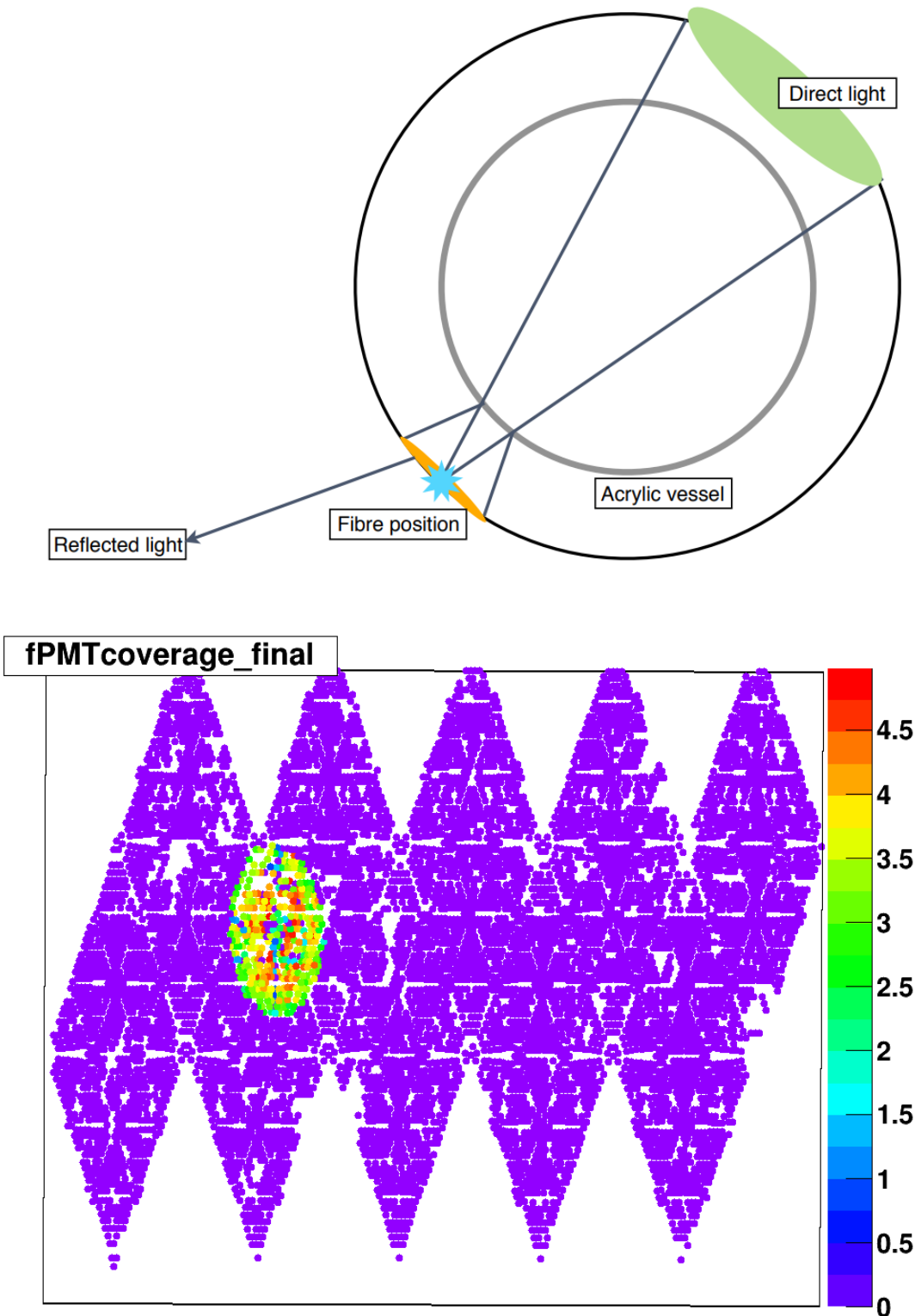
Figure 4.15: Top: A sketch representation of TELLIE fibre light shooting photons through the detector, highlighting the direct light and reflected light. Plot from [110]. Bottom: A flat map representation of SNO+ PMTs for TELLIE run. The color represents the occupancy percentage for each PMT. Only the PMTs within 12 degrees angular cut (these are the hit by the direct light) are considered for PCA calibration. The white spots represent offline PMTs, or PMTs that cannot be used for different reasons (status, type).
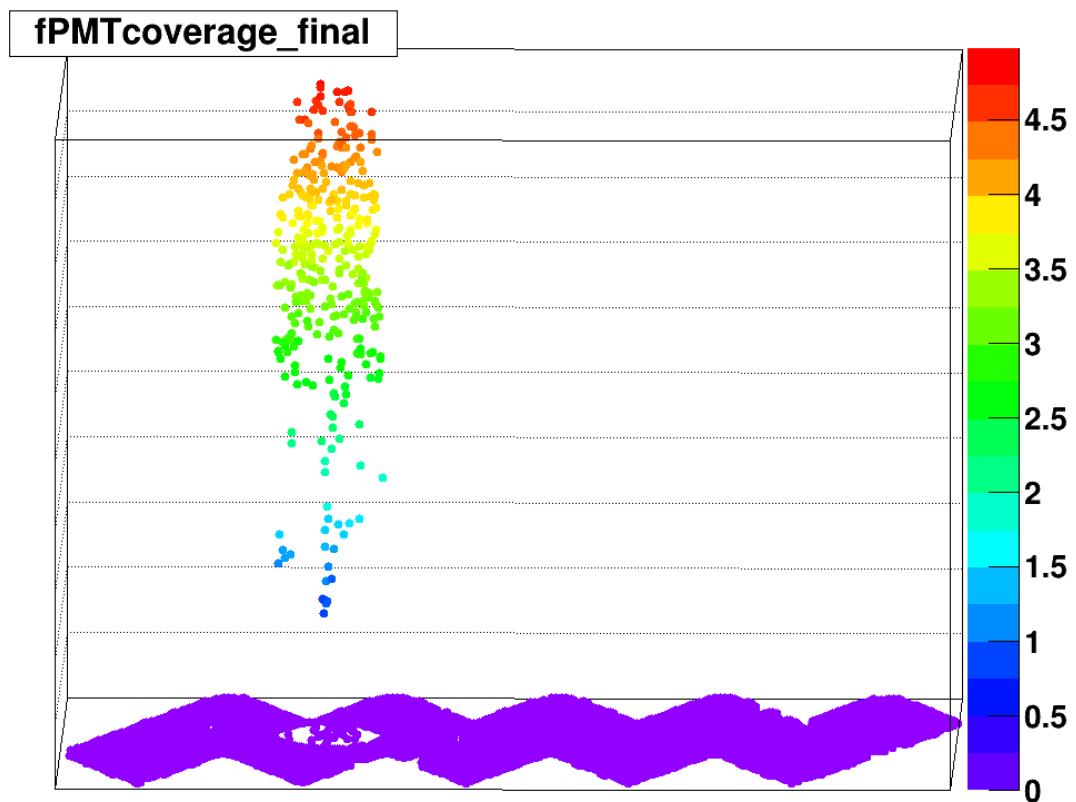
Figure 4.16: A different view of the TELLIE beamspot in TELLIE run. The beamspot represents direct light for single TELLIE fibre, the color represents the occupancy percentage for each PMT. This is commonly the highest in the centre of the beamspot, decreasing with the increasing angle.
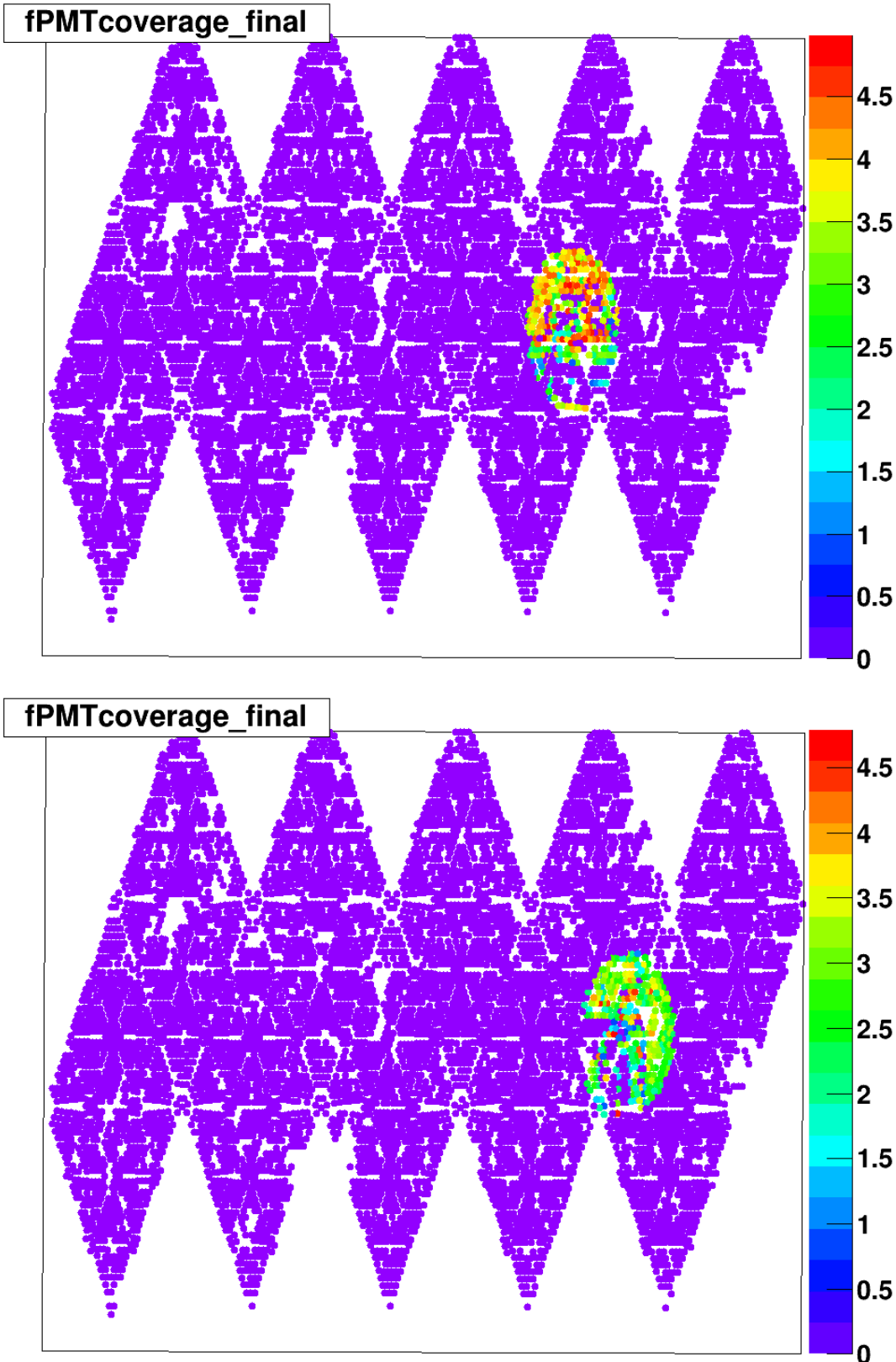
Figure 4.17: Examples of TELLIE beamspots with visible optical effects. The beamspot represents direct light for single TELLIE fibre, the color represents the occupancy percentage for each PMT. There are visible features in the beamspots. These corresponds to physical parts of the detector in the line of direct light between the fibre and the PMTs on the opposite end of the detector. These could be: hold-up or hold-down ropes, belly plates, pipes for filling and removal and more.
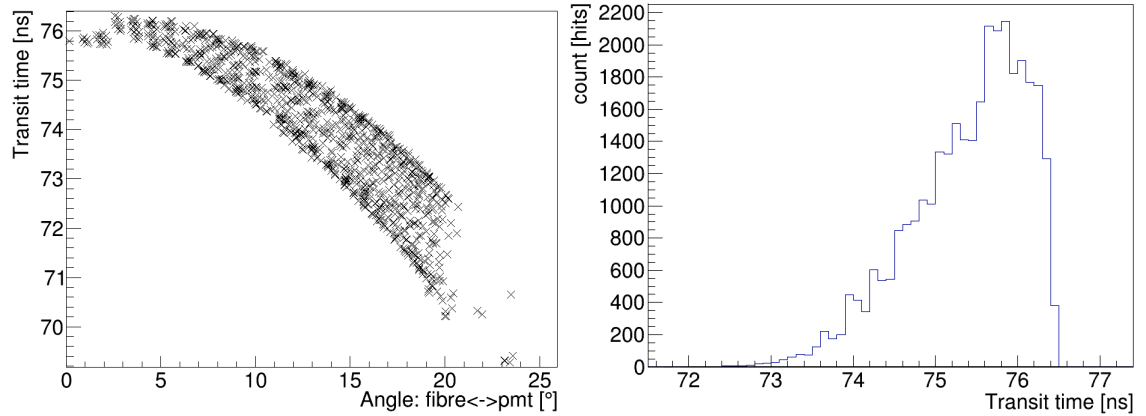
Figure 4.18: Left: Transit time corrections as a function of angle between the PMT and fibre's direction. Each point is a result of the fit of multiple hits for single PMT. Right: Histogram of transit time fits for all PMTs from full PCA dataset. Each PMT only contributes hits for the 'best fibre'.
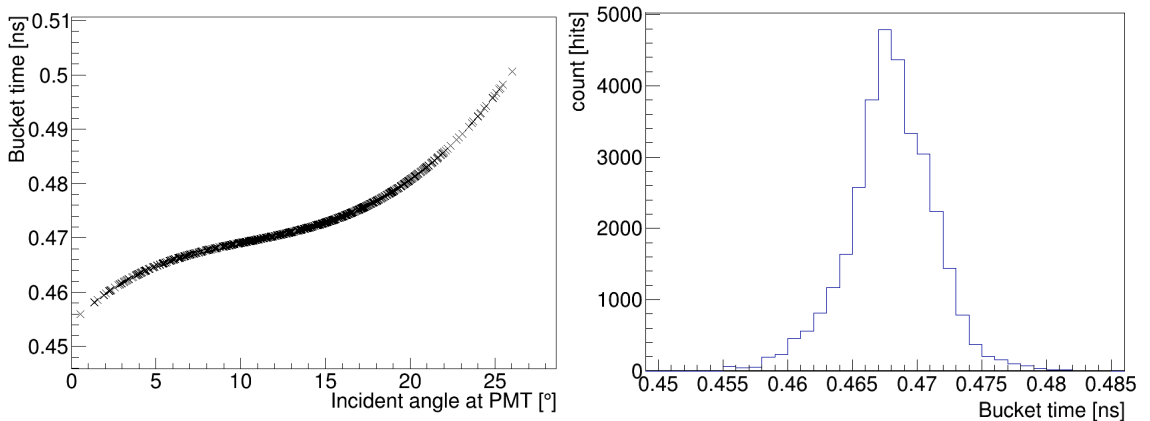
Figure 4.19: Left: Bucket time corrections as a function of incident angle at the PMT. Right: Histogram of bucket times for all PMTs from full PCA dataset. Each PMT only contributes hits for the 'best fibre'.

nanoseconds, peaking at around 0.47 nanoseconds. Again, because only the best fibre is selected when extracting the PCA constants, analysing the full dataset should show very similar range of bucket times. An example of the bucket times for a single fibre from PCA dataset are displayed on the left in Figure 4.19. As can be observed from the same figure, most PMTs in the beamspot get direct hits. Additionally, most PMTs in the full dataset are PMTs in the centre of the beamspots, as expected.

Angular systematic

The angular systematic correction is also applied to the hit time, depending on the angle between the PMT and the fibre's direction. The value of the correction increases with the
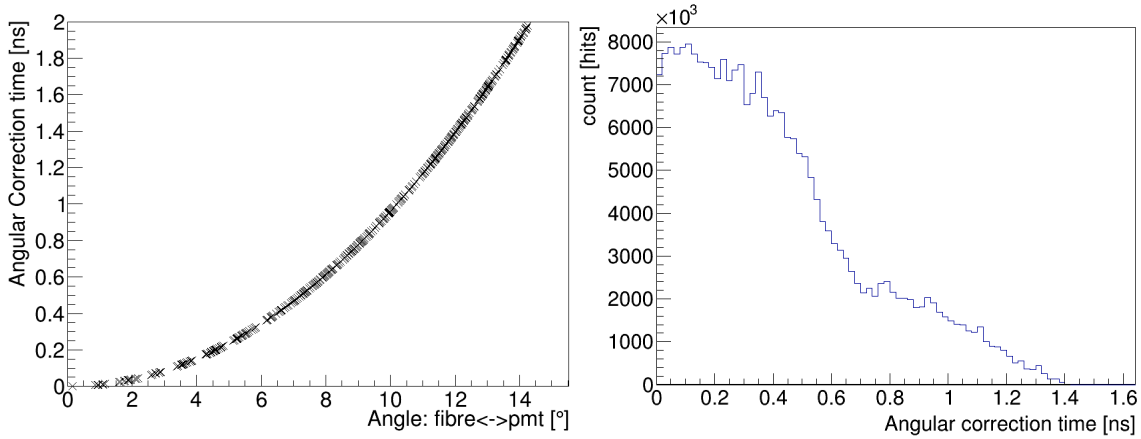
Figure 4.20: Left: Value of the angular systematic correction for single TELLIE fibre. The value is obtained by applying the fit from angular systematic analysis, providing the angle between the fibre and the PMT. The angle is the angle between the fibre's direction and normal to the PMT's center (red dot in Figure 4.9). Right: Histogram of angular systematic corrections for each PMT within one full PCA dataset. Only the best PMT-fibre combination is considered.

angle, as described in the Subsection 4.3.3. It is given by the angular systematic fit per each fibre which comes from the analysis. Regarding the full dataset, the PMTs in the center of the beamspot will experience very small correction, since these are predominantly directly opposite the pulsing fibre. Both observations can be seen in Figure 4.20. The usual angular cut for TELLIE PCA is 12 degrees and, therefore, the effect is not as pronounced. The range is extended in the example plots for better visualization.

Combining the corrections

As seen from the examples of the time corrections, the transit time is the most significant correction to obtain the residual time. Transit time is heavily dependent on the geometry of the detector (therefore, precise and detailed knowledge of the detector geometry and all included components is required). Additionally, the starting and ending positions as well as the starting direction and the incident angle on the PMT are the determining factors. The directions and how they are treated are explained in detail in Section 4.6. It is also worth mentioning here that the bucket time is probabilistic because of the way it is defined and that the angular systematic correction is given by a fit, therefore, also affected by the precision (and errors) of that fit.

During the PCA data-taking, the ECA calibrated PMT hit times are recorded. There are usually 200 000 events for a single run, resulting in few thousands of recorded hit times per PMT. The cuts described in Subsection 4.3.4 are applied. For resulting hits, the best
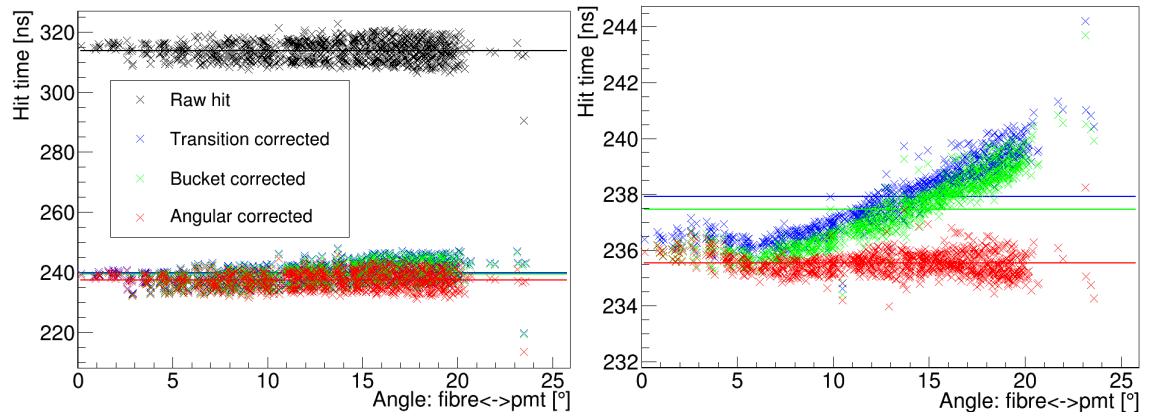
Figure 4.21: Left: Direct light hits as well as corresponding time corrections for Fibre 61, taken from full PCA dataset. The black set are the direct hit times after cuts. The blue set are the residual hit times after correcting for the transit time. Green set has additional bucket time corrections applied. Finally, the red set contains previous corrections as well as the time correction due to angular systematic effect. Right: zoomed version of the left plot, focusing on the time corrections. The colours of the fit lines correspond to different sets.

fibre is selected (the fibre with most valid hits after cuts). For each PMT the direct hit times are recorded and the peak of the histogram is fitted. These direct light peaks for different PMTs are shown in Figure 4.21 in black. Next, the transit time correction is applied for each PMT (this is a constant for a PMT, since it only depends on the PMT and fibre positions and the wavelength of the light). This shifts the overall distribution by up to 80 nanoseconds. Afterwards, the bucket time correction is applied resulting in a minor shift of the overall distribution by $\sim$0.47 ns. The shift is (usually) smaller for smaller angles (the scaling of the bucket time is proportional to the incident angle on the PMT, which is affected by the angle between the PMT and the fibre). The resulting distribution is still affected by the angular systematic. This correction is applied last. The effect of the angular systematic is more pronounced at higher angles. Overall, this brings the distribution of now residual time hits slightly lower and makes it much 'flatter' (following a straight line fit with zero slope). The straight horizontal line is expected after the time corrections, as this represents time of potential event (in this case light leaving the wet end of the fibre). This event has precise (single) time and should be observed as such. Therefore, one of the observables evaluating the 'goodness' (quality) of the time corrections is the variance of the data compared to this straight line. An example of this method of applying the time corrections is shown in Figure 4.21.
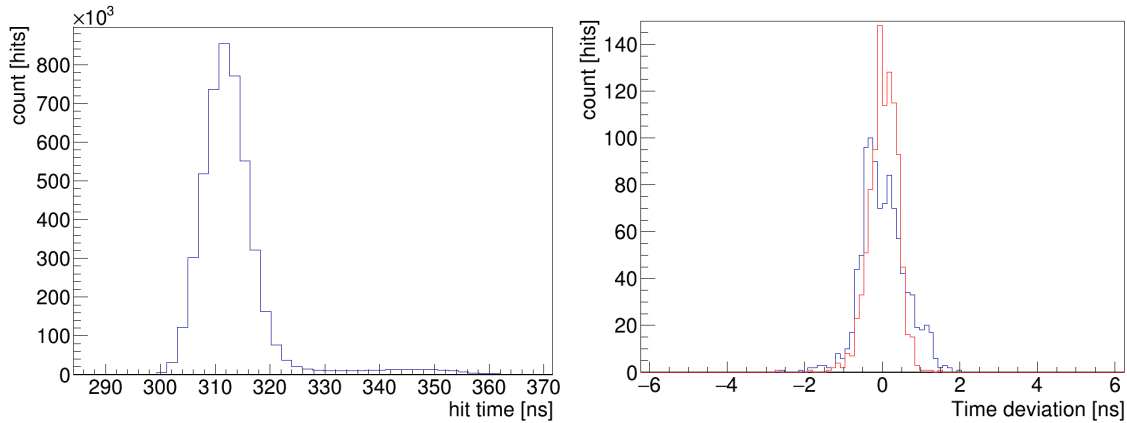
Figure 4.22: Left: Direct hit times as recorded by PMTs for single TELLIE fibre. Right: The evaluation of the time corrections as the deviation of each PMT fit compared to the horizontal line fit. The red set is after all three time corrections were applied.

Example histogram of direct light hits for single TELLIE fibre is shown in Figure 4.22 on the left. These are fit per PMT and shown in Figure 4.21 as the black set. The evaluation of the time corrections is done comparing the variances of the fit PMTs residual times to the horizontal best fit line. This should have smaller variance (a more straight line trend) after the corrections than the original direct light hit times as is the case on the right plot of Figure 4.21.

Once the data is obtained for every single TELLIE fibre, the final hit times can be collected. The sets of raw and collected hit times are presented in Figure 4.23. Obviously, the corrected hit times are shifted to lower values after the corrections, mostly due to the transit time subtraction. Additionally, the outlier PMT hit times, visible as small peaks and troughs, have been smoothed out.

4.4   Overview of delays

As mentioned, there are several delays involved in the calibration process using the TELLIE system. To better appreciate these delays, the whole process of sending a command to fire photons from the fibres to recording a hit on a PMT is presented below. The usual process of using TELLIE to obtain hit time is:

- A command is set to fire photons from TELLIE fibre;

- Photons leave the TELLIE fibre, after a delay;

- The light travels through the detector and hits PMT;
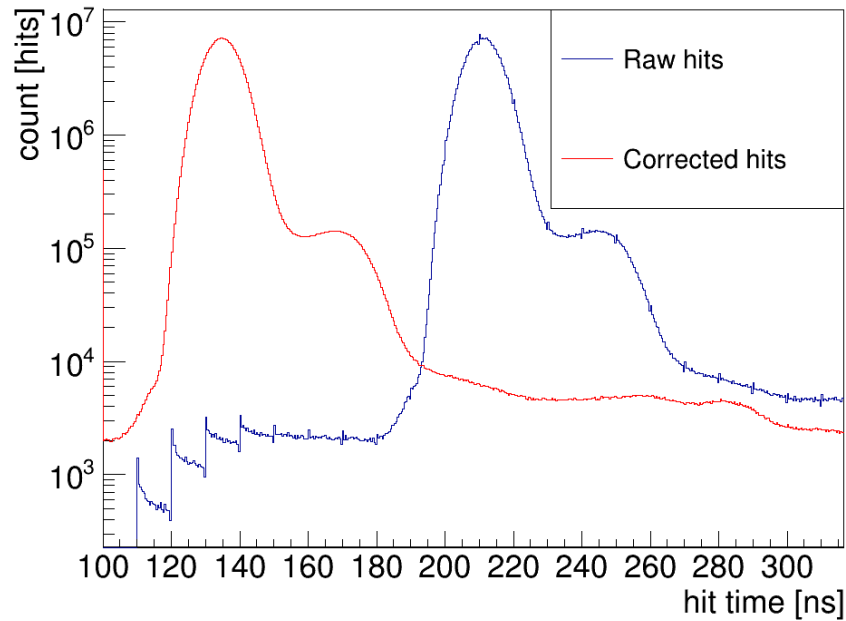
Figure 4.23: Comparison between the raw hit times and hit times corrected for the transit times, bucket times and angular systematic. In addition to the overall shift to lower values, the corrected spectrum is also much smoother. Only the prompt peak is considered for the final fit.

- The discriminator fires after some charge dependent delay ('PCA delay');

- After a chosen delay External Asynchronous (EXTA) trigger is issued with a corresponding Global trigger (GT);

- The event window opens recording everything before the GT;

- The hit times are recorded with respect to t_0.

This procedure is shown in Figure 4.24.

There are several delays involved in this process. A simplified overview of them is further discussed in this section.

These delays, offsets and time values (also shown in Figure 4.25) are:

- **The trigger delay** $= \delta_\mathrm{T} =$ External Asynchronous (EXTA) trigger delay, software setting, fibre dependent. Equal to *trigger_delay* + a constant;

- **The global trigger delay** $= K_\mathrm{GT} =$ Constant time it takes the global trigger signal to get to crates to start collecting data;

- **The software fibre delay** $= \delta_\mathrm{SW} =$ Software delay (tunable), fibre dependent. Corresponds to *fibre_delay*;
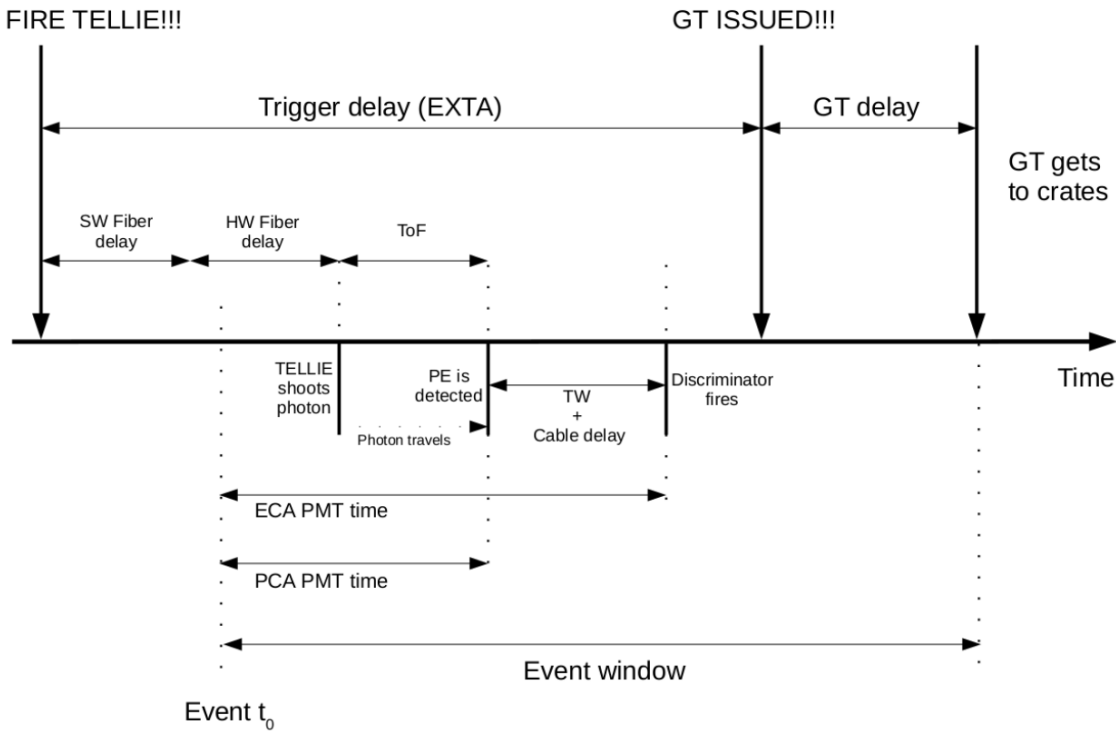
Figure 4.24: Visualization of different delays and offsets during TELLIE data taking.

- **The hardware fibre delay** $= \delta_{\mathrm{HW}} =$ Hardware delay, intrinsic to system, has to be measured, used as input for PCA analysis;

- **The Time-of-Flight (transit time)** $= ToF =$ Photon travel time from fibre to PMT. Includes bucket time and angular systematic correction;

- **the event window** $= K_{\mathrm{W}} =$ Constant 500 ns window that gives t_0 for PMT hit;

- **The ECA PMT time** $= t_{\mathrm{ECA}} =$ Raw PMT hit time [ns]. Not corrected by channel delays;

- **The PCA PMT time** $= t_{\mathrm{PCA}} =$ Hit time after PCA (time-walk and cable delays) corrections [ns];

- **The PCA offset** $= \delta_{\mathrm{PCA}} =$ Charge and channel dependent time correction, requires existing PCA constants (given by laserball).

There are several delays of interest, these can be grouped as:

- *The constants*: Global trigger delay K_{GT}, Event window K_{W};

- *Hit related values*: ECA PMT time t_{ECA}, PCA PMT time t_{PCA}, Time-of-Flight ToF;
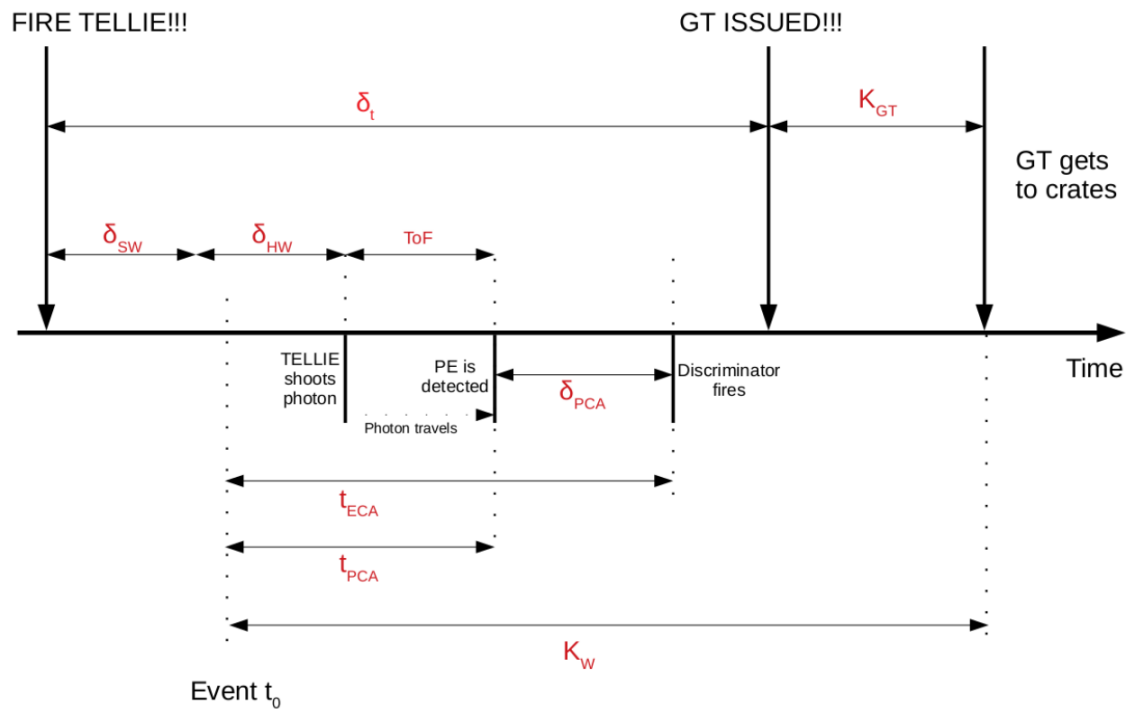
Figure 4.25: Visualization of different delays and offsets during TELLIE data taking.

- *Software set values*: Trigger delay δ_T, Software fibre delay δ_{SW};

- *Analysis related values*: Hardware fibre delay δ_{HW}, PCA offset δ_{PCA}.

4.4.1 Software set values

Trigger delay δ_T

The trigger delay is simply a delay postponing the triggering, ensuring the TELLIE light is recorded in the event window. This is kept constant throughout TELLIE datasets (900 ns) such that the events come approximately in the middle of the event window. This makes it unlikely to lose events if they come earlier or later than expected. It can be set in ORCA[6].

Software fibre delay δ_{SW}

The software fibre delay is a setting that can be set in ORCA and is then applied by variable delay line built onto each TELLIE driver board (therefore being fibre specific). The idea is to ensure the light is emitted from the TELLIE channels (at dry end) at the same time, compensating for board-to-board variations in the time between a primary

---

[6]**ORCA** is an object-oriented real-time control and acquisition: DAQ software interface with the SNO+ detector
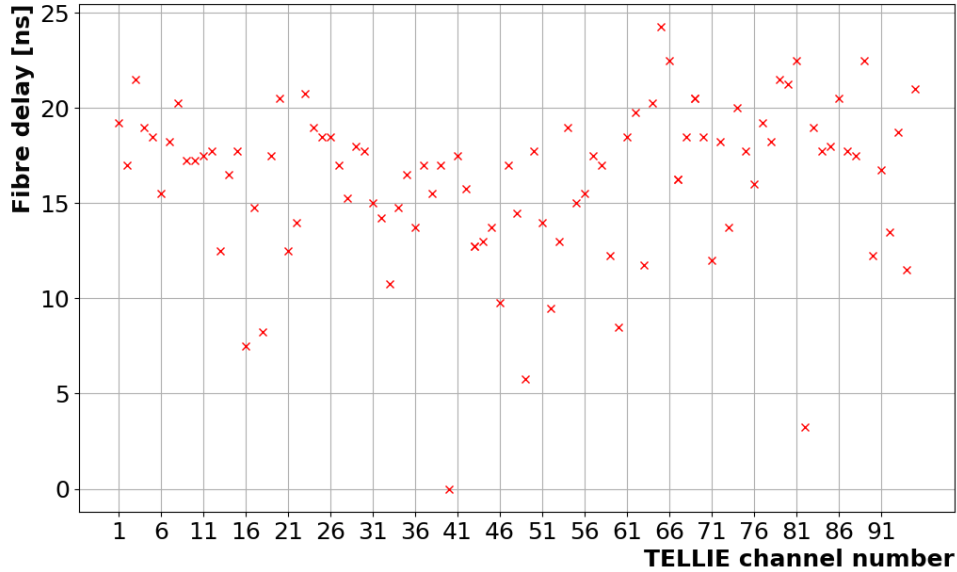
Figure 4.26: TELLIE software fibre delays as a function of the fibre index. These ensure the light emission happens at the same time.

signal being received at the control box and light being produced at the requested channel [111]. The software and hardware delay are complementary to each with the same purpose of (mainly) correcting for LED driver differences. But while the software delay is measured 'offline' as a first order correction, the hardware delay is an exact correction obtained from data. The way these were (re)measured is explained in detail in Section 4.5. There are several factors absorbed in this delay such as: delays caused by physical path length of the BNC cables, the path along the ribbon cable, response of control box chip and response of the individual driver board chips. In theory, this should show visible 'V' pattern due to how the TELLIE rack is routed. The fibre delays are plotted in Figure 4.26.

4.4.2   Analysis related values

Hardware fibre delay $\delta_{\mathbf{HW}}$

This is the time offset between different TELLIE LEDs due to LED board drivers causing the light emission to happen at slightly different time for each LED (assuming same trigger time). This is an exact data-driven correction that is complementary to first order software fibre delay correction. These can be obtained using the method described in Appendix A. However, it is also possible to calculate the values from data if calibrated times are available. From Figure 4.24, it can be seen that

$$\delta_{\mathrm{HW}} = t_{\mathrm{PCA}} - ToF - \delta_{\mathrm{SW}} + \delta_{\mathrm{T}} + K_{\mathrm{GT}} - K_{\mathrm{W}}. \tag{4.6}$$
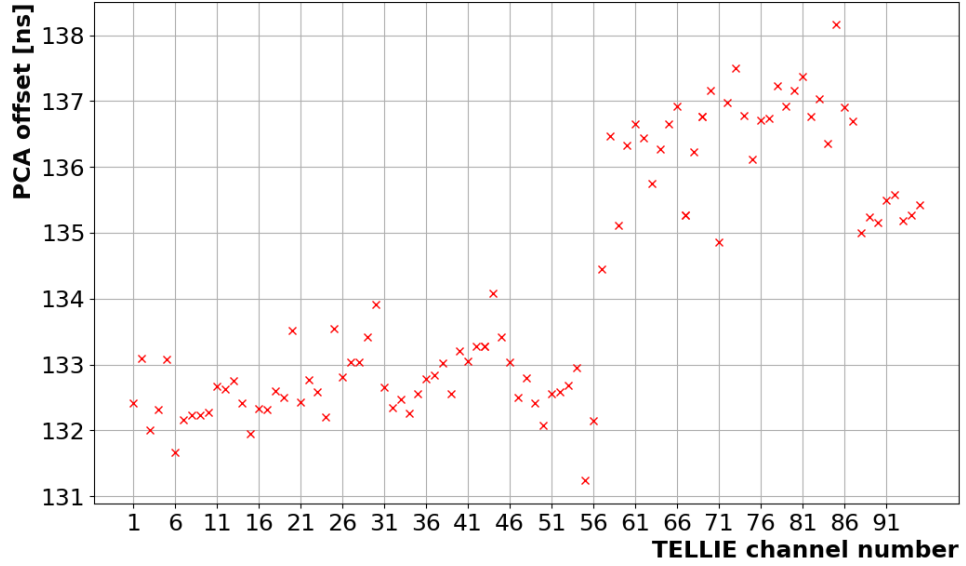
Figure 4.27: TELLIE hardware delay times calculated from PCA calibrated hit times, corrected for the Time-of-Flight, bucket times and angular systematic offset. These are the basis for the hardware fibre delays used as input for TELLIE PCA. Application of the delay ensures the time emission is the same for all fibres. The clear grouping is caused by the way the TELLIE hardware is connected up, with the control box being in the middle, dividing upper and lower boxes. More details on TELLIE are available in Subsection 3.6.2.

Therefore, if PCA calibrated times t_{PCA} are available using previous PCA constants, such as laserball, it is also possible to extract the LED driver offsets for each LED. This has been predominantly done for PCA datasets discussed in this thesis. In that case, the hardware delay is obtained as described in Equation 4.6. Figure 4.27 shows the value of the injection times as a function of the TELLIE fibre. It should be noted that the values presented here are the PCA calibrated hit times corrected for the Time-of-Flight, as well as bucket time and angular systematic offset, but the additional constants are omitted (again, only relative differences are important).

PCA offset δ_{PCA}

Finally, using the hardware fibre delay δ_{HW} it is possible to calculate the PCA offset δ_{PCA} as

$$\delta_{\mathrm{PCA}} = t_{\mathrm{ECA}} - ToF - \delta_{\mathrm{HW}} - \delta_{\mathrm{SW}} + \delta_{\mathrm{T}} - K_{\mathrm{GT}} + K_{\mathrm{W}}. \tag{4.7}$$

The TELLIE hardware delays are sometimes referred to as the fibre pca offsets, which is not the same as the variable PCA offset δ_{PCA} here - which is the time-walk and the cable delay correction in the PCA analysis.

4.5   Remeasuring fibre delays

TELLIE fibre delays are offsets applied to TELLIE fibres at the point of using them from software controlling the SNO+ detector. They delay the emission of the light from each TELLIE channel to ensure that the light leaves the channels at the same time [111]. They are, therefore, channel specific. They were originally measured in 2016 when TELLIE was still being commissioned. There were several changes done to the system, including the addition of AMELLIE (attenuation module), swaps of driver boards, changes of cables, routing and tuning since commissioning. Therefore, these delays were measured again in 2019 after complete deployment and official commissioning was finished for the TELLIE system. The new measurement happened on the site of the detector, directly in the deck clean room to ensure that the running conditions for TELLIE are the same as when it usually runs.

The set-up consisted of:

- A arduino was used as source of external triggers, running at 1 kHz;

- A small Hamamatsu photosensor module;

- An oscilloscope;

- A laptop;

- BNC cables;

- Some additional connectors.

The arduino was set to pulse at 1kHz (same frequency is used for PCA data taking) as external trigger. It was connected to the TELLIE trigger-in port. Laptop was used to communicate with TELLIE control box, sending commands to pulse particular TELLIE channel for specific number of pulses, using the external trigger. The signal-out TEL-LIE port was connected to oscilloscope as well as the trigger signal from arduino. The oscilloscope was then used to calculate the time difference between the signal being sent from arduino and light leaving TELLIE LED. The measured time, therefore, included the physical cable lengths, the ribbon cable connecting TELLIE boxes to the control box and the response of the control box driver. The result of the measurement is the mean value obtained from 1000 pulses after outliers were cut. This was repeated for all available channels. It should be mentioned that this set-up (as well as the place and conditions)

were different to the original measurement. However, only the relative time differences between the channels are important.

To obtain the relative time differences, a channel with the highest PMT hit time is selected. This was channel 40 for both measurements. Then, for each channel, the difference between this time and the PMT hit time for that particular channel is calculated. This is the new value of the (software) fibre delay. Adding this delay to the PMT hit time for the channel results in a constant. This is shown in top plot of Figure 4.28. The difference between the new and old fibre software delays is the bottom plot of the same figure. Additional data is listed in Appendix C.

4.6 Fitted fibre directions

Another improvement to TELLIE PCA analysis was the addition of calculation of TELLIE fibre directions for each dataset. The main reason was to improve the time calibration since precise angular knowledge is essential for several parts of the analysis, such as the definition of the beamspot, the angular systematic correction or the incident angle on the PMT bucket. This analysis was initially done on first PCA dataset in 2017. The details relating to PCA are discussed below, the full details of the analysis are *SNO+ TELLIE PCA data – Fibre installation validation document* [112].

Simplified overview of the fitting procedure is:

- The full dataset data is being considered;

- The PMT occupancy cut is applied (both minimum and maximum) on data;

- In first iteration:

  - The PMTs are grouped together according to the face of the icosahedron they are mounted on, and they are weighted by occupancies;

  - The faces with intensities above 20% of maximal intensity are added to obtain an estimate for the direct light spot (centre of the beamspot);

  - The opposite side of the PSUP provides estimate for the reflected light spot.

- In second iteration:

  - The PMTs within a cone of the estimated light spot (the beamspot) are weighted;
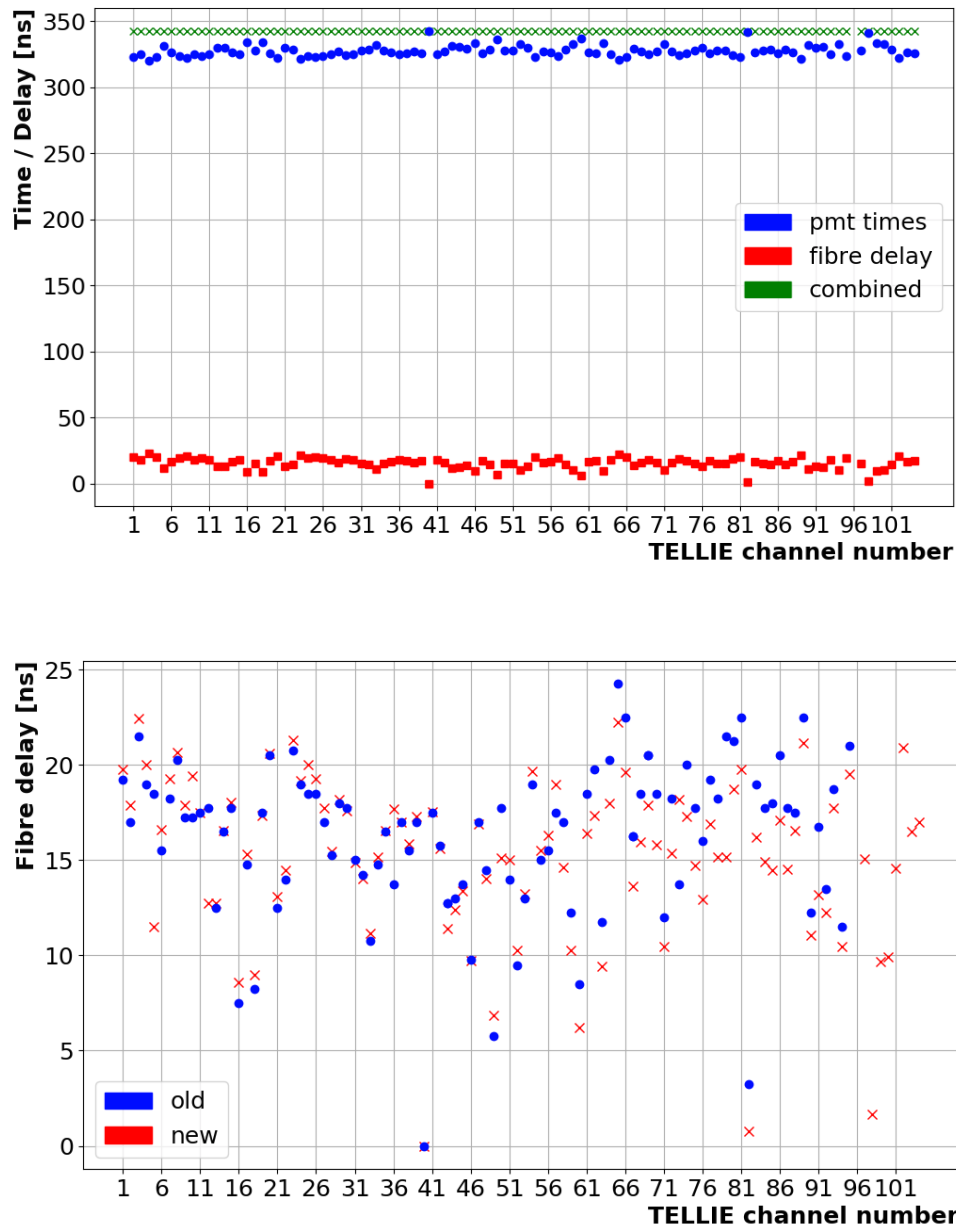
Figure 4.28: Top: A plot representing the remeasurement of TELLIE software fibre delays. The blue points are the mean PMT hit times for each TELLIE channel. Red are new calculated fibre delays. Combining these the green dataset is obtained, producing a constant time for all TELLIE channels. Bottom: Comparison of TELLIE software fibre delays from original measurement during commissioning and new measurement of the same delays on the site of the detector after successful commissioning.
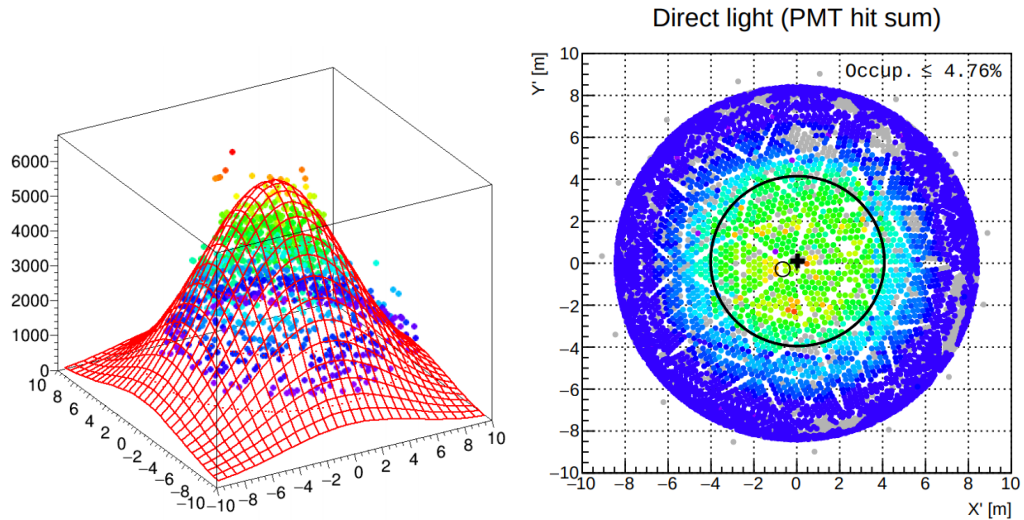
Figure 4.29: Left: Example of fitting direct light spot for single TELLIE fibre using the method described in Section 4.6. Right: Comparing the original (installed) and fitted fibre direction from the same study. Both plots from [112].

— Intensity-weighted position of these PMTs is then the input for a fit.

- In the third iteration:

  — The PMT positions are projected to the plane touching the PSUP sphere;

  — A 2D Gaussian function is fitted to the positions of PMTs within the fibre aperture radius with intensity above 20% of the maximum intensity;

  — Four parameters are obtained: amplitude A, the position on the plane (x, y) and the standard deviation σ.

- The installed fibre positions are loaded from the database;

- The projected light spot (assuming a straight line) is compared to the direct light fit from this study;

- The angle between the projected light and the fitted light spot is calculated.

An example of the fitted direct light spot is shown in Figure 4.29. These fitted directions are then used in the TELLIE PCA analysis to improve the beamspot definition as well as the angular systematic value for each fibre-PMT combination as well as to ensure the incident angle on the PMT that affects the bucket time is as precisely known as possible. The analysis is rerun for each TELLIE dataset that is used for extraction of PCA constants.

4.7   PCA Datasets

There have been several dedicated campaigns to obtain full PCA datasets. As explained before, PCA dataset is data taking session (or multiple) where all 95 TELLIE channels are consecutively used to pulse light into the detector, in separate runs (one per each TELLIE channel), for 200 000 events at 1 kHz frequency. These settings can be customized, but these were found to ensure the required statistics and were used for all consecutive TELLIE PCA datasets. There are several other trigger and delay settings, these were mostly kept constants but were slightly altered in some cases. Table 4.1 contains list of all available dataset with basic settings. Where possible, the datasets were taken as a single session but where this was not possible the sets were taken during sessions in close proximity to each other (never spanning more than 3 days, nominally within 2).

Dataset	Date	Mode	Fibres used	Pulse rate [Hz]	Pulses	Trigger delay [ns]	Software delay [ns]	Avg NHit
1	2017 June	asynchronous	95	1 000	200 000	650	original	35
2	2018 March	synchronous	95	1 000	200 000	1 000	original	40
3	2018 June	synchronous	95	1 000	200 000	900	original	42
4	2018 Sept	synchronous	95	1 000	200 000	900	original	42
5	2018 Dec	synchronous	95	1 000	200 000	900	original	42
6	2019 March	synchronous	92	1 000	200 000	900	original	40
7	2019 Dec	synchronous	95	1 000	200 000	900	remeasured	42
8	2020 May	synchronous	94	1 000	200 000	900	remeasured	42

Table 4.1: Table summarizing all currently available TELLIE PCA datasets. Sets 2-8 were used for TELLIE PCA analysis.

It should be noted that set 1 was taken in different TELLIE mode and as such will not be considered for TELLIE PCA analysis. Additionally, dataset 7 was taken after filling with scintillator has commenced and the last dataset (dataset 8) was taken after half of the detector was filled with scintillator. Due to many optical changes with scintillator filled detector, these two datasets are expected to give slightly different results. As mentioned earlier, there are tuning runs in-between final calibration runs for each fibre to achieve the required light intensity. The full lists of run number for each dataset are listed in Appendix B.

4.7.1   Nearline monitoring

During PCA data-taking, the quality of the data is being monitored almost in real time. In addition to usual detector control tools, there are unique online monitoring

tools to ensure the quality of the TELLIE data as well as the quality of the data for PCA calibration. The TELLIE monitoring looks at the stability of the channel, the event separation and the TAC counts for direct and reflected light; whereas the TELLIE PCA monitoring evaluates the NHit distribution, the PMT occupancies and the time profile of the PMT hits. Example plots from these monitoring tools are shown in Figure 4.30.

Once the data is satisfactory, the generation of PCA constants can proceed as described in Subsection 4.3.1. There are several steps, some of which are run-based (for each TELLIE fibre) and others are global for the full dataset. Some important elements from each part are described below.

4.7.2 Singe run data

Assuming the settings are correct and there is reasonable light intensity data from a stable fibre, the procedure analysis follows as (for each fibre):

- The fibre position is confirmed (so that the correct fibre is firing), this is part of the online monitoring;

- The fibre direction is calculated by fitting the beamspot, as described in Section 4.6;

- The angular systematics parameters are obtained as described in Subsection 4.3.3;

- The beamspot is defined as: normal, online, enabled PMTs within 12 degrees from the fibre direction;

- The occupancy limits are imposed (1% - 5% occupancy) as described in 4.3.4;

- For the hits that passed, the hit times (and charges) are recorded;

- The hit times are corrected for the 3 time corrections: transit time, bucket time and angular systematic;

- The final residual hit times are stored for full dataset analysis.

Example plots for the single fibre analysis steps are shown in Figure 4.31.

4.7.3 Dataset data

After the data from individual TELLIE runs (one for each fibre) is cleaned and the relevant data is stored, the PCA extraction can proceed. Again, there are multiple steps to following analysis:
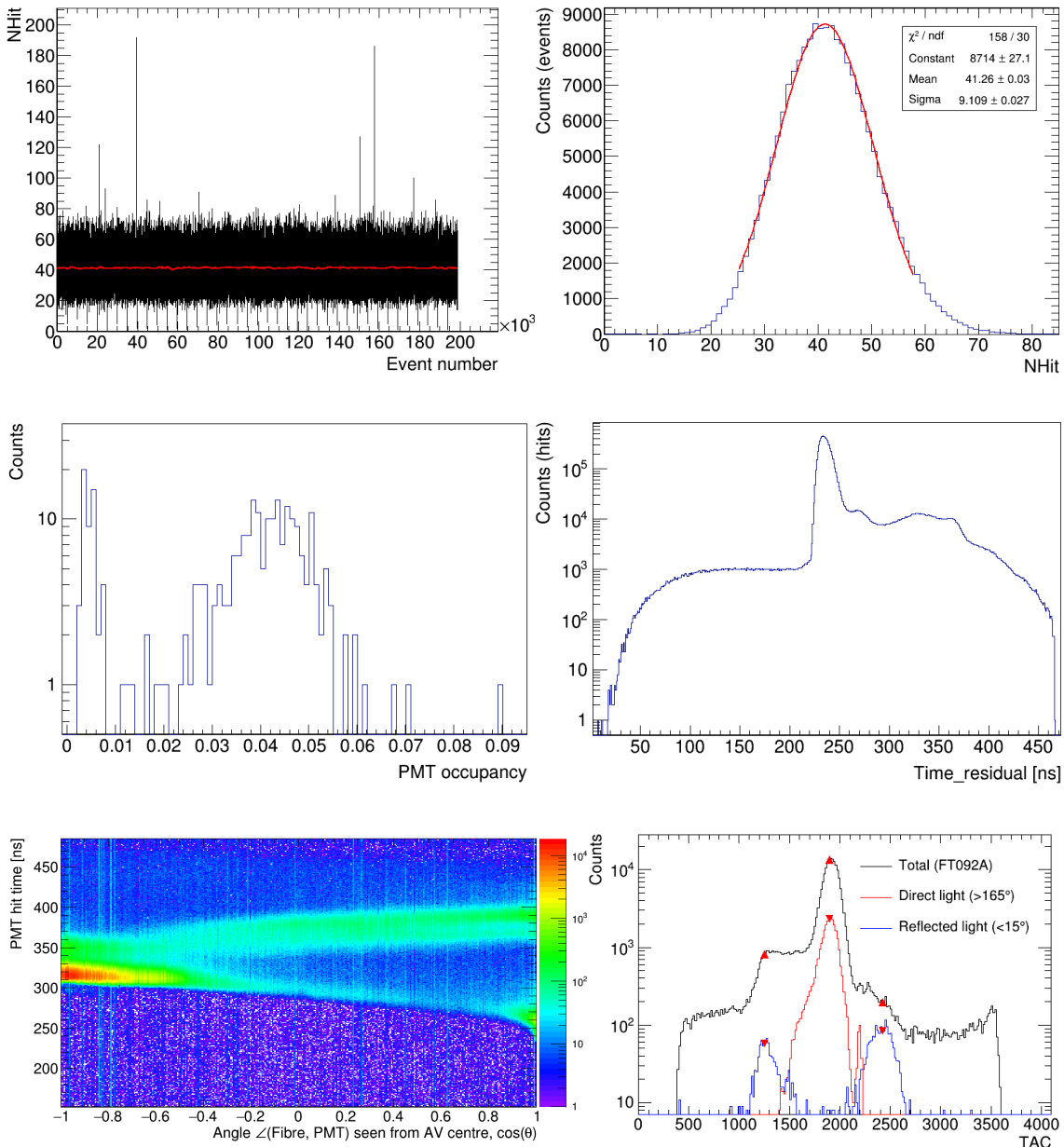
Figure 4.30: Example plots from online monitoring tools used for TELLIE data taking. From top left: 1: Channel stability evaluation by looking at NHit distribution (function of light intensity) over time. 2: Histogram of NHit distribution. The usual desired NHit for PCA run is 40-45. Irregularities in shape of the distribution could point to issues with the fibre. 3: The distribution of PMT occupancies. Since there are cuts applied based on occupancy, this represents what fraction of data can be used for PCA extraction. 4: The log histogram of residual time hits. Again, any uncommon features would point to issues with fibre or the path taken to the PMTs that produced hits. Only the prompt time peak is considered for fitting. 5: A map representing the hit times produced by TELLIE light as a function of an angle between the TELLIE fibre and PMT recording a hit. Clear groups of direct light as well as near and far reflections can be observed. 6: The distribution of light looking at fractions of direct and reflected light. Plots taken from internal online monitoring tools.
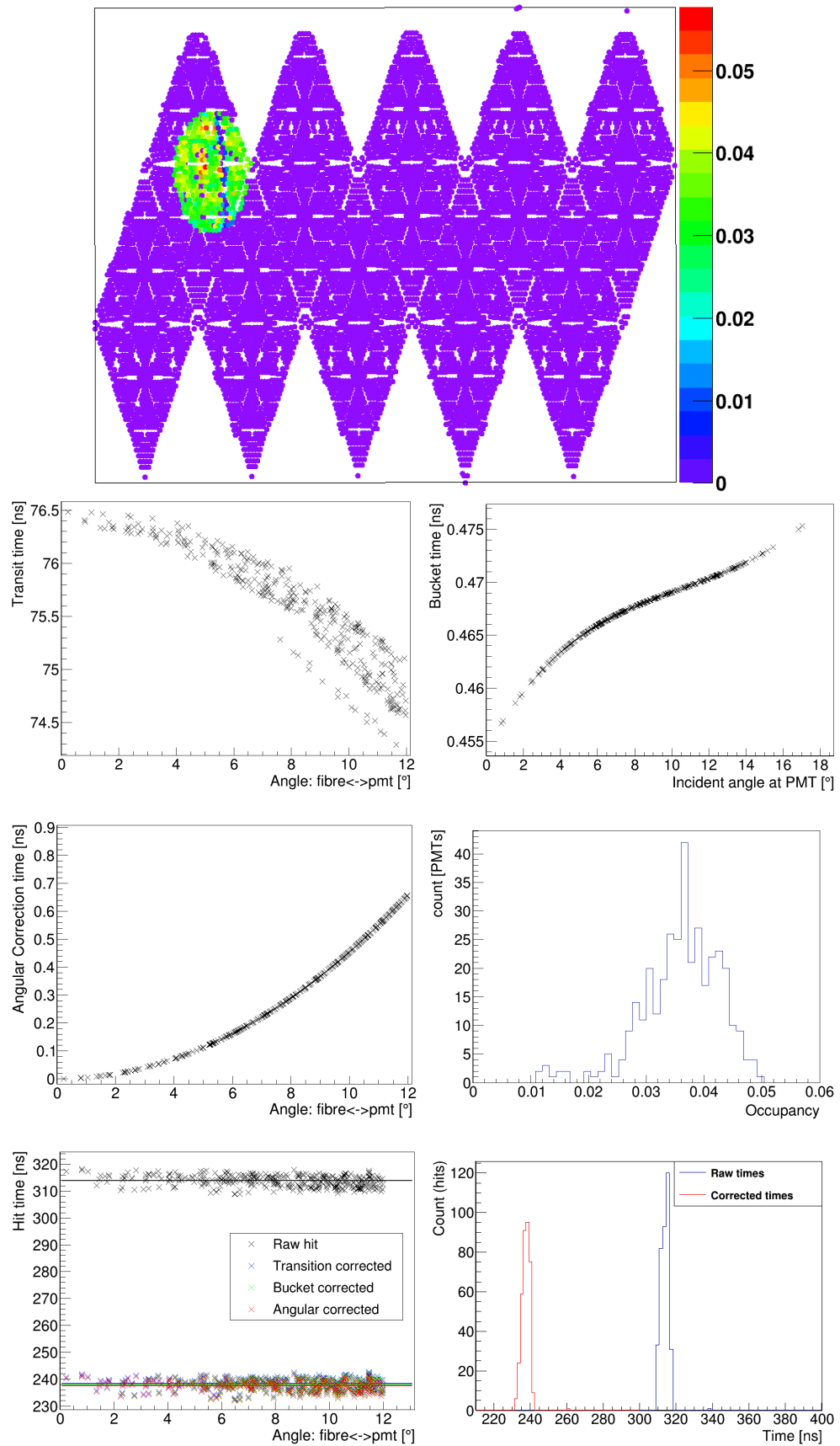
Figure 4.31: Single fibre data - cuts and corrections as described in Subsection 4.7.2. From top: 1: defining beamspot based on the angular cut, 2: transit time correction, 3: bucket time correction, 4: angular systematic correction, 5: PMT occupancy after occupancy cuts, 6: fitting PMT hit times and corrected residual times, 7: log comparison between raw direct hit times and corrected residual times.

- The time offsets between different TELLIE LEDs have to be calculated. As discussed, these can be obtained in two different ways:

  1. calculated as hardware fibre delays δ_{HW} described in Subsection 4.4.2 if previous PCA constants are known (such as close in time laserball calibration);

  2. using the mechanism presented in detail in Appendix A. For purposes of PCA datasets considered in this thesis, the first approach was applied while the second approach was used as cross-check.

- The best fibre is selected for each PMT: the fibre with highest statistics and lowest errors;

- The cable delay for each PMT can now be extracted as a difference to global time offset. This global time offset is usually set so that the variance of all PMTs is the smallest. Only the relative difference to this offset (for all PMTs) is required;

- Since the residual times are now well known, the interpolation points can be calculated per PMT, as described in Subsections 4.2.1 and 4.3.1;

- The final fit can be applied to the interpolation points. These are the final TW calibration values for each PMT;

- Additionally, the three charge variables can be extracted as described in Subsection 4.2.1.

Example plots for the extraction of LED delays are shown in Figure 4.32. Example plots for extraction of charge PCA parameters as well as fitting of interpolation points for time-walk effect are shown in Figure 4.33. Finally, Figure 4.34 is depicting plots for the selection of the best fibre, extracted cable delays as well as the comparison of these delays to previous database values (latest laserball calibration).

4.7.4 Additional data

There is plenty additional data to look at for full PCA dataset. The monitoring of this data is useful. Not only it compares the detector's status between the different datasets and helps evaluating the quality of the calibration, it can also point to any trends with either the electronics or the calibration system.

Some useful examples are:

- A flat map of offline PMTs, these cannot be calibrated and therefore are not used for the analysis; can also be observed on other plots, set to 0;
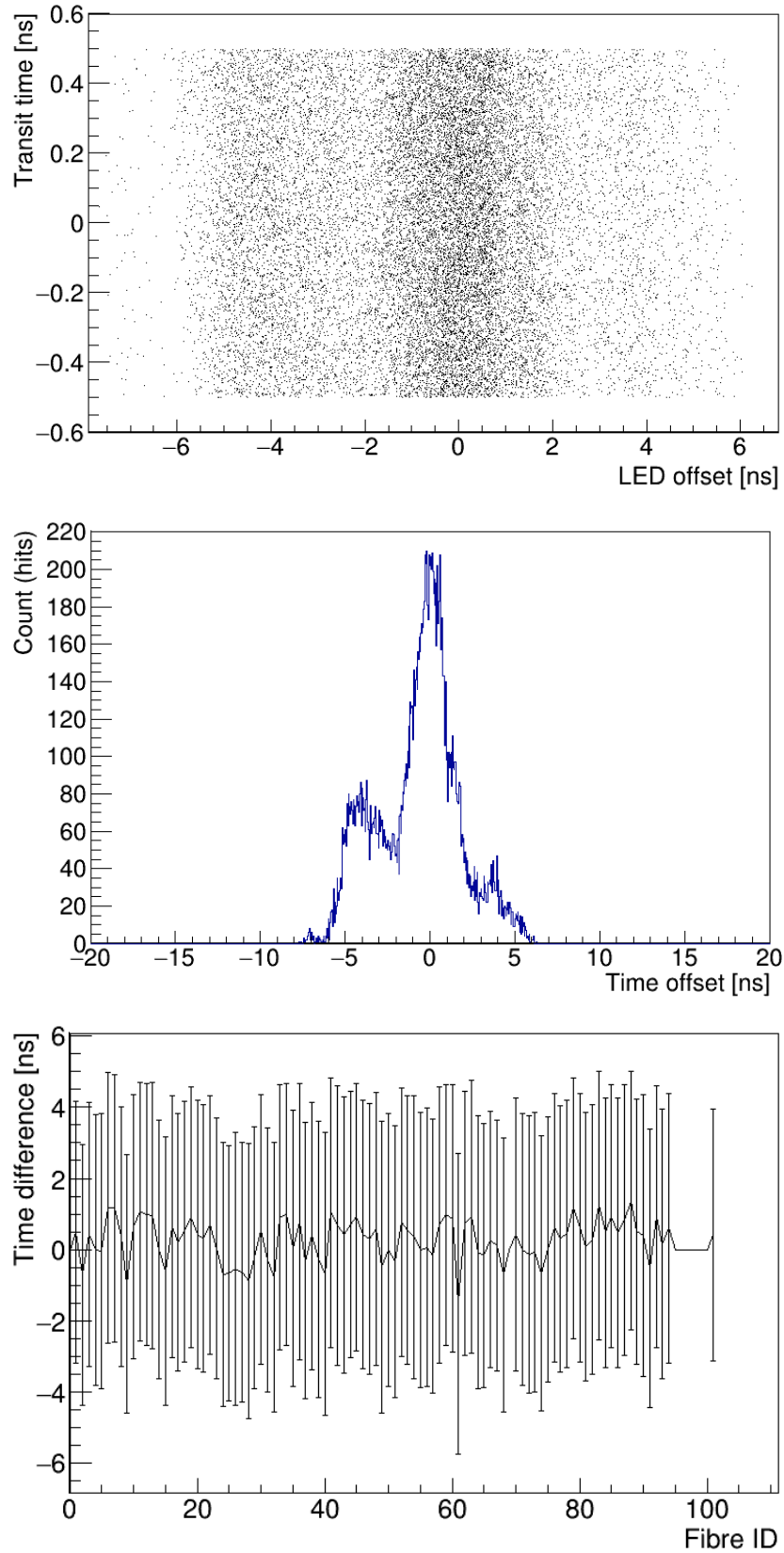
Figure 4.32: Plots related to the relative time offsets between TELLIE LEDs: 1. 2D histogram of transit time differences as a function of the LED pair time offsets, each point is a relative time offset between two LEDs as seen by single PMT; 2. 1D histogram of the median time offsets for each LED pair; 3. 2D graph showing all extracted LED global offsets with error bars versus LED number.
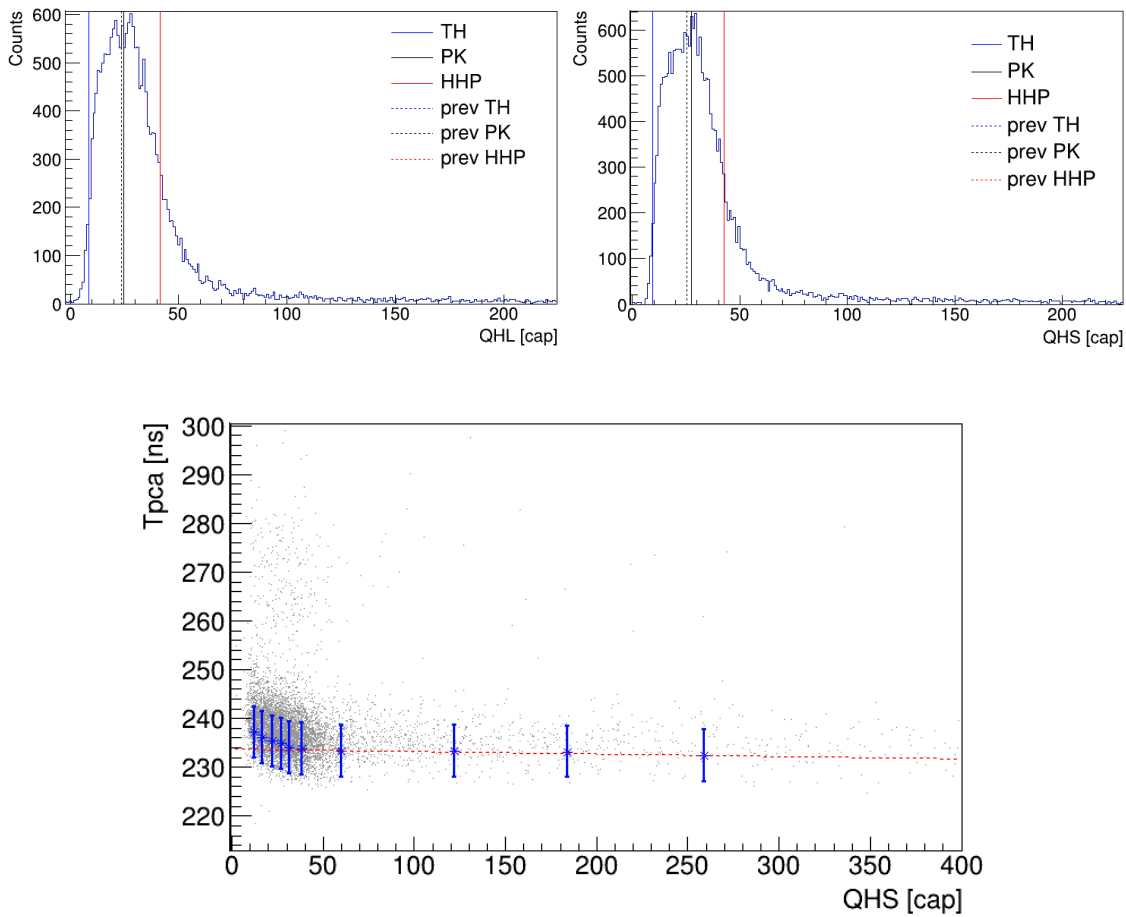
Figure 4.33: Plots related to the extraction of charge parameters as well as the calculation of interpolation points and fit for singe example PMT (3199) from full PCA dataset: 1. QHL charge parameter extraction, compared with previous values; 2. QHS charge parameter extraction, compared with previous values; 3. Fitting of interpolation points for example PMT.
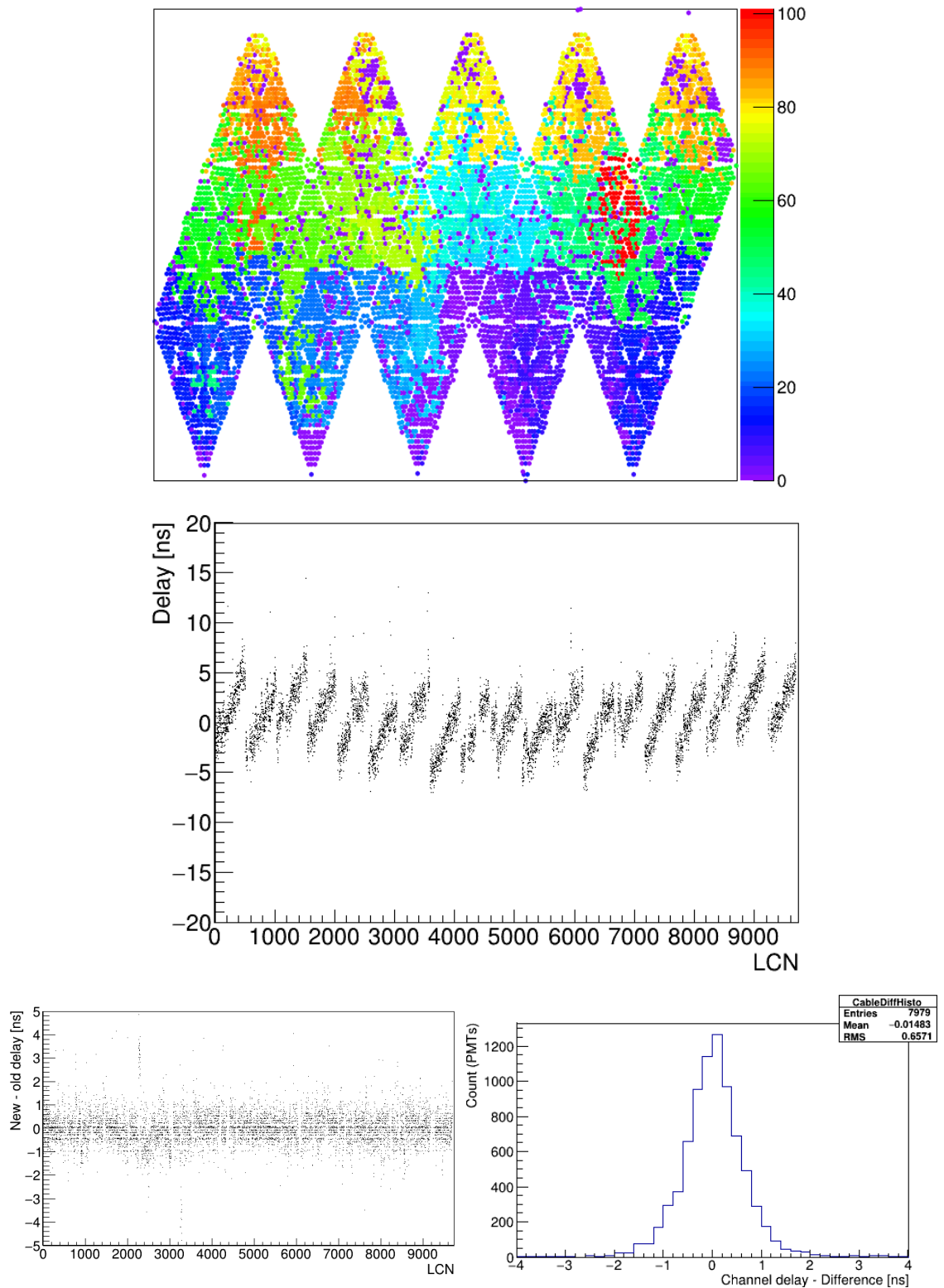
Figure 4.34: Additional plots related to full PCA dataset analysis: 1. Flat map of PMTs showing the best fibre for each PMT in one dataset (the z-axis value is the ID of the best fibre); 2. The final extracted cable delays for each PMT, obtained from TELLIE PCA dataset; 3. Comparison of extracted cable delays to previous database value (laserball extracted cable delays); 4. Same as 3 in the form of a histogram.

- A flat map of hits: the number of events that each PMT triggered on, for all fibres. This approximately corresponds to overall coverage of the detector by TELLIE fibres;

- The LED coverage: the number of LEDs that each PMT was hit by. This represents how redundant the TELLIE system is and how symmetric the distribution of the fibres around the PSUP is.

4.8   PCA Benchmarking

The purpose of benchmarking is to verify the quality of the dataset, to evaluate the divergence from previous dataset, to look at outliers and additionally to test the newly obtained constants. The two aims of PCA are to extract the cable delays as well as the interpolation points for the time-walk effect. Both of these are highlighted in Figure 4.36. There are several parts of benchmarking:

- Comparing the cable delays;

- Comparing the PMT time-walk constants;

- Applying the constants on a control run.

These are discussed in more detail in subsections below.

4.8.1   Cable delays

The cable delays (also called electronics delays) are the delays for each PMT caused by the length of the physical cables, the electronics delay and the transit time inside the PMT itself. They are charge independent [103]. Due to the specific way the dry end electronics is connected, these delays have a unique pattern, they increase depending on the position of the PMT across its card mainly due to the length of the traces. The cards in the same crate usually experience very similar offset however there are offsets between different crates due to different length of the cable to each crate and slightly different electronics delay in each crate. Both the usual pattern across the crates, the increasing delay as well as the progression across cards can be seen in Figure 4.37.

Usually, the evaluation of how good newly obtained set of cable delays is, is to compare it to the closest previous set, as well as looking at the specific patterns mentioned above. To compare the sets, the cable delay for each PMT is taken and the previous value of the cable delay for that particular PMT is subtracted. If the differences are plotted as a function of
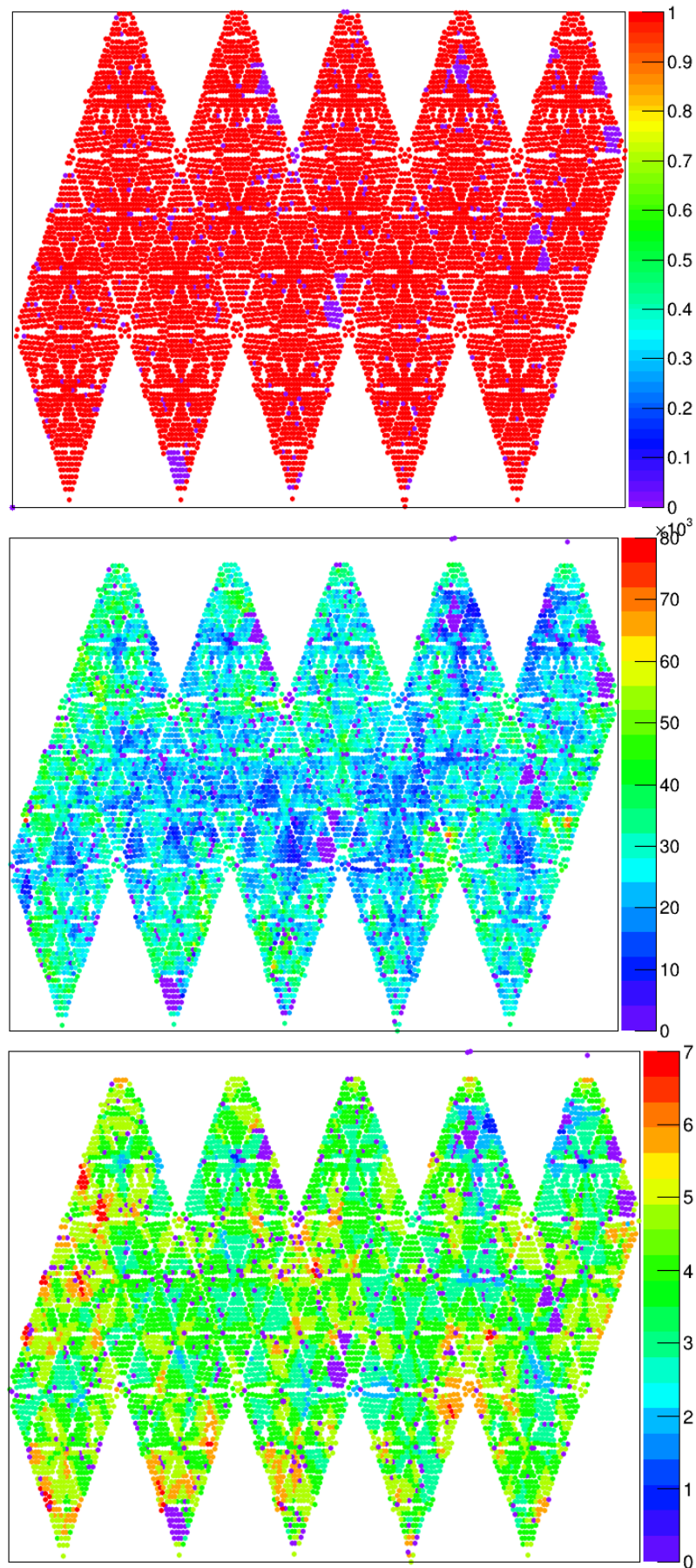
Figure 4.35: Additional plots from TELLIE PCA dataset. 1: A map of offline PMTs, these cannot be calibrated. 2: Hit coverage map of PMTs. 3: LED coverage of the PMT set.
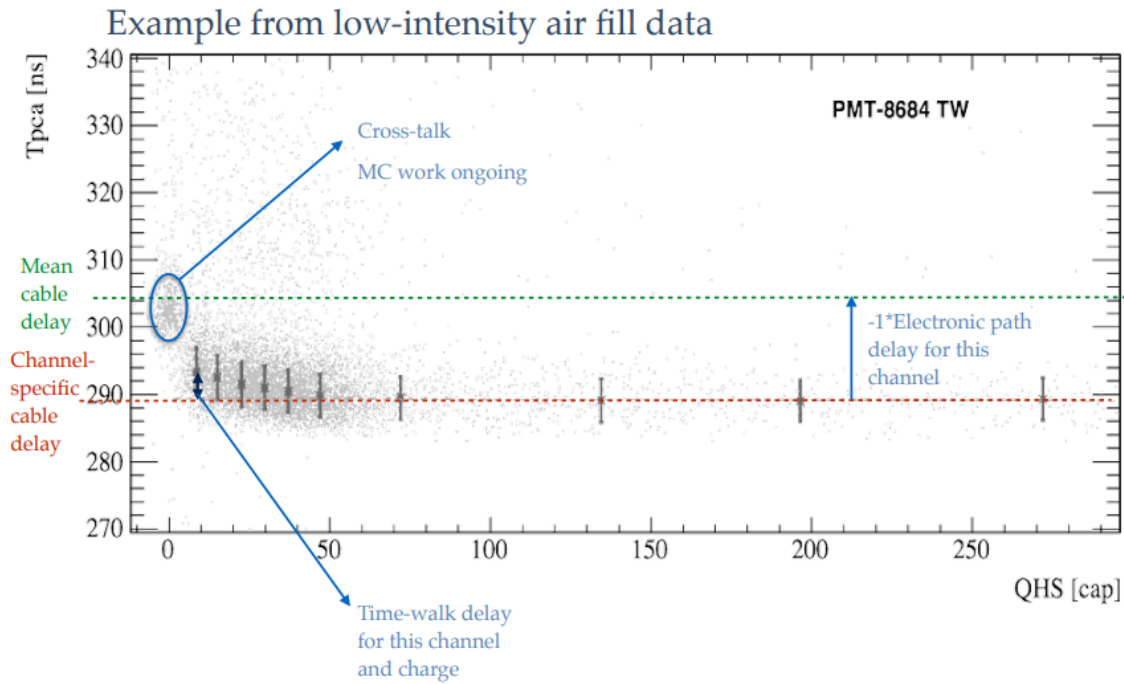
Figure 4.36: Plot of measured charge (QHS [cap]) versus calibrated hit time (T_{pca} [ns]) for and
example SNO+ PMT (8684). The cable delay is the difference between the red and green
horizontal lines while the time-walk delay is highlighted by blue arrow in the bottom portion of
the figure. Plot from [113].

the crate (and card) any systematic effect should be easily observable. Additionally, the
differences can be plotted as a histogram, the mean of this distribution should be close to
0, any significant deviation would suggest a systemic issue with the electronics. The spread
on this distribution then describes the variance of the delays. Some variance is expected,
both due to the changes in the electronics component, 'ageing' of chips, degradation of
cables as well as general maintenance.

Finally, it is useful to observe the cable delays in the flat map space. If there are
significant differences in grouped regions this could suggest issues during data taking.
There can be new items introduces to the detector, such as pipes, or there could have
been changes to the rope system. Changes in the AV position could also slightly change
the delays. These are plotted in Figure 4.38.

Because the histogram version of the comparison are often useful to observe any systemic
shift and also the variance, these were used to compare available datasets. Both mean
and the RMS were considered. Only the corresponding pairs have been compared. These
include:
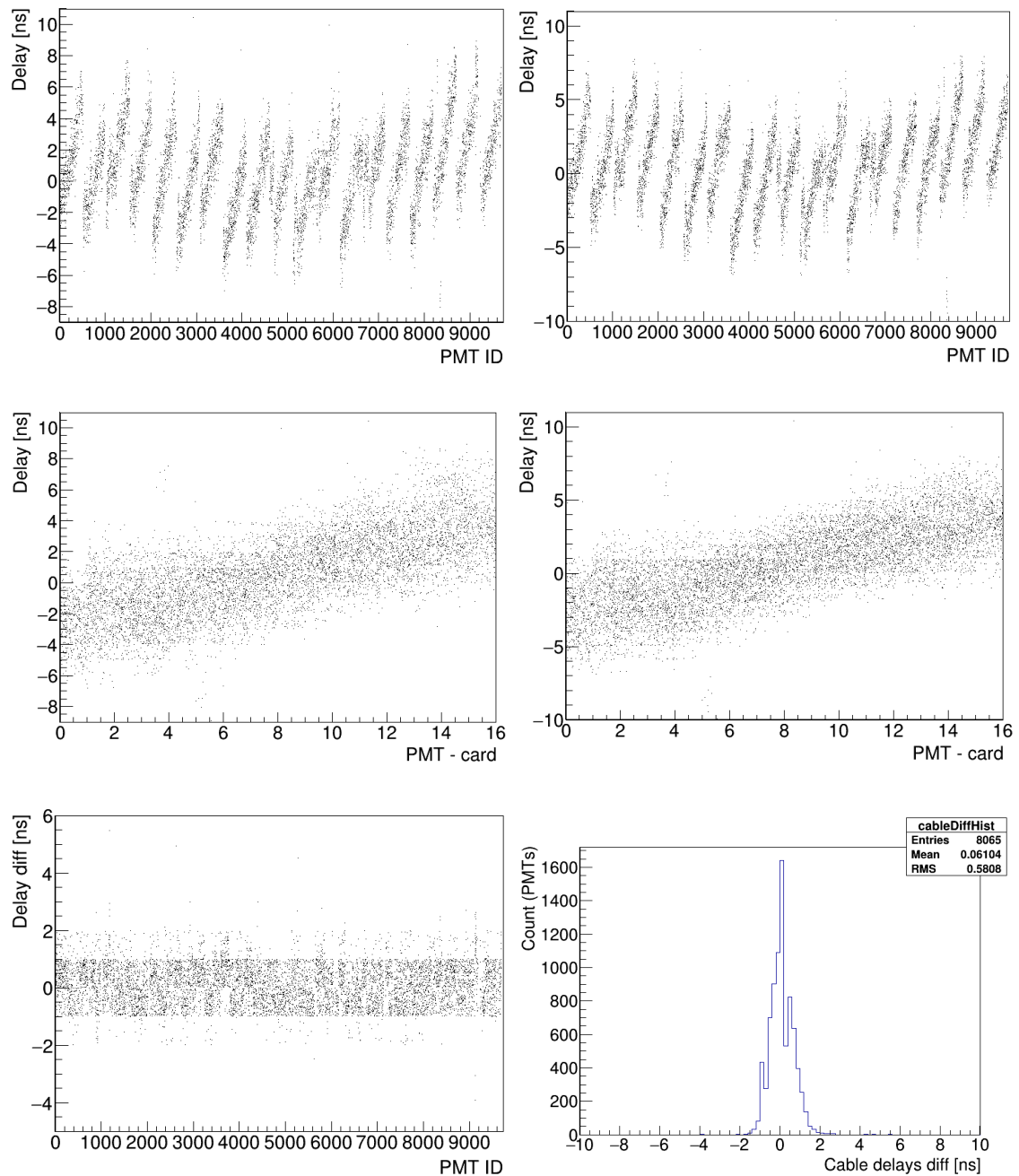
Figure 4.37: Some of the plots used to evaluate the cable delays for a PCA dataset. Top plots are showing full set of cable delays across the detector as a function of PMT ID. The pattern across different PMT crates is clearly observable. Plot on the right is the latest laserball dataset (117567) while the plot on the left is the following TELLIE PCA dataset (117578). Middle plots show the cable delays as a function of PMT card, clearly experiencing the increase in the delay across the card. The bottom plots then show the difference between the two datasets, as a function of the PMT ID on the left and in the form of a histogram on the right.
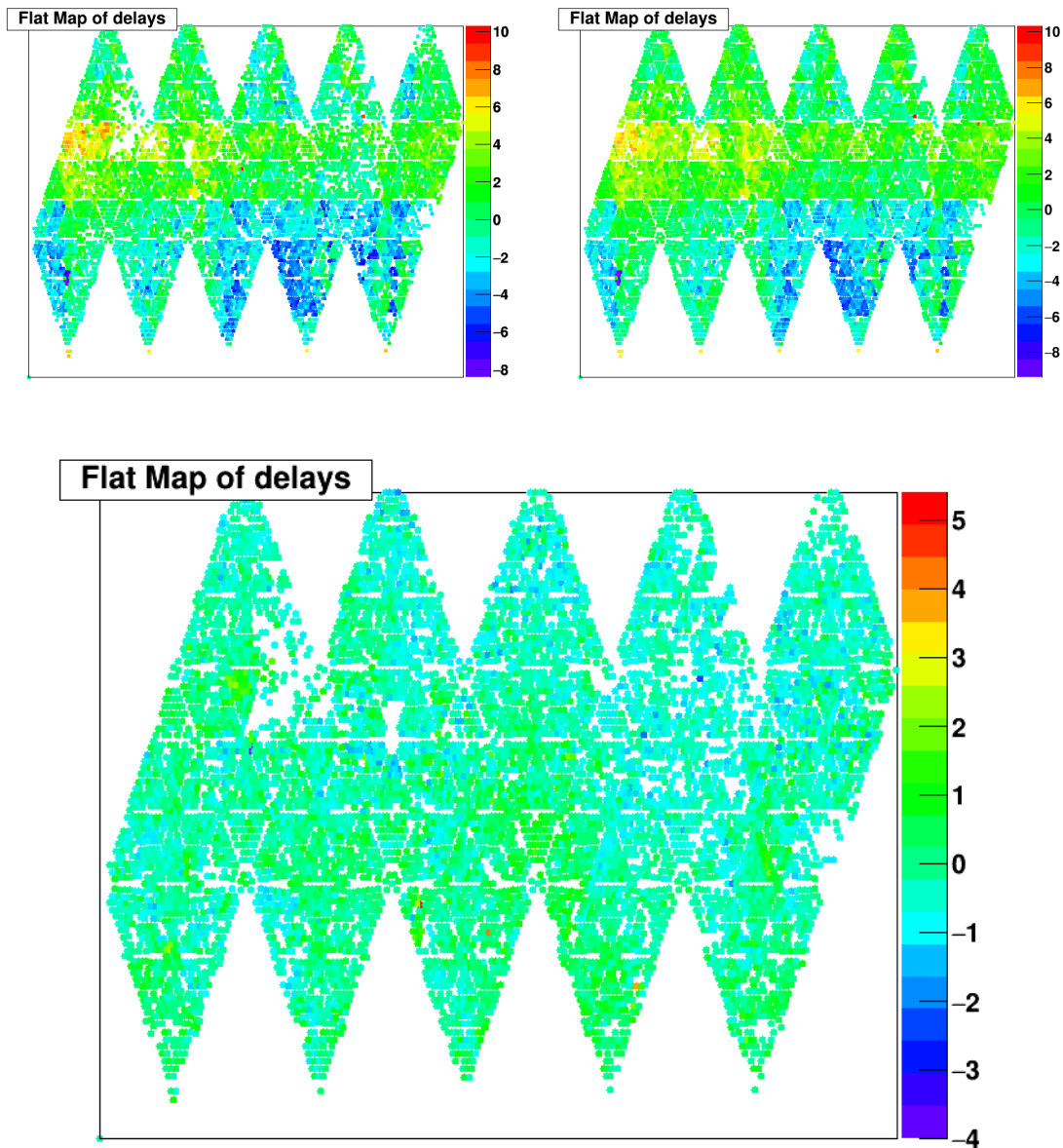
Figure 4.38: The cable delays sets are also visualized in the form of flat maps. This is useful to observe whether the overall pattern is comparable, as well as to see whether there are any new optical effects or outliers that are grouped in this type of visualization. Top right plot is showing the cable delays constants obtained from the most recent laserball data-taking (117567) while the plot on the top left is the complete dataset from the TELLIE PCA data-taking following this laserball run. The bottom plot shows the difference between these cable delays for each PMT. The white spaces are PMTs that were either offline or those where the calibration was not possible due to the checks and cuts. The PMT has to have a valid cable delay calculated in both sets to appear on this plot.

X	LB (110131)	LB (113592)	LB (117567)	TL (110264)	TL (114670)	TL (117578)	TL (201388)	TL (204401)
LB (110131)	X	-0.05546		0.02189				
LB (113592)	-0.05546	X	-0.006433		0.001042			
LB (117567)		-0.006433	X			0.06104	0.01195	0.001768
TL (110264)	0.02189			X	-0.00717			
TL (114670)		0.001042		-0.00717	X	-0.06009		
TL (117578)			0.06104		-0.06009	X	0.03898	
TL (201388)			0.01195			0.03898	X	-0.02296
TL (204401)			0.001768				-0.02296	X

Table 4.2: The comparison of cable delays sets: mean value of the distribution. Value of 0 represents no change to cable delay for a PMT. The mean values are expected to be centred around 0 for a dataset unless substantial work was done on the electronics. A big shift would suggest a systemic change in cable delays, possibly an issue with the calibration. Note that the mean values are comparable between TELLIE and laserball sets.

- A TELLIE set compared to the previous corresponding laserball set;

- (Where no corresponding laserball run is available, the latest laserball run is considered instead. It should be noted that in this case the time difference between the sets is considerable bigger, meaning the detector conditions could have changed);

- A TELLIE set compared to the previous closest TELLIE set;

- A laserball set compared to the previous closest laserball set.

The values obtained from these comparisons are presented bellow. The values of the mean are shown in Table 4.2 while the RMS values are presented in Table 4.3. It can be seen that while the RMS is generally higher for TELLIE datasets, there are no significant differences to the mean values. It should be noted the the bigger spread in the delays is expected for TELLIE. There are several factors to this, such as: the characteristics of the TELLIE pulse (long rise time, bigger pulse width), the scattering as the light travels across the full detector and the fact that there are several calibration sources and the time differences between these have to be accounted for. Plotted histograms are also available as Appendix D.

4.8.2   PMT time-walk effect

The evaluation of the time-walk effect is more complex both because it is a function of charge and time and additionally because the current TELLIE PCA analysis uses laserball PCA constants to calculate the fibre hardware delay. Therefore, given this dependence, the TELLIE time-walk constants are expected to be higher variance data.

X	LB (110131)	LB (113592)	LB (117567)	TL (110264)	TL (114670)	TL (117578)	TL (201388)	TL (204401)
LB (110131)	X	0.4437		0.6061				
LB (113592)	0.4437	X	0.3183		0.6913			
LB (117567)		0.3183	X			0.5808	0.7105	0.6658
TL (110264)	0.6061			X	0.6577			
TL (114670)		0.6913		0.6577	X	0.6783		
TL (117578)			0.5808		0.6783	X	0.6812	
TL (201388)			0.7105			0.6812	X	0.7928
TL (204401)			0.6658				0.7928	X

Table 4.3: The comparison of cable delays sets: RMS value of the distribution. This represents the standard deviation of the differences between the cable delays for each PMT across the two datasets. Value of 0 would represent identical datasets, shifted by the mean value. Some variation in the delays is expected due to changes in electronics, ageing, degradation as well as replacement parts and similar. Note that the RMS is slightly bigger for TELLIE sets, due to the characteristics of the pulse (bigger full-width half-maximum (FWHM)) as well as the scattering over longer path compared to laserball.

The evaluation usually follows similar process as the cable delays, in this case the difference between the straight line fit to high charge end of the data are considered. The slope of fit to each PMT of one set is compared to a slope of the fit to the same PMT of second set. Examples of the comparison plots are shown in Figure 4.39. The results are analogous to the cable delay comparison. The mean values of the differences are very comparable when comparing TELLIE to laserball as comparing laserball to laserball. However, TELLIE data experiences bigger spread of the differences, due to reasons mentioned in the Subsection 4.8.1 above.

4.8.3 Residual times fit

Another benchmarking method for PCA constants obtained from PCA dataset is to apply the constants to a control run. The process is as:

- Select the control run;

- Apply set of PCA constants to calibrate PMTs;

- Obtain PMT hit times (all hits);

- Calculate residual PMT hit times (all hits);

- Fit the prompt time peak of residual hit times (all hits).

- For each PMT: obtain the hit times, calculate residual hit times, fit with Gaussian;

- Collect the Gaussian fits for all PMTs, fit this distribution;
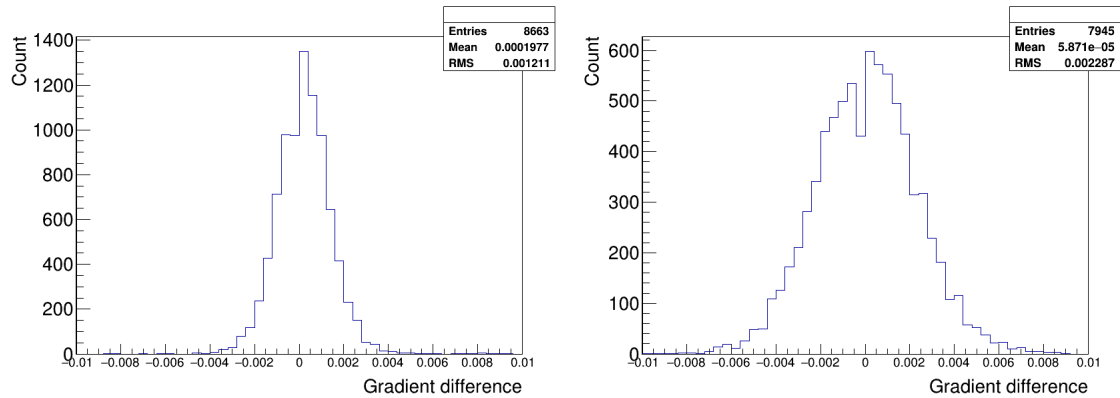
Figure 4.39: Example plots used to evaluate the time-walk effect constants for a PCA dataset. The plot on the left is showing a difference of the time-walk straight line fits (for each PMT) between two consecutive laserball datasets (110131 vs 113592) while the plot on the right is showing the same difference between TELLIE (201388) and closest laserball (117567) set.

- For each PMT: obtain the hit times, calculate residual hit times, extract the median value;

- Collect the median values for all PMTs, fit this distribution.

The central laserball run is selected as a control run. This is because the timings in this type of run are well understood, and the number of reflections is kept to a minimum (the laserball source is in the centre of the AV, the light travels from the centre, through the water, across the AV interface, through the external water and hits the PMT). Two sets of PCA constants are considered for each benchmarking: the laserball constants and the corresponding TELLIE PCA constants. The residual hit times are the hit time corrected for the bucket time and the Time-of-Flight (in TELLIE case it is also corrected for the angular systematic effect). The median is considered because it is used in PCA extraction as it is more reliable than the average since it is less susceptible to being affected by late hits from scattered light, as mentioned. This leaves three values describing the quality of the PCA dataset. If the constants are accurate, the prompt time peak should appear at the same time, while the other fits serve as a cross-check.

The results of benchmarking are listed in Table 4.4. It can be seen that the quality of the PCA datasets from TELLIE is very acceptable, matching the laserball results. The small difference for the 117578 set of constants can be explained by the lower number of PMTs that were calibrated. It should be noted that the RMS reported are the values obtained from the ROOT fit, therefore, representing the standard deviation. The deviation

Dataset	Prompt time peak [ns]	RMS	Gaussian fit [ns]	RMS	Median fit [ns]	RMS	PMTs
LB (110131)	303.8	2.959	303.7	1.426	303.7	1.421	8684
TELLIE (110264)	303.8	3.036	303.8	1.615	303.8	1.63	8354
LB (113592)	297.7	3.165	297.5	1.432	297.5	1.429	8675
TELLIE (114670)	297.7	3.165	297.5	1.432	297.5	1.429	8675
LB (117567)	301.7	3.059	301.5	1.534	301.5	1.541	8756
TELLIE (117578)	301.6	3.16	301.5	1.74	301.5	1.736	8519
TELLIE (201388)	301.7	3.107	301.5	1.631	301.5	1.639	8748
TELLIE (204401)	301.7	3.107	301.5	1.631	301.5	1.64	8748

Table 4.4: Table summarizing the PCA benchmarking for the five available TELLIE PCA datasets in water phase alongside the corresponding laserball sets.

is globally bigger for the TELLIE datasets. This is mostly because the TELLIE constants are (throughout this thesis) obtained using the previous laserball PCA constants - already suggesting the deviation should never be smaller than that of the laserball. The addition of TELLIE specific effect such as the hardware delays, the angular systematic offset, and the offset between the LEDs, add a little more spread. This is expected, and does not take away the fact that TELLIE does not require deployment.

Additionally, the example plots from the benchmarking process are available in Figure 4.40.

4.9   PCA Tables

PCA tables contain data calculated based on each TELLIE PCA dataset. They are necessary in order to complete the extraction of PCA constants. In addition to making the extraction possible, they also serve as a reference point for future reprocessing as well as a measure of stability of the TELLIE system over time for PCA calibration.

PCA table for single dataset consists of:

- The fire name + index;

- The official run number used;

- The pulse width, the trigger delay, the fibre delay;

- The pca offset + width;

- Angular a and angular b parameters;
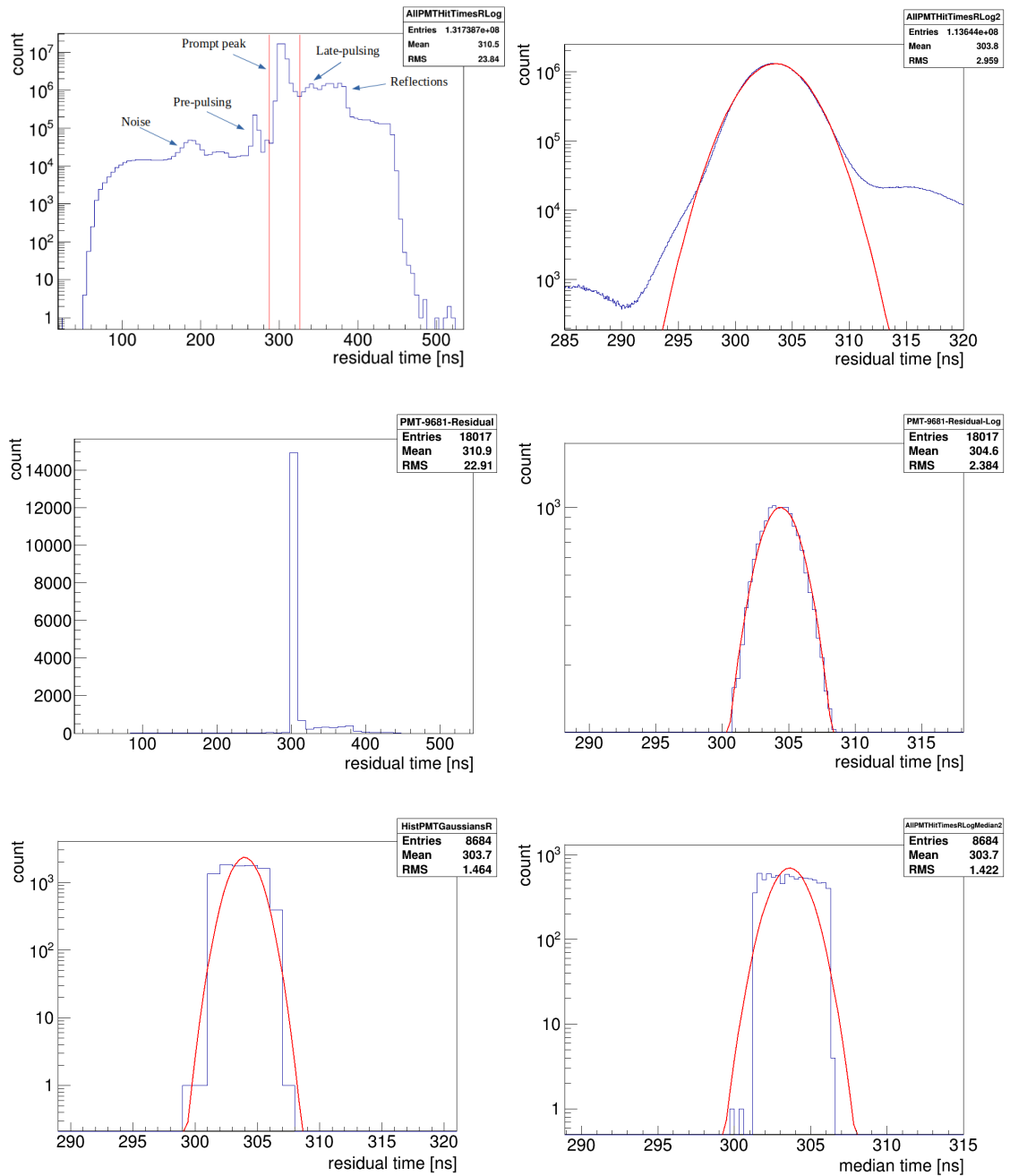
Figure 4.40: Example plots for PCA benchmarking process. From top left: 1: Residual hit times for all hits passing cleaning. 2: Fit to the prompt time peak of the residual times for all clean hits. 3: All clean residual hits for example calibrated PMT. 4: Fit to the peak of the residual hits for the same example PMT, bottom 10% of the data is cut. 5: Histogram of the mean values of the fits to the residual hits for each calibrated PMT in the run. 6: Histogram of the median values of the residual hits for each calibrated PMT in the same run.

- The fibre position;

- The fibre direction.

The **black** items are indexing references, blue items are values set during data-taking while the red values are values that are calculated from collected data that are required for following extraction of PCA constants.

4.9.1 Comparing datasets

This subsection compares the data contained within PCA tables for all official PCA datasets taken in synchronous trigger mode for the water phase of SNO+.

Fibre name, index

The indexing system ensures that data is taken for all fibres during data taking. Additionally, comparisons between different fibres are possible in the future. This is a management system for TELLIE PCA dataset.

Official run number

Before an official TELLIE PCA run is taken the fibre to be used needs to be tuned. This ensures that the fibre is operational, light intensity is as required, the light comes within the event window and that there are no obvious issues such as stability or unknown optical effects. Due to the tuning there are several short runs during PCA data taking that are not suitable for the extraction of the PCA constants. A list of the runs with correct settings (after tuning) is kept to be used for PCA extraction, as well as a reference for what fibre was used to obtain each run. This makes it possible to retake data for specific run if required, to reprocess runs in the future as well as to compare the performance of each fibre over time.
The official run numbers are listed in Appendix B.

Pulse width

One of the available setting for TELLIE fibre is the internal pulse width (IPW). This is a great feature allowing TELLIE fibres to be run at wide range of light intensities, as the intensity is a function of the IPW (inversely proportional). Not only TELLIE sets can be taken at approximately the same light intensity, other additional studies can be performed by selecting different intensity levels. For PCA data, the intensity is tuned to be in SPE

regime, usually around 42 NHit. Additionally, this parameter can be used to evaluate the power stability of the TELLIE calibration system over time.

Delays: trigger, fibre

There are several trigger settings for TELLIE data taking. Overview of all delays is explained in Section 4.4. The trigger delay is kept constant throughout the newer datasets. The are two sets of software fibre delays. The remeasurement process is explained in Section 4.5 while the log of which set was used is listed in Table 4.1.

PCA offsets

The PCA offsets in TELLIE PCA tables are related to the fibre hardware delay as described in the Section 4.4. The value of PCA offset itself is the injection time when light leaves the wet end of the fibre and enters the detector's cavity. Then, the difference of this value to a global time is the actual fibre hardware delay. As explained, these are calculated after the data is taken and require previous PCA constants (laserball set). The calibrated hit times are corrected for the bucket time, transit time and angular systematic effect. Afterwards, the low 10% of the data is cut off. Finally, the remaining hits for single fibre are fitted with Gaussian function. The mean of this fit is the injection time for a fibre. There is also the cross-check option of using the bootstrap method described in Appendix A.

An example fit is shown in Figure 4.42 while the full sets of pca offset values are shown in Figure 4.43.

Angular systematic fits

The angular systematic effect, fit and calculation are all described in Subsection 4.3.3. The calculated values for each dataset, as well as the differences between two consecutive datasets, are shown in Figure 4.44.

Additionally, the angular systematic fits for all fibres (one dataset) are shown in Figure 4.45. In this case the a parameter is set to zero while the b parameter (the only one used for correction) is plotted. This figure represents the time correction applied to PMT hit times as a function of the angle between the fibre and the PMT. The correction is fibre specific and is recalculated for each dataset. Each color line represents a single fibre, the variation between the fibres can be seen.
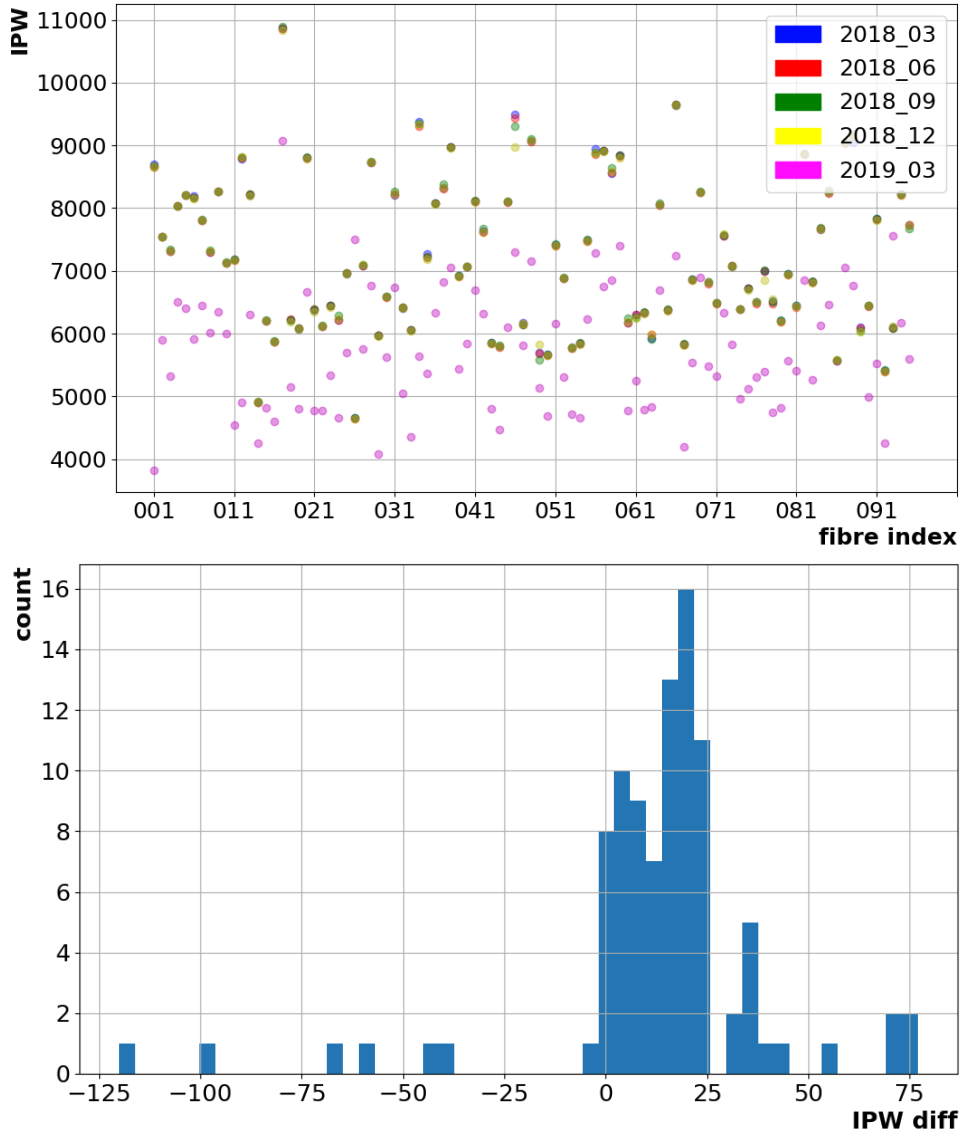
Figure 4.41: Top: plot of IPW settings for each fibre through 5 TELLIE PCA datasets. There is consistency between first 4 dataset suggesting power stability of the TELLIE system. The March 2019 dataset was affected by a power fuse that was damaged. The IPW values returned to nominal after replacement. Bottom: Comparison of required IPW settings to obtain the same light intensity between two TELLIE PCA datasets. Usually the IPW settings are not too sensitive and change of 100 results in single digit NHit shift.
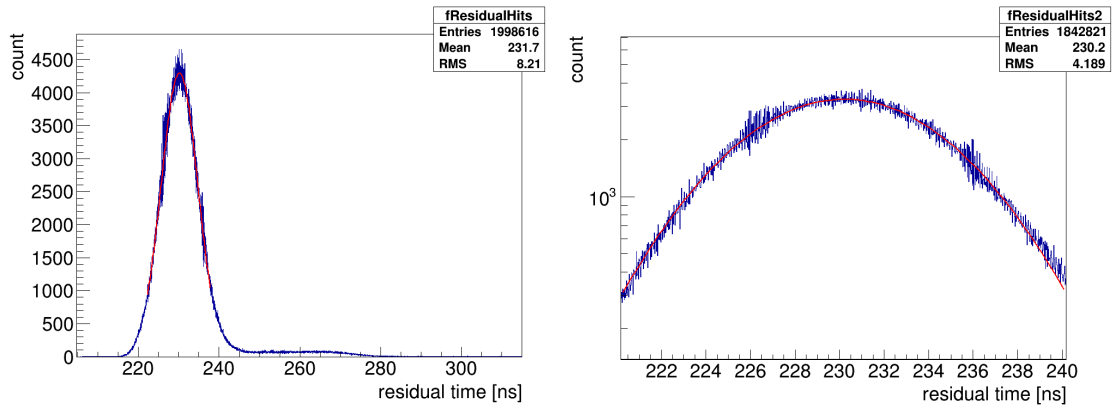
Figure 4.42: Calculating the injection times for example fibre. Left: All residual hits after time corrections for a single fibre. Right: Fit to the peak of the residual times. The mean value is the injection time for this fibre.

Fibre position

The fibre positions that are stored as the fibres were installed are used in the PCA generation process to calculate the TOF for the light. The same constants are used throughout the PCA. However, the positions are recalculated whenever new fibre directions are being evaluated from data for the sole purpose of obtaining these new directions. This is useful check to confirm the correct fibre was being used during data taking as well as to confirm the overall system stability as any big deviation would flag inconsistencies. The way the positions are calculated is explained in Section 4.6. Some example plots are available in Figure 4.46. This figure also shows how the fibres are distributed across the detector. The positions are set to maximise the coverage - every single PMT should ideally be covered by multiple fibres. Almost all PMTs are covered by more than two, making the TELLIE system redundant, meaning that even if some fibres would fail in the future, PMTs should still be covered by other fibres. The coverage is highlighted in Figure 4.35.

Fibre direction

Related to previous subsection, the fibre directions are calculated for each dataset based on the fit to the direct light spot. This is also explained in Section 4.6. Unlike the positions, these are used for the extraction of PCA constants mainly because the definition of the beamspot, which is essential for PCA analysis, is strongly based on the angle between the fibre and the PMT. An example 2D visualization of 3D fibre directions is shown in Figure 4.47.
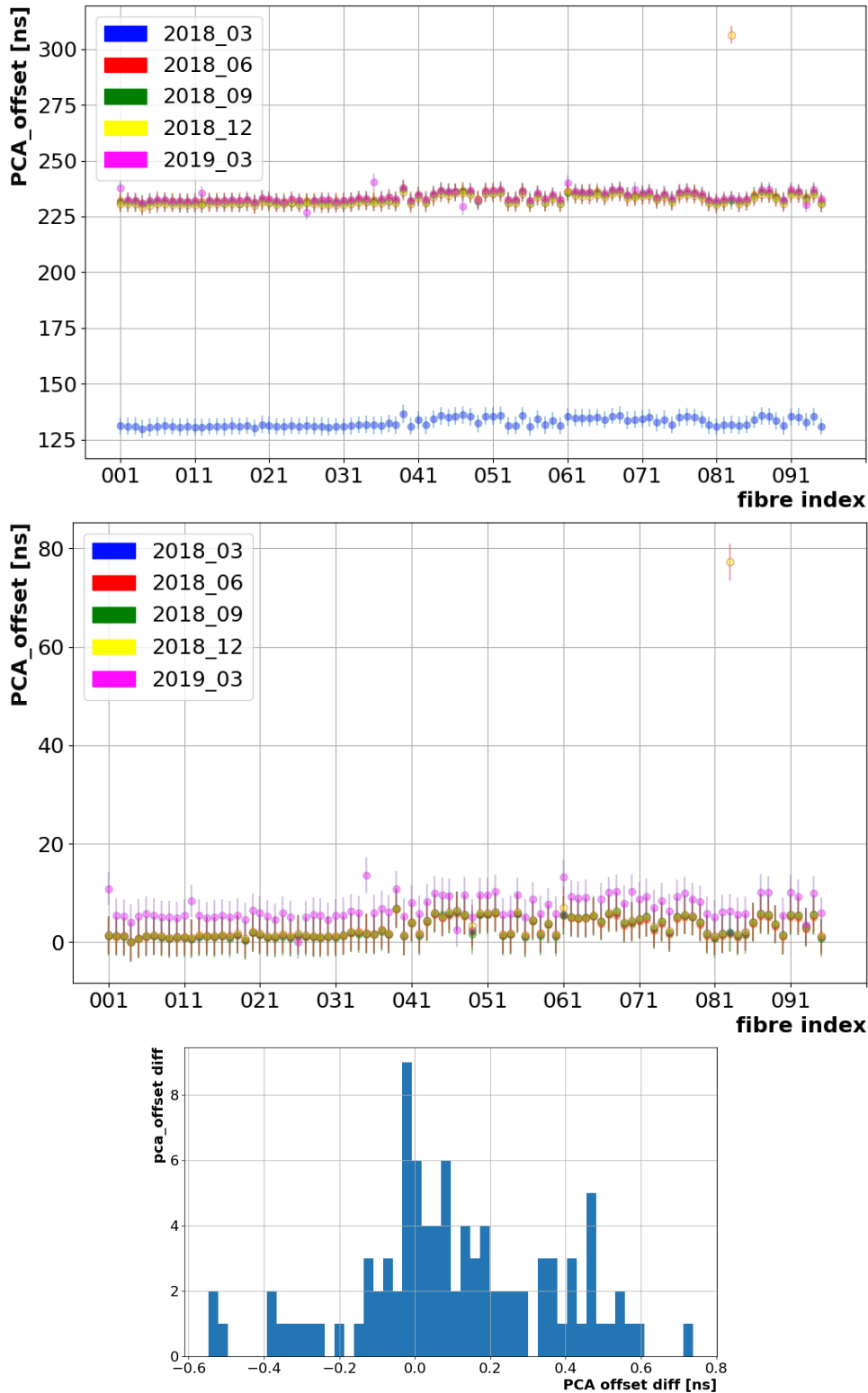
Figure 4.43: PCA offset values for five available TELLIE PCA datasets. Top: The calculated injection times for each fibre throughout the sets. The first dataset was taken with different trigger delay (100 ns difference) causing the injection times to be smaller. Only the relative differences between the fibres in each set are important. Middle: The relative injection times (these now represent the fibre hardware delay). The last dataset shown in the plot was taken with defect power fuse. Bottom: histogram showing the difference in fibre hardware delays between two TELLIE PCA datasets. Small differences can be expected due to: new offline PMTs, new installed objects such as pipes, shifts in AV positions, any hardware changes or maintenance.
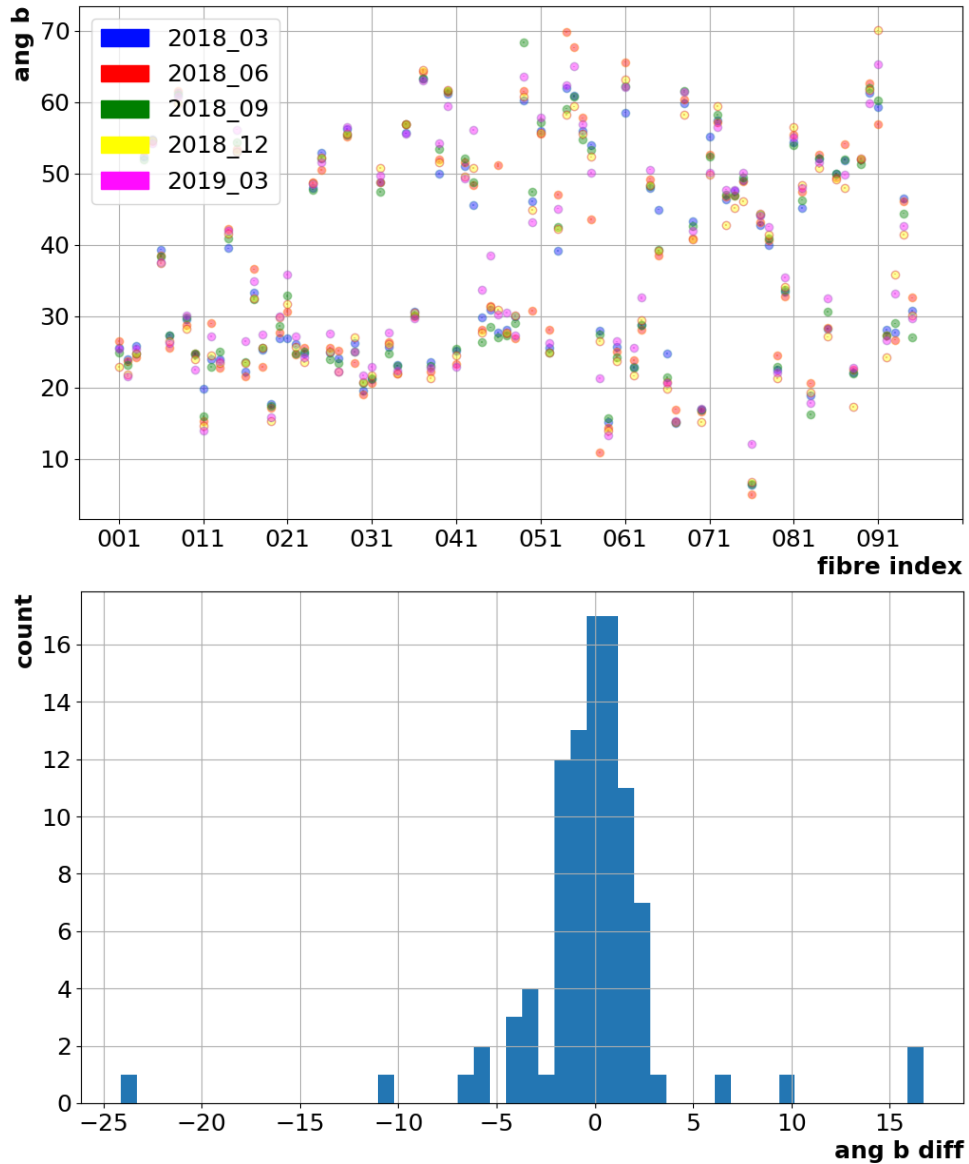
Figure 4.44: Plots related to the b parameter of the angular systematic fit. Top: The b parameter for each fibre throughout the available datasets. Bottom: Histogram of differences of the b parameter for the fibres between two consecutive datasets. Because these are calculated as fit to data, small differences are expected due to factors such as: offline PMTs, occupancy, AV shift, hardware changes and similar.
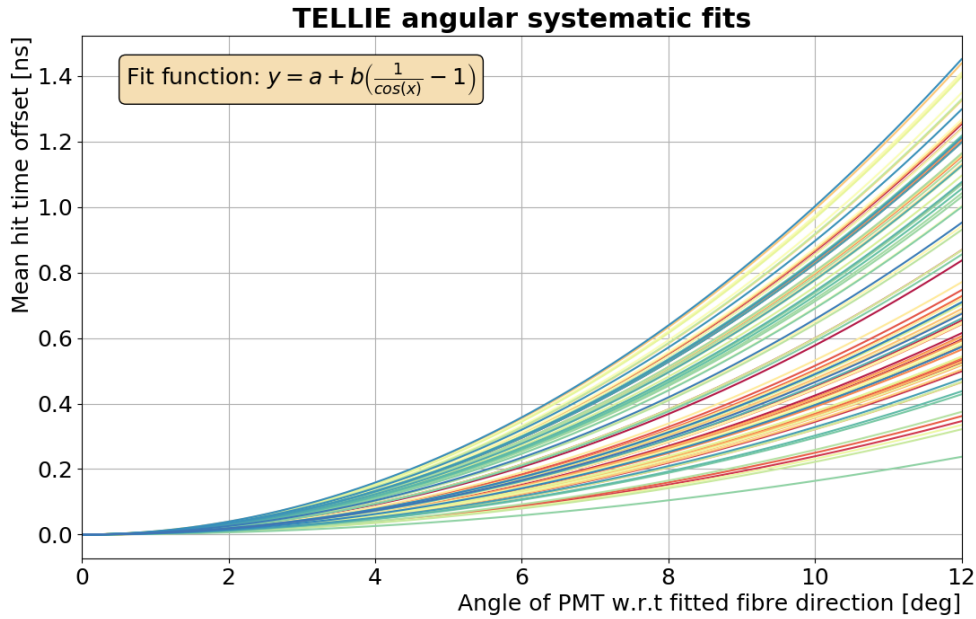
Figure 4.45: Angular systematic fits for all TELLIE fibres, one dataset. Each color represent single TELLIE fibre. Only the b parameters are being used, they affect the slope of the correction with increasing angle.

4.10 Related topics

This section gives insight into some other TELLIE (PCA) related topics that should be mentioned alongside this chapter.

4.10.1 Missing EXTA triggers

During TELLIE running, a small number of EXTA triggers can get 'stolen' by other trigger types, most notably ESUMHI and PULSEGT due to trigger pile-up (more on triggers in Subsection 3.3.3). In some cases there is an associated MISS trigger bit, but this is not always the case [114]. This is not very frequent, as it only occurs at a rate of less than 10 events in 200 000. Until the time of writing of this thesis, TELLIE was always run in dedicated manner, as described in Section 4.3. In the dedicated mode, the missing triggers are not of particularly great importance as they can be easily tagged and recovered. The tagging is based on:

- Knowing the TELLIE pulse frequency, therefore, the expected pulse separation;

- Knowing the expected group of PMTs to record light (the beamspot);

- Knowing the approximate NHit;
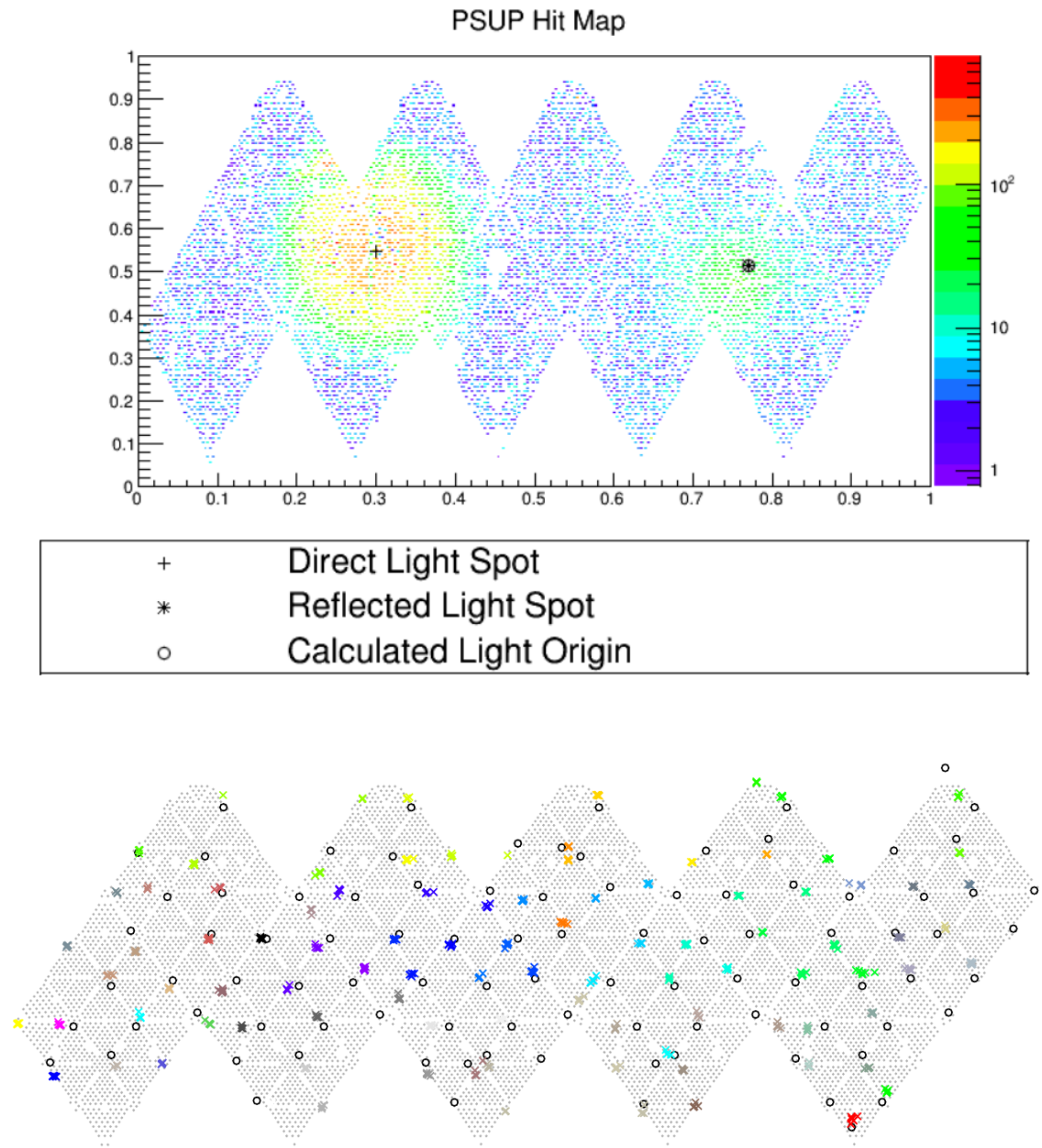
Figure 4.46: Top: Recalculating fibre position using fit to direct and reflected light spot for example TELLIE fibre. Bottom: Position for each TELLIE fibre as calculated for each dataset shown on PMT flat map representation.
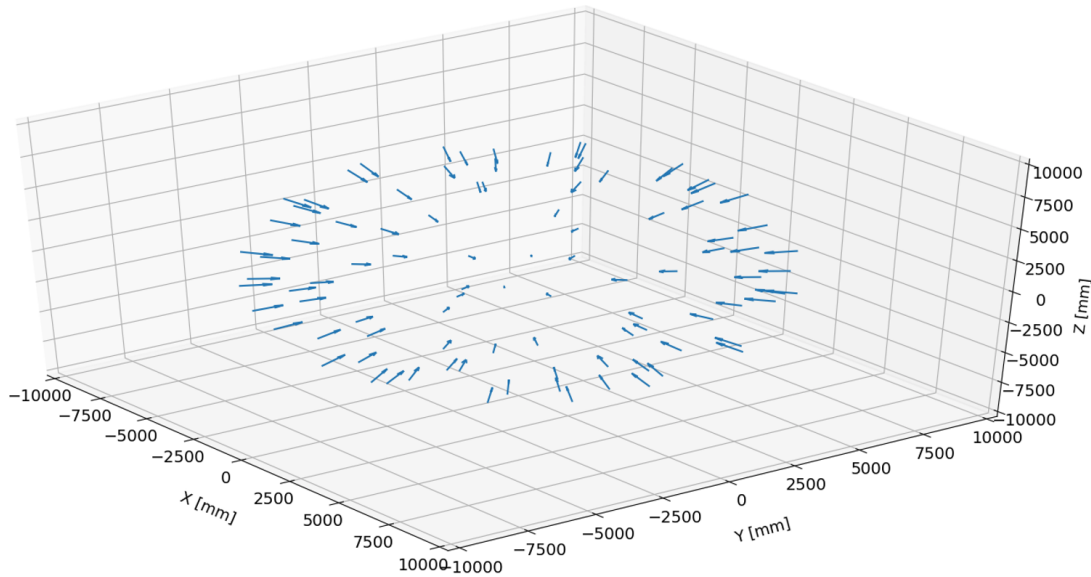
Figure 4.47: A two-dimensional visualization of the calculated fibre directions for example PCA dataset.

- Knowing the total number of events.

Using the tagging method, the events can be iterated through and any event not having the EXTA trigger bit fulfilling the tagging conditions can be recovered.

An example plot showing the pulse separation for a single TELLIE subrun is shown in Figure 4.48. As can be seen in the plot, a single event was found that fulfilled the tagging procedure and was associated back to the TELLIE signal.

4.10.2 TELLIE automation

Another possibility of taking TELLIE calibration data is to run TELLIE automatically (or autonomously, to a certain extend). There are several options how to do this which are discussed in this subsection.

TELLIE automation is planned to have two parts: the automation of data-taking and the automation of processing and analysis.

Data-taking

If the data-taking is to be automated, there needs to be a way to monitor and adjust the intensity of the light being injected into the detector. The most obvious way would to be to look at the EXTA-NHit, however, this is not immediately available (events need to be built and fed back, introducing delay and issues with matching). Therefore, the internal
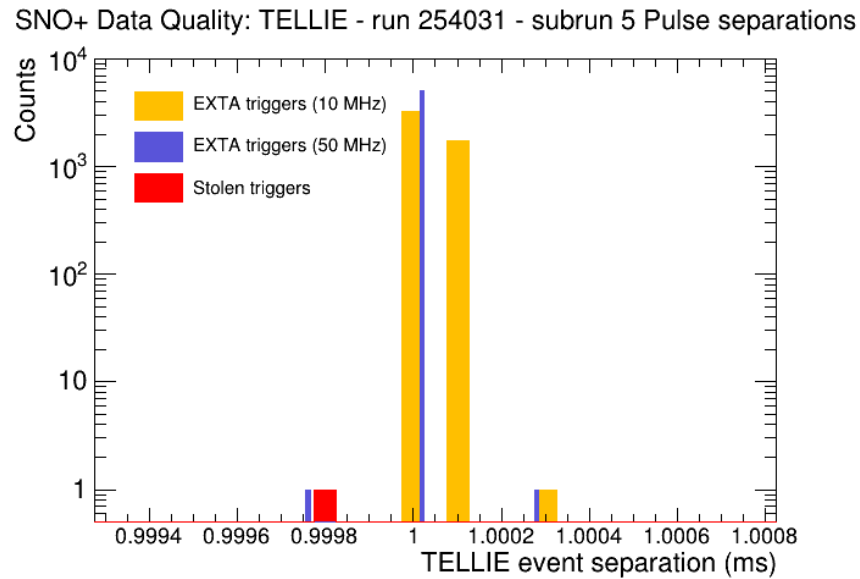
Figure 4.48: An example plot showing the separation of TELLIE pulses for a single subrun (5000 events). A single event was stolen and recovered. Times using both 10 MHz and 50 MHz clocks are shown.

reading from TELLIE - the PIN value - could be used instead. The PIN values correspond to the real light intensity, are readily available, have been shown to be quite sensitive to light intensity changes and have been measured to be stable over time [115, 116].

To successfully automate the running, fibre profiling will be mandatory. Each fibre will require two profiling curves. These are:

- **The calibration curves**: relating IPW to PIN;

- **The tuning curves**: relating PIN to NHit.

The calibration curves can be obtained by scanning the PIN response at specific IPW values. The tuning curves can then obtained via nearline analysis. The goal of the profiling is to reliably relate IPW (variable that can be controlled at run time) to NHit (detector's measure of light intensity).

These procedures are outlined in [115, 116]. The plan is to re-profile the fibres as required.

Regarding the data-taking itself, there are (at least) two viable options:

- **The automated dedicated running**: this version is similar to current TELLIE PCA procedure described in Section 4.3 with the change that no human intervention or monitoring would be required. The fibres would shine light for set number of

events at a specific frequency, one after each other, until the full dataset was taken. No tuning would be required since the profiling would provide the required settings;

- **The automated continuous running**: this method would collect TELLIE PCA data alongside the normal physics data collection. The suggested method would be to run TELLIE at reduced frequency (50 Hz), alternating the PULSEGT and EXTA triggers to ensure zero overlap. This could introduce missing triggers, but this was proven to be recoverable in Subsection 4.10.1.

There are advantages and disadvantages to each option. To mention the main ones, the dedicated running would result in much cleaner datasets with tagged events but a lot of physics dead time. Continuous running would require a careful offline analysis to clearly distinguish TELLIE calibration events from physics events, and would need to run for longer to collect the same order of statistics but would minimize physics dead time.

Another point to mention is that there are several options to control TELLIE for the automation. While ORCA has been used as the main controller in the past, the procedure can in principle be ported to a stand-alone platform. The details of the process are in development at the time of writing.

Processing and analysis

The processing automation would simply require to obtain the PCA constants from the collected dataset (regardless of the method used to collect the dataset). This includes correcting the recorded hit times for the time corrections explained in Subsection 4.3.3, recalculating the required fits, extracting the PCA constants and, finally, benchmarking the results, while monitoring the quality of the data.

Most of the pieces required for processing automation are available at the time of writing. Some unification of global settings, interface to databases and monitoring are still required. This step is also in development.

4.10.3   Charge monitoring

As described in Subsection 4.2.1, in addition to removing the time offsets, PCA is also responsible for monitoring of PMT charge profiles. The monitoring process tracks the three parameters of the distribution: threshold, peak and high-half point. Every time new PCA constants are obtained, the values of these parameters are compared to the last set

of constants. This is done on per PMT basis, as well as globally for the detector. One such comparison is presented in Figure 4.49.

4.11   Conclusion

SNO+ uses an array of photo-multiplier tubes to detect the light in the detector. These PMTs have an intrinsic discriminator threshold used to distinguish the real photo-electrons from the dark current. The aim of the calibration process for the PMTs is to account for this discriminator effect, to ensure accurate time response by removing the relative offsets between the PMTs, and to monitor the gain of the PMTs over time. The calibration process proceeds via the collection of calibration data, the correction for several time effects, and the generation of pca constants.

Additional calibration system called TELLIE was developed for SNO+. The system consists of multiple optical fibres that are permanently mounted on the PSUP. Therefore, this system is external and does not require the deployment inside the AV, which is crucial to minimise the potential contamination of the scintillator.

The time effects present for the TELLIE calibration data were analysed. The transit time and the bucket time corrections are generic for any calibration system, and these were proved to be in the expected range of < 80 ns and < 0.5 ns, respectively. There are two additional TELLIE specific corrections: the angular systematic effect caused by the modal dispersion (< 2 ns), and the relative offsets between the LEDs. After both are corrected for, the measured hit times were observed to have lower spread around a mean fit value.

A detailed overview of all time delays in the TELLIE data taking was produced. These are well understood, and the dependence on the laserball is explained - TELLIE is a complementary system to the LB.

A comparison of the TELLIE calibration results to the LB results was presented for the available TELLIE datasets. There is a great agreement for the two systems. The slightly bigger RMS spread of the TELLIE data is expected due to the aforementioned dependence on the LB constants, as well as the fact that multiple light sources are used for the data collection.
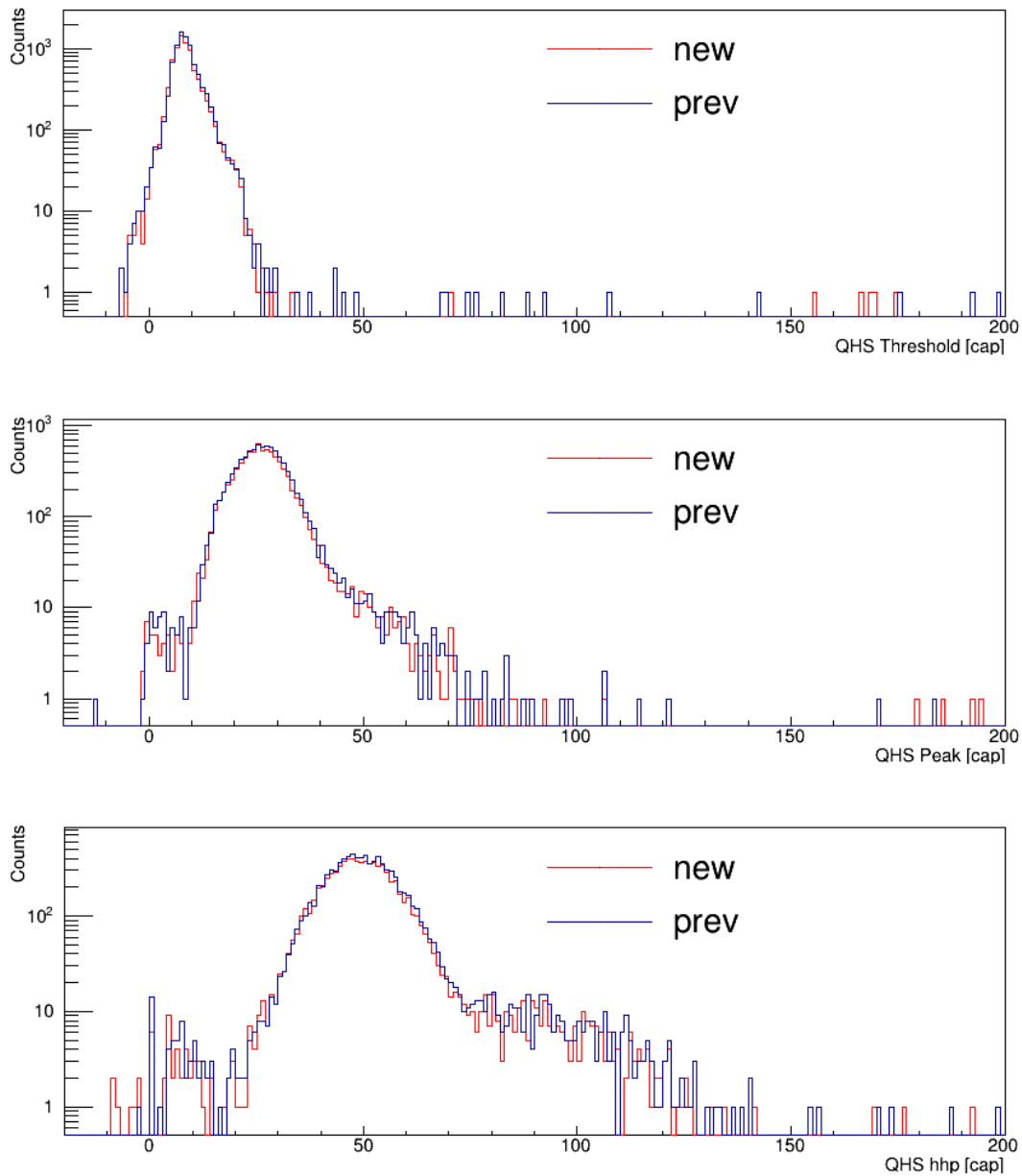
Figure 4.49: Example of QHS charge monitoring for PCA. All three parameters of the charge distribution are considered. The plots compare the latest laserball dataset with the closest TELLIE dataset.

A study of the PCA tables - including the parameters and the fits obtained from the TELLIE data - shows reasonable stability of the system over time. The small deviations are understood and fixes were applied (fuse replacement) or are in the process of being implemented (isolation work).

In conclusion, the TELLIE system fits the purpose of being able to calibrate SNO+ PMTs to the required precision. It does require periodic deployment of the LB, however, it greatly minimises the frequency of the deployments. It is recommended that this source is used for the PMT calibration. To reduce the physics dead time and the manpower requirements the automation of the system should be considered, and the options for this procedure were presented.

Chapter 5

Supernova Detection

How wonderful that we have met with a paradox. Now we have some hope of making progress.

NIELS BOHR

5.1 Introduction

As described in Chapter 2, the SNO+ detector is sensitive to SN neutrinos from the SN explosions in our Galaxy. These are expected to come in a short duration burst ($\mathcal{O}(10)$ s). Most of the observable events should happen within the first 2 s of the burst and the signal is expected to be uniformly distributed across the detector. A burst detection mechanism, with the goal of recognising such a burst, was developed by the author for SNO+. Part of this mechanism is carried over from previous system while most of the mechanism is developed anew alongside additional monitoring features.

This chapter will focus on the SN detection system developed for SNO+. Firstly, the software that is used to detect SNe bursts is described. Then, RAT[1] processors used to analyse the bursts are characterized alongside the online monitoring that is available. Any related alarms to burst detection are described after that. The trigger efficiency is evaluated, as well as the use of a dynamic threshold for the trigger. Additionally, there are examples of the most common types of events registered by the `Burst Trigger` presented. Finally, the process and status of connecting to the global SuperNova Early Warning System (SNEWS) is described.

---

[1] **RAT** is the reactor analysis tool: the software package used to simulate the SNO+ detector.

5.2   Burst Trigger: software

There are two main software packages used to readout the detector data and check for a burst. While the purpose of the `BufferScripts` (BS) package is to ensure the newly written data by the SNO+ `Event Builder` is immediately being evaluated for bursts, the `Stonehenge` (SH) package contains the logic for the `Supernova Burst trigger`. These two packages are described in detail below.

5.2.1   Buffer scripts

The software package `BufferScripts` (BS) is used to ensure the data is sent to be analysed for bursts as soon as possible. The standard way the data is being handled in SNO+ is in subruns of fixed size of one Gigabyte (999,940,000 bytes specifically [117]). This can take a different amount of time depending on the event rate and trigger thresholds, but usually takes between 4 to 5 minutes for the detector when it is fully filled with scintillator. Regardless, waiting for a subrun to be fully written and closed would introduce significant delay before the data could be analysed. This is not usually an issue for other data analyses but it poses a big problem when dealing with potential supernova-like signals. The aim is to be able to send out a reliable alert as soon as possible (more details in Section 5.10). Therefore, the data is instead divided into small pieces and passed to `SH` immediately as it's written out by the SNO+ `Event Builder`.

SNO+ Event Builder

The `SNO+ Event Builder` (or the `Builder` for short) reads raw PMT, MTC and CAEN data from the data stream server and organizes it into events based on global trigger ID. The output is written to file and dispatched for online monitoring [117]. The flow is organized into four threads: ORCA Reader, `Event Builder`, Recorder and Dispatcher. The ORCA Reader thread reads data from ORCA and writes it to internal circular buffers (one buffer for MTC/FEC data, another for CAEN and one more for header records). The MTC and FEC data is build into events by assembling MTC words and FEC data of the same GTID. These are then transferred to Recorder. The Recorder thread maintains a list of data-stream records and inserts them at the proper position in the data-stream as the events are written to disk. Finally, the Dispatcher thread sends the data to the dispatcher - program responsible for the distribution of the data.

In rare cases something goes wrong, the Builder is forced to output PMT bundles without having assembled them into an event with their corresponding MTC data. These are

called orphan events and are distinguished by having all zeros in the trigger word.

L2

The `L2 Trigger` system is a software trigger that runs nearline between the `SNO+ Event Builder` and the propagation of data to the data grid (online). The purpose of the `L2 Trigger` was to allow the detector to be run at low threshold for SN detection while not retaining this low energy data permanently [118]. Even though the system is not run for the original purpose, it still contains the SN buffer and is currently used for the sole purpose of detecting a supernova-like signal.

Regarding the architecture, the trigger system consists of a set of ZDAB[2] utilities in a C++ program called `Stonehenge`, which forms the bases of the `L2 Trigger`, together with a set of bash scripts that handle file movements, launching, and monitoring of jobs. These are controlled by a `L2 master` scripts with user interface [118].
The major components of the `L2 Trigger` system are:

- The `L2 component`: `master` script, controls the system;

- The `client component`: script to identify newly written data and launches `Stonehenge` passing the data;

- The `convert component`: runs the RAT jobs to convert ZDAB files to RAT format;

- The `manager component`: manages disk space;

- The `pushnlug script`: pushes data to nearline analysis server.

Only the `L2 master` script and the `client` are currently being used for the purpose of SN monitoring. The other scripts are either unused or are superseded by other scripts. The overview of the system with connection to the `Event Builder` is displayed in Figure 5.1.

The `L2 master` script can start and stop the three main components of the `L2 system`: `client`, `convert` and `manager` scripts. It also tracks the Process Group IDs (PGIDs) of these processes in file. Additionally, it ensures that necessary files and directory structures are present when starting, and, if not, constructs them.

---

[2]**ZDAB** is a file format in which raw data from SNO/SNO+ runs is stored.
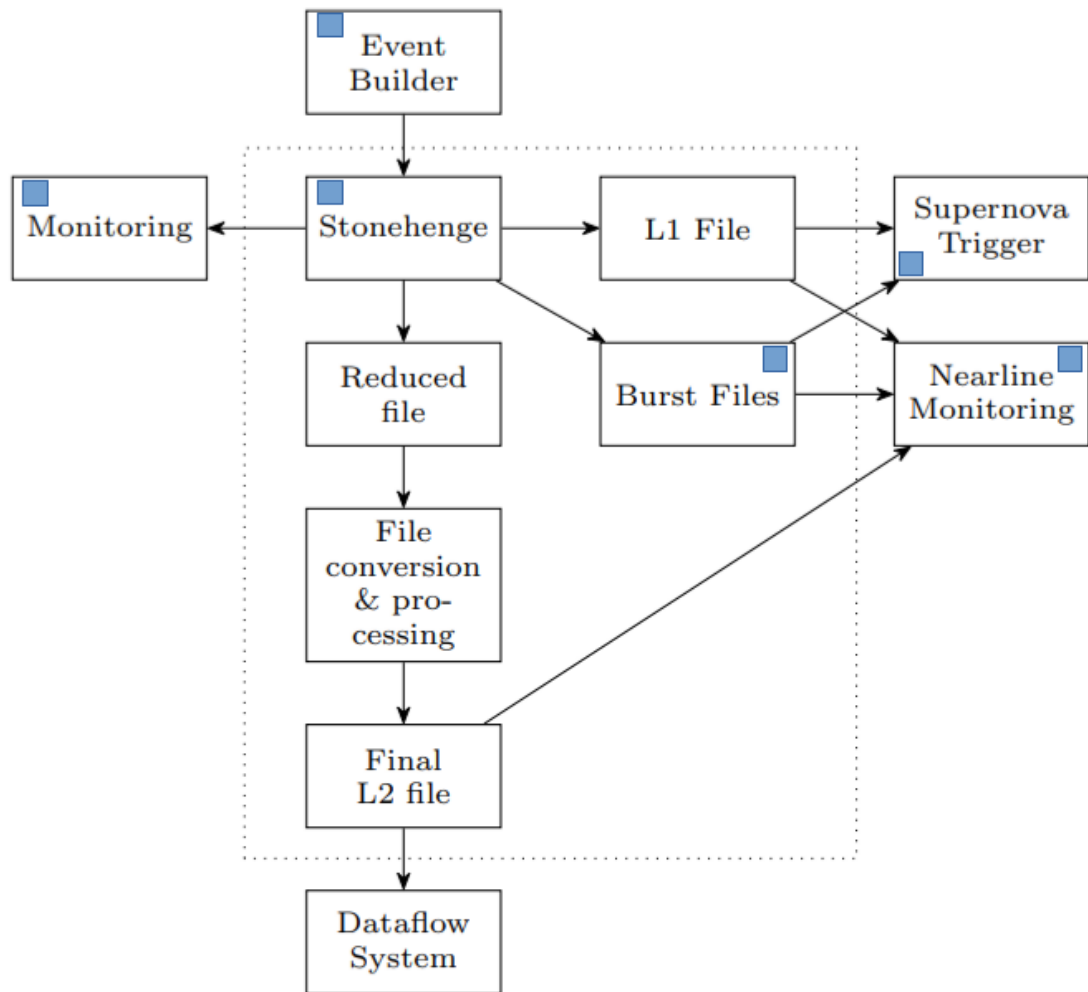
Figure 5.1: Component diagram for `Level Two Trigger`. Items marked with blue square are part of the `Supernova Trigger` system and were modified as part of the rework of the `Supernova Burst Trigger` discussed in this thesis. Original diagram from [118], modified.

Client

The `client` script is responsible for passing newly written raw detector data to the `Stonehenge` package that contains the logic to detect bursts. `Stonehenge` runs over a single ZDAB file and exits upon reaching the end of file record. Therefore, the `client` launches `SH` for each subfile in succession. It reads the filesystem of raw data written by the `Event Builder`, identifies the oldest file which has not yet been processed and launches `SH` passing the location of this file. There is logic in place to check the SH's exit code and retry the same file up to three times in the event of failure [118]. Afterwards the file is logged and skipped so that the detection is not delayed. Also, if the return code is positive, the next file is passed. To minimize any lag, the `client` checks for new data with high frequency. A list of served files as well a list of files to be processed next is kept and updated periodically.

In addition to passing new files to `SH`, `client` also passes additional arguments, such as the configuration file. This is described in Subsection 5.2.3. Further, `client` updates the Redis database (more details in Subsection 5.4.1) for each file, categorising data-files into being processed, done and failed groups. These groups can be monitored via online monitoring, Section 5.4.

5.2.2   Stonehenge package

`Stonehenge` is the heart of the `BT` system. It's a C++ program that handles ZDAB files as the come off the `Event Builder`. The main logic for detecting bursts is contained within this software. In addition to that, it can record event rates and perform simple cuts [118].

The main goal of the `SN Trigger` is to have low latency monitoring for SN-like bursts. Furthermore, `SH` deals with ZDAB files and packed events, instead of the common way of using RAT software to handle SNO+ events. Because of these reasons and not to bias the data in any way, the only parameters that are used for burst detection are event times, relative times and the number of hit PMTs (NHit) which is a function of energy. There is no event reconstruction in terms of event position or charge, even though this can be theoretically added if required.

There are several setting that are customizable via the configuration file and some settings are also affected by the run type.

5.2.3 Burst declaration logic

The basis of the `Burst Trigger` declaration is detection and monitoring of short bursts of relatively high energy events. A burst is said to begin when a sufficiently large number or sufficiently energetic (measured using NHit at this stage) events occurs within a specified time interval. The burst is said to end when the rate of these large events drops below another threshold.

In practice, the declaration is slightly more complex. There is a two second sliding window that counts events above a particular NHit threshold. The two seconds are chosen because most events in a SN explosion are expected to be ejected within the first two seconds of the burst. Nonetheless, this, along with other settings, is customizable. Regarding the NHit threshold, originally there was just one value set for this parameter. However, the `Trigger` was reworked to accommodate four independent logical buffers: 3, 5, 7, and 10 event buffer. This allows for more customizability and increases the sensitivity, given that lower energy events can be considered, without overwhelming the trigger system. The number in the name represents the event threshold, i.e. the required number of events that need to be detected within the sliding window. Each of these logical buffers has different NHit threshold. The full details of how these are set is discussed in Subsection 5.2.3.

In addition to the four logical buffers that only keep track of the events above their threshold value, there are two functional buffers that keeps track of all events regardless of NHit value. One of them stores the times of the events, while the second one contains the ZDAB records of the event with all available data. Therefore, the logical buffers are used to determine whether a burst occurred, while the functional buffers are used to write out a burst file if the burst was declared. Additionally, this allows one to store events going to recent past. This means that a burst file can contain events before the burst itself was declared, making it easier to determine whether the signal is supernova-like. In line with this PRE window that can be written out for a burst, there is similar POST window that is also included with the burst once a burst was declared finished.

Burst declaration process

To summarize, the `SNO+ Supernova Burst Trigger` functions as follows:

- Two functional buffers keep track of all events regardless of the NHit. Events are

dropped from the buffers if they are more than X seconds older than the start of the sliding window, t_0;

- Events are being counted within the 2 seconds sliding window, starting at t_0. If the event is above a threshold for any one of the four logical buffers, the time of this event is added to that particular logical buffer. Events are dropped from these buffers if they are older than the 2 seconds;

- If any one of these four logical buffers contains at least the required number of events (3 events for 3 event buffer, 5 for 5 and so on) **the burst is declared**. This means at least the threshold number of events was recorded within the sliding window;

- It should be noted that the declaration period can take up to 2 seconds, but can also be much shorter than that. As soon as the required number of events is recorded, time t_1 is marked as the last event that was counted, finishing the declaration section;

- The logic to extend the burst follows. If there is any new event that is above the **extending NHit threshold** and is within the extending window dt from the t_1 initially, or from the last event that extend the burst, the burst gets extend, marking t_{end} as the time of the last event that extended the burst. Time t_{end} can be overwritten by any other new event, as long as this event passes the extending NHit threshold and is within dt from t_{end}. The minimum time period between t_0 and t_{end} is set to one second;

- Once there are no new events that would extend the burst (so no new high NHit events within specific time, dt), **burst end** is declared. Events are still being added to the functional buffer holding the ZDAB records until Y seconds after t_{end};

- Once the events are collected, the burst is written to a burst file. This means all ZDAB records from the functional buffer holding them are written to a ZDAB burst file, covering the whole time range: ***PRE(X) + declaration + extending + POST(Y)***.

The declaration logic is depicted in Figure 5.2. Additional details:

- **ALL** = all events, regardless of NHit
- **TH (left)** = a threshold event, any event above set threshold value
- **TH (right)** = logical (threshold) buffers
- **BUF** = functional buffers (time and ZDAB records)
- **X/Y** = special time windows to store all events before and after the burst
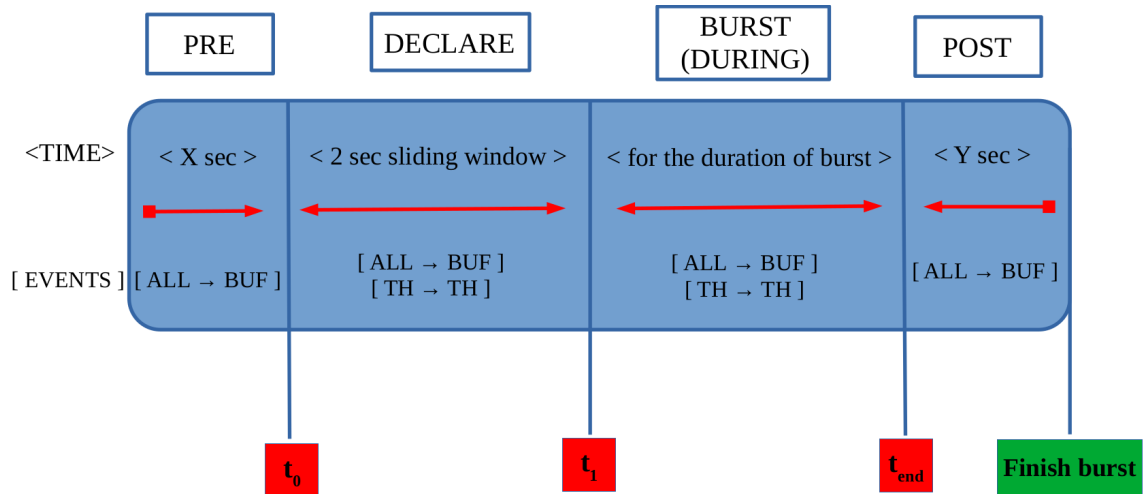
Figure 5.2: `SNO+ Supernova Burst Trigger` logic. The four time windows are marked at the top, while the important time points are marked at the bottom. Within the blue box, the top half represents the time part of the burst, while the bottom portion depicts what happens to events in relation to the multiple buffers in the `Burst Trigger` architecture. Details are described in Subsection 5.2.3.

- **Finish burst** = write the events stored in functional buffer to a file. This includes events from $(t_0 - X)$ until $(t_{end} + Y)$.
- **DECLARE** = the declaration window of 2 seconds. Threshold events are being added (as counts) to logical buffers while all events are being stored in the functional buffers. If any one logical buffer passes the threshold number of events, burst is declared. t_0 and t_1 are set.
- **Burst duration** = the burst is declared from t_0 until t_{end}
- t_0 = time of the first event in the sliding window of the declaration part
- t_1 = time of the last event in the sliding window of the declaration part. The difference between them is not necessarily 2 seconds. As soon as any one of the logical buffers passes the threshold number of events the burst is declared and the times are set.
- t_{end} = either 1 second from t_1 or 1 second after the last threshold event, whichever is later. Threshold events are extending the burst as long as they come within the set time difference from the last threshold event.

This means the length of the burst is variable. Not only the X,Y and dt can be set as needed, but the length of the **declaration window and the extending window are both case dependent**. The declaration window depends on how fast (or close to each other) the threshold events arrive. This can range from 0 up to 2 seconds maximum, at which point the old events are being dropped. Then, the extending window is dependent on

new high NHit events arriving within dt. There can be no such events, or many depending on the burst. There is a hard limit of **42 seconds**[3] after which the burst is ended and written out. In the case the burst was supposed to continue, a new one will be started, slightly overlapping the old one so that no events are lost. There are multiple reasons for this time limit. Firstly, the expected length of the burst is much shorter, therefore, a burst of this length suggests an unphysical signal. Secondly, the burst is only analysed after it is written out. Therefore, in this case, we can analyse this part of the burst and observe it via the online monitoring. This allows for much faster response rather than waiting an unknown length of time before processing the burst. Thirdly, the hard limit removes a lot of potential issues with event mixing. The internal clock assigning times for events rollovers as a consequence of the limits of C++ integer(32) type variable. The hard limit is well within the rollover limits. There is also a minimal length limit contained in the t_{end} variable. This value can get extended, but in case of no new threshold events, it is either set to be equal to t_1, if the difference between t_0 and t_1 is more than 1 second or set to t_0 plus 1 second otherwise. This means the minimal length of normal burst is 1+X+Y seconds if there are no new extending events. Setting X and Y to 1 second, this results in: one second of PRE window, 1 second for the declaration window (t_0 until t_{end}) and 1 second of the POST window. Therefore, the minimal length of a normal burst is 3 seconds (normal burst is a burst that ends when no extending events are recorded). The variable length is used to accommodate different burst types while only storing events of interest. It accounts for the expected SN signal length with overhead while making the analysis as prompt as possible.

The use of PRE and POST windows helps spotting any trends affecting the burst, making it easier to distinguish physics-like bursts from burst caused by electronics effects. It should be noted that no bursts are lost with the addition of the X and Y windows. If there are new threshold events in the Y window that did not extend the current burst (because they were no longer within dt, these would count towards a new burst, meaning the Y section of one burst can overlap with X section of another burst. This ensures that no potential bursts are lost due to the new logic.

---

[3]Number 42 was chosen because it's close to the maximum range of `int32` variable, which is 2,147,483,647. Using 50 MHz clock, this allows for a maximum of 42.95 seconds. Additionally, a burst longer than this is unlikely to originate from a SN burst.

Logical buffers

This part describes the NHit thresholds for the four logical buffers. A study was performed, with the purpose to analyse the expected energies and rates of events in a SN burst, allowing to set detector thresholds to a level where the sensitivity of the detector to SN bursts is maximized without overwhelming the data-acquisition systems. The study is as follows [119]:

- Two SN Monte Carlo (MC) models from the `SNUGen` package are selected: LS220_s27.0co (27 solar mass progenitor) and LS220_z9.6co (9.6 solar mass progenitor). The first model is an example Fe core-collapse SN, while the second model is an electron-capture SN, these were selected to cover a wide range of possible signals;

- Three distances to the SN are selected: 10, 30 and 50 kpc;

- The event burst thresholds are: 3, 5, 7 and 10 (the number of events to trigger a burst);

- The time window is set to 2 seconds;

- The full background data for fully filled SNO+ detector is considered;

- The sensitivity is defined as: the probability of the SN signal passing the trigger threshold (assuming Poisson distribution);

- Inverse beta decay events are counted from SN signal (counting high NHit events, no coincident events are investigated);

- The aim is to retain the highest sensitivity of the `Trigger` while the bursts from predicted backgrounds should not exceed the order of one per month (more in Section 5.10);

- The number of background bursts by NHit value is analysed;

- The final sensitivity as a function of the NHit value is obtained.

The study for model LS220_z9.6co is shown in Figure 5.3 while the results are summarized in Table 5.1.

Configuration file

As mentioned, the `Trigger` is designed with customization in mind. There are several parameters that can be tuned as needed. These are listed here:
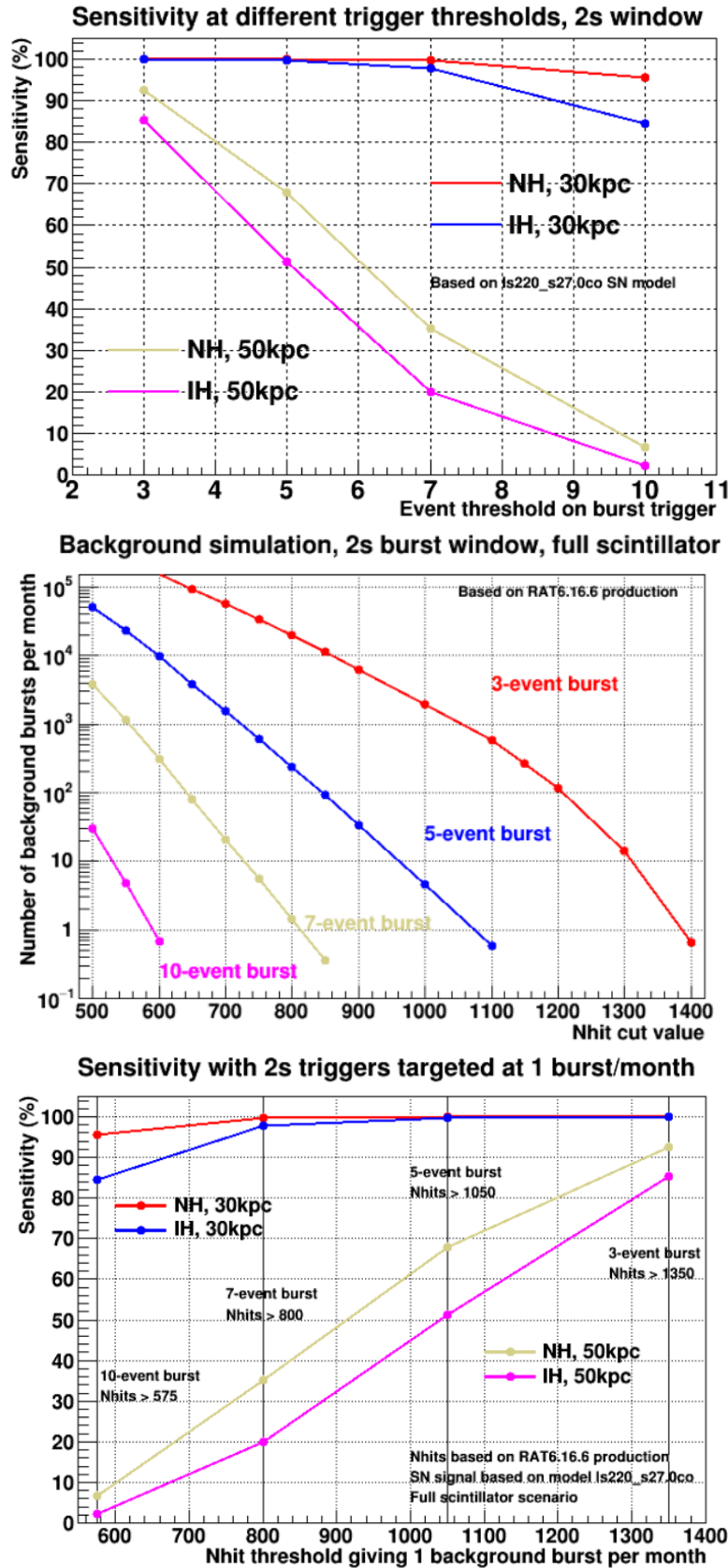
Figure 5.3: Results of the sensitivity study to calculate the NHit thresholds for `SN Burst Trigger` logical buffers using model LS220_z9.6co. Top: Sensitivity as a function of the event threshold for single `SNUGen` model. Four buffers, two distances and both hierarchies are presented here. Middle: The number of background bursts as a function of the NHit value for the four logical buffers. There rate of events is lower for higher NHit values. Bottom: Sensitivity against the NHit threshold value giving one background burst per month. Plots from [119, 120].

Logical buffer	3-event	5-event	7-event	10-event
NHit value	1350	1050	800	575

Table 5.1: Current NHit threshold values for the logical buffers of the `SN Burst Trigger`.

- **The burstwindow**: the length of the sliding window used for counting events in logical buffers that could trigger a burst. Also marked as declaration part;

- **The xwindow**: the time window before the burst window that should be written out to the burst file. Also called PRE time window;

- **The ywindow**: the time window after the burst window that should be written out to the burst file. Also called POST time window;

- **The extwindow**: the length of the extending window. Events coming within this time from the last threshold event extend the length of the burst. This corresponds to the dt;

- **The extnhit**: the threshold NHit value for the events to extend the burst;

- **The threeevsnhit**: the NHit threshold value for the 3-events logical buffer;

- **The fiveevsnhit**: the NHit threshold value for the 5-events logical buffer;

- **The sevenevsnhit**: the NHit threshold value for the 7-events logical buffer;

- **The tenevsnhit**: the NHit threshold value for the 10-events logical buffer;

- **The lengthlimit**: the time limit for the longest a burst can be;

- **The bitmask**: the bitmask determines which events should be saved regardless of NHit. Any events whose trigger word shares a bit with this bitmask is automatically saved.

The configuration files ensures that the settings can be changed while the `Trigger` is operational. It also allows the possibility of changing the NHit threshold values which is especially useful during the scintillator fill period where the activity of the detector changes significantly.

Stonehenge

`Stonehenge` is the main software package that contains the logic of the `SN Burst Trigger`. It processes events from the `Event Builder` fed by the `client`. It has modular

design and uses the following packages [118]:

- **The curl package**: handles posting of messages and alarms to the monitoring system;

- **The config package**: handles parsing the configuration file;

- **The snbuf package**: handles the `Burst Trigger` logic;

- **The redis package**: handles the connection to the Redis database (Subsection 5.4.1) to store rate information;

- **The output package**: handles the writing of finished bursts to the disk.

Supernova buffer

The `supernova buffer` interprets the main burst logic as defined earlier in the chapter. This is the `snbuf` module of `Stonehenge`. There are few additional features that should be discussed.

Timestamps

One major issue is how to handle event timestamps that may arrive out of order. This can happen due to a misread clock bit or due to a problem in the `Builder`. The events are always processed sequentially and cannot reasonably go backwards or look ahead. Because we decided to prioritize a fast SN monitoring process over a complex one with a pointer indexing system to enable reordering, it was decided that events must be stored in the functional buffer in order. Therefore, events with unordered timestamps must be dealt with.

The algorithm was designed as follows: any event with a 0 timestamp (orphan) has the timestamp set to the timestamp of the previous event, a single disordered event is treated the same way. If there is second disordered event in a row, the timestamp of this new event is now assumed to be the correct time. However, if there is an ongoing burst it has to be written out due to the ordering argument. This is one of the few end conditions for a burst.

End conditions

There are five end conditions, where the ongoing burst has to be finished. One is the normal end condition while four denote an abrupt end of the burst. These are:

- 0: the normal end condition, when there are no new threshold events within the extending window;

- 1: when the end of file (subrun) was reached;

- 2: when there is more than one event our of order;

- 3: when the burst is longer than the length limit;

- 4: when there are clock jumps.

Each of these conditions causes the burst to be finished and written to the burst file. However, if the burst conditions are still satisfied, the burst continues and another burst file is created. Due to possible overlap of PRE and POST sections as well as the flexibility of the sliding window, no events are lost due to any of these end conditions.

Handling file boundaries

The recording of the data follows the specific structure formed of runs and subruns. To maximize the sensitivity to SNe, the file boundaries have to be dealt with. Whenever a subrun ends the state of all buffers are written to disk and then loaded back into the memory at the beginning of the next file. Currently the functional buffers are written as ZDAB files, while the logical buffers are kept as text. The ordering of events is rechecked. If a burst is ongoing, it is finished and written to a burst file. If the burst conditions are still satisfied when the new subrun starts, a new burst is declared. No events are lost.

Event quality checks

There are several checks applied in the `snbuf` module:

- A check that events go forward in time;

- A check that time doesn't jump too far ahead;

- A consistency between the 10 MHz clock and 50 MHz clock times is being monitored;

- A check for re-triggers;

- A check for the event ZDAB structure;

- A check that the time, NHit, and trigger word are sensible.

Additionally, important parameters are sent for online monitoring. More debugging information is available in log files.

Implementation of the logic

The `Supernova Burst Trigger` logic is implemented in the `snbuf` module. This includes but is not limited to:

- The check for run type: this allows for different settings to be applied depending on the run type. This is important since the thresholds often need to be increased for maintenance-like runs;

- The events are analysed, added to appropriate buffers depending on the NHit;

- The events are dropped from buffers if they expire;

- The check for the burst start: this requires counting the number of events in the logical buffers;

- The extending logic is implemented here: new threshold events move the end of the burst;

- The length of the burst is checked: this ensures that both the minimal length is adhered to as well as the maximal length is not exceeded;

- All end conditions are reviewed;

- The burst file is opened when required;

- The events are written from the functional buffer to the file on the disk on burst finish;

- The state, buffers and counters are stored on file rollovers;

- Finally, the `RAT Burst processors` are called to analyse a burst once it's fully written out. These are described in detail in Section 5.3.

Burst numbering

It's important to keep a system of numbering for the bursts. This ensures that they are ordered, can be easily linked to the run they were created for, it's easy to track which burst came first and it's also possible to see whether there is anything common between bursts that come close in time to each other.

The hierarchy that is kept is using the run number, subrun number and the counter of the bursts within that subrun. The counter increases for the bursts as they come in time. An example would be: *270168_003_0*, this is the first burst for subrun 3 in the run 270168.

5.3   Burst Trigger: processors

Once the burst file is closed by the `Burst Trigger`, a suite of RAT processors and scripts is run over it. This is done in order to analyse events, extract observables, clean the data, post alarms[4] if necessary, create basic plots and make them available for online monitoring. The whole system is structured into three levels as:

- `Level 1`: This includes everything up to writing the burst out, the `Software Trigger` itself that detects a burst from raw detector data;

- `Level 2`: This level provides immediate analysis of the burst, including the most obvious observables;

- `Level 3`: Data cleaning is applied to the burst and the observables are re-evaluated, this step also includes posting alarms if necessary.

`Level 1` has been described until now, `Level 2` and `Level 3` are described in detail below. A possible method for `Level 4` - a reconstruction of SN observables - is suggested in Chapter 6.

5.3.1   Level 2

The purpose of the `level 2` processor is to provide immediate analysis of the burst and make it available for monitoring. Speed is the priority.

Both `Level 2` and `Level 3` processors are similar in the way they approach the data:

- At the start, counters are initialized and basic plots are prepared;

---

[4]SN alarms: every detected burst alarms in a form of email. If the burst is found to be significant (more in in Section 5.5), an associated alarm is also posted to the detector alarm application that is being monitored by detector shifters, and additional message is also posted to the SNEWS network (Section 5.10).

- The time of the burst is set to be the time of the first event of the burst (it should be noted that two times are considered, local time as well as UTC time);

- The time **in run** when the burst occurred is calculated;

- Status of the PMTs is evaluated, vectors are initialized;

- Events are looped over chronologically, for each:

  - The NHit is obtained and stored: both raw and cleaned (cleaned NHit has cross talk hits removed);

  - The time of the event is obtained (the 50 MHz clock is used) and stored;

  - The time difference to previous events is also stored;

  - The trigger bits are collected;

  - The PMTs are looped over and the hits are recorded, this makes it possible to see the distribution of the hits across the electronics space (crates, cards and channels) to evaluate isotropy;

  - The counts of total events and entries are kept;

  - For the first and last event, the global trigger ID is stored (GTID). This makes it easier to locate the events if needed.

- Once the events are looped over, the data is analysed as:

  - The NHit plots are filled;

  - The time plots are filled;

  - For PMTs, the occupancies are calculated in order to cut any PMTs that have significantly higher occupancy, these likely correspond to flashers[5];

  - Flat maps[6] of hits are created.

- The plots created above are written out to root file;

- Additional processes are called to make data available online as well as to continue with `Level 3` processing.

---

[5]**A flasher event**: a specific detector event, usually produced by an arc inside a PMT, causing light that is detected on the other side of the detector [117].

[6]**A flat map** is a type of plot where SNO+ PMTs are shown in 2D view, with dots/markers representing individual PMTs. Because the shape of the structure holding the PMTs is spherical, the visualization is form of a map projection, where the sphere is 'sliced', similar to an orange peel. The positions on the flat map correspond to true positions, i.e. the top portion is the neck of the detector.

The `Level 2` processor is aimed to provide immediate overview of the burst, looking at the very basic observables that could help identify the burst without complex reconstruction. The readily available variables that are considered are the times of events, the number of hit PMTs, the distribution of the hits across the detector, the number of hit PMTs as a function of time and some basic statistics such as the number of events and the length of the burst.

5.3.2 Level 3

`Level 3` processor aims to apply data cleaning on the burst. This is done by removing events that are very like not physics events (and, therefore, not SN events). A common approach to cleaning is applied: processors are used to identify and tag instrumental backgrounds in the data, including electronics cross talk and PMT flasher events.

Data cleaning bits

As mentioned, the SN burst data is special as it usually involves many high energy events which is also the case for some instrumental issues such as breakdowns. Therefore, the cleaning bits that are applied need to be evaluated with SN signal in mind.

The cleaning bits that are being applied:

- **Ring of fire**: Checks for rings associated with front-end electronics. This type of event is associated with noise in the front-end (FE) electronics that is worst in the outer channels on the Front-End-Card (FEC). Also checks if most hits come from single crate;

- **Crate isotropy**: Checks that hits are unevenly distributed in the electronics space. These events are associated with noise in the FE electronics that causes noise hits on adjacent channels;

- **NHit cut**: Flags events below a NHit value. Very low NHit events are usually noise;

- **Flasher geo cut**: Cut that tries to flag flasher events. Looks for events with a cluster of hits, either a cluster of PMTs near each other on the PSUP or a cluster of electronic channels on the same FEC. The idea is that a flasher event will create a very high charge hit that may induce cross talk hits on nearby channels or flash bright enough to light up adjacent tubes;

- **Threshold flasher cut**: Designed to look for flasher and shark-fin[7] events occurring next to channels that have their discriminator threshold maxed. That would cause the flasher not to produce cross talk on several nearby channels;

- **Charge vs NHit**: Since most of the noise is bipolar, events triggering on noise will have much lower charge than expected. This cut identifies noise events by looking at the charge compared to the NHit;

- **Charge cluster**: Cuts Wet End Breakdowns (WEB), flashers and shark-fins by looking for clusters of hits in the electronics space surrounding a high charge hit;

- **Charge vs time**: Looks for flashing PMTs where a hit has charge many counts above mean that also occurs much earlier than mean hit time;

- **Neck cut**: Tags neck events. Looks for events with many neck PMTs hit or events where a neck tube has a bad charge and is hit much earlier than the average time of hits in the bottom hemisphere;

- **Junk cut**: Cuts events where a PMT had more than one hit, which should not be physically possible;

- **Zero-zero cut**: Tags events where the last two hex digits of the GTID are zero. This is required to deal with rollover issue for orphan hits with bad GTIDs ending in 00.

Some examples of special cleaning bits that are intentionally not applied because they select against close SN bursts:

- **Empty crate**: Bit that tries to cut high NHit event that are not evenly distributed among the crates. Because the detector is kept up even in non-ideal states in case a SN goes off, this bit is omitted;

- **Owl cut**: Cuts events with too much activity in the outer PMTs. This is expected for SN signal;

- **Missed count burst cut**: The front-end electronics has a limited buffer which can fill up during high rate bursts. A missed count bit is flagged once a hit arrives where all cells already contain data. This cut searches for events where many channels have missed counts. High rate bursts are expected for close SN signal;

---

[7]The **shark-fin** event is characterized by one channel with high charge while its neighbouring channels show no charge, but fire on 'pickup' noise.

- **Atmospheric**: Designed to cut atmospheric neutrino events by looking at high NHit event followed by a slightly less high NHit event within short time windows. This selects against SN burst;

- **Polling cut**: The DAQ system has few different measurements that are done on a run-by-run basis. During these measurements the hardware can increase the amount of noise. The timing hardware tags these polling periods. However, these are very low NHit and quite localised, therefore, to increase the sensitivity this cut is also omitted.

A study was performed to find the effect of selected data cleaning cuts on both MC (`SNUGen`) and bursts collected from real data. Results of the study are shown in Figure 5.4. The cleaning bits in use do not affect MC signal in any significant way, meaning, if real SN data is as predicted, it should be preserved by data cleaning.

Muon cleaning bits cannot be used in their current form as they strongly cut SNUGen data. Real muon events are being tagged by other cleaning bits and are therefore cleaned from real bursts.

In `Level 3`, the data is analysed almost identically to `Level 2`, with the addition of data cleaning. Each event is checked for any flags applied by the data cleaning bits described above. Some additional plots are created with regards to the clean events as well as cut events. Plots from `Level 2` and `Level 3`, alongside additional data that is stored is discussed in Section 5.4. Also, if the clean burst passes certain thresholds, alarms are raised. These are discussed in Section 5.5.

The overview connecting the raw data to RAT `Level 2` and `Level 3` processors as well as online monitoring is shown in Figure 5.5. A more detailed overview is presented in Appendix E.

5.4   Online monitoring

Since the purpose of the `SN Burst Trigger` is to alarm whenever a supernova-like signal is detected, it is important to make the data available for review. There is a full suite of monitoring tools available online to review for every burst. The online monitoring offers data coming from the RAT processors, both `Level 2` and `Level 3`. The data is stored in two different databases and the plots are stored on storage server.
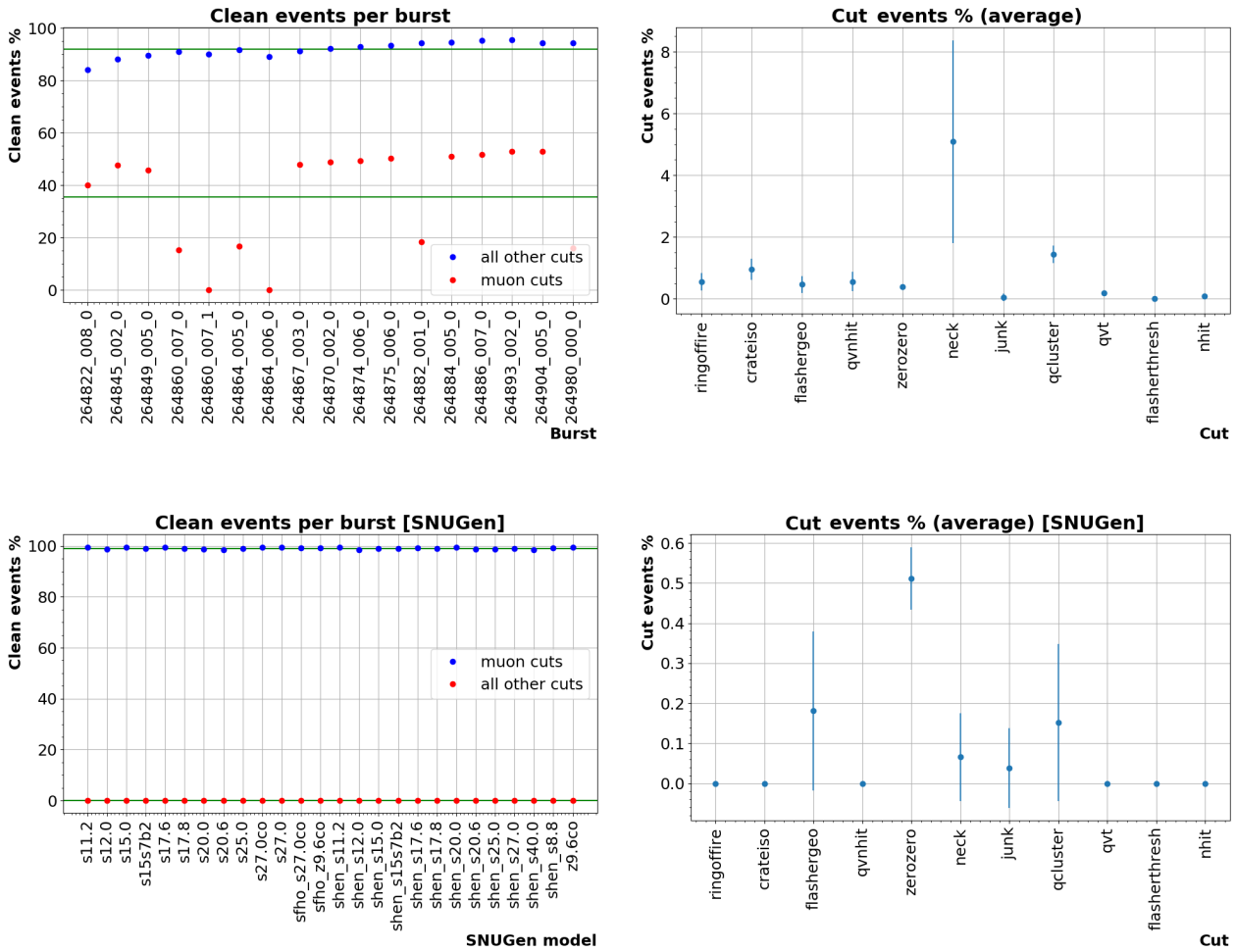
Figure 5.4: Analysis of L3 cuts. The selection of cleaning bits was applied to group of real data bursts as well as SNUGen MC bursts. The current selection of cleaning bits was found not to affect SNUGen signals significantly.
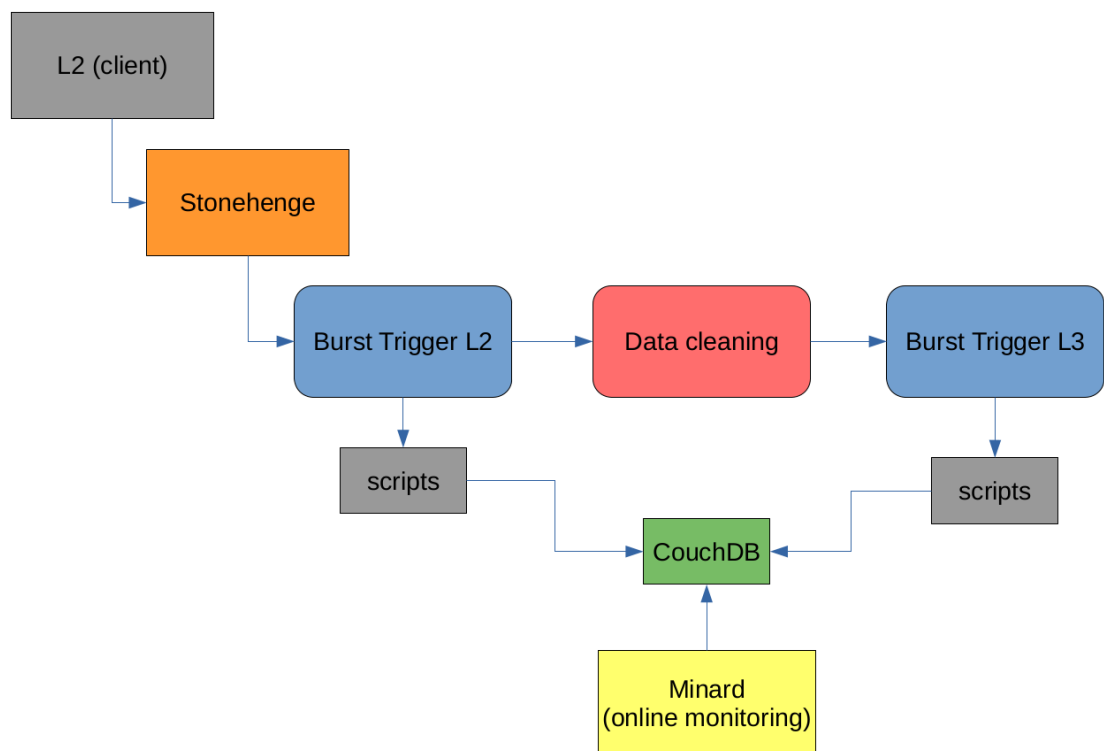
Figure 5.5: Simplified overview of the `Supernova Burst Trigger` system. The elements are grouped by color: scripts are simple pieces that link or control the data flow, Stonehenge contains the logic for declaring the bursts, RAT processors analyse burst files extracting the data and making plots, CouchDB holds the list and basic data for each burst and Minard is the name for the server (and system) hosting the online monitoring.

5.4.1 Redis database

Redis, or Remote Dictionary Server, is an open source in-memory data structure stored most often in the form of key-value database [121]. For purposes of the `Burst Trigger`, several elements are stored in a Redis database:

- The NHit threshold values for the four logical buffers;

- The lengths of several time windows for the `Burst Trigger`: declare window, pre window, post window and extending window;

- The `Stonehenge` configuration;

- The threshold for high NHit events.

Redis is used in place of other key-value database because the values stored here are often needed for short time period only and can later be overwritten. It is not often necessary to hold the values for longer. This improves the speed and reduces the storage needed.

5.4.2 CouchDB database

CouchDB is a schema-free database management system. The CouchDB server hosts named databases that store unique documents. These documents are the primary unit of data and consist of any number of fields and attachments. This type of database is used throughout the experiment with the `Burst Trigger` also utilizing the same approach [122]. Example information stored in burst CouchDB database for each burst is:

- `THe stonehenge` settings: NHit thresholds for the four logical buffers, time lengths for the windows (declare, pre, post, extending), extending NHit threshold;

- Which buffer triggered the burst;

- The burst end condition;

- The burst identification: run number, subrun number, burst number within the subrun;

- The burst time and date (local and UTC);

- The burst size (number of recorded events);

- The burst length;

- The average NHit;

- The number of recorded hits;

- The number of triggers;

- The first and the last global trigger IDs to easily locate the events;

- Names and paths for the burst file and plots.

5.4.3 Level 2

The online monitoring specific to the `Supernova Burst Trigger` was made a part of the common online monitoring page for the SNO+ experiment. There are two sections, one for each level of the processing. Both follow the same general structure but there are some additional features for the `Level 3`. Each section consists of three parts: an overview page, a list page and a page with details of a specific burst.

Overview page

The overview page informs the user about the current status of the `Burst Trigger`. It reflects the current rate of the events being built by the `Event Builder`, the rate of events being processed by `Stonehenge`, the number of orphans, the number of bursts, current GTID and the current run. Additionally, the settings stored in Redis database are shown as well as the lists of ZDAB files according to their status: being processed, done, failed and similar.

Examples of these are presented here: Figure 5.6 shows the monitoring overview, Figure 5.7 is a view of the `Stonehenge` settings loaded from the Redis database and Figure 5.8 shows the lists of ZDAB files and their category.

List page

The list page loads data from the CouchDB database. It loops through all available bursts, ordering them by the run number, subrun number and the burst number within that subrun. This means the most recent bursts are listed first. Some basic information is presented in the table. This includes: date, time, number of events, length, average NHit, GTID range, buffer that triggered the burst, burst end condition and some of the `Stonehenge` settings. An excerpt of the table is shown in Figure 5.9.
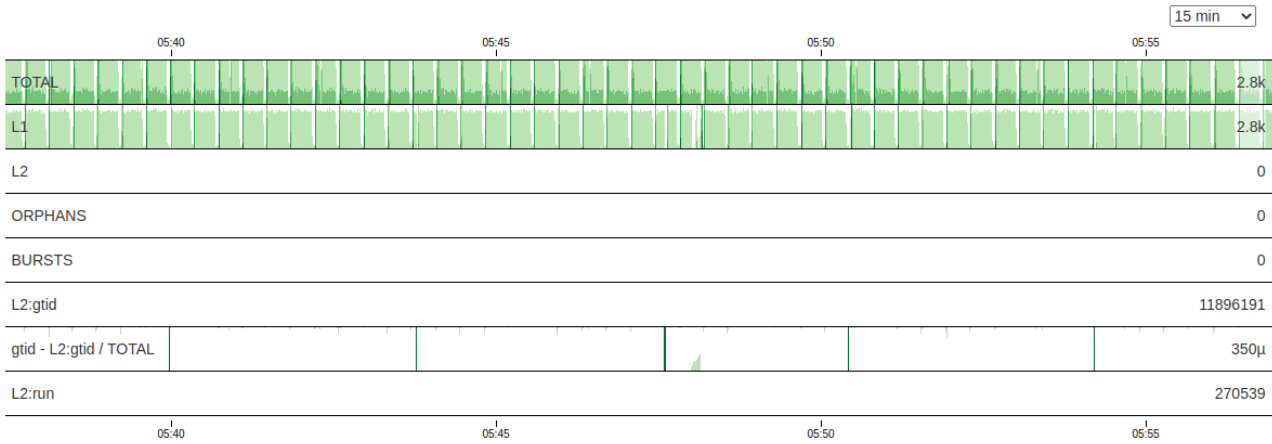
Figure 5.6: Monitoring overview of the `Level 2` of the `Supernova Burst Trigger` as available as the part of the online monitoring suite. It shows some basic properties such as: the rate of raw events (TOTAL), the rate of events processed by the `Burst Trigger (L1)`, any detected orphans, declared bursts, current GTID and run.

3Evt [NHit]	5Evt [NHit]	7Evt [NHit]	10Evt [NHit]	Window [s]	Pre [s]	Post [s]	Ext [s]
1630	1000	795	700	2	1	1	1

Figure 5.7: The view of currently applied `Stonehenge` settings as seen on the `Level 2` overview page of the online monitoring.

Being Processed

SNOP_0000270539_002.zdab   a few seconds ago

Waiting for RAT

RAT

Done

SNOP_0000270520_008.zdab   17 hours ago

Failed

Figure 5.8: Lists of ZDAB files according to their status as seen on the `Level 2` overview page of the online monitoring.

Details

SH End: 0=normal, 1=end of file reached, 2=events out of order, 3=too long, 4=clock jumps

Run	SubRun	Burst	Date	Time	# Events	Length [s]	NHit(avg)	GTID range	Buffer	SH 3Evt	SH 5Evt	SH 7Evt	SH 10Evt	SH End
270539	8	0	5 May 2021	17:23:41	9127	3.06246	62.6752	16588622 - 16597748	3	1630	1000	795	700	0
270537	5	0	5 May 2021	15:10:03	8852	3.0001	64.4971	9868647 - 9877499	3	1630	1000	795	700	0
270536	7	0	5 May 2021	14:19:37	5384	1.78349	63.9915	976359 - 981742	3	1630	1000	795	700	2
270535	13	0	5 May 2021	13:39:55	11890	4.01762	60.1017	10725612 - 10737502	3	1630	1000	795	700	0
270534	13	0	5 May 2021	12:40:20	9110	3.00033	58.93	281860 - 290969	3	1630	1000	795	700	0

Figure 5.9: The list page contains the table presenting the data for bursts loaded from the CouchDB database. These are ordered in reverse chronological order. Some basic data for each burst is shown.

Detail page

Each line in the table shown in Figure 5.9 represents a single burst detected by `Stonehenge` and analysed by the `Level 2` RAT processor. The table itself only shows some details that can help categorize the burst. However, the run number represents a hyperlink to a detail page containing all details for that particular burst. The detailed pages is separated into tables and plots as follows:

- Tables:

    - **General information**: The basic information for the burst: run, subrun, burst numbers, run type, date, time, date UTC, time UTC;

    - **Burst details**: The basic parameters of the burst: length, size, average NHit, hits, triggers, GTIDs;

    - **Stonehenge settings**: `Stonehenge` settings used to detect the burst: buffer that trigger the burst, end condition, declare window, pre window, post window, extending window, logical buffers thresholds, extending threshold;

    - **Other details**: Details regarding files: burst ZDAB file, processed ROOT file.

- Plot sections:

    - **NHit plots**: There are two NHit plots available. First plot focuses on low NHit events (below 500). This should help distinguish the signal from nominal backgrounds. Second plot focuses on all events, regardless of NHit, in a log scale. This highlights if there are any peaks around specific NHit values and what the overall distributions looks like. It should be reminded that the NHit values correspond to energy. There are specific energy peaks expected for a SN signal;

    - **Time plots**: There are three time plots. The time spectrum shows the distribution of events across the length of the burst. This helps to distinguish whether the events come in little bursts, which could point to electronics issue. The second plot shows the number of events over the length of the burst in cumulative fashion. The event rate for the successful SN signal is expected to decay over time with most events within the first two seconds or so. This could be easily spotted using this plot. The last plot shows the time differences between the events. The inverse beta decay channel specifically has a unique

signature for the neutron capture that has distinct time profile. Features similar to that could be captured using this plot;

- **Time vs NHit plot**: The time-NHit plot may be the most useful plot to determine the burst type. The plot shows the NHit of events as a function of the time. The data is binned, the z-axis represents the number of events in each bin by color. The plot also shows the NHit value used to declare the burst as well as the extending NHit threshold as horizontal lines, red and pink respectively. Several burst classes were defined using the features from this plot, more details are available in Section 5.8;

- **Crate / Card / Channel distribution**: The CCC plots display the distribution of the hits across the detector's readout electronics. The SN signal is expected to be uniformly distributed across the PMTs. If there is a specific crate or a few neighbouring crates standing out this usually points to a breakdown or similar issue. It should be noted that the plots are normalized per number of active, online channels;

- **Triggers plot**: Simple plot showing the distribution of triggers for all events in the burst. Makes it possible to notice any trigger related issues.;

- **Flat map plot**: The flat map shows the occupancy of PMTs across the detector. This helps in identifying whether the events in the burst are localized, whether there are any PMTs that stand out such as flashers or shark-fins, crates that are breaking down, or generally point to any known electronics issues or features of known physics events such as muons, Michel electrons and similar. Again, the SN signal should be very uniform.

The `Level 2` tables for burst *269750_5_3* are presented in Figures 5.10, 5.11, 5.12 and 5.13 while the `Level 2` plots for the same burst are shown in Figures 5.14, 5.15, 5.16, 5.17 and 5.18. These figures are a representation of the data that is stored and presented via online monitoring for each detected burst. If a real SN burst is detected, this data would be used to make a preliminary decision on categorising the burst.

5.4.4 Level 3

The `Level 3` sections follow the same structure with some differences relating to the data cleaning.

General information

Parameter	Value	Note
Run	269750	Run number where burst occured
SubRun	5	Subrun number where burst occured
Burst #	3	Burst number within subrun
Run type	Physics, Bubblers On, Cavity Recirculation ON, Scint. Fill	Type of run, calibration, run bits
Date	8 Apr 2021	Sudbury date
Time	01:02:16	Sudbury time
Date UTC	8 Apr 2021	UTC date
Time UTC	06:02:16	UTC time

Figure 5.10: `Level 2` detailed page table: General information. This table contains the burst ID (including the run number, subrun number and burst number), local date and time, UTC date and time and the type of run which includes any tags for the run that could point to unusual conditions.

Burst details

Parameter	Value	Note
Burst length	5.01477	[s]
Burst size	16108	# events
Avg NHit	99.5739	
Hits	1603933	
Triggers	40283	
First GTID	15011112	GTID of first event
Last GTID	15027220	GTID of last event

Figure 5.11: `Level 2` detailed page table: Burst details. This table describes the basic properties of the burst such as the length, the number of events, average NHit and similar.

Stonehenge settings

Parameter	Value	Note
SH Buffer	5	Logical buffer that triggered burst
SH End	0	Burst end condition (0:normal,1:EoF reached,2:out of order,3:too long,4:clock jumps)
SH Window	2	[s] Declaration window
SH Pre	1	[s] Pre-declaration window
SH Post	1	[s] Post-declaration window
SH Ext	1	[s] Extending window
SH Nhit 3 Evs	1630	NHit threshold for 3 event logical buffer
SH Nhit 5 Evs	1000	NHit threshold for 5 event logical buffer
SH Nhit 7 Evs	795	NHit threshold for 7 event logical buffer
SH Nhit 10 Evs	700	NHit threshold for 10 event logical buffer
SH Nhit Ext	700	NHit threshold for extending

Figure 5.12: `Level 2` detailed page table: `Stonehenge` settings. The settings used to declare this burst are presented in this table. The settings can change when the detector status changes to improve sensitivity. It also serves as control for the declaration logic.

Other details

Parameter	Value	Note
ROOT file	269750_5_3.root	
ZDAB file	burst_0000269750_005_3.zdab	

Figure 5.13: `Level 2` detailed page table: Other details. Some additional details relating to the burst are listed in this table, such as the raw burst file and the processed file.
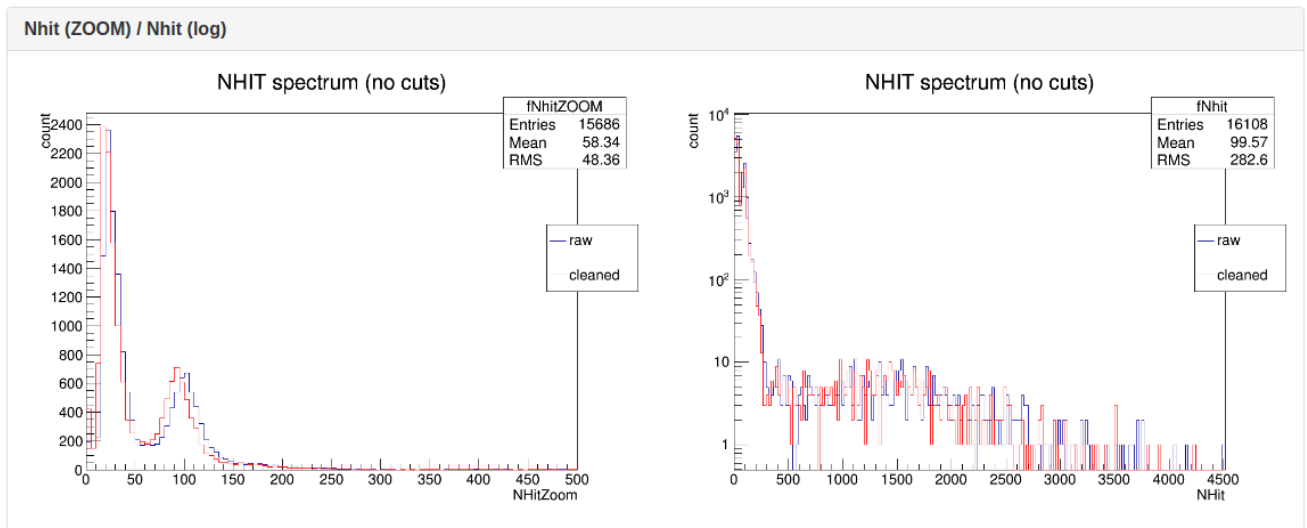
Figure 5.14: `Level 2` detailed page plots: NHit (ZOOM) and NHit (log). Two datasets are shown, raw and cleaned (cross talk is removed) events. The left plot is zoomed over lower end of the distribution where most of the backgrounds are present while the right plot covers the whole range in log scale to easily distinguish significant peaks.
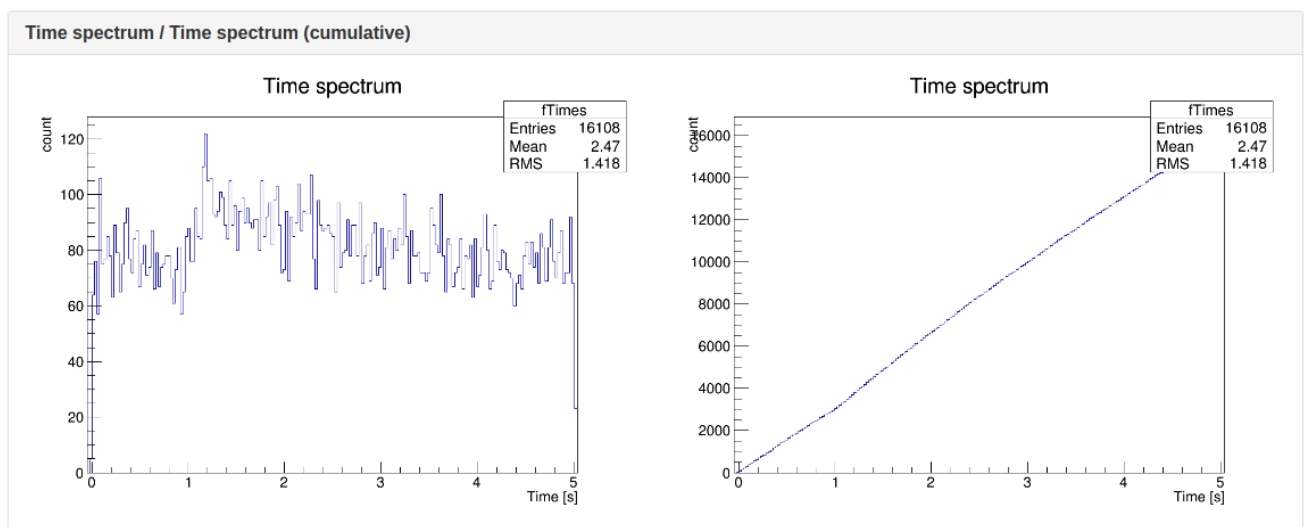
Figure 5.15: `Level 2` detailed page plots: Time spectrum and Time spectrum (cumulative). The left plot shows the distribution of events (in very narrow bins) over the length of the burst. The right plot is a cumulative version of the same distribution. These help notice whether the event rate is constant or changing throughout the burst and whether there are mini-bursts present, which could point to issues with electronics. Additionally, the (common) SN-like burst should have decreasing event rate over time, with most events coming in the first two seconds or so. This could be easily observed in a plot of this type.
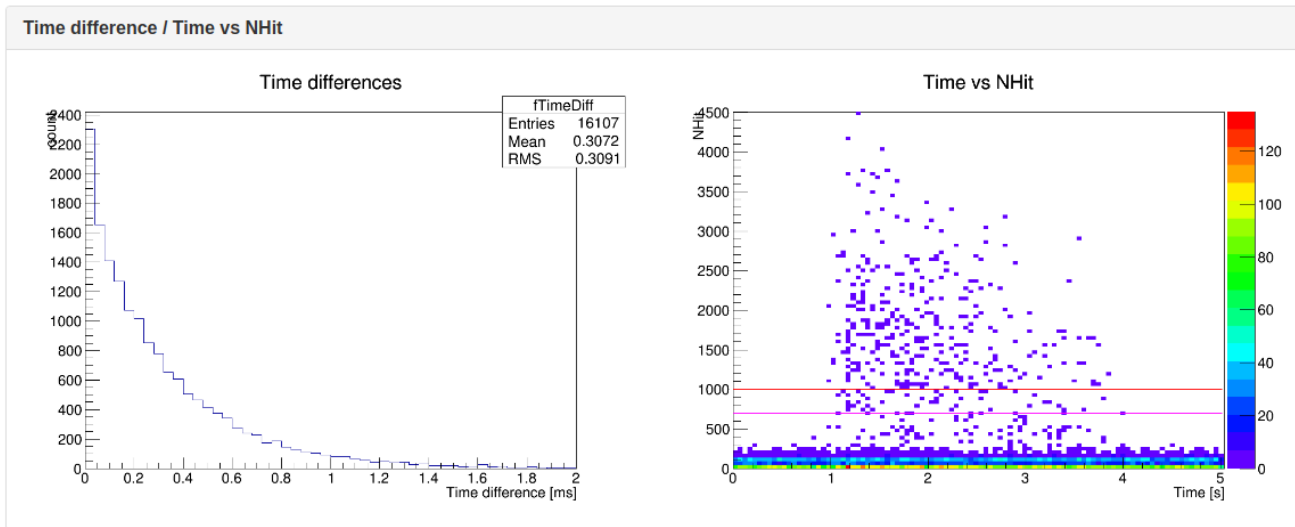
Figure 5.16: `Level 2` detailed page plots: Time difference and Time versus NHit plots. The first plot shows the time difference between the events in a burst, this makes it possible to notice a triggering issues versus potentially physical events. The time versus NHit plot maybe the most useful plot to evaluate the burst type. It shows the time of the events on the x-axis, the NHit of the events on the y-axis and because it is a histogram, the data is binned, with the color representing the number of events in respective bins, visualized by a color scheme. The plot also shows the two NHit threshold values, one for the buffer that triggered the burst and one for the extending process. Different classes of bursts have significant features that can be observed in this type of a plot. Some of these are discussed in the Section 5.8.
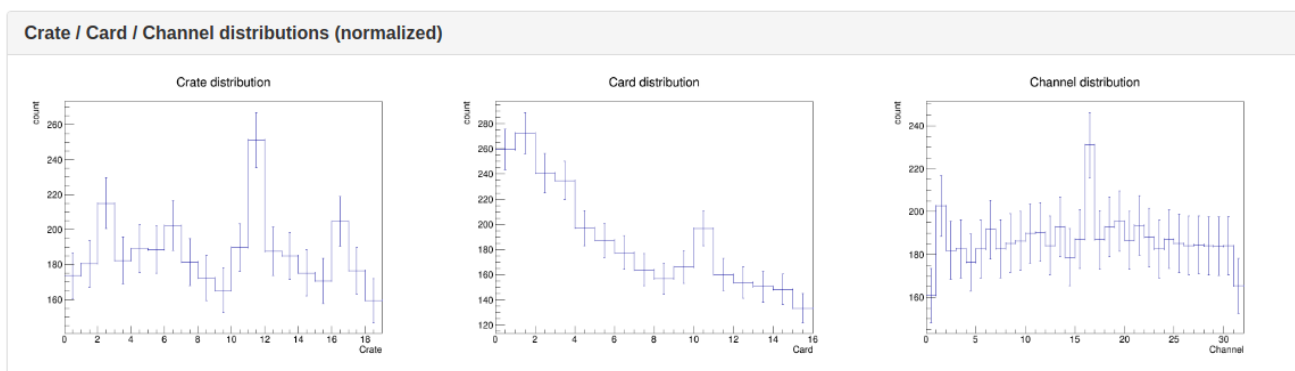
Figure 5.17: `Level 2` detailed page plots: the Crate, Card and Channel distributions. The plots in this section shown the distribution of hits across the detector's electronics. The uniformity of the burst can be determined. Additionally, some types of breakdowns show unique features in these plots. These are, again, discussed in Section 5.8. It should be noted that the data is normalized per number of online, active PMTs per each unit, being it the crate or card.
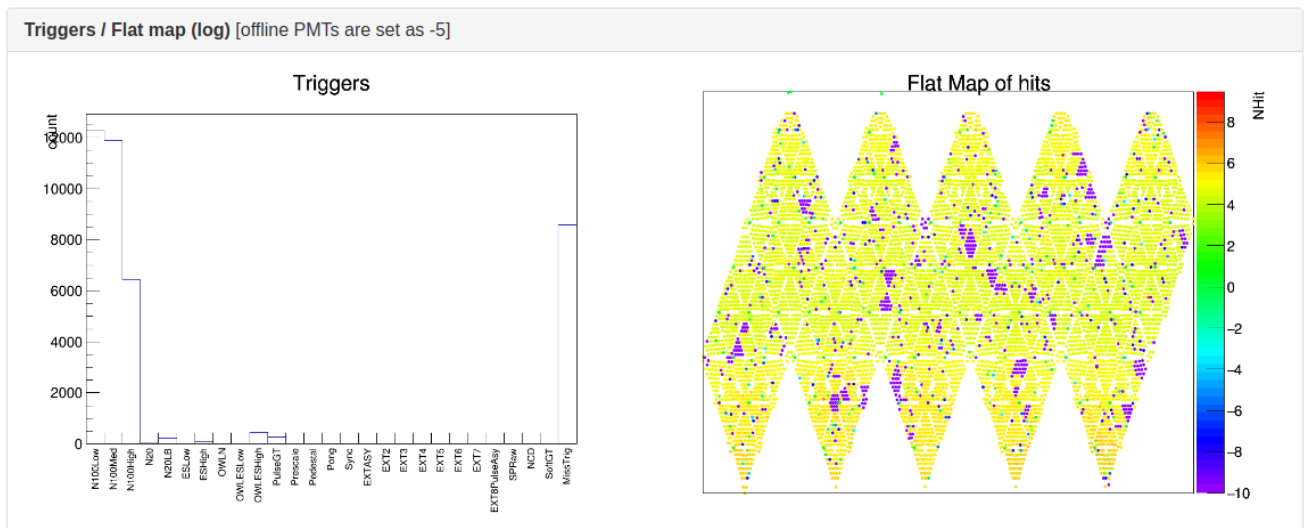
Figure 5.18: `Level 2` detailed page plots: the triggers and the flat map of hits. The trigger plots shows the distribution of the events in the burst by the trigger type. Only some are associated with physics data-taking. Additionally, any issues with triggers can be spotted. The flat map is useful to highlight whether there was specific localization of the burst events. It can also point to unique features such as flasher PMTs, shark-fins and similar. Only the sum of events is shown, so it is not necessarily easy to distinguish individual events such as muons if they were present. During the detector fill with scintillator, increase in sensitivity around the water-scintillator interface could be seen on this type of plot.

Status	Cuts
✅ Applied:	junkcut, flashergeocut, qvt, thresholdflashercut, qcluster, qvnhit, nothingcut, nhitcut, zerozerocut, ringoffire, neckcut, crateisotropy
❌ Not Applied:	caencut, ftscut, emptycrate, owlcut, missedmuonfollower, missedcountburstcut, itctimespreadcut, muontag, pollingcut, prescalecut, pedcut, atmospheric, tpmuonfollowercut

Figure 5.19: Overview of the cuts for the `Level 3` of the `Supernova Burst Trigger` as available as the part of the online monitoring suite. Because the cuts are being reworked as the detector transitions between different phases they can be turned on or off as appropriate.

3Evt [NHit]	5Evt [NHit]	7Evt [NHit]	10Evt [NHit]	Window [s]	Pre [s]	Post [s]	Ext [s]	High NHit
1630	1000	795	700	2	1	1	1	500

Figure 5.20: Similar to `Level 2`, an overview of the `Stonehenge` settings is shown on the `Level 3` overview page. One additional parameter that is important for `Level 3` is the High NHit threshold, where events above this value are uniquely treated as they count towards the alarm threshold.

Overview page

The overview page for `Level 3` lists currently applied data cleaning cuts loaded from CouchDB, NHit and time settings loaded from Redis database and list of processed ZDAB files grouped according to their status. The page is made as dynamic as possible, showing information that can change at any point without the need to change the design of the page. The main purpose here is the monitoring of current settings and the progress of the processed files. Examples are listed in Figures 5.19, 5.20 and 5.21.

List page

The list page for `Level 3` is very similar to `Level 2`, loading available data from CouchDB in reverse chronological order by the burst ID. The table still includes some basic information such as date, time, the number of events and `Stonehenge` settings but there is additional data relating to the data cleaning: the number of survived events, the

Burst L2		DC - pass 1		DC - pass 2	
270567_000_0	2 days ago				
Burst L3		**Done**		**Failed**	
		270607_002_0	11 hours ago		

Figure 5.21: Lists of ZDAB files according to their status as seen on the `Level 3` overview page of the online monitoring. There are additional groups available compared to `Level 3`, corresponding to multiple passes of data cleaning.

Details

SH End: 0=normal, 1=end of file reached, 2=events out of order, 3=too long, 4=clock jumps
Check: 0=not checked, 1=checked by algorithm, 2=checked by person

Run	SubRun	Burst	Date	Time	# Events	Clean events	High NHit	Survived	Length [s]	NHit(avg)	SH End	Check	Note
270539	8	0	5 May 2021	17:23:41	9127	8491 93.03%	29	3 10.34%	3.06246	56.9482	0	0	
270537	5	0	5 May 2021	15:10:03	8853	8300 93.75%	28	2 7.14%	3.0001	57.0567	0	0	
270536	7	0	5 May 2021	14:19:37	5384	5004 92.94%	20	3 15.00%	1.78349	56.2256	2	0	
270535	13	0	5 May 2021	13:39:55	11891	11129 93.59%	21	2 9.52%	4.01762	57.2744	0	0	
270534	13	0	5 May 2021	12:40:20	9110	8466 92.93%	14	1 7.14%	3.00033	55.6961	0	0	

Figure 5.22: The `Level 3` list page focuses on the data cleaning related parameters such as the number of surviving events. Specifically the number of surviving high NHit events is relevant for alarms. The note section can be used for burst classification.

number of events above the high NHit threshold and the number of survived events above the high NHit threshold. Some variables are present that were also included in `Level 2`, such as the length and the average NHit, but in this case these represent the cleaned burst. Finally, there is a note column that contains a classification of the burst as written in the review section of the burst detail page (more details in the Section 5.4.4). An excerpt of the table is shown in Figure 5.22.

Detail page

Again, following the scheme of `Level 2`, every[8] detected burst is run through the data cleaning and the processed with `Level 3` RAT processor. The processors produces data and plots for each burst. These are used to classify the burst. In the case the burst is similar to a SN signal, alarms are also posted. There is a detail page available for each processed burst. The detail page contains tables, plot sections and review section:

- Tables:

    - **General information**: This table contains the general information for the burst: run number, subrun number, burst number, date and time. Additionally, the run type is loaded here. These represent the detector conditions when the burst was declared. Some of these may be a hint towards the burst origin, for example the 'DCR bit' means people were accessing the detector clean room or the 'Scintillator Fill bit' suggests increased detector activity due to fluids being recirculated inside the AV. The relevant `Stonehenge` settings are listed here, the buffer that triggered the burst and the end condition. Total number

---

[8]The logic was recently updated and obviously wrong bursts are thrown out at `Level 2` stage and won't reach `Level 3`.

of entries is listed as well;

- **High NHit events**: This table reports cleaning statistics for events above the high NHit threshold. These are relevant for declaration of alarms;

- **Clean burst**: Statistics of the events that passed the data cleaning: length, size, average NHit, triggers, hits and GTID;

- **Cut burst**: Statistics of the events that were flagged by the data cleaning;

- **Cuts statistics**: Summary of the cut events by cut type. Red bits are being counted but are not used to cut the events;

- **Other details**: Details regarding files.

- Plot sections:

  - **Event statistics**: A pie chart to summarize clean and tagged events in the burst. Second chart also shows the relative ratios of the data cleaning bits;

  - **Time-NHit plots**: This section contains four time-NHit plots: the original `Level 2` version, the same plot for clean events only, scatter plot showing the dataset of clean events and the dataset of cut events in the burst and finally, the scatter plot of the cut events by the cut type;

  - **NHit plots**: The first two plots in this section are the same as `Level 2` but show the data for the clean events only. Two additional plots show the data by the cleaning bit;

  - **Time plots**: The first two plots are the same as `Level 2` but show two datasets, for the clean events and for the cut events in the burst. There is an additional plot showing the time profile by cleaning bit. Finally, there is a plot for a few specific cleaning bits of interests (muon related and CAEN data) that are tagged but not used for event cutting;

  - **Crate — Card — Channel distribution**: The same version of the plots for hit distribution, showing the set for clear and cut events;

  - **Triggers plot**: Again, showing the data in two sets: clean and cut;

  - **Flat map plot**: Two separate flat map plots in this case. One for each set of events (clean, cut). Offline PMTs are marked as -5 (purple color).

- Review section: This section is used to classify the burst, it has two parts. The summary is what is shown in the list table. The notes section is intended for detailed notes.

General information

Parameter	Value	Note
Run	269750	Run number where burst occured
SubRun	5	Subrun number where burst occured
Burst #	3	Burst number within subrun
Run type	Physics, Bubblers On, Cavity Recirculation ON, Scint. Fill	Type of run, calibration, run bits
Date	8 Apr 2021	Sudbury date
Time	01:02:16	Sudbury time
Date UTC	8 Apr 2021	UTC date
Time UTC	06:02:16	UTC time
SH Buffer	5	Logical buffer that triggered burst
SH End	0	Burst end condition (0:normal,1:EoF reached,2:out of order,3:too long,4:clock jumps)
Total entries	16109	
Total events	16109	

Figure 5.23: `Level 3` detailed page table: General information. Lists the basic details of the bursts, including the ID, date, time, the initial and end conditions, number of entries and importantly also shows the run type which lists different detector conditions at the point of burst detection.

Example tables, plots and view of the review section are all available in Figures: 5.23, 5.24, 5.25, 5.26, 5.27, 5.28, 5.29, 5.30, 5.31, 5.32, 5.33, 5.34, 5.35 and 5.36. As is the case for `Level 2`, these figures are a representation of the data that is stored and presented via online monitoring for each detected burst. If a real SN burst is detected, this data would be the basis used to make a preliminary analysis, forming the decision on whether to send appropriate alarms, such as an alarm to SNEWS.

High NHit events

Parameter	Value	Note
Threshold	500	NHit threshold defining high NHit event
Total	422	# of high NHit events
Clean	1 0.24%	# of clean high NHit events, % of surviving events

Figure 5.24: `Level 3` detailed page table: High NHit events. The table shows the statistics for the events that are above the high NHit threshold. These are used to declare the final alarm, if specific conditions are met. These are described in Section 5.5.

Clean burst

Parameter	Value	Note
Burst length	5.01477	[s], this includes the PRE and POST windows
Burst size	14513 90.09%	# events, % of surviving events
Avg NHit	58.1231	
Triggers	37031	
Hits	843538	
First GTID	15011112	GTID of first event
Last GTID	15027220	GTID of last event

Figure 5.25: `Level 3` detailed page table: Clean burst. This table lists the basic parameters of the clean events of the burst. These include: the length, number of events (and what percentage these represent from all events in the burst) and more.

Cut burst

Parameter	Value	Note
Burst length	5.00917	[s], this includes the PRE and POST windows
Burst size	1595 9.90%	# events, % of cut events
Avg NHit	476.738	
Triggers	3252	
Hits	760395	
First GTID	15011116	GTID of first event
Last GTID	15027200	GTID of last event

Figure 5.26: `Level 3` detailed page table: Cut burst. Basic parameters for the events cut by data cleaning.

Cuts statistics

Parameter	Value	Note
nhitcut	2 0.01%	Flag events below chosen nhit value
zerozerocut	63 0.39%	Tags when last two hex digits of the gtid are zero (bad orphans)
ringoffire	21 0.13%	Checks for rings – associated with FE electronics
crateisotropy	42 0.26%	Check hits are unevenly distributed in electonics space
flashergeocut	155 0.96%	Flashers – events with a cluster of hits (PMTs near each other)
neckcut	1321 8.20%	Neck events: many neck tubes hit or bad charge, hit earlier than avg time of hits
junkcut	0 0.00%	Event where channel has more than one hit
qcluster	441 2.74%	WEB, flashers, sharkfins by looking for clusters of hits in ES
qvt	33 0.20%	Flashers where there is lower charge in flashing tube
qvnhit	120 0.74%	Noise events by looking at charge compared to nhit (noise will have lower charge)
thresholdflashercut	0 0.00%	Flasher and sharkfins that occur next to channel with maxed discriminator threshold
caencut	15689 97.39%	
muontag	0 0.00%	
tpmuonfollowercut	16107 99.99%	
missedmuonfollower	12820 79.58%	

Figure 5.27: `Level 3` detailed page table: Cuts statistics. A breakdown of cut events by cleaning bit. Red bits are of interest and are being monitored but are currently not used to cut events.

Other details

Parameter	Value	Note
Input file	DC2_0000269750_005_3.root	
Output file	L3_269750_5_3.root	

Figure 5.28: `Level 3` detailed page table: Other details. Lists the names of the input and output files.
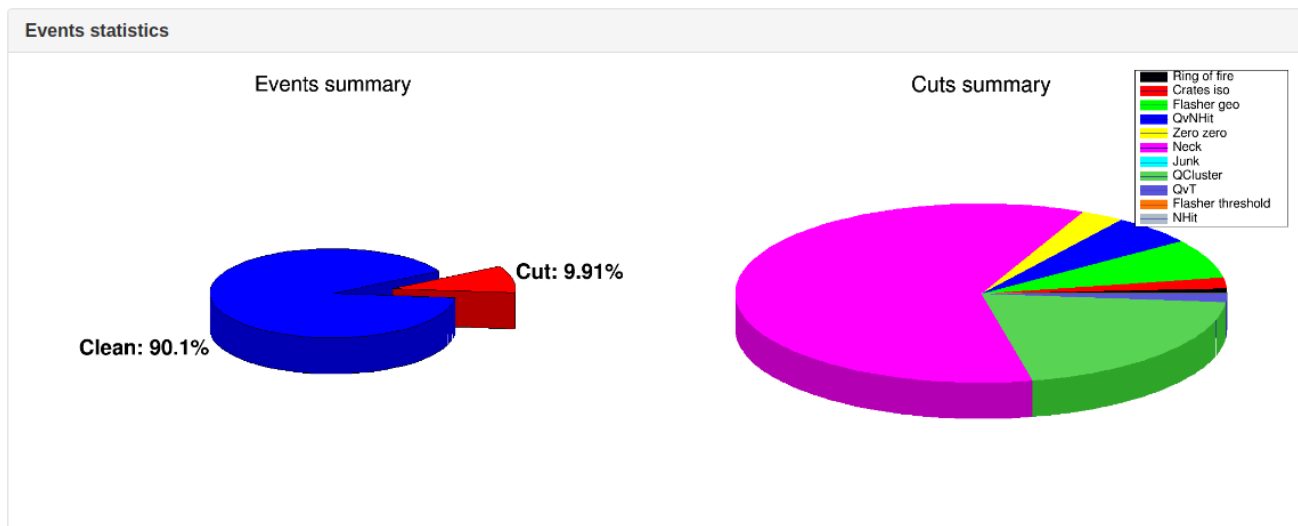
Figure 5.29: `Level 3` detailed page plots: Events statistics. Simple pie chart diagrams. Plot on the left shows the percentage of cut and clean (surviving) events. Right plot shows the relative ratios of cut events by the clearing bit.
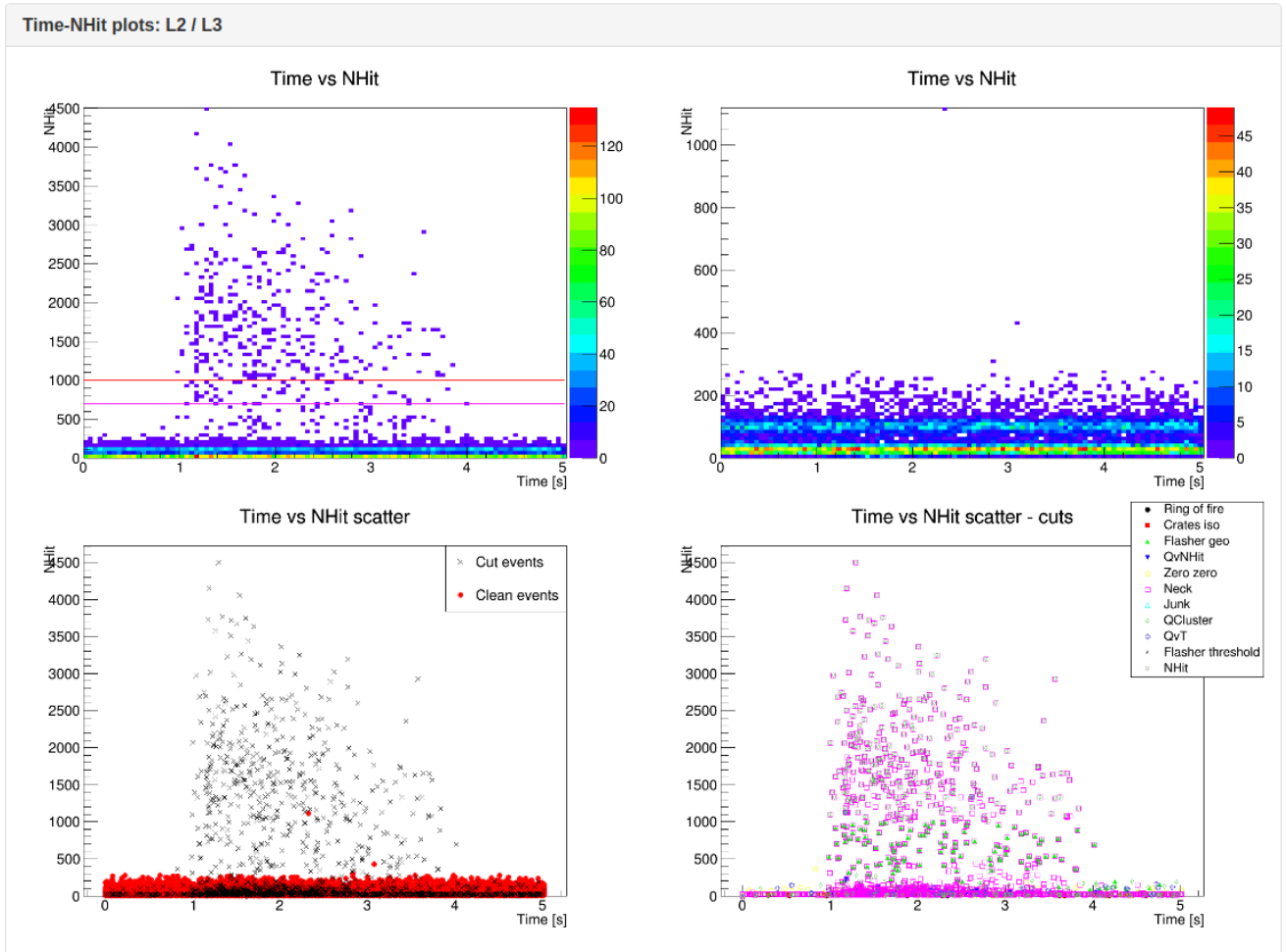
Figure 5.30: `Level 3` detailed page plots: Time-NHit plots. This section offers the simple comparison between the events in `Level 2` and `Level 3`. The top left plot shows the original burst, as shown in `Level 2` detail page. The top right plot shows the events that are clean, not tagged by data cleaning. The bottom left scatter plot shows all events, using dot for events that survived the cleaning and **x** for the events that were cut during the cleaning process. The remaining plot shows the cut events by clearing bit.
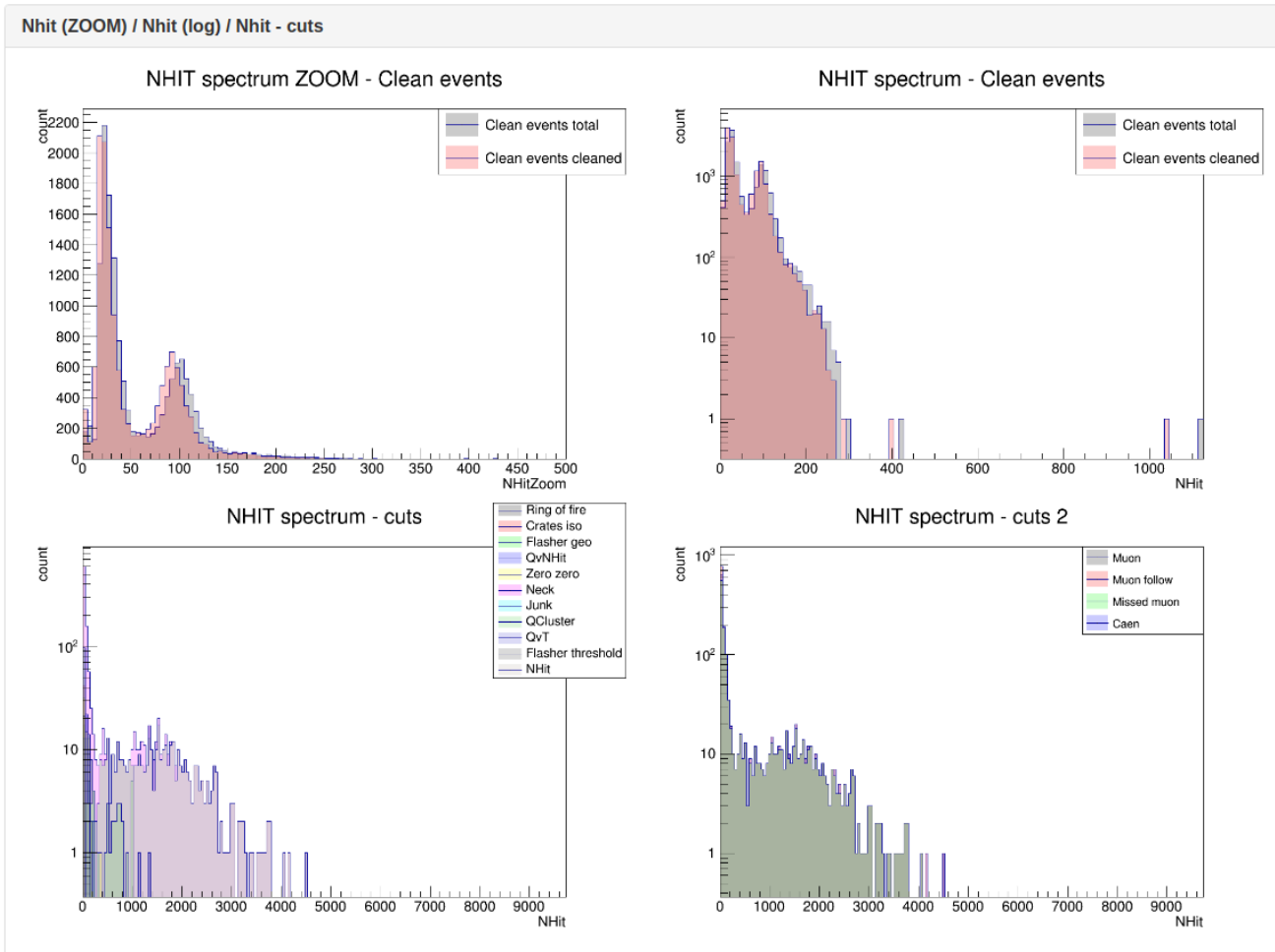
Figure 5.31: `Level 3` detailed page plots: NHit section. Top plots follow the `Level 2` format: left plot is a zoomed version over low NHit end while the right plot is a global overview over the full NHit range in log scale. Two datasets are shown, the raw and cleaned (cross talk removed) events of the survived burst. The bottom plots show the full range in log scale but show the cut events by the cleaning bits used to tag them.
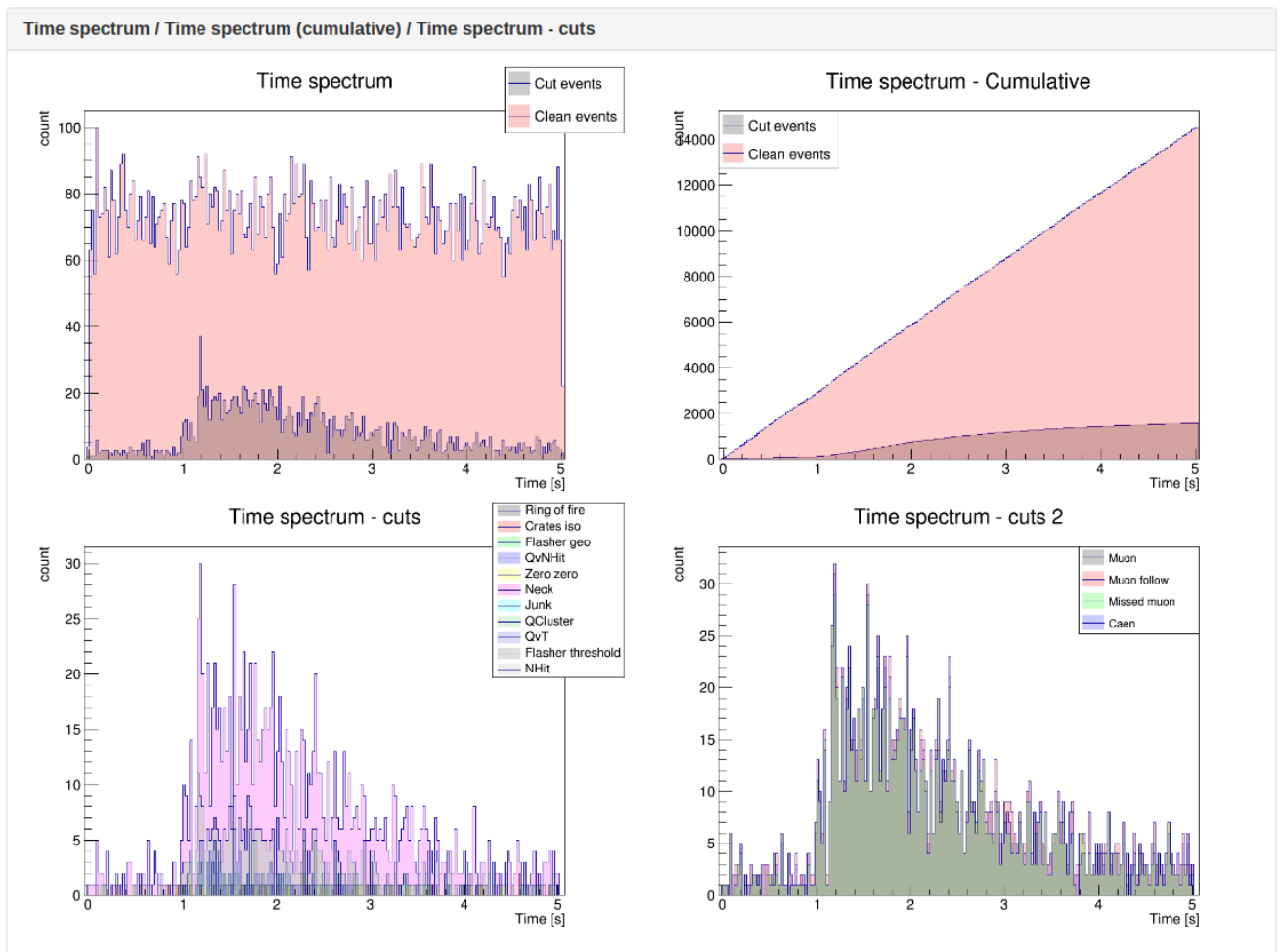
Figure 5.32: `Level 3` detailed page plots: Time section. Similar to NHit section. Top plots re-use `Level 2` format but show two datasets: clean and cut events. Bottom plots show the time spectrum of cut events by the cleaning bits that flagged the event.
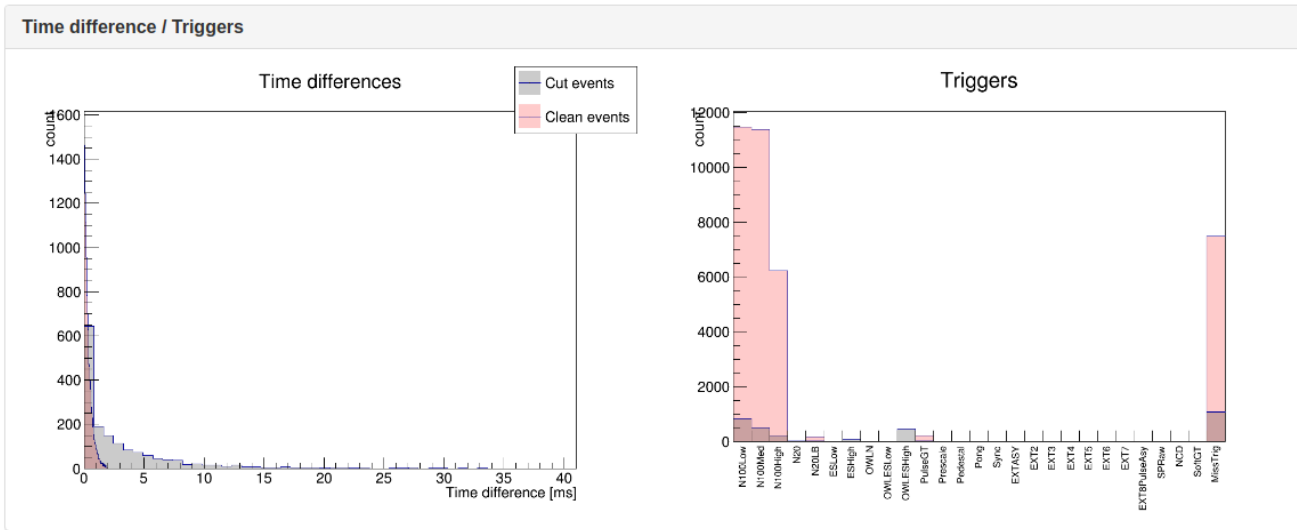
Figure 5.33: `Level 3` detailed page plots: Time differences and triggers. Alike to `Level 2`, the time differences and the hits by trigger type are plotted here. As is the case for `Level 3` plots, two datasets are shown, clean and cut events.
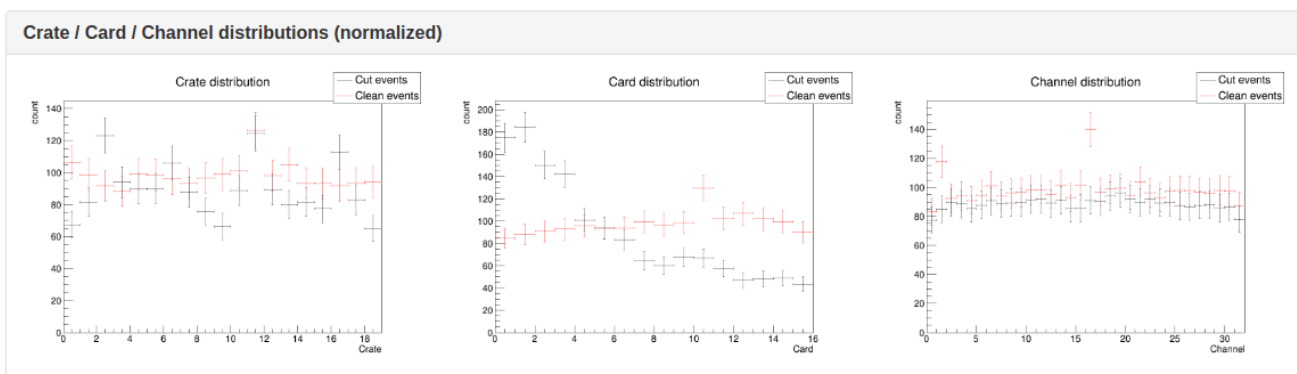
Figure 5.34: `Level 3` detailed page plots: Crate, Card and Channel distribution. These normalized plots per the number of active channels show the distribution of hits across the electronics for the clean and cut events datasets.
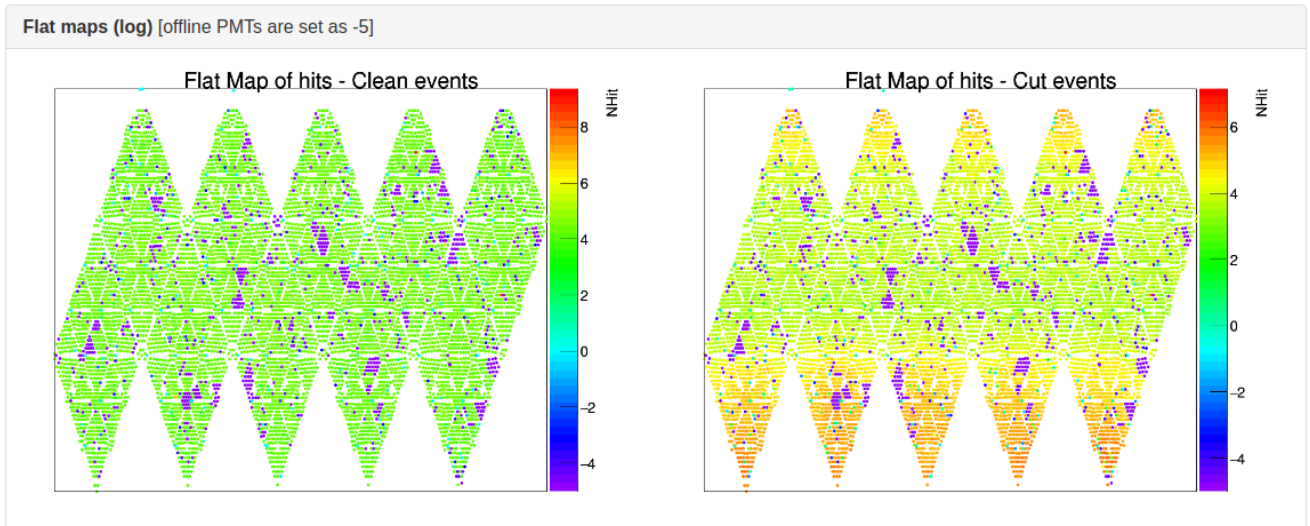
Figure 5.35: `Level 3` detailed page plots: Flat maps. Left plot is the flat map of the PMTs showing the PMT occupancy for the clean events. The right plot shows the cut events data only. Offline PMTs are marked as -5 (purple color).

Figure 5.36: `Level 3` detailed page section: Review. This section is intended to be used to review and classify the burst with the option to leave notes. The summary is then present on the `Level 3` list page. There are several known burst categories as described in Section 5.8.

5.5   Alarms

5.5.1   Alarm conditions

The main purpose of the `Burst Trigger` is to monitor for SN-like burst and alarm in the case of detecting one. The burst detection and monitoring was described above. In addition to the monitoring page containing details and preliminary analysis, there is an 'alarm' in the form of an email notification for each detected burst. However, there is a higher level alarm when special conditions are met. The reason for the higher level alarm is to notify about the most significant bursts that consist of high energy physics events that have survived the data cleaning. This would suggest a possible SN-like signal. The conditions are:

- At least **60**% of high NHit events must survive (the high NHit threshold is dynamic, currently set to **500** NHit);

- At least **4** such events must exist;

- At most **1** alarm per month.[9]

These conditions are summarized in the high NHit section for each burst and are also available in the list table of `Level 3`. The main reason for the one alarm per month limit is the connection to the SNEWS coincidence server. This is detailed in Section 5.10. Because of the responsibility and associated consequences of SNEWS reporting a SN signal, they limited the false alarm rate of experiments to at most one per month. For experiments exceeding this rate, the significance of their input is reduced, therefore, staying within this boundary is essential (exceeding the rate basically means any following alarm will be ignored).

5.5.2   Conditions analysis

This subsection analyses whether the alarm conditions are reasonably set to detect a SN signal.

High NHit threshold

The NHit limit value is determined by two main factors. One is the expected energy of the SN events and another one is the frequency of background events perturbing this

---

[9]This is not a condition to declare the final alarm but the goal is to have one such alarm per month, therefore, this value affects how other other parameters are tuned.
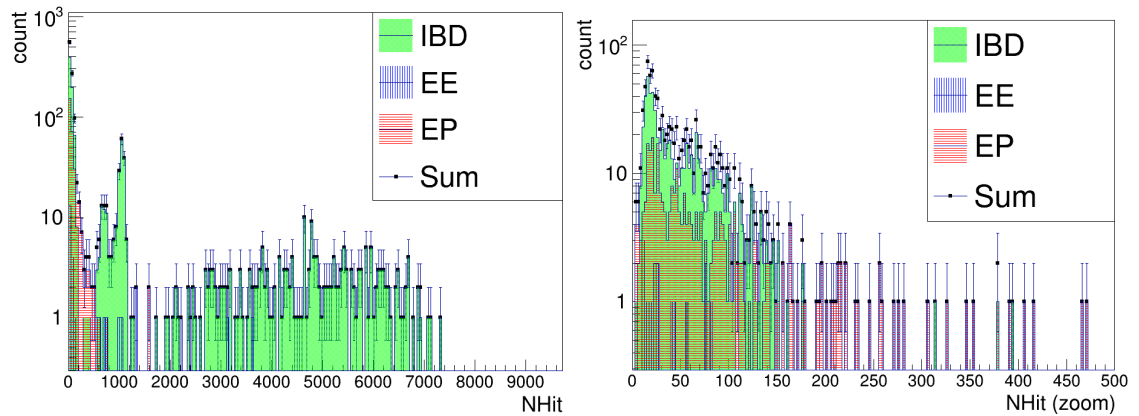
Figure 5.37: The NHit spectrum as detected by the fully filled SNO+ detector for an example Monte Carlo SN model (LS220-s27.0co) at 10 kpc, normal hierarchy. All three interaction channels available to RAT are included, in addition to the sum of the three, essentially representing the full SN spectrum.

energy range. For the expected energy of SN events an example Monte Carlo model was used using `SNUGen` (Section 6.3). The model was LS220-s27.0co, the three available interaction channels were used: inverse beta decay, elastic neutrino-electron scattering and elastic neutrino-proton scattering, the distance was set to 10 kpc (which is approximately most likely distance to a SN in the galaxy [35]), the normal hierarchy was assumed and the SNO+ detector was chosen as a target.

The NHit distribution plots for this model are shown in Figure 5.37. The significant features of the distribution are the neutron capture peak following the IBD events at 2.2 MeV, this corresponds to ~1100 NHit depending on precise detector loading, and the very high NHit end, which is basically background free, caused by the initial IBD event. The second plot is zoomed over the lower NHit range. This shows that the interaction channels are commonly lot lower than the 500 NHit value, which is the current high NHit limit. The sum of the three channels is also shown in the same figure.

Surviving percentage limit

Regarding the percentage of surviving events, this is adjusted to reach the desired frequency of alarms. A study was undertaken to confirm that the current cleaning cuts do not clear any of the SN signal across many models - Subsection 5.3.2. This subsection will highlight this in detail on two models in particular. Data from these two SN models was used as an input to the `Burst Trigger` and the surviving percentage was evaluated. The models were chosen as the likely best and worst case scenario by the number of events,

Run	SubRun	Burst	Date	Time	# Events	Clean events	High NHit	Survived	Length [s]	NHit(avg)	SH End	Check	Note
444444	0	0	18 Sep 2014	19:35:00	210	161 76.67%	109	109 100.00%	0.487491	2039.34	0		
333333	0	0	18 Sep 2014	19:35:00	970	715 73.71%	465	461 99.14%	9.09479	1997.09	0		
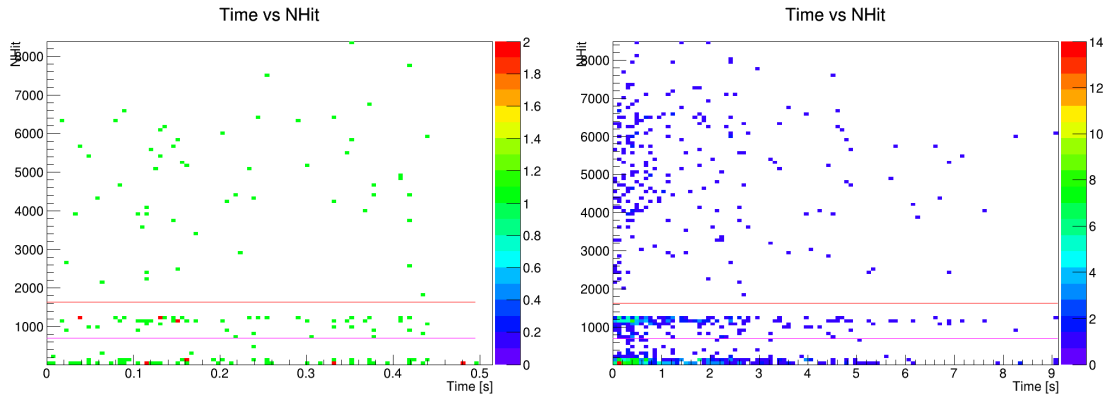
Figure 5.38: Applying data cleaning to SN Monte Carlo data. The left plot, and also the run marked as 444444 represents the electron-capture SN data while the right plot, the run marked as 333333 is the Fe core-collapse SN model. No data is cut for the first model, while only 0.86% of events are cut for the second (these are flagged by the zero-zero cut which is a consequence of how the MC data is treated).

these are: LS220-s27.0co (Fe core-collapse SN) and LS220-z9.6co (electron-capture SN) respectively. Plots from the study are shown in 5.38. It is clear that current data cleaning cuts do not affect the high energy data.

5.5.3   Rate of alarms

Finally, the rate of alarms was evaluated empirically. A selection of bursts covering approximately two months of real data taking was collected. These bursts were evaluated for the number of total events, the number of clean and surviving events, and the same parameters as a function of the NHit value. The plots are presented in Figures 5.39, 5.40 and 5.41.

The data shows that the majority of bursts has a low event number. This is because most bursts are either caused by few high NHit events only, with the rest of the burst being filled with the usual background events, and because many bursts are cut short due to breakdowns resulting in events out of order, prematurely ending the burst.

Regarding the surviving percentage, it is high for most bursts. However this only holds true while considering all events in the burst regardless of the NHit. The number of clean events drops of at much higher rate than the number of cut events. This is because most of the burst consists of the background events that are low NHit. The events that are cut are usually caused by issues with electronics which are often higher in NHit.

Finally, looking specifically at Figure 5.41, one can observe the surviving probability as a function of NHit. By simple counting of lines, it is possible to see that there are exactly two bursts that have higher surviving percentage than 60% above 500 NHit. Because the data covers approximately two months that results in approximately the ideal rate.

5.6 Trigger efficiency

The efficiency of the `Supernova Burst Trigger` is discussed in this section. `SNUGen` software (Monte Carlo) was used for this study, specifically two models: LS220-s27.6co (Fe core-collapse SN) and LS220-z9.6co (electron-capture SN). These are, as mentioned above, the best and worst case scenarios that are available, respectively (by the number of events). The fully filled SNO+ detector is used and normal hierarchy is assumed. The distance range of 10 to 140 kpc is used. These limits were chosen as the efficiency should be well saturated at the low end and mostly determined by statistics at the high end. The concept to obtain the data at each point was termed 'smart sampling'. For each model:

- The full available time range is used;

- Both AV events and external water events are assumed (i.e. the full detector);

- Data is simulated at 1 kpc, in multiple jobs of 5 events, to speed up the computational time;

- Separate ROOT files are combined to a single final data file;

- For the distance range, the data is sampled from this final data file;

- The number of events (and event type for each) to sample is determined by the `SNUGen` software, without the need to simulate them;

- One hundred iterations of sampling are performed at each point, in steps of 1 kpc.

Once the data is sampled, the efficiency is evaluated using RAT processor that mirrors the `Stonehenge` software. There is a two seconds window counting events above particular NHit threshold (the four logical buffers, as described in Subsection 5.2.3). If any one of these exceeds specific threshold values (3, 5, 7 or 10 events) this would be flagged as triggered. The NHit threshold values are as used by the `Burst Trigger`. Plots from the study are shown in Figures 5.42, 5.43 and 5.44.
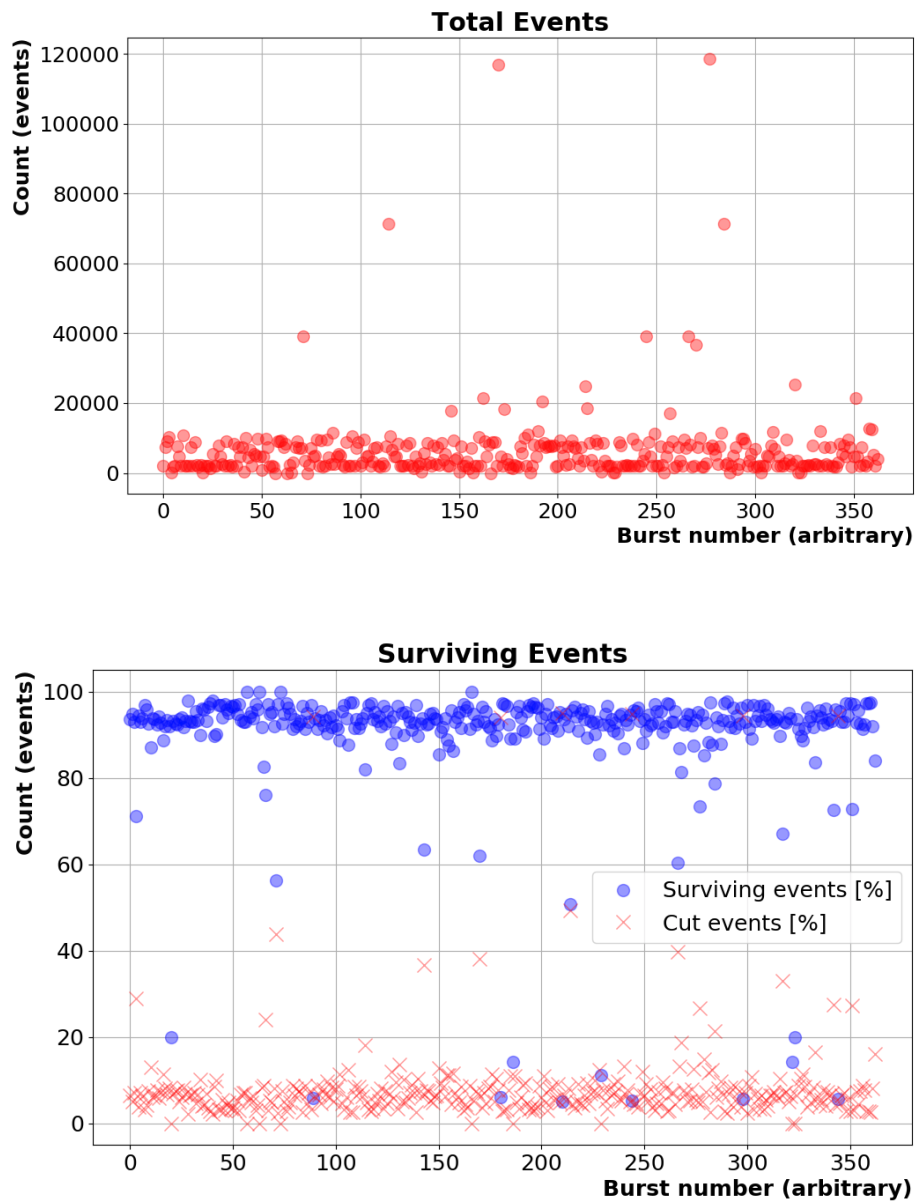
Figure 5.39: Rate of alarms study: Total events in a burst (top) and the surviving percentage of events (bottom) for the selection of burst covering approximately two months of real data taking. This is considering all events, regardless of NHit.
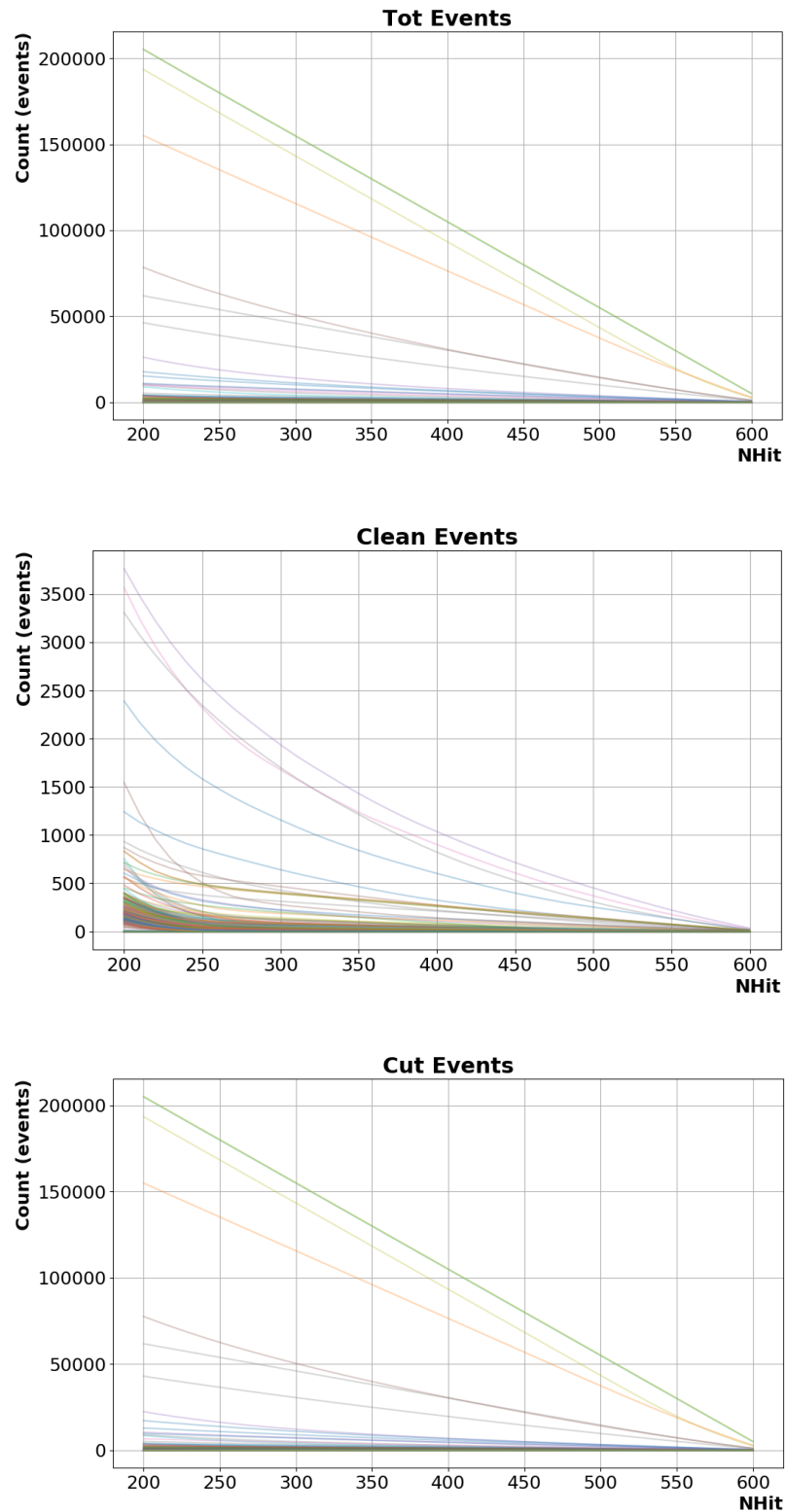
Figure 5.40: Rate of alarms study: Statistics as function of NHit value for the selection of bursts covering two months of real data taking. Each line here represents a single burst. The clean events decrease more exponentially-like with the increasing NHit value while the cut events show more linear decrease.
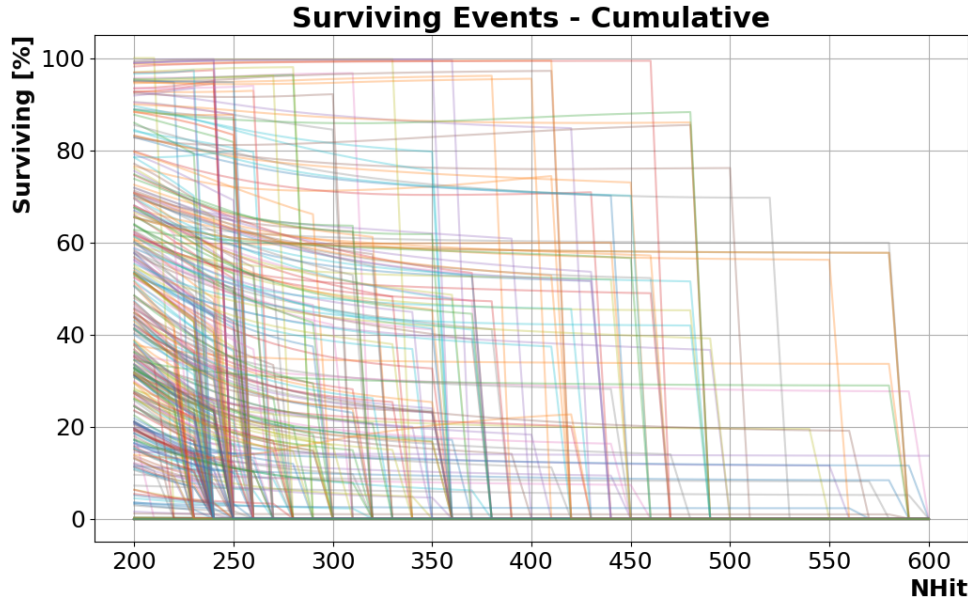
Figure 5.41: Rate of alarms study: the surviving probability as a function of NHit value for the selection of bursts covering two months of real data taking. Each line represents a single burst.

Looking at the data, the average NHit of the events does not change much with distance, and is almost the same across the two models. This is because the same interaction channels are present, with specific energies. The error bars represent the standard deviation. The increase in deviation is caused by the low number of events at high distances. In some cases low energy scatter events are detected while in other cases these are IBD events. For the number of events, these follow the expected exponential decay rate as a function of the distance. The difference between the models is also most pronounced at the short distances, while a plateau is reached at higher distance where the difference is negligible. Regarding the efficiency of each buffer, the lower number, higher NHit buffers have higher efficiency and it decreases with the increasing number of events (and lowering NHit threshold). The reason behind this is that the limiting condition is usually the number of events while the NHit value is often above the threshold.

For the final trigger efficiency, the individual buffers are combined, where a single buffer that triggered counts as a global pass (or global trigger). Therefore, the final trigger efficiency is higher than that of individual buffers. The final trigger efficiency is expected to be almost 100% for the SNe occurring around the galactic edge and above 90% up to the far galactic edge, therefore, very high efficiency for SN in the galaxy. The efficiency starts to drop faster beyond that with about 70% for the Large Magellanic Cloud (LMC). The large dependency on the many different models that clearly exist should also be taken into account.
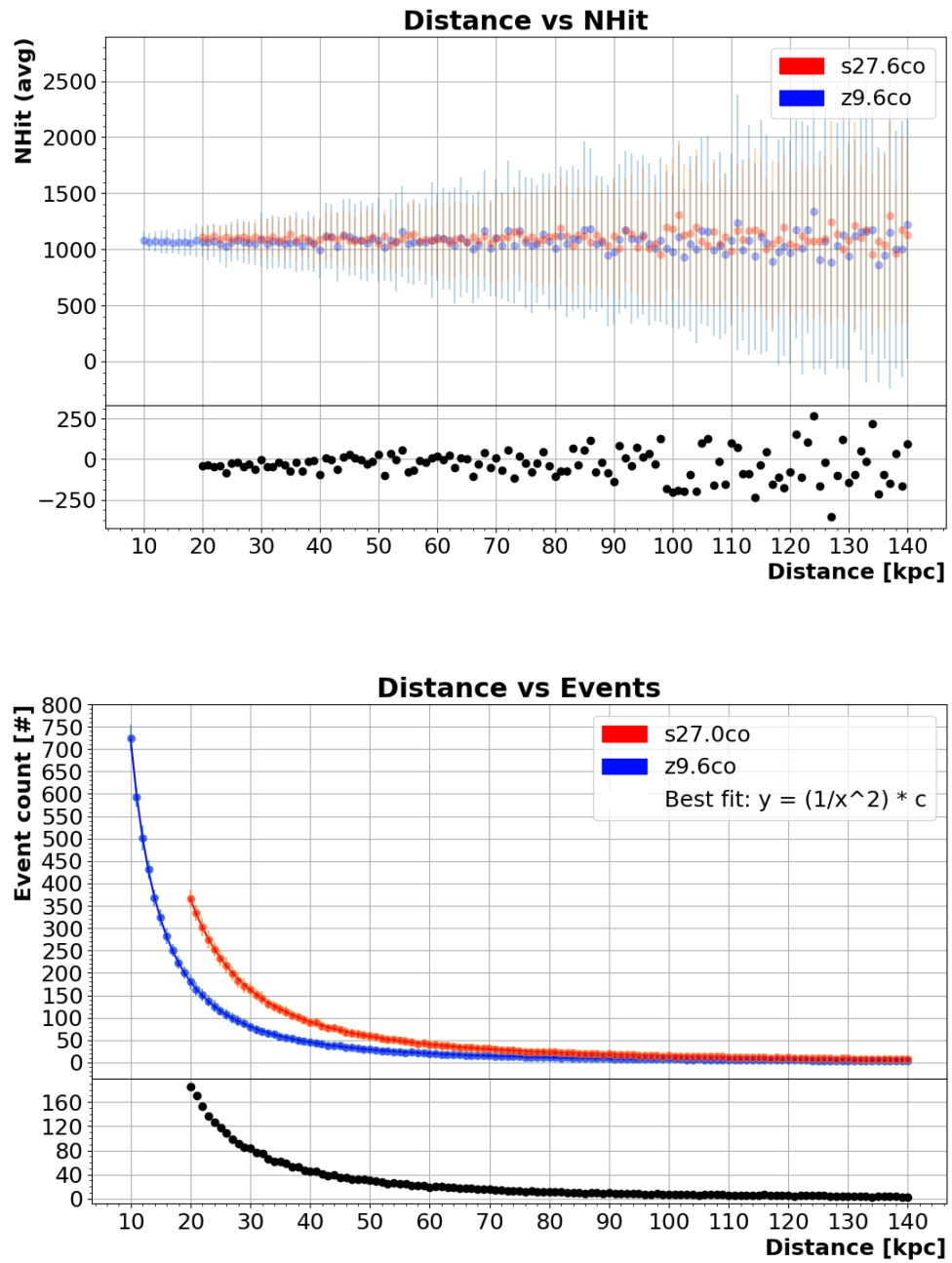
Figure 5.42: Data for the trigger efficiency study. Two models were used. The bottom portion of each plot is the difference between the two models. The error bars here represent the standard deviation as each point is obtained from hundred iterations.
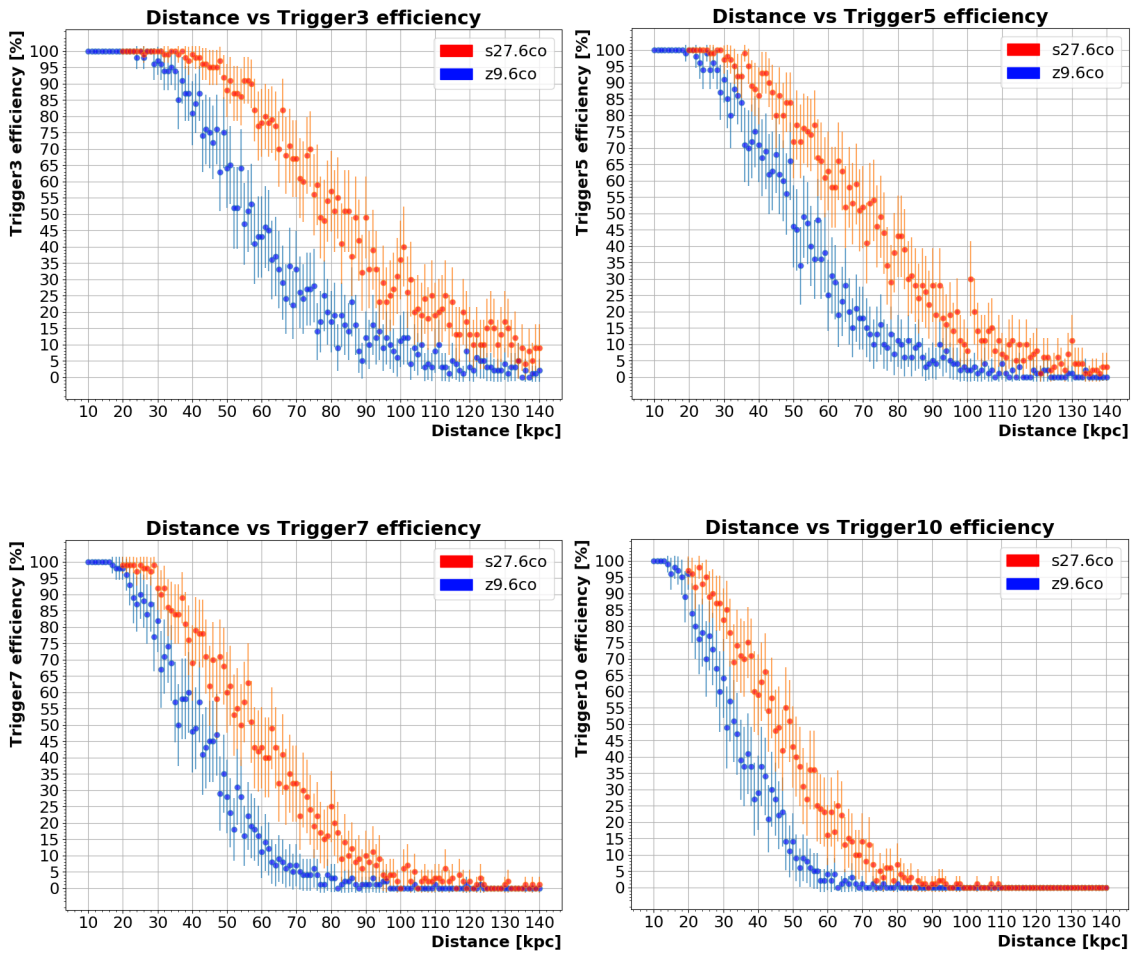
Figure 5.43: Data from the trigger efficiency study. The plots here represent the trigger efficiency for each logical buffer. Each point is obtained from hundreds iterations. The error bars represent the standard deviation.
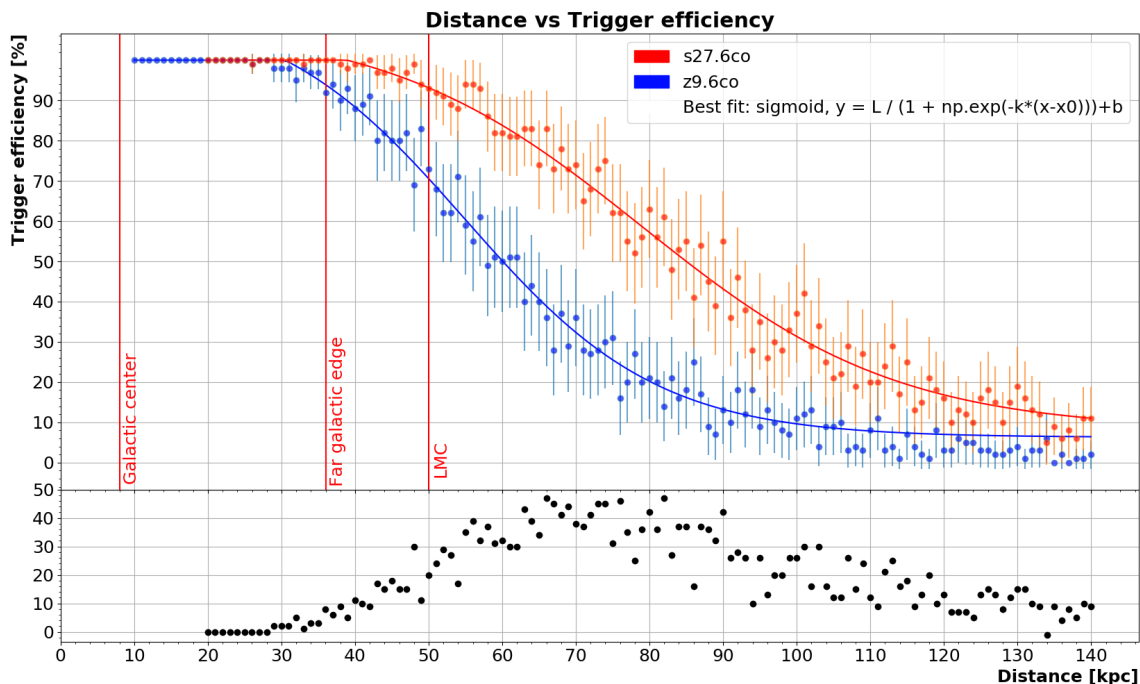
Figure 5.44: Data from the trigger efficiency study. The final trigger efficiency obtained by combining the data from four logical buffers. The bottom portion of the plot represents the difference at each point. Few significant galactic distances are marked with red vertical lines (LMC = Large Magellanic Cloud).

Additionally, there are several interaction channels that are not included within the `SNUGen` software at all, such as interaction with the carbon nuclei. These could increase the efficiency even more.

However, the study was done using MC data and assuming ideal detector conditions. For distances that are very close, some data may be lost due to the limitations of the DAQ system, specifically the FIFO buffers. These are investigated in Subsection 5.11.1.

It should be noted that the star density (and, therefore, the probability of a SN) is very low beyond the LMC. SN probabilities from two separate sources are shown in Figure 5.45. The `SNO+ Supernova Trigger` efficiency is estimated to be close to 100% for SNe at these distances.

5.7 Dynamic threshold

Because the `Burst Trigger` was first established during the phase when the detector was being filled with scintillator, the detector's activity was changing quite rapidly from day to day. This meant if the threshold for the `BT` was set too low in order to increase the sensitivity, sometimes the detector's activity could have increased suddenly, causing
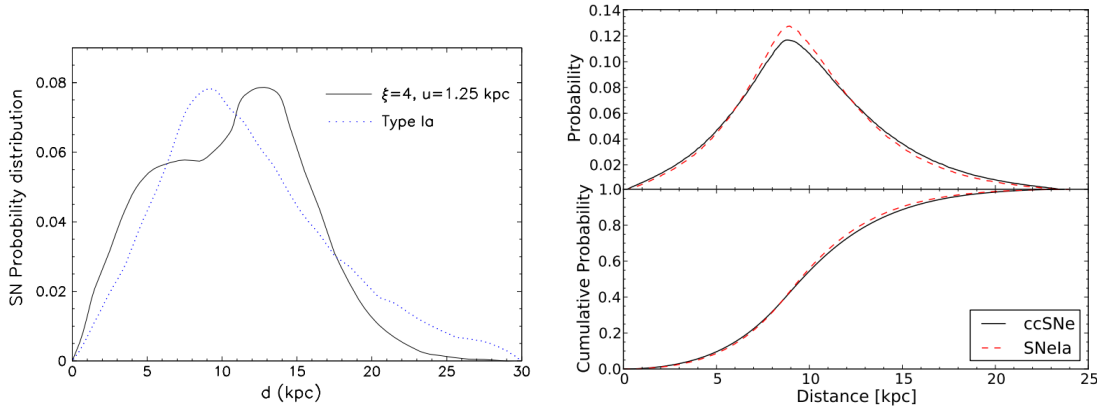
Figure 5.45: SN probability as a function of SN distance. Left plot: SN probability vs. distance from the Sun for a simple model of progenitor distribution (continuous curve). In comparison also the SN distribution for Type Ia SNe is shown (dotted curve). From [123]. Right plot: The differential (top panel) and cumulative probability (bottom panel) of the distance to SN in the Milky Way, from [35].

detection of a high number of bursts in short time period. In order to deal with these changes of detector activity while maintaining very good sensitivity to SN bursts, a dynamic threshold monitoring was designed. The main purpose was to monitor the activity, specifically related to filling with scintillator, and to adjust the threshold for the logical buffers of the `SNO+ BT` accordingly.

The method that was applied was to scan selection of real detector data from period of about a month to extract the lowest NHit at which a burst would be detected. This means keeping the width of the sliding window constant (at two seconds) and keeping the number of required events to trigger the threshold constant, while varying the threshold NHit to detect a burst. An example plot is shown in Figure 5.46. Once the NHit is found, the integral is calculated from zero up to this value (instead of just the value of the integral, the percentage of the full area is used, a "percentage integral"). This is repeated for the selection of the real data. It was found that the percentage integral value is very similar even thought the NHit value for the first burst does change. An average of this percentage integral value is now assumed.

The data is periodically evaluated (usually each day for the previous day) and the NHit spectrum is plotted. The NHit value corresponding to this global percentage integral value is obtained and used as an NHit threshold input for the `BT` (plus some constant, to make sure this is not on the edge of creating many bursts). A plot of this NHit value is made available online, alongside the level of the scintillator interface, which is what strongly

affects the NHit value. This is shown in Figure 5.46 as well. The varying detector activity can be seen as the scintillator level changes.

5.8 Burst Trigger: burst ZOO

Analysing multiple bursts it was found that many follow similar patterns, meaning similar events often have comparable features that can be observed using the basic plots of the `Level 3 BT`. These can, therefore, be used to classify the bursts into known types. The most recurring types were found to be:

- A muon-like burst;

- A crate trip burst;

- A breakdown burst (or often burst of bursts);

- Other types of bursts;

- A SMELLIE burst.

Most visible features of each category are discussed in this section. Plots showing the unique patterns are also available here.

5.8.1 Muon-like burst

This type of burst is the most common by far. The three seconds length is a consequence of the `BT` design, allowing for a second long pre and post windows. Also, if the declaration window is too short (the high NHit events comes fast after each other) it is set to a minimal length of one second. There is usually a low number of high NHit events coming close after each other, perceived as a column at 1 second. These are always cleared by data cleaning. This kind of burst usually ends with the normal end condition. These were thought to be muon events, but some differences were found. A real muon is also presented in Subsection 5.8.6. These are now believed to be mostly flasher events. A selection of plots from the online monitoring is available in Figure 5.47.

5.8.2 Crate trip burst

The crate trip burst is a burst caused by a short, usually not severe issue with electronics that is quickly resolved. As most non-physics bursts, it often ends in condition 2 (events out of order) or 4 (clock jumps). It exhibits visible peak of high NHit events at 1 second
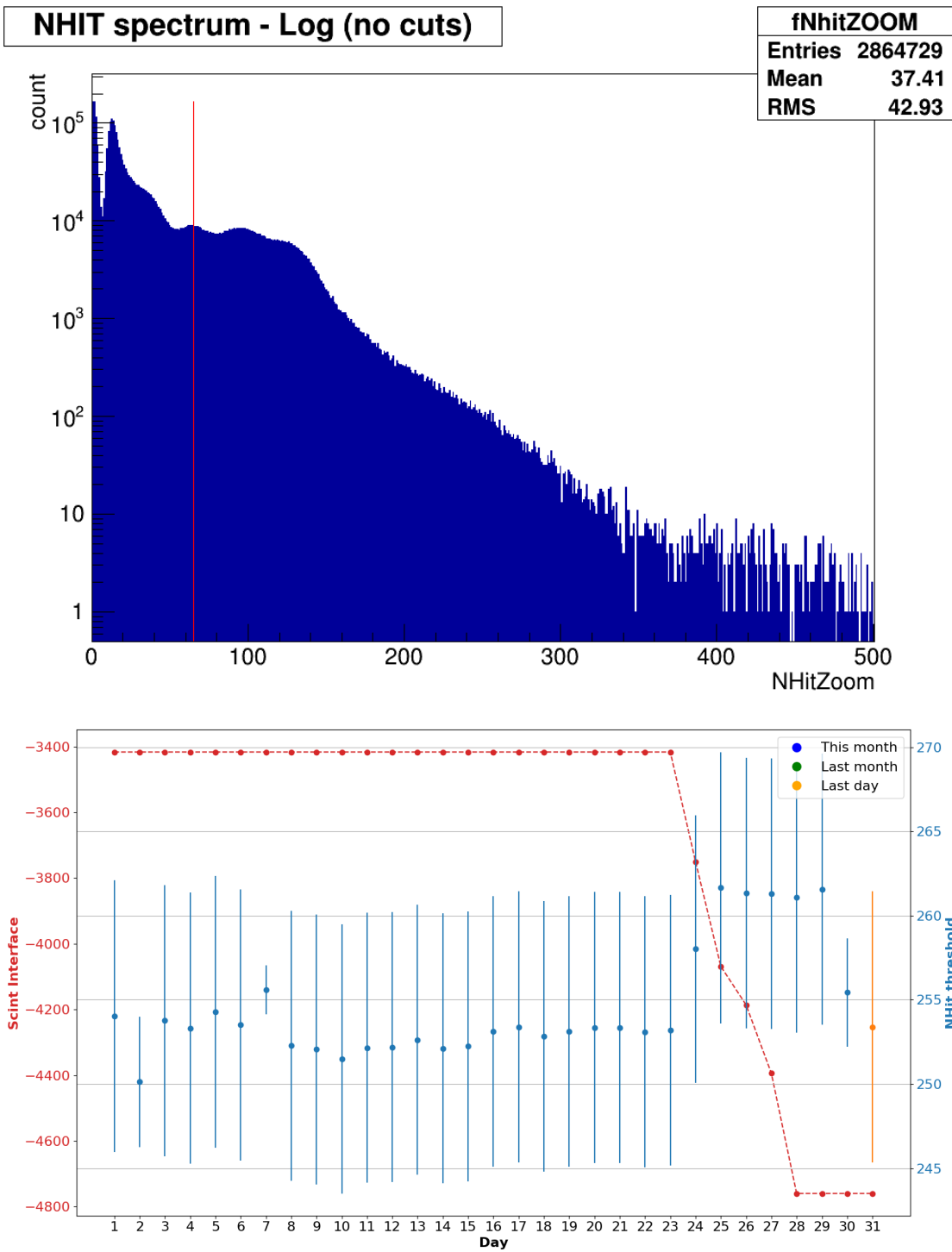
Figure 5.46: Dynamic threshold study. Top plot shows the NHit distribution for an example run (real data). The red vertical line represents the lowest NHit value to cause a single burst. This is the method to obtain the percentage integral. The bottom plot is an example of the dynamic threshold monitoring as available online. Clear correlation between the scintillator interface level and the NHit threshold value, that represents the activity inside the detector, can be observed.
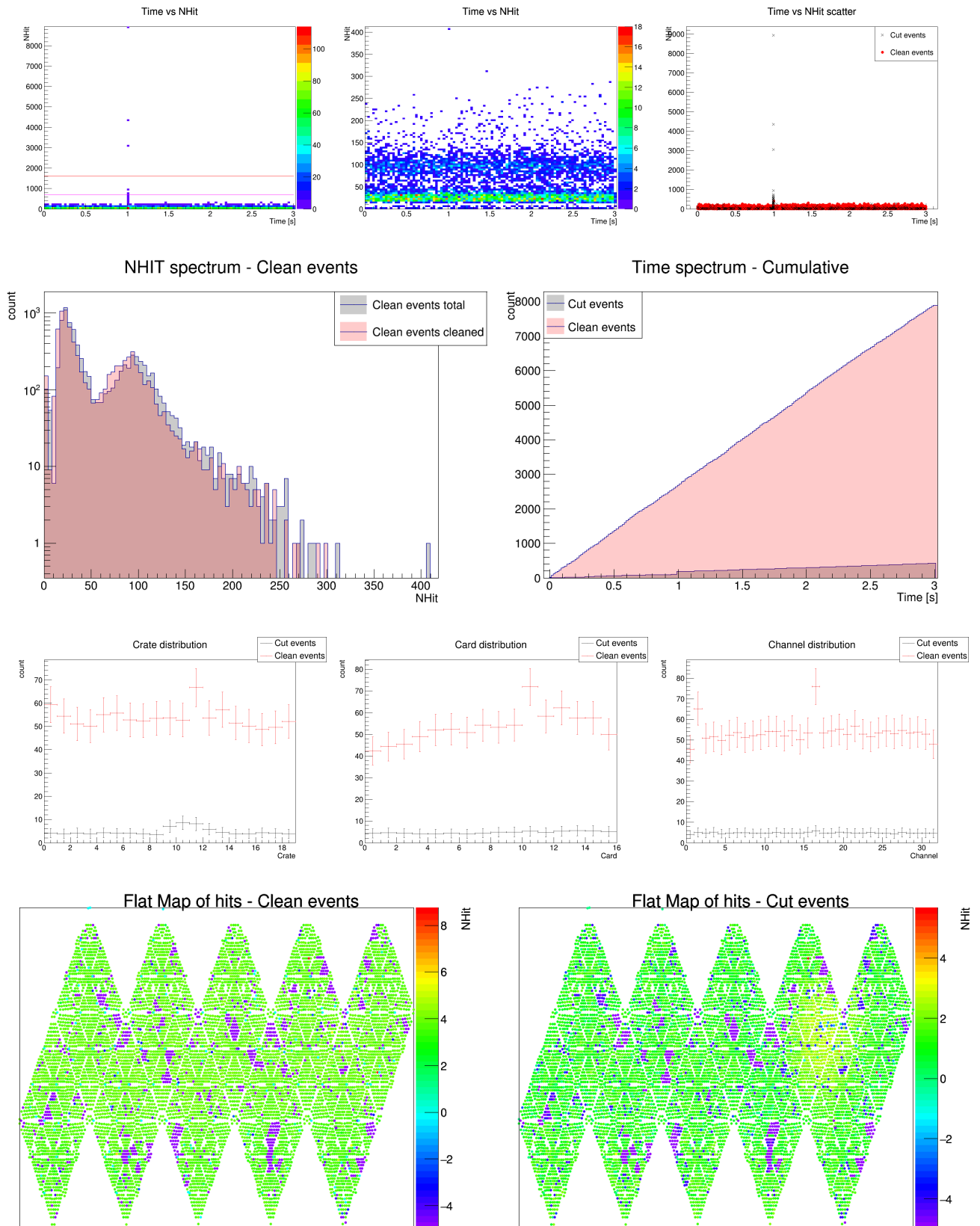
Figure 5.47: Burst ZOO: a muon-like burst. The most common type of a burst. Around three seconds long with signature column of high NHit events at (exactly) 1 second as seen on the time-NHit plot (top left). Little bump visible on the cumulative time spectrum plot at 1 second. No clear feature in the CCC distribution or flat map.

that is wider than just a column, often with visible high energy preceding events. The crate distribution often shows a clear bump of cut events for at least one crate, often also affecting neighbouring crates. Data cleaning cuts the high NHit events as is often the case for non-physics events. A selection of plots from the online monitoring is available in Figure 5.48.

5.8.3 Breakdown burst

This is the most severe type of a burst. Many high NHit events, commonly structured in columns (i.e. arriving at the same time) are visible on the time-NHit plot. Most events are cleared by data cleaning (regardless of NHit). The flat map of cut events usually reports high number of hits across the full detector. Also often ends in end condition 2 or 4. This means the burst ends prematurely, sometimes multiple bursts are created for a breakdown because of that.

The wet-end-breakdown (WEB) is a subtype of the breakdown burst that is less severe, and often more localized.

A selection of plots from the online monitoring for the breakdown is available in Figure 5.49 while a WEB event is shown in 5.50.

5.8.4 Other types

These bursts are unlike the other categorised types of bursts. They are usually caused by increased detector activity. These were most often found to be linked to a start of detector filling with scintillator. Other times they were caused by personnel accessing the detector clean room[10] or similar (uncommon) activities. The most significant feature is that a high number of high energy events passes the data cleaning - therefore, these are not obviously tagged as an instrumental backgrounds including the electronics cross talk and PMT flasher events. The particular example presented in Figure 5.51 is from a seismic event detected in Sudbury on the 15th January 2021 [124] that was detected by the `BT`.

5.8.5 SMELLIE burst

This is a burst created by one of the calibration systems, SMELLIE. It is included here mostly to highlight the variance of the `BT` usage and the monitoring tools. The calibration system laser pulses light at specific frequency at approximately constant energy that is

---

[10]The access to the detector clean room is logged and if the work is expected to be disruptive, this is also flagged in the run type. This information is available for the burst on the monitoring page.
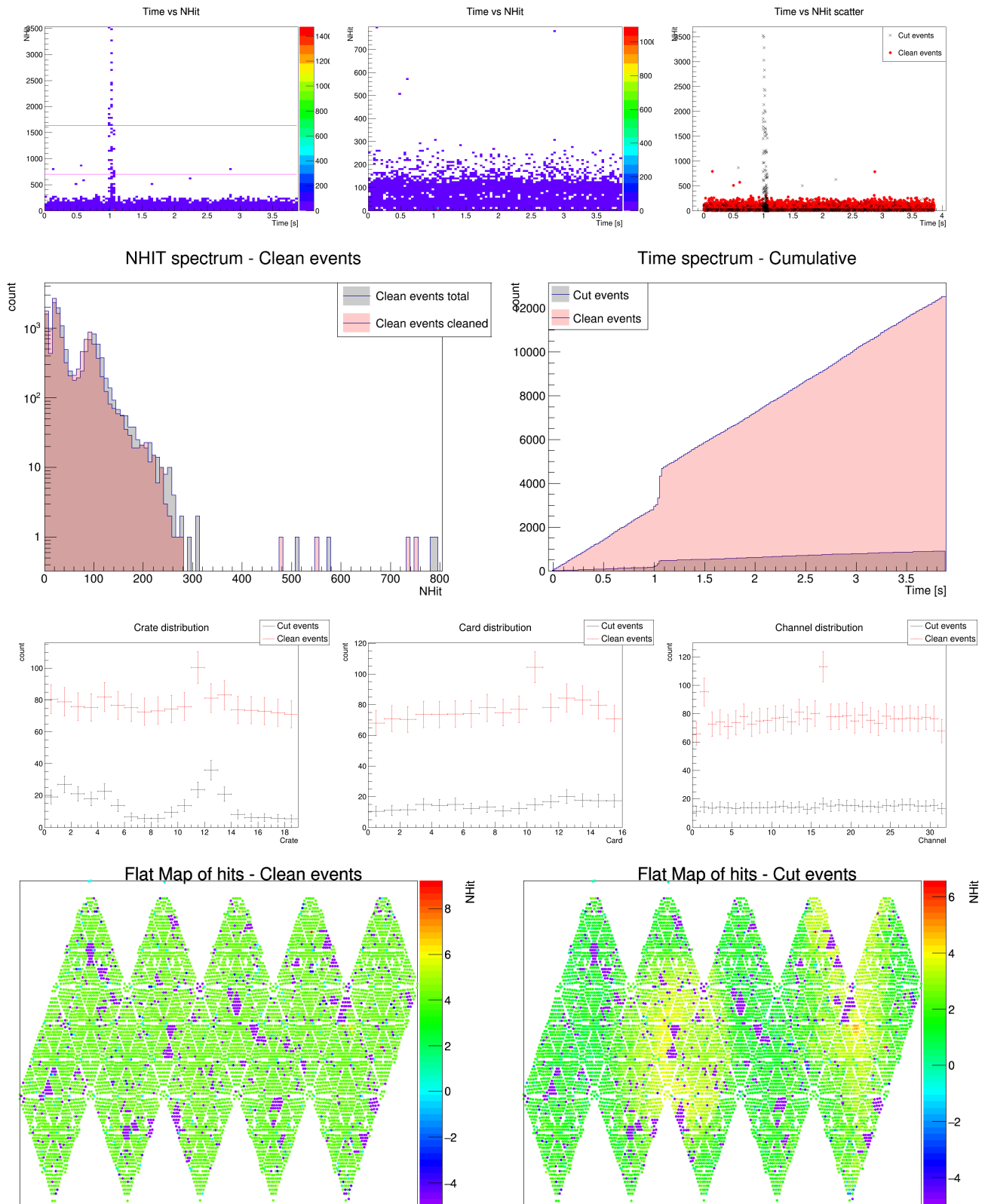
Figure 5.48: Burst ZOO: a crate trip burst. High number of high NHit events at 1 second visible on the time-NHit plot, usually preceded by few build-up events. Lasts longer and has more high NHit events than the muon-like burst. Visible signature is a bump of at least one crate (possibly affecting neighbouring crates) in the CCC distribution plot. Additionally, flat map shows a "slice" of PMTs with high number of hits (due to how the PMTs are distributed, details in Chapter 3) with the PMTs on the other side of the detector usually seeing an increase in the amount of light, although lower than the crate experiencing issues. A noticeably bigger bump at 1 second can be seen on the cumulative time spectrum plot.
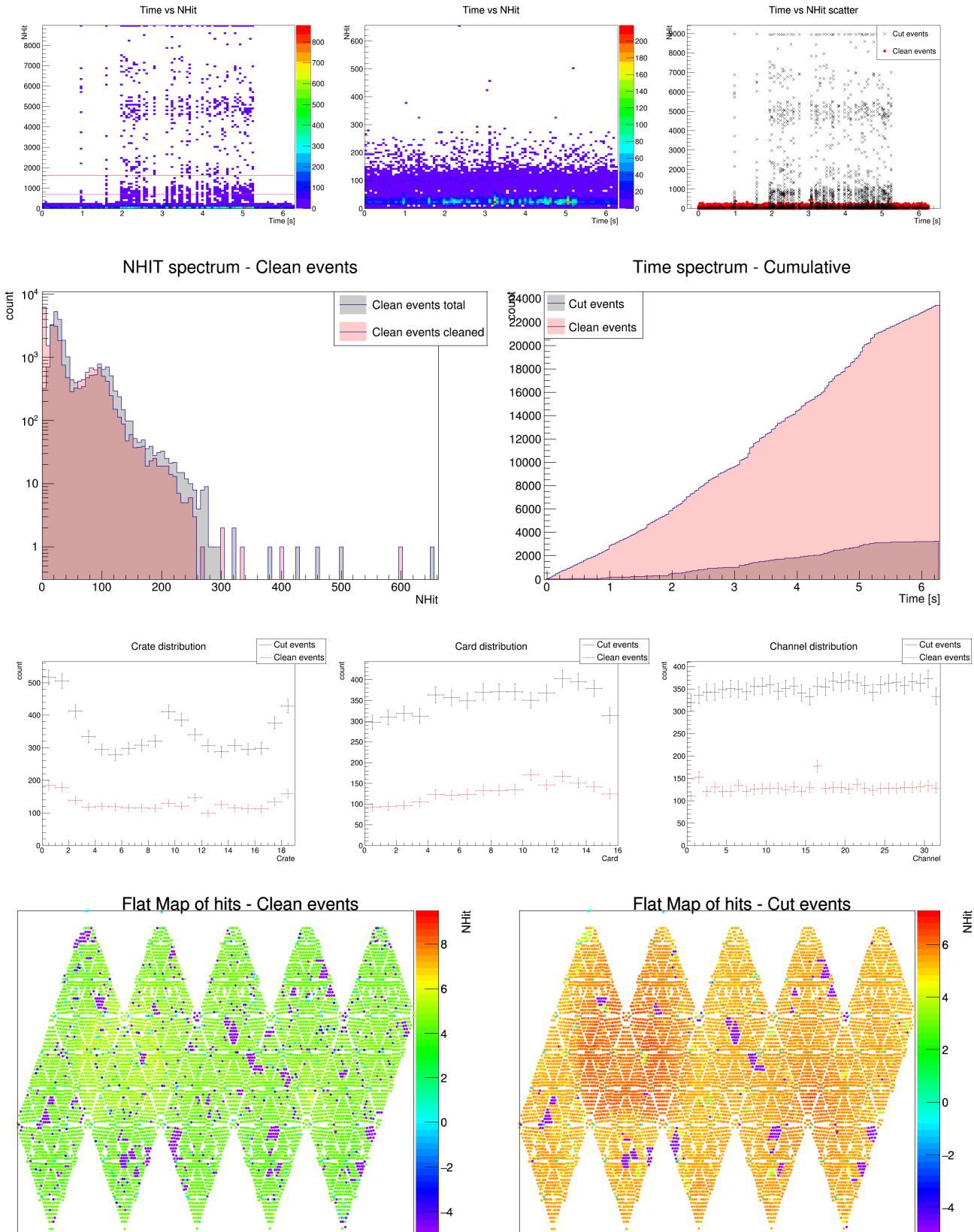
Figure 5.49: Burst ZOO: a breakdown burst. Visible signature is the high number of high NHit events, usually distributed in columns, seen on the time-NHit map, lasting for considerably longer than a crate trip. Another hint is the number of events cut by data cleaning being higher than the number of surviving events, this can be seen in the CCC distribution plots and the flat map plot of cut events.
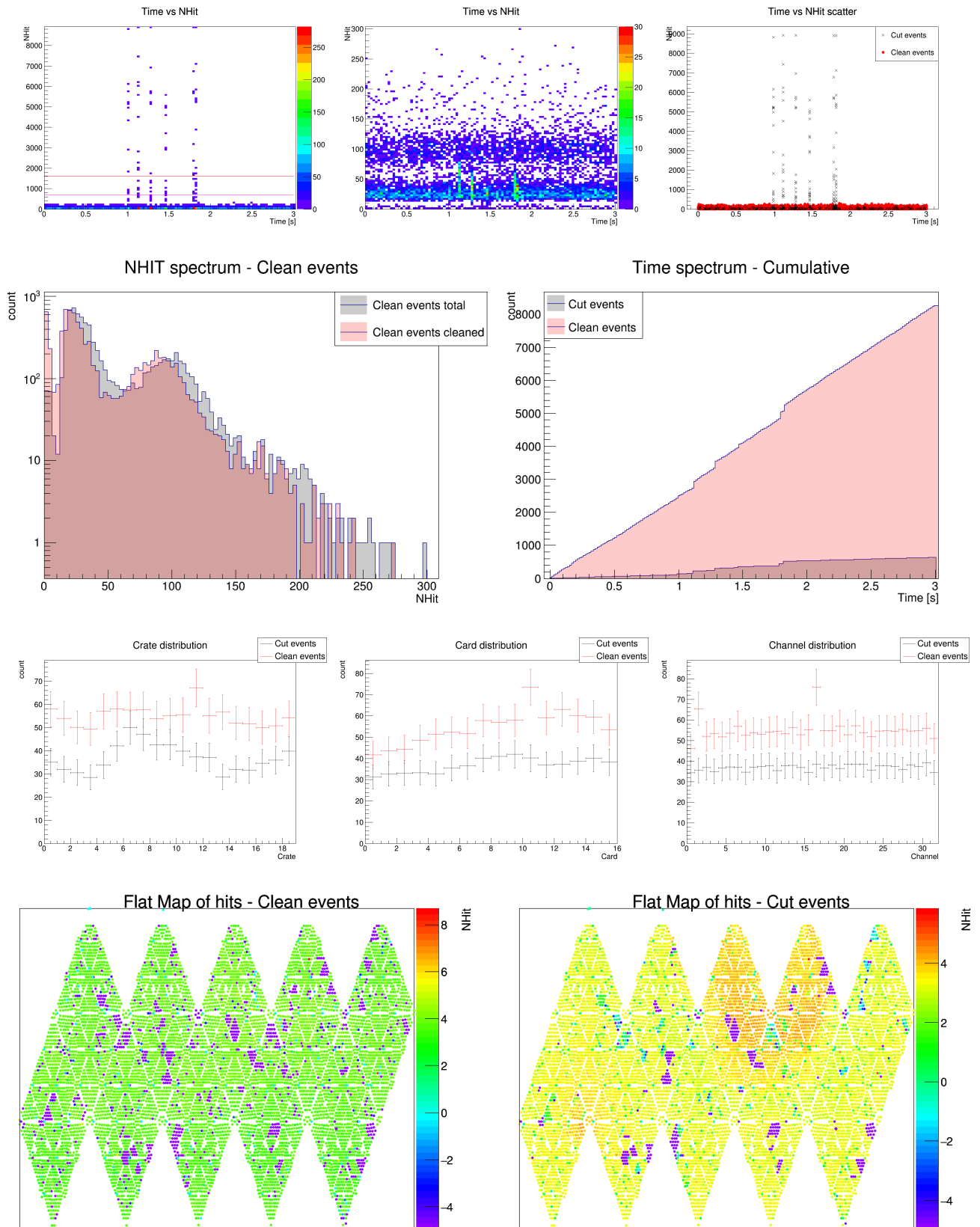
Figure 5.50: Burst ZOO: a wet-end-breakdown burst (subsection of breakdown bursts). Very similar to crate trip burst, usually more severe. The are multiple columns of high NHit events and these are more spread out than in the full breakdown burst type. Commonly showing a bump of cut events in the crate distribution plot and multiple bums in the cumulative time plot. Often also presents itself as few slices or quite localized zone of higher number of recorded hits on the flat map of cut events.
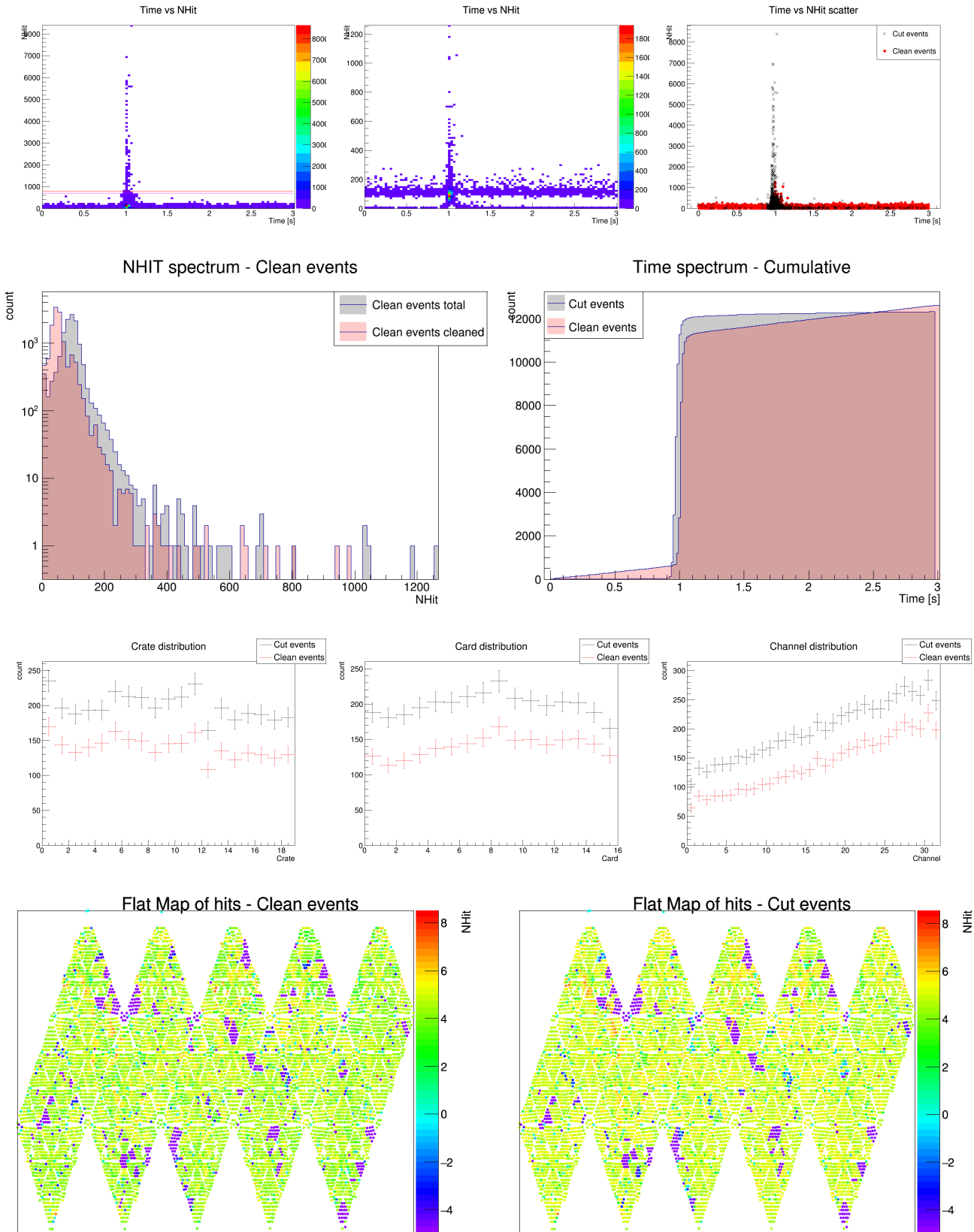
Figure 5.51: Burst ZOO: other type of burst. Usually unlike the aforementioned types, often a consequence of significant detector activity. In some cases these can be a result of detector filling. This particular example was caused by a seismic event caused by earthquake in Sudbury area on January 15th, 2021[124]. An outstanding signature is the number of high NHit events surviving the data cleaning, as can be see on the `Level 3` time-NHit plot (top middle).

visibly above the detector's background rate. These events are all cut by data cleaning but a nice beamspot is visible on the flat map of cut events. A selection of plots for this type of the burst from the online monitoring is available in Figure 5.52.

5.8.6 Bursts caused by real muons

As a part of the study to understand and classify bursts, especially the muon-like bursts, a real muon event was found and processed as if it were a burst. Because this is not exactly a burst, it had to be processed slightly differently. The whole subrun containing the muon event is taken into consideration. Therefore, the burst is a lot longer and contains many events (that are not muons) as well as the muon event. The example plots are shown in Figure 5.53. The noticeable difference is that the high NHit event, which is the muon, does not appear on a column in the time-NHit plot. Actually, for most real muons there is only one, occasionally two high energy events. Additional steps were taken to try to distinguish the real muons and muon like events. A view using xsnoed (an event viewer software) was made of the highest NHit event and three following events. These plots are shown in Figure 5.55 for real muon and in Figure 5.54 for the muon-like event. The plots that are shown are the maps of the PMTs of the SNO+ detector. While the top plot is (by now well known) flat map of PMTs, the bottom plot is the PMT crate map - a map of PMTs by their allocation within the electronics space. The color in this case represents time of the reported hit by each PMT.

Even by a brief look, these events are very different. The first event of the muon-like burst seems to be caused by several PMTs in the bottom left part of the detector (flat map) and there is much clearer boundary between the PMTs around this 'heat spot' and PMTs on the other side of the detector. The real muon shows a smoother transition between the heat spot and other PMTs. But most importantly, this initial event is followed by a spree of what seems to be breakdown-like events in the case of the muon-like burst. These are quite distinct. The most obvious marks are the empty horizontal lines in the crate map (top right section of the figure) and 'confetti' events, where there is a high number of hit PMTs, that report times that are completely unrelated, resulting in very colourful plot (as seen in bottom section of the figure). These following events are the rest of the high NHit events that form the column of energetic events for the muon-like bursts.

The real muon, meanwhile, is followed by much lower NHit events. These are localized around the heatspot of the muon entry point to the detector - this is the light that bounces around after the muon travels through the scintillator and excites electrons which
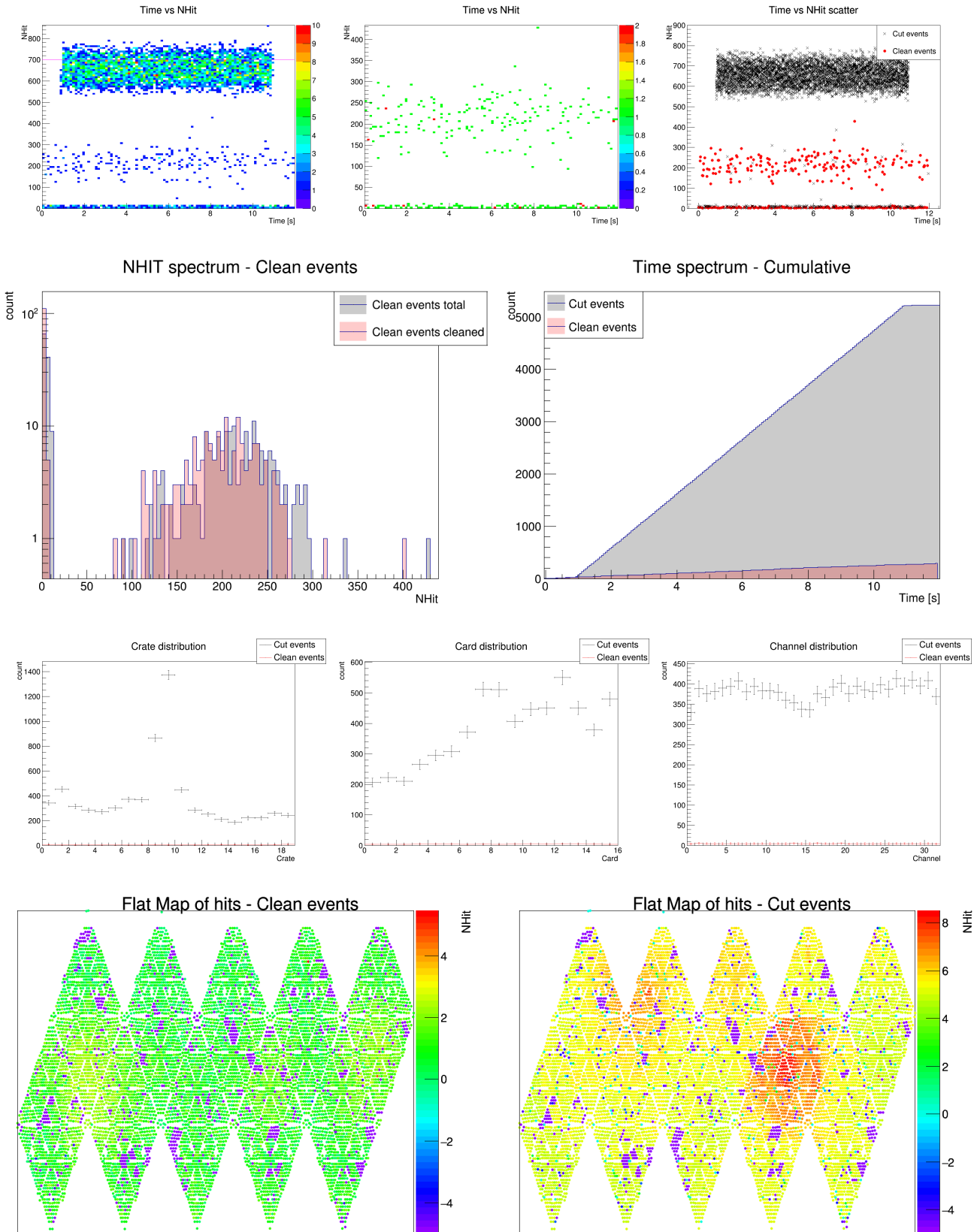
Figure 5.52: Burst ZOO: SMELLIE burst. A burst caused by a calibration system. Signature features include: high NHit events at constant frequency, low rate of background events, clear beamspot on the flat map.

consequently drop back, emitting photons.

The study was repeated for several real muons and muon-like events. It was found that real muons are rarely followed by enough high energy events to be detected as bursts by the `BT`. Most of the muon-like events are, therefore, high energy events (can be physics events but do not have to be) that are energetic enough to cause a surge of follower high NHit events.

5.8.7 SNUGen MC

Additionally, to have a baseline, a SN MC (using `SNUGen`, described in Section 6.3) was run through the `BT`. It was detected, and created a burst that was analysed. The basic plots are shown in Figure 5.56

The data shows the expected features of SN signal, such as:

- There are many high energy events;

- There are visible peaks at energy points of interests (such as 1100 NHit roughly corresponding to the 2.2 MeV γ, a result of the neutron capture, or even higher energy IBD events);

- The burst is about ten seconds long, with most of the events within the first two seconds;

- The events are uniformly distributed across the detector;

- The events are physics-like, not being tagged by data cleaning.

In addition to the Monte Carlo data, a SN source is under construction to be deployed inside the detector. The main purpose of the source is to test the response of detector for a SN-like signal. This includes both, a response in the case of detecting SN signal as well as stress testing the electronics to find out the limiting event rate, which can be used to calculate the closest possible SN that can be handled by the detector without data loss (Subsection 5.11.1).

5.9 Burst statistics

In addition to the burst monitoring, an overall burst statistics analysis was performed on bursts from the start of the year 2021, the threshold setting were kept constant throughout this period. However, several significant operations were performed during this time, such
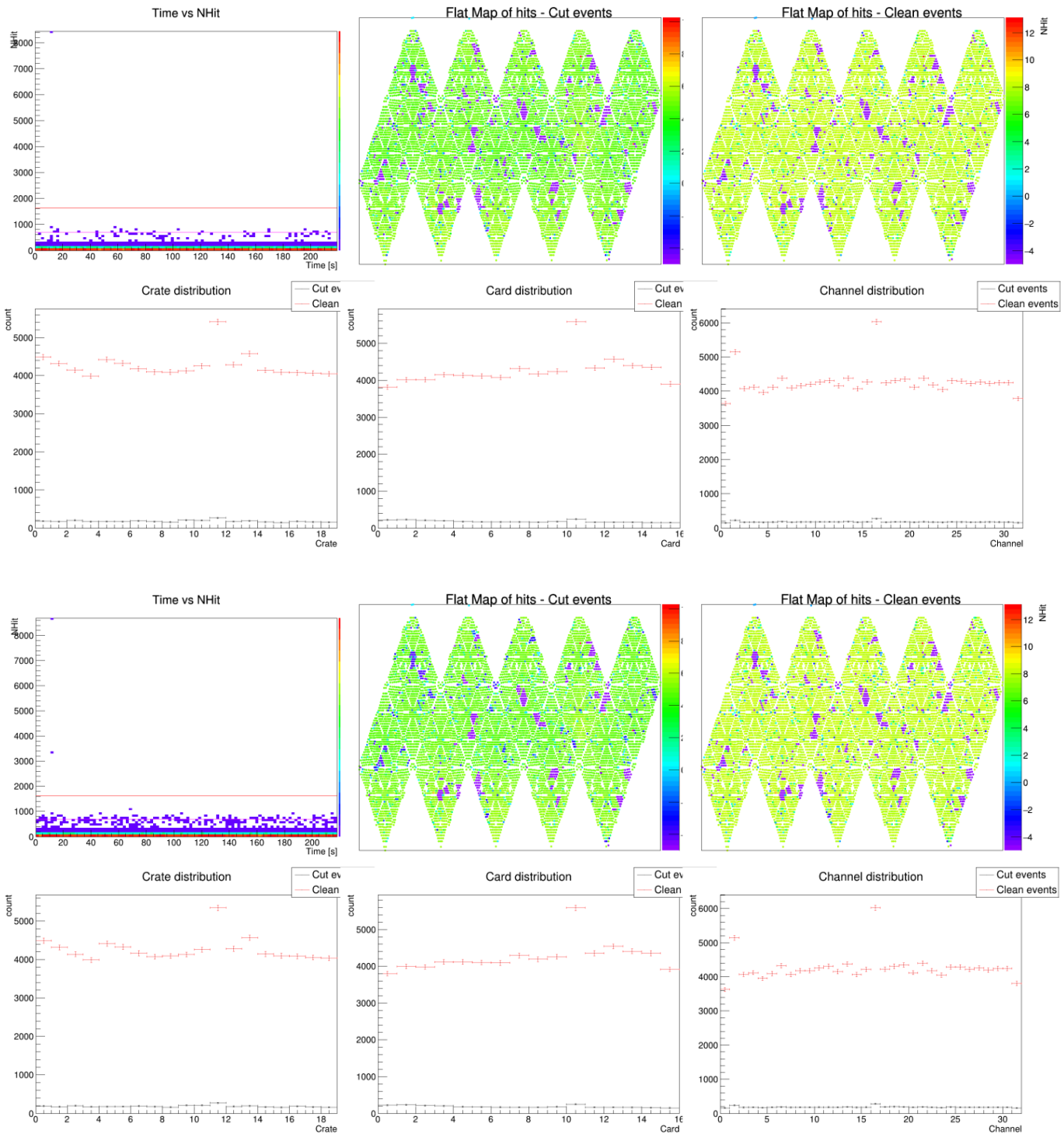
Figure 5.53: Burst ZOO: `Level 3` basic plots for two real muon events. The whole subrun is processed in this case, as these muons would not trigger a burst on their own. The noticeable feature is that there is no column of high energy events in the time-NHit window. Instead, only one or two high NHit events are present at most.
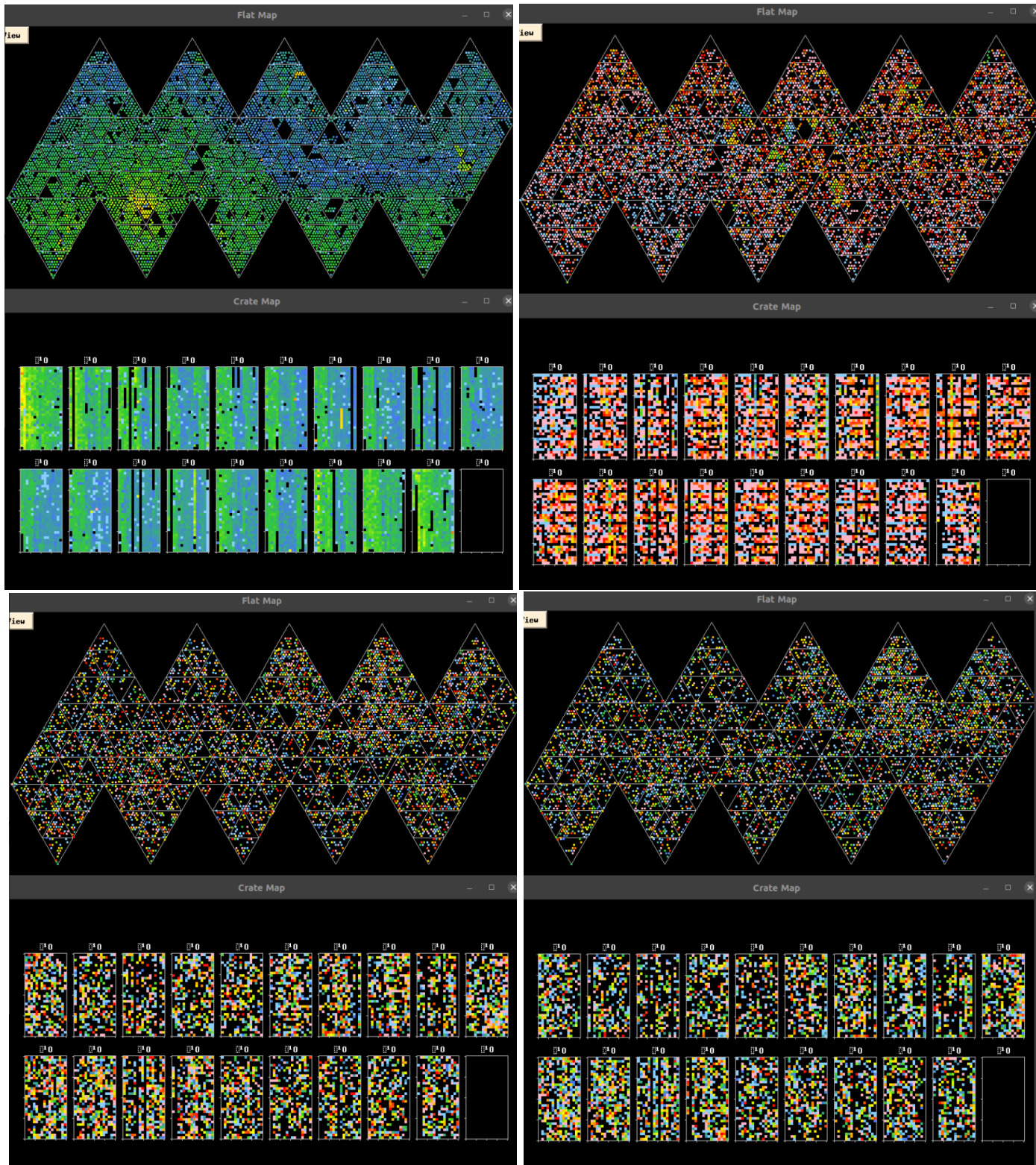
Figure 5.54: Burst ZOO: the XSNOED view of the muon-like burst. Only the highest NHit event (causing the burst) and three immediately following events are shown. The figure consists of four separate plots. Each part is a flat map of PMTs and a crate map of PMTs for single detected event. The color represents the hit time. The obvious trait is that the follower events are high NHit with features of a breakdown.
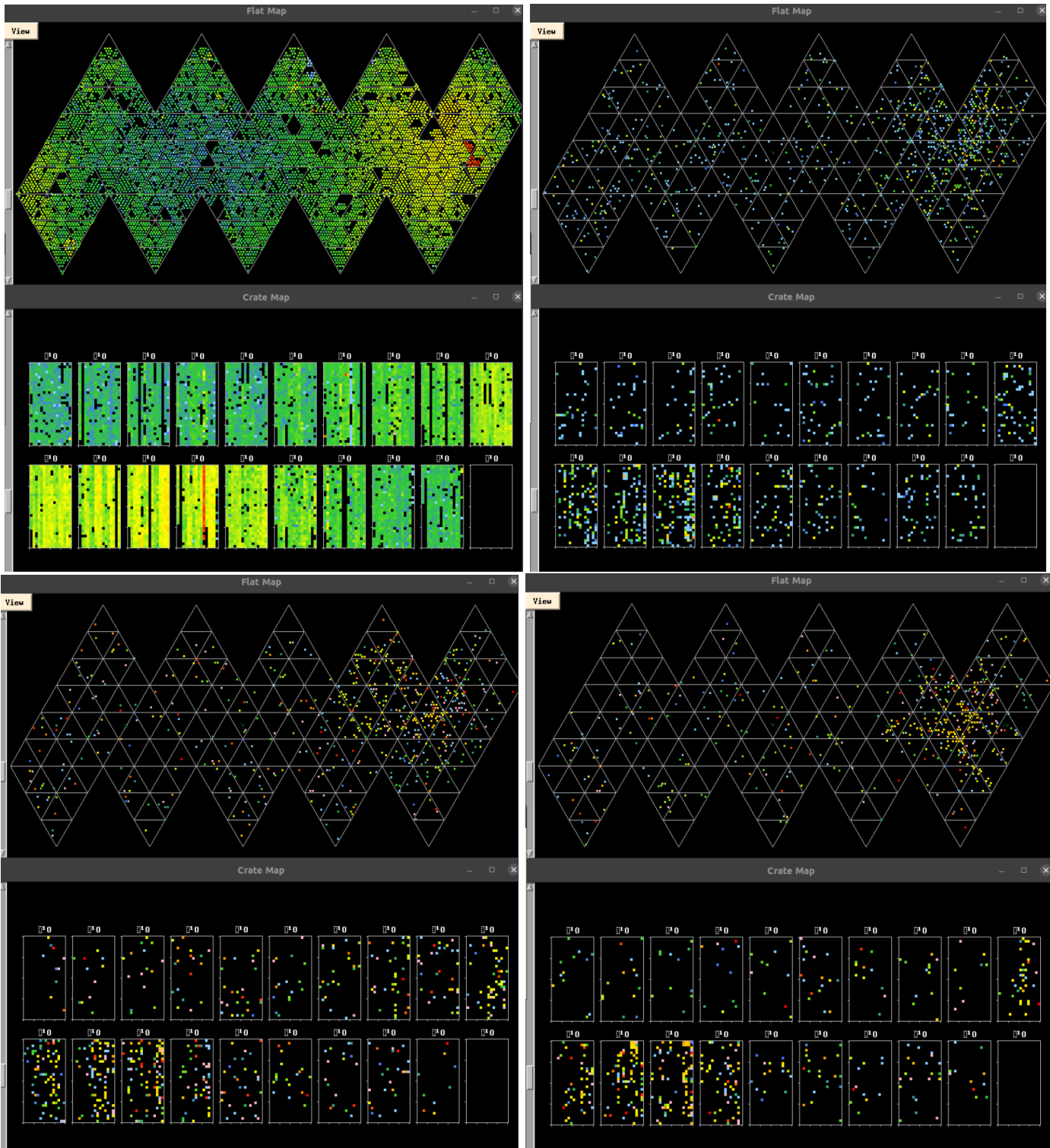
Figure 5.55: Burst ZOO: the XSNOED view of a real muon event. This is noticeably different to muon-like burst. The following events are not as high energy. The light is located around the muon entry position. The activity promptly decreases after entry.
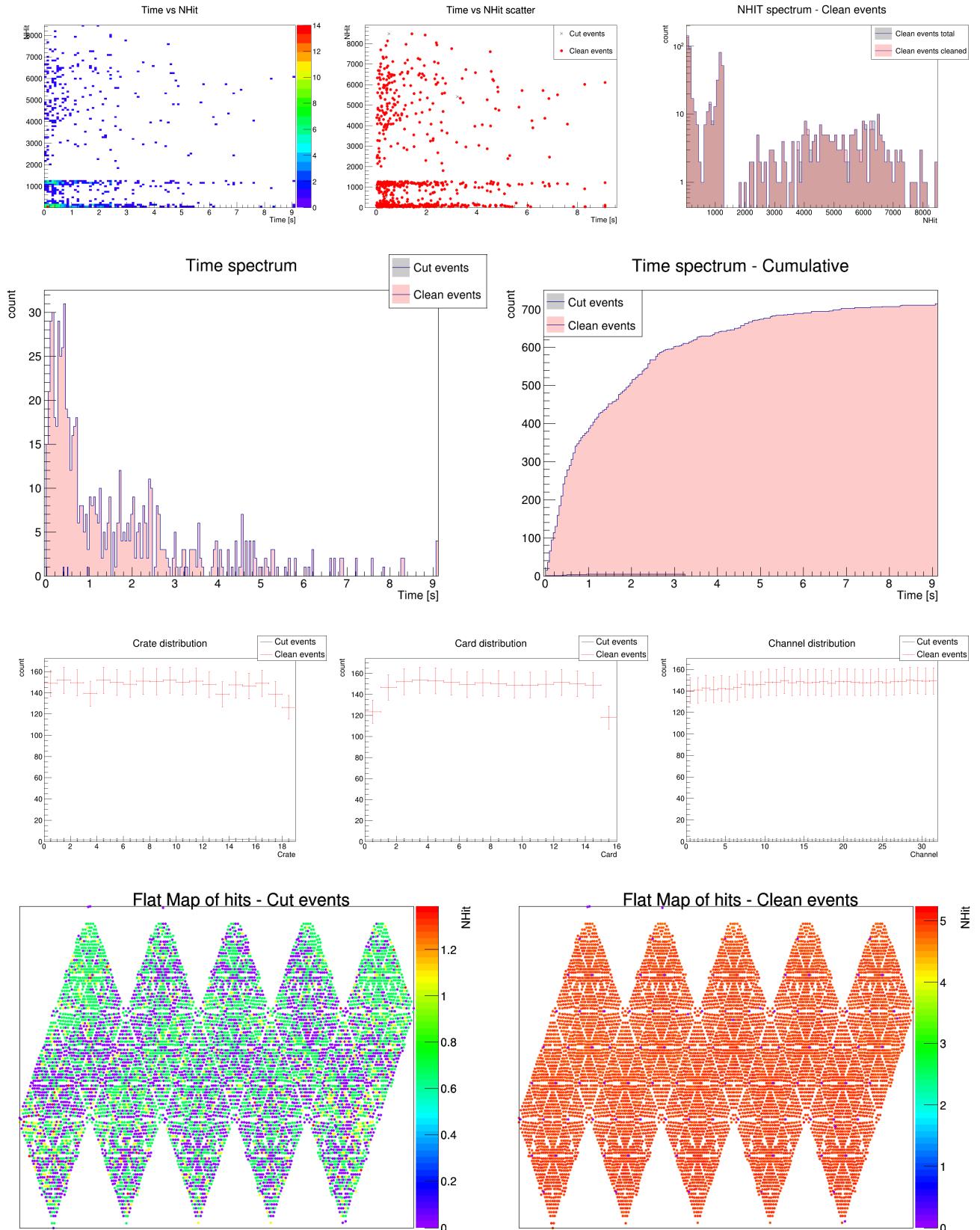
Figure 5.56: Burst ZOO: `SNUGen` data. The basic `Level 3` plots for a SN Monte Carlo simulation data (LS220_s27.0co model at 10 kpc). The expected features of a SN signal can be observed.
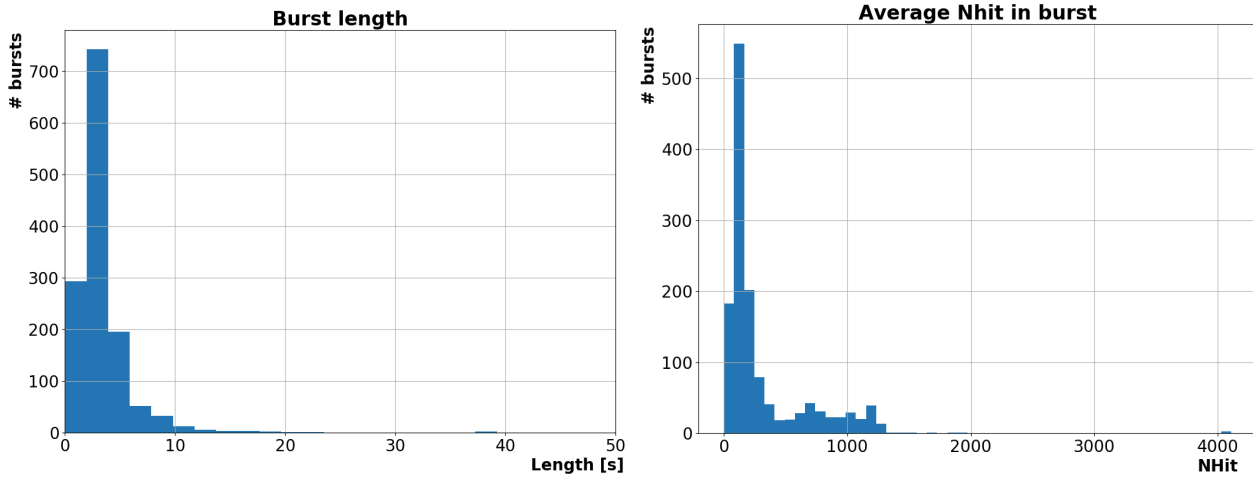
Figure 5.57: Burst statistics: Length and NHit. There is significant peak at 3 seconds for the length distribution, corresponding to the expected average length of a burst. Regarding the average NHit, it peaks at < 300, with very few bursts averaging above 1200 NHit.

as water extraction from the bottom of the AV to finish the scintillator fill as well as removal of pipes previously used for filling. Therefore, not all detector conditions were consistent. Plots from the overview are available in Figures 5.57, 5.58, 5.59 and 5.60.

Regarding the length of the burst, the majority of bursts that end with normal end condition - meaning no more extending events within extending window - are 3 seconds long. This is because of the logic to declare the burst, which allows for at least one second declaration window and one second of pre and post time frames. As mentioned, if the threshold events within the two second long sliding window come close in time to each other, the declaration window is set to be at least one second long. Sometimes the declaration window is a bit longer than this (the events declaring the burst are spread along the sliding window) and other times there are few extending events following the declaration window. These bursts are, therefore, slightly longer than the minimum three seconds. For the events ending in other conditions than the normal end, these are most often shorter than the three seconds standard length.

For the average NHit, the value is usually much lower than the threshold values. This is because the logic of the burst declaration writes out all events, regardless of NHit. The high NHit values usually contribute very little considering the number of events in the burst. Therefore, this value is dominated by the background events. In this case, the bursts with very high average NHit are breakdown bursts that are usually extremely short, ending with end condition 2 or 4, consisting mostly of the breakdown events only. Looking at the logical buffer that triggers the burst, the buffers requiring fewer events
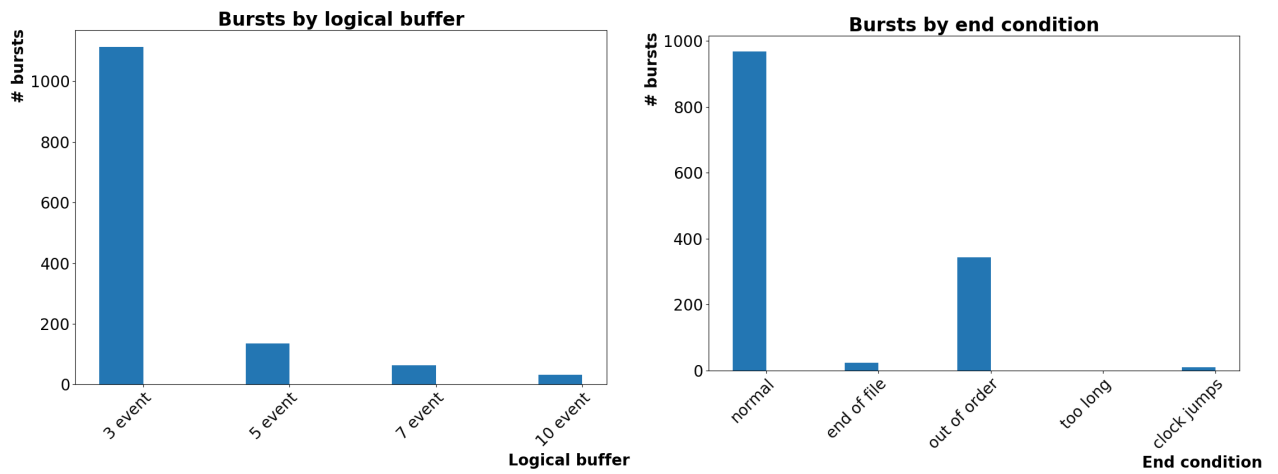
Figure 5.58: Burst statistics: Logical buffer and burst end condition. The lower event buffers are higher in frequency. Majority of bursts ends with normal end, while about a quarter ends in "events out of order" condition.
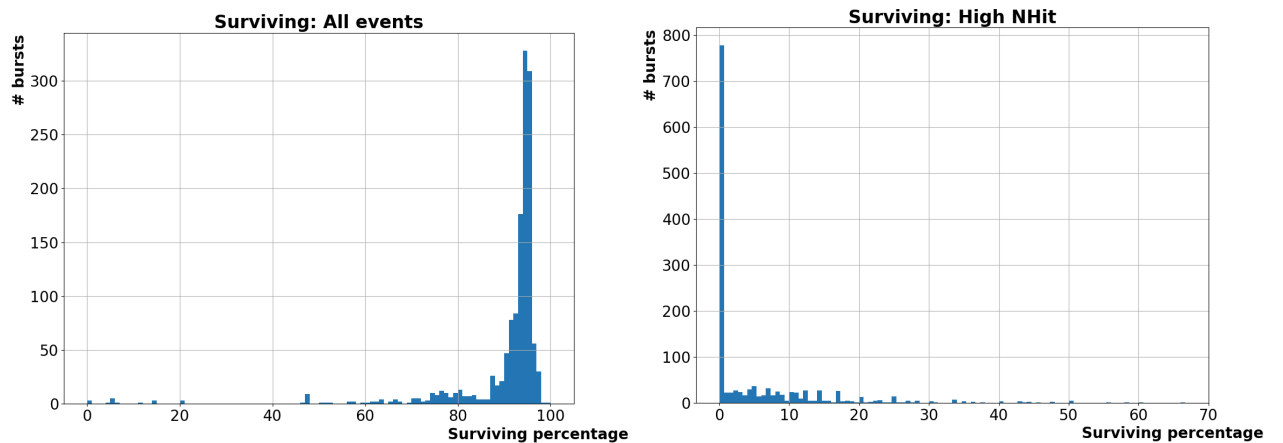
Figure 5.59: Burst statistics: Surviving percentage for all events and surviving percentage for high NHit events. Left plot shows the surviving events (events untagged by data cleaning) for all events in a burst while the right plot shows the survivability for the high NHit events only, these are used to declare the final alarm.
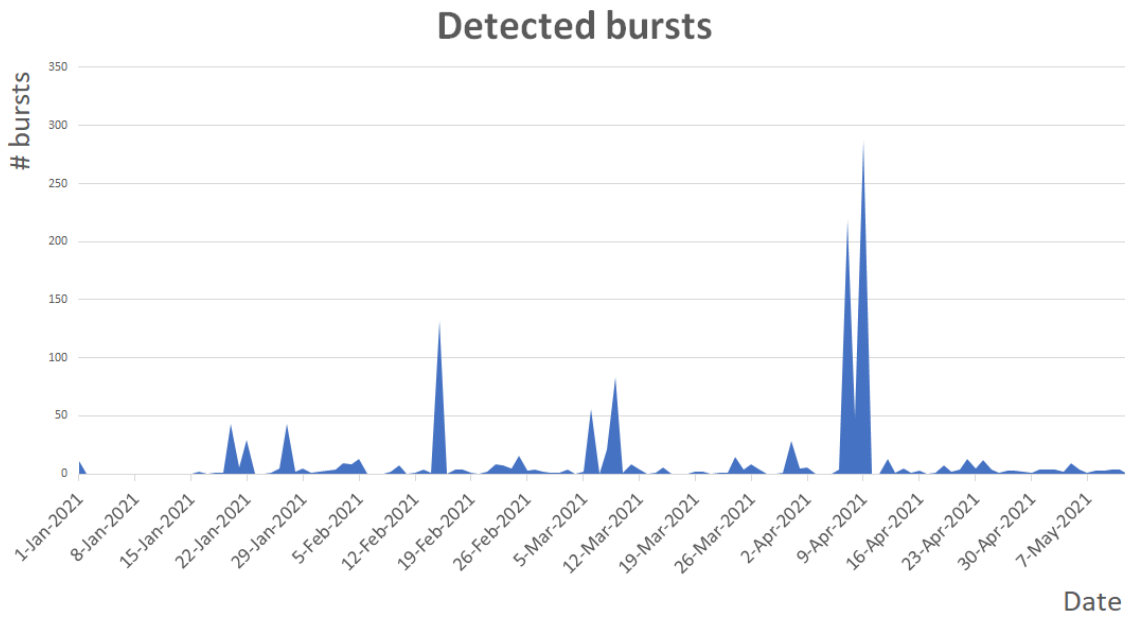
Figure 5.60: Burst statistics: Distribution of bursts by date. The peaks in the distribution suggest a detector breakdown, or a significant increase in detector activity. Outside of that, the nominal burst activity is relatively low.

(even though of higher NHit) are much more frequent, with the frequency decreasing considerably with increasing limit on the number of events. The predominant portion of the detected bursts is triggered by the three-event buffer. Sometimes, these are bursts caused by muons with high energy follower events, other times these are caused by a screamer PMTs. In some cases this is a very short breakdown incident. It is important to keep in mind that all buffers have quite high NHit threshold value, above the nominal background events. Therefore, the bursts caused by the higher number event buffers are usually more serious. However, it should be mentioned that even if there are multiple (more than 5) really high NHit events, the logic checks for the lower number buffers first, and therefore, several bursts declared as bursts triggered by the 3-event buffer could also satisfy the conditions for other buffers.

The end condition is either 0 or 2 for almost all bursts. Again, the normal condition mean there were no more events that would extend the burst while the events out of order condition flags bursts where there are issues with time being assigned to events, usually suggesting an issue with the data acquisition system. The reason why these bursts are also considered, is because a close-by SN could potentially result in such a high number of events that the read out electronics would be overwhelmed, resulting in similar issues. In this case, the potential signal would be split into multiple bursts, but as long as the data is not lost it would be processed by the `burst trigger`. A study looking into how close a SN

can be to still be detected and processed without issues is mentioned in Subsection 5.11.1. Looking at the plots of events surviving the data cleaning, these explain why it is necessary to focus on the high NHit events only. The percentage of surviving events regardless of NHit is usually quite high, with not too much of a spread. Lot of these events are background events. The high NHit events are usually either physics events with high energy or breakdown-like events and these can be distinguish with reasonable precision.

For the distribution of bursts by date, there are significant peaks where the number of bursts was very high. These are either detector breakdowns (the very high peaks) or periods where there was significantly increased detector activity (actions regarding detector filling, water extraction, PPO mixing, removal of pipes and other direct interventions). This is supported by the fact that the periods with low burst rate are periods where no underground activity was taking place (such as early January). Therefore, the rate of bursts is clearly affected by the activity of the detector (or the medium). With the recent addition of re-evaluation of burst at `Level 2`, the number of significant bursts had dropped significantly.

5.10 SNEWS

A core-collapse SN in the our galaxy would bring a wealth of scientific information, such as the properties of the neutrinos and about the nature of the core collapse. The important and unique feature of the neutrino signal specifically is that it is prompt - hours or even days before the electromagnetic signal [125, 126]. This is the main reason the `BT` is designed with aim to minimize latency. As such, the observation of the neutrino signal from a SN can provide early alert that can give astronomers a chance to make observations of early turn-on of the SN light curve. Observing the signal early allows probing of the progenitor star's surroundings - effects such as binary companions or other unexpected effects. In some cases there can be no associated optical signal but neutrinos are still expected to be observed for such SN [125]. For the purposes of providing astronomical community with a prompt alert for a galactic SN as well as to optimize global sensitivity to SN neutrino physics by cooperative work and downtime coordination, the SuperNova Early Warning System (SNEWS) collaboration was formed [125].

The SNEWS collaboration is an international group of experimenters from several SN neutrino-sensitive experiments. They serve as a coincidence trigger between the world's neutrino detectors [126]. These currently include: Super-K (Japan), LVD (Italy),

IceCube (South Pole), KamLAND (Japan), Borexino (Italy), Daya Bay (China) and HALO (Canada) [127, 126]. The SNO experiment was also a member while it was active. SNO+ is currently finishing internal testing, with the ambition to connect to the SNEWS test channel in the near future. The main method of detecting bursts is based on a central coincidence computer receiving signal from the involved experiments [125]. In other words, whenever any local automated SN monitor detects a SN-like signal in one of the participating detectors, an alarm is send over the internet to remote server (the coincidence server). Whenever there is a coincidence of alarms between experiments, SNEWS reports this to interested parties [126, 128].

5.10.1 Coincidence alarms

In addition to the advantages of the early warning, there are other benefits from system involving neutrino signal from multiple detectors. If only weak signals are recorded (as is the case for distant SN) a coincidence between signals coming from different detectors increases the sensitivity. Moreover, requiring the coincidence even for highly sensitive detectors reduces background and increases the confidence in the alarm, as widely separated laboratories are highly unlikely to be correlated [125]. Finally, the concept of coincidence makes the automated process possible and allows for potential determination of the direction of the source (pointing) [125]. As of writing, there was no coincident alarm recorded nor has any core-collapse event been detected within the lifetimes of the currently active experiments.

The strength of the coincidence alarm is that the false alert rate can be decreased to nearly zero, which is realistically impossible for a single experiment [125, 126]. This is strongly supported by the SNEWS approach to reduction of false alarms. Based on analysis of rates of different types of alarms and the number of active experiments (as can be seen in [125]) SNEWS put a condition on alarm rate for all participating experiments of no more than 1 per week [125]. The `SNO+ BT` was tuned to allow up to 2 alarms per month.

In the case of the detection of a SN-like burst - a L3 burst passing thresholds for final alarm, as described in Section 5.5 - an alarm is also sent to SNEWS coincidence server (currently to local copy of the same server). This alarm consists of [125]:

- **The date**: the date when burst was detected;

- The exact **timestamp**: nanosecond precision of the first event in the burst;

- **The level**: the significance of the alarm, ranges from test, to possible, to confirmed; also allows for retracting;

- **The experiment ID**: the assigned ID of the experiment reporting the burst.

5.10.2   SN shifting

In order to interface the burst detection a scheme for SNO+ SN shifting was developed. The duties of a SN shifter include [129]:

- To monitoring both the pre-supernova monitor (currently being finalized for SNO+, for more details see [130]) and the `Supernova Burst Trigger`;

- To confir that these systems are operational;

- To revie any L3 bursts, including classification;

- To be on call for SN related alerts;

- In case of potential SN-like burst (a burst passing final alarm thresholds), the duties are:

  - To verify the burst;

  - To confirm the SNEWS alarm was sent;

  - To confirm or retract this alarm;

  - To contact the SN response team;

  - (Possibly) To start additional analysis tasks.

SNO+ SN shifting has recently started, with 24/7 monitoring. The exact details are being adjusted by the experiment at this time [131, 129, 132].

5.11   Related topics

This section gives insight into some other topics related to SN detection that should be mentioned alongside this chapter.

5.11.1 Supernova test using ELLIE

An analysis of the trigger efficiency by distance was done to estimate how far a SN signal can be to still be detected by SNO+ detector. Another study was performed to investigate how close a SN can be to be properly detected and the data stored (without loss). The limiting factor in this case is not to detect enough energetic events to trigger on, but instead the ability of detector's DAQ system to deal with short duration burst of many events.

Ideally, this would be tested with a source capable of creating SN like signal. A SN source like that is currently in development (more details in Subsection 3.6.3). Regardless, in the meantime, the detector's ability to cope with bursts of thousands of events was tested using the ELLIE system. ELLIE signal is intrinsically different to what is expected from SN signal; ELLIE generally fires photons at set frequency and set light intensity for specified duration. The intensity and frequency does not change over the duration of a single cycle (burst in this case). However, the frequencies and intensities can be changed for subsequent repetitions in order to scan the response until the limitations of the readout system are found.

The method of testing had to accommodate for the mode used to create the light signal. Three different TELLIE fibres covering distinct portions of the detector were used (one after another). Three high NHit points were chosen, approximately at the peaks of the expected SN signal. Then, each fibre was run at each NHit set-point (consecutively), increasing frequency with each iteration until a point where some data loss occurred was reached. Several reasons for the data loss were observed, such as failure of the `Event Builder`, overflow of the FIFO buffers, PMT reporting bad data and more. More details can be found in [133, 134, 135].

Once these limits are known, the expected SN spectra by distance can be compared to these limits to extract the distance at which the data would be (likely) lost. There are, of course, several assumptions made, such as assuming that if the detector can deal with the first two seconds of the signal, it can deal with the rest of the burst with no issues. Another assumption is that the SN signal is comparable to TELLIE signal at the center of the beamspot. Regardless, the study also served as a very good stress test for the detector's readout system.
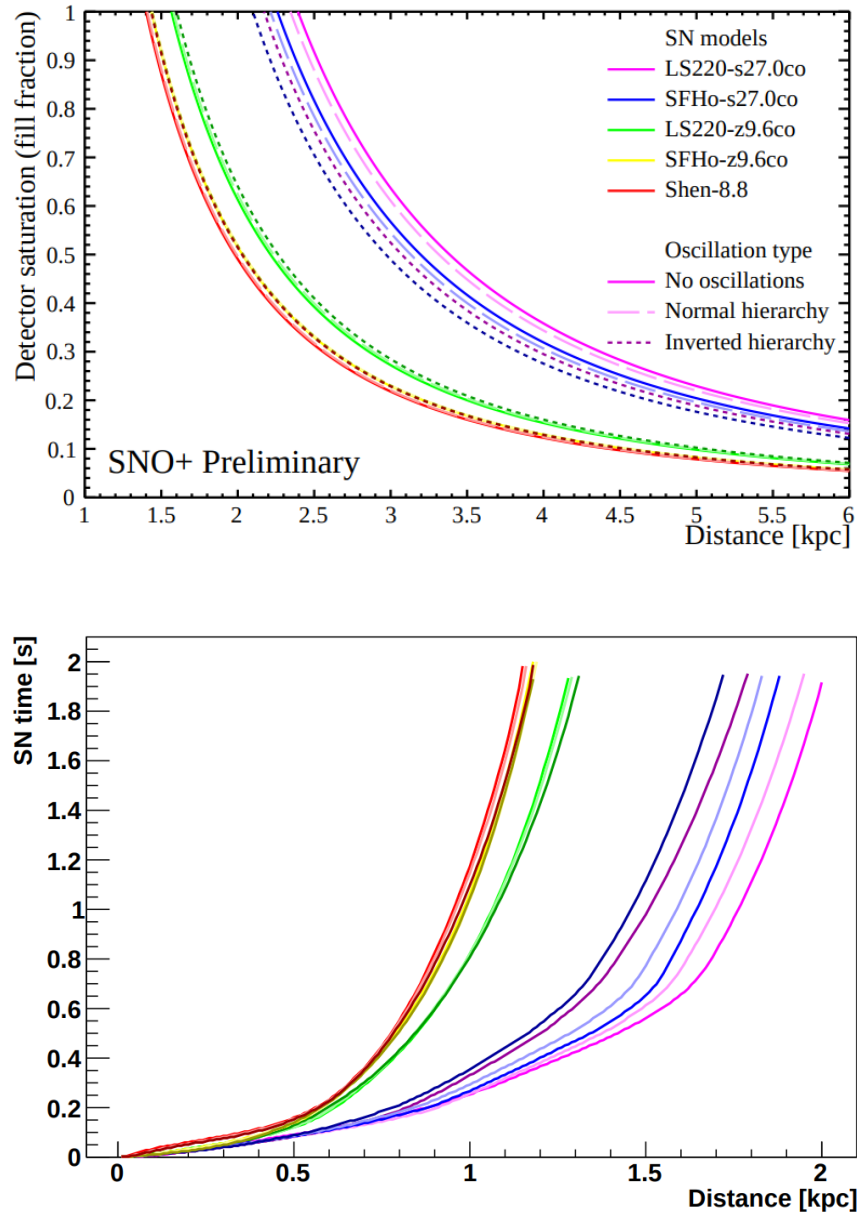
Figure 5.61: Results of the study using ELLIE system to determine SNO+ sensitivity to close SNe. Top plot: saturation of the detector as a function of SN distance for selection of SN models. Saturation of one corresponds to the detector failing to record some (at least one) events in a burst. Bottom plot: The time it takes to reach saturation of one per model. Plots from [136, 134].

The results of the study are shown in Figure 5.61. Full saturation of the detector is estimated to occur between 1.4 - 2.4 kpc, depending on the model [136]. The chance of the next SN saturating the detector was estimated between 0.4% and 2.8% [134], assuming probabilities introduced in Figure 5.45. Additionally, the study also presents the time to detector saturation in the bottom plot of the same figure. The time here represents when a saturation of one (failing to record an event) would occur for each model as a function of distance.

5.11.2   Time to stabilize

The dynamic threshold for the `SN BT` (Section 5.7) was developed because the detector's activity was changing significantly during the periods where scintillator was being added to the AV. This study investigated the extend of the change of activity as well as the time it takes for the detector to stabilize - or return to the pre-fill order of activity.

The method of the study was to use `Stonehenge`, the realistic trigger, and look for the number of detected bursts as a function of NHit. Runs were analysed immediately after filling and for few following days.

The results of the study are presented in Figure 5.62. The top plot of the figure highlights the change in detector activity. While the green run (immediately after fill) contains many high NHit events and would create bursts at relatively high NHit values, the blue run (before the fill) does not consist of such high NHit events and the bursts would only be declared at lower NHit values. The red run (few days after the fill) is in the transition period, when the activity is returning to pre-fill levels.
Bottom plot shows several runs following the fill cycle, analysed using the same method. The color represents the time since the filling in days. It can be observed that the activity steadily lowers and returns to the approximate levels preceding the fill. The estimated time it takes is 3.5 to 4 days, which roughly corresponds to the half-life of radon (3.8 days [137]), which is introduced during the fill.

5.11.3   Frequency of threshold events

At the time of commissioning of the BT, a study was performed to investigate the frequency of threshold events - these are events that would contribute to the counts of logical buffers of the `BT` (more details in Subsection 5.2.3). Therefore, the results of the study would point to the frequency of the bursts. A coincidence of multiple events of
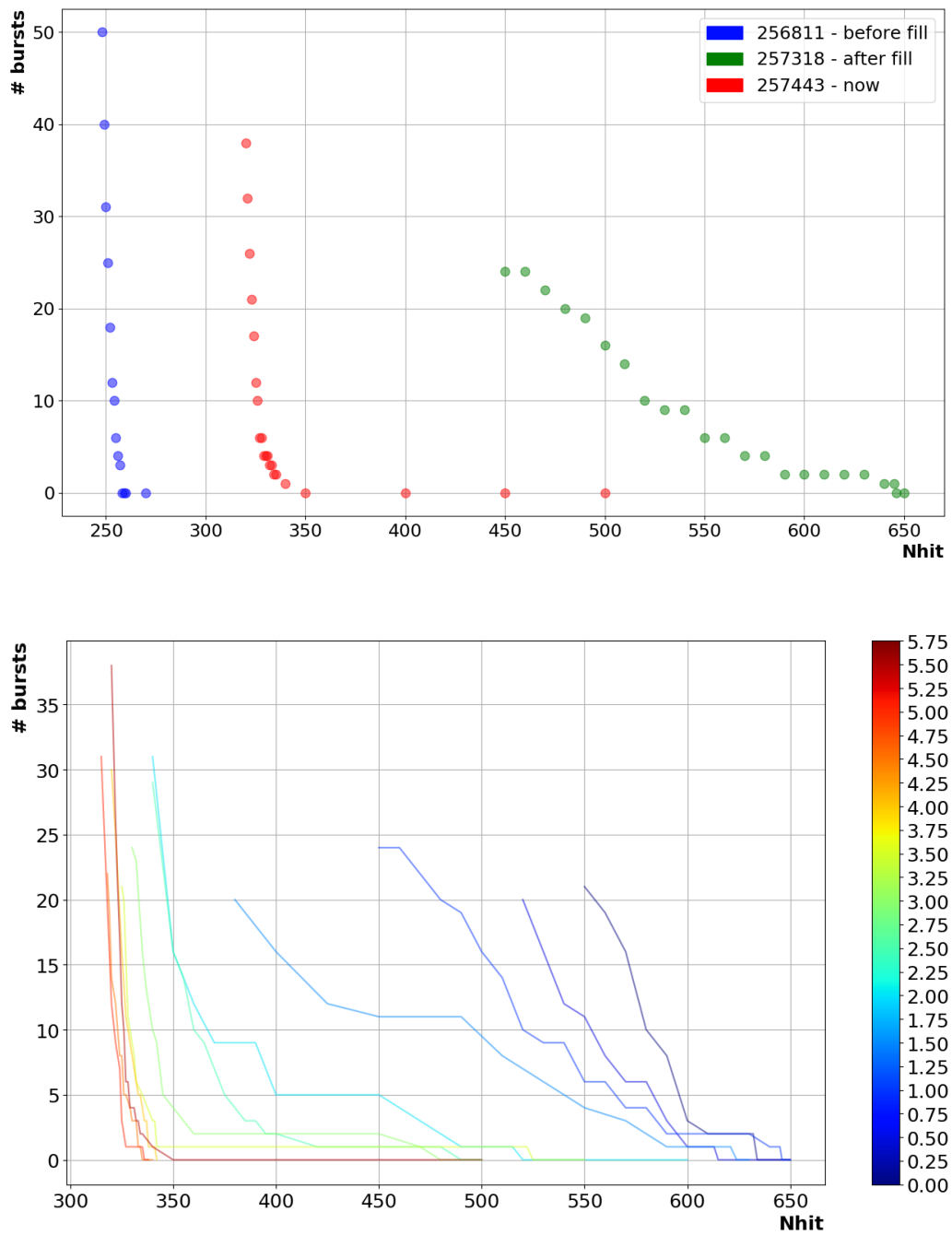
Figure 5.62: Results of study with focus on the time it takes for the detector activity to stabilize after filling with scintillator, from the perspective of the `Burst Trigger`. The color palette (bottom plot) represents the time since last fill in days. Details of the study alongside discussion are presented in Subsection 5.11.2.

particular NHit is required to declare a burst, however, the frequency of these coincidences is still affected by the frequency of the events themselves.

The frequency of TH events was evaluated on a set of data from one day of physics running with common detector settings. The results of the study are available in Figure 5.63. Looking, for example, at the frequency of events at around 1000 NHit, these appear at rate of approximately nine per hour. To fulfil the requirements of the five-event logical buffer, **five** events within **two** seconds would be required. Thus, bursts are not likely to originate from random coincidences of background events.

It should be noted that the distribution of events as a function of NHit follows an exponential distribution. Therefore, even small changes to the TH values for the high-event buffers would result in a sizeable change in frequency.

5.12   Conclusion

A `Supernova Burst Trigger` was designed and developed by the author, based on an older software package. The goal of the trigger is to provide fast (minimal delay), live (processing real data), and sensitive trigger to alert in the case of detecting SN-like signal.

The design of the trigger includes several buffers that increase the sensitivity. The length of each burst is not set, it is possible to extend the burst if additional high energy events are detected, and there are pre and post periods allowing for the analysis of trends within the burst. The trigger itself is multi-level, with the detection being separated from the data cleaning. The design is very modular: the threshold settings, the time windows, as well as the cleaning bits, can be set through the configuration file. There are also multiple start and end conditions for the burst that can be monitored. Additionally, the thresholds settings can be set dynamically by analysing the activity in the detector.

In addition to the trigger, a full monitoring suite was developed. This is promptly available online for each detected burst. It interfaces with the database and the underground systems to provide all available details relevant for the burst, including several plots highlighting the basic characteristics of the burst. Using this monitoring, it is possible to distinguish the SN-like bursts from the bursts caused by other means, such as the issues with electronics, therefore, working as a breakdown monitoring system as well. It has successfully triggered on an earthquake.
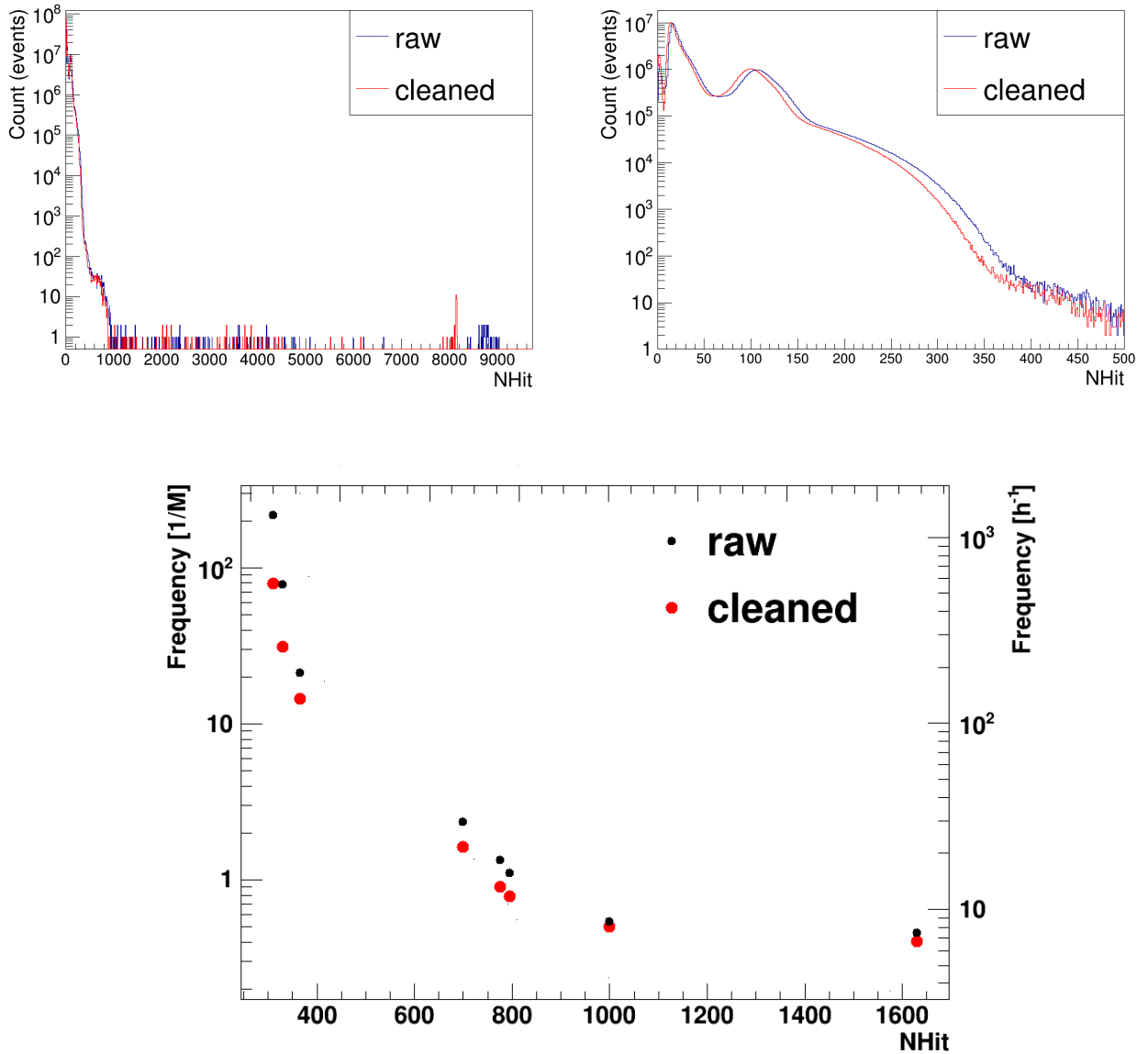
Figure 5.63: Results of the study with focus on the frequency of threshold events. These are important for the `Burst Trigger`. Top plots show the distribution of events as a function of NHit for a period of a day (right plot is zoomed over lower portion of the spectrum). Bottom plot indicates the frequency of events at specific NHit points of interest. The frequency is expressed in events per million events (left axis) and events per hour (right axis). The raw as well as cleaned data is considered.

A burst ZOO was produced to facilitate the understanding and the classification of the bursts. This is used during the SN shifting, a procedure established to verify that the burst trigger is operational, also involving the review of the bursts. Furthermore, automated alarms are produced when the system is not running, when the bursts are detected, as well as when a significant SN-like burst is observed.

The rate of this final alarm is tuned to comply with the SNEWS requirements. A connection of SNO+ to SNEWS is nearing completion at the time of writing.

Additionally, the efficiency of the `SN trigger` was evaluated using a method mimicking the real trigger across a range of distances for both the core-collapse and the electron-capture SN models. It was found that the trigger has almost perfect efficiency up to the galactic center and >90% efficiency up to the far galactic edge. Therefore, it is extremely likely SNO+ will detect a SN explosion in our galaxy.

Finally, a study was performed to evaluate how close a SN can be to not overwhelm the detector readout system. The limit was determined at 1.4-2.4 kpc, depending on the model.

Chapter 6

Supernova Sensitivity

> *I don't see the logic of rejecting data just because they seem incredible.*

> Fred Hoyle

6.1 Introduction

The main goal of this chapter is to estimate the sensitivity of SNO+ to SN neutrinos during the scintillator phase and beyond.

The chapter first introduces neutrino interaction channels that are relevant for SN detection. Afterwards, the focus is on the SN Monte Carlo generator used for SNO+ SN analyses - `SNUGen`. The process of generating SN data is described first, detailing the method of generating events, the interaction channels that are considered, the available models and the final conversion to format that can be used with SNO+ analysis software. The potential reconstruction and use of external water events was attempted, in order to use as much of the available detector as possible.

Following that the `SNUGen` data is analysed by the interaction channel, the event position within the detector, and by the SN distance. This is done to explore how diverse SN bursts can be and how that affects the detector response. A look into the effect of different neutrino mass hierarchies and equations of state is also included.

Subsequently, the analysis of backgrounds significant for SN signal is presented. This includes comparison of the backgrounds to SN signal in order to suggest analysis strategies to mitigate these backgrounds.

The SNO+ sensitivity to SN neutrinos during the full scintillator fill phase is evaluated afterwards. The focus is on the the observables that can be directly extracted from a

SN signal by SNO+. The method of tagging, its performance, reconstruction related obstacles, as well as the corrections to the energy that are required are all outlined in this section.

The analysis of these extracted neutrino spectra, the extraction of the energy of the explosion, and look into the signatures of the black hole formation during SN finalize the chapter.

The idea is to understand the SN signal and devise a procedure that could extract the observables once such a signal is detected. If efficient, this can be built onto the current `SN Burst Trigger`.

6.2 Neutrino interactions

This section describes the relevant SN neutrino interaction channels. These treat neutrinos by flavour, where ν_μ and ν_τ are usually treated together as ν_x, and accordingly, $\bar{\nu}_\mu$ and $\bar{\nu}_\tau$ are grouped as $\bar{\nu}_\mathrm{x}$.

SNO+ is a big, underground, shielded, high-purity liquid scintillator with relatively low backgrounds and as such is sensitive to multiple SN interaction channels. Additionally, having both water and liquid scintillator as detection media allows for even better sensitivity, due to the access to interaction channels exclusive to each media, such as the neutrino interactions on ^{16}O for water, and neutrino interactions on ^{12}C in scintillator. Furthermore, the overall mass of the detection media is bigger, if both scintillator and water regions of SNO+ detector are taken into account. However, there are different neutrino cross sections in the two media and some of the channels can, in fact, form a background to each other. This is the case for channels that do not have an option to be tagged (no clear prompt and delayed signal) and have overlapping energy ranges, such as the $\nu - e$ reaction and the inclusive ^{12}C transitions, explained later in the chapter.

6.2.1 Cross sections

Exact knowledge of the neutrino cross sections is crucial to understand the interaction rates. Regarding the data for cross sections, these are related to the interactions that are included with `SNUGen`. The analytical cross sections that can be calculated internally are:

- The Inverse Beta Decay (IBD);

- the Neutrino Electron Scattering ($\nu - e$);

- the Neutrino Proton Scattering ($\nu - p$).
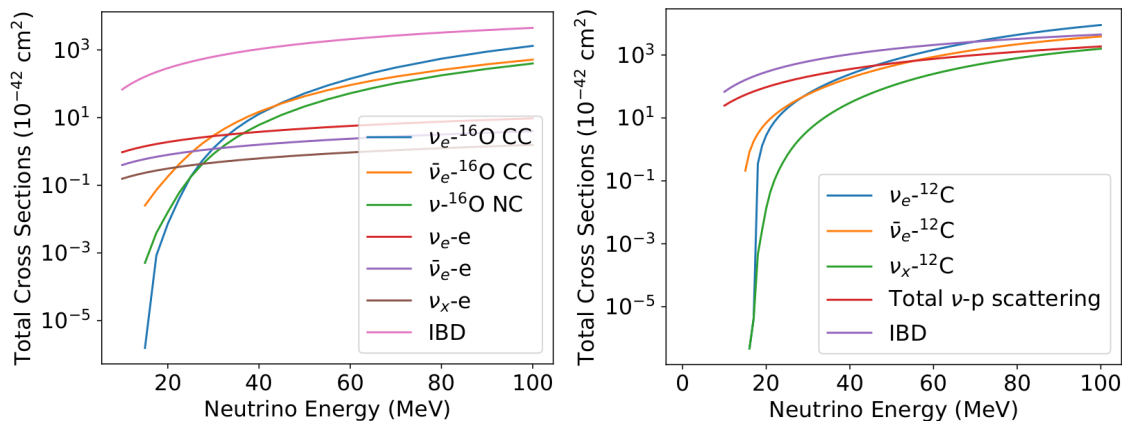
Figure 6.1: Cross sections for SN neutrino interactions relevant for SNO+. Left plot shows channels visible to external water part of SNO+. Plot on the right shows channels visible to scintillator part of SNO+. The $\nu_e - e$ scattering is also present in the scintillator but is omitted to increase the clarity of the plot. Both figures from [43].

These analytical cross sections are well understood and are calculated using the SM.

In addition to these, there are nuclear cross section tables available. These are:

- The ^{12}C tables [138];

- The ^{16}O tables [139].

For these interactions with nucleons, numerical evaluations are required, introducing systematic uncertainties. The tables for tellurium are not readily available and, therefore, `SNUGen` can currently be only used to estimate the sensitivity for pure water phase and the scintillator phase of the SNO+ experiment. It should be mentioned that the addition of tellurium is not going to affect the SNO+ sensitivity to SN neutrinos significantly. The major change will be the change to mass and the density of target nuclei for SN neutrinos.

There are different interactions visible to water than to liquid scintillator of SNO+. Therefore, in some cases (and in `SNUGen`) the SNO+ detector is treated as two separate detectors: LS[1] detector (the AV[2] filled with LAB[3]) and Water-Cherenkov detector for the region of external water. Comparison between cross sections of SN neutrinos relevant for each of these regions is shown in Figure 6.1. The details of each channel, alongside (simplified) calculation of tier cross section, are described in the following section.

---

[1]Liquid scintillator.

[2]Acrylic vessel.

[3]Linear alkylbenzene.

$$\bar{\nu}_e + p \rightarrow e^+ + n$$
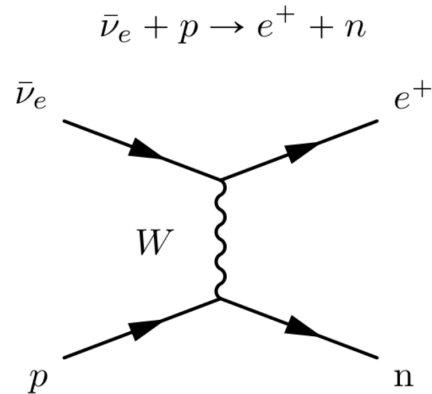
Figure 6.2: The Feynman diagram for IBD interaction.

6.2.2 Analytical interactions

Inverse Beta Decay

The inverse beta decay (IBD) is a nuclear reaction involving an electron antineutrino scattering off a proton, resulting in a positron and a neutron. The interaction proceeds via the exchange of the W^+ boson. The Feynman diagram is available as Figure 6.2. The cross section of this process exceeds those for scattering off electrons, protons and nuclei by few orders of magnitude, especially at energies below $\sim$20 MeV [140]. As such, it is a major component of the overall SN neutrino signal, with highest cross section for almost the whole energy range.

Specifically considering the conditions of the SNO+ detector, the resulting positron annihilates with an electron while the neutron captures on a proton, after it thermalises. If the neutron captures on ^{1}H, this produces 2.22 MeV de-excitation γ-ray and happens after $O(200 \ \mu s)$, therefore, giving quite unique and clear signature [141, 142, 143]. This happens in 99% of the cases [144]. Additionally, it can also capture on the ^{12}C of the LS, where the γ-ray has an energy of 4.945 MeV [145].

There is an energy threshold of $E_\nu = 1.806$ MeV for this reaction [146], outlined in Eq. 6.1.

$$E_{\text{thr}} = \frac{(m_{\text{n}} = m_{\text{e}})^2 - m_{\text{p}}^2}{2m_{\text{p}}} \approx 1.806 \text{ MeV}. \tag{6.1}$$

Regarding the cross section, it is well described by the approximation (accurate to the permille level [147])

$$\sigma_{\text{tot}}(E_{\bar{\nu}_{\text{e}}}) = 10^{-43}\text{cm}^2 p_{\text{e+}} E_{\text{e+}}^{\text{tot}} E_{\bar{\nu}_{\text{e}}}^{-0.07056+0.02018\ln E_{\bar{\nu}_{\text{e}}} - 0.001953\ln^3 E_{\bar{\nu}_{\text{e}}}}, \tag{6.2}$$

$$E_{\text{e+}}^{\text{tot}} \approx E_{\bar{\nu}_{\text{e}}} - (m_{\text{n}} - m_{\text{p}}). \tag{6.3}$$

where the $p_{\text{e+}}$ is the momentum of the positron, $E_{\text{e+}}^{\text{tot}}$ is the total energy, $E_{\bar{\nu}_{\text{e}}}$ is the energy of the antineutrino and m_{p} and m_{n} are the masses of the proton and neutron respectively. All stated energies are in MeV.

The visible energy of the interaction is related to the incoming antineutrino energy, Eq. 6.4 [28] as

$$E_{\text{vis}}^{\text{p}} = E_{\text{e+}} + 2m_{\text{e}} = E_{\nu} - (m_{\text{n}} - m_{\text{p}}) - m_{\text{e}} + 2m_{\text{e}}, \tag{6.4}$$

substituting Eq. 6.3.

Neutrino - Electron scattering

All flavours of neutrinos and antineutrinos can interact with electrons through the elastic scattering process

$$\overset{(-)}{\nu}_{\alpha} + e^- \rightarrow \overset{(-)}{\nu}_{\alpha} + e^-, \tag{6.5}$$

where: $\alpha = e, \mu, \tau$. There is no associated threshold given the initial and final states are the same, only redistribution of energy and momentum is present [7]. Feynman diagrams for electron neutrino processes are pictured in Figure 6.3, for electron antinuetrino process in Figure 6.4 and for heavier neutrino flavours in Figure 6.5.

While the ν_{e} and $\bar{\nu}_{\text{e}}$ experience both neutral current and charged current interactions, heavier neutrinos only contribute via the neutral current interaction - this is considering neutrino energies that can be achieved during a SN, $E_{\nu} < O(100 \text{ MeV})$. For these energies, the mass of μ and τ is too big to interact via charged current. For the electron (anti)neutrino processes: $\nu_{\text{e}} + e^- \rightarrow \nu_{\text{e}} + e^-$ and $\bar{\nu}_{\text{e}} + e^- \rightarrow \bar{\nu}_{\text{e}} + e^-$, the effective Lagrangian
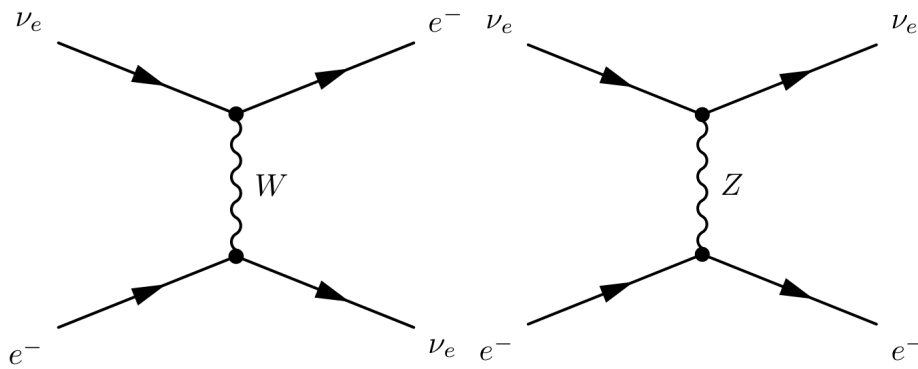
Figure 6.3: The Feynman diagrams for ν_e- e scattering processes available to ν_e. Charged current on the left, neutral current on the right.

Figure 6.4: The Feynman diagrams for $\bar{\nu}_e$- e scattering processes available to $\bar{\nu}_e$. Charged current on the left, neutral current on the right.
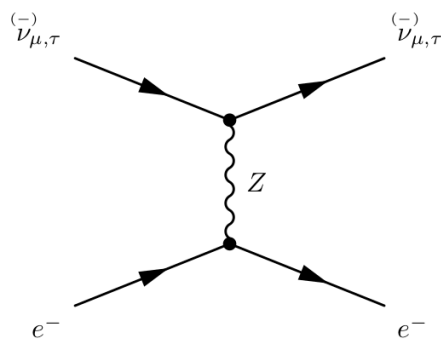
Figure 6.5: The Feynman diagrams for ν_x- e $(\bar{\nu}_x$- $e)$ scattering process available to ν_x $(\bar{\nu}_x)$.

Process	Total cross section	Value [s/MeV^2]
$\nu_{\mathrm{e}} + e^-$	$(G_{\mathrm{F}}^2 s/4\pi)[(1 + 2\sin^2\theta_{\mathrm{W}})^2 + \frac{4}{3}\sin^4\theta_{\mathrm{W}}]$	93
$\bar{\nu}_{\mathrm{e}} + e^-$	$(G_{\mathrm{F}}^2 s/4\pi)[\frac{1}{3}(1 + 2\sin^2\theta_{\mathrm{W}})^2 + 4\sin^4\theta_{\mathrm{W}}]$	39
$\nu_{\mathrm{x}} + e^-$	$(G_{\mathrm{F}}^2 s/4\pi)[(1 - 2\sin^2\theta_{\mathrm{W}})^2 + \frac{4}{3}\sin^4\theta_{\mathrm{W}}]$	15
$\bar{\nu}_{\mathrm{x}} + e^-$	$(G_{\mathrm{F}}^2 s/4\pi)[\frac{1}{3}(1 - 2\sin^2\theta_{\mathrm{W}})^2 + 4\sin^4\theta_{\mathrm{W}}]$	13

Table 6.1: The total neutrino-electron elastic scattering cross sections. Values from [7].
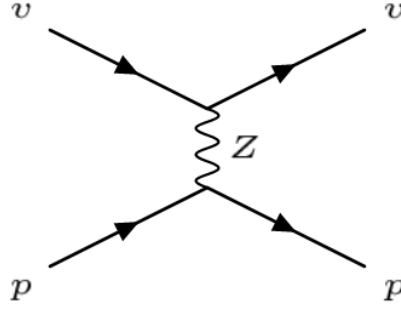
Figure 6.6: The Feynman diagram for $\nu + p \to \nu + p$ scattering process.

in compact form is shown in Eq. 6.6, and Eq. 6.7 shows the effective Lagrangian for the $\overset{(-)}{\nu}_{\mathrm{x}} + e^- \to \overset{(-)}{\nu}_{\mathrm{x}} + e^-$ processes [7].

$$\mathcal{L}_{\mathrm{eff}}(\overset{(-)}{\nu}_{\mathrm{e}}e^- \to \overset{(-)}{\nu}_{\mathrm{e}}e^-) = -\frac{G_{\mathrm{F}}}{\sqrt{2}}[\overset{(-)}{\nu}_{\mathrm{e}}\gamma^\rho(1 - \gamma^5)\nu_{\mathrm{e}}][\bar{e}\gamma_\rho((1 + g_{\mathrm{V}}^{\mathrm{l}}) - (1 + g_{\mathrm{A}}^{\mathrm{l}})\gamma^5)e]. \tag{6.6}$$

$$\mathcal{L}_{\mathrm{eff}}(\overset{(-)}{\nu}_{\mathrm{x}}e^- \to \overset{(-)}{\nu}_{\mathrm{x}}e^-) = -\frac{G_{\mathrm{F}}}{\sqrt{2}}[\overset{(-)}{\nu}_{\mathrm{x}}\gamma^\rho(1 - \gamma^5)\nu_{\mathrm{x}}][\bar{e}\gamma_\rho(g_{\mathrm{V}}^{\mathrm{l}} - g_{\mathrm{A}}^{\mathrm{l}}\gamma^5)e]. \tag{6.7}$$

Finally, regarding the cross sections, it can be seen from the Lagrangians that they are all proportional to G_{F}^2. The total values are written in Table 6.1, these are known to better than 1%. Considering the values in this table, the approximate ratios are [7]:

$$\sigma_{\nu_{\mathrm{e}}} : \sigma_{\bar{n}u_{\mathrm{e}}} : \sigma_{\nu_{\mathrm{x}}} : \sigma_{\bar{\nu}_{\mathrm{x}}} \simeq 1 : 0.42 : 0.16 : 0.14.$$

There are no coincidences that can be used to tag these events.

Neutrino - Proton scattering

All (anti)neutrinos can elastically scatter on a proton via the exchange of a Z boson, $\nu + p \to \nu + p$, thus making this channel the one with the highest event yield (no kinetic

energy threshold), even though the total cross section is much smaller than the one for IBD. An unique feature of this channel is that the proton recoil can provide spectral information about the nutrino flux. The exact cross section predicted by the SM can be found in [148]. Considering SN energies, the cross section simplifies to

$$\frac{d\sigma}{dE_\mathrm{p}}(E_\nu) = \frac{G_\mathrm{F}^2 m_\mathrm{p}}{2\pi E_\nu^2}[(c_\mathrm{V} \pm c_\mathrm{A})^2 E_\nu^2 + (c_\mathrm{V} \mp c_\mathrm{A})^2 (E_\nu - E_\mathrm{p})^2 - (c_\mathrm{V}^2 - c_\mathrm{A}^2)m_\mathrm{p} E_\mathrm{p}], \qquad (6.8)$$

where: E_ν is the energy of the incoming neutrino, E_p is the proton recoil energy, c_A and c_V are the axial-vector coupling constants. The upper signs refer to neutrinos and lower to anti-neutrinos [149].

The values of the coupling constants are

$$c_\mathrm{V} = \frac{1 - 4\sin^2\theta_\mathrm{W}}{2},$$

and:

$$c_\mathrm{A} = \frac{g_\mathrm{A}(0) \cdot (1 + \eta)}{2},$$

where: θ_W is the effective weak mixing angle, the value of $\sin^2\theta_\mathrm{W} = 0.23155$ is assumed and the axial proton form-factor is $g_\mathrm{A}(0) = 1.267$ [150]. η, the proton strangeness, represents the strange-quark contribution [151]. This is currently measured to be $\eta = 0.12 \pm 0.07$ [148].

Integrating Eq. 6.8 yields the total cross section as

$$\sigma_\mathrm{tot}(E_\nu) = \int_0^{E_\mathrm{p}^\mathrm{max}} \frac{d\sigma}{dE_\mathrm{p}}(E_\nu)dE_\mathrm{p}, \qquad (6.9)$$

$$E_\mathrm{p}^\mathrm{max} = \frac{2E_\nu^2}{m_\mathrm{p} + 2E_\nu}. \qquad (6.10)$$

Here, the $E_\mathrm{p}^\mathrm{max}$ is the maximum proton recoil energy, achieved when the neutrino is scattered completely backwards. The η is the main source of uncertainty - about 13% - and the assumption of its value significantly affects the cross section [28]. It should be mentioned that it is not possible to extract the proton's direction in the scintillator medium.

Proton quenching

SNO+ uses linear alkylbenzene (LAB) as the scintillating medium. The energy response of the LS detector is not linear due to energy quenching of the scintillator. The light output
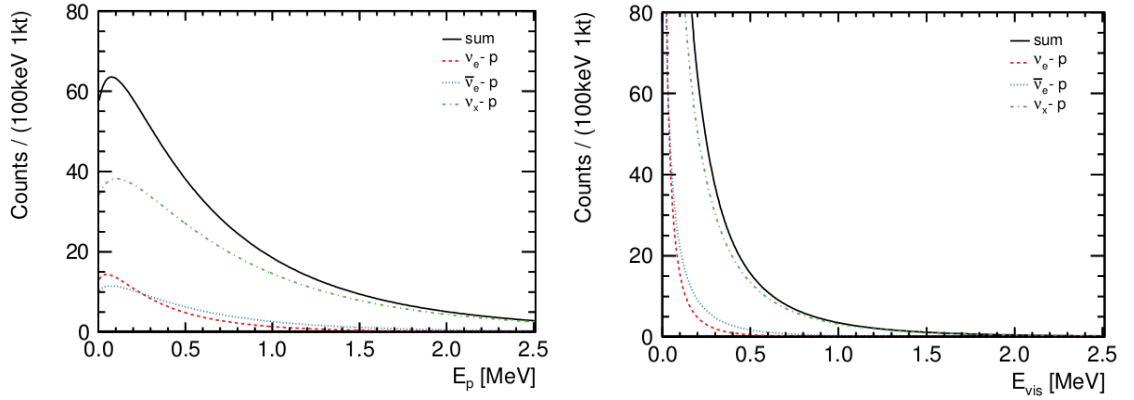
Figure 6.7: True (left) and visible (right) proton recoil spectrum in LAB, using $k_{\mathrm{B}} = 0.0096$ cm/MeV. Plots from [28].

of the scintillator is constrained by the energy deposit density dE/dr [152]. The general formula is

$$\frac{dL}{dr} = S\frac{\frac{dE}{dr}}{1 + kB\frac{dE}{dr} + kC(\frac{dE}{dr})^2}.\tag{6.11}$$

here dL/dr is the change in the light output over distance, S is the scintillation efficiency, dE/dr is the energy deposit density, k is the probability of quenching and B is the constant of proportionality linking the local density of ionized molecules at a point along the particle's path to the specific energy loss [153]. Because k and B only ever appear as a product, they act as one parameter called the Birks' constant [154] and k_{C} is the second order parameter [152]. These constants depend on the material.

With quenching present, the light output of the scintillator is reduced. The reason behind this is different level of ionisation (ionisation strength). If several strong ionising particles deposit energies over a short distance, the excited molecules close to each other can recombine in a specific process that does not result in photon emission, thus reducing the light yield [28]. The Birks' constant for protons in LAB (used in SNO+) has been measured as 0.0096 ± 0.0003 cm/MeV [43]. The effect on the visible energy is shown in Figure 6.7.

It should be mentioned that the quenching described above refers to the ionisation quenching. Impurity quenching also exists, where the light output is likewise affected due to impurities present in the scintillation medium. In some cases the impurities do not scintillate when excited, in other cases they do scintillate, therefore, altering the wavelength distribution and the time profile [43].

6.2.3 Interactions with nuclei

SN neutrinos can also interact with individual nucleons, which are abundant in the liquid scintillator medium.

The neutral current interaction has a signature γ emitted as a consequence of a nucleon being promoted to a higher energy level within the nucleus and subsequently decaying to the ground state after the neutrino interaction. This interaction is available to all neutrinos regardless of flavour. For high enough energy neutrinos a nucleon can be fully ejected from the nucleus.

Additionally, there is a charged current channel available to electron (anti)neutrinos. A ν_e can turn neutron into a proton with the electron emission while $\bar{\nu}_e$ can turn a proton into neutron emitting positron. The resulting (changed) nuclei are often unstable and decay shortly after. These decays can sometimes be used to tag these $\nu - X$ events [139]

$$\nu + X \to \nu' + X^* \to X + \gamma, \tag{6.12}$$

$$\nu + X \to \nu' + Y + n/p. \tag{6.13}$$

The total cross sections of these interactions are affected by many variables, such as the effect of other nucleons, the attraction between the ejected lepton and the daughter nucleus and more. Also due to this complexity, as well as due to the scaling with energy, these interactions are not perfectly understood. There are several proposed methods to calculate the cross sections at different energy levels [155].

Interactions with ^{16}O

The ^{16}O atoms are one of the potential targets for SN neutrinos. These are only available in the external water part of the SNO+ detector during the fully filled phase and later.

Charged current There are two main charged current interactions, described below.

$$\nu_e + {}^{16}\text{O} \to {}^{16}\text{F} + e^-. \tag{6.14}$$

The electron neutrino interaction has an energy threshold of 15.4 MeV. The ^{16}F then decays immediately and γ is released with 538 keV energy. The resulting ^{15}O atom decays again via beta decay, the final energy is ≈ 2.8 MeV.

$$\bar{\nu}_e + {}^{16}\text{O} \rightarrow {}^{16}\text{N} + e^+. \tag{6.15}$$

For the electron antineutrino, this interactions has a threshold of 11.4 MeV. The ${}^{16}\text{N}$ nuclei decays (a) via beta decay (68%) to and electron with endpoint energy of 4.3 MeV and γ with 6.14 MeV or (b) directly to the ground state ${}^{16}\text{O}$ (26%) releasing electron with endpoint energy of 10.4 MeV or (c) to other, higher excited levels of ${}^{16}\text{O}$ (rest), causing a lower energy e and one or more γ rays [43].

Neutral current Neutral current interactions are also physically possible on ${}^{16}\text{O}$ nuclei. For neutrinos of 25 MeV and more [156] a nucleon can be directly ejected from the nucleus, as [157]

$$\nu + {}^{16}\text{O} \rightarrow \nu + p + {}^{15}\text{N}^*, \tag{6.16}$$

$$\nu + {}^{16}\text{O} \rightarrow \nu + n + {}^{15}\text{O}^*. \tag{6.17}$$

In the case of ${}^{15}\text{N}$, this nuclei is radioactively stable. The ${}^{15}\text{O}$ decays the same way as described in the charged current case.

Interactions with ${}^{12}\text{C}$

Similar to interaction in external water, neutrinos can interact with ${}^{12}\text{C}$ nuclei in the scintillator molecules. Again, the charged current interactions are only available to electron (anti)neutrinos while the neutral current is experienced by all flavours.

Charged current The charged current interactions are described in Eq. 6.18. The daughter isotopes are, as in the case of Oxygen, unstable. ${}^{12}\text{B}$ decays via β^- decay to (a) the ground state ($Q = 13.37$ MeV) or (b) to an excited state of ${}^{12}\text{C}^*$. Meanwhile ${}^{12}\text{N}$ decays via β^+ decay. The ground state transition has $Q = 17.34$ MeV, excited ${}^{12}\text{C}$ states are also possible. The half lives of the transitions to ground states are 20.2 and 11.0 ms respectively. Values from [158].

$$\nu_e + {}^{12}\text{C} \rightarrow {}^{12}\text{N} + e^-, \tag{6.18}$$

$$\bar{\nu}_e + {}^{12}\text{C} \rightarrow {}^{12}\text{B} + e^+. \tag{6.19}$$

The ν_e interaction comes with energy threshold of 17.3 MeV while the $\bar{\nu}_e$ has energy threshold of 14.4 MeV [159].

Neutral current   The neutral current interaction is shown in Eq. 6.20. The γ ray produced has distinct energy of 15.1 MeV, therefore, serves as unique feature that can be used to tag these events. This is only available for higher energy neutrinos and was measured by the KARMEN experiment for neutrinos with energy of 29.8 MeV. The cross section of this interaction was measured as $(3.2 \pm 0.5(\text{stat}) \pm 0.4(\text{sys})) \times 10^{-42}$ cm^2 [160].

$$\nu + {}^{12}\text{C} \rightarrow {}^{12}\text{C}^* \rightarrow {}^{12}\text{C} + \gamma. \tag{6.20}$$

There are additional interactions possible where a nucleon is ejected from the ^{12}C nucleus for both NC and CC. These are listed in Eq. 6.21 - 6.26 [138] where X means the cross section is summed over all final states and ν indicates NC available to all neutrino flavours [161].

All cross sections of the SN neutrinos interactions with ^{12}C nuclei are shown in Figure 6.8.

$$\nu + {}^{12}\text{C} \rightarrow \nu' + X + n, \tag{6.21}$$

$$\nu + {}^{12}\text{C} \rightarrow \nu' + X + p, \tag{6.22}$$

$$\nu_{\text{e}} + {}^{12}\text{C} \rightarrow X + e^- + n, \tag{6.23}$$

$$\nu_{\text{e}} + {}^{12}\text{C} \rightarrow X + e^- + p, \tag{6.24}$$

$$\bar{\nu}_{\text{e}} + {}^{12}\text{C} \rightarrow X + e^+ + n, \tag{6.25}$$

$$\bar{\nu}_{\text{e}} + {}^{12}\text{C} \rightarrow X + e^+ + p. \tag{6.26}$$

6.2.4   Summary of interactions in LAB

The summary of the relevant neutrino interactions with LAB is listed in Table 6.2. It should be mentioned that this calculation was performed assuming 1 ktonne of LAB, which is slightly more than the final volume of SNO+ AV. Therefore, the final predictions for event numbers would be slightly lower, at around 78%, corresponding to the 780 tonnes of liquid scintillator inside the SNO+ AV [77].

The summary for external water is quite similar with the addition of interactions with ^{16}O, which are only possible for the external water region. The target densities are different in this case (some more details can be found in Table 6.3). A study considering external water events is presented in Subsection 6.5.2. Due to results of this study and additional reasons described in Section 6.8, external water events are not used to determined the
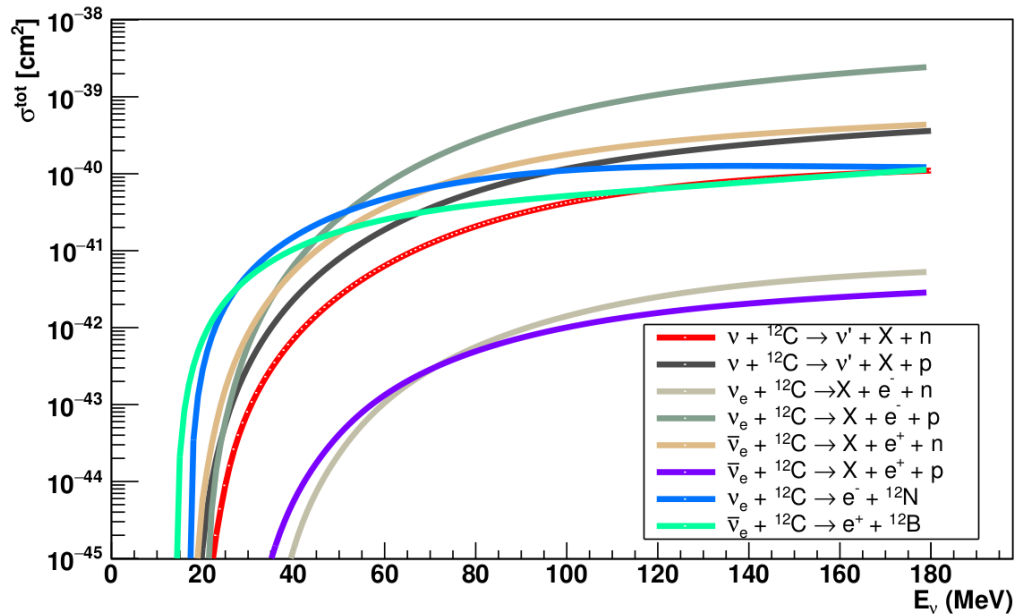
Figure 6.8: Cross sections of interactions of SN neutrinos with ^{12}C nuclei. ν indicates NC channel, available to all neutrinos regardless of flavour. X labels cross sections summed over all possible final states. Figure from [43].

overall sensitivity, but can be considered in the future, once the reconstruction methods are adopted.

6.2.5 Visible energy

Example visible energies for each channel are presented in Figure 6.9. These follow analysis done in [28] that assumes a reference SN neutrino fluence (also the basis for `SNUGen`) using analytical description for a SN at a distance of 10 kpc and total neutrino energy of 300 foe[4] [28]. For detection medium, 1 ktonne of pure LAB is assumed and SNO+ geometry is used. The energy resolution is $\frac{6\%}{\sqrt{E_{\text{vis}}(\text{MeV})}}$, which is worse than the current SNO+ prediction. For more details please refer to [28].

6.3 SNUGen

The software used to generate the neutrino signal from a SNe is called `SNUGen` and is used throughout this chapter. It mainly consists of C++ code that builds into an application that is used to generate neutrino fluxes by interaction channel for each neutrino flavour.

---

[4]**A foe** is a unit of energy, equal to 10^{44} joules or 10^{51} ergs, usually used to express the large amount of energy, such as the energy released by a SN.

Channel	Current	Process	Target density $[10/\text{cm}^3]$	Events $[1/\text{ktonne}]$
Elastic proton scat.	NC	$\nu + p \rightarrow \nu' + p$	6.275	550.1 ± 15.4
				$(152.4 \pm 4.3)^{\dagger}$
Inverse beta decay	CC	$\bar{\nu}_{\text{e}} + p \rightarrow n + e^+$	6.275	249.6 ± 1.3
Elastic electron scat.	NC / CC	$\nu_{\text{e}} + e^- \rightarrow \nu_{\text{e}}' + e^-$	29.08	8.2^*
Elastic electron scat.	NC	$\bar{\nu}_{\text{e}} + e^- \rightarrow \bar{\nu}_{\text{e}}' + e^-$	29.08	3.5^*
Elastic electron scat.	NC	$\nu_{\text{x}} + e^- \rightarrow \nu_{\text{x}}' + e^-$	29.08	2.7^*
Elastic electron scat.	NC	$\bar{\nu}_{\text{x}} + e^- \rightarrow \bar{\nu}_{\text{x}}' + e^-$	29.08	2.4^*
Nuclei int.	CC	$\bar{\nu}_{\text{e}} + {}^{12}\text{C} \rightarrow {}^{12}\text{B} + e^+$	3.763	9.0 ± 0.9
Nuclei int.	CC	$\nu_{\text{e}} + {}^{12}\text{C} \rightarrow {}^{12}\text{N} + e^-$	3.763	3.5 ± 0.4
Nuclei int.	NC	$\nu + {}^{12}\text{C} \rightarrow {}^{12}\text{C}^* + \nu'$	3.8	56.2 ± 11.2
Nuclei int. + nucleon emission	CC	$\nu_{\text{e}} + {}^{12}\text{C} \rightarrow {}^{11}\text{C} + p + e^-$	3.763	0.2 ± 0.1
Nuclei int. + nucleon emission	CC	$\bar{\nu}_{\text{e}} + {}^{12}\text{C} \rightarrow {}^{11}\text{B} + n + e^+$	3.763	0.2 ± 0.1
Nuclei int. + nucleon emission	NC	$\nu + {}^{12}\text{C} \rightarrow {}^{11}\text{B} + p + \nu'$	3.763	2.1 ± 0.6
Nuclei int. + nucleon emission	NC	$\nu + {}^{12}\text{C} \rightarrow {}^{11}\text{C} + n + \nu'$	3.763	0.6 ± 0.2

Table 6.2: SN neutrino interaction channels in liquid scintillator. For the densities, clean LAB is assumed. Regarding the events, these were calculated in [28] with 1 ktonne of LAB using reference SN at 10 kpc with no MSW effect. Uncertainties on the event rates are defined only by the uncertainties in the corresponding cross sections. †Trigger threshold of 200 keV assumed. *The uncertainty is $< 1\%$ in the SM.
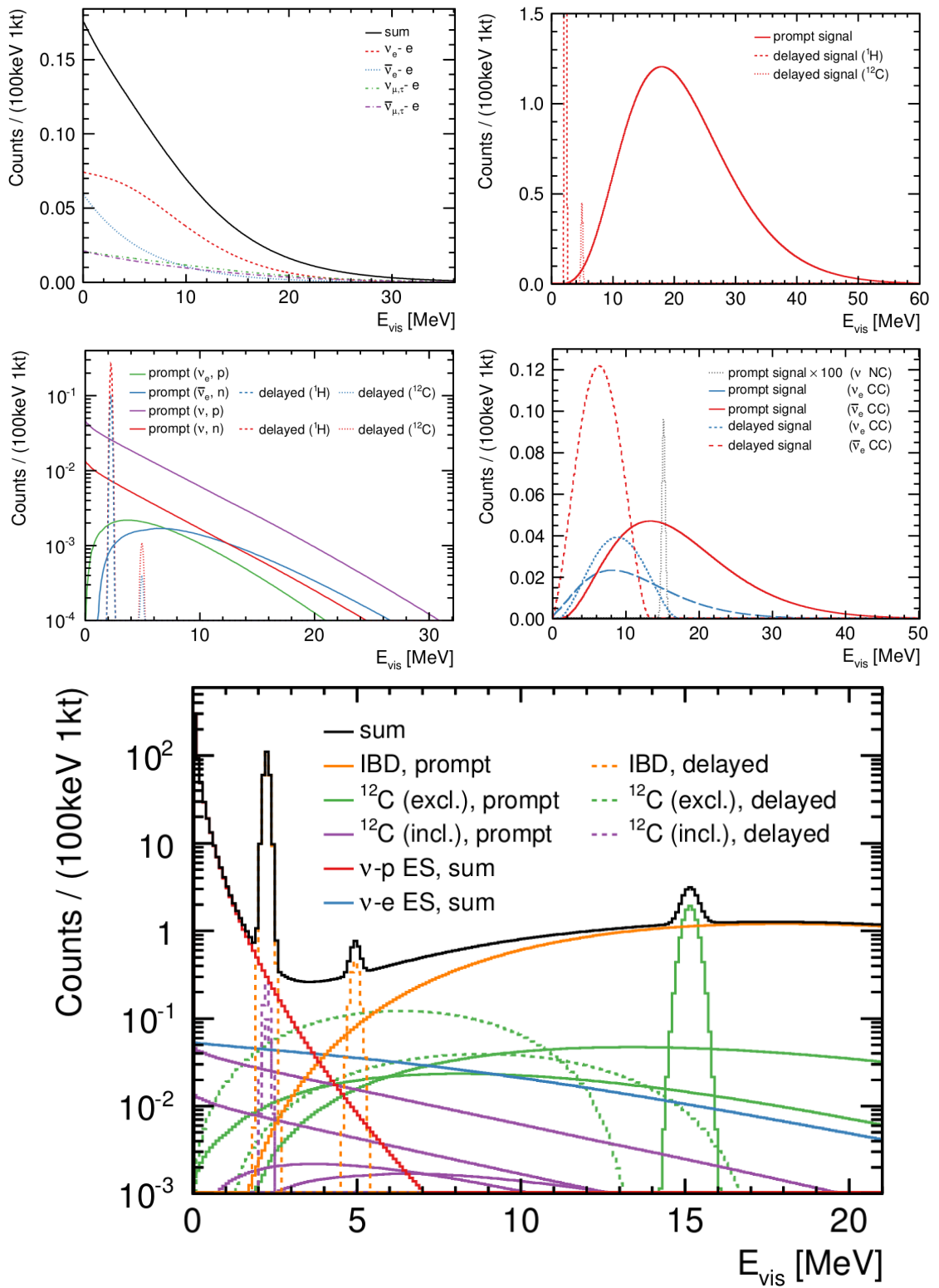
Figure 6.9: From top left: visible energy for $\nu - e$ elastic scattering interactions, visible energy for IBD interactions, inclusive and exclusive $\nu - {}^{12}C$ interactions visible energy and finally, the visible energy spectra of all detection channels in liquid scintillator. All figures from [28].

The procedure is described later. There is additional set of python scripts available to further extend the functionality. As an example, one of these converts the `SNUGen` output to a format readable by SNO+ RAT[5] software. The program was originally written by Belina von Krosigk and Torben Ferber. It was later extended by Mark Stringer [43].

`SNUGen` requires input files specifying the average energy of neutrinos, the luminosity and the pinching parameter for each neutrino flavour (ν_{e}, $\bar{\nu}_{\mathrm{e}}$, ν_{x}, $\bar{\nu}_{\mathrm{x}}$). These input files are provided by the Garching supernova group [162]. The simulations are performed using the PROMETHEUS-VERTEX code [163, 164, 165] for several progenitors and multiple equations of state (EOS). The data considered in this chapter uses a set of 1D models with progenitor masses ranging from 8.8 $\mathrm{M}_\odot$ to 40.0 $\mathrm{M}_\odot$. Three EOS are used: the Lattimer-Swesty [166] (LS), SFHO [167] and stiffer[6] EOS of SHEN [168].

6.3.1 Process

Input data

As mentioned, the input to `SNUGen` consists of data files provided by the Garching group. These are based on their spherically symmetric 1D simulations with different progenitors and equations of state. The files provide the time-dependent luminosity $\mathcal{L}$, the pinching parameter β, the mean energy $\langle E \rangle$, second and third energy moments $\langle E^2 \rangle$ and $\langle E^3 \rangle$ for each ν_{e}, $\bar{\nu}_{\mathrm{e}}$, ν_{x} and $\bar{\nu}_{\mathrm{x}}$ at many timestamps. The steps in time are not linear, for time periods where the changes in the simulated values are big (for example the core bounce), there are proportionally more steps allocated. The exact time range depends on the model, but the files always start before the core bounce and go well beyond the accretion phase, therefore, the neutronization burst is always included. The values provided are used to evaluate the neutrino spectra during each step.

Neutrino spectra

The neutrino spectra evaluation follows the Eq. 6.27 where L_0 is the luminosity in MeV, $\langle E \rangle$ is the mean energy of the neutrinos, and β is the pinching parameter that is defined in Eq. 6.28. The $\langle E^2 \rangle$ is the mean of the squared energy and $\langle E \rangle^2$ is the squared value of the mean energy.

$$\frac{dL}{dE} = L_0 \frac{1.0}{\langle E \rangle^2} \frac{(1+\beta)^{1+\beta}}{\Gamma(1+\beta)} \frac{E^\beta}{\langle E \rangle} e^{\frac{-(1+\beta)E}{\langle E \rangle}} . \tag{6.27}$$

---

[5]The reactor analysis tool: the software package used to simulate the SNO+ detector.

[6]'Stiff' in this context means that the remnant contracts slower [31]. A stiffer EOS leads to a less compact remnant. The antonym is 'soft'.

$$\beta = \frac{2 - \frac{\langle E^2 \rangle}{\langle E \rangle^2}}{\frac{\langle E^2 \rangle}{\langle E \rangle^2} - 1}. \tag{6.28}$$

The evaluation process calculates the neutrino fluences for a fixed number of time bins that can be configured before runtime. There are two time-stepping methods available to evaluate the spectra as well as two integration methods to integrate (6.27) with respect to energy. The time stepping methods are:

- **The continuous method**: treating L_0, β and $\langle E \rangle$ as continuous functions of time, evaluating the equation at fixed intervals, interpolating between the data points given by the input;

- **The specific method**: evaluating spectra at each input time.

The final spectrum is obtained by averaging per bin, weighted by the width of particular bin. The energy integration methods are:

- **The numerical method**: using a GSL integration library [169] to give precise numerical integral value before binning the data;

- **The crude method**: a crude midpoint rule integration method is used.

Number of events

To obtain the resulting distribution of interacting neutrino energies (per bin) from the spectra, it is convoluted with the cross sections for each interaction. The cross sections for IBD, $\nu - p$ and $\nu - e$ are obtained analytically and are available as part of `SNUGen` by default. There are other cross sections available that were calculated numerically . These are all detailed in next section, Section 6.2.

To obtain the number of interactions for specific detector a scaling factor calculation is used. This is as follows

$$S = \frac{1}{d^2}(\frac{M}{\rho}\eta\tau), \tag{6.29}$$

where:

- **The** $\frac{1}{d^2}$ is the inverse square law, scaling due to distance from SN;

- **The number of targets** (the second term, in brackets) consists of:

Detector	Medium	Mass [ktonne]	Density $[\frac{g}{cm^3}]$	Target densities $(\frac{1}{cm^3})$			
				e	p	^{12}C	^{16}O
SNO+	LS	0.780	0.867	2.929e23	6.686e22	3.803e22	0
SNO+ : Fiducial	LS	0.450	0.867	2.929e23	6.686e22	3.803e22	0
SNO+ : Water	Water	1.00	1.000	3.346e23	6.686e22	0	3.346e22
SNO+ : External Water	Water	2.121434	1.000	3.346e23	6.686e22	0	3.346e22
Super-K	Water	50	1.000	3.346e23	6.686e22	0	3.346e22

Table 6.3: `SNUGen`: available detectors. The available detectors are different iterations of the SNO+ detector and the Super-K detector. The table also lists the target densities for each target that is considered by `SNUGen`.

- **The** M: the fiducial mass of the detector;

- **The** ρ: the density of the detector (medium);

- **The** $\eta\tau$: the target density, representing the number of targets per cm^3.

Additionally, `SNUGen` also provides the energy distribution for the daughter (outgoing) particles for the three default interactions (IBD, $\nu - p$ and $\nu - e$ scattering). The visible energy is also provided as a function of the chosen detector. This is calculated as

$$E_{\text{vis}} = E_\nu - \Delta - m_{\text{e}}, \qquad \text{(Water Cherenkov)} \qquad (6.30)$$

$$= E_\nu - \Delta + m_{\text{e}}. \qquad \text{(Liquid Scintillator)} \qquad (6.31)$$

The value of Δ is dependent on several factors, such as energy resolution, efficiency, energy quenching and more.

It should be noted, that the LS detector gains additional $2m_{\text{e}}$ due to γ annihilation event. This is not observable in the water Cherenkov detector [43].

6.3.2 Detectors

Because `SNUGen` is a bespoke software made specifically for SNO+, the available detectors mostly represent different phases or parts of the SNO+ detector, and additionally, Super-K detector for comparison. These are listed with details in the Table 6.3. It should be noted that the external water is treated as a separate detector, therefore, when the full SNO+ detector in the full scintillator phase is considered, both "SNO+" and "SNO+: External Water" detector options should be combined.

Parameter	$|\Delta m^2_{12}|$ [eV^2]	$|\Delta m^2_{13}|$ [eV^2]	$|\Delta m^2_{32}|$ [eV^2]	$\sin^2(2\theta_{12})$	$\sin^2(2\theta_{13})$	$\sin^2(2\theta_{23})$	δ_{CP}
Value	$7.50e^{-5} \pm 0.20e^{-5}$	0.00232 ± 0.00012	0.00232 ± 0.00012	0.857 ± 0.024	0.095 ± 0.010	1.0 ± 0.0	$3.141593 * 1.08$

Table 6.4: `SNUGen`: oscillation parameters. These include the neutrino mass splitting values, the mixing angles and the charge-parity (CP) violation parameter.

Parameter	$|V_{\text{ud}}|$	$|V_{\text{us}}|$	$|V_{\text{cd}}|$	$|V_{\text{cs}}|$	m_{p} [$\frac{\text{MeV}}{\text{c}^2}$]	m_{n} [$\frac{\text{MeV}}{\text{c}^2}$]	m_{e} [$\frac{\text{MeV}}{\text{c}^2}$]	η: strange content
Value	0.97377	0.2257	0.23	0.957	938.272046	939.565379	0.510998928	0.12

Table 6.5: `SNUGen`: other physics parameters. These are the relevant Cabibbo-Kobayashi-Maskawa elements, the masses of proton, neutron and electron, and the assumed content of strange quarks inside a proton.

6.3.3   Physics parameters

The default values of main physics parameters were used throughout the analysis. The oscillation parameters are listed in the Table 6.4 and other physics parameters are listed in the Table 6.5. The values were provided by the author of `SNUGen` using the best known fit values.

6.3.4   Interactions

The interaction channels available in `SNUGen` follow the interactions described in Subsection 6.2. The IBD, $\nu - e$ elastic scattering and $\nu - p$ elastic scattering cross sections are calculated internally by `SNUGen` as described in the Subsection 6.3.1. For $\nu - nuclei$ interactions with ^{12}C and ^{16}O, these are provided externally in form of tables.

6.3.5   Models

Currently available `SNUGen` models are listed in Table 6.6.

The available models were chosen to cover a wide range of progenitor masses: from 8 M$_\odot$ to 40 M$_\odot$, which covers the predicted range of progenitor masses for SN explosions. Different SN types are also considered, including core-collapse and electron-capture SNe. Additionally, most models are available with multiple equations of state. The list also includes the LS220-s27.0co model, which is one of the most studied and most understood models. This one was used for more detailed studies throughout this thesis. More details are available in Section 6.5.

Model	Progenitor mass [M$_\odot$]	Time limit [s]	EOS
s8.8	8.8	8.9	SHEN
z9.6co	9.6	12, 13.6	LS220, SFHO
s11.2	11.2	0.5	LS220, SHEN
s12.0	12.0	0.5	LS220, SHEN
s15.0	15.0	0.5	LS220, SHEN
s15s7b2	15	0.5	LS220, SHEN
s17.6	17.6	0.5	LS220, SHEN
s17.8	17.8	0.5	LS220, SHEN
s20.0	20.0	0.5	LS220, SHEN
s20.6	20.6	0.5	LS220, SHEN
s25.0	25.0	0.5	LS220, SHEN
s27.0	27.0	0.5	LS220, SHEN
s27.0co	27.0	15.4, 11.2	LS220, SFHO
s40.0	40.0	0.5	SHEN
s40.0c-bh	40.0	2.1	LS220
s40s7b2c-bh	40	0.57	LS220

Table 6.6: `SNUGen`: available models. Additional notes: **c** = includes mixing-length convection in the proto-neutron star, **o** = includes nucleon self-energy shifts in the charged current neutrino-nucleon interactions, **bh** = black hole formation model, **s7b2** = rapidly mass-accumulating accretion layer. If there are multiple time limits, these corresponds to the multiple equations of state used, written in order.

6.3.6 Run-level parameters

To obtain specific SN neutrino spectra using `SNUGen`, a configuration file is provided and the `SNUGen` process is the followed. These settings include:

- **The group name**: current options are Garching (using models provided by the Garching group) or analytical;

- **The name of the model**: selecting input data file by model name. These are described in the Subsection 6.3.5;

- **The start and end time**: the time limits between which to bin data;

- **The hierarchy**: either normal or inverted. This affects the mass splitting values;

- **The MSW effect**: binary choice of including or excluding the Mikheyev-Smirnov-Wolfenstein (MSW) effect [13];

- **The energy integration method**: either numerical or crude, as described in Subsection 6.3.1;

- **The time stepping method**: either specific or continuous, mentioned in Subsection 6.3.1;

- **The number of time bins**: the number of bins used to evaluate the spectrum at;

- **The experiment**: only one detector from the Table 6.3 can be selected at a time;

- **The distance**: any positive number can be used, this is used as input to the calculation of the scaling parameter. It will eventually result in zero events at very high distances, affected by Poisson fluctuations;

- **The interactions**: any combination of interactions can be used (from one up to all). These are detailed in Subsection 6.2;

- **The global parameters**: these are listed in Table 6.5;

- **The oscillation parameters**: these are summarized in Table 6.4;

- **The input for backgrounds**: currently, only the events coming from (α, n) interactions are considered as backgrounds.

6.3.7 Linking to RAT

A method was developed to convert the output of `SNUGen` to a list of events that can then be used as MC input to the SNO+ analysis software - RAT. There are several parameters that can be specified. These are:

- **The inner AV events**: input file to be processed for inner AV events;

- **The external events**: input file to be processed for the external water events;

- **The output file**: the name of the output;

- **The seed**: the seed to be used for random number generator;

- **The file distance**: the distance used to generate the input files;

- **The SN distance**: the distance to be used for SN;

- **The SN direction**: the relative SN direction to the detector.

After the parameters are specified, the input files are read. The data parsing is done per interaction. For each time bin in the `SNUGen` files the neutrino energy is sampled, the time of each event is generated uniformly within the time bin. Afterwards, and the energies and direction to SN are used to calculate the kinematics of each interaction. Details for these are in [43]. Finally, the distribution of the ejecta energy and direction are used to sample the final energy and direction of each event. The position of each event is generated uniformly either within the inner AV region (0 - 6 m radius) for inner AV events and, similarly, the external events are uniformly distributed between 6.05 and 9 m.

After the interaction is processed, the participating particles are written to an output file. The details that are kept are:

- **The status**: this refers to the state of the particle, generally 1 refers to scattered particle while 2 is a sign of incoming particle or particle originally at rest;

- **The pdg**: this is the Particle Data Group [170] identifier for the particle;

- **The child1**: this is the daughter particle #1;

- **The child2**: this is the daughter particle #2;

- **The px**: the momentum of the particle along the x-axis;

- **The py**: the momentum of the particle along the y-axis;

- **The pz**: the momentum of the particle along the z-axis;

- **The m**: the mass of the particle [GeV];

- **The delta-time**: the time offset from the start;

- **The x**: the x position;

- **The y**: the y position;

- **The z**: the z position.

This file, termed *hepevt* file, containing the particles, their positions and kinematics is then used as an input to RAT analysis software, where each particles is simulated within SNO+ geometry.

Currently, `SNUGen` only contains the precise kinematics for the IBD, $\nu - e$ and $\nu - p$ interactions. The interactions with nuclei are missing at present, mostly because of the lack of literature on their kinematics and the complexity of the final states the nuclei could end in.

6.4   Visualization

To better appreciate the fluxes of different neutrino types during a SN burst, a simple visual representation is presented in Figure 6.10. The time range covers everything provided by the model. Data for ν_e, $\bar{\nu}_e$, ν_x and $\bar{\nu}_x$ is shown, each in a separate row. The three sections roughly represent different phases of a SN burst: neutralization, accretion and cooling (details in Chapter 2). It can be seen that the flux is dominated by the ν_e, which peaks first, and forms most of the burst that is the easiest to detect, however, this is not the case for average energy.

Similarly, Figure 6.11 shows ν_e data visualized in similar manner for the three different LS220 models: a reference LS220-s27.0co, LS220-z9.6co because it is an example of electron-capture SN and, finally, LS220-s40.0c-bh being a model that leads to a black hole formation (BH). An obvious feature of the BH model is increasing average energy throughout the spectrum (as described in Section 6.9).
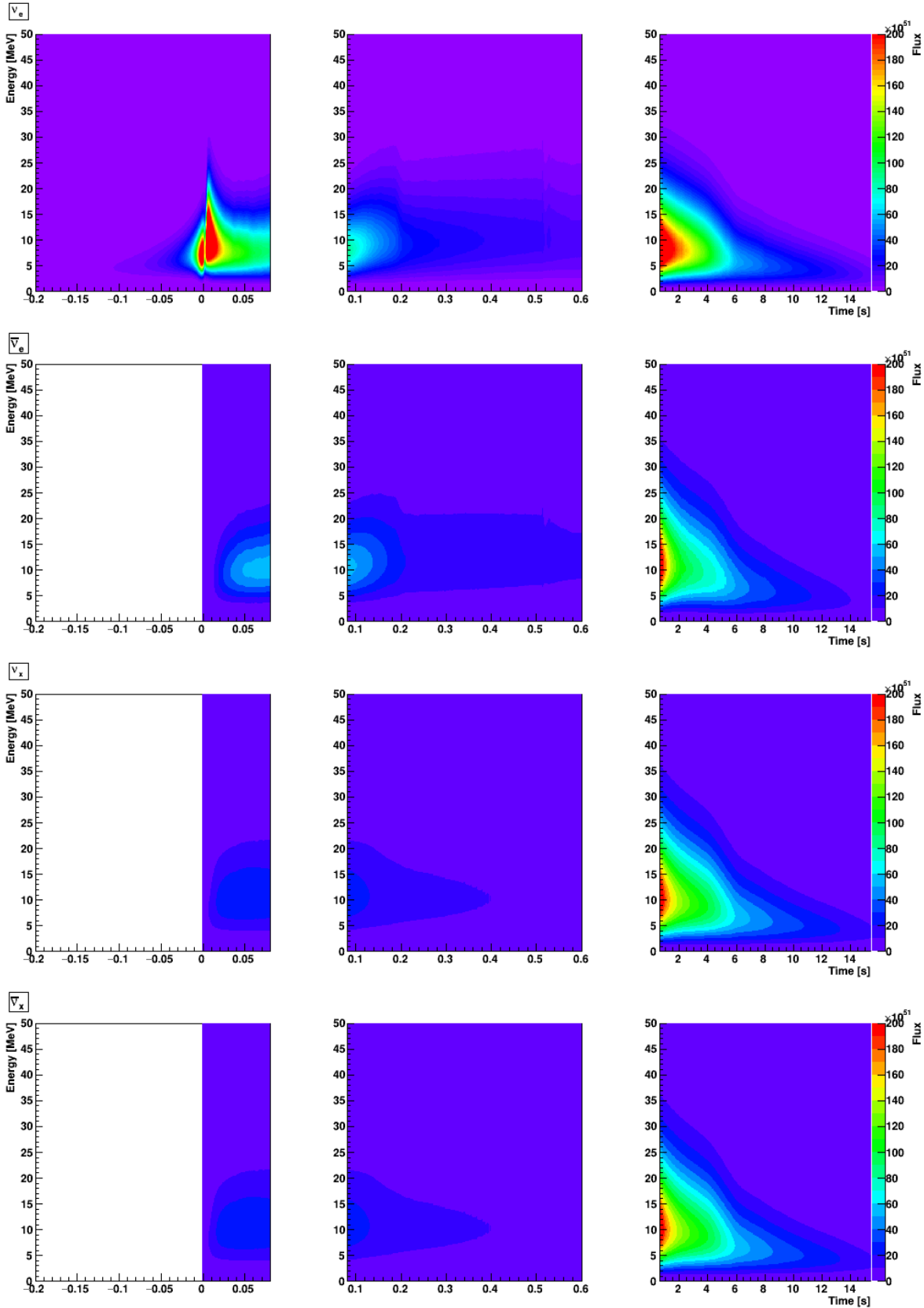
Figure 6.10: Visual representation of a reference SN model: LS220-s27.0co. The three signal parameters are presented: time, energy, and flux, all as binned data. Each section (row) represents data for different neutrino flavour. Columns represent phases of a SN burst: the neutronization burst, accretion phase and cooling. The data is not normalized per bin. White sections used where no data is provided by the model.
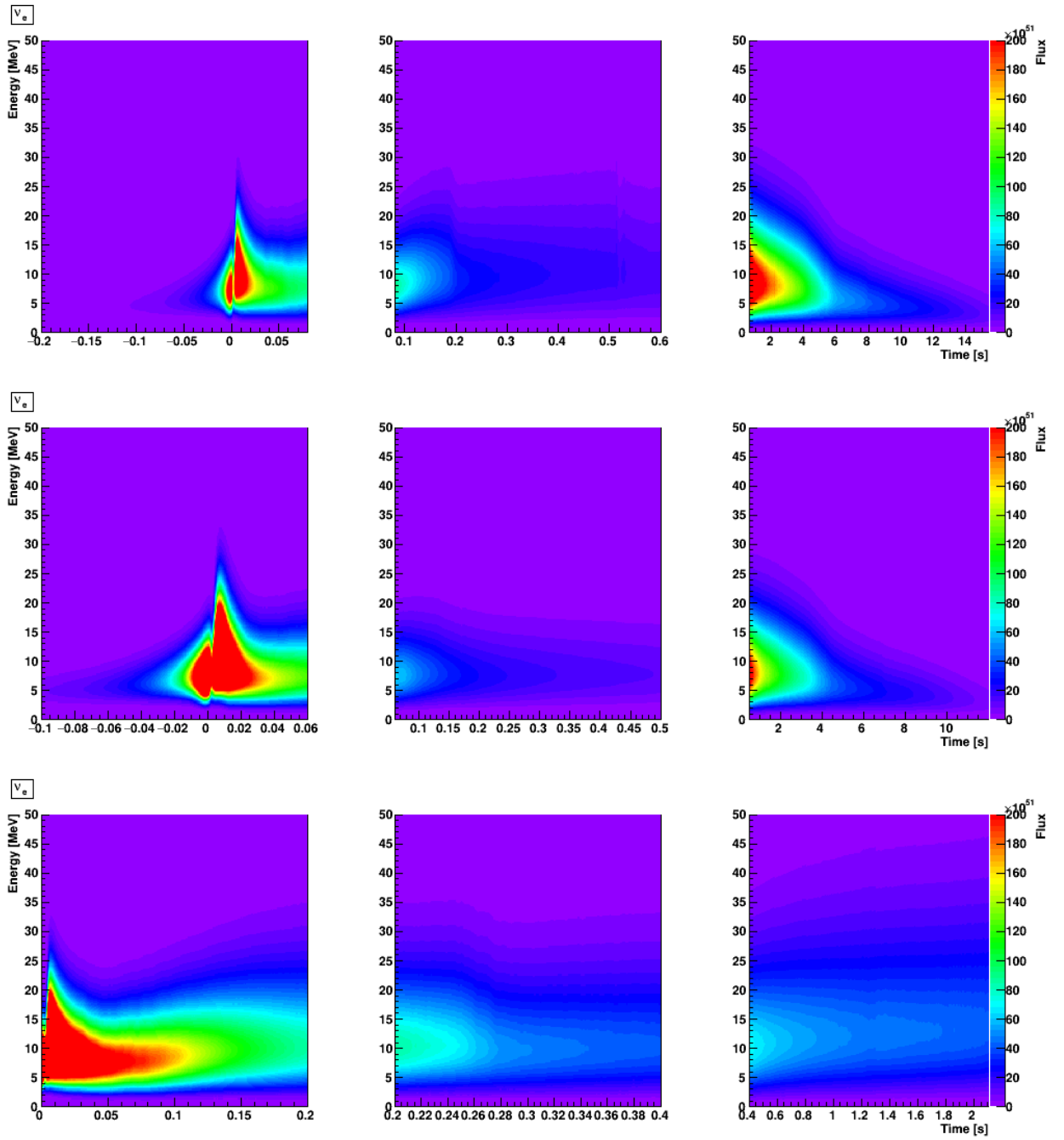
Figure 6.11: Comparison of visual representation of multiple SN models: LS220-s27.0co, LS220-z9.6co and LS220-s40.0c-bh. Only ν_e data shown. Plots are not time-normalized, the full range provided by the models is shown.

6.5   SNUGen studies

This section focuses on the available models via `SNUGen` and the initial analysis. Firstly, an overview of the basic characteristics of these models is made. Secondly, a more in-depth overview if the go-to model is presented. Finally, the effects of parameters such as different equation of state, the MSW effect or the distance are evaluated.

The models used throughout are time-dependent models provided by the Garching group and are described in: [33, 123, 164, 165, 166, 168, 171, 172, 173].

6.5.1   SNUGen models

The Table 6.7 lists the `SNUGen` models that were analysed in this section. With the addition of two black hole models, that are presented later in separate section (Section 6.9), these combined represent all SN models currently present within `SNUGen`.

The generated flux settings used to obtain the event numbers and subsequent analyses were kept constant throughout. All models are considered at 10 kpc, with normal mass ordering. Regarding the `SNUGen` settings, energy integration method 2 was used and time stepping method 1. The number of time bins was set to 1000. The AV column represent the 'SNO+ detector', while the combined column considers 'SNO+ detector' for inner AV and additionally 'SNO+: External Water' for the external region.

Plots in Figure 6.12 show the range and variability between the available `SNUGen` models. They cover wide range of masses, starting from 8.8 $M_\odot$ up to 40.0 $M_\odot$, which is the theoretical limit above which a star turns directly into a black hole without a SN (calculations are uncertain due to uncertainties in the models) [174]. Most models (with the exception of the very smallest and the biggest progenitor) are available with two different equations of state (EOS). This allows for a comparison of the effect of the choice of EOS. Regarding the average NHit - that can be seen in the top right plot of the Figure 6.12 - there is clear distinction between the AV only datasets and combined AV + EXT datasets. This is expected due to the Cherenkov detection in water, producing little light compared to scintillator [36]. For models from the same dataset, the average NHit is comparable - there is no clear correlation between mass and average NHit. This is expected, as the produced neutrinos interact via the same channels. One notable feature is that in some cases the LS220 model has higher average NHit than other EOS model of the same mass when considering the AV case only, and lower when considering the combined case - i.e. there is a reversal of the order when the two datasets are considered for the same mass.

	Time limits [s]		AV				AV + EXT			
MODEL	tSTART	tEND	HEPEVT evs	RAT entries	RAT events	NHit average	HEPEVT evs	RAT entries	RAT events	NHit average
LS220										
S11.2	-0.1	0.4963	143	143	196	1735	325	325	365	1350
S12.0	-0.1	0.4963	216	216	346	1975	473	473	557	1274
S15.0	-0.1	0.4963	314	314	513	1975	688	688	843	1285
S15s7b2	-0.1	0.4963	247	247	407	2001	397	397	502	1398
S17.6	-0.1	0.4963	237	237	437	2048	520	520	643	1310
S17.8	-0.1	0.4963	317	317	542	2105	605	605	784	1319
S20.0	-0.1	0.4963	216	216	301	1700	455	455	537	1397
S20.6	-0.1	0.4963	353	353	579	2091	770	770	976	1298
S25.0	-0.1	0.4963	440	440	842	2141	908	908	1158	1301
S27.0	-0.1	0.4963	274	274	451	2001	526	526	645	1320
S27.0co	-0.1	15.4388	616	616	970	2003	1208	1208	1372	1114
z9.6co	-0.1	11.9900	314	314	451	1987	643	643	723	1246
SFHO										
S27.0co	-0.1	11.1688	600	600	846	1871	1209	1209	1448	1386
z9.6co	-0.1	13.6220	325	325	422	1951	597	597	640	1259
SHEN										
S8.8	-0.06	8.9090	298	298	415	2052	530	530	577	1299
S11.2	-0.1	0.4963	138	138	210	2025	275	275	327	1307
S12.0	-0.1	0.4963	189	189	322	2208	389	389	514	1459
S15.0	-0.1	0.4963	296	296	508	1929	582	582	797	1449
S15s7b2	-0.1	0.4963	188	188	304	2103	403	403	486	1285
S17.6	-0.1	0.4963	222	222	338	2045	452	452	549	1326
S17.8	-0.1	0.4963	274	274	497	2170	601	601	766	1318
S20.0	-0.1	0.4963	205	205	312	2146	355	355	436	1225
S20.6	-0.1	0.4963	346	346	578	2042	690	690	939	1433
S25.0	-0.1	0.4963	356	356	640	1986	817	817	1016	1363
S27.0	-0.1	0.4963	254	254	434	2119	482	482	608	1307
S40.0	-0.1	0.4963	323	323	605	2229	658	658	853	1351

Table 6.7: `SNUGen` models with their corresponding time limits and extracted event numbers for both HEPEVT files and RAT files. Average NHit for each model is also shown. The table contains models for the three available EOS (in `SNUGen`). The data presented is for SNO+ detector, divided into the AV region only, and combined AV and External regions.
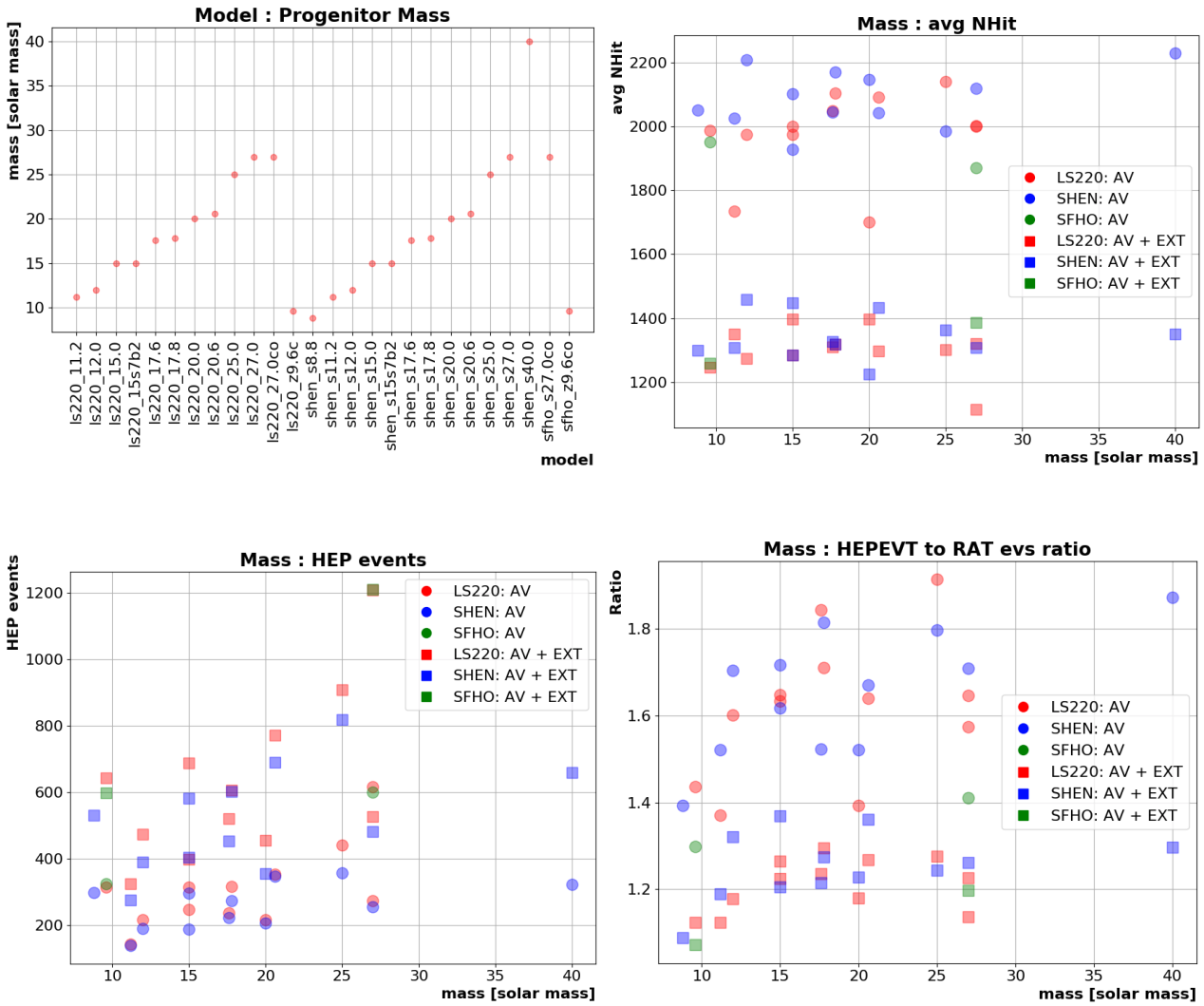
Figure 6.12: Comparison of `SNUGen` models. Top left: overview of models by mass. Top right: Average NHit by mass. Bottom left: The number of HEPEVT events by model. Bottom right: The ratio of HEPEVT events to RAT events.

Considering the number of HEP events (bottom left plot of the same figure), there is a general slight increase in the number of events as a function of the progenitor mass, however, the deviations between different EOS often affect the final number of events more. As expected, there are always more events for the combined AV + EXT cases.

Finally, the bottom right plot of the same figure shows the ratio between the number of RAT events to HEPEVT events. A single MC input event (HEPEVT event) can cause several detector events. These are caused be the scattering events, ionisation events, Bremsstrahlung events, interactions with nuclei - any interaction of the simulated particle with the detector. There is a visible difference between the set considering the external water region (which is much lower) as well as observable difference between different EOS.

6.5.2 External water events

Tracking MC

A brief analysis of SN events in the external water region was attempted. This is mainly interesting due to the potential directional information via the reconstruction of the charged particle's interaction vertex and usage of the Cherenkov ring pattern [36]. The disadvantage of water as a detection medium for SN neutrinos is the difference in light yield which is $\sim 50 \times$ smaller for water compared to scintillator. The Cherenkov threshold values are 0.8 MeV for electrons and 1400 MeV for protons. Therefore, proton are always invisible as are sub-MeV electrons. However photons carry directional information and can be used for SN pointing [36]. Additionally, the interaction with ^{16}O are only present in the light water region, not in LAB.

As a first step, a detailed look into the MC generation was made. This uses `SNUGen` HEPEVT file as input, where the detector was specified as *SNO+: External Water*. These observed interactions were:

- **The $\nu - e^-$ scattering**: Available to all ν types. The involved particles were ν and e^-. Observed electron interactions were:

  - Cherenkov radiation into optical photon;

  - Electron ionisation - this can crate optical photons or other electrons;

  - Bremsstrahlung - resulting in γ which can Compton scatter, finally ending as optical photons.

- **The $\nu - p^+$ scattering**: Available to all ν types. Observed particles were ν and p^+. Observed proton interactions were:

  – Hadronic ionisation into optical photon.

- **The Inverse Beta decay events**: Available to $\bar{\nu}_e$ only. Observed particles were n and e^+. Observed neutron interactions:

  – A neutron scatter on proton that goes through hadronic ionisation;

  – Neutron interacts with ^{16}O nuclei, causing ionisation, later decays radioactively;

  – Neutron finally captures on proton, resulting in deuteron and γ.

  Observed positron interactions were:

  – Interaction were very similar to e^-, most of the time causes Cherenkov radiation creating optical photons or can cause electron ionisation or Bremsstrahlung;

  – They always ends in annihilation with e^-, producing two γs.

Inner AV to External water events - comparison

Afterwards, a comparison between the data from the acrylic vessel region (only), and combined AV + External water region was made.

For this comparison, the 'go-to' model is used: this is LS220-s27.0co. To remind, this is a 1D collapse and explosion simulation of 27 $M_\odot$ progenitor that includes the nucleon self-energy shifts in the charged current neutrino-nucleon interactions [123]. It has been the most studied model, and therefore, the most understood. It also allows for more extensive comparison, since more studies are available for this particular model. The inner AV uses reconstruction aimed at the scintillator while the water events are fitted with fitter tuned for water. It should be mentioned that the results are preliminary at this stage, as the SNO+ processing and reconstruction routines are still being developed for the full scintillator phase. This also includes fitting external water events during scintillator phase. Due to this, the efficiency of the water fitter specifically is not great. Additionally, events that pass through both media can also be mis-reconstructed or not reconstructed at all. Figures 6.13, 6.14 and 6.15 represent the comparison. The left side of the figures is the AV region events while the right side corresponds to events from external water. In some cases the interactions are divided based on the interaction channel. The names are as: **EE** = neutrino - electron elastic scattering, **EP** = neutrino - proton elastic scattering and **IBD** = inverse beta decay interaction.
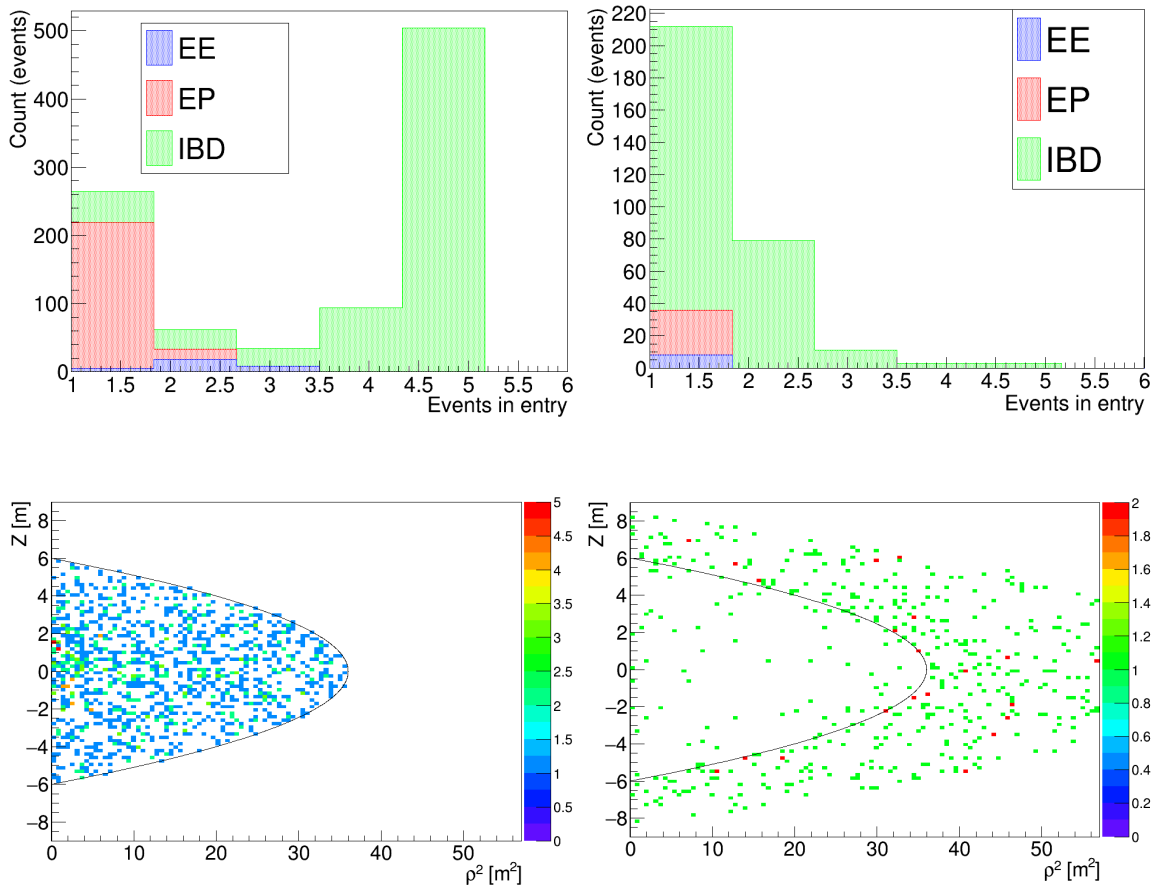
Figure 6.13: Comparing AV events to external water events: multiplicity (top) and reconstructed position (bottom). Left side is the AV region only, right side is the external water region. Multiplicity represents the number of simulated detector events caused by single HEPEVT interaction (entry). Here, the interactions are distinguished according to the interaction channel. For positions reconstruction, the color scale represents the number of events in each bin. The edge of the AV is depicted as black half-ellipse. The histograms are overlaid, not stacked.
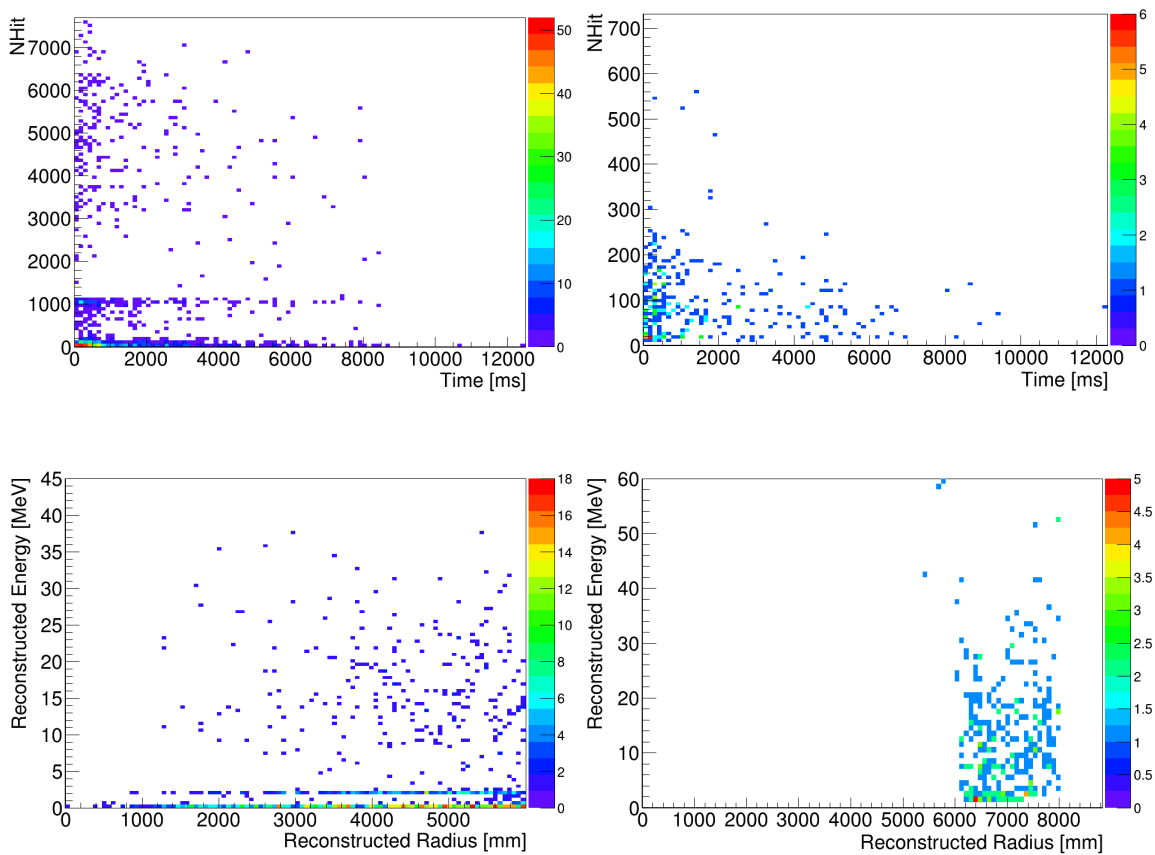
Figure 6.14: Comparing AV events to external water events: NHit over time (top) and reconstructed energy as a function of reconstructed radius (bottom). There are significantly more events reconstructed inside the AV due to aforementioned reconstruction challenges. In both cases most events come early on. There is also an obvious group of events around 2.1 MeV, which corresponds to the γ released after the neutron capture. There are some really high energy events reconstructed inside the AV for the external set, these are likely miss-reconstructed.
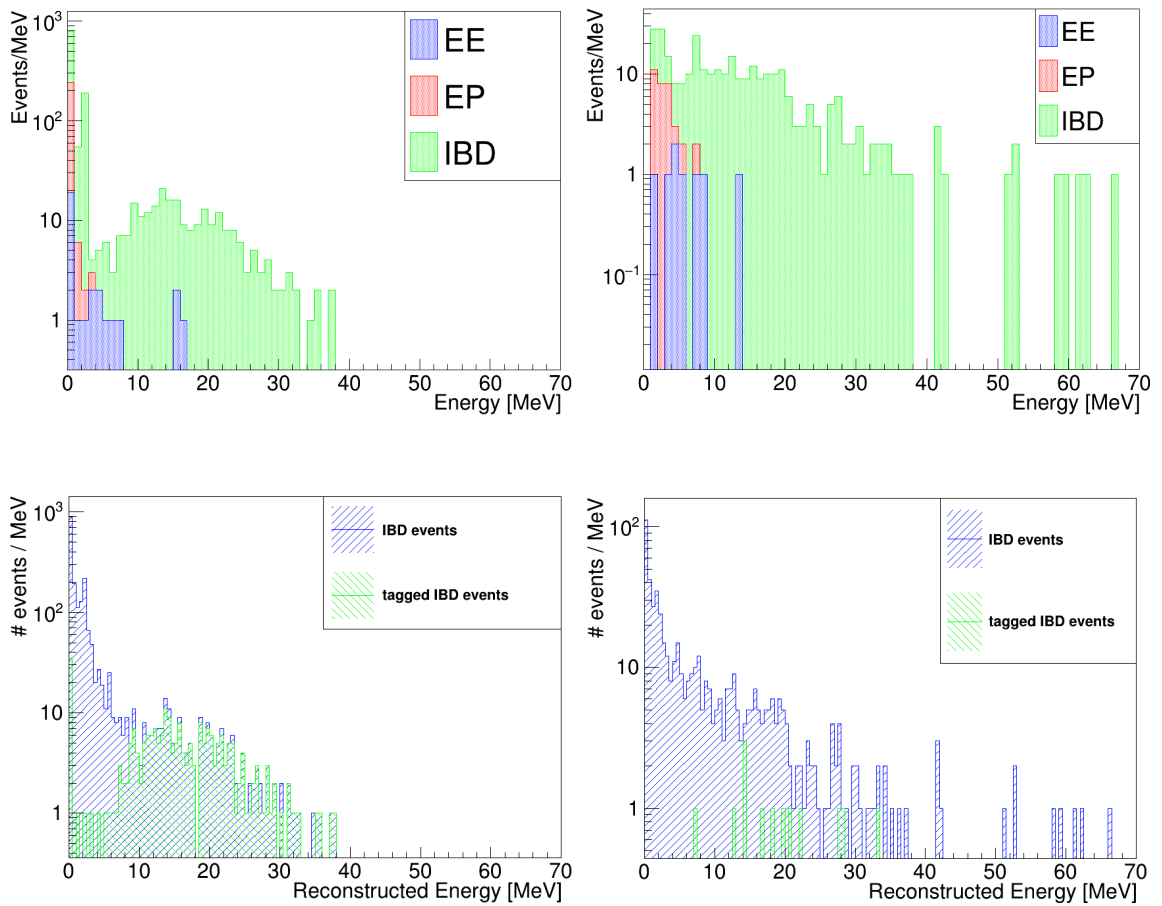
Figure 6.15: Comparing AV events to external water events: overall energy distribution (top) and IBD tagging (bottom). Note the difference in number of events. The tagging is particularly inefficient for the external events. Different reconstruction cuts and binning is used (between top and bottom portion of the figure, always constant for the particular comparison), resulting in slightly different energy distribution for tagging plots. These are overlaid histograms.

Due to the combination of the issues with external water events: low multiplicity, low reconstruction efficiency (currently), miss-reconstructions, low ability to tag events and low overall sensitivity to such events (detector trigger thresholds are set for scintillator, requiring a lot more NHit than events in water generally produce) the external water events have not been used for the remainder of analyses in this thesis. However, the advantage of such events (additional interaction channel and possibility to point) should be recognised, and once the reconstruction is tuned, these events can increase the SN detection sensitivity and provide additional information.

6.5.3 The default model

The LS220-s27.0co model overview is presented in this subsection. Firstly, the physics parameters as given by `SNUGen` are shown. Secondly, simple reconstruction using the SNO+ analysis software is displayed. Finally, analysis using this model as input to the `Burst Trigger` is made.

The settings for `SNUGen` MC generation are the same as for previous comparison of inner and external events: 10 kpc distance, normal mass ordering, 1000 time bins, no MSW effect.

Snugen signal

The flux parameters for this model are shown in Figure 6.16, they are analogous to most available models. The model presented here differs from the model in Section 2.8 slightly. Even though the mass of the progenitor is the same, different EOS and/or specific elements affecting the neutrino production could have been used. The overview model presented in Section 2.8 comes from [32], while the model here (and all models throughout) is produced by the Garching group for use with `SNUGen`. The full overview of all parameters for all available models is listed in Appendix F.

The pinching parameter β is very similar for all neutrino groups after about 0.7 s, while the very early times show high pinching for the ν_e. While the ν_x and $\bar{\nu}_x$ distributions are identical, the $\bar{\nu}_e$ also appears to have the same shape, shifted to higher values of β.

Similar trend is also visible for the luminosity $\mathcal{L}$, where the early discrepancy for ν_e is even greater. The $\bar{\nu}_e$ equalizes at around 0.1 s, and all three distributions are almost identical from 0.55 s onwards. Therefore, in the early milliseconds, the flux consists of mostly ν_e, with minimal contributions from other neutrino flavours. Between 0.1 s and 0.7 s, where the ν_e and $\bar{\nu}_e$ are equal, both the ν_x and $\bar{\nu}_x$ display about two thirds of the luminosity.
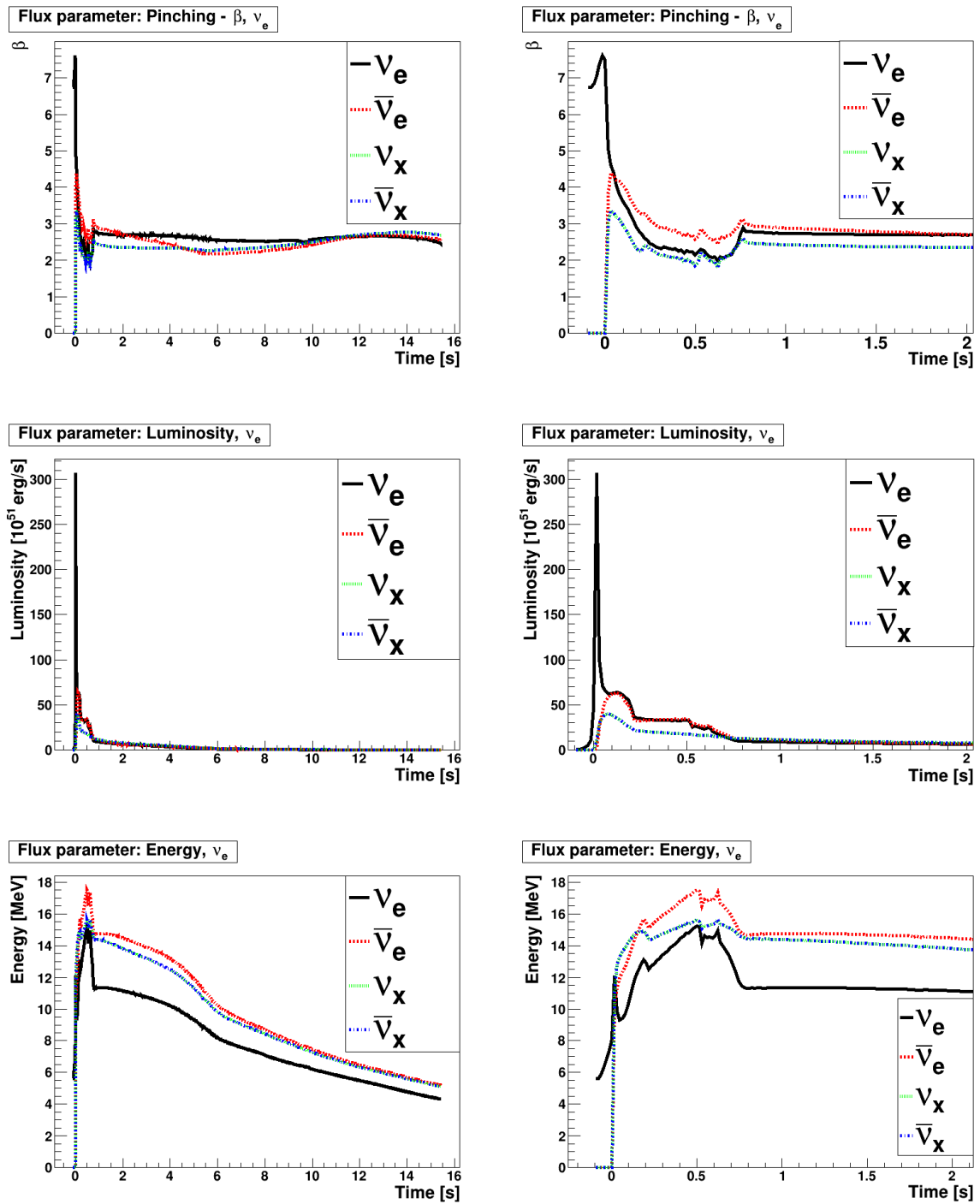
Figure 6.16: The flux parameters over time for the time-dependent go-to model as given by the Garching group: the pinching parameter at the top, luminosity profile in the middle, energy distribution at the bottom. These are essential for the `SNUGen` process to obtain number of events and energies. Plots on the right of the figure are zoomed over the first two seconds of the burst duration, where much bigger deviation is seen. Distributions are plotted per neutrino group, as described in 6.2.

Regarding the average energy $\langle E \rangle$ distributions, there is a brief period (approximately 0 to 0.2 s) that exhibits highest average energies from the ν_x and $\bar{\nu}_\mathrm{x}$ groups, however, from about 0.2 s onwards, $\bar{\nu}_\mathrm{e}$ displays the highest average energy by more than 2 MeV. In this case, the ν_x and $\bar{\nu}_\mathrm{x}$ are again identical. The ν_e distribution is almost identical to $\bar{\nu}_\mathrm{e}$ after the burst onset, however shifted to comparably lower energies. It should also be noted that the different burst phases strongly affect all flux parameters but are perhaps most visible in the energy distributions. After a somewhat violent burst period at the start, it is possible to observe a slow exponential decay in energies between about 1 to 6 seconds, subsequently, there is almost linear decrease.

Figure 6.17 displays the number of events for the go-to model, by the interaction channel. First thing to note is that while the electron elastic scattering and proton elastic scattering channels are available for all neutrino flavours, the inverse beta decay is only available to the $\bar{\nu}_\mathrm{e}$. Additionally, the electron scattering contribution is significant, relative to the other two channels. The shape of the distributions for different neutrino groups for ν - p and ν - e are somewhat similar with relative shifts between the groups, with ν_e producing a big visible peak (outburst of events) at the very beginning of the signal. The $\bar{\nu}_\mathrm{x}$ and $\bar{\nu}_\mathrm{x}$ have almost identical distributions.

For the ν - e channel, this is dominated by ν_e throughout and the general order is

$$\nu_e > \bar{\nu}_e > \nu_x = \bar{\nu}_x. \tag{6.32}$$

The ν - p channel has the same outburst at the start, followed by a period dominated by ν_x and $\bar{\nu}_\mathrm{x}$. Generally, the order after the initial peak is

$$\nu_x = \bar{\nu}_x > \bar{\nu}_e = \nu_e. \tag{6.33}$$

Most events are generated within the first second, with the majority within the first half-second. Again, the different phases of the burst strongly affect the event rate, causing visible changes to the spectra. There are several bumps visible for the first second, followed by fast drop (this seems to be faster for ν - e channel). There are fewer events after 2 seconds and almost none after 6 seconds.

The combined event distribution over time and the final energy distributions for all `SNUGen` interactions (for this particular model) are presented in Figure 6.18. It is clear that most events are produced via the IBD and ν - p interaction channels with much lower
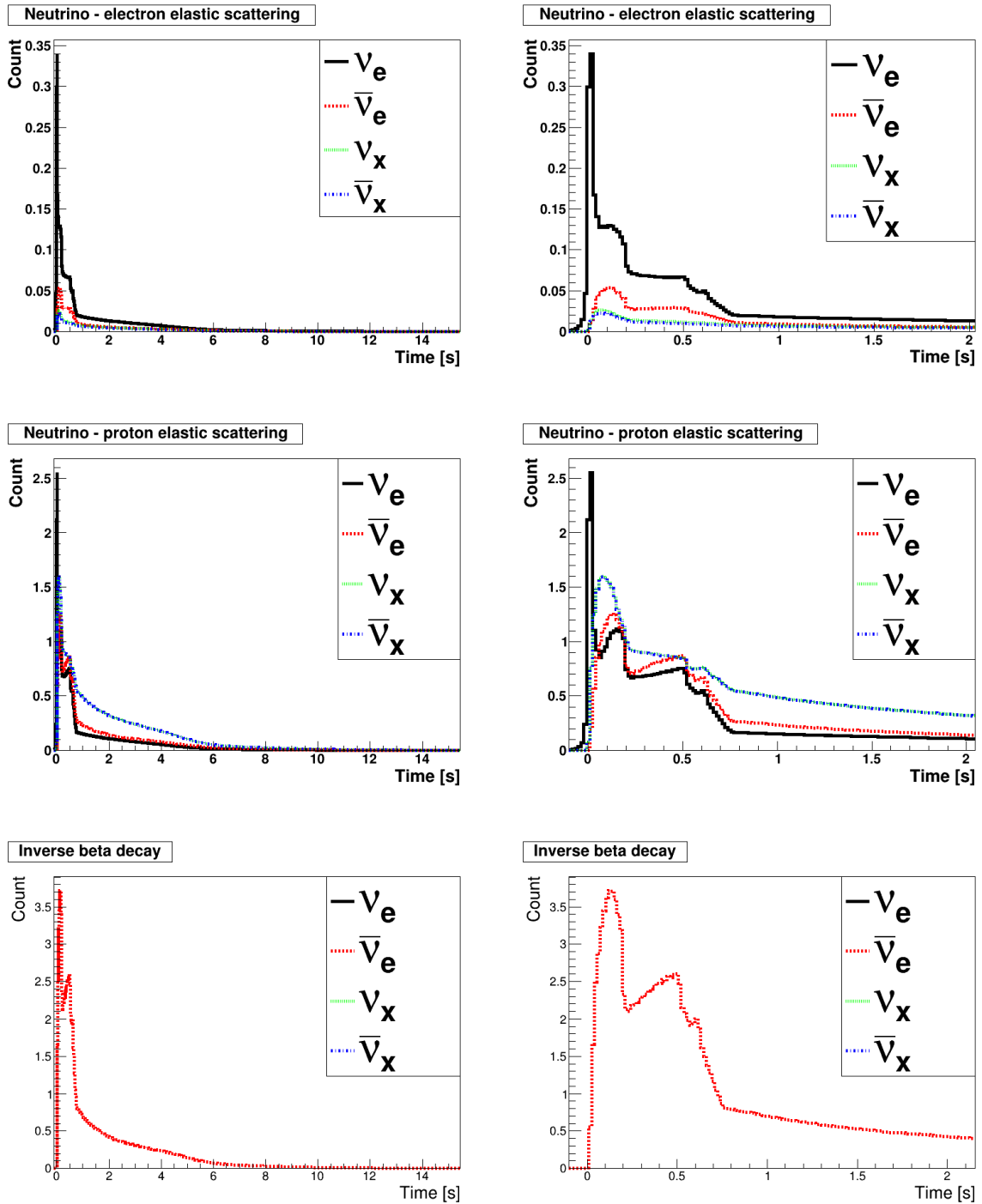
Figure 6.17: The event distributions as the function of time for the go-to model. Only the three interaction channels that are available for RAT are included. Right portion of the figure is zoomed over the first two seconds. Data is shown per neutrino group.
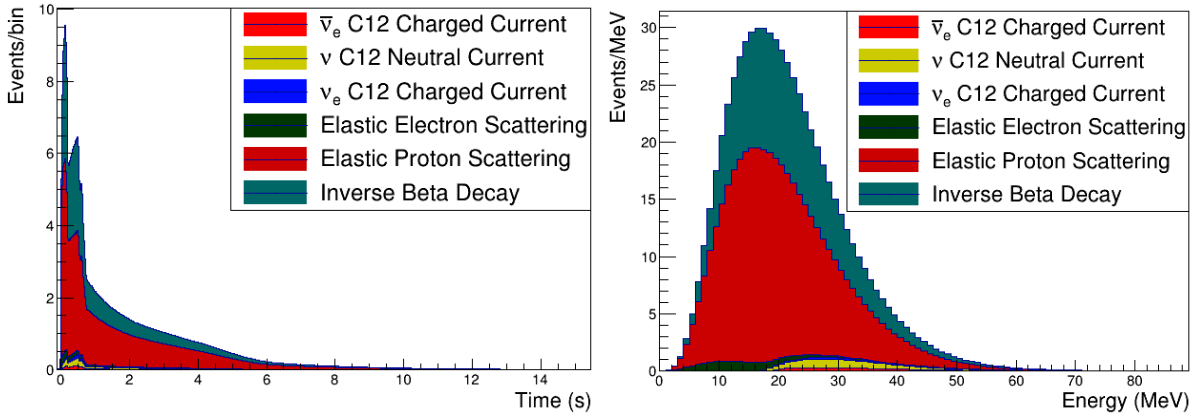
Figure 6.18: The overall event distribution over time and energy distribution for the go-to model. All interaction channels available to `SNUGen` are shown. The data is presented per interaction channel.
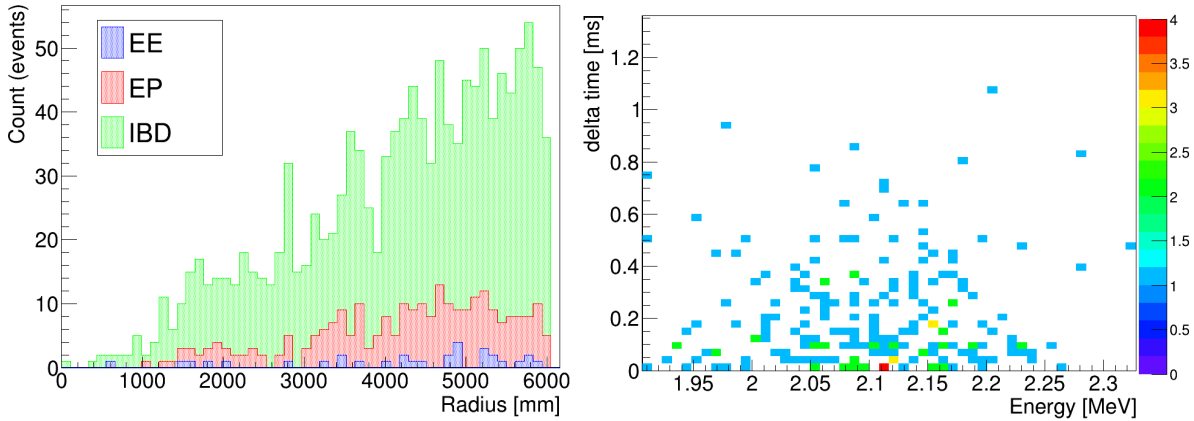
Figure 6.19: Fitting events using RAT for the go-to model. The uniform distribution of AV events up to the edge of the AV is shown on the left. The right plot shows the distribution of the IBD events around the neutron capture γ energy as a function of delta time.

contribution from ν - e. All ^{12}C contributions are almost negligible. Again, there is a turbulent period with high activity after the initial peak, followed by visible second peak. Afterwards, there is a fast drop-off period with subsequent slow decrease over longer time period.

The energy distribution is the same with respect to relative contributions. For the two main channels, the distributions seems to be represented by a skewed Gaussian distribution with a tail-like structure towards the higher energies. The IBD channel has a slightly higher mean. The interactions on carbon nuclei have significantly higher mean of the energy distribution but very small total count of events.

Reconstruction

The reconstruction of the go-to model has been outlined in Subsection 6.5.2 with some additional plots in the Figure 6.19.

Regarding the multiplicity of events (Fig 6.13) we see that specifically the IBD entries cause multiple detector events. This is expected as both daughter particles (neutron and positron) readily interact. The neutron's scattering on a proton, capture on the proton, positron's Cherenkov radiation, Bremsstrahlung and final annihilationism with electron all contribute to this count. Regarding the events inside the acrylic vessel, these are uniformly distributed (Fig 6.13, Fig 6.14, Fig 6.19). Figure 6.14 highlights both, the times these events are detected at, alongside their associated number of hit PMTs (NHit). For the time, most events come very early on and most within the first 2 seconds. There are clear groups of events, specifically below 300 NHit, around 1000 NHit and between the 2000 to 8000 NHit. With respect to the reconstructed energy (Fig 6.15), the higher portion of the spectrum consists almost entirely of IBD events. The neutron capture peak is visible at approximately 2.2 MeV. The IBD tagging is further described in Subsections 6.8.1 and 6.8.2.

Using Burst Trigger

The go-to model data was analysed using the `Level 3 burst processor`. This would be an output similar to capturing real SN signal, if it's analogous to the model. Plots are presented in Figure 6.20.

Some of the more obvious observables can be seen in the plots (Figure 6.20). These observables are:

- The events are uniformly distributed;

- Most events come early in the burst (most under two seconds);

- The highest peak in NHit distribution is at very low NHit: these are mostly ν - p events and scatters;

- There is a clear peak at 1000 NHit, corresponding to the neutron capture from IBD events;

- There are several higher energy events, with broad distribution between 2000 to 8000 NHit - these are the positron energies from IBD events.
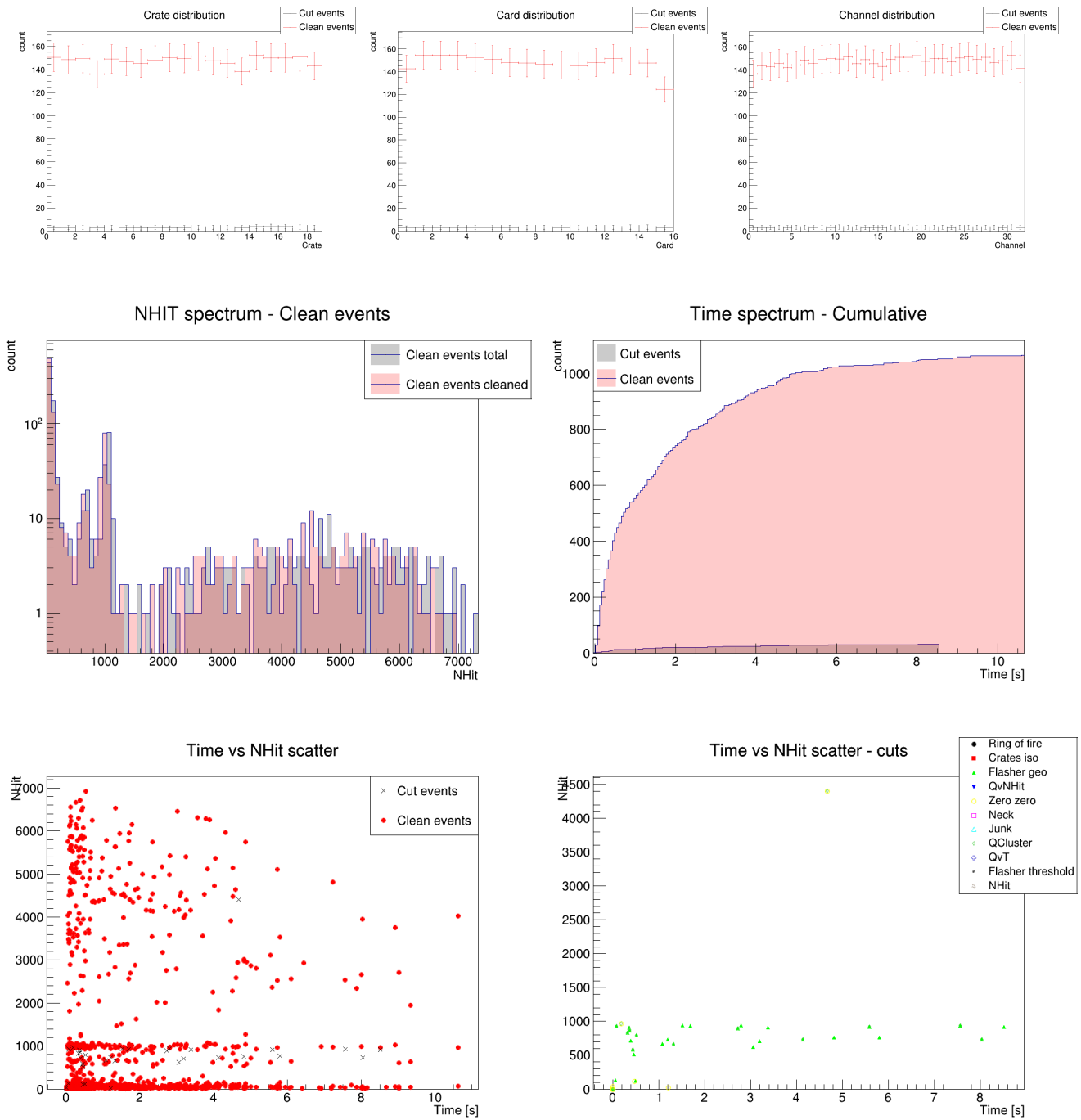
Figure 6.20: Using `Burst Trigger` processor on the go-to model. The expected features of a SN signal can be observed from the simple analysis by the `BT`. Bottom plots show the results of data cleaning applied on the burst.

Regarding data cleaning, 97.7% of all recorded events would be marked as clean by currently applied data cleaning. There is a total number of 1411 events, with 32 events flagged and cut. Regarding the high NHit events (> 500 NHit), which are used to determine whether to post the final alarm (including alert to SNEWS), 30.5% of all events were high NHit, with 93.7% of them surviving the data cleaning. The current thresholds for final alarm are at least 60% surviving, and at least 4 such events. In this case, a final alarm would be issued.

6.5.4   Hierarchy study

The effect of the hierarchy - or neutrino mass ordering - on the SN signal is probed in this subsection. Because the neutrino ordering is unknown at the time of writing of this thesis, the possibility of extracting the hierarchy given a detected SN signal by SNO+ is evaluated.

Two models are considered, the LS-s27.0co (go-to) model and LS-z9.6co model. Both models include the mixing-length treatment of proto-neutron star convection [123]. As was the case for the study of `BT` efficiency (Section 5.6), the models are chosen as example cases for the iron core-collapse SN and an electron-capture (EC) SN.
The settings to generate the signal data were kept in line with other studies: distance set to **10** kpc, **all available interactions** are considered, the time and energy methods are 1 and 2 respectively, 1000 time bins are used and **6% energy resolution** is assumed. Only the **scintillator portion** (the AV) of the SNO+ detector is considered. The time of the simulation is normalized for the shorter model.

The focus of the comparison is the IBD events as these are the easiest to tag. The full reconstruction method is detailed in Section 6.8. The comparison for go-to model is shown in Figure 6.21 while the EC SN is shown in 6.22. In both cases the normal ordering case produces more events although the energy distributions are fairly similar. The difference is much more pronounced for the go-to model, suggesting this is heavily model dependent. The ability to distinguish the hierarchies is, therefore, mostly driven by the shape of the event distribution of the IBD interaction channel. If there are special features to the shape, as is the case for the go-to model, these could be told apart by a fit to the number IBD events over time of the SN signal (details in Subsection 6.8.6). It should be mentioned that the `SNUGen` input parameters are identical. More detailed study is presented in [43].
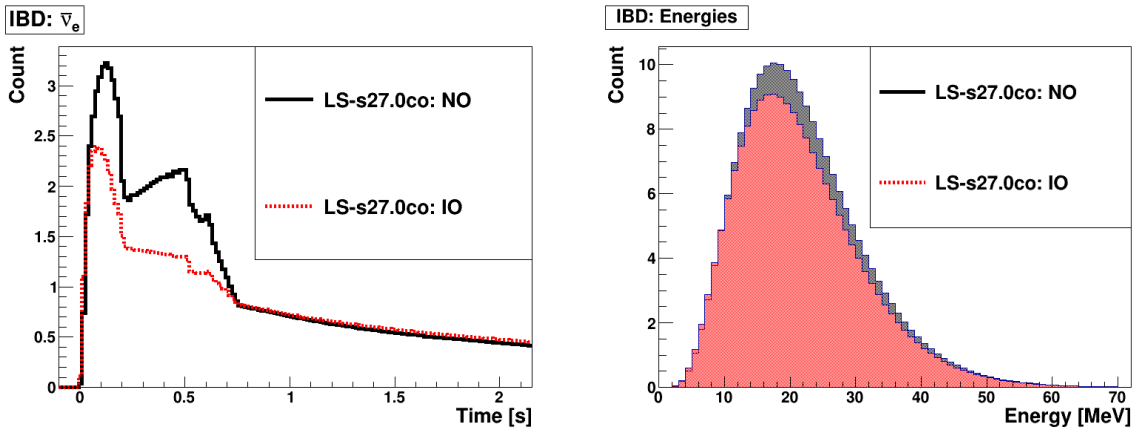
Figure 6.21: Comparison of the effect of the choice of neutrino mass ordering for the LS-s27.0co model. NO refers to the normal ordering, IO is the inverted ordering. IBD related distributions shown only.
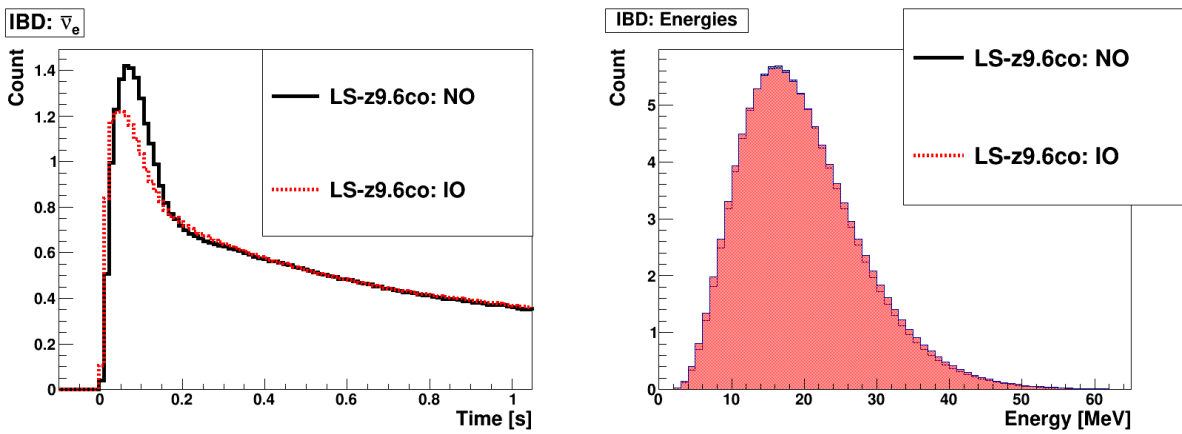
Figure 6.22: Comparison of the effect of the choice of neutrino mass ordering for the LS-z9.6co model. NO refers to the normal ordering, IO is the inverted ordering. IBD related distributions shown only.

6.5.5 Equation of State study

The choice (or in many cases new definition) of the equation of state has significant effect on the outcome of SN simulation. This is due to complexity of the SN as such and the extreme conditions that are present during the explosion, ranging from density several times that of the nuclear saturation density, the presence of strange baryons, strangeness and issues with convergence. Because many processes are still not fully understood the SN EOS tend to vary. The EOS also affects whether the explosion is successful or not [175]. The consequences of using different EOS to generate SN signal are analysed here. The same overall settings were used to investigate the effect of the equation of state.

The comparisons are shown in Figure 6.23 for the lighter s11.2 progenitor and in Figure 6.24 for the more common s27.0co progenitor. The first noticeable effect of the use of different energy of state is the change to the flux parameters: luminosity $\mathcal{L}$, the pinching parameter β and the mean energy $\langle E \rangle$. These are altered due to the changes to the physical processes behind the explosion. Overall, the SHEN models tend to have higher pinching parameter resulting in lower number of events and slightly lower mean energy, except for the later parts of the burst in the s27.0co progenitor case.

Regarding the observables, the effects are of similar order as the effect of different hierarchy. The LS models generally express a slightly higher mean in the energy distribution and achieve higher maximum energies but the differences, at 10 kpc, are not very significant. For the distribution of $\bar{\nu}_e$ IBD events, both progenitor display features in the distribution, which are generally the traits that can be detected when reconstructing the data. These are, as most other observables, strongly dependent on statistics.

6.5.6 Study by distance

Statistics are, naturally, strongly dependent on the distance of the SN explosion to the detector due to the inverse proportionality between the intensity and distance. The effect of varying the distance for a single SN model is shown in Figure 6.25. The model used is the LS-s27.0co. All settings - baring the distance - are kept constant. The distance is in this case the independent variable, while the IBD related observables are the dependent variables.

Figure 6.25 clearly shows that the mean of the energy distribution and the width remain unchanged, only the number of the events is changed. Regarding the shape of the
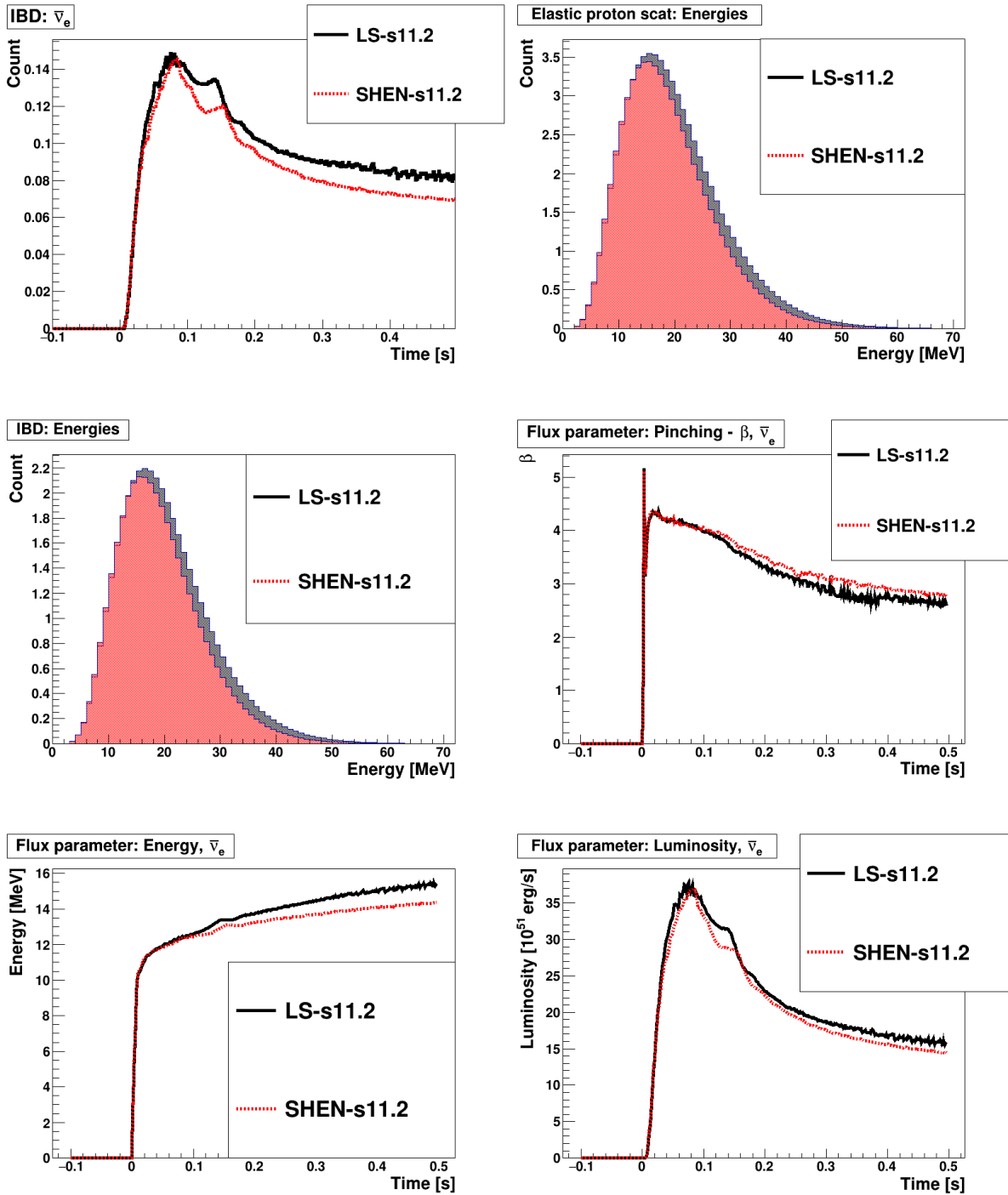
Figure 6.23: Comparison of the effect of the equation of state on the LS-s11.2 model. LS refers to the Lattimer-Swesty [166], SHEN refers to the stiffer Shen [168] EOS. The input parameters differ in this case and are also shown.
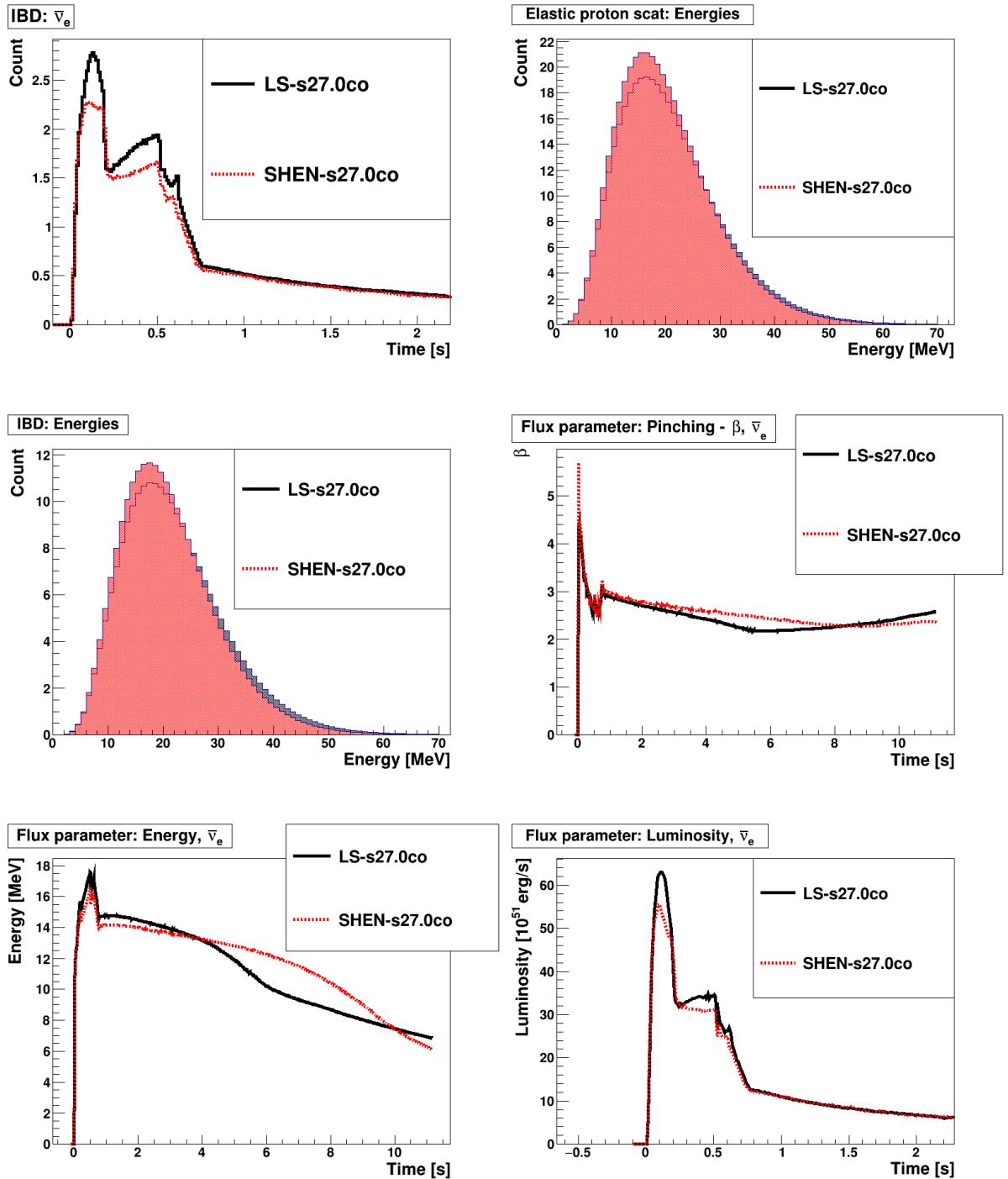
Figure 6.24: Comparison of the effect of the equation of state on the LS-s27.0co model. The input parameters differ in this case and are also shown. The event distribution is zoomed over the first two seconds, where most of the features are visible.
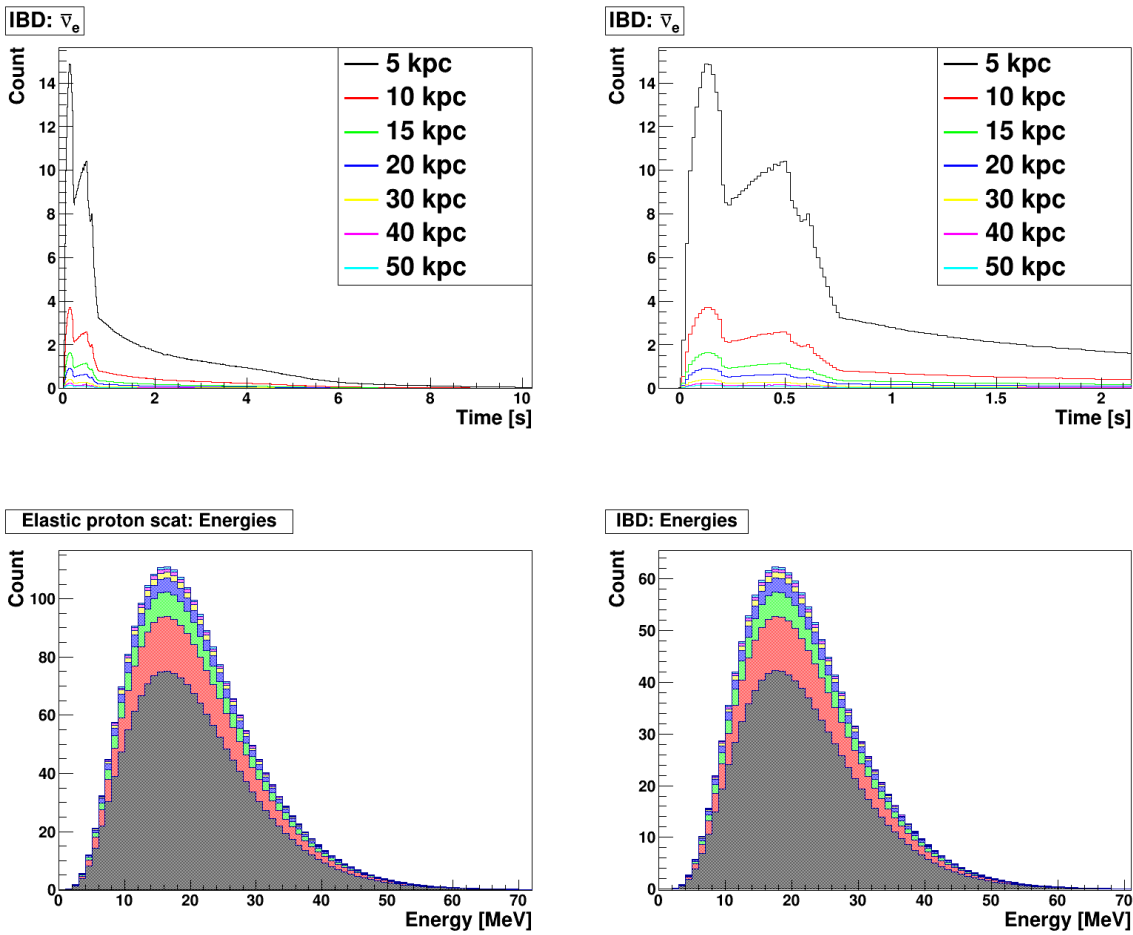
Figure 6.25: The effects of varying the distance of the SN explosion to the SNO+ detector, for the LS-s27.0co model. Seven distances are analysed, only relevant observables for detection with SNO+ are shown. In this case, the energy distribution plots (bottom half) uses the stack drawing option. Top right plot is zoomed over the first two seconds, where most of the features are visible.

distribution of events, this is also unchanged, only the amplitude changes (global shift of the whole distribution). If the event distribution can be reconstructed (more on that in Subsection 6.8.6), the distance of the exploded star could be estimated. This is obviously more accurate for closer SNe.

The effects of the distance on the SN signal are also shown in the trigger efficiency study, Section 5.6.

To conclude the studies of the effects of various parameters: some consequences of the parameters can be observed. This is especially true if the affected observables include IBD events and IBD energy distribution since these are easily tagged. It should be mentioned that different parameters can convolve and cannot always be separated. Therefore, to extract an observable, some knowledge of the data is required. For example, it is possible to extract the distance if a model (type) of the progenitor is known. Similarly, the hierarchy can be fitted for if the model is known. If both the progenitor and the distance are well known, it could be possible to point towards which EOS is more accurate. All in all, there is lot to be gained from detection and reconstruction of SN signal, especially since SN physics is heavily data limited. However, collaboration between the neutrino experiments and the astronomy community is preferred to maximize the potential learning.

6.6   Supernova backgrounds

This section aims to describe the major contributions to the background for a SN signal in the SNO+ detector. The advantage of a SN signal is high overall energy of the events, especially for the IBD channel (relative to SNO+). Because most backgrounds are typically low energy, with orders of magnitudes lower rates considering just the timespan of a SN burst, the contamination of the signal is relatively low if reasonable volume cuts are applied. In addition to this, significant source of the background is the AV itself, while the SN signal can be detected across the detector.

Detection of the IBD channel will be considered separately as the backgrounds for it are significantly different.

Additionally, the effect of the addition of the PMT noise is studied.

6.6.1   IBD channel

The IBD interaction channel is almost background free due to the high energy. There are two types of backgrounds: true IBD events and mimicked IBD events, and both types can

be caused by SN and non-SN events. The non-SN IBD events are caused by geo neutrinos and reactor neutrinos. These are expected to reach a rate $\mathcal{O}(10^{-5})$ ktonne$^{-1} \cdot$ s^{-1} [144, 54, 141] and, being several orders of magnitude lower than the SN IBD rate, can be fully neglected.

True IBD events

The background coming from the **true IBD events** is created by the $\bar{\nu}_e$-induced inclusive ^{12}C transition. In this case the incoming neutrino energy is not unequivocally assigned to positron energy as in the case of the more common IBD of a free proton. In addition to that, due to combination of positron signal and quenched proton recoil events, no distinct prompt energy can be assigned to the parent neutrino. However, because the event signature is identical, these true ^{12}C transitions form a source of background to the SN IBD channel. The predicted rate for this reaction is 0.1 ktonne$^{-1} \cdot$ s^{-1} [28]. This is highlighted in Figure 6.26.

Mimicked IBD events

Scattering of neutrinos on ^{12}C and random coincidences with uncorrelated events can create **mimicked IBD events**. The fast neutron, released from the inclusive ^{12}C transition, produces the prompt signal via proton or carbon scattering, followed by the capture signal once it thermalizes. The expected rate is 0.3 ktonne$^{-1} \cdot$ s^{-1} [28] and as such is the largest background to SN IBD events. Regarding the random coincidence events, where an uncorrelated event can fulfil the IBD coincidence trigger condition by chance, the rate of these depends on the rate of the events and the specific conditions of the coincidence trigger. The observed rate for non-SN events found in detectors such as Borexino and KamLAND was found to be $< 10^{-6}$ ktonne$^{-1} \cdot$ s^{-1} [141, 144]. These rates were considering lower energy distributions, and because the rate of events from radioactive backgrounds drops rapidly with higher energies, the real rate of these events should be even lower for SN IBD events. Random coincidences from SN events depends on the SN distance. The rate for these was estimated in [28] to be 6.4×10^{-5} ktonne$^{-1} \cdot$ s^{-1} and is, therefore, negligible compared to IBD signal rate.

To summarize, the IBD interaction channel for SN neutrinos is almost completely background free. The highest contributor to the background is the inclusive ^{12}C transition.
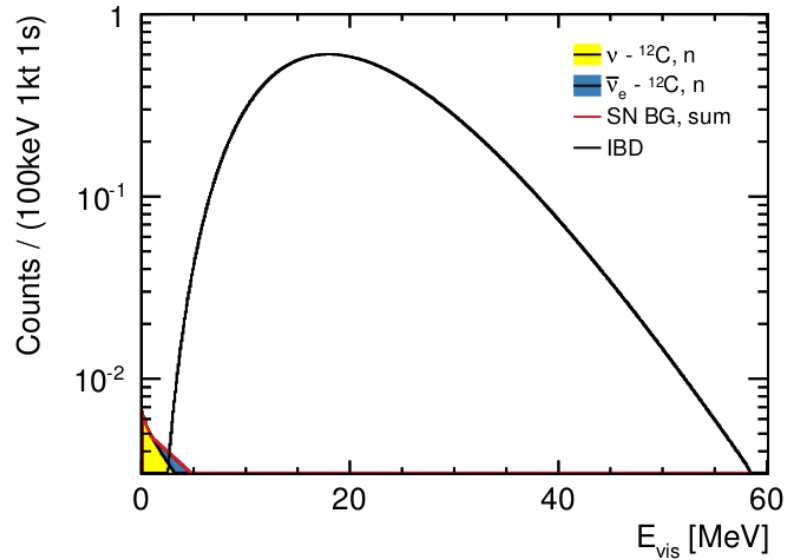
Figure 6.26: Comparison between SN IBD signal and self-induced backgrounds consisting of inclusive ^{12}C transitions. An energy resolution of $\frac{6\%}{\sqrt{E_{\text{vis}}(\text{MeV})}}$ was assumed. Figure from [28].

This results in a rate of (0.4 ± 0.1) ktonne$^{-1} \cdot$ s^{-1} [28]. Considering usage of IBD tagging and possibly an energy cut, this is insignificant.

6.6.2 $\nu - p$ and $\nu - e$ scattering channels

Other interaction channels are more sensitive to the backgrounds due to the lower overall energy and no clear tagging options. The background events due to the detector itself (ropes, steel structure, PMTs) were measured to be negligible [43]. However, the intrinsic radioactivity of the scintillator and the events from the surfaces of the acrylic vessel form backgrounds at the energy range of the scattering events caused by SN neutrinos.

Intrinsic scintillator background

Linear alkyl benzene (LAB) is the liquid scintillator used in SNO+. A small percentage of the carbon atoms within the organic compound is the ^{14}C isotope (about 10^{-18} g/g$_{\text{LAB}}$ [43]). It cannot be removed by any chemical purification procedure and, therefore, forms an isotropic background of low energy. The decay's endpoint is 0.16 MeV [176] with a half-life of 7730 years [177].

AV backgrounds

The origin of the background events from the surfaces of the AV is radon. Radon atoms were embedded within the AV during the construction of the SNO detector, when it was

exposed to the mine air that is rich in radon. This was not a problem for SNO, where the tolerance for low energy backgrounds was high due to it being water Cherenkov detector, affected by the Cherenkov threshold. This is 0.8 MeV for electrons, 160 MeV for muons and 1400 MeV for protons [178]. The radon decay chain consists of several steps, most of which release energies well below the Cherenkov threshold. These are relevant for SNO+, having $\sim50\times$ times higher light yield in scintillator phase compared to SNO, looking at fundamental physics processes at lower energies with greater resolution [77]. Removal of the radon daughters was investigated during SNO+ water phase but was found to be prohibitive [43].

The decay chains of two most common radon isotopes are shown in Figure 6.27. In addition to several isotopes having long half-lives, the radon daughters exist in ionic form and tend to deposit on to the acrylic, implanting ~100 nm below the surface [77]. The most significant isotopes to the background are the ^{210}Bi and ^{210}Po. ^{210}Bi is a daughter particle of ^{210}Pb, formed by β^- decay with $T_{1/2} = 22.26$ years and $E = 0.06$ MeV. ^{210}Bi then decays into ^{210}Po through another β^- decay, with $T_{1/2} = 5.01$ days and $E = 1.16$ MeV [179]. Finally, a stable ^{206}Pb is produced via α decay, releasing α particle with 5.30 MeV endpoint energy and $T_{1/2} = 138$ days.

This lead chain forms two different backgrounds. The more significant one is when the radon daughters embedded within the AV decay and deposit energy into the scintillator. These are termed AV surface backgrounds and due to the location can be reduced with a fiducial volume cut [43].

The second source is leaching[7], where nuclei from the acrylic can leach into the scintillator. This was tested with a table top setup and the leaching rates were measured [77, 181]. The rates are being controlled with several assays[8] throughout the experimental running. The main mitigation strategy is rigorous purification of the deployed material, including recirculation of the water inside and outside of the AV [77].

The predicted rates for the radon daughters are shown in Table 6.8. The bulk type indicates the leached events while the AV surface corresponds to the embedded atoms within the AV. Additionally, the reconstructed energies for these events are shown in Figure 6.28. It can be seen that the bulk events are not very sensitive to the radial

---

[7]Leaching in this context means loss or extraction of the material from a carrier into a liquid.

[8]An assay is an investigative procedure for assessing and/or measuring the presence, amount, or functional activity of a target entity.0
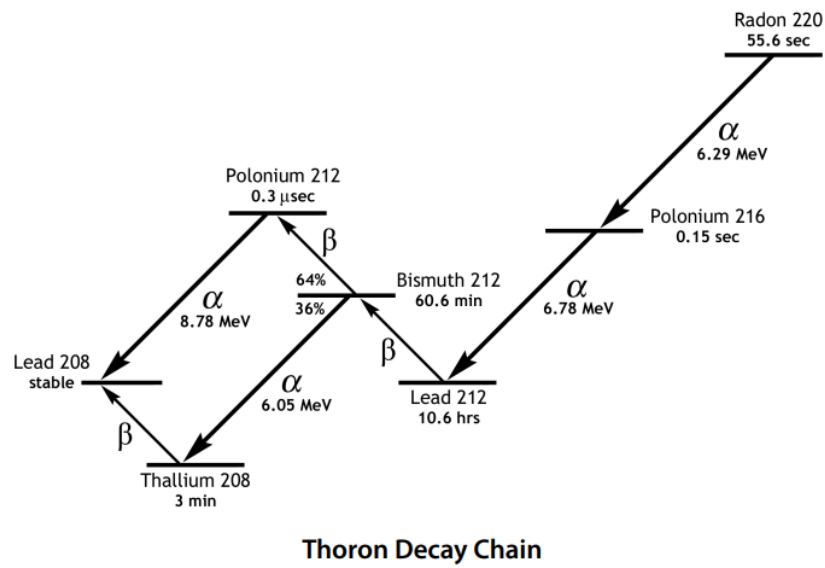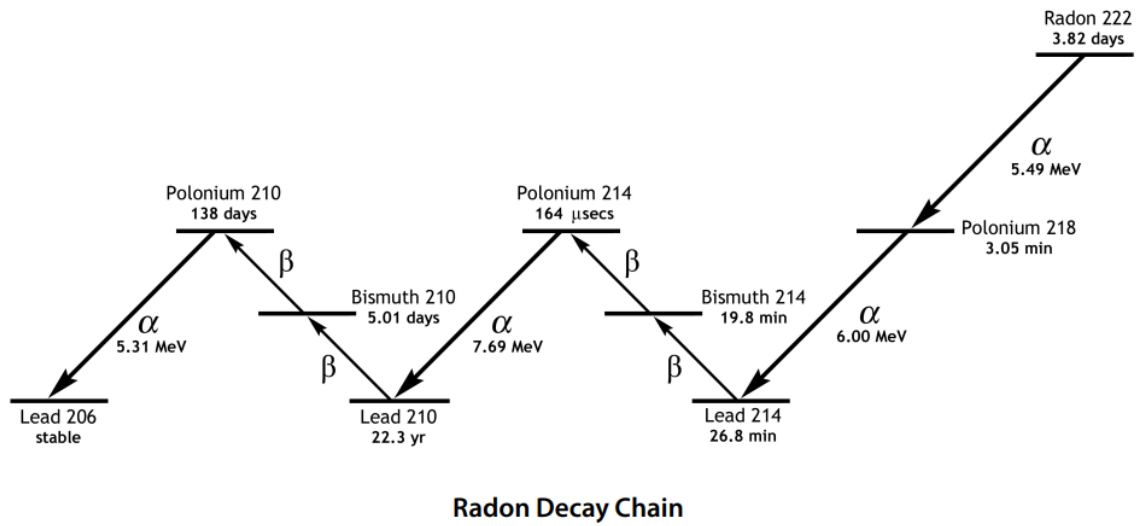
Figure 6.27: Decay chains of two most common radon isotopes: ^{222}Rn and ^{220}Rn, produced from uranium and thorium decays respectively. Figure from [180].

Isotope	Type	Rate [yr^{-1}]	Rate [Hz]	Count in 10 s, 5.3 m FV [%]
^{14}C		4.08 x 109	129.29	78
^{210}Pb	Bulk	1.93 x 108	6.12	85
^{210}Bi	Bulk	1.93 x 108	6.12	70
^{210}Po	Bulk	2.03 x 108	6.43	68
^{210}Pb	AV surface	3.04 x 1010	963.34	35
^{210}Bi	AV surface	3.04 x 1010	963.34	5.3
^{210}Po	AV surface	3.12 x 1010	988.69	1.8

Table 6.8: The raw expected rates for the backgrounds relevant for a SN burst during the pure scintillator phase of SNO+. The numbers are obtained from [182] and additional discussion is available in [61] and [28]. Additionally, the last column represents the remaining percentage of events after 5.3 metres FV cut is applied.
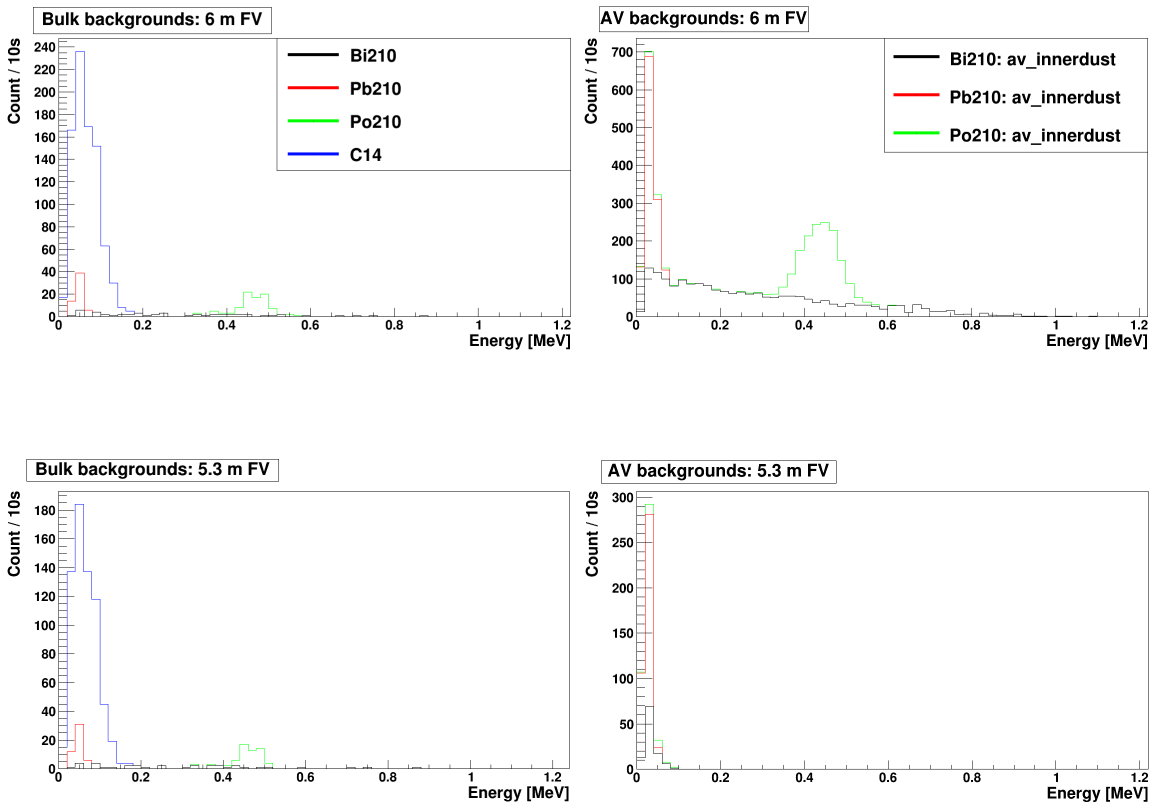
Figure 6.28: Reconstructed energies for both bulk and AV surface backgrounds relevant for SN signal in SNO+. The total counts are reconstructed for the duration of 10 seconds. The top portion considers 6 meters fiducial volume while the bottom only counts events within 5.3 meters.

# Events	Clean events		High NHit	Survived		Length [s]	NHit(avg)
1284	1107	86.21%	405	401	99.01%	13.8334	1136.11
1300	1113	85.62%	405	401	99.01%	13.8334	1130.59

Figure 6.29: Addition of PMT noise to a SN MC burst. The top row is the original burst while the bottom row is the same datafile with the addition of PMT noise.

cut while the events embedded in the AV reconstruct closely to the AV. The effect of surface events, therefore, can be minimalized by using appropriate radial cut. The bulk backgrounds are quite isotropically distributed and the decrease in the total count is proportional to the total volume (plots are not normalized per volume). These, therefore, cannot be cleaned with a radial cut, but because they are very low in energy, a reasonable energy cut would dispose of them.

6.6.3   PMT noise

Additionally, to simulate real detector response as precisely as possible an introduction of PMT noise to the burst data was made. The PMT noise is an intrinsic noise rate, often referred to as dark current, which results from thermal excitation at the single electron level. These thermal electrons can mimic a photoelectron from the PMT's photo-cathode. Because of this, these noise hits cannot be distinguished from true hits caused by incident photons [183].

There is a RAT processor available to add PMT noise at rate and distribution that was measured to reflect the real rate. The addition of this effect to the SN MC is presented in Figure 6.29.

The effect of the PMT noise addition is (as expected):

- There is an increase in the total number of events (16 new events);

- There is slight increase in clean events (10 get cut, 6 are flagged clean);

- These noise events do not affect the high NHit portion of the burst (all new introduced events are low NHit);

- The average NHit of the burst is lowered (the noise events are low NHit).

Therefore, if such events are present during data-taking of real SN burst, these will definitely not affect the triggering efficiency and, given an energy cut, will not affect reconstruction and fitting in any way.

6.7 Signal to background analysis

This section analyses SN signal data compared to the backgrounds. The signal data is obtained using `SNUGen`. Two backgrounds sources (data files) are considered. One is obtained using available MC for backgrounds with the predicted rates. The duration is set to ten seconds, in line with the length of the SN signal. The other one is obtained from data recorded during a period of relatively high backgrounds.

6.7.1 Backgrounds - MC

The MC backgrounds come from the available generators used to mimic the expected backgrounds. The geometry is set to be the fully filled SNO+ detector with scintillator. The rates are as expected during the scintillator phase. In addition, other detector settings, such as the trigger thresholds, the concentration of PPO, and the number of online PMTs are all set to fully reflect the real conditions as were at the time of generating the backgrounds dataset.

The sources of the backgrounds that were included are the acrylic vessel itself, the LAB, the dust, hold up and hold down ropes, PMTs, external water, rocks and air. All (radioactive) isotopes that are available for MC production were added, this includes: ^{228}Ac, ^{39}Ar, ^{8}B, ^{7}Be, ^{210}Bi, ^{212}Bi, ^{214}Bi, ^{11}C, ^{13}C, ^{14}C, ^{17}F, ^{13}N, ^{15}O, ^{18}O, ^{40}K, ^{85}Kr, ^{234}Pa, ^{210}Pb, ^{213}Pb, ^{214}Pb, ^{210}Po, ^{212}Po, ^{214}Po, ^{216}Po, ^{218}Po, ^{224}Ra, ^{226}Ra, ^{228}Ra, ^{220}Rn, ^{222}Rn, ^{130}Te, ^{228}Th, ^{230}Th, ^{232}Th, ^{234}Th, ^{208}Tl, ^{210}Tl, ^{234}U, ^{238}U. Backgrounds from solar neutrinos, $\beta - \gamma$ and $\alpha - n$ processes are also included. As mentioned, all available generators were used to create 10 seconds of data, using currently estimated rate. The data was then combined.

The reconstructed data from this simulation is shown in Figure 6.30. It can be seen that the majority of the events are around the edge of acrylic vessel. Regarding the energy, almost all of the events fall below 1 MeV, with few higher energy events being again positioned close to the AV.

6.7.2 Backgrounds - Data

The 'background' to the SN signal was also estimated from real detector data (that is not SN signal). To take the worst possible set, the data was taken from a period of high overall backgrounds, just after the completion of the bulk fill with scintillator. Several scintillator and water recirculations were taking place and the overall activity was high
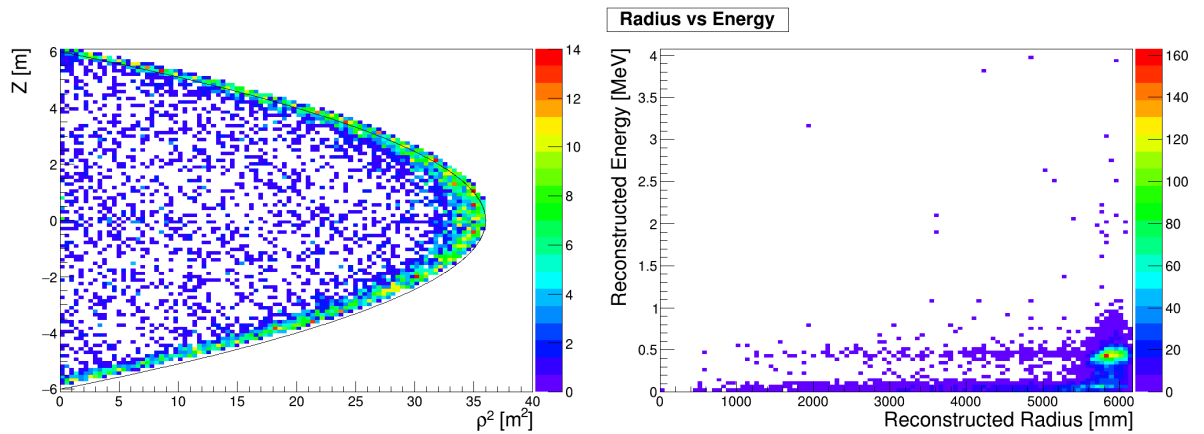
Figure 6.30: Reconstruction of 10 seconds of background events from MC simulation. All backgrounds available for simulation are included with current best estimates of the rates for the SNO+ inner AV region filled with pure scintillator. Detector settings are identical to real running conditions at the time.
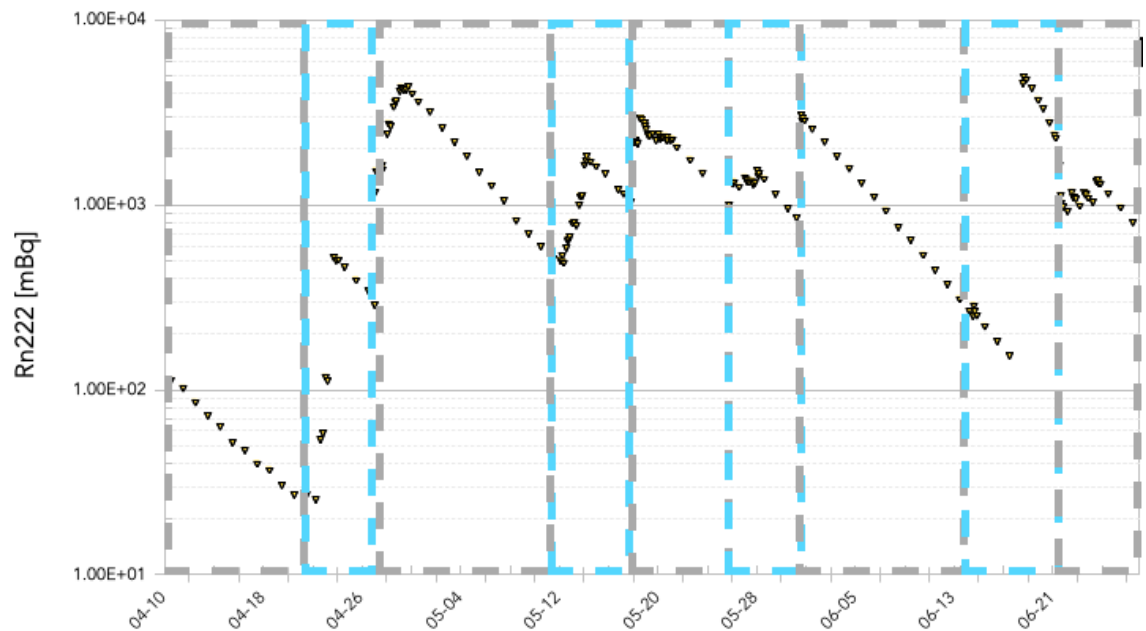
Figure 6.31: Measured ^{222}Rn background for the SNO+ detector over the period of approximately three months when the scintillator filling was nearing completion. The measured data is obtained from SNO+ backgrounds group after verbal communication.
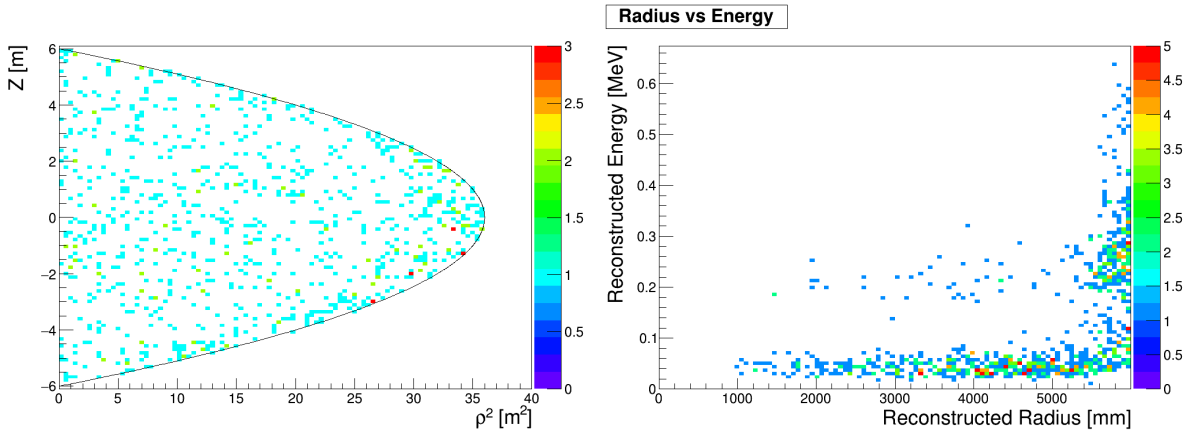
Figure 6.32: Reconstruction of 10 seconds of real data taken by SNO+ detector during a period of highest ^{222}Rn background just after scintillator fill was completed. Only the events inside the AV are considered.
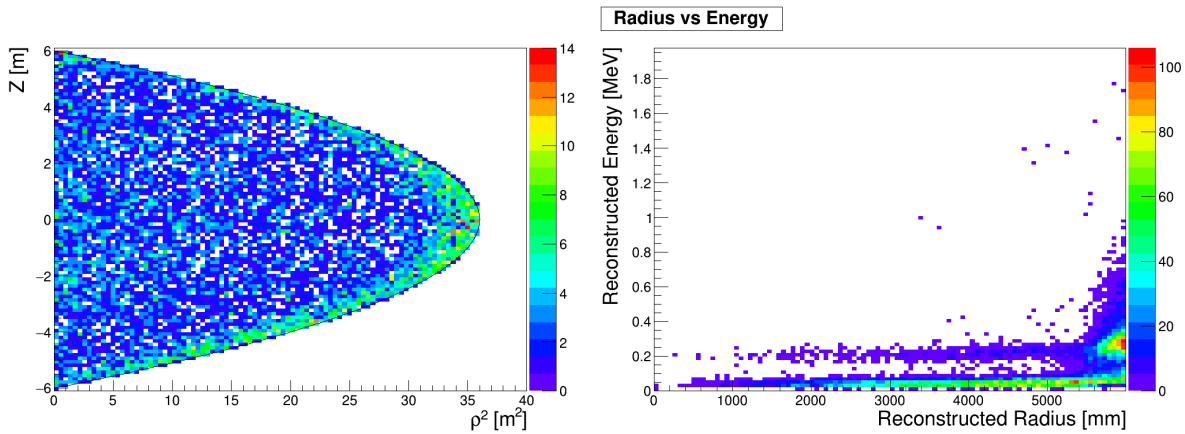
Figure 6.33: Reconstruction of a single subrun (approximately 1.5 minutes) of real data taken by SNO+ detector during a period of highest ^{222}Rn background. Only the events inside the AV are considered.

compared to periods before. This is highlighted in Figure 6.31. The data considered in this subsection is part of run 271122, taken on 23$^{\rm rd}$ May 2021.

To describe the detector conditions at the time: the bulk scintillator fill has just recently completed, there is a high radon rate (measured at later date) at this date, the AV recirculation (usual reason for radon ingress) is ongoing, there is little remaining water puddle at the bottom of the AV that is being drained, and the PPO concentration is uniform. ^{222}Rn and ^{212}Pb are the only backgrounds that seem to have the position changing with time. ^{210}Po and ^{210}Bi are uniform. ^{222}Rn is the major contributor to the backgrounds.

Figure 6.32 shows events reconstructed from this exact period, for the duration of 10 seconds, to match the likely SN signal (and also the length of the go-to model data). In
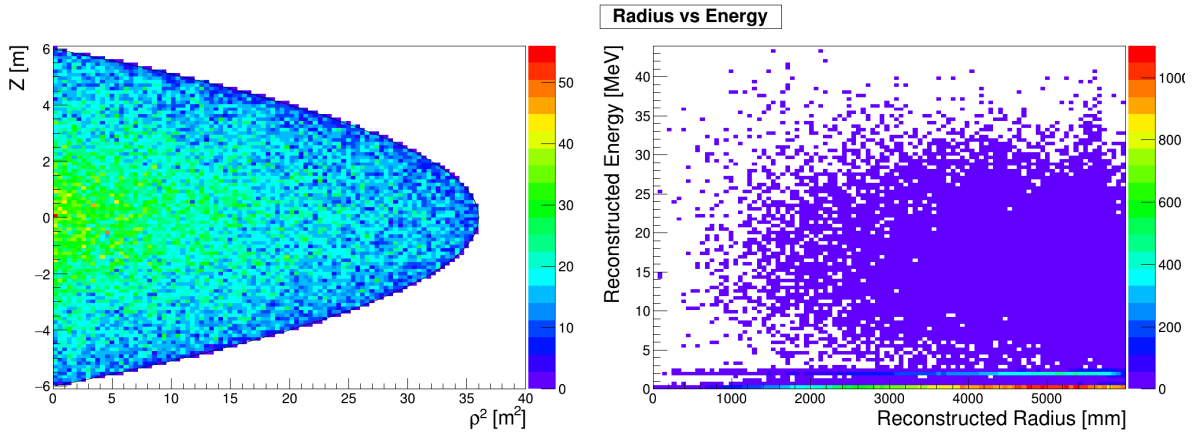
Figure 6.34: Reconstruction of 100 simulations of SN go-to model (LS220-s27.0co). Only the events inside the AV are considered. Detector settings are identical to real running conditions at the time of highest backgrounds.

addition to that, data from a full subrun - approximately 1.5 minutes[9] - is available in Figure 6.33. While the 10 seconds of data does not show as clear of a correlation with the edge of the AV, this is clearly visible for the full subrun set. The energies in this case are lower than the simulation for the backgrounds with all events being below 2 MeV.

6.7.3 Signal - MC

The SN signal was generated using `SNUGen`. One hundred bursts of the go-to model (LS220-s27.0co) were generated for better evaluation of the statistics, these are averaged (where appropriate) to get values corresponding to a single burst. The settings were kept constant at 10 kpc, normal hierarchy with no MSW effect. As with other sets, only the internal events (events within the AV) are considered. The detectors settings (including thresholds, status of the PMTs, PPO concentration and geometry) were set to reflect the real conditions as during the data taking of other datasets.

The reconstruction of the SN MC signal is presented in Figure 6.34. There are visible differences between the SN signal data compared to any set of the background data. The events are more uniformly distributed, with no clear increase in the number of events around the AV edge. The energies are significantly higher, with (at least) three distinct groups: below 1 MeV, around 2 MeV and at higher energies between 3 to 40 MeV (these correspond to the NHit peaks mentioned in Subsection 6.5.3).

---

[9]The average length of a subrun is between 4 and 5 minutes currently, however, this was the last subrun in a run, which is usually shorter.
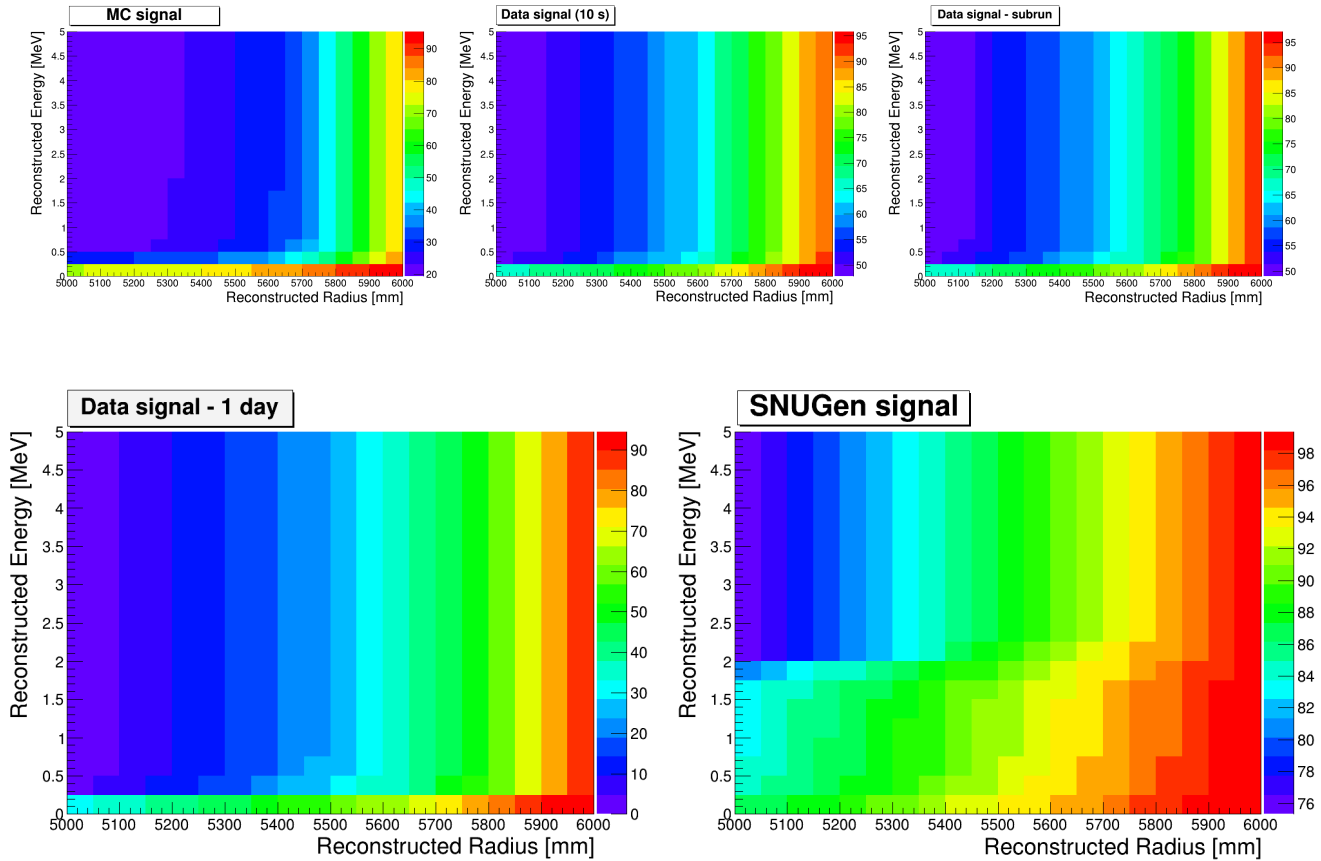
Figure 6.35: Analysis of distribution of SN background events to SN signal events. The plots show reconstructed radius versus the reconstructed energy. The z-axis scale shows the remaining percentage of events up to the specific value. Five datasets are shown (from top left): backgrounds MC results (10 s), real data (10 s), real data (1.5 minutes), real data (1 day) and `SNUGen` MC (10 s, 100 bursts).

6.7.4 Signal comparison and cuts

Finally, all previously introduced datasets are plotted in the form of reconstructed energy against the reconstructed radius in a cumulative format, Figure 6.35. The idea is to use these distribution to make it possible to suggest a sensible cut - both in terms of radius and energy - that would cut most of the background events while preserving the SN signal. The z-axis (colour) represents the percentage of surviving events of each particular set, if a cut was made at the specific selection of radius and energy. For example, looking at the very first plot in the figure (MC signal), only about 20% of the events are above 0.5 MeV, within the 5.3 meters.

To obtain the final values of cuts, the bottom plots of Figure 6.35 are considered. These represent one full day of real detector data during a period with of backgrounds (a likely worst case scenario) and a SN signal, consisting of 100 burst to increase the statistics. The

suggested radial cut to use would be approximately 5.3 meters and the energy cut around 1 MeV is advised. These values would cut ∼85% of backgrounds while ∼88% of SN signal would be preserved.

It should be noted that a function extracting the most efficient cuts could be made at this point, however, because a significant factor in this study is reconstruction efficiency, which is to be improved for the full scintillator fill, there is no urgent need to do so at this point.

6.8   SNO+ sensitivity

The sensitivity of SNO+ to SN signal is evaluated here. The applied method uses the IBD events from SN signal, applies tagging to distinguish such events, and attempts to reconstruct these events. Finally, after accounting for the difference between the visible and true neutrino energy, the reconstructed events are compared with the original distributions.

This could, in essence, serve as an inspiration for potential `Level 4 Burst Trigger` - a set of analysis methods to extract observables from detected SN signal.

There are several reasons to only use IBD events, even at the cost of lowered sensitivity. These reasons are:

- These are the highest energy events and, therefore, are (likely) easier to be detected;

- The IBD interaction channel contributes the most to the total number of events;

- Due to the two reasons above, in the case of SN that is farther away, these would contribute the most to the signal;

- There is a clear tagging option available for these events (described in 6.8.1);

- The impurity becomes lower as the distance becomes greater [43];

- Events above a certain (comparably low) energy threshold are essentially background free.

It should be mentioned that the neutrino proton elastic scattering channel is also quite significant. However, there are several reasons to not use this channel for the reconstruction, specifically relating to the SNO+ full scintillator phase. Some of the more important reasons are:

- There is no clear tagging method for these events;

Delayed Energy [MeV]	Time window [μs]	Position cut [mm]	Tagging efficiency [%]
2.04 <E <2.82	0.5 <t <660	1600	72
2.0 <E <3.0	0.5 <t <660	1600	75
1.9 <E <3.1	0.5 <t <660	1600	79
1.9 <E <3.1	0.5 <t <660	2000	83
1.9 <E <3.1	0.5 <t <700	2000	84
1.9 <E <3.1	0.5 <t <800	2000	88

Table 6.9: Tuning cut parameters for tagging of inverse beta decay events. The final percentage is evaluated as the number of tagged IBD entries over all IBD entries. The tagging efficiency for events is lower.

- The energy of these events is strongly quenched;

- The average energy is quite low (< 500 keV) [28];

- There is a big overlap with background events, especially below < 200 keV [28];

- Only $\sim$30% can theoretically be detected, even with lowered thresholds [28].

6.8.1   IBD tagging - method

A tagging method similar to that described in [184] was used. The base of the method is to search for the neutron capture event that releases a γ which has a clear energy signature. This is either between $1.8 < E < 2.6$ MeV if the capture happens on proton or between $4.0 < E < 5.8$ MeV for captures on carbon nucleus. The reason for the range is due to reconstruction precision and energy resolution, the γ itself is of precise energy. Once the event is identified, previous events within the specified time window are iterated through to search for the prompt positron signal. The time constraint on the prompt event is set to be between 0.5 μs and 660 μs before the delayed event. In addition to that, a position cut is applied, restricting the two events to be within 2 m of each other. Finally, an energy cut is applied for the prompt positron, in order to make sure the event is not a random coincidence from other channels or backgrounds. This was initially set to be $E_{\mathrm{p}} > 1$ MeV as was described in Subsection 6.7.4 and later increased to $E_{\mathrm{p}} > 3$ MeV which further increased the efficiency. Finally, only events within $r < 5300$ mm radius are considered (inner AV events), as a result of the signal to background study in Subsection 6.7.4.

The tagging efficiency of scintillator detectors such as SNO+, KamLAND and Borexino is usually quite high, in the order of 80-90% [185, 54]. The cuts described above were tuned and efficiencies evaluated. The tuning is present in Table 6.9. The final values used throughout the analyses were:

- **The energy of delayed event**: between 1.9 and 3.1 MeV[10], the distribution of IBD events around the expected value of 2.2 MeV is highlighted in Figure 6.19;

- **The maximum allowed distance between the prompt and delayed event**: 2000 mm;

- **The time window for prompt event**: between 0.5 and 800 μs;

- The parameters mentioned above are used for tagging, for the final evaluation additional cuts are used, these come from Subsection 6.7.4 where only events within **5.3 m fiducial radius** are considered;

- Finally, a **3 MeV energy** cut is applied to ensure no miss-tagged events are present.

6.8.2 IBD tagging - statistics

The tagging efficiency presented in Table 6.9 considers IBD entries only. There are multiple events created in the detector as a result of single IBD entry and these all require valid reconstruction and tagging. To evaluate the tagging efficiency on event basis, the tagging method was applied to over 100 `SNUGen` data files. All of these have the same settings applied as for previous analyses (go-to model and signal to background study). The go-to model is used, SNO+ detector selected, the three interaction channels available to RAT are included (IBD, ν - p scattering, ν - e scattering), the distance is 10 kpc, only the AV region is considered, normal hierarchy is assumed and there is no MSW effect applied.

A major factor in the study is the performance of SNO+ software (RAT) to fit (reconstruct) events. This is required for both energy and position and as such is essential for tagging and overall reconstruction. The fitter used for the study is the 'scintFitter', a method in development for the full scintillator phase of the SNO+. As of the time of writing, this particular collection of fitting algorithms is not perfectly coordinated as SNO+ is mostly focusing on the analysis of recently finished partial fill phase. Therefore,

---

[10]The wider range for this search is a combination of the energy threshold limit (Subsection 6.2.2), the energy resolution and the reconstruction efficiency.
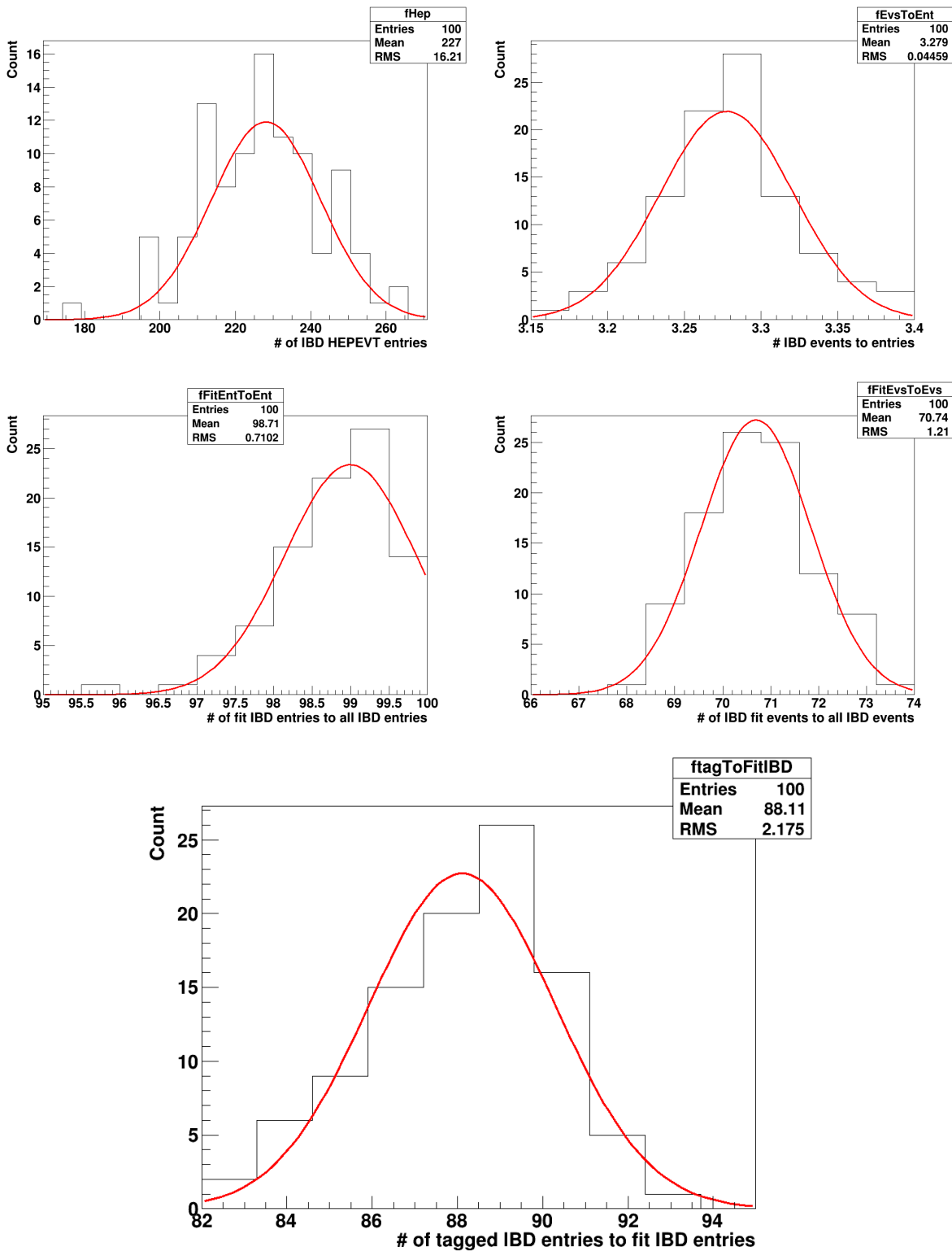
Figure 6.36: Analysis of the fitting and tagging performance for the reconstruction of SN signal. One hundred simulations of the go-to model at 10 kpc were analysed. The tagging (and high efficiency) of IBD events is essential for SN reconstruction. Single MC entry can create multiple events. This is the clean case - simulation considering ideal detector conditions.

the performance is expected to improve greatly over time. Nevertheless, the analysis is attempted regardless and can be retried at later time with more accurate fitting procedures in place.

As can be seen in Figure 6.36, the performance of the fitter was estimated to be about 70.7% for all events, about 98.7% for all entries, and the IBD tagging efficiency was found to be approximately 88.1%. There are several events associated with single entry: these are scatters and the final neutron capture all caused by single IBD interaction. These are the reason for lower fitting efficiency for all events compared to all entries: the low energy scatter events are often harder to reconstruct. Additionally, events close to the AV are also harder to reconstruct due to higher background rates and more complex optics resulting in higher chance of total internal reflection.

The overall expected number of IBD events can be seen in the very first plot of the same figure, showing that approximately 227 IBD events are expected for this particular model at around the most likely distance for a SN (10 kpc).

The analysis will examine two cases:

- The 'clean' case: this is running simulation as is, considering ideal conditions;

- The 'realistic' case: this type assumes realistic detector conditions, including settings such as: trigger thresholds, trigger efficiency, offline PMTs, realistic PPO concentration and more. Settings were chosen to be as during high backgrounds period, just after completion of scintillator fill.

Figure 6.37 shows the fitting and tagging performance for the case of realistic detector conditions. In this case, more events can be seen for each entry caused by higher backgrounds and coincidences. The tagging efficiency is little lower, at 87.1%.

6.8.3 Reconstructing positrons

One significant property of the reconstruction is that fitted energy is reported in units of electron-equivalent energy[11]. This means that an additional correction is required when reconstructing some other known particles. Specifically for positrons, the positron annihilation must be taken into account. In SNO+, positrons readily annihilate with electrons that are abundant throughout the detector. The most likely final state is an annihilation

---

[11]The PMT response is usually calibrated by the electronic recoil events. The energy of other events (such as nuclear recoil) is therefore expressed in the electron-equivalent energy.
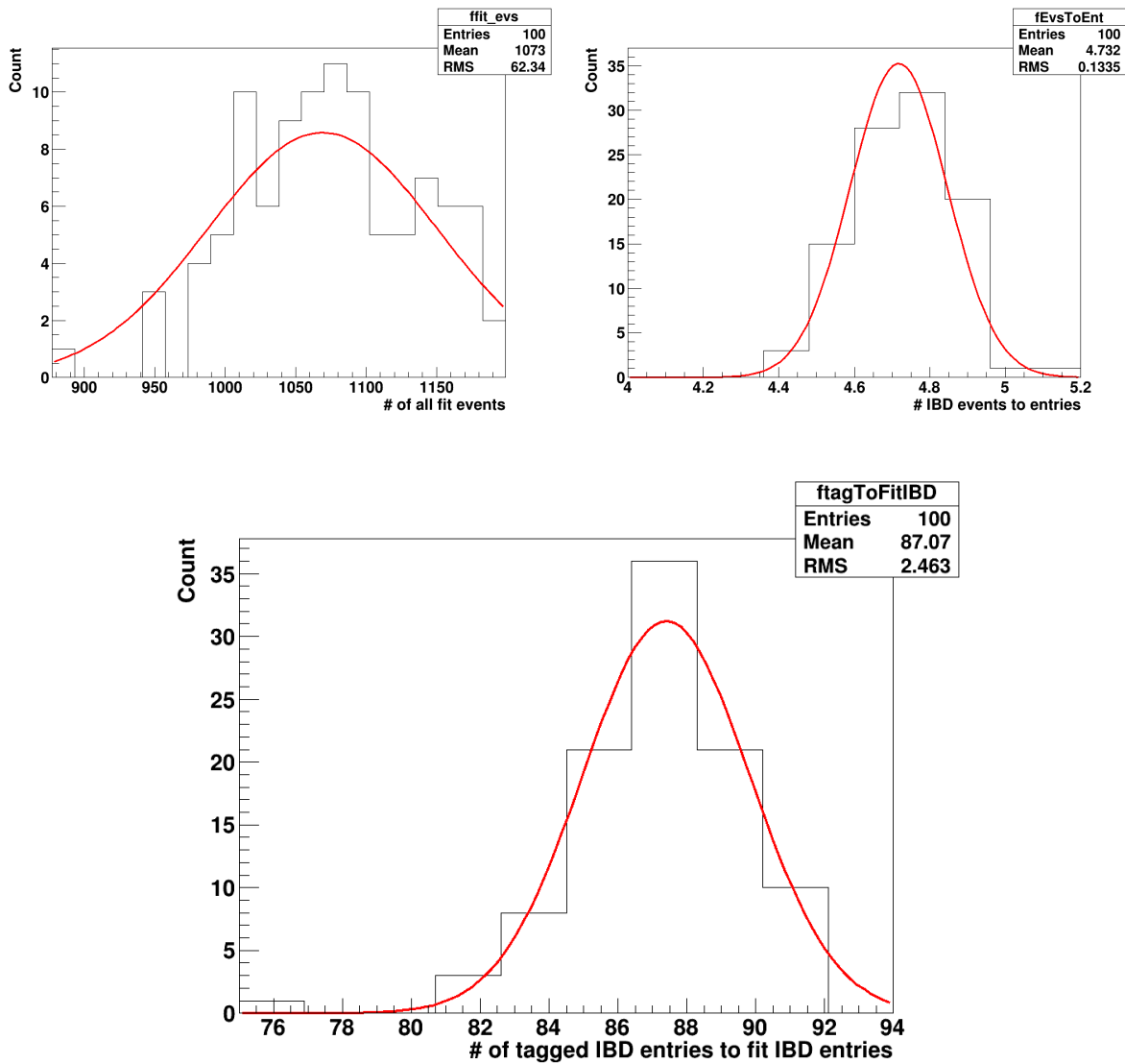
Figure 6.37: Analysis of the fitting and tagging performance for the reconstruction of SN signal. One hundred simulations of the go-to model at 10 kpc were analysed. This is the realistic case - simulation considering realistic detector conditions.
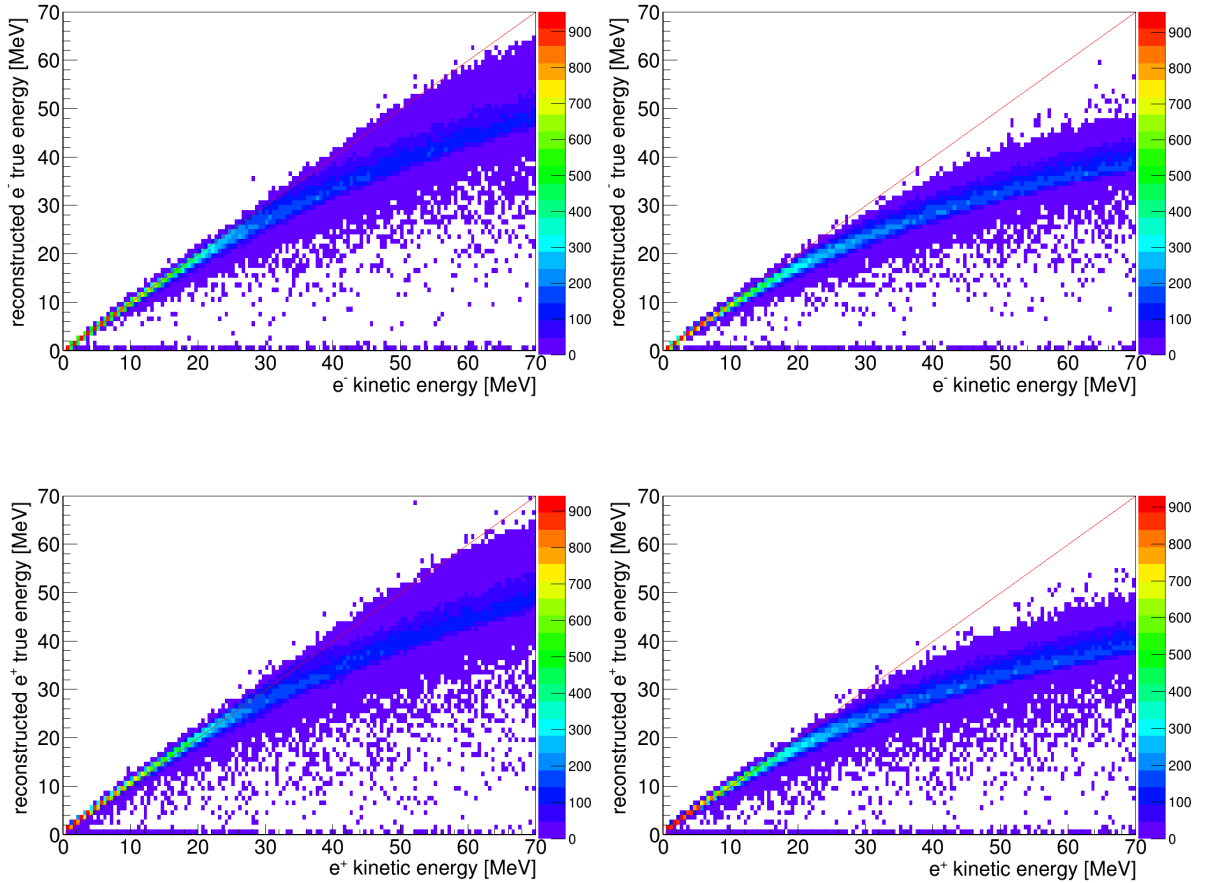
Figure 6.38: Reconstruction of energy for high energy electrons and positrons. Plots for electrons at the top, positrons at the bottom. The left side is the case of clean simulation while the right side considers realistic detector conditions. Two distinct effects can be observed: over-fitting of energy at lower energies for positrons and under-fitting of energies that scales with increasing energy.

with the creation of two photons, each with the energy equal to the electron's rest energy of 0.511 MeV [186]. This energy is normally included in the reconstructed positron kinetic energy and, therefore, the annihilation photons must be subtracted. Because the IBD events are observed through the positron interaction, this correction is to be applied during energy reconstruction of SN IBD events.

To confirm the presence of the energy over-fit for positrons, as well as to observe any additional effects of reconstruction of higher energy events, a study was performed. The details of the study are:

- 1000 electrons (positrons) were simulated at 0.5 MeV steps;

- The study covered the range from 0.5 MeV to 70 MeV (essentially the whole range

of SN IBD energies);

- Both clean and realistic cases were analysed;

- Other settings were kept the same as throughout other SN analyses: SNO+ detector, AV filled with scintillator;

- The same fitting procedures were used.

The results of the study are presented in Figure 6.38. Two effect can be observed: there is over-fitting of positron energy at lower end and there is global under-fitting of reconstructed energy for both electrons and positrons, with the difference increasing as a function of initial kinetic energy. This second effect is described in Subsection 6.8.4. The first effect is caused by the positrons annihilation as described above, and can be fixed by simple subtraction of $2 \times$ electron's rest energy.

6.8.4   Energy correction

In addition to the correction due to positron annihilation, there are some other effects in reconstruction of high (in terms of SNO+) energy particles. As visible in Figure 6.38 there is an under-fit of the energy that gets bigger with the kinetic energy. This effect is present for both electrons and positrons and is more pronounced for the case of realistic simulation. There are several sources for this effect. These are:

- The higher light yield for scintillator;

- The saturation of the PMTs;

- The multi-hits on PMTs (most significant, described below);

- The coordination (energy calibration) range is mostly focused on lower energies.

At higher energies, the number of scintillation photons that are produced in an event is proportional to the deposited energy. The number of collected photo-electrons (p.e.) will also scale proportionally [187]. However, some p.e. are lost to the pile up of multiple hits on a single PMT. This could be corrected for by using the total charge collected by each PMT, however, this is not a great estimator of the number of p.e. at low hit multiplicity [187]. There are several possible techniques to deal with this problem, such as PMT segmentation, however the effect of missed p.e. is still a strong factor that affects the reconstruction. This can be seen in Figure 6.39 where the single photo electron fraction decreases rapidly with increasing event energy.
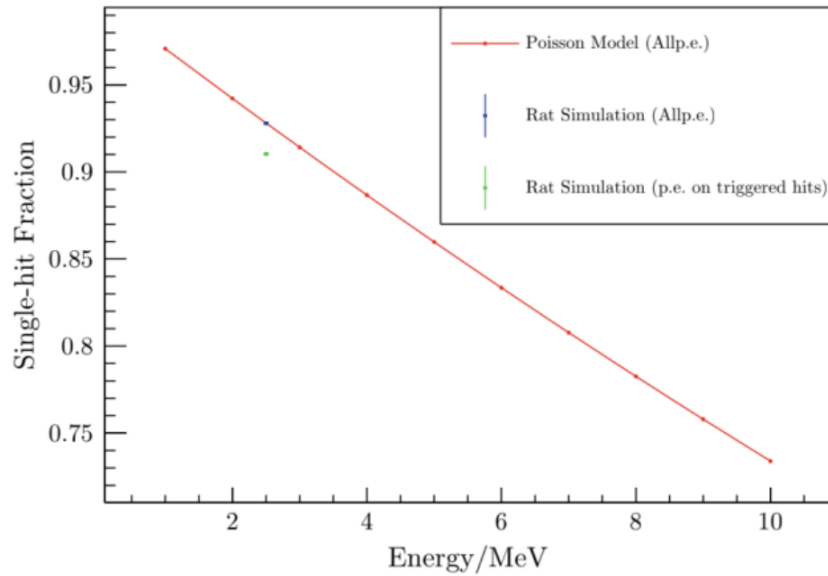
Figure 6.39: The fraction of p.e. that hit a PMT with no other p.e. as a function of event energy in SNO+. Figure from [187].

For the purposes of this thesis, with the specific purpose of reconstructing high energy IBD events from SN, an energy correction was designed and applied to the SN data. The correction function was estimated from the study presented in Subsection 6.8.3 and, therefore, is not dependent on the SN data itself. The energy correction is present in Figure 6.40, while the effect of the correction is shown in Figure 6.41. The reconstructed energy correlates well with the initial kinetic energy of the positron. Finally, the ratio of the reconstructed positron energy to the initial positrons kinetic energy is highlighted in Figure 6.42. The ratio is now approximately one, with wider distribution for the realistic simulation, as is expected. Generally, the energy resolution gets worse with increasing energy.

6.8.5 Reconstructed energy spectrum

After correcting the energy reconstruction, the overall energy distribution of the SN signal can be fitted for. 100 bursts of the go-to model at 10 kpc with the usual settings are used. There are several sets used throughout. These are:

- The `SNUGen` **input**, as provided by the Garching group, more details in Section 6.3;

- The **Monte Carlo (MC) set**: as read by the analysis software, raw data before simulation and reconstruction;

- The **reconstructed set**: events after reconstruction and correction;
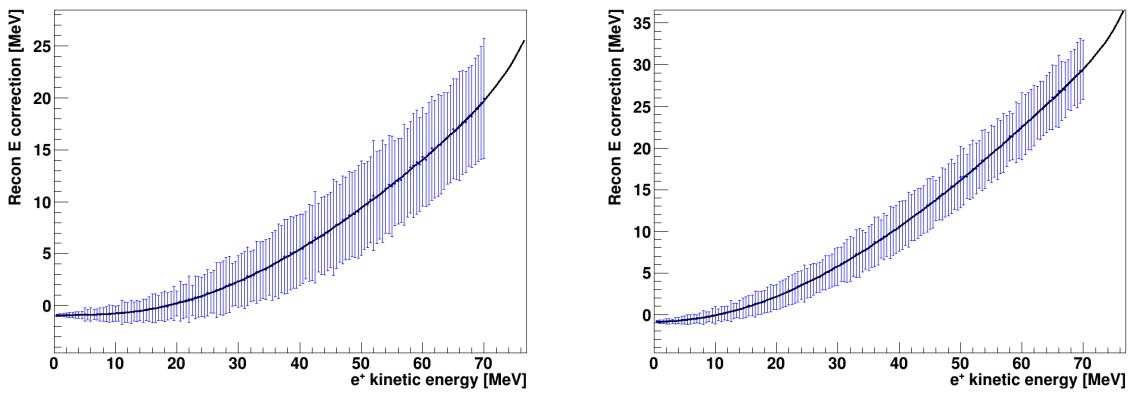
Figure 6.40: The energy correction function for clean simulation (left) and realistic simulation (right). The correction accounts for multi photo-electron hits on PMTs as well as positron annihilation energy reconstructed for positrons (shift by 1.02 MeV).
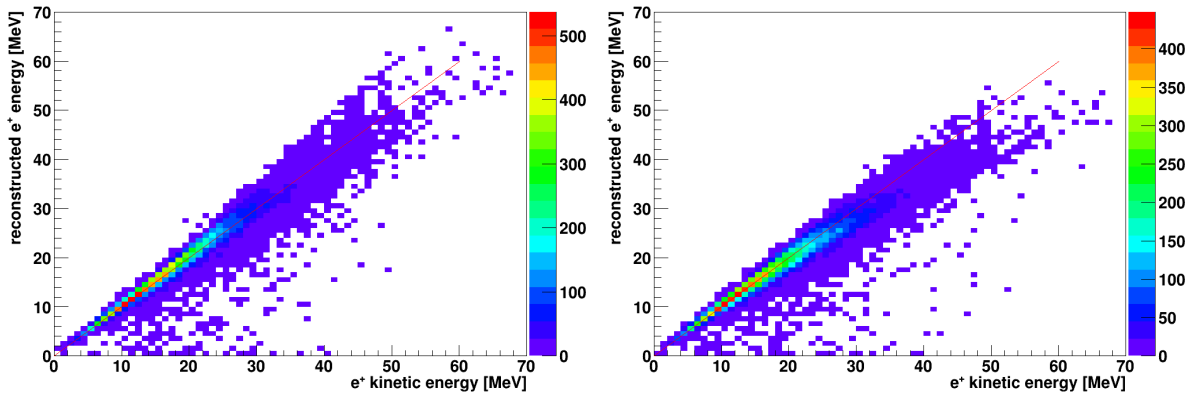
Figure 6.41: Reconstruction of high energy positrons using the energy correction function. Left: clean simulation. Right: realistic simulation.
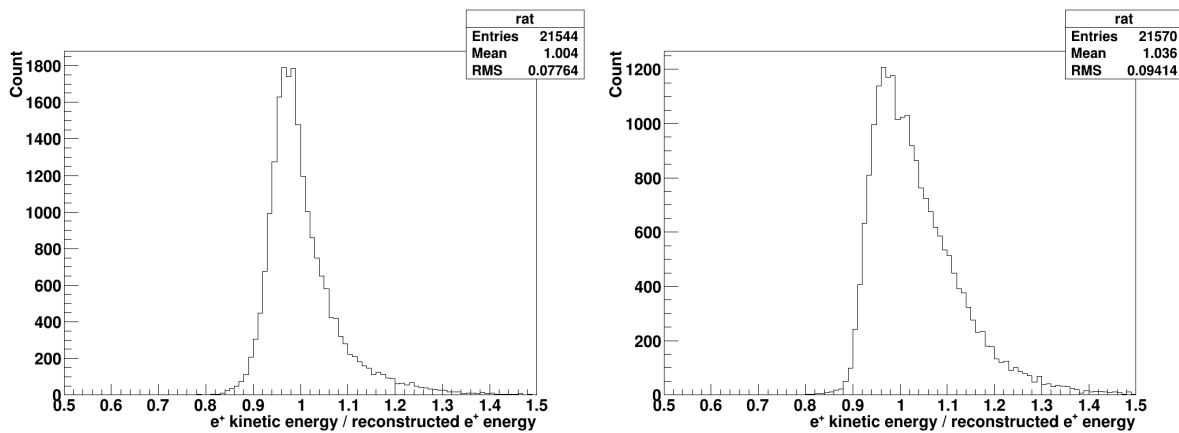
Figure 6.42: The ratio of reconstructed positron energy to original positron kinetic energy after correcting for the various effects using the energy correction function. Left: clean simulation. Right: realistic simulation.

- The **tagged set**: events tagged by the IBD tagging method;

- Additionally, **cut versions** of the latter 3, as determined by the signal study (Subsection 6.7.4) are also used.

The results of the fit are presented in Figure 6.43. The generally high fitting efficiency and energy correction allow for very high match between the MC and reconstructed sets. The tagging set exhibits a slightly lower peak of the distribution, as should be expected due to some IBD events not being tagged. Generally, the shape seems to follows the original MC set nicely, with the highest difference of ∼3 events per MeV at the peak of the distribution. Figure 6.44 shows the sets that pass cut criteria of at least 3 MeV energy and within 5.3 meters of fiducial volume. Here, the correlation between the reconstructed and tagged set is even better, however, to obtain the original distribution the events lost to the cuts would have to be accounted for - a mere normalization by volume could be successful at doing so.

6.8.6 Reconstructed neutrino spectra

Another observable that can be obtained using an efficient IBD tagging procedure is the distribution of events over time. In addition to actually detecting a SN, the knowledge of the time profile could allow for reconstruction of the neutrino spectra. For instance, if a model is known (provided by astronomers) the single fit to IBD $\bar{\nu}_e$ events distribution would allow for complete reconstruction of other neutrino types and channels, since the ratios of these are often stable. Additionally, if the spectrum has significant features, especially in the first 2 seconds or so where the flux is high, this could help differentiate between models, which in turn, would lead to better understanding of the SN explosion mechanism.

Plus, the time reconstruction is separate to the energy reconstruction, therefore, the issues with high energy do not affect this reconstruction.

The reconstruction of events over time confirms the trends observed with energy distributions. The MC set fluctuates around the `SNUGen` input, with the variance caused by the Poisson sampling of events when generating the spectra. The reconstruction set follows very closely with the little difference caused by the few events that fail to get fitted. This is likely to improve in the future when the fitting procedures are optimized for the scintillator phase of SNO+. The tagging efficiency is of the expected order, resulting in an
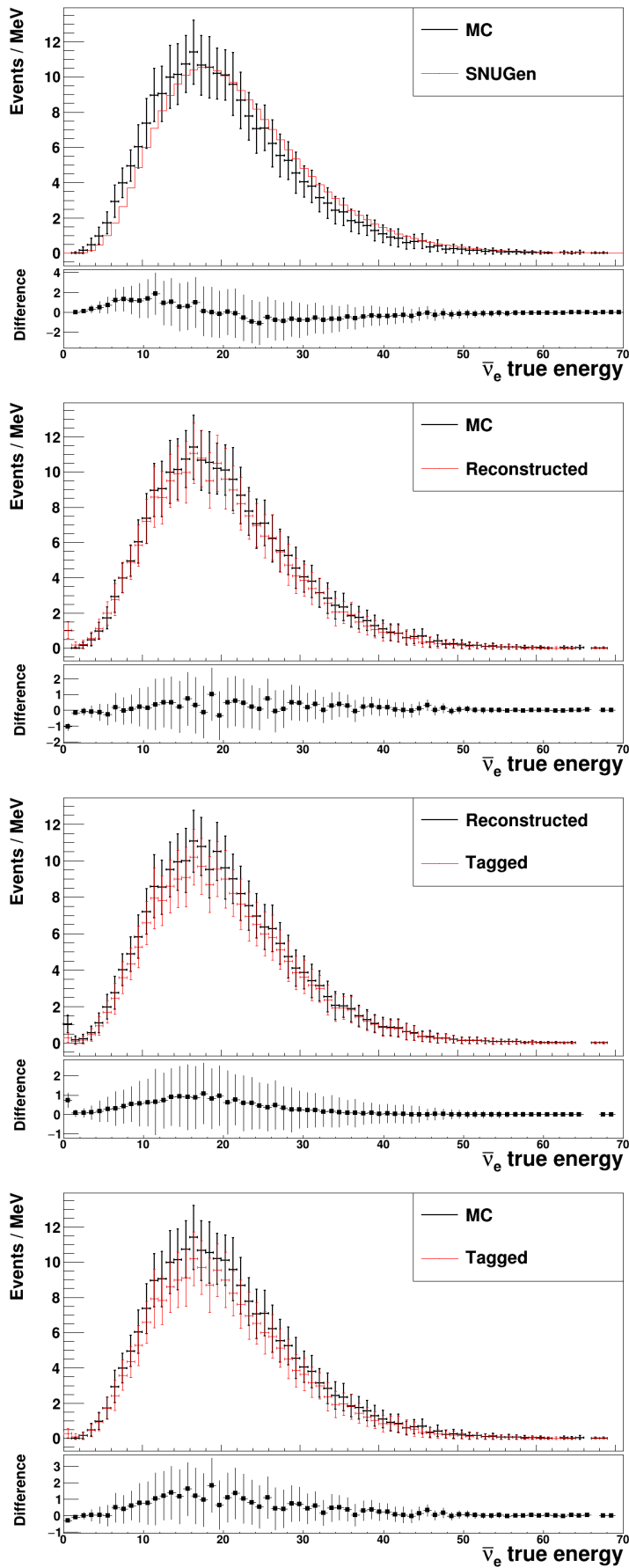
Figure 6.43: Reconstruction of the `SNUGen` go-to model energy distribution using SNO+
Reactor Analysis Tool (RAT). Energy correction is applied. Comparisons between various sets
are shown.
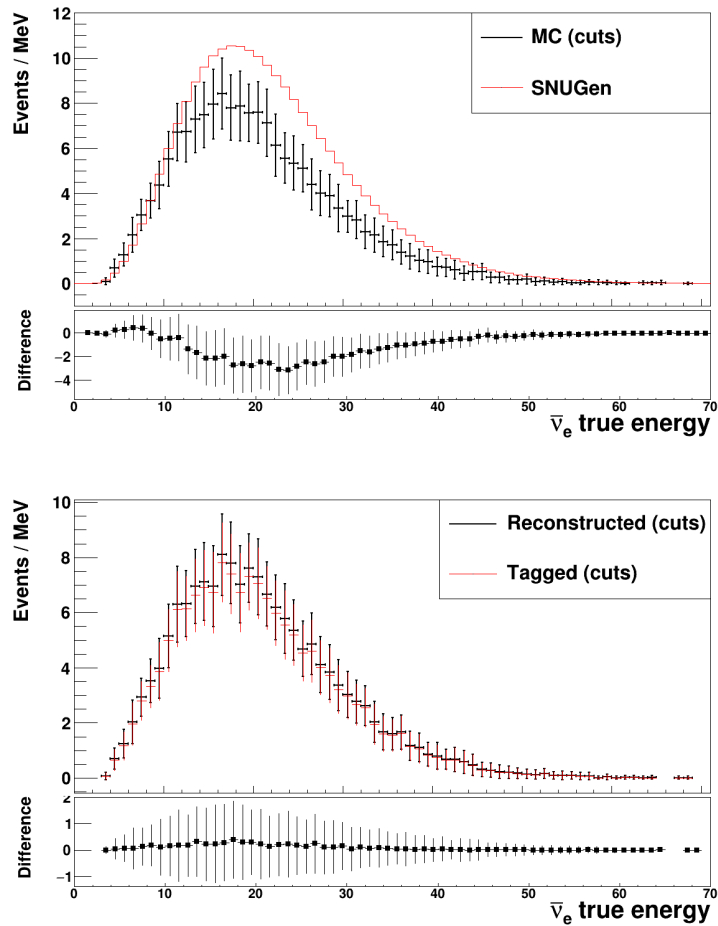
Figure 6.44: Reconstruction of the `SNUGen` go-to model energy distribution using SNO+ Reactor Analysis Tool (RAT). Energy correction is applied. Additional plots for datasets with applied cuts.
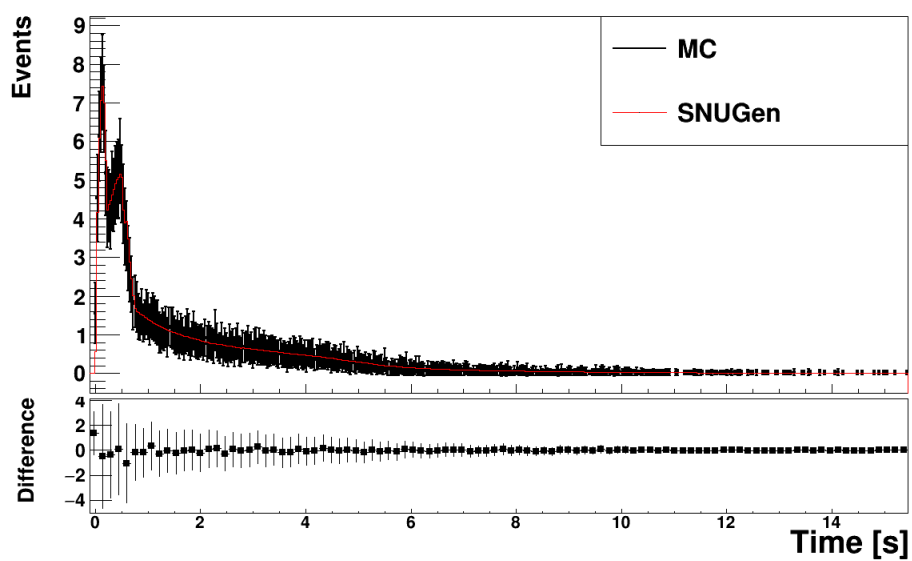
Figure 6.45: Reconstruction of the `SNUGen` go-to model events distribution using SNO+ Reactor Analysis Tool (RAT). Full length of the signal is shown.
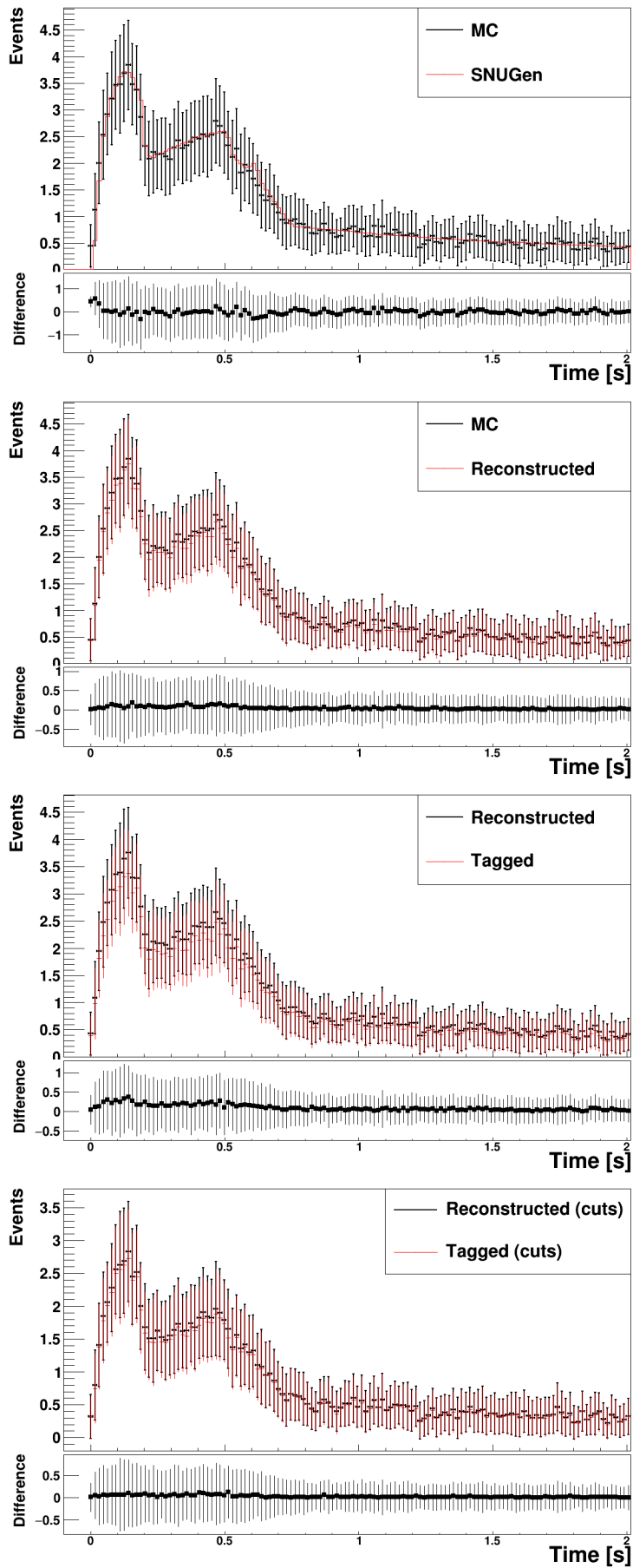
Figure 6.46: Reconstruction of the `SNUGen` go-to model events distribution using SNO+ Reactor Analysis Tool (RAT). Initial two second period shown, comparisons between various sets presented.

overall shift in the distribution, but the shape is reproduced quite accurately. Finally, if the sets reconstructed with the use of cuts are used, the tagging becomes almost identical to the reconstructed set, which is useful in tracing the features in the spectra.

6.8.7 Reconstructed energy over time

Finally, if both energy and time distributions are fitted, an average energy over time can also be reconstructed. These tend to change between various models, especially for models resulting in black holes, where the average energy is generally higher and continuously rising throughout the burst. These are shown in Figure 6.47.

6.8.8 Energy of explosion

Even though this is not the focus of this thesis, it should be mentioned that the ability to reconstruct the energy distribution of the SN signal allows for the fit to spectral $\bar{\nu}_e$ parameters, namely the average energy $\langle E_{\bar{\nu}_e} \rangle$, the pinching factor $\beta_{\bar{\nu}_e}$, and the total energy $\epsilon_{\bar{\nu}_e}$.

The set of these parameters, $\mathbf{a} = (\langle E_{\bar{\nu}_e} \rangle, \beta_{\bar{\nu}_e}, \epsilon_{\bar{\nu}_e})$ can be determined by a procedure based on the fit to the analytical description of the SN neutrino fluence (Eq. 6.34), multiplied by the total IBD cross section σ_{tot}, to the reconstructed $\bar{\nu}_e$ spectrum [28].

$$\frac{d\Phi(\boldsymbol{a})}{dE} = \epsilon_\alpha \frac{(1+\beta_\alpha)^{1+\beta_\alpha}}{\Gamma(1+\beta_\alpha)} \frac{E^{\beta_\alpha}}{\langle E_\alpha \rangle^{\beta_\alpha+2}} \exp\left[-(\beta_\alpha+1)\frac{E}{\langle E_\alpha \rangle}\right]. \tag{6.34}$$

The best fit values can be obtained by the minimization of negative log-likelihood function of the set, $-2\ln L(\boldsymbol{a})$, Eq. 6.35. In the equation, $g(E_{\nu,j}|\boldsymbol{a})$ is the probability density function (PDF) of the reconstructed energies that are normalized to the number of expected events K according to Eq. 6.36 [28].

$$-2\ln L(\boldsymbol{a}) = -2 \cdot \left[\sum_{j=1}^{J} \ln(g(E_{v,j}|\boldsymbol{a})) - \int_0^{E_\nu^{max}} g(E_\nu'|\boldsymbol{a})dE_\nu\right]. \tag{6.35}$$

$$\int_0^{E_\nu^{max}} g(E_{\nu\prime}|\boldsymbol{a})dE_\nu = K. \tag{6.36}$$

Finally, the normalized PDF is shown in Eq. 6.37. In addition to the reconstructed energy, the number of protons in the scintillator volume N_p, the IBD tagging efficiency ϵ_{IBD}, the total IBD cross section σ_{tot}, and (maybe most importantly) the distance to the SN d need to be known.
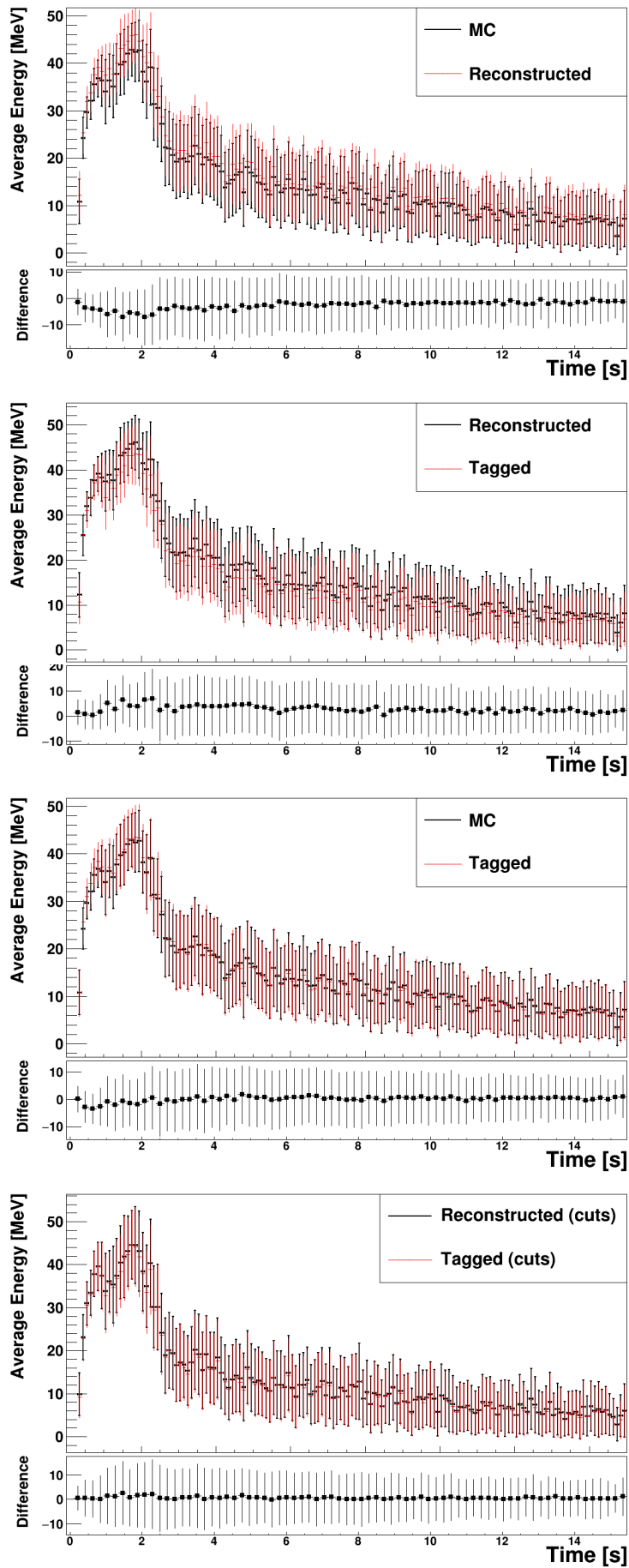
Figure 6.47: Reconstruction of the `SNUGen` go-to model average energy over time using SNO+ Reactor Analysis Tool (RAT). Comparisons between various sets presented.

$$g(E_\nu|\boldsymbol{a})dE_\nu = \epsilon_{\mathrm{IBD}} \cdot \frac{N_{\mathrm{p}}}{4\pi d^2} \cdot \frac{d\Phi_{\bar{\nu}_{\mathrm{e}}}}{dE}(\boldsymbol{a}) \cdot \sigma_{\mathrm{tot}}, \tag{6.37}$$

$$= \epsilon_{\mathrm{IBD}} \cdot \frac{N_{\mathrm{p}}}{4\pi d^2} \cdot \epsilon_{\bar{\nu}_{\mathrm{e}}} \frac{(1+\beta_{\bar{\nu}_{\mathrm{e}}})^{1+\beta_{\bar{\nu}_{\mathrm{e}}}}}{\Gamma(1+\beta_{\bar{\nu}_{\mathrm{e}}})} \frac{E^{\beta_{\bar{\nu}_{\mathrm{e}}}}}{\langle E_{\bar{\nu}_{\mathrm{e}}}\rangle^{\beta_{\bar{\nu}_{\mathrm{e}}}+2}} \exp\left[-(\beta_{\bar{\nu}_{\mathrm{e}}}+1)\frac{E}{\langle E_{\bar{\nu}_{\mathrm{e}}}\rangle}\right] \cdot \sigma_{\mathrm{tot}} \tag{6.38}$$

Additional details about the fitting procedure and results of a fit to MC data is available in [28].

Once the total IBD $E_{\bar{\nu}_{\mathrm{e}}}$ is known, the total energy of the explosion can be estimated. First, the total $E_{\bar{\nu}_{\mathrm{e}}}$ can be evaluated by comparing the energy contributions of $\bar{\nu}_{\mathrm{e}}$ via all interaction channels, knowing the contribution of the IBD channel. Following that, the relations between total energies carried away by different neutrino types can be used to estimate the final total energy of the explosion. These rations are, of course, model dependent but procedures to approximate them are known. One of them is presented in [188], estimating the ratios as: $E_{\nu_{\mathrm{e}}}$: 17-22%, $E_{\bar{\nu}_{\mathrm{e}}}$: 17-28% and $E_{\nu_{\mathrm{o}}}$: 50-66%.

6.9 Black hole formation during SN

Due to the gravitational collapse, SN explosion may lead to the formation of a neutron star or a black hole in the central part of the massive star [172]. This final state is still one of the key issues in stellar physics [189]. Massive stars between $\sim 8\mathrm{M}_\odot$ and $\sim 100\mathrm{M}_\odot$ lead to various phenomena, such as core-collapse SNe, hypernovae and failed SNe, with the outcome being strongly dependent on the properties of the progenitors, namely the masses, rotations and profiles [23, 189]. The black hole end of life is inevitable for stars beyond ~ 40 M$_\odot$ [174]. This collapse is triggered by very intense matter accretion onto the proto-neutron star [189].

Failed SN from non-rotating massive stars are one of possible channels that could result in a black hole. These are also accompanied by the neutrino burst present during a successful SN, however, while the neutrino signal from common SN lasts for several seconds (or tens of seconds) with a gradual decrease of average energies and luminosities, black hole forming failed SN burst shows unique signatures: short(er) duration, and increase of both luminosities and average energies in time. Another significant observable feature is the sudden termination of the signal once the black hole is formed [189]. This signal may be used to probe the EOS of nuclear matter [190]. Importantly for this thesis, the neutrino burst from a failed SN forming a black hole can be detectable at the terrestrial neutrino

detector facilities [189].

Regarding the duration of the burst, the formation usually occurs within ∼0.4-1.5 seconds after core bounce. After the bounce, the central object is acquiring mass at very high rate. The PNS[12] is usually formed almost immediately, while in ordinary SNe this formation takes place in ∼0.3 seconds [191, 192]. The mass increases gradually and the dynamical collapse to a black hole occurs at the end point, which depends on the progenitor and EOS. If the length of this signal can be accurately measured, the critical mass can be inferred through the mass increase [189].

Besides the features, the probability of such event should be also mentioned. Because the aforementioned event of non-rotating black hole formation with its short neutrino burst is linked to heavy stars, the occurrence rate is also proportional to the fraction of massive stars having large masses for intense accretion without significant rotation. Such stars comprise ∼30% of massive stars [189], which is not insignificant. It was estimated that the rate of black hole formation could be comparable to the rate of normal core-collapse SNe [193]. Indeed, there have been observations of faint SNe from massive stars without significant rotations, which may be of the origin considered here [194].

6.9.1   Features of the signal

The two available models that result in black hole in `SNUGen` are LS220-s40.0c-bh [195, 25] and LS220-s40s7b2c-bh [173, 195]. The 's7b2' term refers to rapidly mass-accumulating accretion layer, resulting in shorter burst of ∼0.57 seconds, while the former model lasts ∼2.1 seconds, making both of these clearly shorter than the go-to burst. More details on models are available in Subsection 6.3.5.

The spectral parameters are presented in Figure 6.48, where they are compared to core-collapse SN models. The expected features can be observed in the distributions of spectral parameters: the average energies are generally higher than for core-collapse models and they keep constantly increasing. Regarding the luminosity, it is also much higher compared to successful SN models, and although not constantly increasing - there is a big peak at the point of collapse - they remain higher throughout the burst.

Looking at the energy distribution and the event rate over time, Figure 6.49, these also carry the features explained above. The mean energy is relative higher than common models. Maybe the most distinct is the the number of events over time, where the rate keeps increasing throughout, after an initial blimp after the core bounce. As expected,

---

[12]**PNS** = Proto-Neutron star.
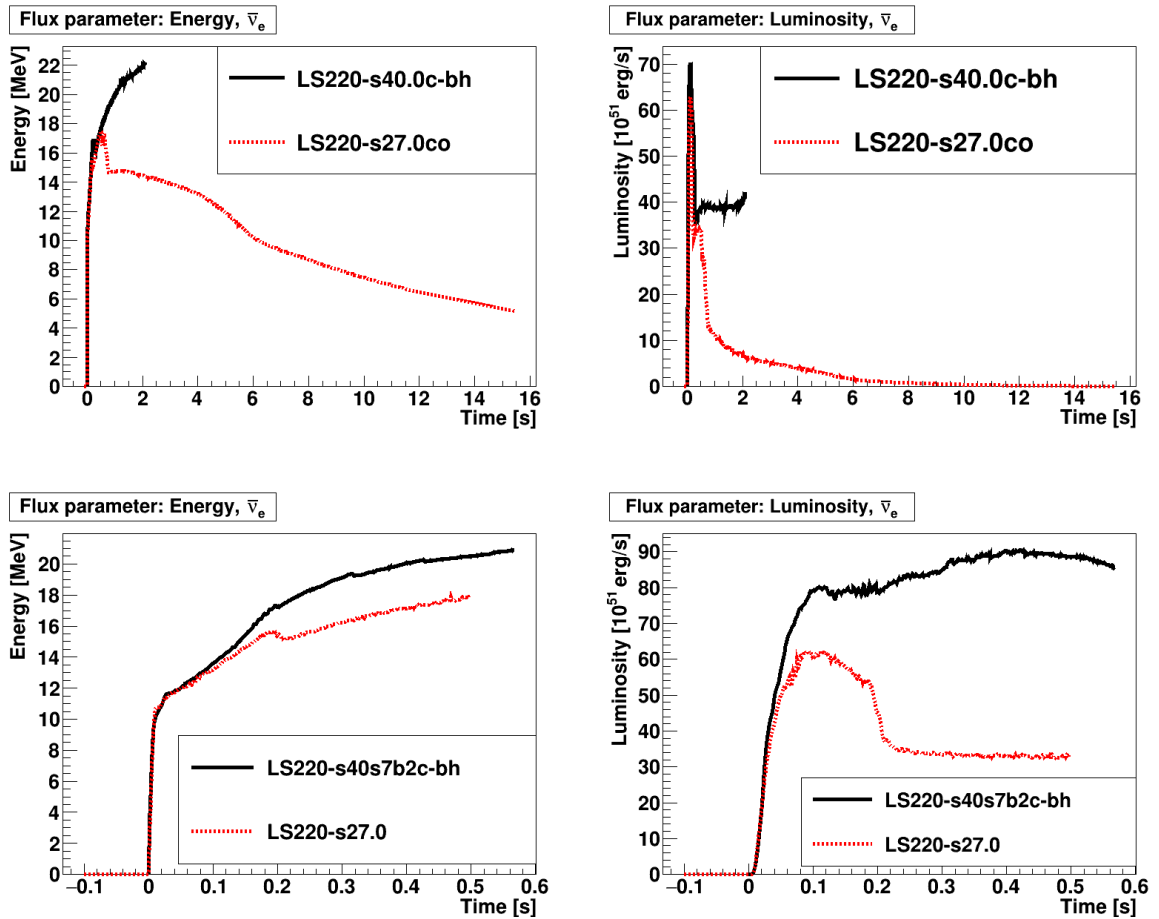
Figure 6.48: Comparison of spectral parameters between two available models resulting in black hole and common core-collapse models. Top plots are for LS220-s40.0c-bh, while bottom plots show LS220-s40s7b2c-bh. Both average energy plots (left) and luminosity plots (right) show the expected differences of the spectral parameters for black hole models.
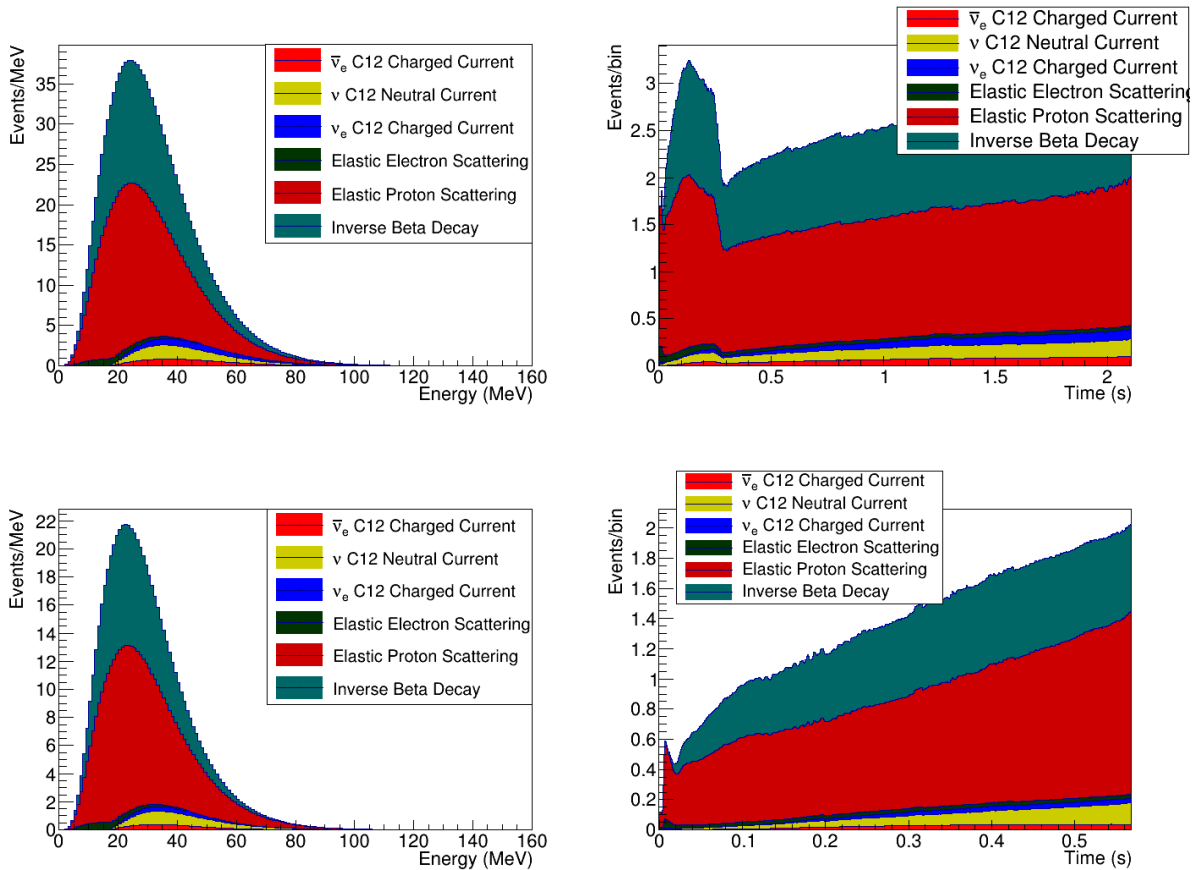
Figure 6.49: Energy distribution and event rate profile for the two black hole models: LS220-s40.0c-bh (top) and LS220-s40s7b2c-bh (bottom).

the LS220-s40s7b2c-bh model with rapid accretion displays more rapid increase but for shorter period of time, consistent with expectations.

6.9.2 Reconstructing models

The same reconstruction process was used as for the go-to model, considering only inner AV events of the fully filled SNO+ scintillator detector. Example plots are presented in Figure 6.50. The same energy correction as described in Subsection 6.8.4 was applied. It can be seen in the time vs NHit plot that the event rate is slightly increasing over time. The reconstructed energy can be observed in the other plot, where the energy correction brought the reconstructed e^+ energies closer to the true energies.

While these bursts are both quite short compared to other expected lengths of SN bursts, they have appreciable higher average energy. Because the basis of the BT is the energy of the events (more precisely NHit, which is a function of energy) these bursts, if they were to take place, would pass the thresholds for the SNO+ Supernova Burst Trigger.
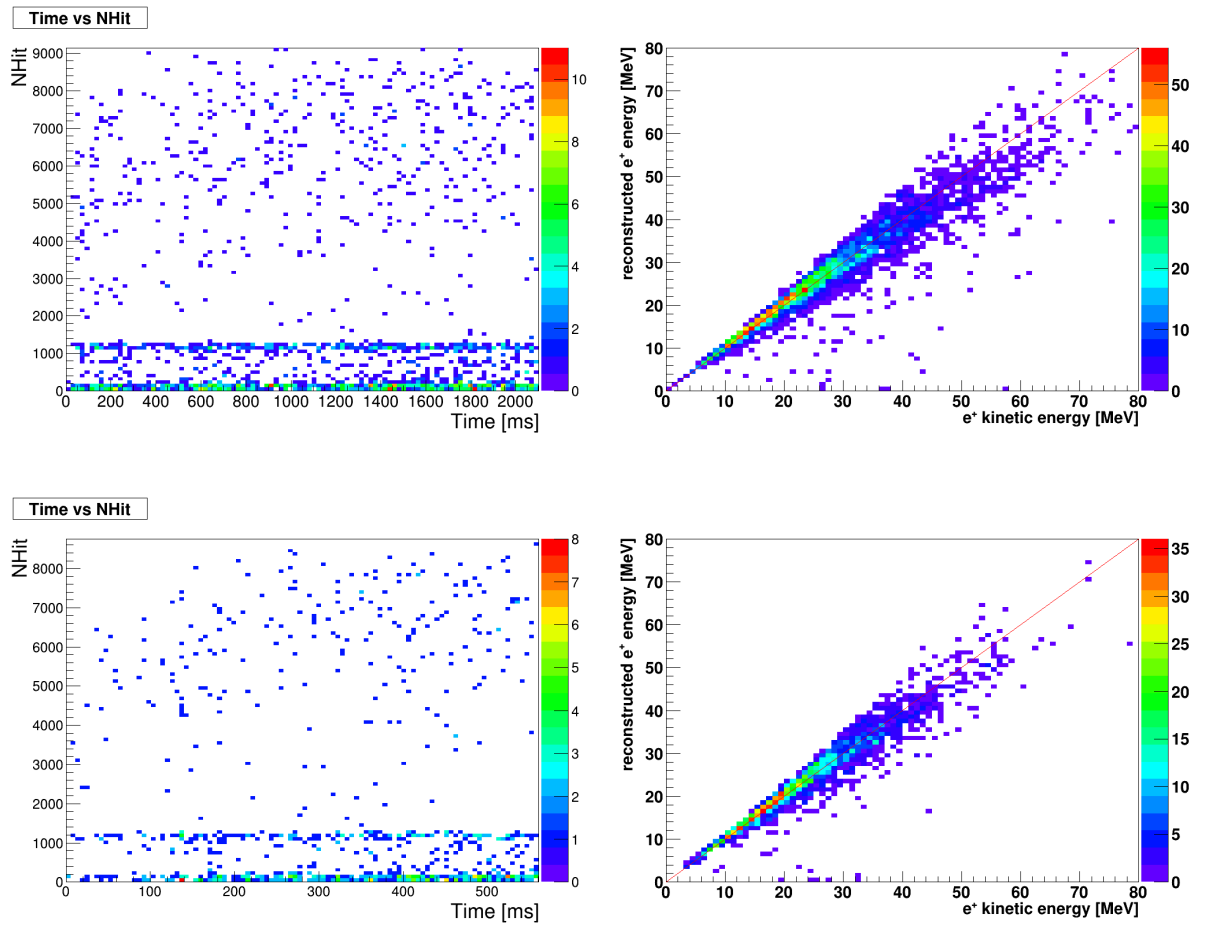
Figure 6.50: Basic reconstruction of the two black hole models, LS220-s40.0c-bh (top) and LS220-s40s7b2c-bh (bottom).

6.9.3   Fitting observables

Finally, the reconstruction of both available black hole models was attempted. Again, the same settings are used for consistency, the most important being: 10 kpc distance, SNO+ fully filled with scintillator, inner AV events only. The fit uses the same procedure of tagging of IBD events (Subsection 6.8.1). This time, only 10 iterations of simulation of each model are used, therefore, the statistics are lower.

The results of the fits can be seen in Figure 6.51 for LS220-s40.0c-bh model and in Figure 6.52 for LS220-s40s7b2c-bh model.

In both cases, the tagging method successfully follows the shape of both the energy distribution and the event rate distribution with a small shift downwards, corresponding to the sum of reconstruction efficiency and tagging efficiency. Even though the assumed detector conditions are likely better then the real conditions would be, it should be mentioned that this method uses IBD events only, and these are - as mentioned in Section 6.6 and in Subsection 6.7.4 - almost free of backgrounds. Additionally, the reconstruction algorithm for full scintillator phase is likely to improve in the near future.

Finally, while the most accurate fit would be the most useful, it is important to keep in mind that to determine whether a burst is potentially from a black hole formation, there are features that should be anticipated. These features are:

- A short(er) burst, in order of just few seconds;

- The peak in events at the start, then increasing throughout;

- A higher mean energy;

- The (maybe most importantly) energy should be increasing over time;

- A sudden cut-off of the signal.

All of these features can be seen in the fitted spectra. These are, however, strongly statistics dependent.

6.10   Conclusion

The chapter summarised the relevant SN interactions channels for SNO+, giving estimates for the number of events and the expected energy distributions. Likewise, `SNUGen` - the SN MC generator - was described in detail, explaining the method to create the expected neutrino fluxes. All available SN models were discussed, listing their basic properties.
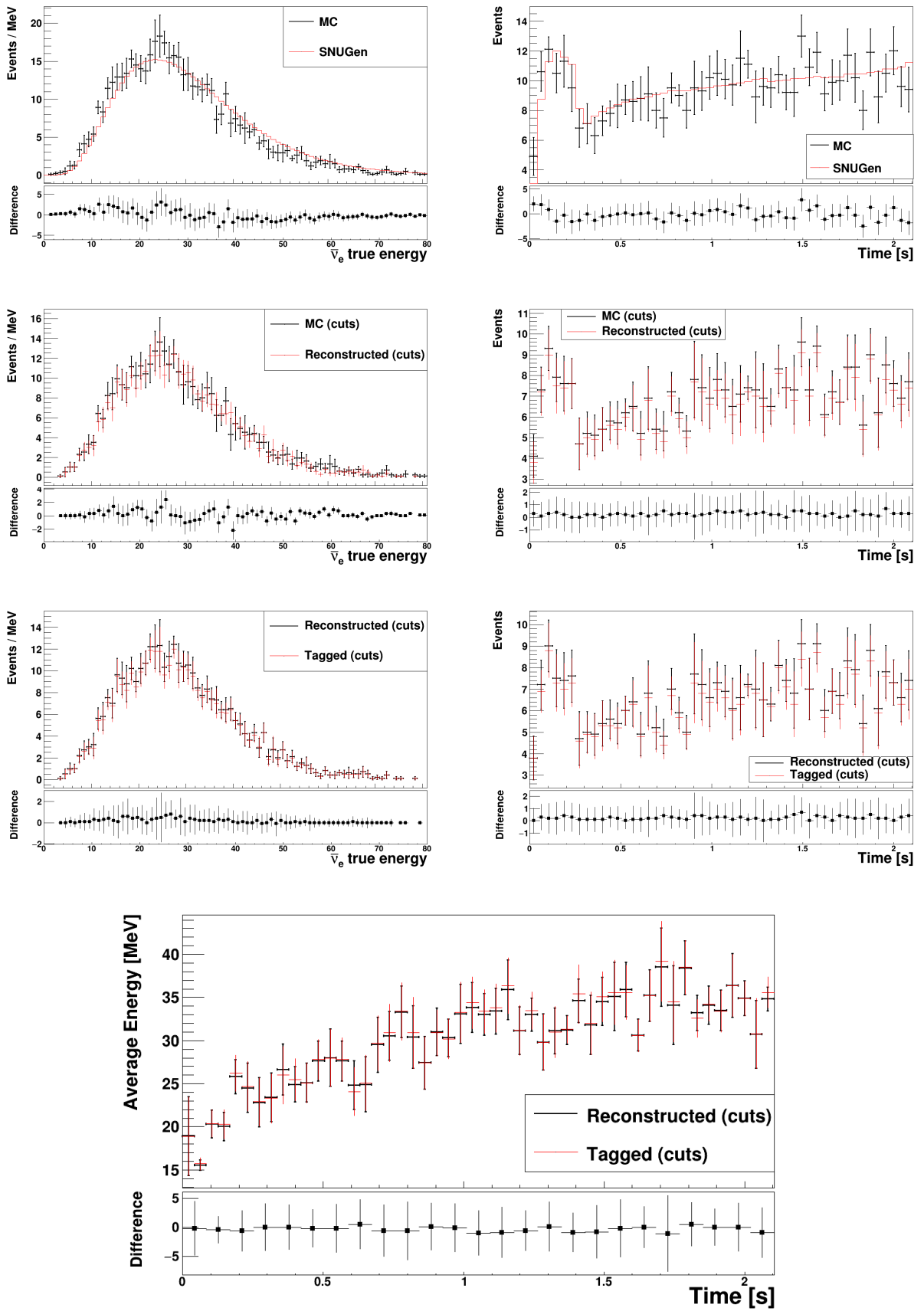
Figure 6.51: Results of IBD tagging and fit to observables: LS220-s40.0c-bh model.
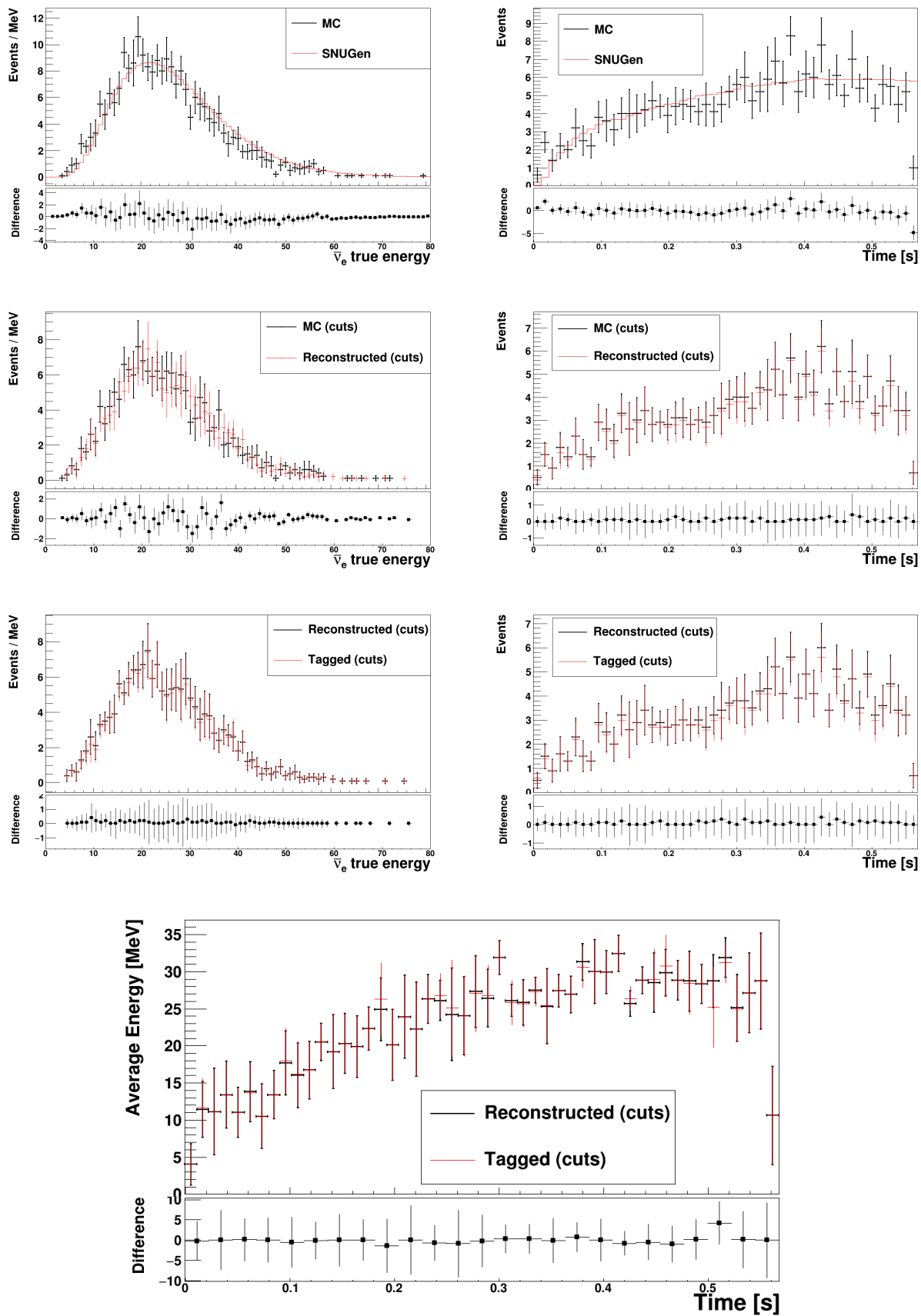
Figure 6.52: Results of IBD tagging and fit to observables: LS220-s40s7b2c-bh model.

The LS220-s27.0co model was selected as the default model and was fully analysed. This included the description of the features of the signal, the expected detector response, the reconstruction, and the view of the burst created by this model using the `SN Burst Trigger`. In addition to that, studies were performed to evaluate the impact of the hierarchy, the equation of state, the event position within the detector, and the SN distance, on the neutrino signal and the response of the detector. In most cases, the effect was visible in the distribution of events over time, although in the EOS study, this is strongly dependent on the mass of the progenitor. The effect of the distance is likely the most pronounced, and if the model is known, it could be possible to estimate the distance to the SN.

Another analysis was performed to suggest the effective reconstruction cuts on the SN signal that would preserve most of the signal while cleaning most of the backgrounds. Several approaches were considered, including pure MC as well as real detector data from the period of high background rates. The final suggested cuts are 1 MeV energy cut and 5.3 meters fiducial volume cut. These were estimated to cut ∼85% of backgrounds while preserving ∼88% of the signal. The method itself could be repeated at later time (for example during Te loading) to give new estimations.

The later portion of the chapter described the possible reconstruction methods to use when a real SN-like signal is detected. This includes the IBD tagging method with ∼87% efficiency and the energy correction that corrects the reconstructed energy for the high energy positrons expected for this signal. Both of these were then used to reconstruct and analyse the energy distribution, the events distribution, and the events over time for an example SN burst. It was shown that depending on the statistics (mainly the number of events), the features of the SN signal can be recognised by SNO+. The same conclusion was found for a signal produced by a model leaving a black hole remnant.

All in all, the reconstruction methods, the tagging method, and the energy correction described in this chapter could be used as a basis for a Level 4 stage of the `SN Burst Trigger`. This could serve as a quick method to distribute the basic observables of the detected SN signal to the public.

Chapter 7

Conclusion

My goal is simple. It is a complete understanding of the universe, why it is as it is and why it exists at all.

STEPHEN HAWKING

SNO+ is a multi-purpose detector that reuses the SNO detector with several changes and upgrades. One significant change is the detection medium. The water was replaced by the liquid scintillator. The filling process alongside the quality assurance procedures were outlined in this thesis. Another upgrade includes the deployment of the new external calibration system - TELLIE. This system, alongside the general maintenance, tuning, and stability studies were described.

An accurate energy and time calibration is essential to properly reconstruct the physics events in a detector. One of the uses of the TELLIE system is the calibration of the PMTs. The procedure to obtain the calibration data using this system and the correction methods that are used to correct for multiple time offsets were expressed. The system was found to be functional and capable of calibrating the PMT array to the desired accuracy. TELLIE is a complementary system and requires periodic deployment of the laserball, however, it lowers the required frequency of deployment, which minimises the chance of contamination. The stability of the new calibration system was monitored throughout various datasets and was found to be satisfactory.

Supernovae explosions are extremely energetic events happening throughout the Universe. They are the only source of heavy elements found inside the planets. Additionally, they release 99% of the binding energy of a star in the form of a short burst of neutrinos. These provide a window inside the core of a star, where the conditions are more extreme

than anywhere else. Therefore, detecting these neutrinos is paramount to learn about the neutrinos and to look for new physics.

To detect this burst of neutrinos, the `Supernova Burst Trigger` was designed and built for SNO+. It is a fast, live, multi-level trigger devised to detect and alert whenever a burst of high energy neutrinos is observed. The design is modular, the detection settings are easily modifiable, and a dynamic study of the activity of the detector is running alongside it to maximise the sensitivity without overwhelming the detector. The BT also serves as a breakdown control tool.

The efficiency of this trigger was evaluated and found to be >90% up to the far galactic edge.

An online monitoring platform was built to interface with the BT. It provides a prompt analysis of the detected burst, focusing on the main observables of the signal. It is used during supernova shifting to analyse and classify detected burst. The classification is based on the burst ZOO - a collection of bursts, grouping bursts of similar origin based on the features detected by the BT.

A set of automated alarms was also developed, allowing SNO+ to join the SNEWS network. This process is currently being finalised.

Several aspects of the BT are based on the supernova MC generator - `SNUGen`. The overview of how it generates the neutrino fluxes, samples the rates and energies, and creates events readable by the analysis software was presented in this thesis. This includes the summary of all available progenitor models with their properties.

A full analysis was performed using one of these models - LS220-s27.0co - looking at the features of the signal and the response of the detector. Similarly, an analysis was performed to evaluate the effects of the hierarchy, the equation of state, and the distance on the neutrino signal. They all affect the signal to an extend, and require high statistics and efficient reconstruction.

To increase the efficiency of the reconstruction, a study was performed to determine the best cuts to use to clean any detected signal from the backgrounds. It is suggested that 1 MeV energy cut and 5.3 m fiducial volume cut are used, based on the distribution of the backgrounds.

Finally, a reconstruction procedure was produced to be used in the case of the detection of the SN signal. It could be used as a Level 4 stage of the `SN Burst Trigger`. The

procedure is based on the IBD tagging method described in the thesis that is estimated to be ~87% efficient. Another significant component is the correction of the reconstructed energy of the tagged IBD events. It was found that high energy positrons are reconstructed with lower energies due to multiple effects, and a correction function was generated to improve the energy reconstruction. The usage of the reconstruction cuts, the IBD tagging method, and the energy correction results in the accurate reconstruction of the SN signal, including the energy distribution, the distribution of events over time, and the profile of energy over time. Depending on the statistics, it is possible to recognise features in the signal. This also applies to the models resulting in a black hole remnant. This method could be used to analyse prompt observables of the SN signal, if needed.

Bibliography

[1] Carlo Giunti and Kim Chung Wook. *Fundamentals of Neutrino Physics and Astrophysics.* Oxford Univ., Oxford, 2007. 4, 5, 35

[2] M. L. Perl, G. S. Abrams, A. M. Boyarski, M. Breidenbach, D. D. Briggs, F. Bulos, W. Chinowsky, and et al. Evidence for anomalous lepton production in $e^+ - e^-$ annihilation. *Phys. Rev. Lett.*, 35:1489–1492, Dec 1975. 5

[3] K. Kodama, N. Ushida, C. Andreopoulos, N. Saoulidou, G. Tzanakos, P. Yager, B. Baller, and et al. Final tau-neutrino results from the donut experiment. *Physical Review D*, 78(5), Sep 2008. 5

[4] Kamiokande Collaboration. Evidence for oscillation of atmospheric neutrinos. jul 1998. 5

[5] M. Cribier, M. Spiro, and D. Vignaud. *La lumiere des neutrinos.* Collection "Science Ouverte.". Editions du Seuil, 1995. xvi, 6

[6] John F. Beacom. The diffuse supernova neutrino background. *Annual Review of Nuclear and Particle Science*, 60(1):439–462, Nov 2010. 6

[7] Carlo Giunti and Kim Chung Wook. *Fundamentals of Neutrino Physics and Astrophysics.* Oxford Univ., Oxford, 2007. xiii, 7, 36, 251, 253

[8] Brent Follin, Lloyd Knox, Marius Millea, and Zhen Pan. First detection of the acoustic oscillation phase shift expected from the cosmic neutrino background. *Physical Review Letters*, 115(9), Aug 2015. 7

[9] A. Yu. Smirnov. Solar neutrinos: Oscillations or no-oscillations?, 2017. xvi, 7, 8, 10, 11, 44

[10] K Zuber. Neutrino physics, 2012. 8, 9

[11] Sunny Vagnozzi. *Weigh them all! - Cosmological searches for the neutrino mass scale and mass ordering.* PhD thesis, 06 2019. xvi, 10

[12] Boris Kayser. Neutrino Physics. jun 2005. 9, 39

[13] A. Yu. Smirnov. The MSW effect and Solar Neutrinos. may 2003. 9, 267

[14] Steve Boyd. Neutrino Mass and Direct Measurements. 2013. 12, 14, 15

[15] Patrick Cheryl. Neutrinoless $\beta\beta$ decay: physics that matters (... but doesn't anti-matter). 2019. 12, 13

[16] V.M. Carballo, M.A. Chefdeville, M.P. Decowski, M. Fransen, H Graaf, W. Koppert, and Jurriaan Schmitz. Applications of gridpix detectors. *Journal of Instrumentation*, 5, 02 2010. xvi, 13

[17] Joachim Kopp. Theoretical neutrino physics). 2019. 13, 14

[18] Dina Prialnik. *An Introduction to the Theory of Stellar Structure and Evolution.* 2000. 16

[19] Richard B Larson. The physics of star formation. *Reports on Progress in Physics*, 66(10):1651–1697, Sep 2003. 16

[20] Raman Prinja. PHAS 1423 – Astrophysics. 2012. xvi, 16, 17, 18, 20

[21] Hans-Thomas Janka, Florian Hanke, Lorenz Huedepohl, Andreas Marek, Bernhard Mueller, and Martin Obergaulinger. Core-collapse supernovae: Reflections and directions. *Progress of Theoretical and Experimental Physics*, 2012, 11 2012. xiii, xvi, xvii, 17, 25, 27, 38

[22] Stellar Evolution, 1 2021. [Online; accessed 2021-09-23]. xvi, 17

[23] A. Heger, C. L. Fryer, S. E. Woosley, N. Langer, and D. H. Hartmann. How massive single stars end their life. *The Astrophysical Journal*, 591(1):288–300, Jul 2003. xvii, 18, 19, 22, 23, 321

[24] Conrad Chan, Bernhard Müller, Alexander Heger, Rüdiger Pakmor, and Volker Springel. Black hole formation and fallback during the supernova explosion of a 40 $M_\odot$ star. *The Astrophysical Journal*, 852(1):L19, Jan 2018. 18

[25] L. Hüdepohl. Neutrinos from the formation, cooling, and black hole collapse of neutron stars. 2014. 20, 322

[26] Enrico Cappellaro and Massimo Turatto. Supernova types and rates. *Astrophysics and Space Science Library*, page 199–214, 2001. xvii, 21

[27] J. C. Niemeyer, M. Reinecke, and W. Hillebrandt. Models of Type Ia Supernova Explosions. mar 2002. 21

[28] Belina von Krosigk. *Measurement of proton and α-particle quenching in LAB based scintillators and determination of spectral sensitivities to supernova neutrinos in the SNO+ detector.* PhD thesis, jun 2015. xiv, xxxix, xlii, 21, 22, 31, 251, 254, 255, 259, 260, 261, 294, 295, 298, 306, 319, 321

[29] S Chandrasekhar. Stars, their evolution and their stability. *Rev. Mod. Phys.; (United States)*. 22

[30] Hans-Thomas Janka. Explosion mechanisms of core-collapse supernovae. *Annual Review of Nuclear and Particle Science*, 62(1):407–451, Nov 2012. 23

[31] H. Thomas Janka, Florian Hanke, Lorenz Huedepohl, Andreas Marek, Bernhard Mueller, and Martin Obergaulinger. Core-collapse supernovae: Reflections and directions, 2012. 24, 27, 262

[32] Hans-Thomas Janka. Neutrino emission from supernovae. *Handbook of Supernovae*, page 1575–1604, 2017. xvii, xviii, 24, 26, 27, 28, 29, 30, 31, 32, 280

[33] S. E. Woosley, A. Heger, and T. A. Weaver. The evolution and explosion of massive stars. *Rev. Mod. Phys.*, 74:1015–1071, Nov 2002. 28, 272

[34] M. Kachelrieß, R. Tomàs, R. Buras, H.-Th. Janka, A. Marek, and M. Rampp. Exploiting the neutronization burst of a galactic supernova. *Physical Review D*, 71(6), Mar 2005. 30

[35] Shunsaku Horiuchi and James P Kneller. What can be learned from a future supernova neutrino detection? *Journal of Physics G: Nuclear and Particle Physics*, 45(4):043002, Mar 2018. xiii, xxxv, 32, 33, 35, 36, 209, 218

[36] Kate Scholberg. Supernova neutrino detection. *Annual Review of Nuclear and Particle Science*, 62(1):81–103, Nov 2012. 33, 34, 35, 272, 275

[37] K. Nakamura. Present status and future of Kamiokande. *Conf. Proc. C*, 890928:297, 1989. 35

[38] IMB experiment homepage. `http://www-personal.umich.edu/~jcv/imb/imb.html`. Accessed: 2021-09-20. 35

[39] Baksan experiment homepage. `http://www.inr.ru/bno.html`. Accessed: 2021-09-20. 35

[40] V Dadykin, V. Yakushev, P Korchagin, V. Korchagin, Alexey Malgin, F. Ryassny, O. Ryazhskaya, and et al. The research program of the liquid scintillation detector (lsd) in the mont blanc laboratory. 09 1985. 35

[41] Rodolfo Valentim, Jorge E. Horvath, and Eraldo M. Rangel. Evidence for two neutrino bursts from sn1987a. *International Journal of Modern Physics: Conference Series*, 45:1760040, Jan 2017. 36

[42] Guido Drexlin, Volker Hannen, Susanne Mertens, and C. Weinheimer. Current direct neutrino mass experiments. *Advances in High Energy Physics*, 2013, 10 2012. xviii, 37

[43] Mark Stringer. *Sensitivity of SNO+ to supernova neutrinos*. Phd thesis, 2019. xviii, xxii, xxxix, 36, 40, 41, 44, 47, 54, 58, 59, 86, 91, 108, 249, 255, 257, 259, 262, 264, 268, 287, 295, 296, 305

[44] R. M. Bionta et al. Observation of a Neutrino Burst in Coincidence with Supernova SN 1987a in the Large Magellanic Cloud. *Phys. Rev. Lett.*, 58:1494, 1987. 36

[45] J. N. Bahcall and S. L. Glashow. Upper limit on the mass of the electron neutrino. *nat*, 326(6112):476–477, April 1987. 36

[46] L. Wolfenstein. Neutrino oscillations in matter. *Phys. Rev. D*, 17:2369–2374, May 1978. 39

[47] S. P. Mikheyev and A. Yu. Smirnov. Resonance Amplification of Oscillations in Matter and Spectroscopy of Solar Neutrinos. *Sov. J. Nucl. Phys.*, 42:913–917, 1985. 39

[48] H. A. Bethe. Possible explanation of the solar-neutrino puzzle. *Phys. Rev. Lett.*, 56:1305–1308, Mar 1986. 39

[49] Amol S. Dighe and Alexei Yu. Smirnov. Identifying the neutrino mass spectrum from a supernova neutrino burst. *Physical Review D*, 62(3), jul 2000. 40

[50] Irene Tamborra. Supernova neutrinos: Theory, 2016. xviii, 41, 42

[51] Huaiyu Duan, George M. Fuller, J. Carlson, and Yong-Zhong Qian. Simulation of coherent nonlinear neutrino flavor transformation in the supernova environment: Correlated neutrino trajectories. *Phys. Rev. D*, 74:105014, Nov 2006. 41

[52] Overview of the SNOLAB facility and Current Programme Evolution. `https://indico.cern.ch/event/439062/contributions/1085691/attachments/1143592/1638849/snolab-future-projects-workshop-150824-facility-and-program-rev-1.pdf`. Accessed: 2021-09-10. 43

[53] A. Bellerive, J.R. Klein, A.B. McDonald, A.J. Noble, and A.W.P. Poon. The sudbury neutrino observatory. *Nuclear Physics B*, 908:30–51, Jul 2016. xix, 43, 44, 51, 57, 69, 78

[54] G Bellini, J Benziger, D Bick, G Bonfini, D Bravo, M. Buizza Avanzini, B Caccianiga, and et al. Cosmogenic backgrounds in borexino at 3800 m water-equivalent depth. *Journal of Cosmology and Astroparticle Physics*, 2013(08):049–049, Aug 2013. 44, 294, 307

[55] James R. Sinclair. *Positioning and timing calibration of SNO+*. PhD thesis, 2015. xviii, xx, 45, 47, 48, 49, 72, 78, 97

[56] Jack Dunger. *Topological and Time Based Event Classification for Neutrinoless Double Beta Decay in Liquid Scintillator*. PhD thesis, 2018. 44, 61

[57] Y Yamaguchi and K Oyanagi. Mechanical Properties of Urylon, a Polynonamethylene Urea Fiber. *Journal of the Textile Machinary Society*, 13(12):855–861, 1960. 44

[58] P G Jones. *Background rejection for the neutrinoless double beta decay experiment SNO+*. PhD thesis, University of Oxford, 2011. xix, 46

[59] James R. Sinclair. *Positioning and Timing Calibration of SNO+*. Phd thesis, 2015. 47, 51, 86, 102

[60] J. Benziger, L. Cadonati, F. Calaprice, E. de Haas, R. Fernholz, R. Ford, C. Galbiati, and et al. The nylon scintillator containment vessels for the borexino solar neutrino experiment. *Nuclear Instruments and Methods in Physics Research Section A: Accelerators, Spectrometers, Detectors and Associated Equipment*, 582(2):509–534, Nov 2007. 48

[61] S. Andringa, E. Arushanova, S. Asahi, M. Askins, D. J. Auty, A. R. Back, Z. Barn-ard, and et al. Current status and future prospects of the SNO+ experiment. *Advances in High Energy Physics*, 2016:1–21, 2016. xiv, xix, 48, 52, 54, 55, 56, 298

[62] Kalpana Singh, P. Gorel, Aksel Hallin, Carsten Krauss, and Zachary Petriw. Under-water photometry system of the SNO+ experiment. *Journal of Physics: Conference Series*, 1342:012130, 01 2020. 48

[63] M. R. Anderson, S. Andringa, M. Askins, D. J. Auty, N. Barros, F. Barão, R. Bayes, and et al. Measurement of neutron-proton capture in the SNO+ water phase. *Physical Review C*, 102(1), Jul 2020. 48

[64] S. N. Ahmed et al. Constraints on nucleon decay via 'invisible' modes from the Sudbury Neutrino Observatory. *Phys. Rev. Lett.*, 92:102004, 2004. 48

[65] E. Arushanova. Development of an 90y calibration source and rejection of pileup backgrounds in the SNO+ experiment. 2018. xix, 49, 54, 56, 69

[66] A scintillator purification plant and fluid handling system for SNO+. 2015. xix, 52, 54

[67] M.R. Anderson, S. Andringa, L. Anselmo, E. Arushanova, S. Asahi, M. Askins, D.J. Auty, and et al. Development, characterisation, and deployment of the SNO+ liquid scintillator. *Journal of Instrumentation*, 16(05):P05009, May 2021. 52

[68] L. Pickard and B. Tam. Scintillator QA Plenary. SNO+ internal document SNO+-doc-5872-v1, 2019. 53

[69] Morgan A. D. Askins. *Search for Invisible Neutron Decay in the SNO+ Water Phase.* PhD thesis, 2018. 53, 57, 60, 66

[70] R. Arnold, C. Augier, J. Baker, A. S. Barabash, A. Basharina-Freshville, S. Blondel, M. Bongrand, and et al. Measurement of the $\beta\beta$ decay half-life of te130 with the nemo-3 detector. *Physical Review Letters*, 107(6), Aug 2011. 53

[71] Matthew Redshaw, Brianna J. Mount, Edmund G. Myers, and Frank T. Avignone. Masses of te130 and xe130 and double-β-decay q value of te130. *Physical Review Letters*, 102(21), May 2009. 54

[72] G. Prior. The SNO+ experiment physics goals and background mitigation, 2017. 55

[73] R. Alves, S. Andringa, S. Bradbury, J. Carvalho, D. Chauhan, K. Clark, I. Coulter, and et al. The calibration system for the photomultiplier array of the SNO+ experiment. *Journal of Instrumentation*, 10(03):P03002–P03002, Mar 2015. 55, 57

[74] Ashley R. Back. *Probing new physics mechanisms in neutrinoless double-beta decay with SNO+*. PhD thesis, 2017. 56, 62

[75] J. Klein, M. Neubauer, M. Newcomer, and R. Van Berg. The SNO Trigger System. SNO+ internal document SNO+-doc-827-v1, 1997. 59

[76] James Waterfield. *Optical calibration system for SNO+ and sensitivity to neutrinoless double-beta decay.* PhD thesis, University of Sussex, April 2017. xix, 60

[77] SNO+ Collaboration, :, V. Albanese, R. Alves, M. R. Anderson, S. Andringa, L. Anselmo, E. Arushanova, S. Asahi, and et al. The SNO+ experiment, 2021. 60, 258, 296

[78] S Agostinelli, J Allison, K Amako, J Apostolakis, H Araujo, P Arce, M Asai, and et al. Geant4—a simulation toolkit. *Nuclear Instruments and Methods in Physics Research Section A: Accelerators, Spectrometers, Detectors and Associated Equipment*, 506(3):250–303, 2003. 61

[79] I. Antcheva, M. Ballintijn, B. Bellenot, M. Biskup, R. Brun, N. Buncic, Ph. Canal, and et al. Root — a c++ framework for petabyte data storage, statistical analysis and visualization. *Computer Physics Communications*, 180(12):2499–2512, Dec 2009. 61

[80] R. Bonventre, G. Orebi Gann, M. Schwendener, S. Seibert, M. Strait, and J. Wilson. Event Display Committee Recommendations. SNO+ internal document SNO+-doc-1962-v1, 2013. 62

[81] Data-flow Documentation. `https://snoplus.github.io/data-flow-documentation/`. Accessed: 2021-09-18. 63

[82] B. Aharmim, S. N. Ahmed, J. F. Amsbaugh, J. M. Anaya, A. E. Anthony, J. Banar, N. Barros, and et al. Measurement of the ν_e and total 8b solar neutrino fluxes with the sudbury neutrino observatory phase-iii data set. *Physical Review C*, 87(1), Jan 2013. 66

[83] B.A. Moffat, R.J. Ford, F.A. Duncan, K. Graham, A.L. Hallin, C.A.W. Hearns, J. Maneira, and et al. Optical calibration hardware for the sudbury neutrino observatory. *Nuclear Instruments and Methods in Physics Research Section A: Accelerators, Spectrometers, Detectors and Associated Equipment*, 554(1-3):255–265, Dec 2005. xix, 68, 69

[84] Robert Stainforth. *Characterising the Optical Response of the SNO+ Detector.* PhD thesis, U. Liverpool (main), 2016. 69

[85] Edward Leming. TELLIE Usermanual (v1). SNO+ internal document, 2015. 71, 86

[86] Matthew Strait. Summer 2015 Supernova Plenary. SNO+ internal document SNO+-doc-3420-v1, 2015. 71

[87] Martti Nirkko. Umbilical Flasher Object (UFO) design. SNO+ internal document, 2018. 73

[88] Rongqing Hui and Maurice O'Sullivan. *Characterization of Optical Devices*, pages 259–363. 12 2009. 75

[89] Michal Rigan. UFO measurements. SNO+ internal document SNO+-doc-7121-v1, 2021. 76

[90] E. Leming, R. White, J. Sinclair, S. Peeters, J. Waterfield, M. Stringer, and M. Nirkko. TELLIE hardware manual. SNO+ internal document SNO+-doc-4486-v1, 2017. xx, xxi, 79, 80, 81, 82, 83, 85, 86

[91] E. Falk, J. Lidgard, M. I. Stringer, and E. Turner. Commissioning of ellie for SNO+, 2017. 86

[92] Jose Maneira, Matthew Mottram, Simon Peeters, James Sinclair, and James Waterfield. Characterisation Procedure for TELLIE LED Drivers. SNO+ internal document SNO+-doc-3148-v2, 2016. 87

[93] C. Mills and M. Rigan. TELLIE HW maintenance report - 25_Jan_2019. SNO+ internal document SNO+-doc-5491-v1, 2019. 87

[94] Michal Rigan. TELLIE Hardware work report - Feb 2019. SNO+ internal document SNO+-doc-5542-v1, 2019. 87

[95] Michal Rigan. TELLIE Electronics Upgrades - July 2019. SNO+ internal document SNO+-doc-5857-v1, 2019. 88, 89

[96] Ch. Mills, M. Nirkko, and M. Rigan. TELLIE - recent UG work. SNO+ internal document SNO+-doc-6422-v3, 2020. 89

[97] Michal Rigan. TELLIE isolation boards tests. SNO+ internal document SNO+-doc-6255-v1, 2020. 93

[98] Michal Rigan. TELLIE Isolation boards - hardware work plan. SNO+ internal document SNO+-doc-6260-v1, 2020. 93

[99] TELLIE Inventory. `https://epp-wiki.hpc.susx.ac.uk/SnoPlus/TELLIEInventory`. Accessed: 2021-09-17. 93

[100] Tellie_hardware_status. `https://docs.google.com/spreadsheets/d/1m6w9x162qPbOOEpruCQORSqrlMgiGSu35oala6uIpp0/edit#gid=0`. Accessed: 2021-09-17. 93

[101] TELLIE debugging manual. `https://users.sussex.ac.uk/~mr514/TELLIE_debugging_manual.pdf`. Accessed: 2021-09-17. 93

[102] R. Alves, S. Andringa, S. Bradbury, J. Carvalho, D. Chauhan, K. Clark, I. Coulter, and et al. The calibration system for the photomultiplier array of the SNO+ experiment. nov 2014. xxiii, 96, 97, 98, 113, 115

[103] Freija Descamps. PCA calibration with SNO + RAT. SNO+ internal document SNO+-doc-1987-v5, 2016. xxii, 96, 99, 100, 102, 103, 104, 105, 106, 107, 140, 356, 357

[104] James Cameron. *The Photomultiplier Tube Calibration of the Sudbury Neutrino Observatory*. Phd thesis, 2001. 97

[105] Orebi Gann, Gabriel. ECA Calibration / Uncalibration in SNO+. SNO+ internal document SNO+-doc-1236-v1, 2010. 98

[106] Richard Taplin. *The Use of Photomultipliers in SNO*. Phd thesis, 1995. 98

[107] Robert Stainforth. *Characterising the Optical Response of the SNO+ Detector*. Phd thesis, 2016. 107

[108] Robert Stainforth. PMT Bucket Time / RAT::DU::GroupVelocity. SNO+ internal document SNO+-doc-3138-v6, 2015. xxiii, 108, 109

[109] Martti Nirkko. Angular systematic evaluation using TELLIE PCA data. SNO+ internal document SNO+-doc-4748-v1, 2017. xxiii, 110, 111, 112

[110] Freija Descamps. SNO+ External Light Calibration. SNO+ internal document SNO+-doc-3926-v1, 2016. xxiii, 116

[111] E. J. Leming, R. White, J. Sinclair, S. Peeters, J. Waterfield, and M. Stringer. TELLIE hardware manual (v1). SNO+ internal document SNO+-doc-4486-v1, 2016. 126, 128

[112] Martti Nirkko. SNO+ TELLIE PCA data – Fibre installation validation document. SNO+ internal document SNO+-doc-4442-v5, 2017. xxv, 129, 131

[113] Freija Descamps. PCA update. SNO+ internal document SNO+-doc-2644-v1, 2014. xxvii, 142

[114] Martti Nirkko. TELLIE features and plans. SNO+ internal document SNO+-doc-5610-v1, 2019. 156

[115] Martti Nirkko. TELLIE automation plan. SNO+ internal document SNO+-doc-5756-v1, 2019. 159

[116] Michal Rigan. TELLIE Automation - plan. SNO+ internal document SNO+-doc-6957-v1, 2021. 159

[117] A. Mastbaum, E. Caden, K. Labe, A. LaTorre, E. Marzec, T. Pershing, and L. Kormos. SNO+ Detector Operator Manual. SNO+ internal document, 2019. 165, 180

[118] Kevin Labe. Report and User Guide for the Level 2 Trigger System. SNO+ internal document SNO+-doc-2842-v2, 2016. xxix, 166, 167, 168, 176

[119] Jia-Shian Wang. Supernova burst trigger study. SNO+ internal document SNO+-doc-6079-v1, 2019. xxx, 173, 174

[120] Jia-Shian Wang. Supernova burst trigger study - update. SNO+ internal document SNO+-doc-6079-v1, 2021. xxx, 174

[121] redis. `redis.io`. Accessed: 2021-05-05. 186

[122] CouchDB. `https://docs.couchdb.org/en/stable/intro/overview.html`. Accessed: 2021-05-05. 186

[123] Alessandro Mirizzi, Irene Tamborra, Hans-Thomas Janka, Ninetta Saviano, Kate Scholberg, Robert Bollig, Lorenz Hudepohl, and Sovan Chakraborty. Supernova

Neutrinos: Production, Oscillations and Detection. jul 2015. xxxv, 218, 272, 276, 287

[124] Vale confirms multiple seismic events at Creighton Mine. `https://northernontario.ctvnews.ca/vale-confirms-multiple-seismic-events-at-creighton-mine-1.5269552`. Accessed: 2021-05-12. xxxvii, 222, 226

[125] Pietro Antonioli, Richard Tresch Fienberg, Fabrice Fleurot, Yoshiyuki Fukuda, Walter Fulgione, Alec Habig, Jaret Heise, and et al. Snews: the supernova early warning system. *New Journal of Physics*, 6:114–114, Sep 2004. 237, 238

[126] Alec Habig. Snews: A neutrino early warning system for galactic sn ii. *AIP Conference Proceedings*, 2000. 237, 238

[127] SNEWS: SuperNova Early Warning System. `https://snews.bnl.gov/`. Accessed: 2021-05-12. 238

[128] Kate Scholberg. Snews: The supernova early warning system. *AIP Conference Proceedings*, 2000. 238

[129] S Andringa, R. Bayes, C. Kraus, L. Lebanowski, S. Peeters, M. Rigan, J. Rumleskie, and et al. Supernova Shifter Instructions. SNO+ internal document SNO+-doc-6976-v1, 2021. 239

[130] Janet Rumleskie. *SNO+ Sensitivities to Pre-supernova and Supernova Neutrinos*. PhD thesis, 2021. 239

[131] S Andringa, R. Bayes, C. Kraus, L. Lebanowski, S. Peeters, M. Rigan, J. Rumleskie, and et al. SNO+ supernova response. SNO+ internal document SNO+-doc-6665-v1, 2020. xlv, 239, 371

[132] Jeff Tseng. SN Reaction Strategy. SNO+ internal document SNO+-doc-6832-v1, 2021. 239

[133] Janet Rumleskie. Supernova testing with TELLIE. SNO+ internal document SNO+-doc-6180-v1, 2019. 240

[134] Janet Rumleskie. (SN)ELLIE April 2020 Testing. SNO+ internal document SNO+-doc-6462-v1, 2020. xxxviii, 240, 241, 242

[135] Janet Rumleskie. (SN)ELLIE Testing. SNO+ internal document SNO+-doc-6363-v1, 2020. 240

[136] M. Rigan and J. Rumleskie. Supernova sensitivities. SNO+ internal document SNO+-doc-6802-v1, 2021. xxxviii, 241, 242

[137] N. Rupp. Radon background in liquid xenon detectors. *Journal of Instrumentation*, 13(02):C02001–C02001, Feb 2018. 242

[138] Takashi Yoshida, Toshio Suzuki, Satoshi Chiba, Toshitaka Kajino, Hidekazu Yokomakura, Keiichi Kimura, Akira Takamura, and Dieter H. Hartmann. Neutrino-nucleus reaction cross sections for light element synthesis in supernova explosions. *The Astrophysical Journal*, 686(1):448–466, Oct 2008. 249, 258

[139] E. Kolbe, K. Langanke, and P. Vogel. Estimates of weak and electromagnetic nuclear decay signatures for neutrino reactions in super-kamiokande. *Phys. Rev. D*, 66:013007, Jul 2002. 249, 256

[140] Artur M. Ankowski. Improved estimate of the cross section for inverse beta decay, 2016. 250

[141] G. Bellini, J. Benziger, S. Bonetti, M. Buizza Avanzini, B. Caccianiga, L. Cadonati, F. Calaprice, and et al. Observation of geo-neutrinos. *Physics Letters B*, 687(4-5):299–304, Apr 2010. 250, 294

[142] P. Jean and N. Guessoum. Neutron-capture and 2.22 mev emission in the atmosphere of the secondary of an x-ray binary. *Astronomy & Astrophysics*, 378(2):509–521, Nov 2001. 250

[143] S. Dazeley, A. Bernstein, N.S. Bowden, and R. Svoboda. Observation of neutrons with a gadolinium doped water cherenkov detector. *Nuclear Instruments and Methods in Physics Research Section A: Accelerators, Spectrometers, Detectors and Associated Equipment*, 607(3):616–619, Aug 2009. 250

[144] S. Abe, T. Ebihara, S. Enomoto, K. Furuno, Y. Gando, K. Ichimura, H. Ikeda, and et al. Precision measurement of neutrino oscillation parameters with kamland. *Physical Review Letters*, 100(22), Jun 2008. 250, 294

[145] J. E. Lynn, S. Kahane, and S. Raman. Analysis of slow neutron capture by Be-9, C-12, and C-13. *Phys. Rev. C*, 35:26–36, 1987. 250

[146] Vincent Fischer. Beta-decay emitted electronic antineutrinos as a tool for unsolved problems in neutrino oscillation physics, 2015. 250

[147] Alessandro Strumia and Francesco Vissani. Precise quasielastic neutrino/nucleon cross-section. *Physics Letters B*, 564(1-2):42–54, Jul 2003. 251

[148] L. A. Ahrens et al. Measurement of Neutrino - Proton and anti-neutrino - Proton Elastic Scattering. *Phys. Rev. D*, 35:785, 1987. 254

[149] John F. Beacom, Will M. Farr, and Petr Vogel. Detection of supernova neutrinos by neutrino-proton elastic scattering. *Physical Review D*, 66(3), Aug 2002. 254

[150] J. Beringer et al. Review of Particle Physics (RPP). *Phys. Rev. D*, 86:010001, 2012. 254

[151] Giulia Pagliaroli, Carolina Lujan-Peschard, Manimala Mitra, and Francesco Vissani. Neutrinos from pion decay at rest to probe the proton strangeness in an underground lab, 2013. 254

[152] M. S. Yang, Z. Y. Yu, J. Cao, X. L. Sun, B. X. Yu, and G. P. An. Measurement of proton quenching in a lab based liquid scintillator, 2018. 255

[153] J B Birks. Scintillations from Organic Crystals: Specific Fluorescence and Relative Response to Different Radiations. *Proceedings of the Physical Society. Section A*, 64(10):874–877, oct 1951. 255

[154] T Matulewicz. Quenching of scintillation in BaF2 for light charged particles. *Nuclear Instruments and Methods in Physics Research Section A: Accelerators, Spectrometers, Detectors and Associated Equipment*, 325(1):365–366, 1993. 255

[155] E Kolbe, K Langanke, G Martínez-Pinedo, and P Vogel. Neutrino–nucleus reactions and nuclear structure. *Journal of Physics G: Nuclear and Particle Physics*, 29(11):2569–2596, Oct 2003. 256

[156] K. Langanke, P. Vogel, and E. Kolbe. Signal for supernova muon-neutrino and tau-neutrino neutrinos in water Cherenkov detectors. *Phys. Rev. Lett.*, 76:2629–2632, 1996. 257

[157] T. Mori, R. Yamaguchi, M. Sakuda, A. M. Ankowski, O. Benhar, S. K. Singh, J. G. Morfin, and et al. The γ -ray production in neutral-current neutrino-oxygen interaction in the energy range above 100 mev. 2011. 257

[158] F Ajzenberg-Selove. Energy levels of light nuclei A = 11–12. *Nuclear Physics A*, 248(1):1–152, 1975. 257

[159] C. Lujan-Peschard, G. Pagliaroli, and F. Vissani. Spectrum of supernova neutrinos in ultra-pure scintillators. *Journal of Cosmology and Astroparticle Physics*, 2014(07):051–051, Jul 2014. 257

[160] B Armbruster et al. Measurement of the weak neutral current excitation C-12(nu(mu) nu'(mu))C*-12(1+,1,15.1-MeV) at E(nu(mu)) = 29.8-MeV. *Phys. Lett. B*, 423:15–20, 1998. 258

[161] A. Gando, Y. Gando, K. Ichimura, H. Ikeda, K. Inoue, Y. Kibe, Y. Kishimoto, and et al. Search for extraterrestrial antineutrino sources with the kamland detector. *The Astrophysical Journal*, 745(2):193, Jan 2012. 258

[162] Garching core collapse archive. https://wwwmpa.mpa-garching.mpg.de/ccsnarchive/archive.html. Accessed: 2021-06-01. 262

[163] Markus Rampp and H.-Thomas Janka. Spherically symmetric simulation with boltzmann neutrino transport of core collapse and postbounce evolution of a 15 $m_\odot$ star. *The Astrophysical Journal*, 539(1):L33–L36, Aug 2000. 262

[164] Pasquale D. Serpico, Sovan Chakraborty, Tobias Fischer, Lorenz Hüdepohl, Hans-Thomas Janka, and Alessandro Mirizzi. Probing the neutrino mass hierarchy with the rise time of a supernova burst. *Physical Review D*, 85(8), Apr 2012. 262, 272

[165] Bernhard Müller and Hans-Thomas Janka. A new multi-dimensional general relativistic neutrino hydrodynamics code for core-collapse supernovae. iv. the neutrino signal. *The Astrophysical Journal*, 788(1):82, May 2014. 262, 272

[166] James M. Lattimer and F. Douglas Swesty. A Generalized equation of state for hot, dense matter. *Nucl. Phys. A*, 535:331–376, 1991. xlii, 262, 272, 290

[167] Andrew Steiner, Matthias Hempel, and Tobias Fischer. Core-collapse supernova equations of state based on neutron star observations. *The Astrophysical Journal*, 774, 07 2012. 262

[168] L. Hüdepohl, B. Müller, H.-T. Janka, A. Marek, and G. G. Raffelt. Neutrino signal of electron-capture supernovae from core collapse to cooling. *Phys. Rev. Lett.*, 104:251101, Jun 2010. xlii, 262, 272, 290

[169] Mark Galassi, Jim Davies, James Theiler, Brian Gough, and Gerard Jungman. *GNU Scientific Library - Reference Manual, Third Edition, for GSL Version 1.12 (3. ed.)*. 01 2009. 263

[170] PDG Identifiers. `https://pdg.lbl.gov/2020/pdgid/PDGIdentifiers.html`. Accessed: 2021-06-21. 268

[171] Evan O'Connor and Christian D. Ott. The progenitor dependence of the pre-explosion neutrino emission in core-collapse supernovae. *The Astrophysical Journal*, 762(2):126, Dec 2012. 272

[172] H. Shen, H. Toki, K. Oyamatsu, and K. Sumiyoshi. Relativistic equation of state of nuclear matter for supernova and neutron star. *Nuclear Physics A*, 637(3):435–450, Jul 1998. 272, 321

[173] S E Woosley, CA Lawrence Livermore National Lab., and T A Weaver. The evolution and explosion of massive stars ii: Explosive hydrodynamics and nucleosynthesis. 272, 322

[174] Chris L Fryer. Mass Limits For Black Hole Formation. *The Astrophysical Journal*, 522(1):413–418, sep 1999. 272, 321

[175] D. P. Menezes and C. Providencia. Equation of State for supernova explosion simulations. mar 2007. 289

[176] G Audi, A H Wapstra, and C Thibault. The Ame2003 atomic mass evaluation: (II). Tables, graphs and references. *Nuclear Physics A*, 729(1):337–676, 2003. 295

[177] H. Godwin. Half-life of radiocarbon. *nat*, 195(4845):984, September 1962. 295

[178] Kate Scholberg. Supernova Neutrino Detection in Water Cherenkov Detectors. *Journal of Physics: Conference Series*, 309:12028, aug 2011. 296

[179] H M O'Keeffe. *Low energy background in the NCD phase of the Sudbury Neutrino Observatory*. PhD thesis, University of Oxford, 2008. 296

[180] Stephen Robert Hanchurak. Development of a High Sensitivity Radon Emanation Detector. Master's thesis, Alberta U., 2014. xlii, 297

[181] P. Khaghani. Neck sense rope system and leaching studies for sno. Master's thesis, Sudbury U., 2015. 296

[182] M. Chen, V. Lozza, and H. O'Keeffe. Expected radioactive backgrounds in SNO+. SNO+ internal document SNO+-doc-507-v42, 2019. xiv, 298

[183] Kevin Nuckolls. PMT Speci*ic Noise Analysis and Calibration For SNO+. SNO+ internal document SNO+-doc-2629-v2, 2014. 299

[184] S. Abe, T. Ebihara, S. Enomoto, K. Furuno, Y. Gando, K. Ichimura, H. Ikeda, and et al. Precision measurement of neutrino oscillation parameters with kamland. *Phys. Rev. Lett.*, 100:221803, Jun 2008. 306

[185] A. Gando et al. A study of extraterrestrial antineutrino sources with the KamLAND detector. *Astrophys. J.*, 745:193, 2012. 307

[186] C. A. Kierans, S. E. Boggs, A. Zoglauer, A. W. Lowell, C. Sleator, J. Beechert, T. J. Brandt, and et al. Detection of the 511 kev galactic positron annihilation line with cosi. *The Astrophysical Journal*, 895(1):44, May 2020. 311

[187] Jack Dunger. *Event Classification in Liquid Scintillator Using PMT Hit Patterns*. PhD thesis, Oxford U., 2019. xliii, 312, 313

[188] H. T. Janka. Neutrinos from type II supernovae and the neutrino driven supernova mechanism. *Italian Phys. Soc. Proc.*, 40:345–374, 1993. 321

[189] K. Sumiyoshi, S. Yamada, and H. Suzuki. Dynamics and neutrino signal of black hole formation in nonrotating failed supernovae. ii. progenitor dependence. *The Astrophysical Journal*, 688(2):1176–1185, Dec 2008. 321, 322

[190] K. Sumiyoshi, S. Yamada, H. Suzuki, and S. Chiba. Neutrino signals from the formation of a black hole: A probe of the equation of state of dense matter. *Phys. Rev. Lett.*, 97:091101, Aug 2006. 321

[191] Adam Burrows. Supernova Neutrinos. *Astrophysical Journal v.334*, 334:891, November 1988. 322

[192] Yudai Suwa, Kohsuke Sumiyoshi, Ken'ichiro Nakazato, Yasufumi Takahira, Yusuke Koshio, Masamitsu Mori, and Roger A Wendell. Observing Supernova Neutrino Light Curves with Super-Kamiokande: Expected Event Number over 10 s. *The Astrophysical Journal*, 881(2):139, aug 2019. 322

[193] Christopher S. Kochanek, John F. Beacom, Matthew D. Kistler, José L. Prieto, Krzysztof Z. Stanek, Todd A. Thompson, and Hasan Yüksel. A survey about nothing: Monitoring a million supergiants for failed supernovae. *The Astrophysical Journal*, 684(2):1336–1342, Sep 2008. 322

[194] K. Nomoto, N. Tominaga, M. Tanaka, K. Maeda, H. Umeda, Stefan Immler, and Kurt Weiler. Nucleosynthesis in core-collapse supernovae and grb-metal-poor star connection. *AIP Conference Proceedings*, 2007. 322

[195] Rasmus S. L. Hansen, Manfred Lindner, and Oliver Scholer. Timing the neutrino signal of a galactic supernova. *Phys. Rev. D*, 101:123018, Jun 2020. 322

Abbreviations

$0\nu\beta\beta$ neutrinoless double beta decay

1D, 2D one-dimensional, two-dimensional

$2\nu\beta\beta$ double beta decay

ADC analog-to-digital (converter)

AMELLIE attenuation module for embedded LED/laser light injection entity

AV acrylic vessel

BH black hole

BNL Brookhaven National Laboratory

BS brust trigger

BT (supernova) burts trigger

BUF buffer

CAEN CAEN digitizer, instruments housing high speed multichannel flash ADC, local memory and field-programmable gate array for real-time data processing

CAP counts above pedestal

CC charged current (interaction)

CC (SN) core-collapse (when mentioned with SN/SNe)

CCC crate-card-channel (distribution)

CERN the establishment of a European Council for Nuclear Research

CMB cosmic microwave background

CNB cosmic neutrino background

CMOS complementary metal-oxide semiconductor (chip)

CNO carbon-nitrogen-oxygen (cycle)

CP charge-parity (violation)

CRSU control room Sussex university

CTC crate trigger card

DAQ data acquisition

DC direct current

DCR detector control room

E energy

EC electron-capture (supernova)

ECA electronics calibration

EE neutrino-electron elastic scattering (interaction)

ELLIE embedded LED/laser light injection entity

EOS equation of state

EP neutrino-proton elastic scattering (interaction)

ESUM trigger signal, a copy of the PMT pulse

EXT external, sometimes also external water part of SNO+

EXTA external asynchronous (trigger)

FE front-end (electronics)

FEC front-end card

FIFO first-in, first-out (buffer)

FT fibre TELLIE

FV fiducial volume

FWHM full-width half-maximum

GPS global positioning system (time)

GRID grid computing, widely distributed computer resources

GT global trigger

GTID global trigger ID

HEP high energy physics

HEPEVT high energy physics event(s)

HHP high-half point

HW hardware

IBD inverse beta decay

ID identifier

IMB Irvine-Michigan-Brookhaven (experiment)

IO, IH inverted ordering, inverted hierarchy

IP interpolation point

IPW ($I_{\mathbf{PW}}$) internal pulse width

L1 level 1

L2 level 2

LAB linear alkylbenzene

LB laserball

LED light-emitting diode

LESA the lepton-emission self-sustained asymmetry

LMC Large Magellanic Cloud

LPC ligth path calculator

LS liquid scintillator

LSD Mont Blanc liquid scintillator detector

MC Monte Carlo, usually reference to the Monte Carlo simulation

M$_\odot$ solar mass

MPE multi photo-electron (mode)

MS main-sequence (star)

MSW Mikheyev-Smirnov-Wolfenstein (effect)

MTC master trigger card

MTCA+ master trigger card analogue

MTCD master trigger card digital

NC neutral current (interaction)

NHIT(S) (NHit(s)) number of hit photo-multiplier tubes

NO, NH normal ordering, normal hierarchy

NS neutron star

ORCA object-oriented real-time control and acquisition: DAQ software interface with the detector

OWL outward looking PMT(s)

PCA photo-multiplier tube(s) calibration

PE photo-electron

PI pair-instability (SN)

PIC peripheral interface controller (chip)

PIN (diode) is a diode with a wide, undoped intrinsic semiconductor region between a p-type semiconductor and an n-type semiconductor region

PK peak

PMMA polymethyl methacrylate, aka acrylic glass or plexiglass

PMNS Pontecorvo-Maki-Nakagawa-Sakata (matrix)

PMT photo-multiplier tube

PMTIC PMT interface card

PNS proto-neutron star

PPO 2,5-Diphenyloxazole, used as wavelength shifter

PSUP photo-multiplier tubes support structure

Q charge

QA quality assurance

QHL deposited charge over long integration window

QHS deposited charge over short integration window

QLX deposited charge over long integration window, low gain

RAT reactor analysis tool: the software package used to simulate the SNO+ detector

RMS root mean square

ROOT open-source data analysis framework used by high energy physics

SASI the standing accretion shock instability

SCOUT scintillator counter of uranium and thorium

SH stonehenge (software package)

SI self interactions

SM Standard Model

SMELLIE scattering module for embedded LED/laser light injection entity

SN supernova

SNe supernovae

SNEWS supernova early warning system

SNUGEN supernova generator, MC software package

SPE single photo-electron (mode)

SW software

TAC time to amplitude converter

TELLIE timing module for embedded LED/laser light injection entity

TH threshold

TOF Time-of-Flight

TTS time transition spread

TUB trigger utility board

TUBII (TUBii) trigger utility board II

TW time-walk (effect)

UFO umbilical flasher object

UPW ultra-pure water

USB universal serial bus

UTC universal time coordinated, coordinated time scale

UV ultraviolet

V-A Vector-Axial (coupling)

WEB wet-end breakdown

XL3 additional control board for CTC

XSNOED X-SNO-Event-Display, graphical interface to view events

ZDAB file format in which raw data from SNO/SNO+ runs is stored

Appendix A

Method to extract the LED time offsets

Outline of the method to extract relative LED time offsets using overlapping PMTs between two LEDs. This is used in TELLIE PCA. The method is as described in [103].

- Find the position of the prompt time peak (corrected for transit-time) for each $\frac{PMT_i}{LED_j}$ combination that has enough hits. Store this in $tDelta[j][i]$ and also keep track of the list of LEDs that caused a hit in PMT i ($PMTHitBy[i]$).

- Loop over all PMTs, check if a PMT saw light from more than one LED. If so, calculate and store the time-offset between those LEDs as measured by this PMT.

- We now have, for each LED pair, a vector with time-offsets and one with the errors on these time-offsets.

- Then, we can calculate the time offset between each LED-pair by taking the median of the extracted offsets. This is done if at least 20 PMTs registered light from that LED pair.

- We have now extracted time-offsets and the errors on the time-offsets for all LED pairs (a lot of them will not have an extracted time-offset since there will be no overlap between them). This gives us two matrices: the time-offset matrix and the time offset error matrix.

- This is now a classic graph problem: we need to find the lowest-cost (most efficient, error-wise) way to bootstrap all LED times. This means: pick a reference LED and find the lowest-cost tree. This can be done with the Dijkstra algorithm. Then,

find the shortest path solution for each LED as starting point (basically re-do the Dijkstra[1] calculation as many times as there are working LEDs). Finally, we pick the solution with the most resolved LEDs-offsets and the smallest global error.

---

[1]Dijkstra algoritm is desgined to find the shortest (minimum error) path between nodes in a graph [103].

Appendix B

Complete run lists for TELLIE PCA datasets

This Appendix lists the full run lists for all available TELLIE PCA datasets:

Date	2017 June	2018 Mar	2018 June	2018 Sept	2018 Dec	2019 Mar	2019 Dec	2020 May
Mode	Asynch	Synch	Synch	Synch	Synch	Synch	Synch	Synch
Channel	95	95	95	95	95	92	95	94
1	101374	110264	114670	117578	201388	204401	253887	258566
2	101381	110266	114673	117580	201390	204403	253861	258568
3	101386	110268	114675	117582	201392	204409	253827	258570
4	101391	110269	114677	117584	201394	204411	253844	
5	101404	110282	114679	117586	201396	204413	253897	258576
6	101410	110289	114681	117588	201398	204415	253855	258578
7	101414	110293	114683	117590	201401	204418	253882	258580
8	101498	110303	114685	117592	201403	204420	253925	258582
9	101500	110309	114687	117594	201405	204423	253825	258584
10	101502	110314	114689	117598	201407	204425	254035	258586
11	101505	110321	114691	117602	201409	204429	253847	258588
12	101509	110329	114693	117604	201411	204431	253803	258590
13	101512	110337	114695	117606	201413	204437	253938	258592
14	101515	110342	114697	117608	201415	204439	253821	258594
15	101528	110347	114699	117610	201417	204441	253815	258596
16	101530	110350	114701	117612	201419	204442	253865	258811
17	101533	110357	114703	117614	201421	204444	253829	258602
18	101537	110363	114705	117616	201423	204446	253875	258608
19	101543	110367	114707	117618	201425	204448	253805	258610
20	101548	110372	114709	117620	201427	204450	253857	258612
21	101553	110376	114711	117622	201432	204452	254007	258614
22	101558	110385	114713	117624	201434	204454	254027	258616
23	101560	110392	114715	117626	201436	204456	253823	258618
24	101564	110398	114717	117628	201438	204460	253832	258621
25	101567	110403	114720	117630	201440	204462	253929	258623
26	101570	110407	114722	117632	201442	204464	253957	258627
27	101579	110413	114724	117634	201444	204467	253951	258631
28	101705	110415	114726	117636	201446	204469	253911	258633
29	101717	110426	114728	117638	201448	204471	253895	258635
30	101721	110430	114730	117640	201450	204473	253901	258637
31	101726	110434	114732	117642	201452	204475	253867	258639
32	101730	110440	114734	117644	201454	204477	253849	258641

33	101735	110468	114736	117646	201456	204479	253842	258643
34	101740	110477	114738	117654	201462	204481	253863	258645
35	101745	110481	114740	117656	201464	204483	253808	258647
36	101749	110487	114742	117658	201466	204485	253871	258649
37	101756	110496	114744	117660	201468	204487	254009	258651
38	101759	110501	114746	117662	201470	204489	253940	258653
39	101763	110507	114748	117664	201473	204491	254013	258655
40	101771	110510	114750	117666	201475	204493	254015	258657
41	101774	110516	114752	117668	201477	204495	253903	258659
42	101780	110520	114754	117670	201479	204497	253989	258661
43	101787	110578	114756	117672	201481	204499	253893	258663
44	101793	110587	114787	117680	201483	204501	253985	258665
45	101795	110608	114789	117684	201493	204503	254011	258667
46	101799	110614	114794	117686	201504	204505	254005	258669
47	101806	110619	114796	117688	201506	204507	253837	258671
48	101809	110625	114798	117690	201508	204509	254046	258673
49	101811	110637	114800	117692	201510	204511	253885	258675
50	101815	110645	114802	117694	201512	204513	253835	258677
51	101819	110650	114804	117696	201514	204515	253907	258679
52	101822	110660	114806	117698	201516	204517	253947	258681
53	101824	110666	114808	117700	201518	204519	253889	258683
54	101827	110671	114810	117702	201520	204521	253899	258685
55	101831	110700	114812	117704	201522	204523	253811	258687
56	101834	110725	114817	117708	201524	204525	253869	258691
57	101839	110731	114819	117712	201526	204527	254037	258693
58	101842	110736	114821	117714	201528	204529	253983	258695
59	101845	110744	114824	117716	201530	204531	254017	258697
60	101849	110751	114826	117718	201532	204533	254001	258702
61	101852	110757	114828	117720	201534	204535	253996	258704
62	101889	110762	114830	117722	201538	204537	253920	258706
63	101892	110768	114832	117724	201540	204541	253981	258708
64	101895	110773	114834	117728	201542	204543	253964	258712
65	101898	110777	114836	117730	201544	204545	254031	258714

66	101903	110781	115672	117732	201546	204547	254019	258716
67	101905	110785	115674	117734	201548	204549	254003	258719
68	101910	110793	115676	117736	201550	204551	253961	258721
69	101913	110796	115678	117738	201552	204553	253927	258723
70	101915	110800	115682	117740	201554	204555	253916	258727
71	101929	110823	115684	117742	201557	204557	254025	258747
72	101933	110833	115686	117744	201559	204559	253942	258749
73	101944	110841	115688	117746	201561	204561	254033	258751
74	102157	110847	115690	117748	201565	204563	253934	258754
75	102161	110854	115692	117750	201567	204565	253966	258756
76	102165	110858	115694	117752	201569	204567	253998	258760
77	102168	110865	115696	117754	201571	204569	253931	258762
78	102178	110872	115707	117756	201573	204571	254052	258764
79	102183	110878	115711	117758	201575	204573	253959	258766
80	102260	110891	115713	117760	201577	204575	253922	258772
81	102264	110896	115716	117762	201579	204577	253936	258774
82	102268	110902	115718	117764	201581	204579	253973	258776
83	102274	110905	115722	117766	201583	204581	253880	258778
84	102278	110910	115725	117768	201585	204583	253968	258780
85	102281	110932	115728	117770	201587	204585	253905	258782
86	102286	110964	115730	117772	201589	204589	254023	258784
87	102290	110972	115732	117774	201591	204593	254029	258787
88	102293	110997	115738	117776	201595	204595	253955	258793
89	102296	111022	115740	117779	201597	204597	253971	258797
90	102300	111033	115742	117782	201602	204599	253977	258799
91	102304	111036	115744	117784	201606	204601	253979	258801
92	102306	111042	115746	117786	201611	204605	253913	258803
93	102310	111044	115749	117788	201613		253909	258805
94	102313	111050	115751	117790	201617		253987	258807
95	102315	111058	115753	117792	201620		253949	258809

Table B.1: Table listing full run lists for all available TELLIE PCA datasets.

Appendix C

Remeasuring fibre delays - data

This Appendix contains data related to remeasuring TELLIE fibre software delays in 2019. The goal, set-up and additional details of this study are as described in Section 4.6. Additional plots and data are accumulated here.
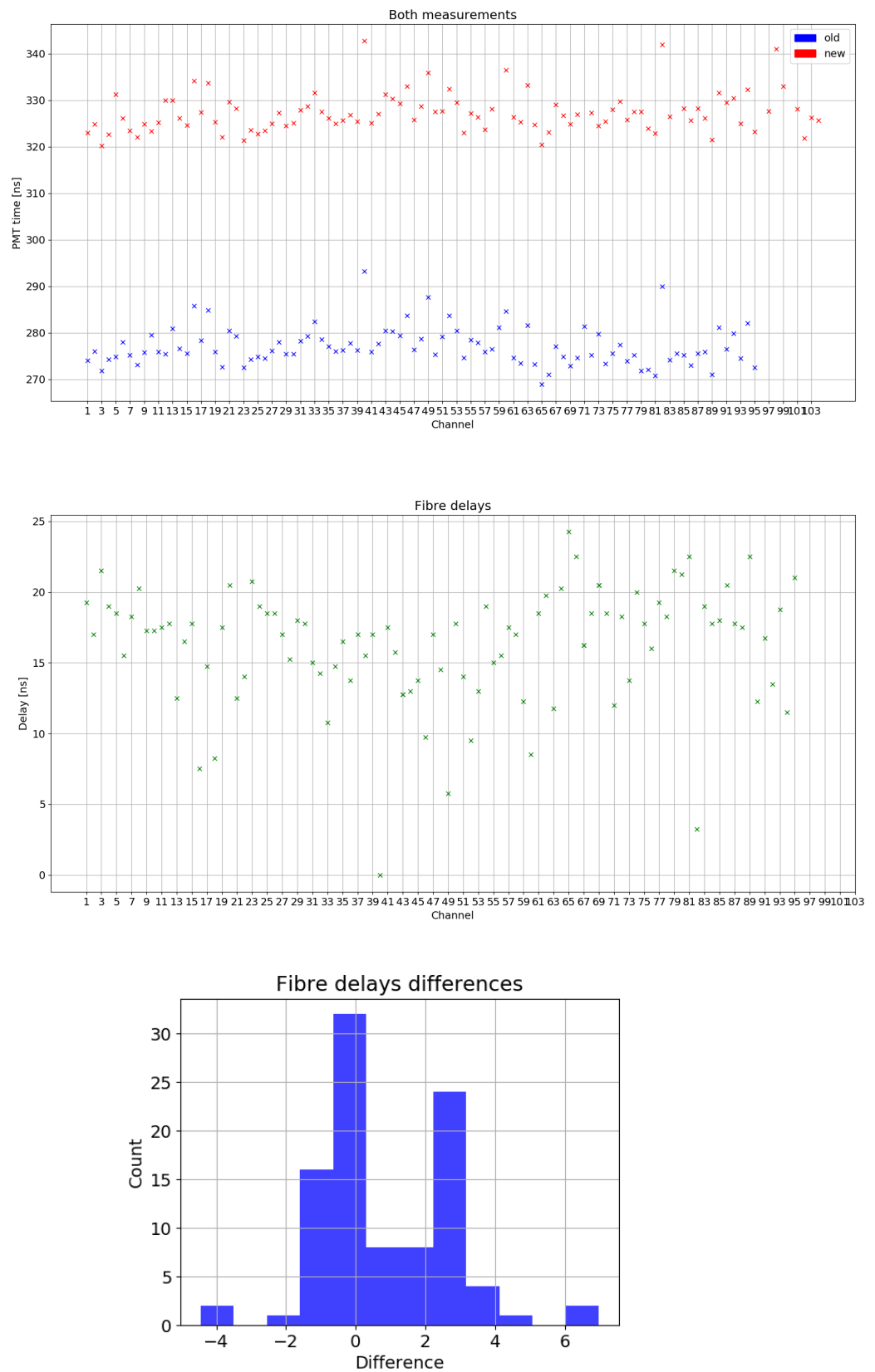
Figure C.1: Top: Mean time of PMT hit times per channel for old and new measurement. Middle: New calculated fibre software delays per channel. Bottom: Histogram of differences between the old and new fibre software delays for each channel.

Channel	Old fibre delay [ns]	New fibre delay [ns]	Difference [ns]	Mean hit time [ns]	Gaussian fit [ns]
1	19.25	19.750271	-0.500271	322.944201	322.9
2	17	17.866683	-0.866683	324.827789	324.8
3	21.5	22.466878	-0.966878	320.227594	320.2
4	19	20.007306	-1.007306	322.687166	322.6
5	18.5	11.512703	6.987297	331.181769	331.1
6	15.5	16.628281	-1.128281	326.066191	326
7	18.25	19.279369	-1.029369	323.415103	323.4
8	20.25	20.668046	-0.418046	322.026426	322
9	17.25	17.8794954	-0.6294954	324.8149766	324.8
10	17.25	19.402843	-2.152843	323.291629	323.3
11	17.5	17.511956	-0.011956	325.182516	325.1
12	17.75	12.720809	5.029191	329.973663	329.9
13	12.5	12.748343	-0.248343	329.946129	329.9
14	16.5	16.541403	-0.041403	326.153069	326.1
15	17.75	18.0485866	-0.2985866	324.6458854	324.6
16	7.5	8.5917841	-1.0917841	334.1026879	334.1
17	14.75	15.299961	-0.549961	327.394511	327.4
18	8.25	8.9673608	-0.7173608	333.7271112	333.7
19	17.5	17.330378	0.169622	325.364094	325.3
20	20.5	20.604509	-0.104509	322.089963	322
21	12.5	13.095391	-0.595391	329.599081	329.5
22	14	14.451265	-0.451265	328.243207	328.2
23	20.75	21.320416	-0.570416	321.374056	321.3
24	19	19.163809	-0.163809	323.530663	323.5
25	18.5	19.996383	-1.496383	322.698089	322.6
26	18.5	19.252528	-0.752528	323.441944	323.4
27	17	17.763448	-0.763448	324.931024	324.9
28	15.25	15.444679	-0.194679	327.249793	327.2
29	18	18.192428	-0.192428	324.502044	324.5
30	17.75	17.584646	0.165354	325.109826	325
31	15	14.880763	0.119237	327.813709	327.8
32	14.25	14.037378	0.212622	328.657094	328.6
33	10.75	11.145302	-0.395302	331.54917	331.5
34	14.75	15.145976	-0.395976	327.548496	327.5
35	16.5	16.560008	-0.060008	326.134464	326.1
36	13.75	17.712795	-3.962795	324.981677	325
37	17	17.011265	-0.011265	325.683207	325.6
38	15.5	15.842764	-0.342764	326.851708	326.8

Channel	Old fibre delay [ns]	New fibre delay [ns]	Difference [ns]	Mean hit time [ns]	Gaussian fit [ns]
39	17	17.306042	-0.306042	325.38843	325.4
40	0	0	0	342.694472	342.7
41	17.5	17.56436	-0.06436	325.130112	325.1
42	15.75	15.618559	0.131441	327.075913	327
43	12.75	11.409918	1.340082	331.284554	331.2
44	13	12.412895	0.587105	330.281577	330.2
45	13.75	13.379523	0.370477	329.314949	329.3
46	9.75	9.712209	0.037791	332.982263	332.9
47	17	16.902663	0.097337	325.791809	325.8
48	14.5	14.015853	0.484147	328.678619	328.6
49	5.75	6.854192	-1.104192	335.84028	335.8
50	17.75	15.130155	2.619845	327.564317	327.5
51	14	15.02904	-1.02904	327.665432	327.6
52	9.5	10.246737	-0.746737	332.447735	332.4
53	13	13.223892	-0.223892	329.47058	329.4
54	19	19.693068	-0.693068	323.001404	323
55	15	15.515796	-0.515796	327.178676	327.2
56	15.5	16.291082	-0.791082	326.40339	326.3
57	17.5	18.993485	-1.493485	323.700987	323.6
58	17	14.62168	2.37832	328.072792	328
59	12.25	10.2484474	2.0015526	332.4460246	
60	8.5	6.201152	2.298848	336.49332	336.4
61	18.5	16.394596	2.105404	326.299876	326.3
62	19.75	17.337142	2.412858	325.35733	325.3
63	11.75	9.433684	2.316316	333.260788	333.2
64	20.25	18.009914	2.240086	324.684558	324.6
65	24.25	22.259949	1.990051	320.434523	320.4
66	22.5	19.614074	2.885926	323.080398	323
67	16.25	13.620212	2.629788	329.07426	329.1
68	18.5	15.956073	2.543927	326.738399	326.7
69	20.5	17.91051	2.58949	324.783962	324.7
70	18.5	15.795299	2.704701	326.899173	326.9
71	12	10.4692819	1.5307181	332.2251901	

Channel	Old fibre delay [ns]	New fibre delay [ns]	Difference [ns]	Mean hit time [ns]	Gaussian fit [ns]
72	18.25	15.387444	2.862556	327.307028	327.3
73	13.75	18.206532	-4.456532	324.48794	324.4
74	20	17.300828	2.699172	325.393644	325.4
75	17.75	14.746569	3.003431	327.947903	327.9
76	16	12.943047	3.056953	329.751425	329.7
77	19.25	16.911962	2.338038	325.78251	325.8
78	18.25	15.159221	3.090779	327.535251	327.5
79	21.5	15.157342	6.342658	327.53713	327.5
80	21.25	18.740882	2.509118	323.95359	323.9
81	22.5	19.773213	2.726787	322.921259	322.8
82	3.25	0.77215	2.47785	341.922322	341.9
83	19	16.218203	2.781797	326.476269	326.4
84	17.75	14.9199156	2.8300844	327.7745564	
85	18	14.490169	3.509831	328.204303	328.1
86	20.5	17.081631	3.418369	325.612841	325.6
87	17.75	14.5185	3.2315	328.175972	328.2
88	17.5	16.571275	0.928725	326.123197	326.1
89	22.5	21.173888	1.326112	321.520584	321.5
90	12.25	11.059547	1.190453	331.634925	331.6
91	16.75	13.208237	3.541763	329.486235	329.4
92	13.5	12.249466	1.250534	330.445006	330.4
93	18.75	17.726788	1.023212	324.967684	324.9
94	11.5	10.468307	1.031693	332.226165	332.4
95	21	19.535349	1.464651	323.159123	323.1
96	Loop-back fibre				
97		15.085094		327.609378	327.5
98		1.669834		341.024638	341
99		9.664982		333.02949	333
100		9.9292638		332.7652082	
101		14.559196		328.135276	328.1
102		20.901841		321.792631	321.8
103		16.490564		326.203908	326.2
104		16.988625		325.705847	325.7

Table C.1: Table summarizing software fibre delays for TELLIE channels. Includes results from the original measurement as well as new on-site measurement. Both mean and Gaussian git values are shown where available. Fibre 96 is a loop-back fibre. For the new measurements, AMELLIE fibres were included as well.

Appendix D

PCA cable delays - comparison

This Appendix contains the histograms comparing the cable delay constants obtained from PCA datasets. These are described in Subsection 4.8.1.
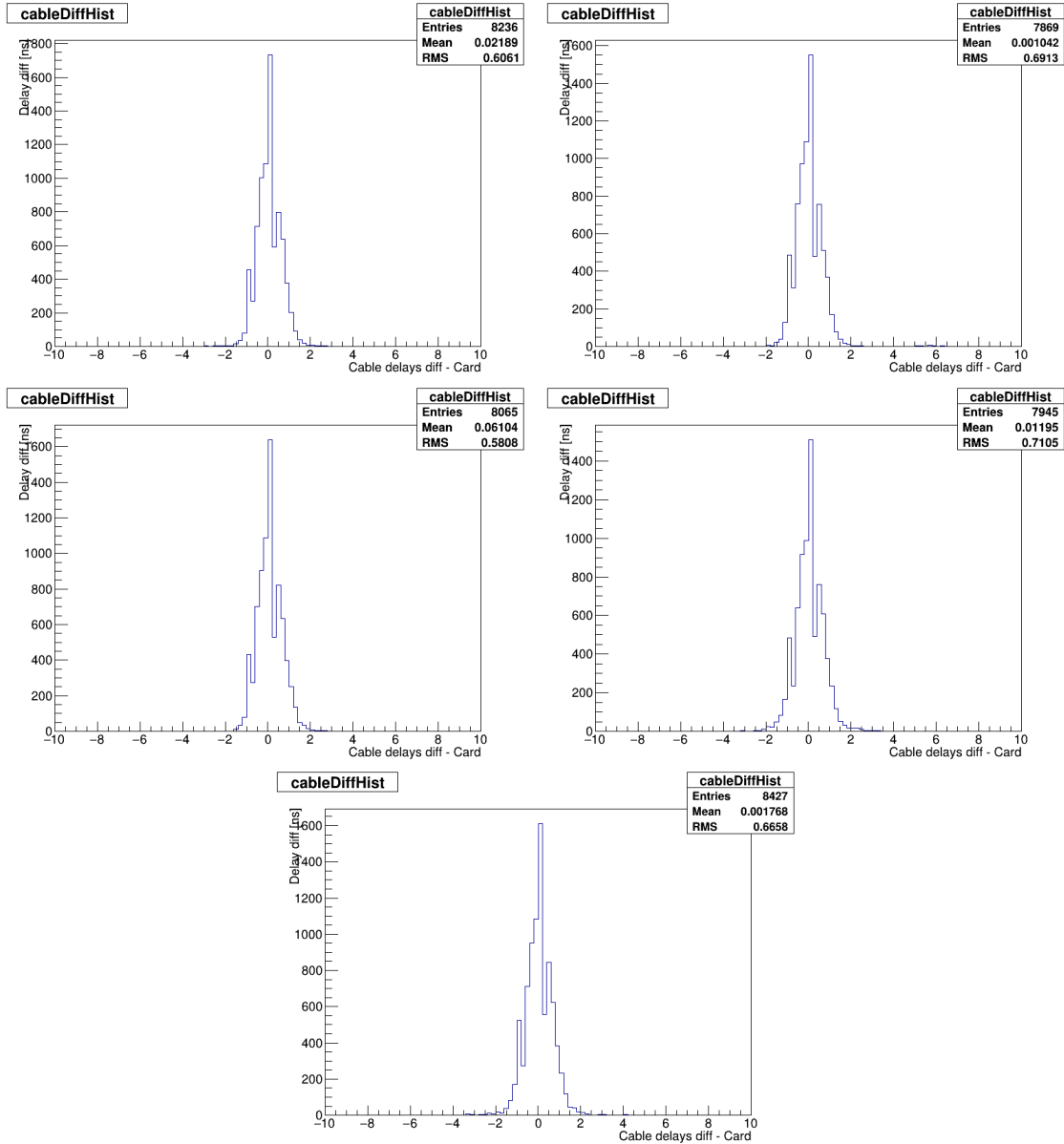
Figure D.1: Comparing TELLIE sets with accompanying closest laserball sets. Plots from top left: TELLIE (110264) vs laserball (110131): March 2018, TELLIE (114670) vs laserball (113592): June 2018, TELLIE (117578) vs laserball (117567): Sept 2018, TELLIE (201388) vs laserball (117567): Dec 2018, TELLIE (204401) vs laserball (117567): March 2019.
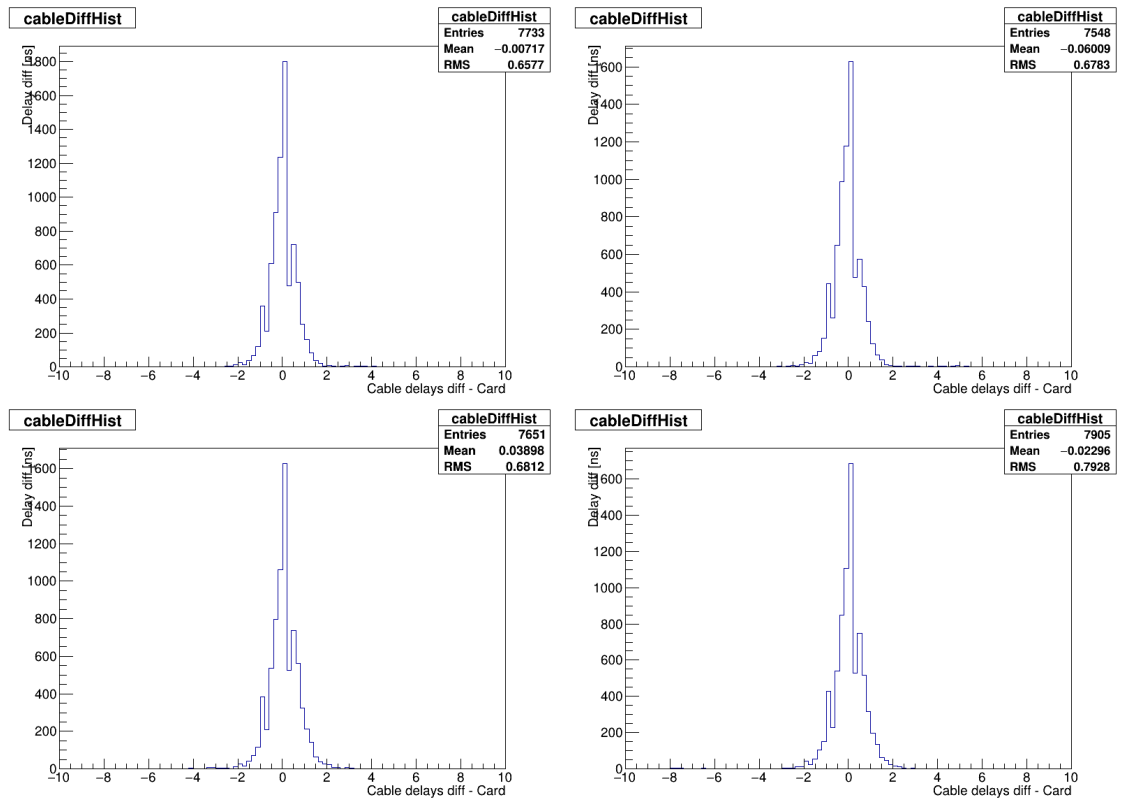
Figure D.2: Comparing TELLIE sets with previous closest TELLIE sets. From top left: TELLIE (110264) versus TELLIE (114670), TELLIE (114670) versus TELLIE (117578), TELLIE (117578) versus TELLIE (201388), TELLIE (201388) versus TELLIE (204401).
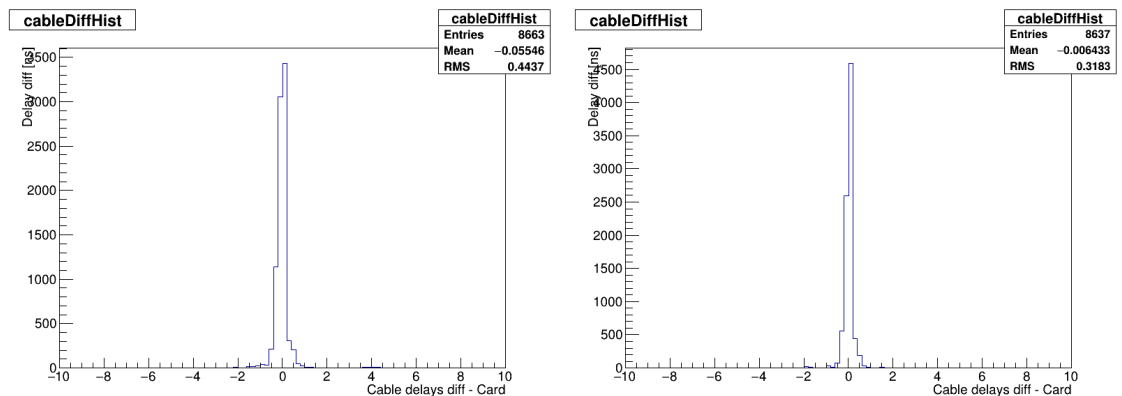
Figure D.3: Comparing laserball sets with previous closest laserball sets. From left: laserball (110131) versus laserball (113592), laserball (113592) versus laserball (117567).

Appendix E

Supernova Burst Trigger - overview

This Appendix shows the full overview of the Supernova Burst Trigger system as described in Supernova Detection.
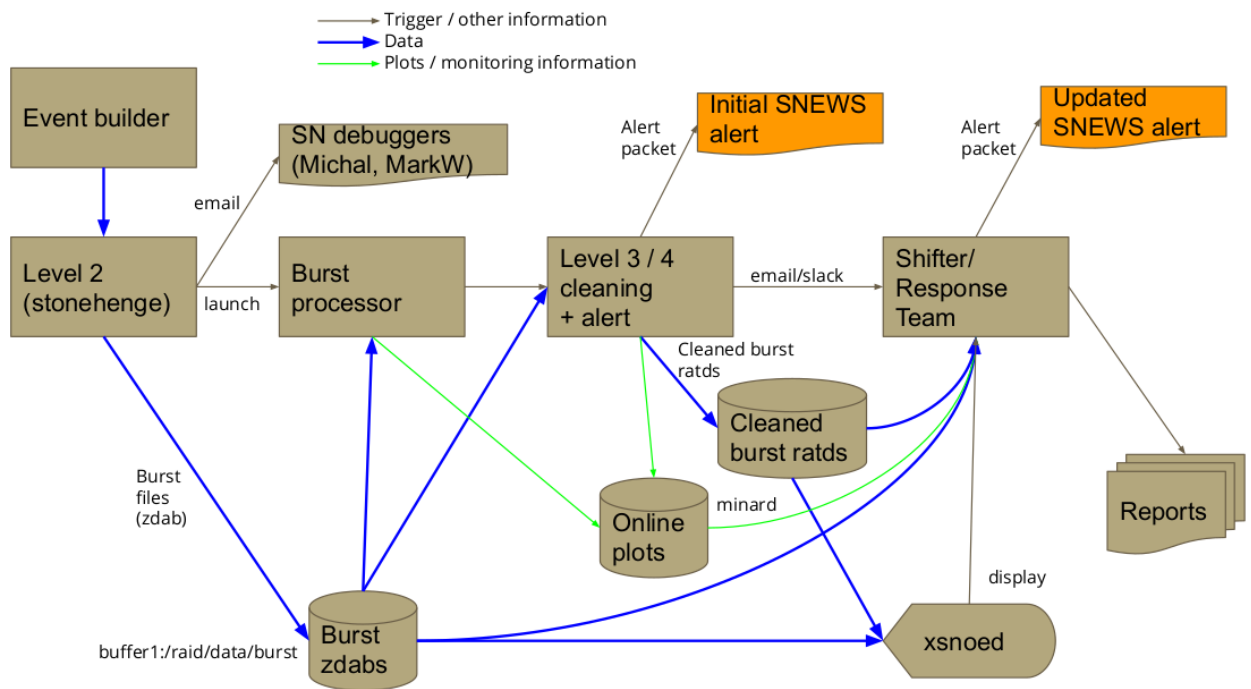
Figure E.1: More detailed overview of the Supernova burst trigger system, including the parts described in the Supernova Detection chapter. This includes the Event builder, Level 2 and Level 3 RAT processors, burst files, data cleaning, online monitoring, alarms and some response actions. Arrows represent the flow of trigger and other information, data and plots and monitoring information. Plot from [131].

Appendix F

SNUGEN: Overview of models

This Appendix shows the full overview of the models available for the SNUGen software, as described in Supernova Sensitivity.

F.1   Basic parameters

F.1.1 LS220 models
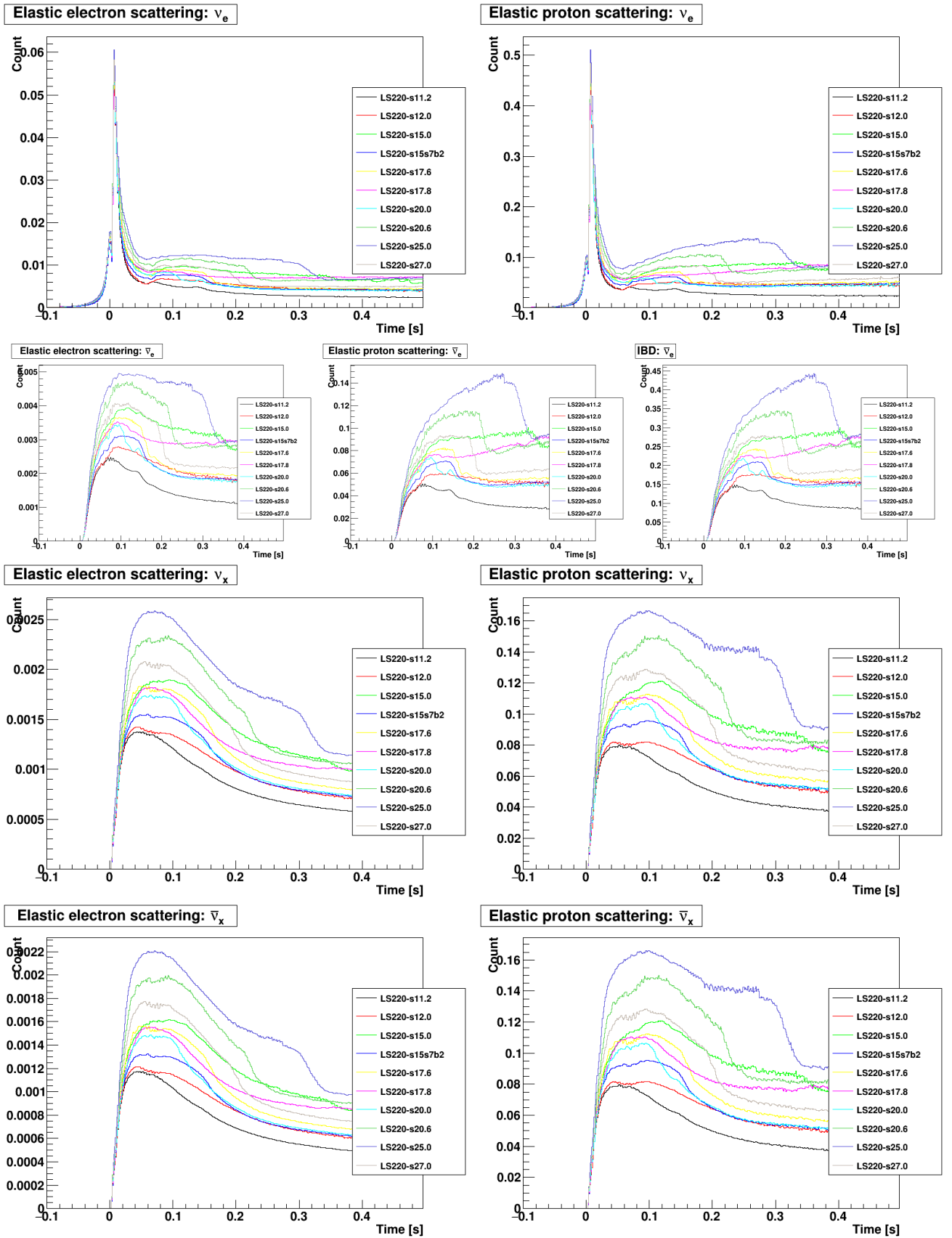
Figure F.1: Flux parameters: Luminosity spectra available for LS220 EOS models.
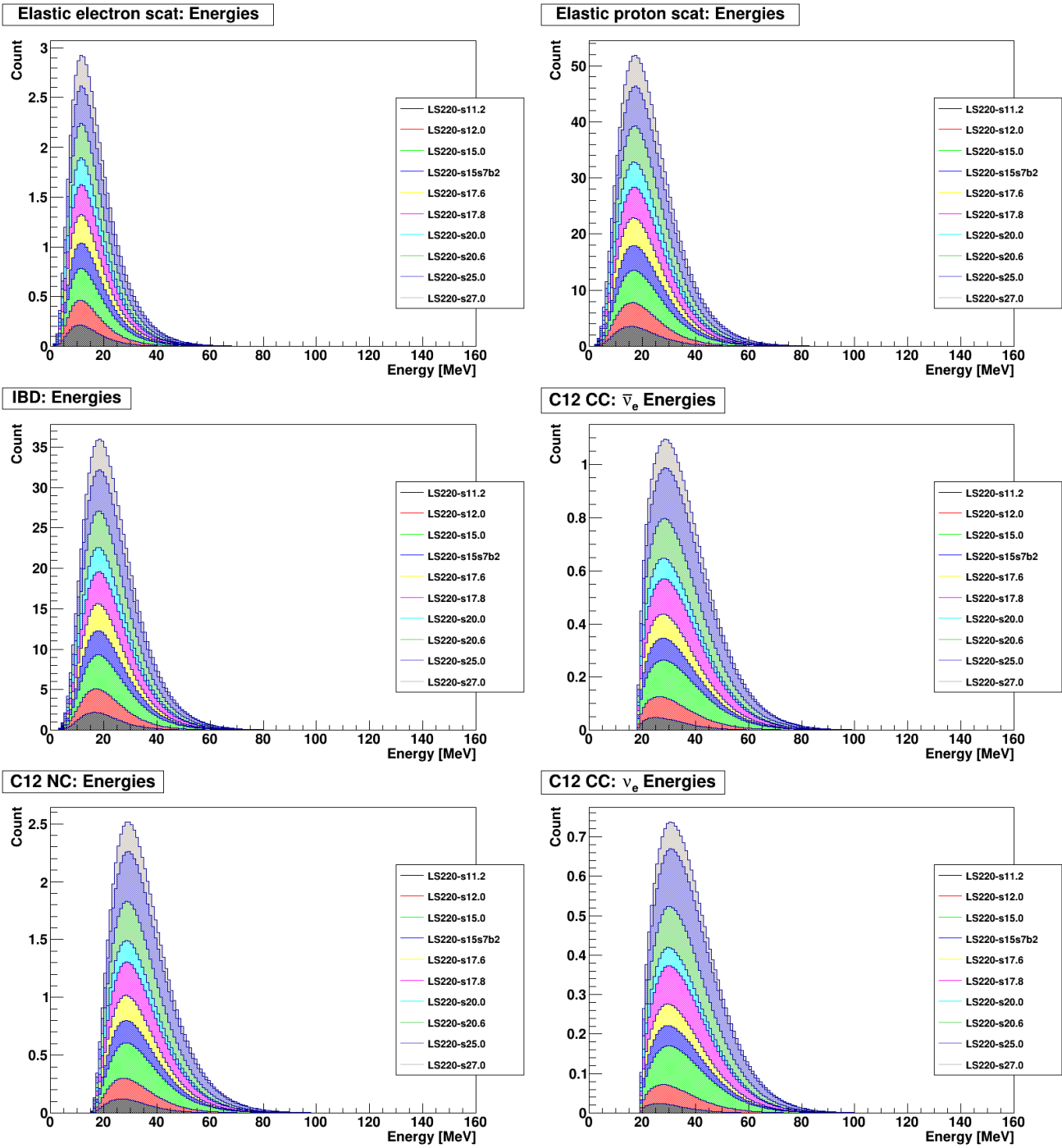
Figure F.2: Flux parameters: Energy distributions for LS220 EOS models.
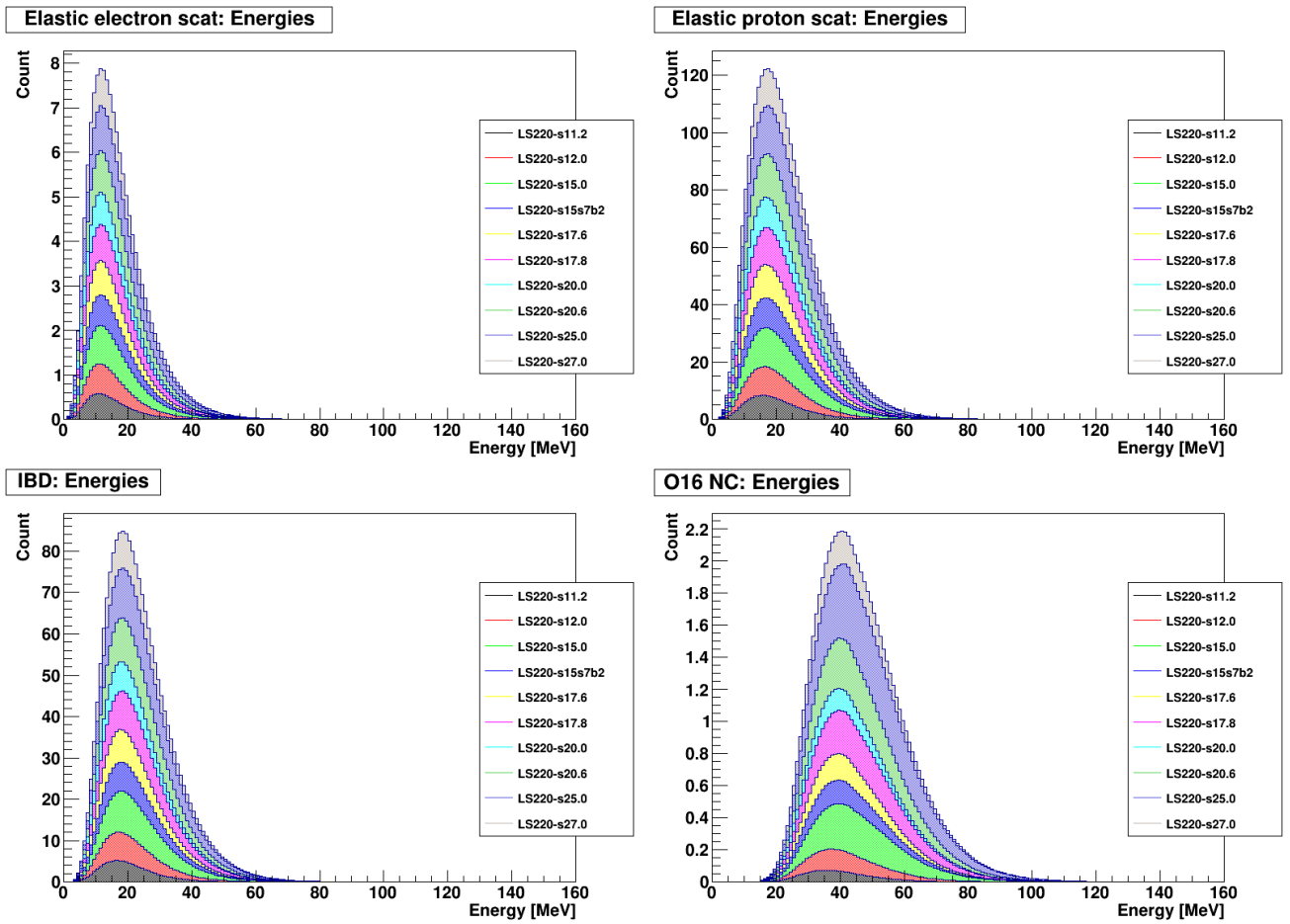
Figure F.3: Flux parameters: Energy distributions for LS220 EOS models.
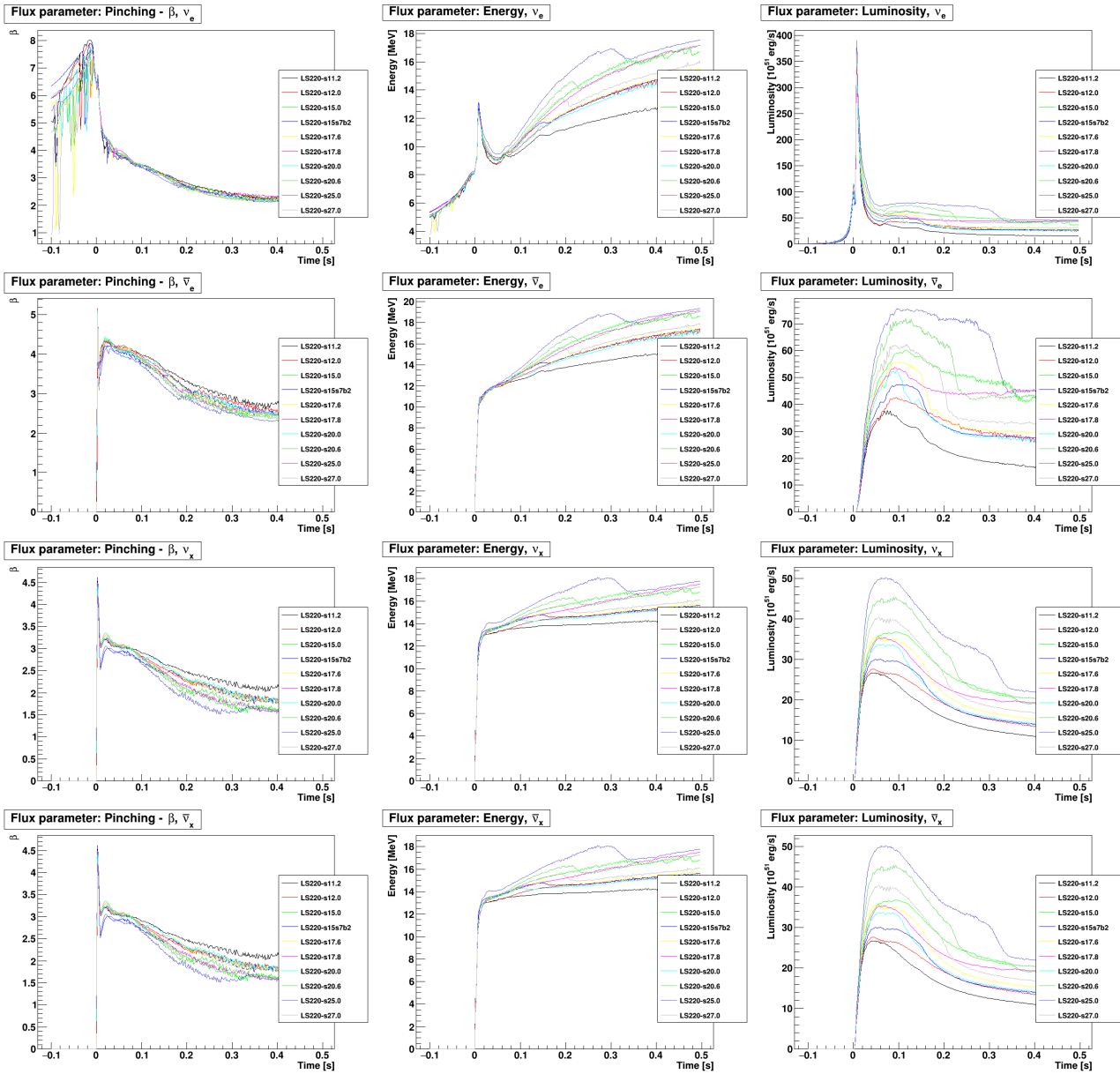
Figure F.4: Flux parameters: Pinching parameter for LS220 EOS models.

F.1.2 SHEN models
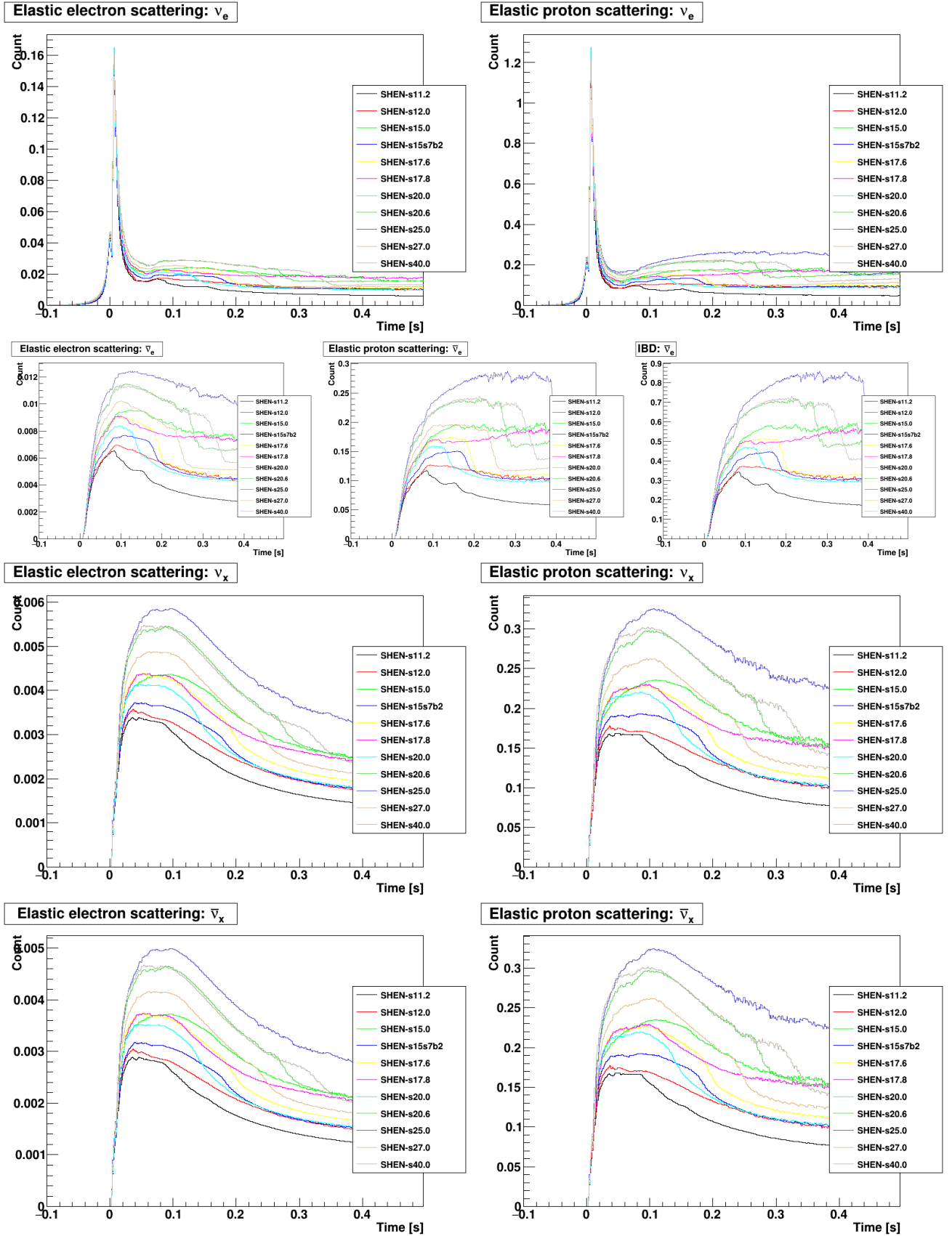
Figure F.5: Flux parameters: Luminosity spectra available for SHEN EOS models.
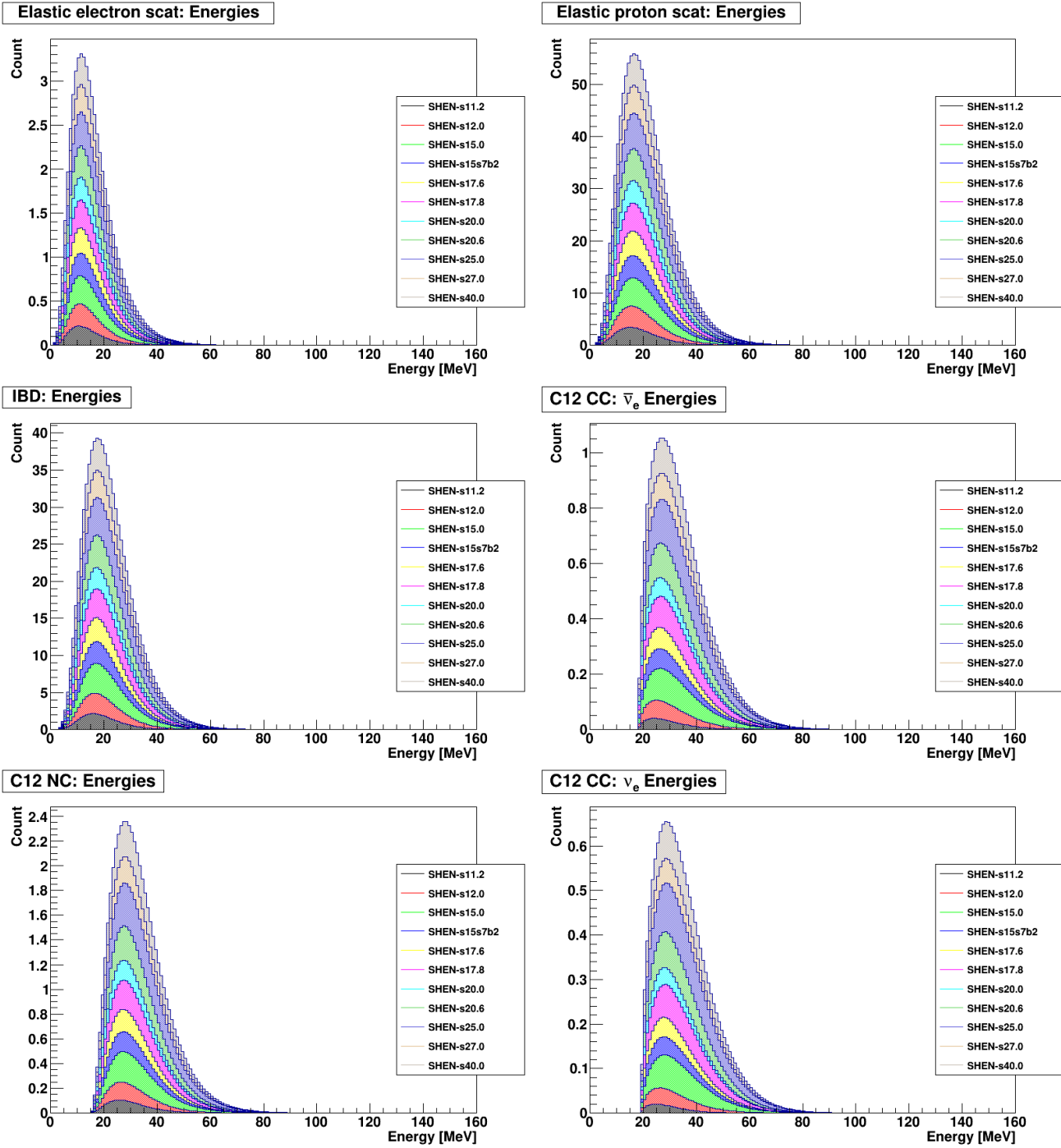
Figure F.6: Flux parameters: Energy distributions for SHEN EOS models.
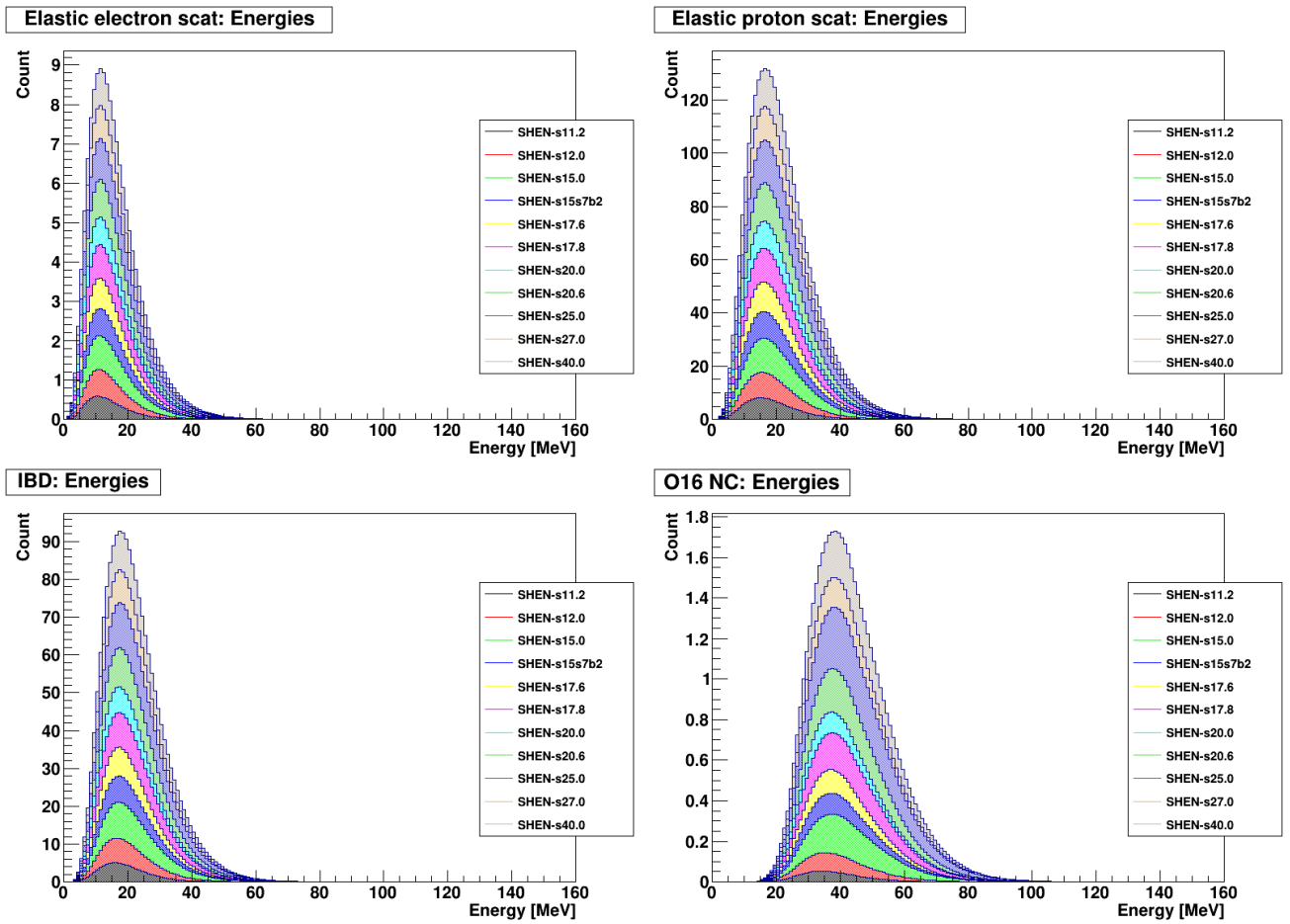
Figure F.7: Flux parameters: Energy distributions for SHEN EOS models.
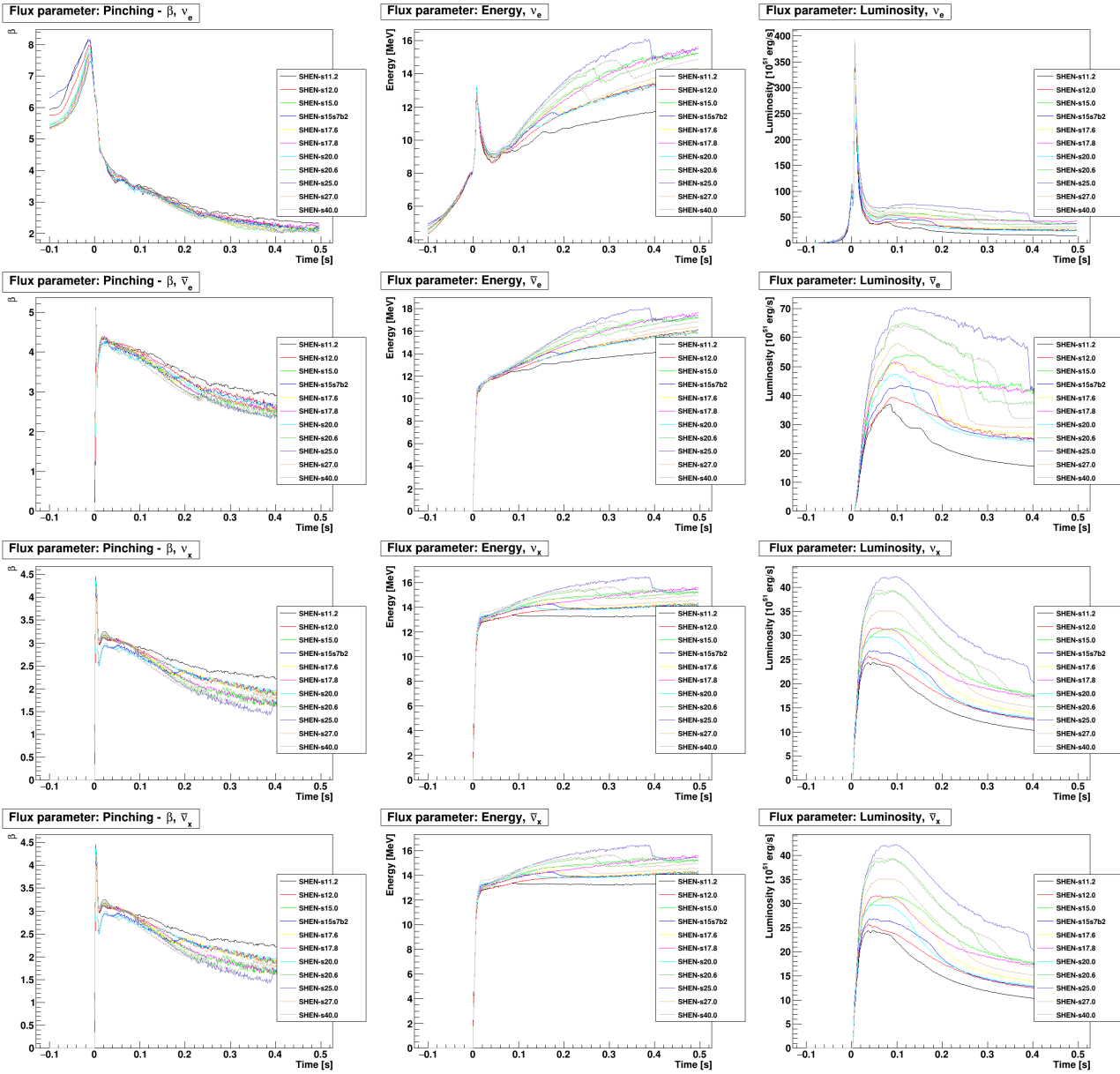
Figure F.8: Flux parameters: Pinching parameter for SHEN EOS models.

F.1.3 Longer models
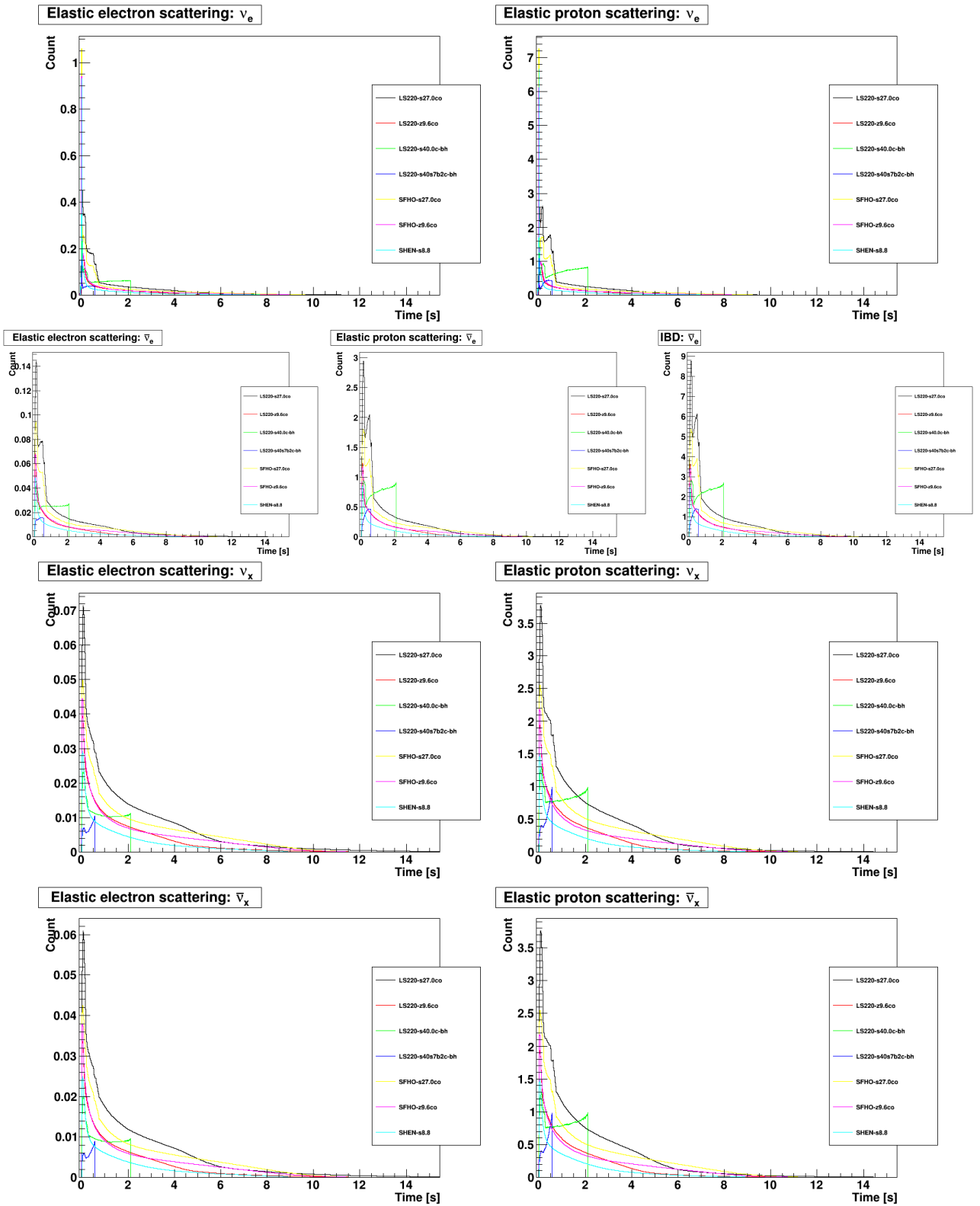
Figure F.9: Flux parameters: Luminosity spectra available for models going beyond 0.5s, combining different EOS.
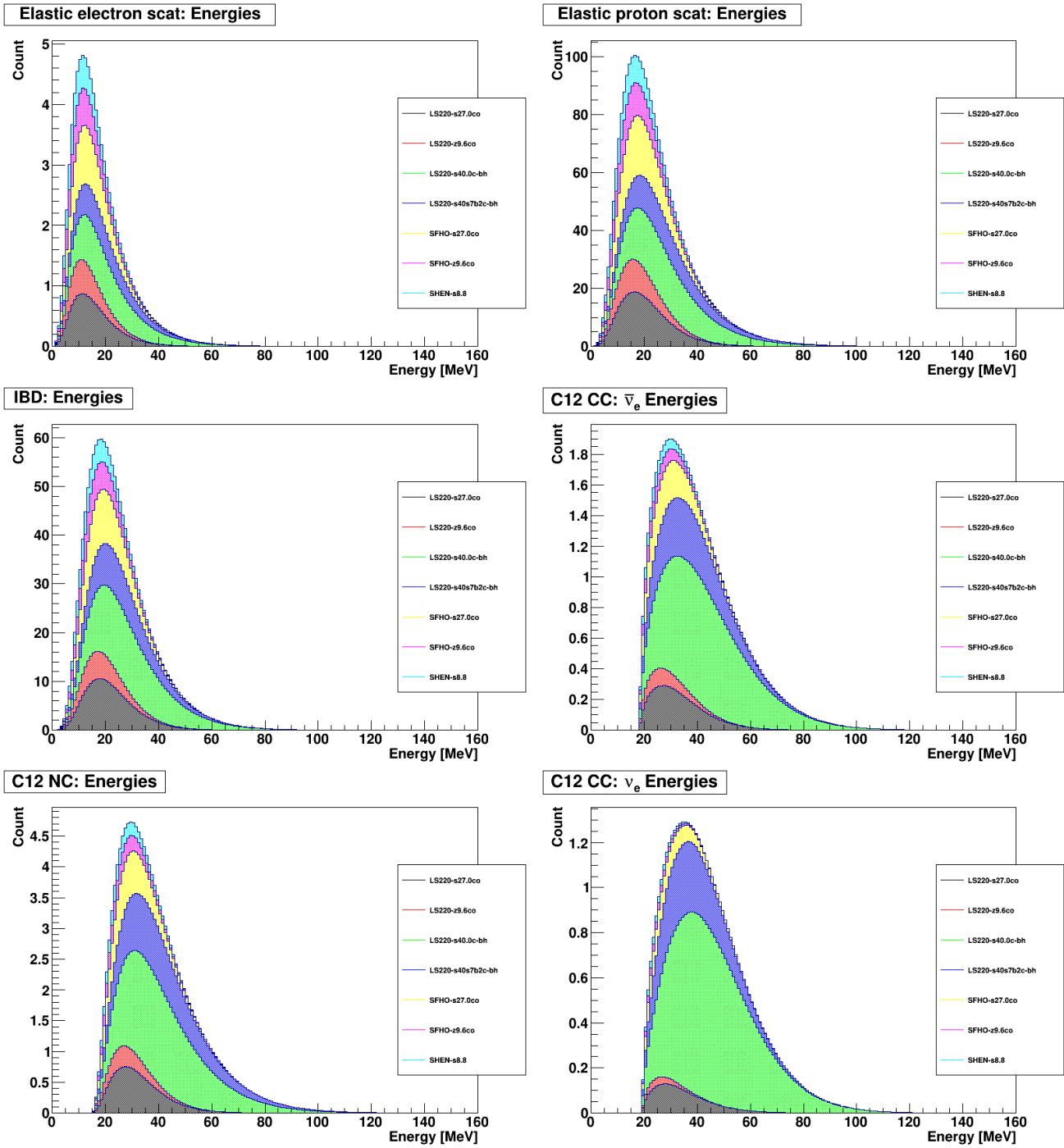
Figure F.10: Flux parameters: Energy distributions available for models going beyond 0.5s, combining different EOS.
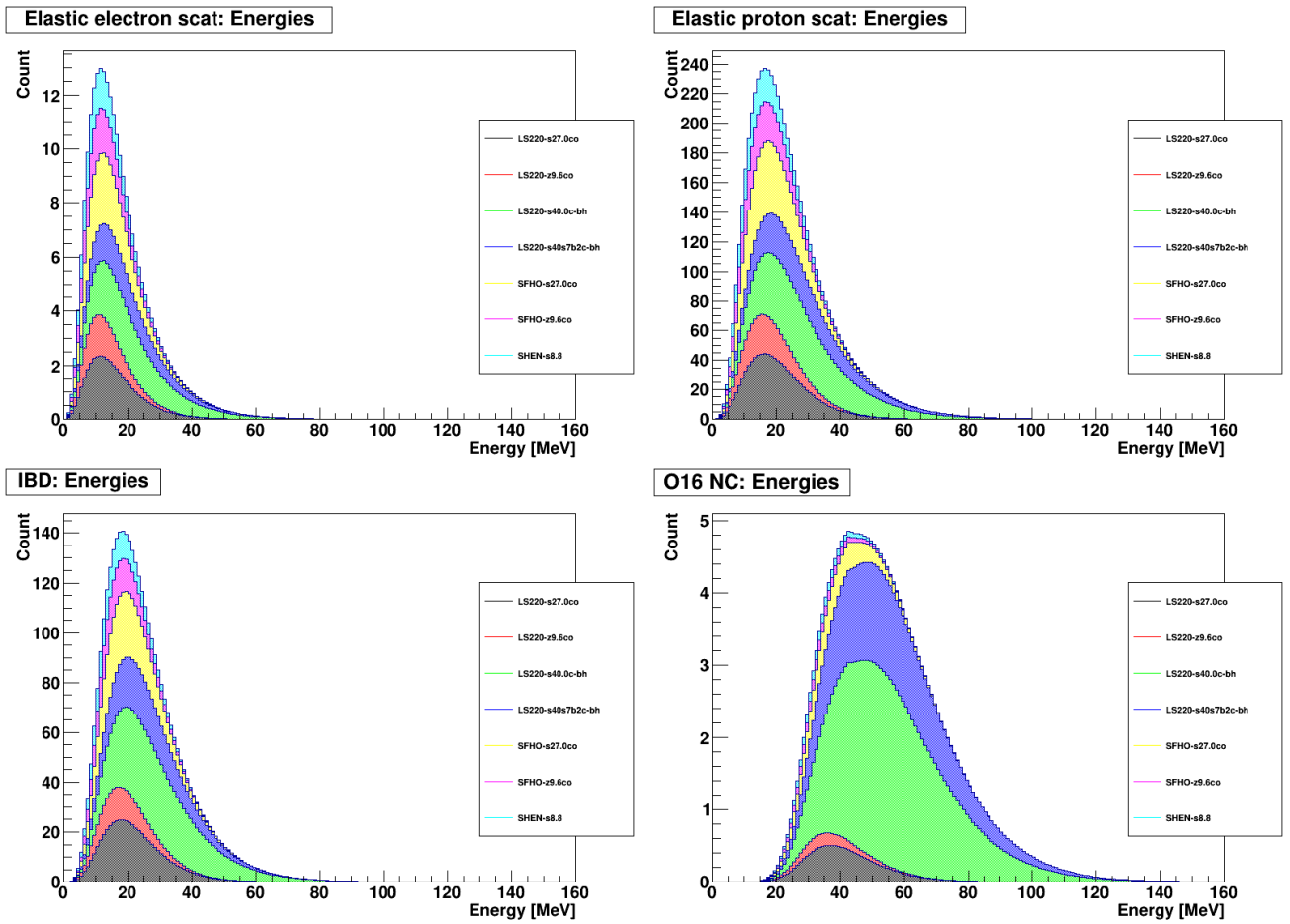
Figure F.11: Flux parameters: Energy distributions available for models going beyond 0.5s, combining different EOS.
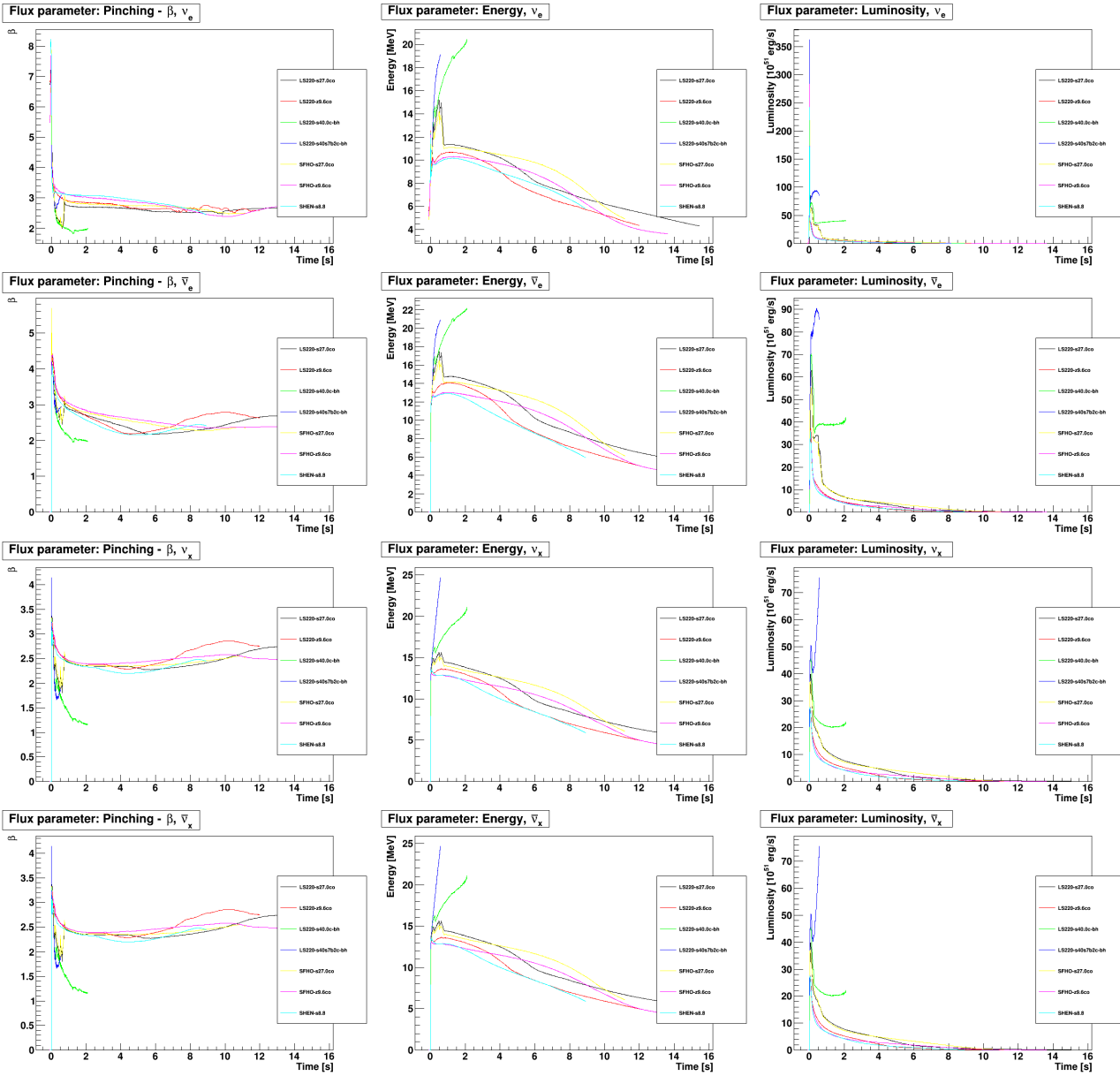
Figure F.12: Flux parameters: Pinching parameter available for models going beyond 0.5s, combining different EOS.

F.1.4 Equation of state
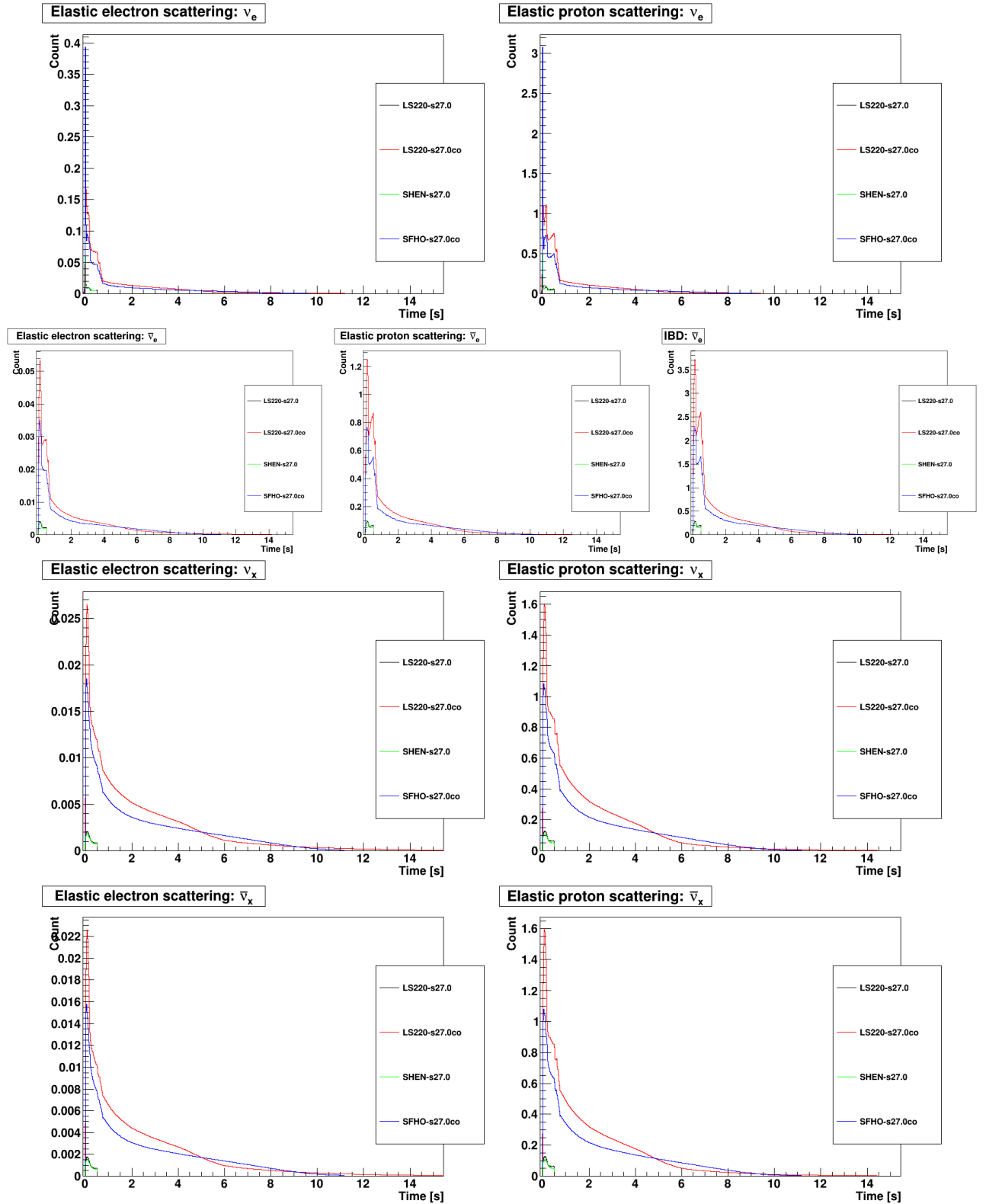
Figure F.13: Flux parameters: Luminosity spectra for two progenitors, using different EOS.
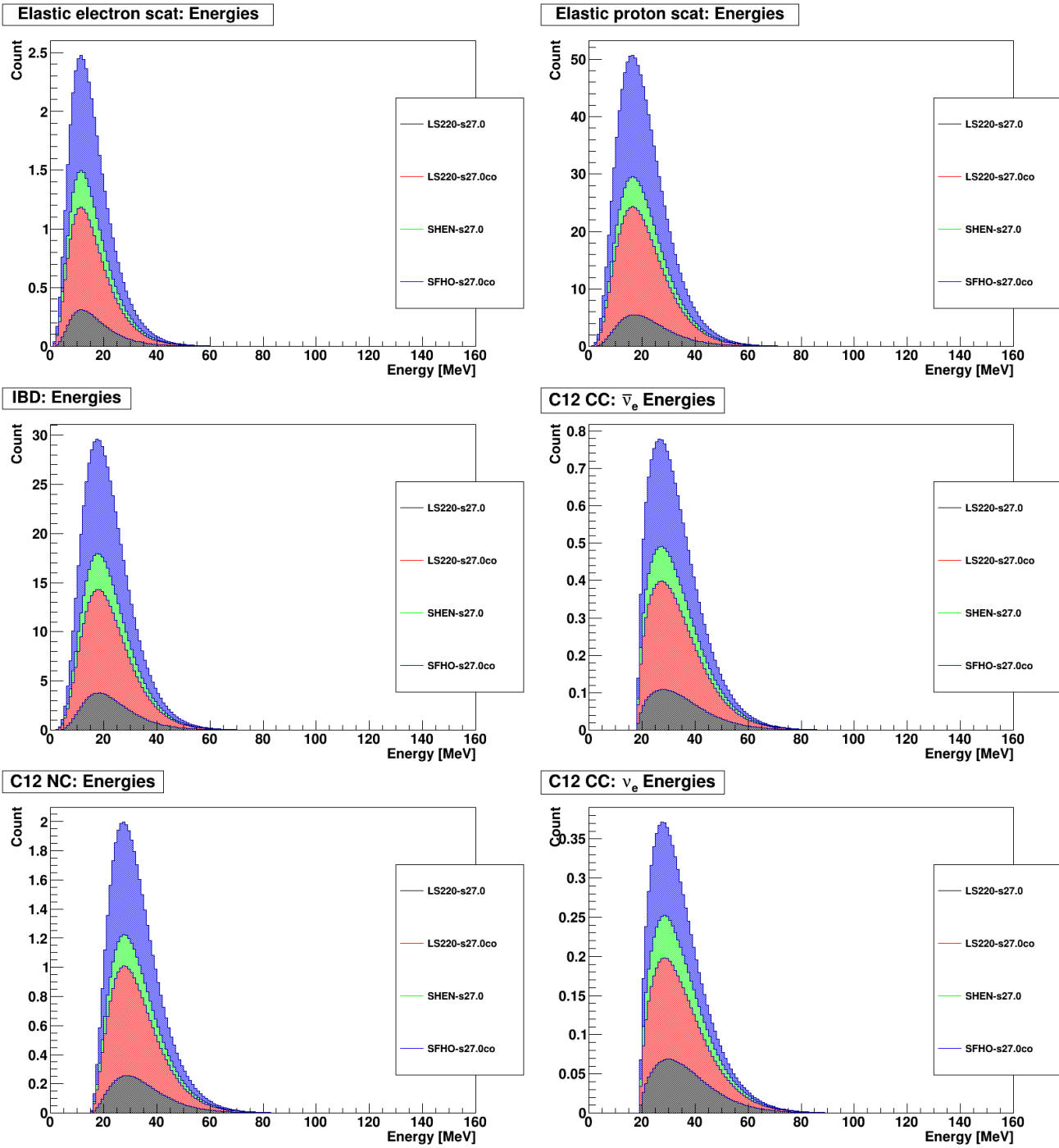
Figure F.14: Flux parameters: Energy distributions for two progenitors, using different EOS.
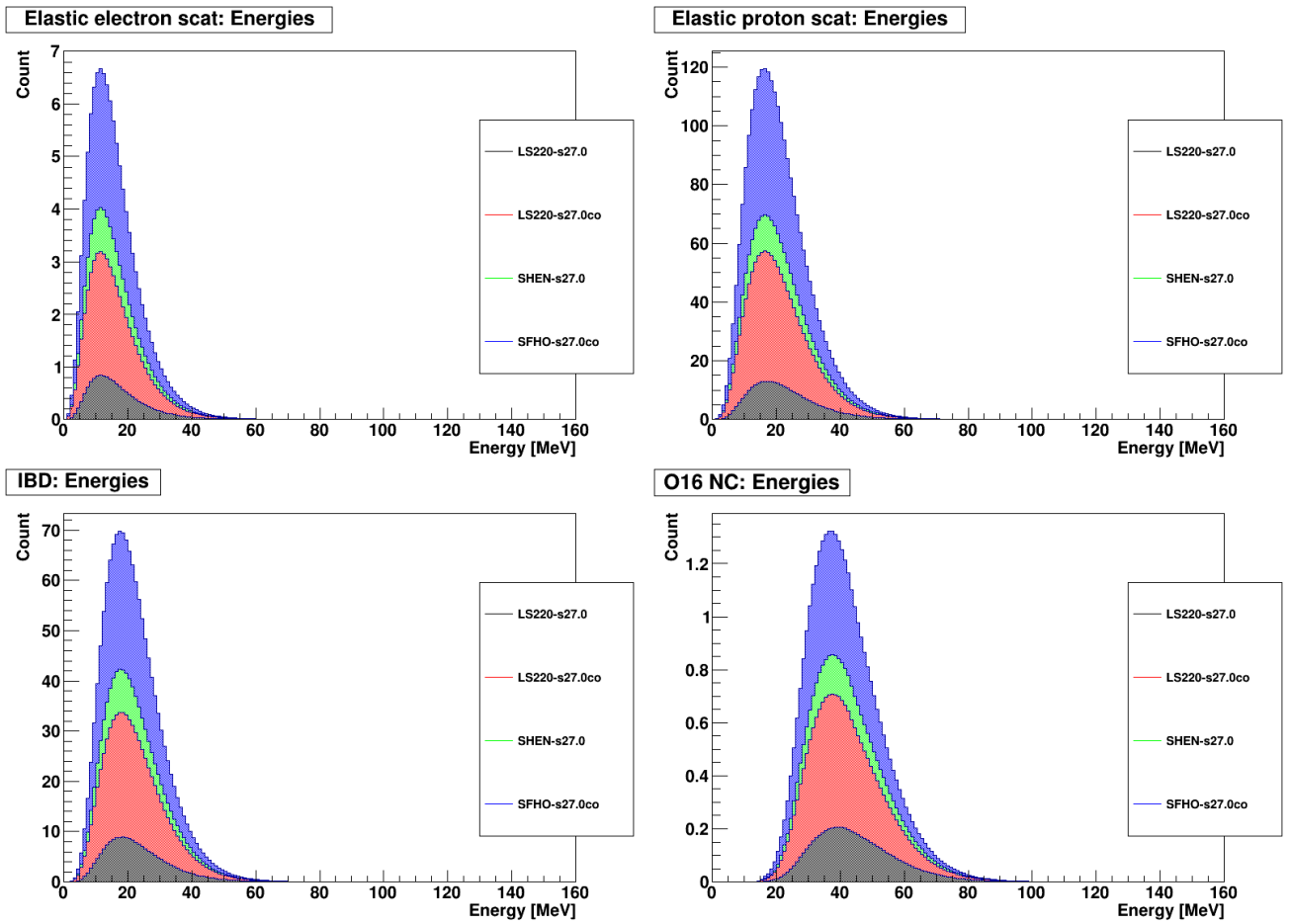
Figure F.15: Flux parameters: Energy distributions for two progenitors, using different EOS.
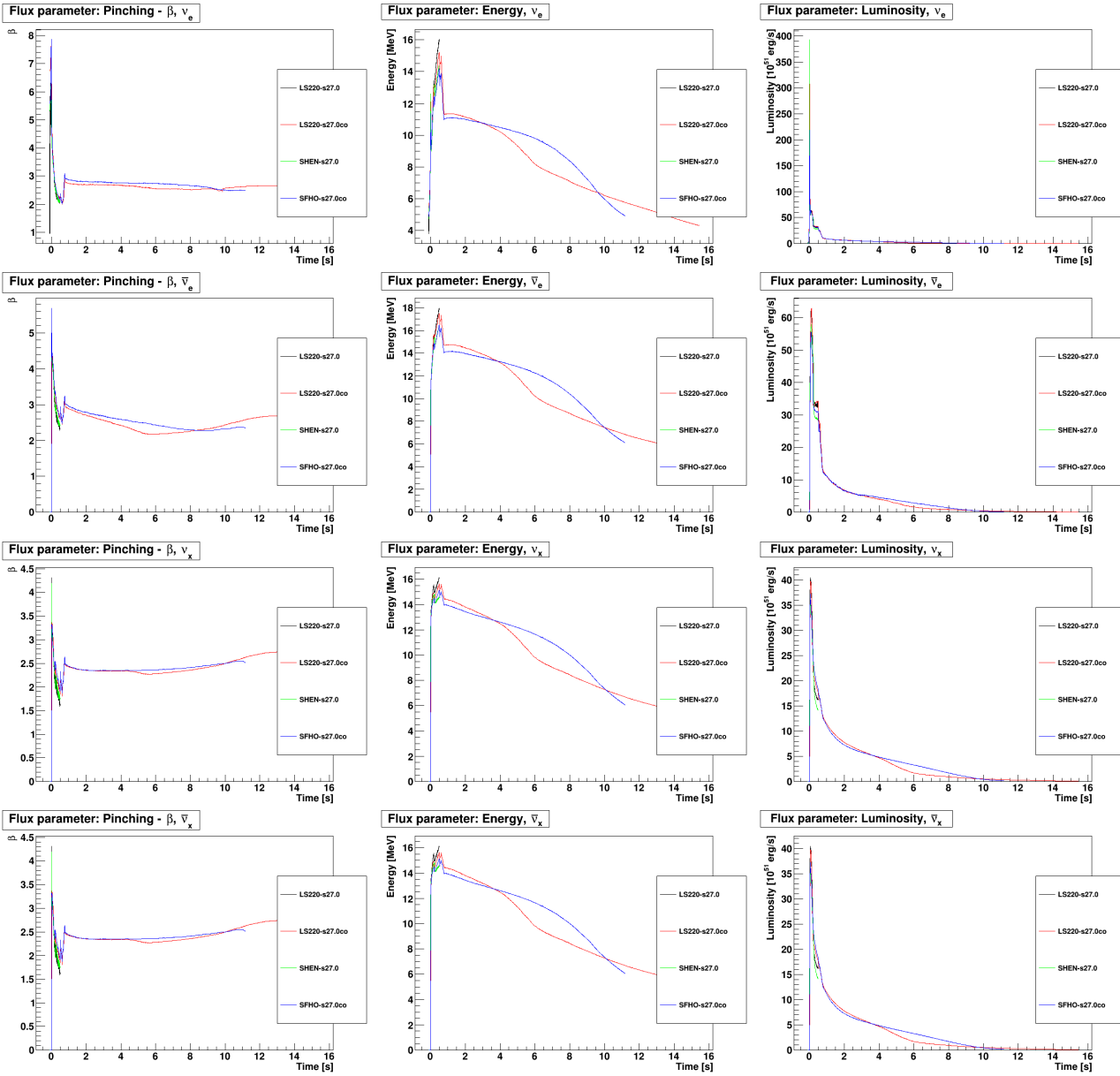
Figure F.16: Flux parameters: Pinching parameter available for two progenitors, using different EOS.

F.1.5 Hierarchy comparison
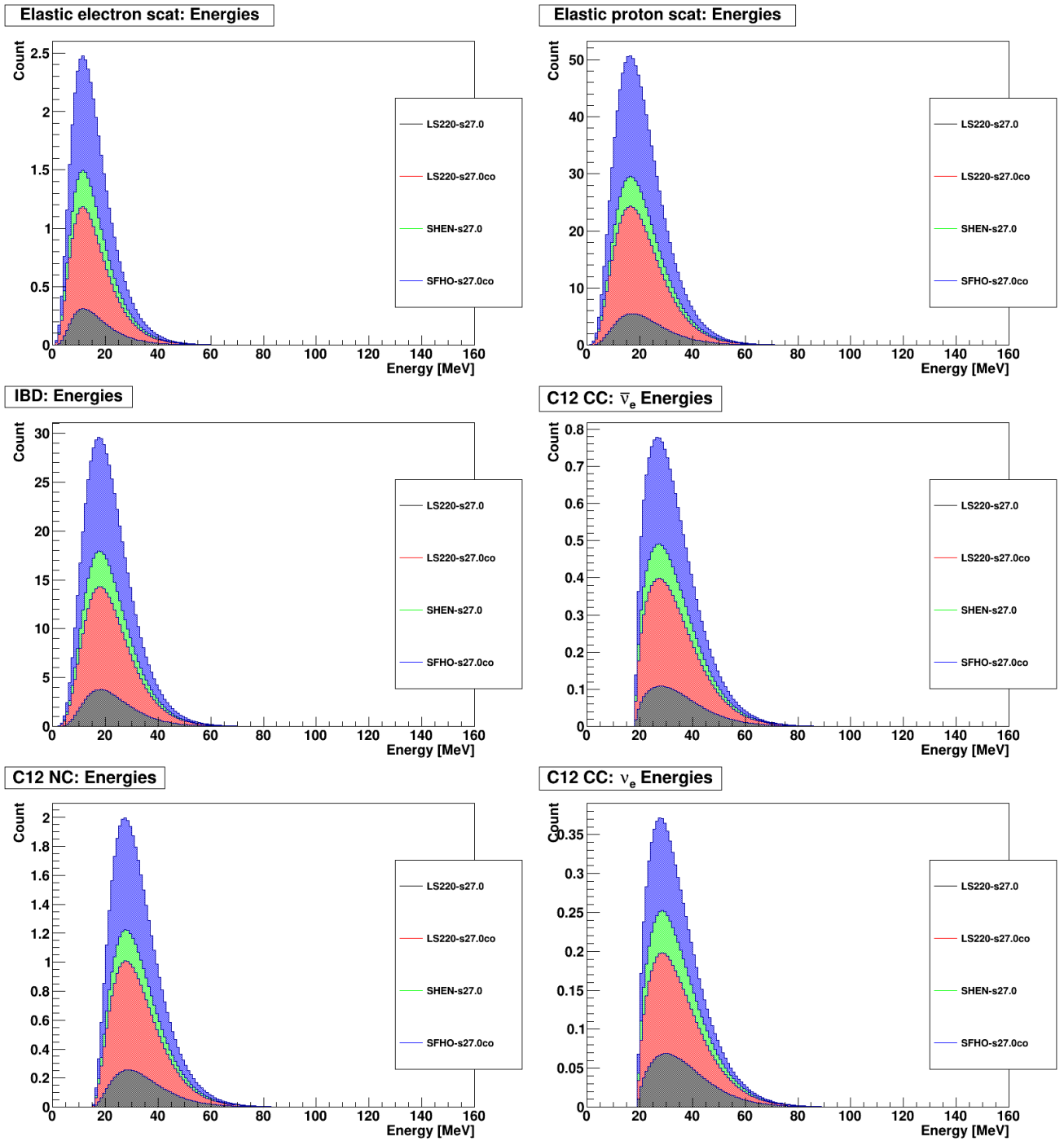
Figure F.17: Flux parameters: Energy distributions for two progenitors, using different hierarchy for neutrino masses.
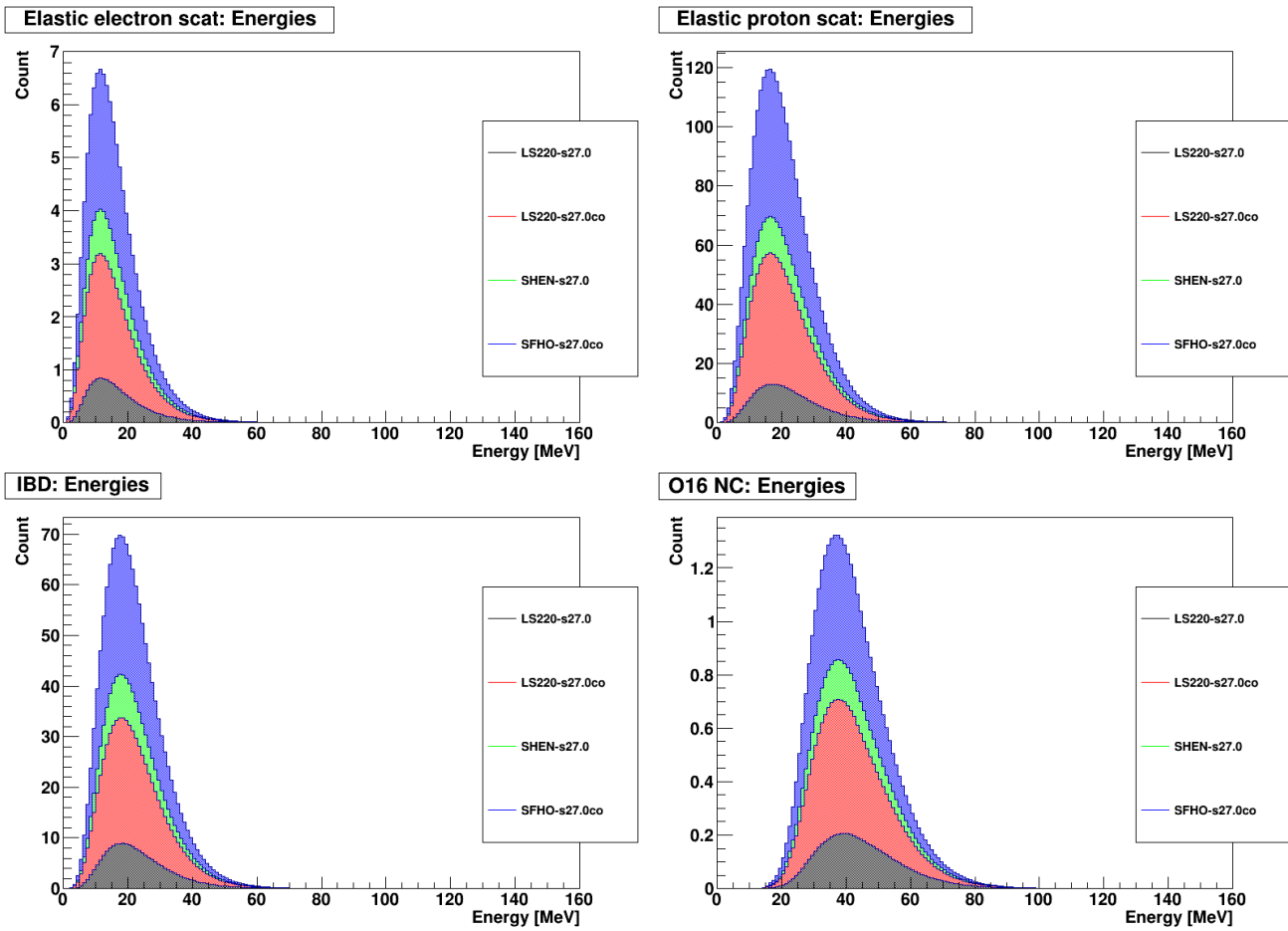
Figure F.18: Flux parameters: Energy distributions for two progenitors, using different hierarchy for neutrino masses.

F.1.6   Mikheyev-Smirnow-Wolfenstein effect
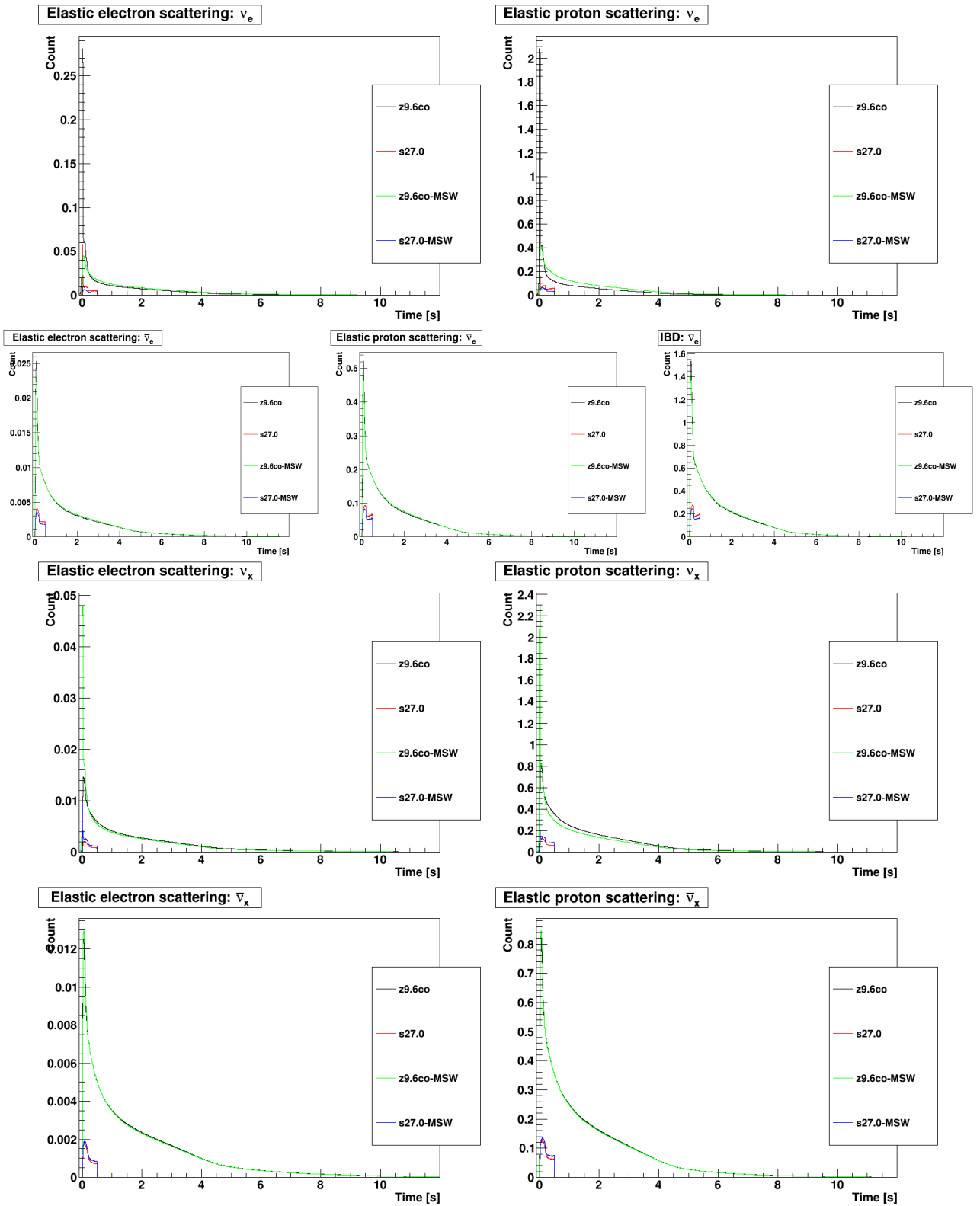
Figure F.19: Flux parameters: Luminosity spectra for two progenitors, one set considering the Mikheyev-Smirnow-Wolfenstein effect and one set without.
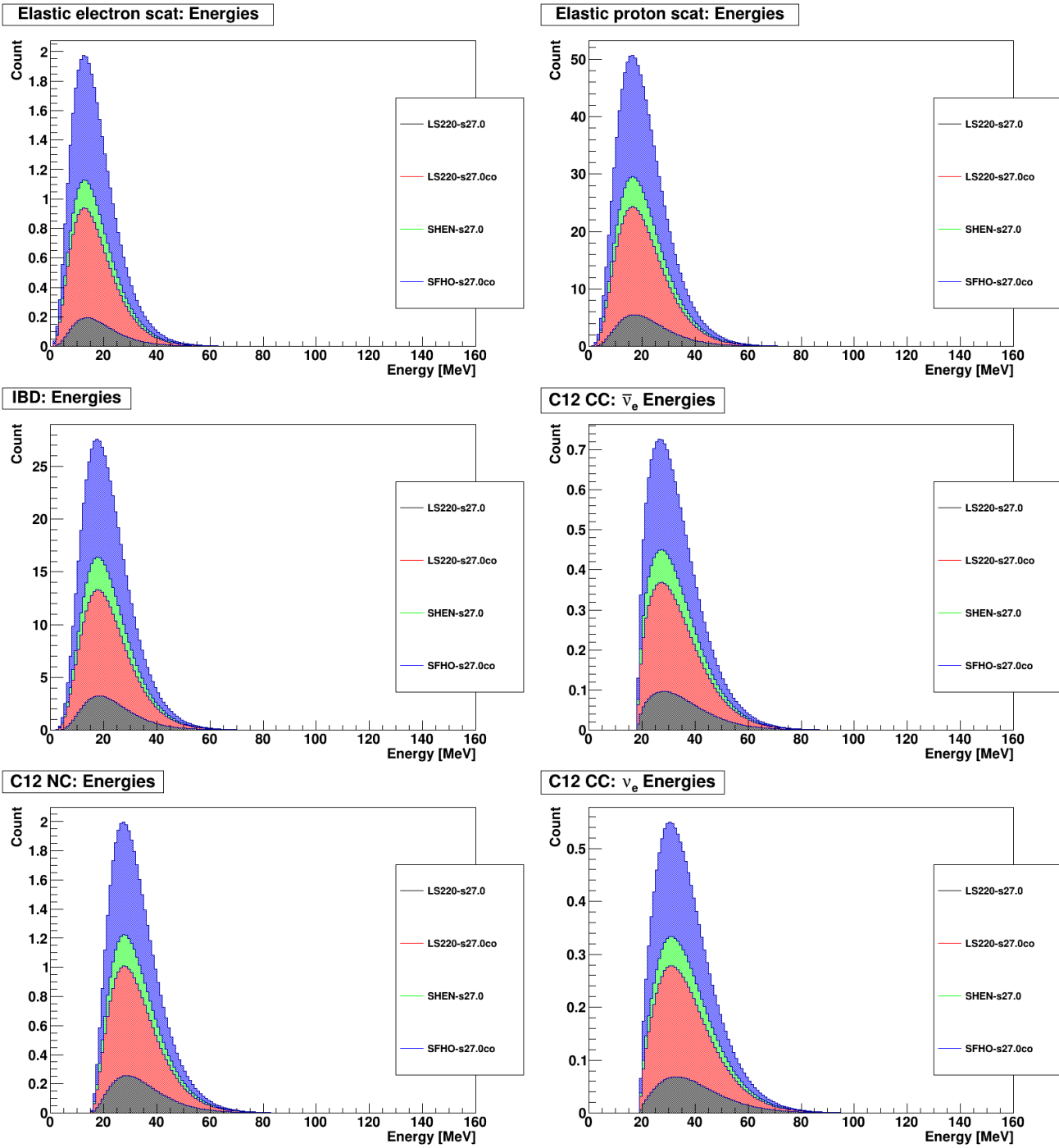
Figure F.20: Flux parameters: Energy distributions for two progenitors, one set considering the Mikheyev-Smirnow-Wolfenstein effect and one set without.
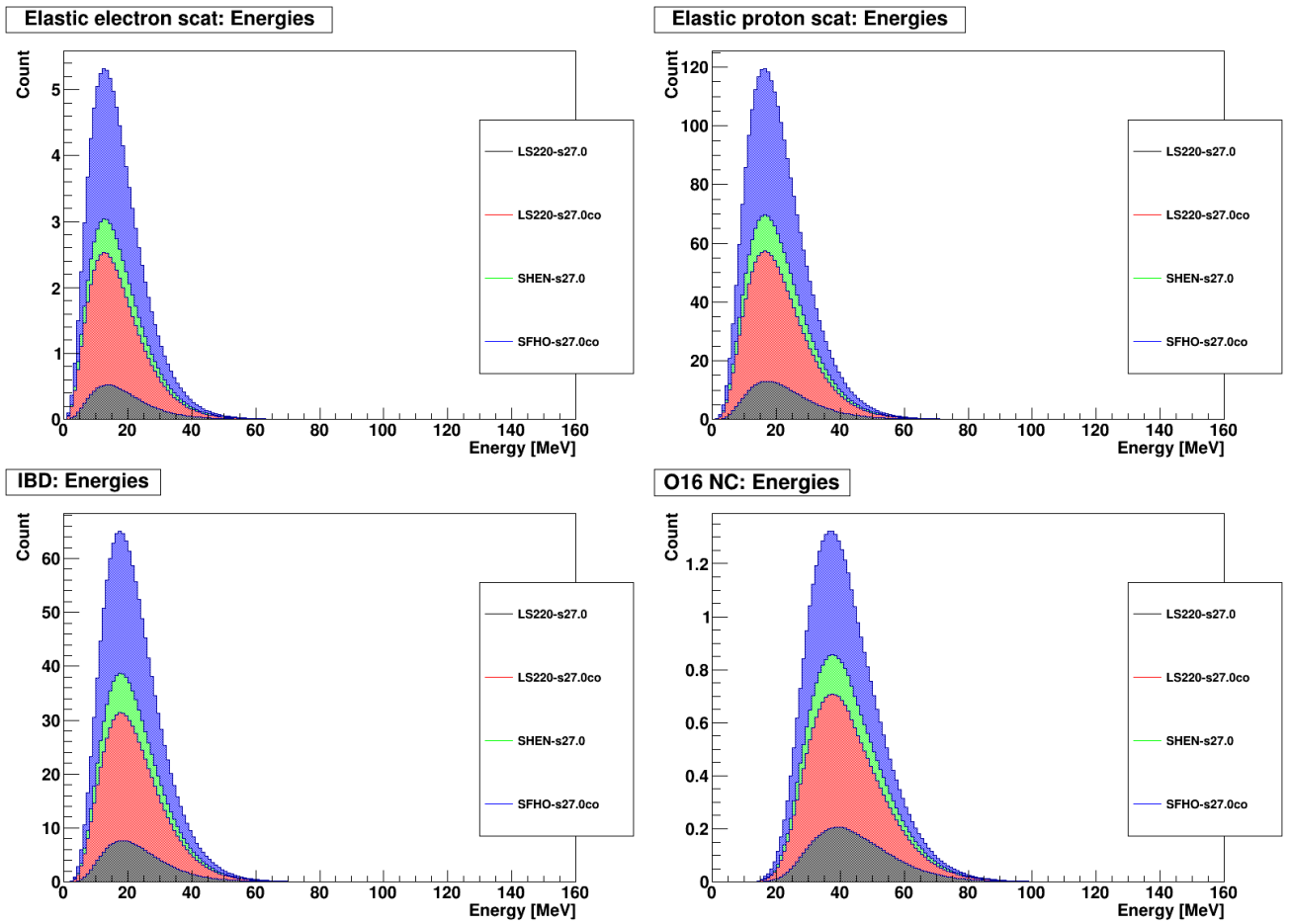
Figure F.21: Flux parameters: Energy distributions for two progenitors, one set considering the Mikheyev-Smirnow-Wolfenstein effect and one set without.

F.2   Time - Energy - Luminosity (TEL) visualisation

F.2.1   LS220 models
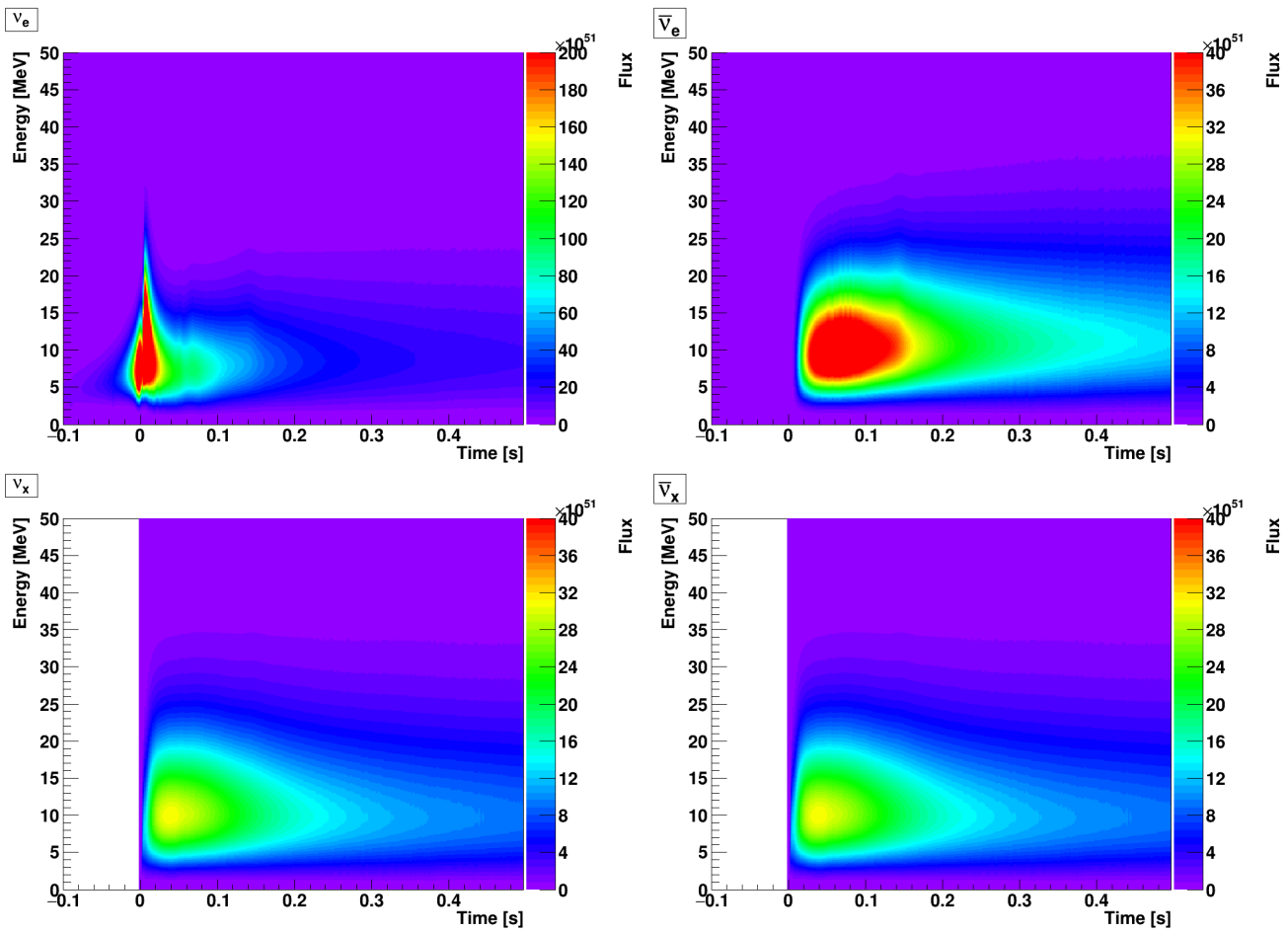
Figure F.22: TEL: LS220-s11.2 model.
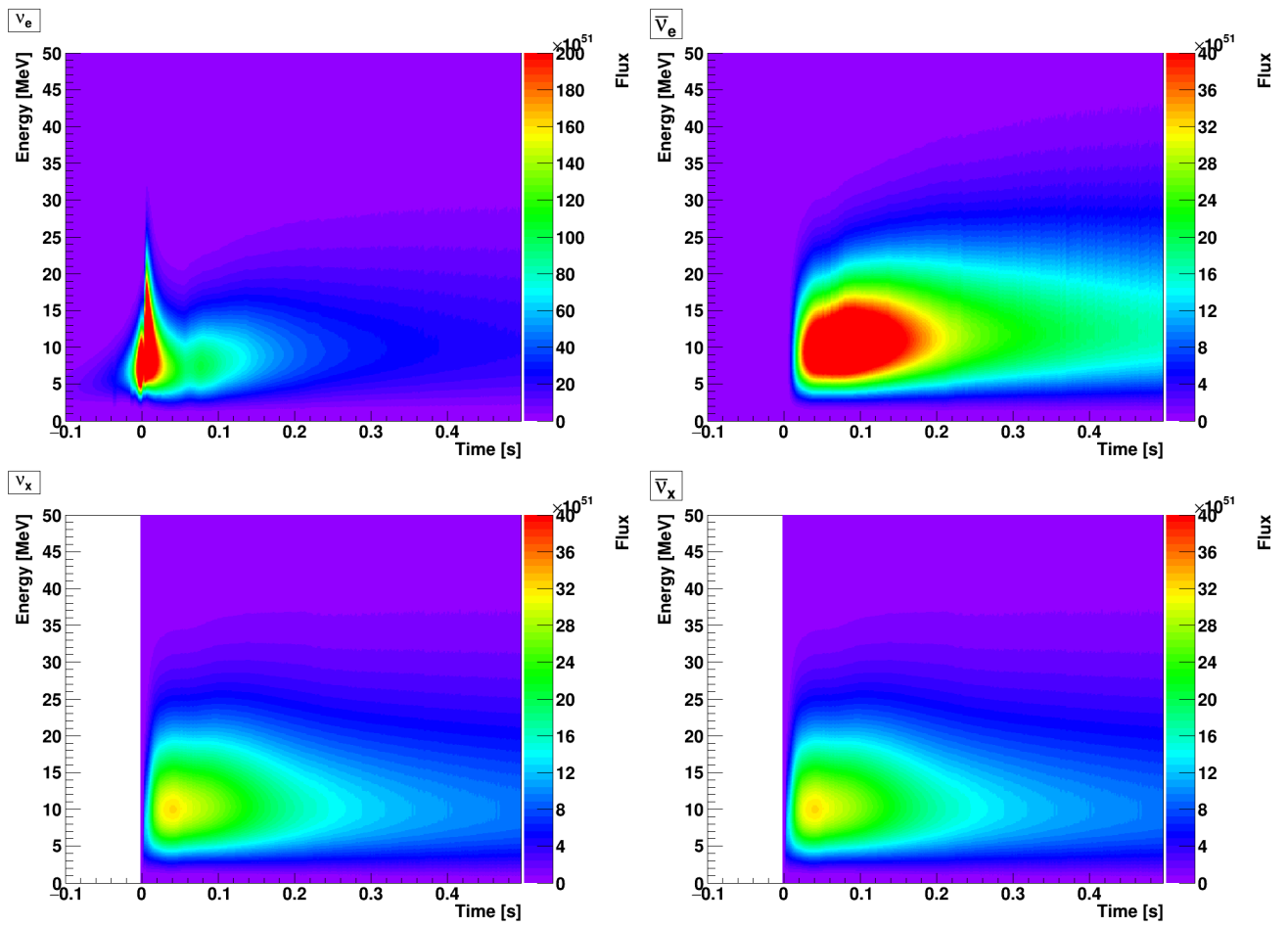
Figure F.23: TEL: LS220-s12.0 model.
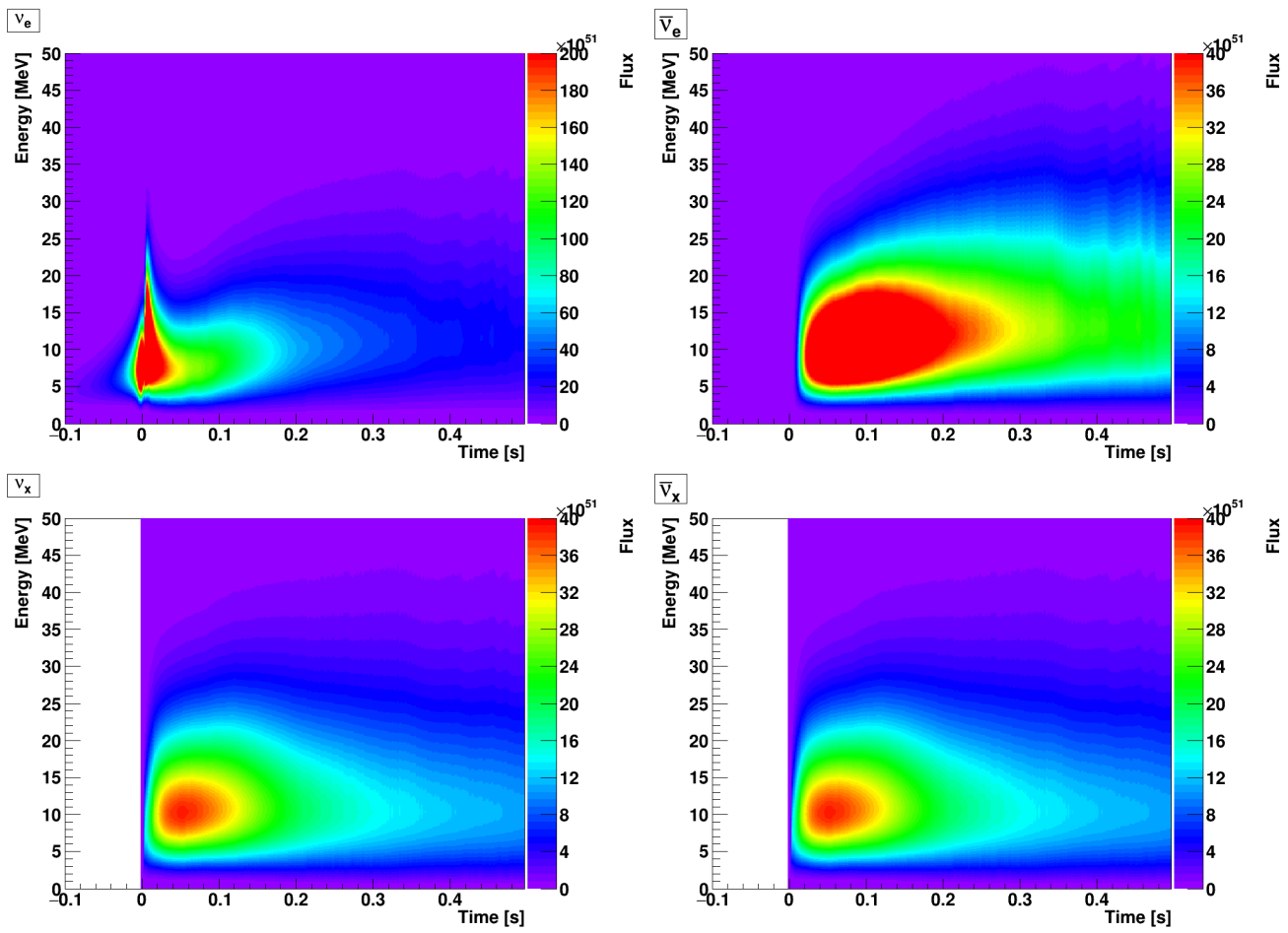
Figure F.24: TEL: LS220-s15.0 model.
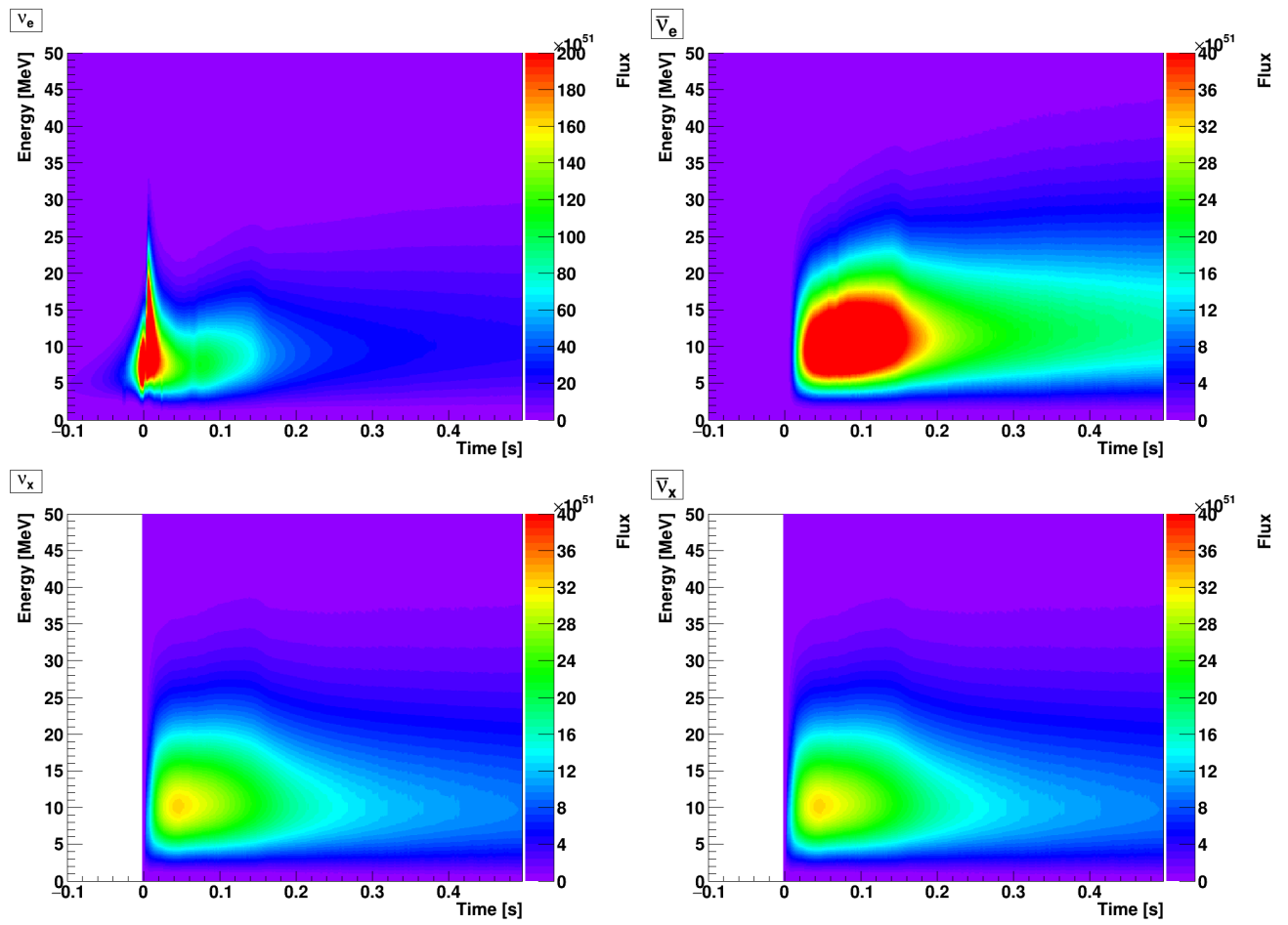
Figure F.25: TEL: LS220-s15s7b2 model.
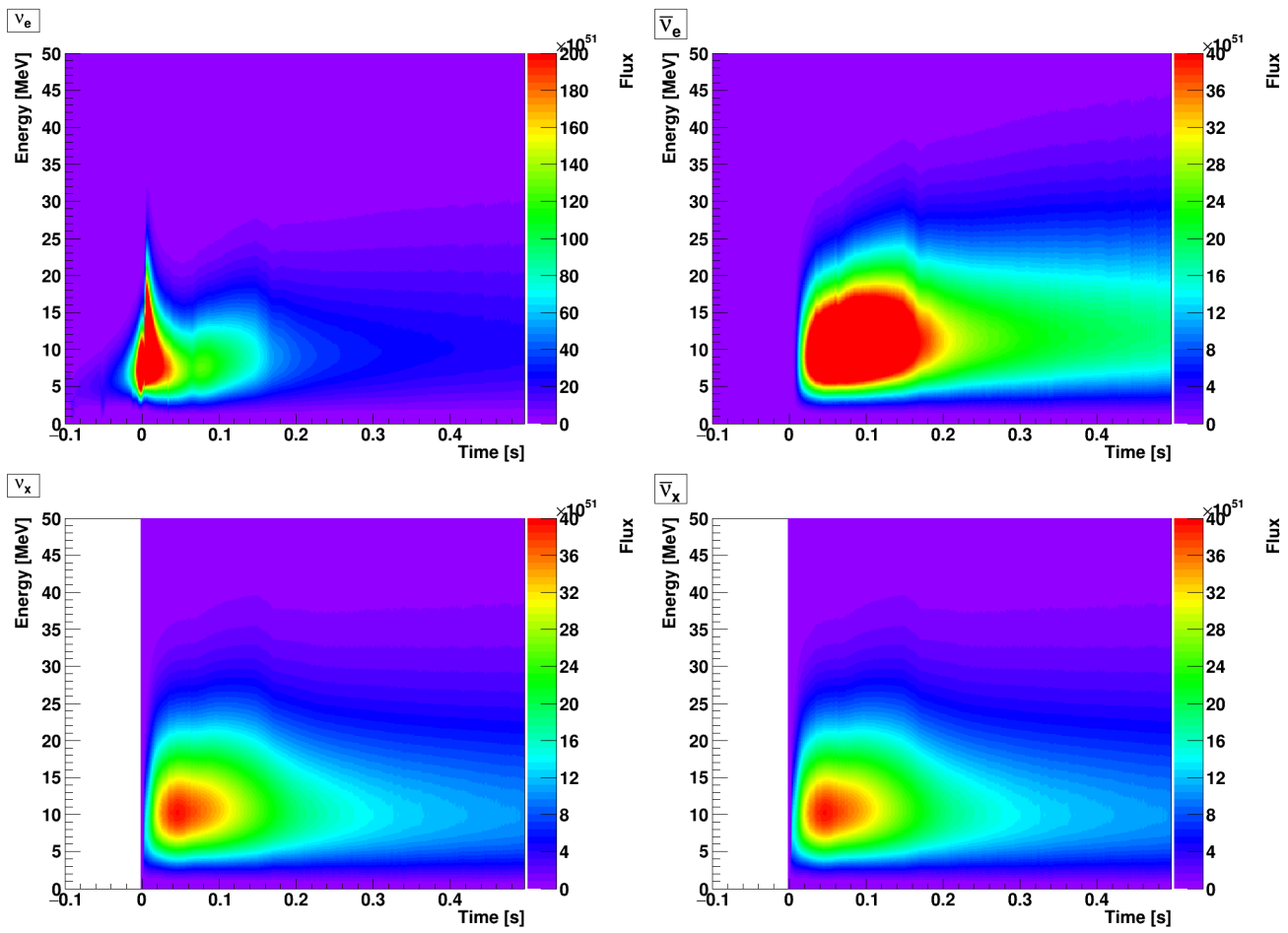
Figure F.26: TEL: LS220-s17.6 model.
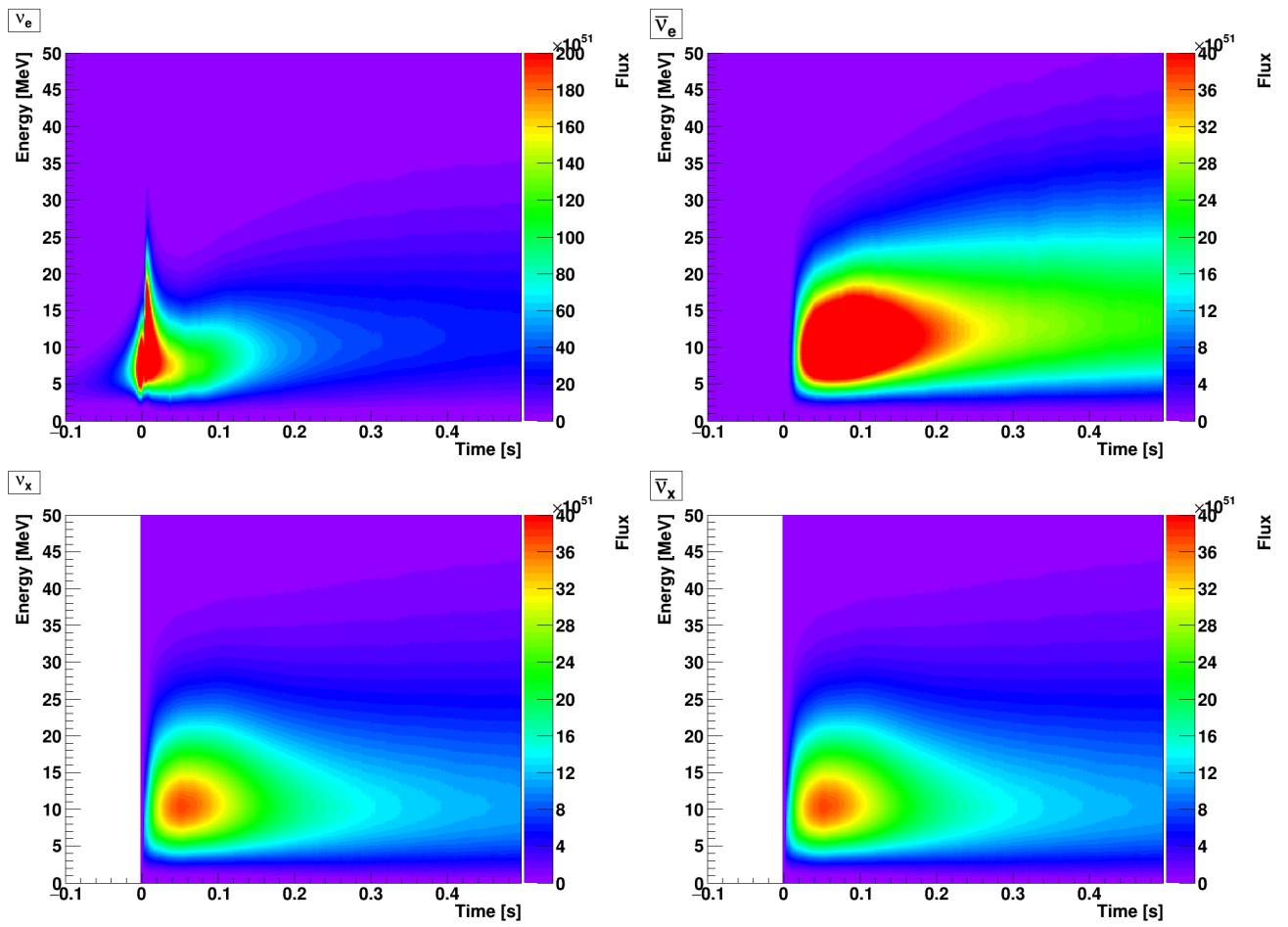
Figure F.27: TEL: LS220-s17.8 model.
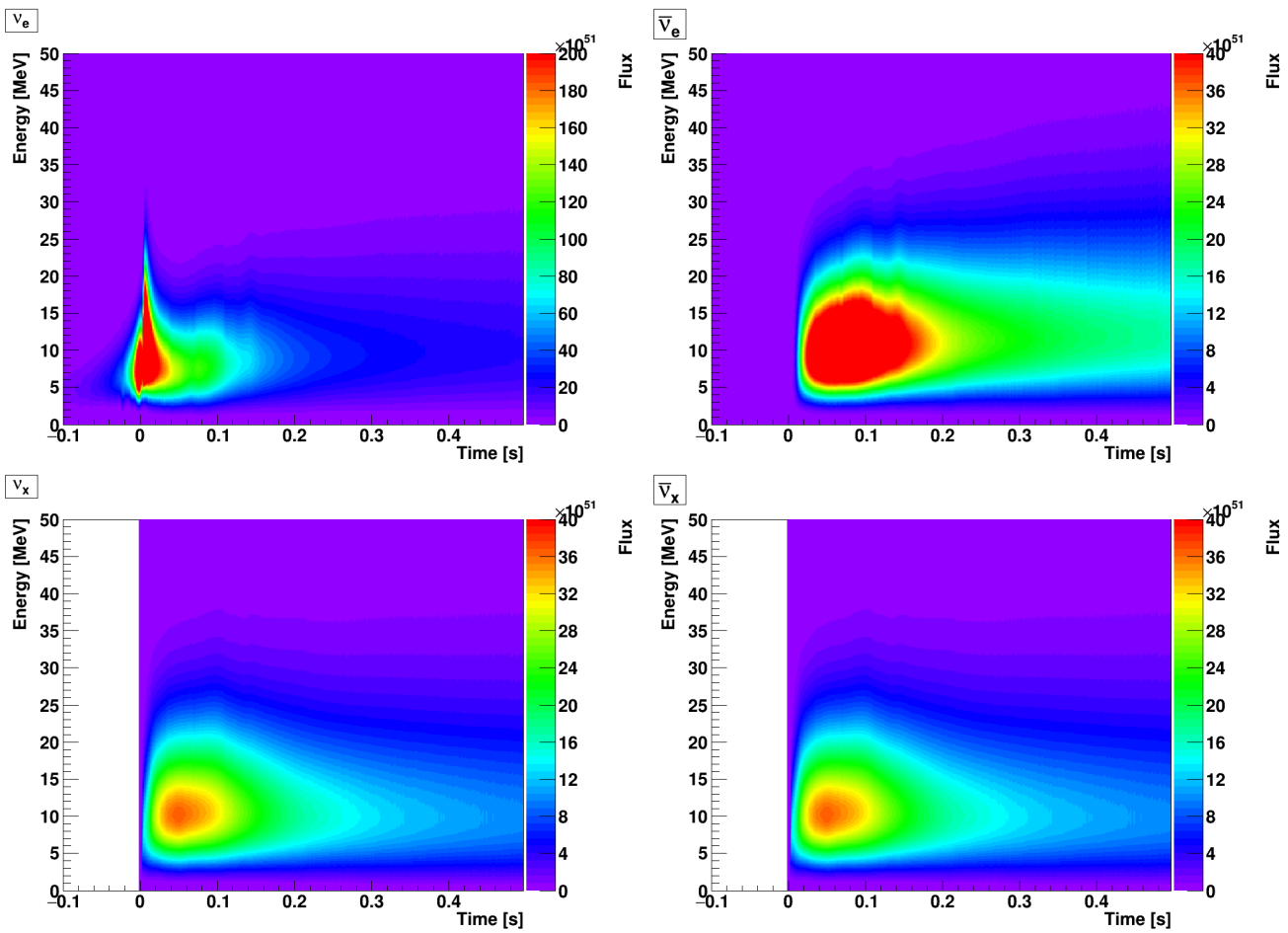
Figure F.28: TEL: LS220-s20.0 model.
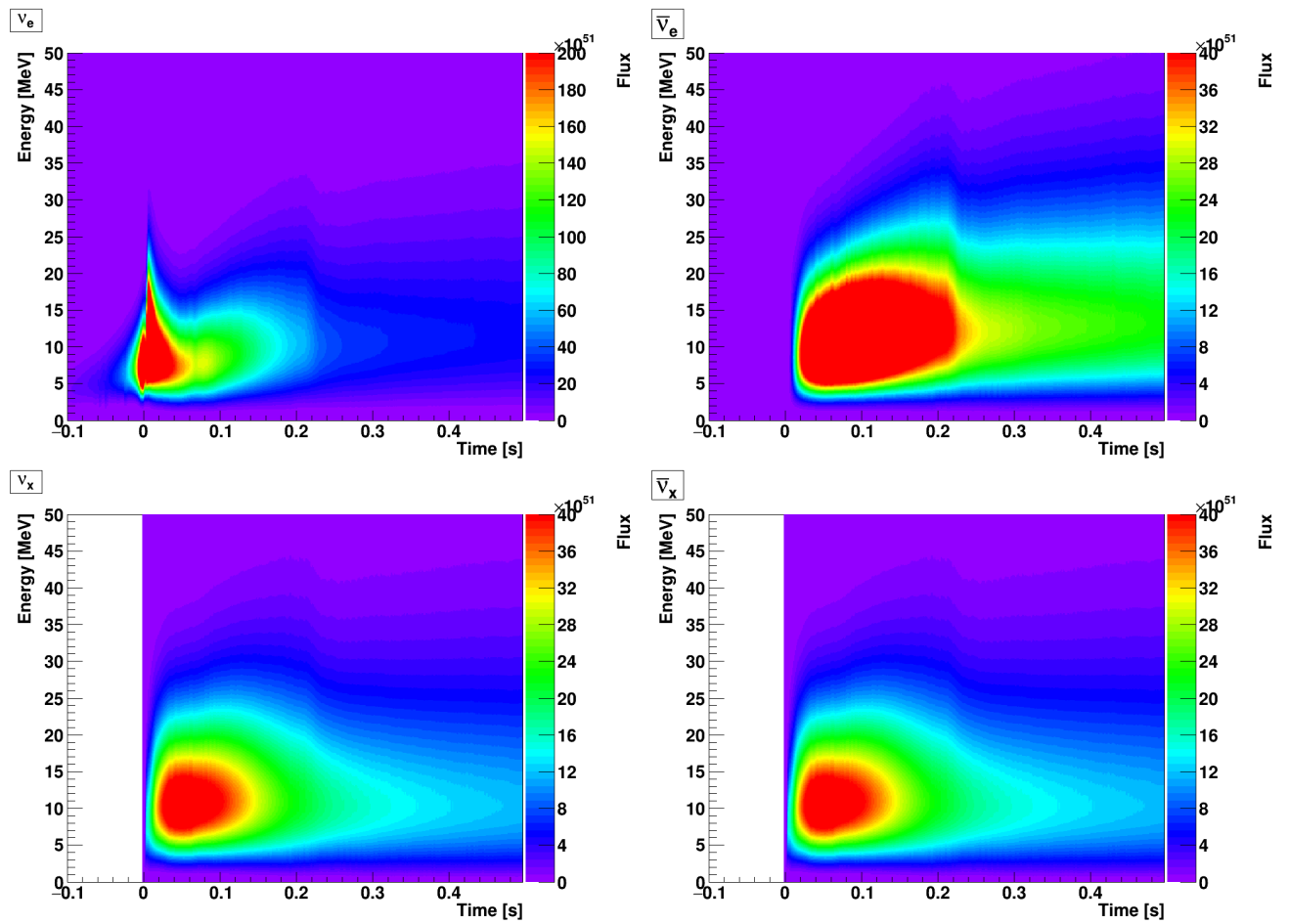
Figure F.29: TEL: LS220-s20.6 model.
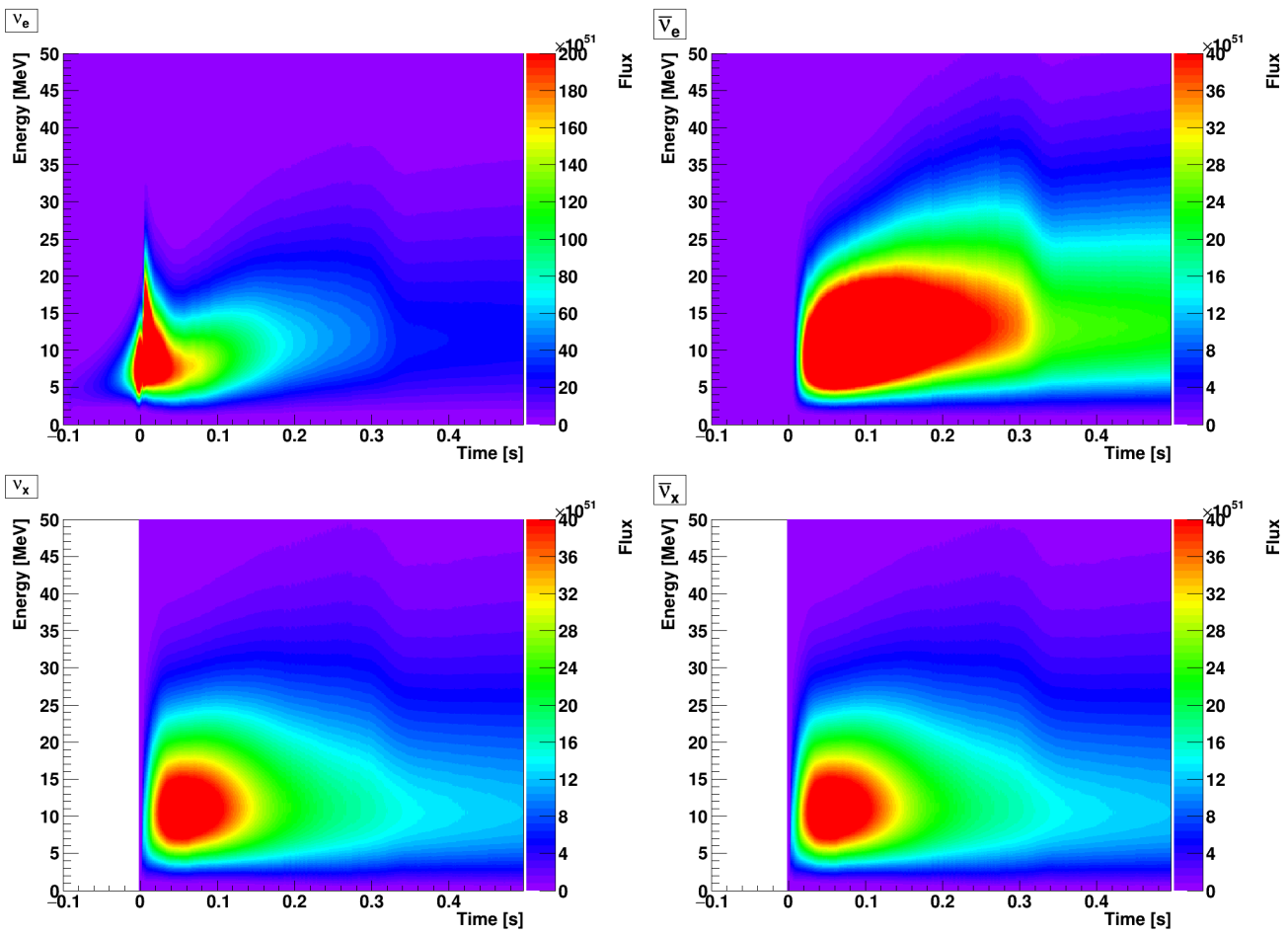
Figure F.30: TEL: LS220-s25.0 model.
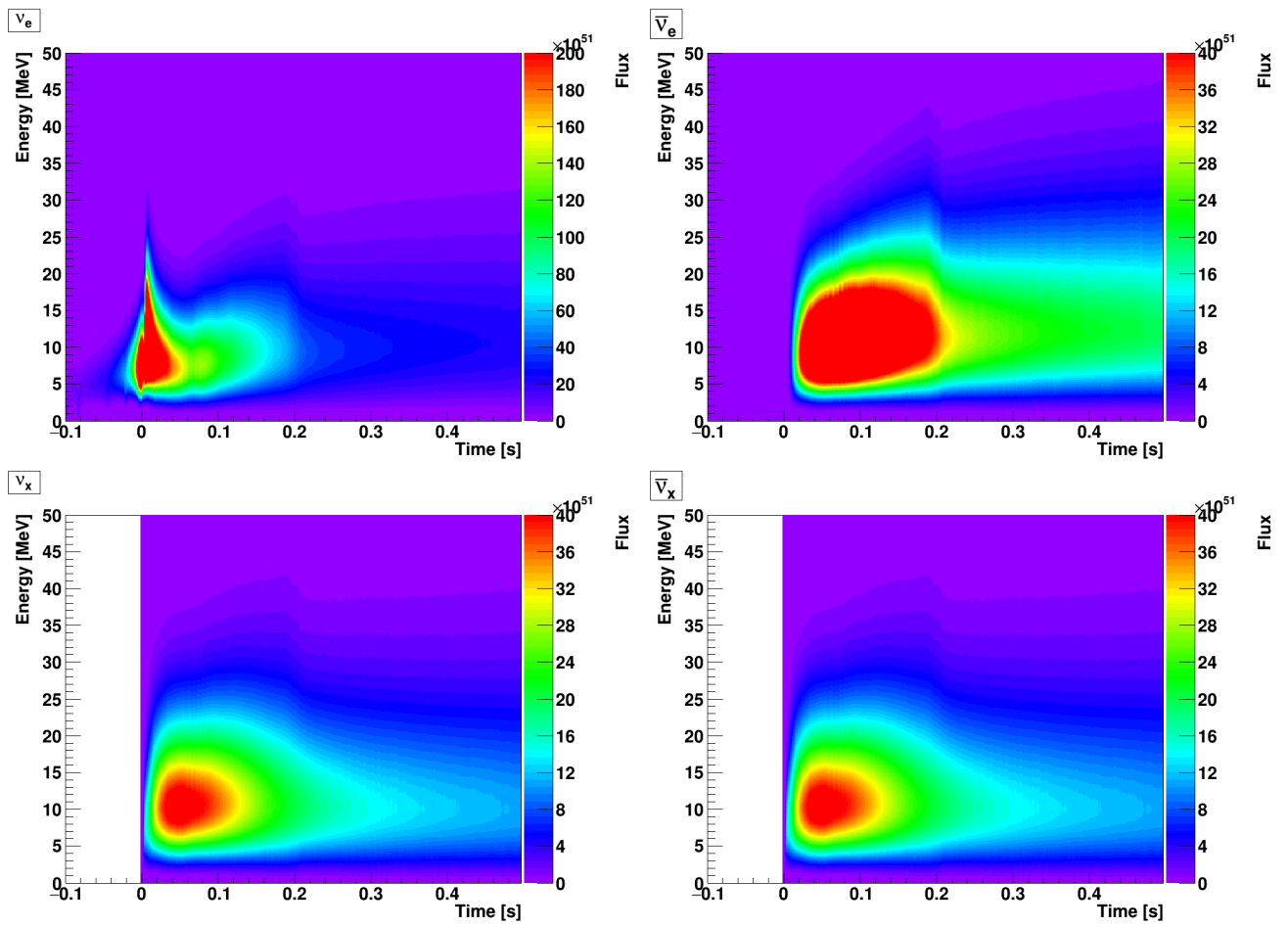
Figure F.31: TEL: LS220-s27.0 model.

F.2.2   SFHO models
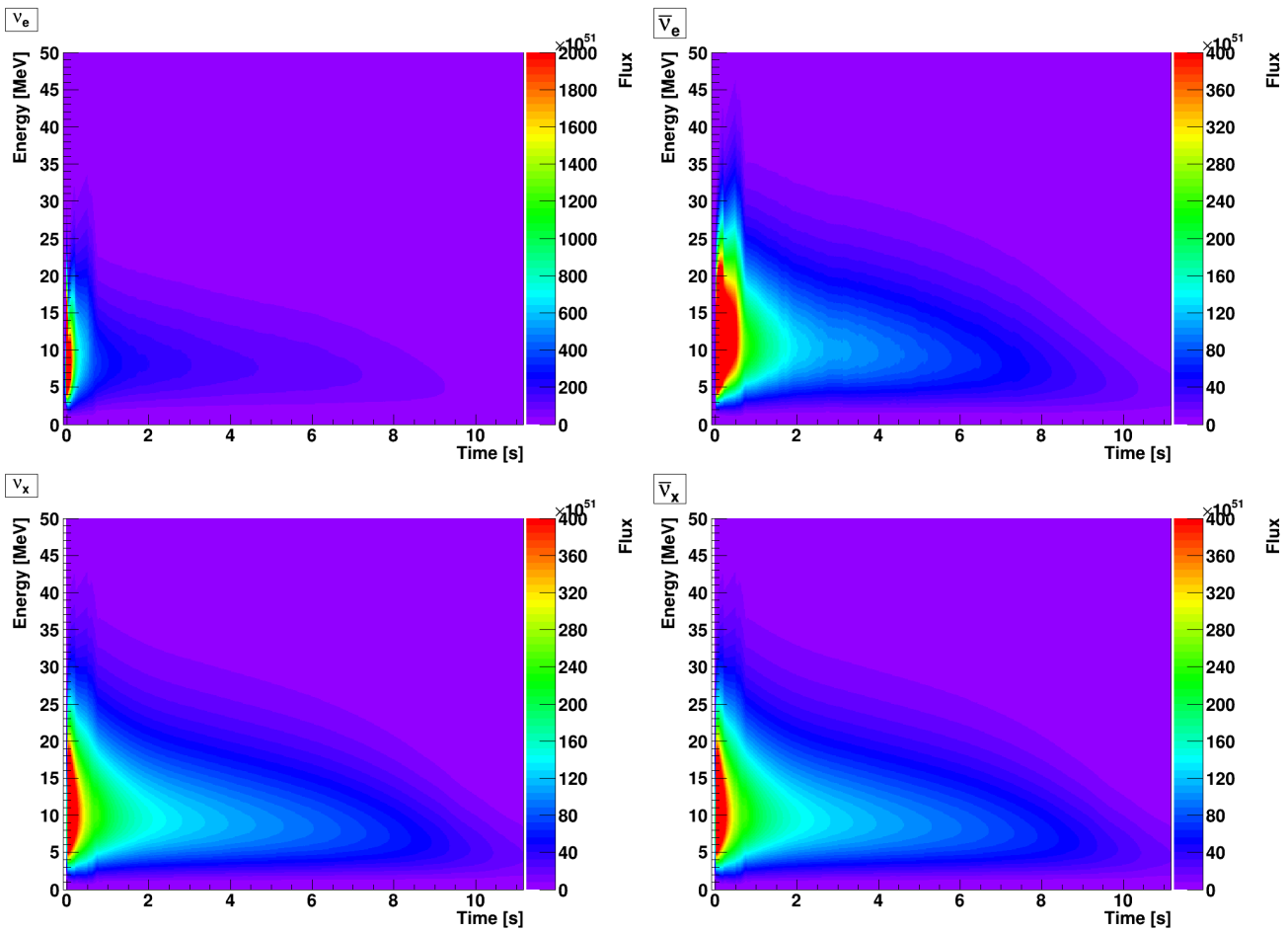
Figure F.32: TEL: SFHO-s27.0 model.
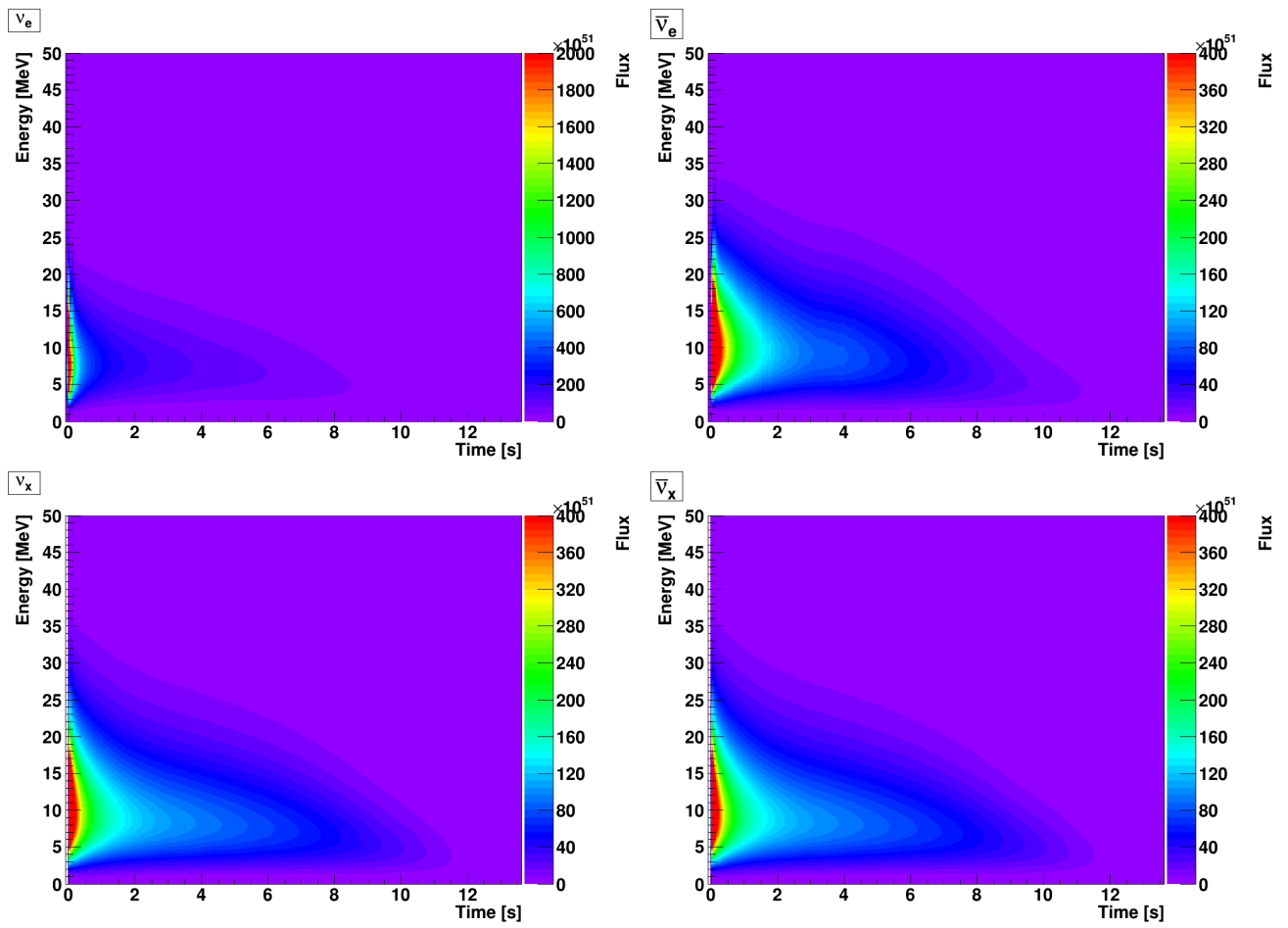
Figure F.33: TEL: SFHO-z9.6co model.

F.2.3   SHEN models
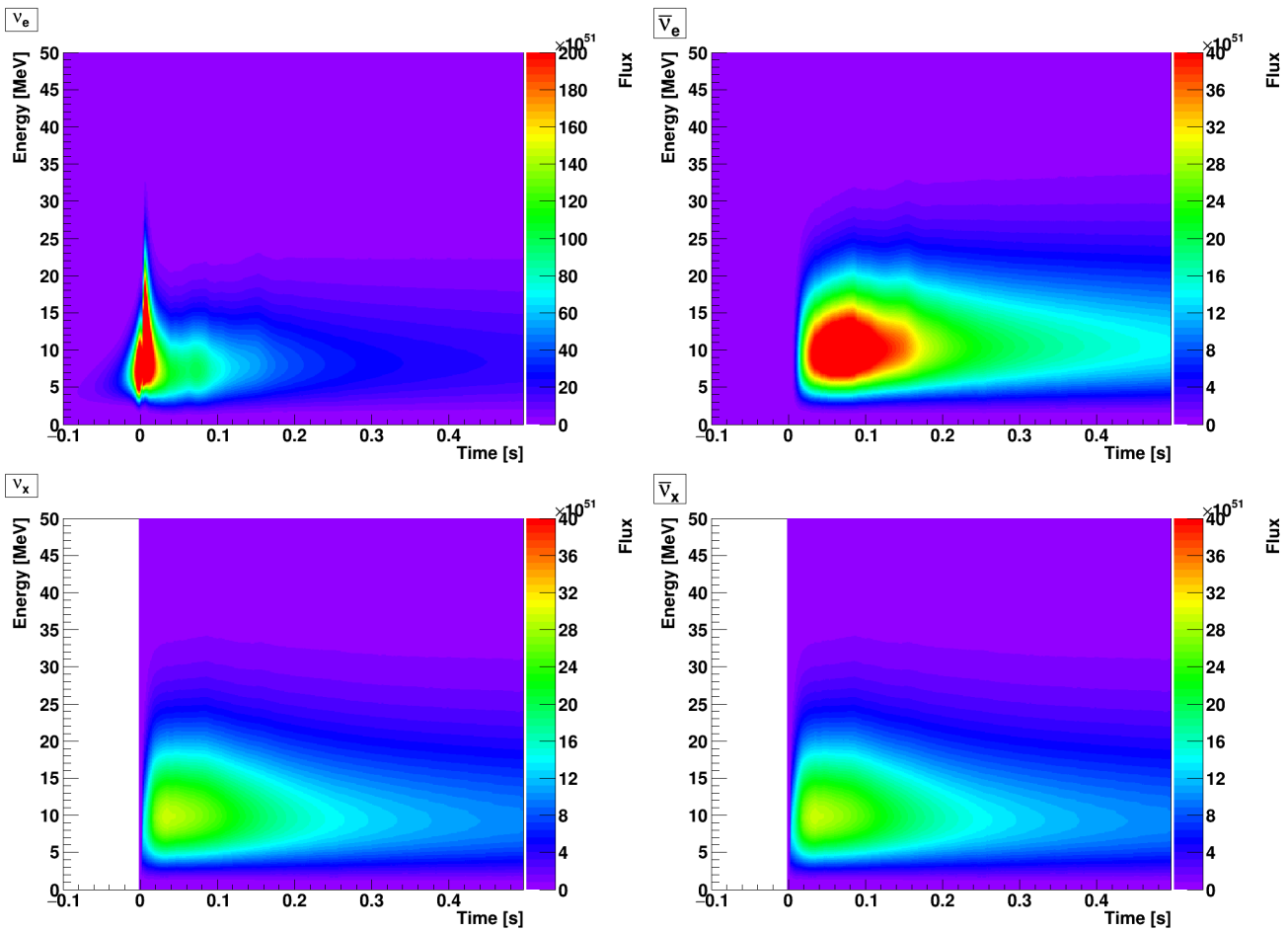
Figure F.34: TEL: SHEN-s11.2 model.
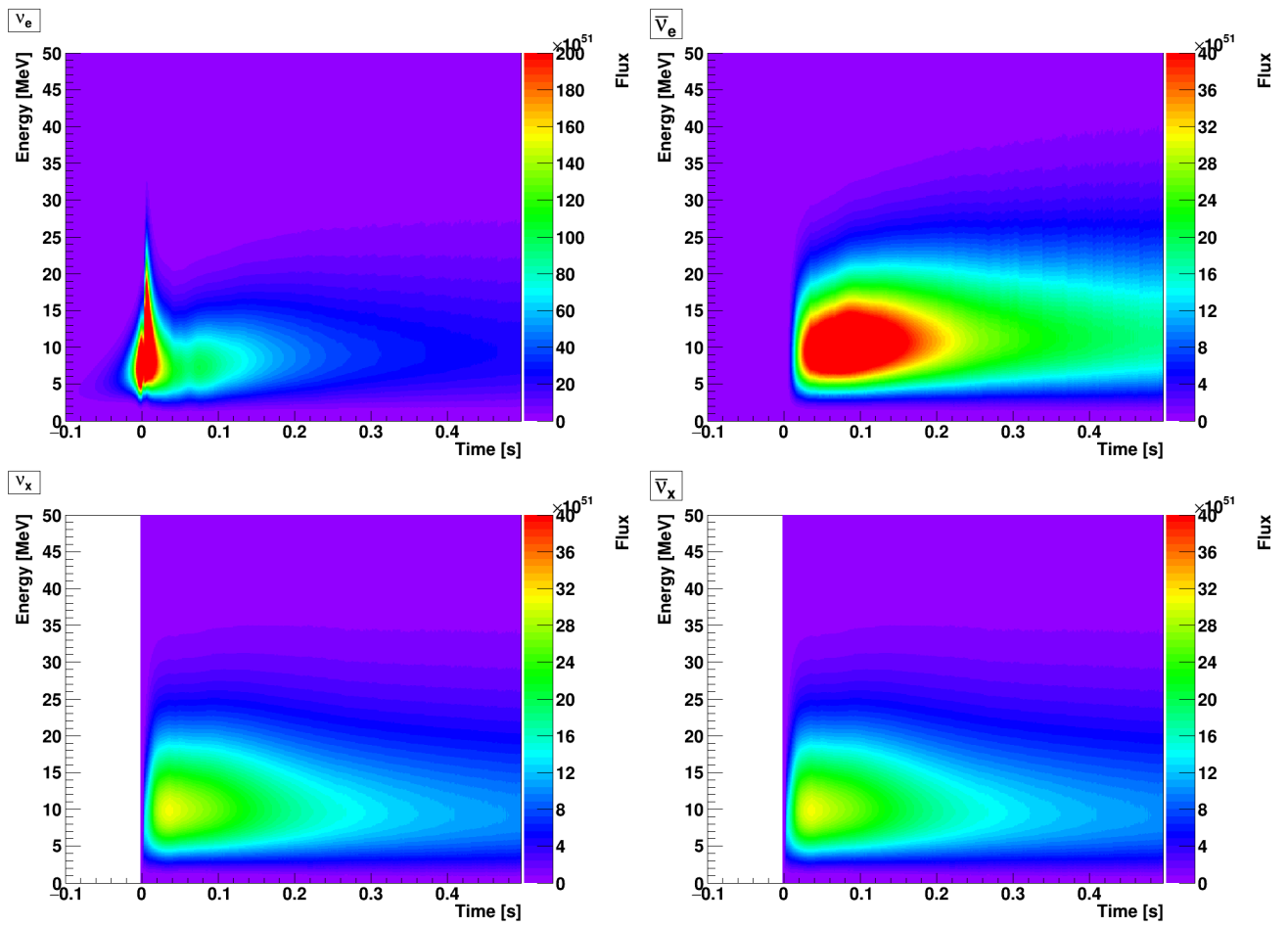
Figure F.35: TEL: SHEN-s12.0 model.
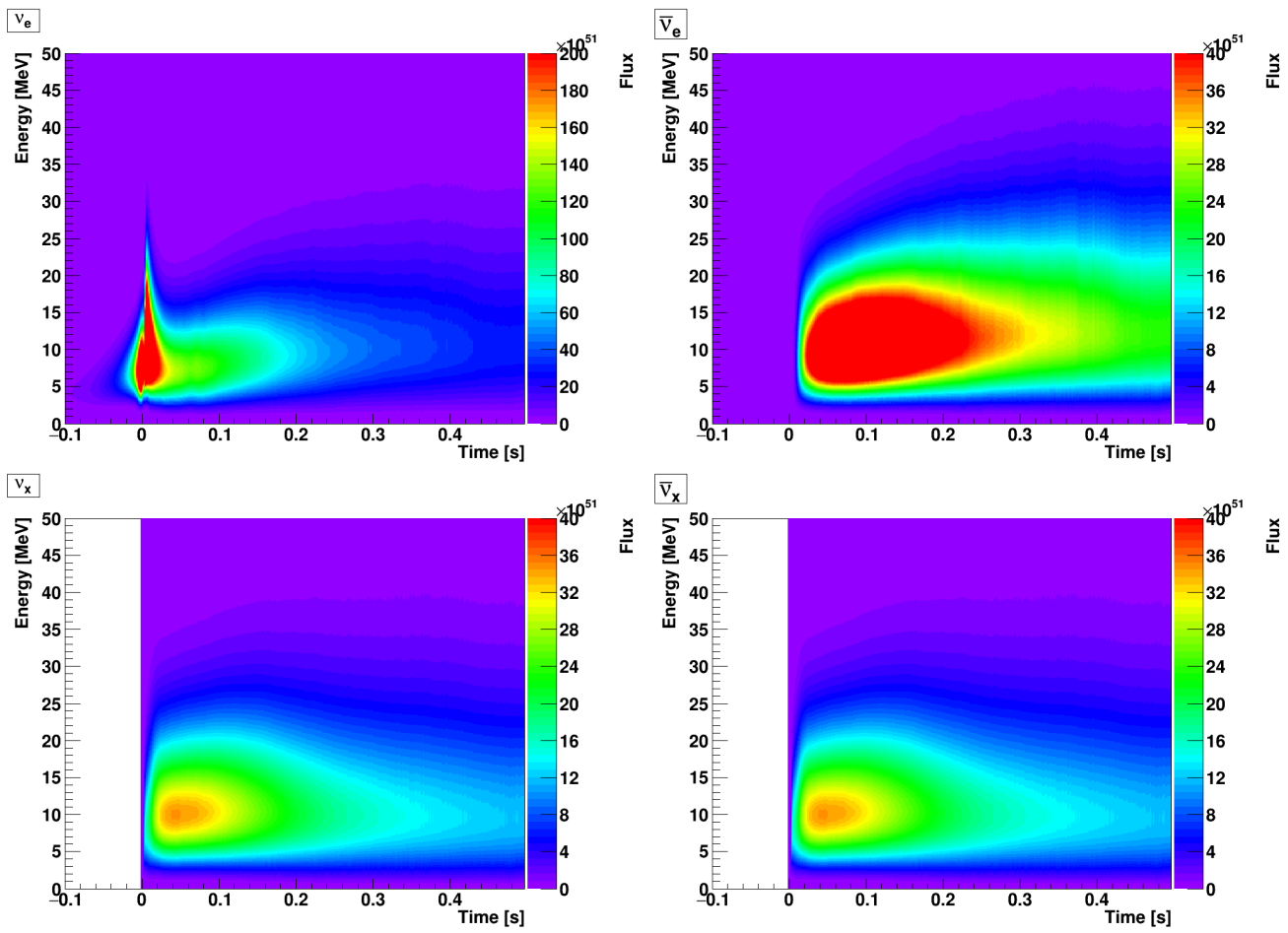
Figure F.36: TEL: SHEN-s15.0 model.
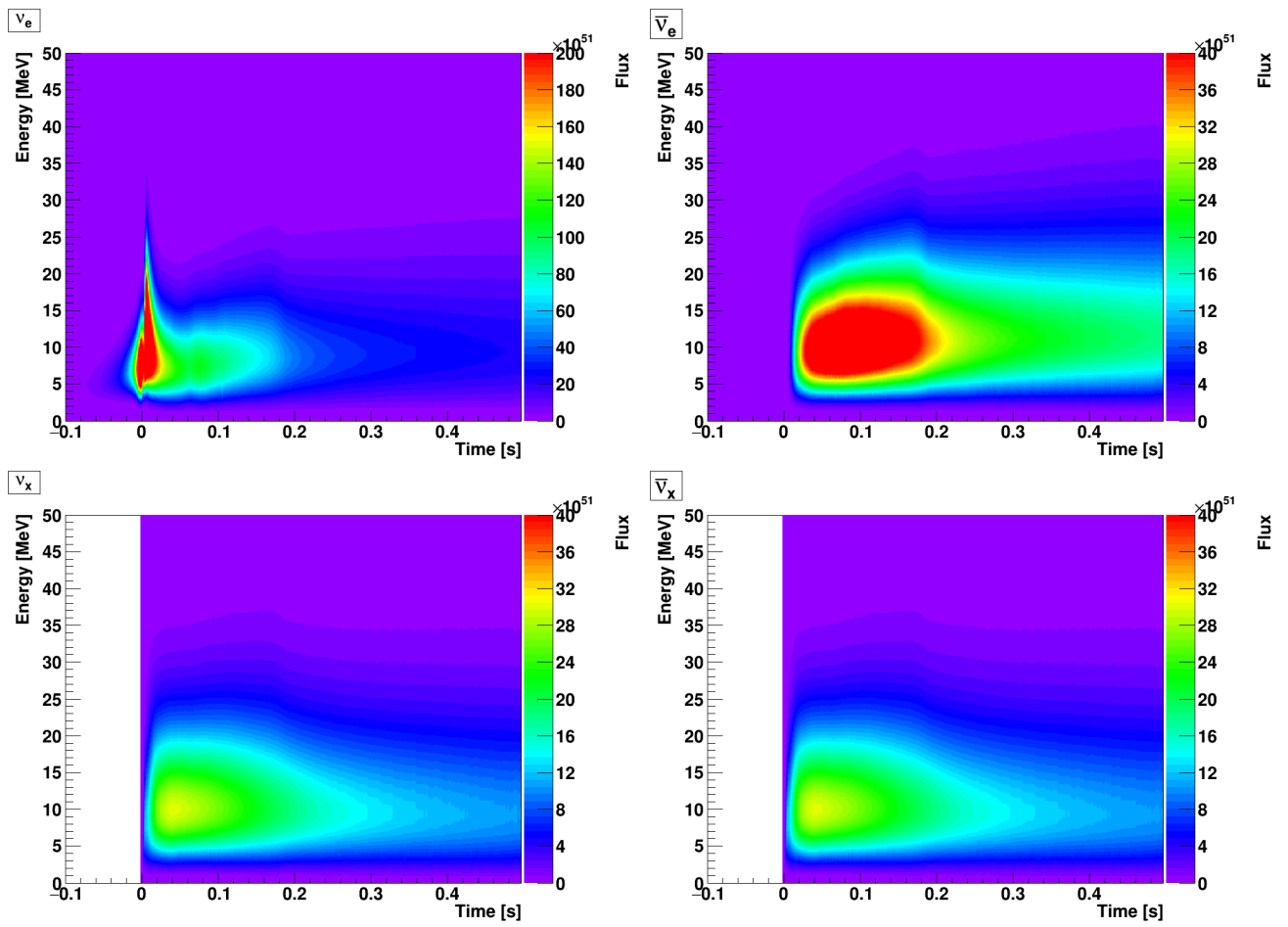
Figure F.37: TEL: SHEN-s15s7b2 model.
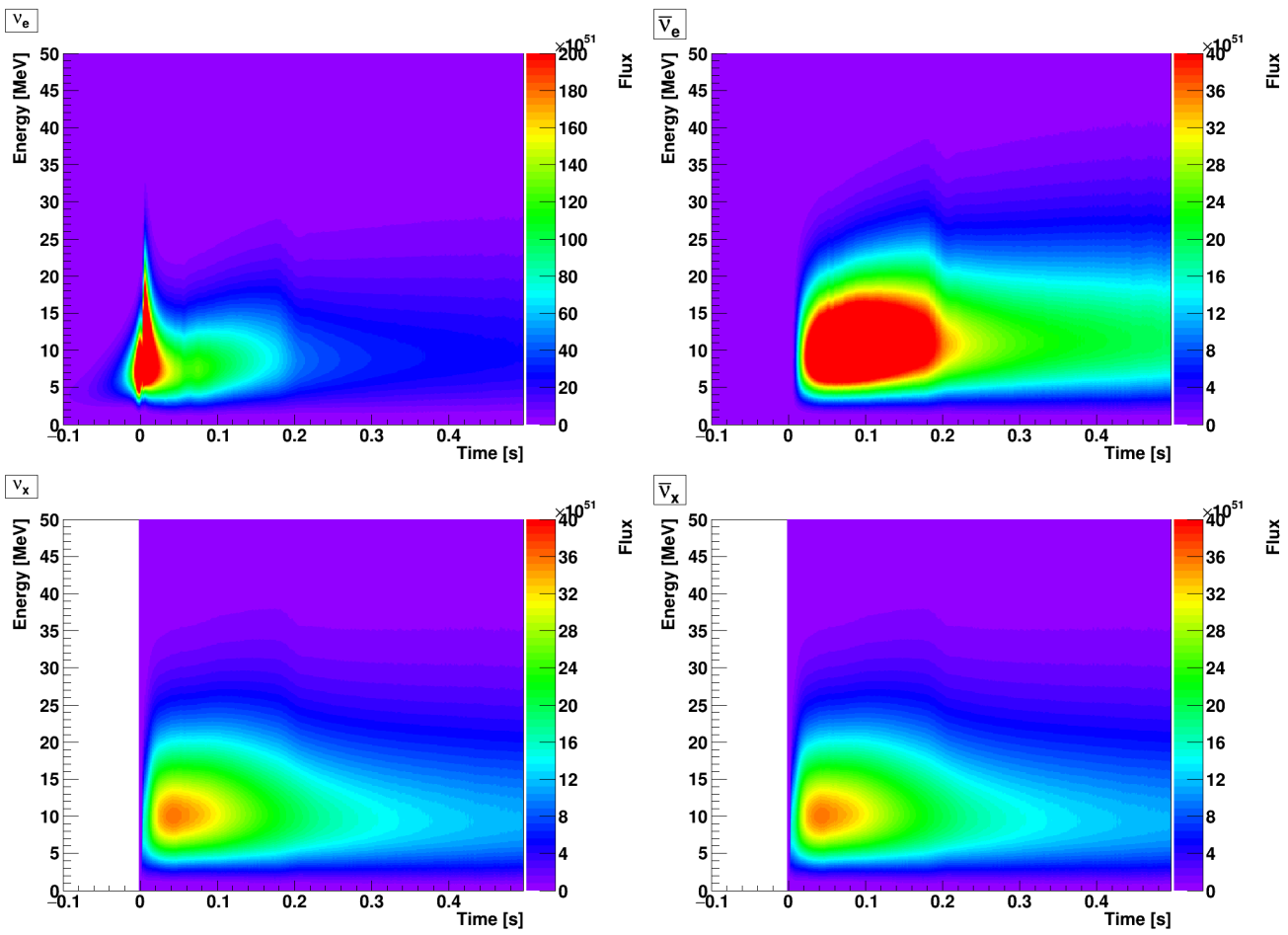
Figure F.38: TEL: SHEN-s17.6 model.
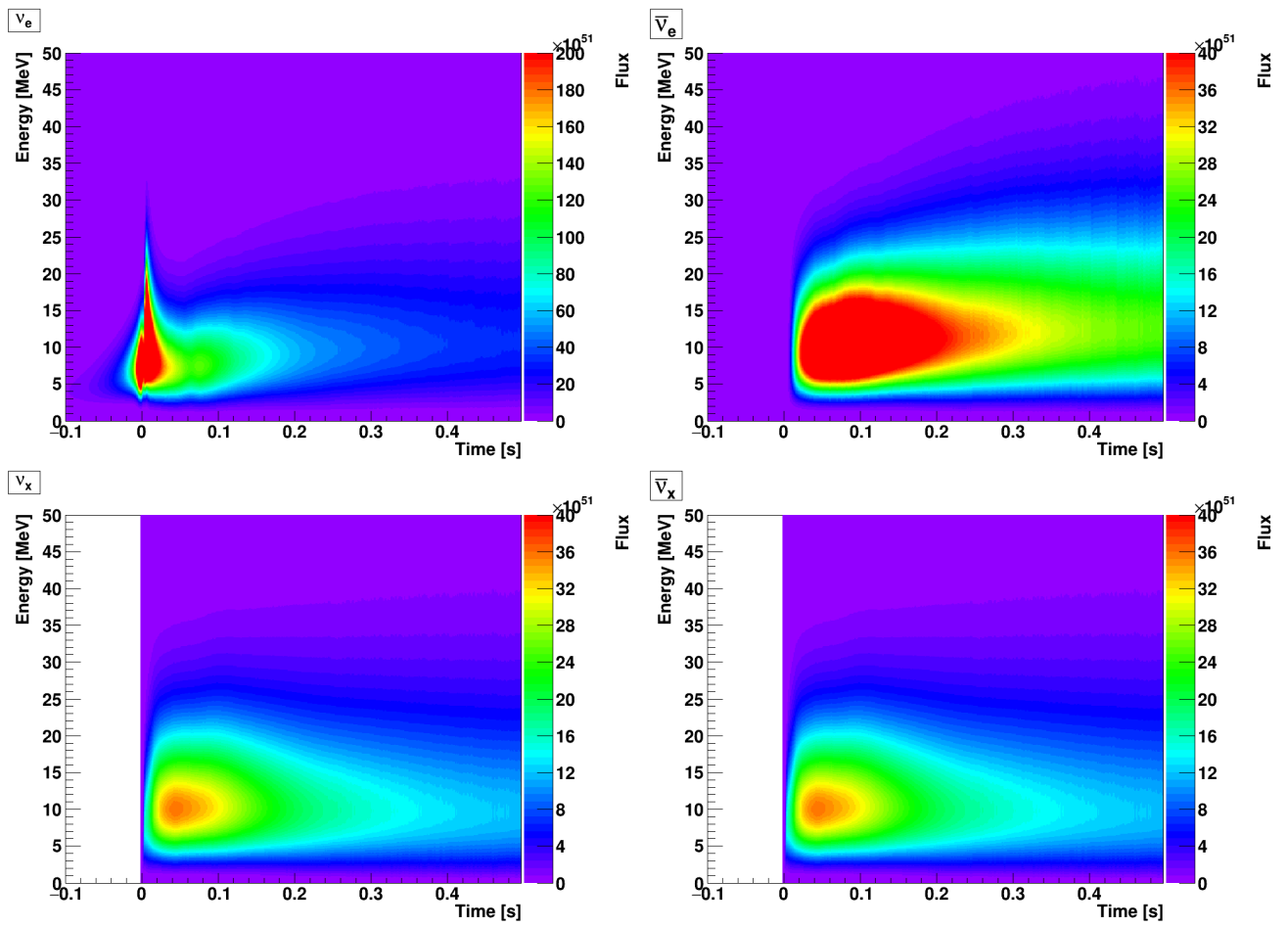
Figure F.39: TEL: SHEN-s17.8 model.
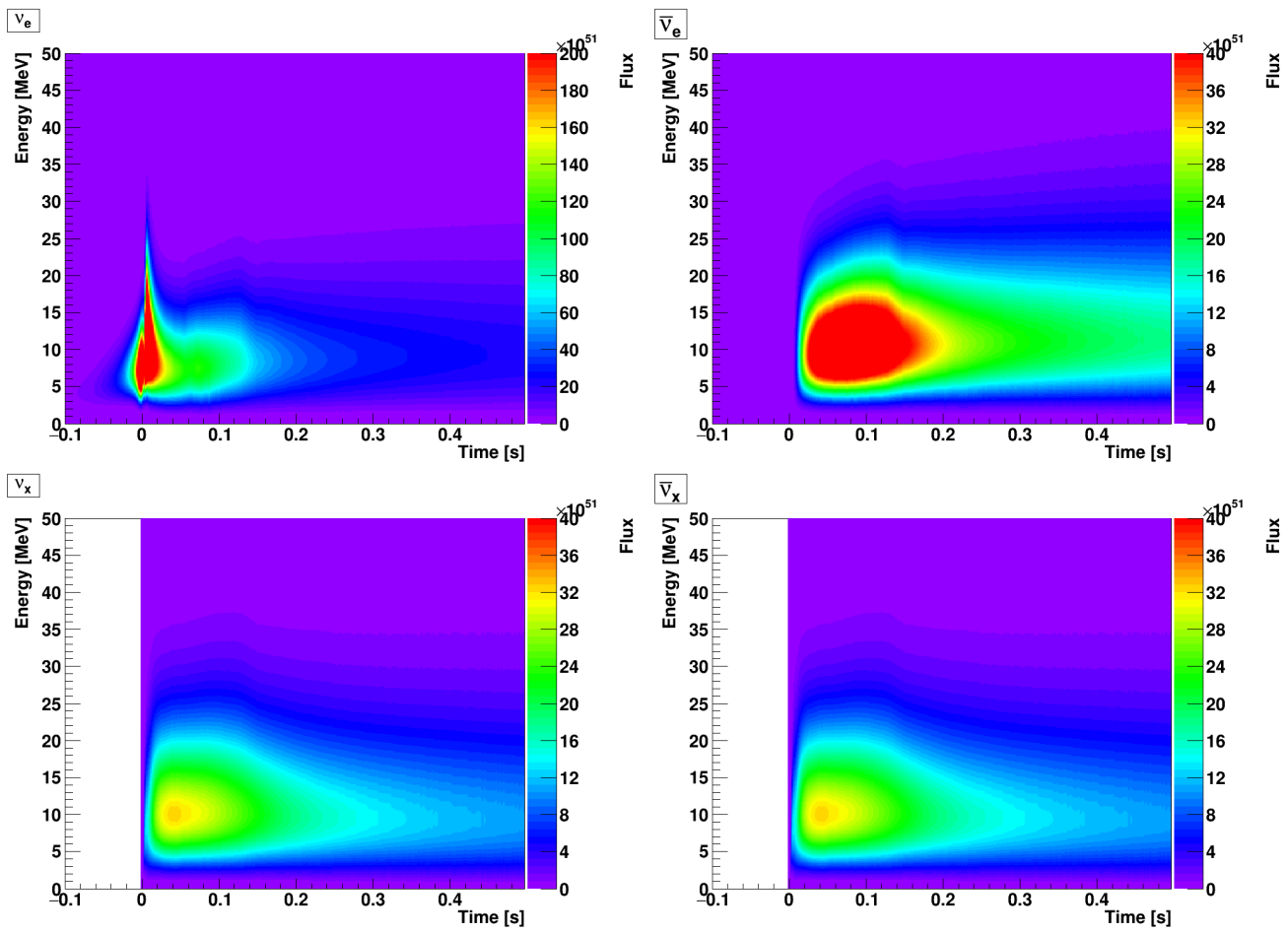
Figure F.40: TEL: SHEN-s20.0 model.
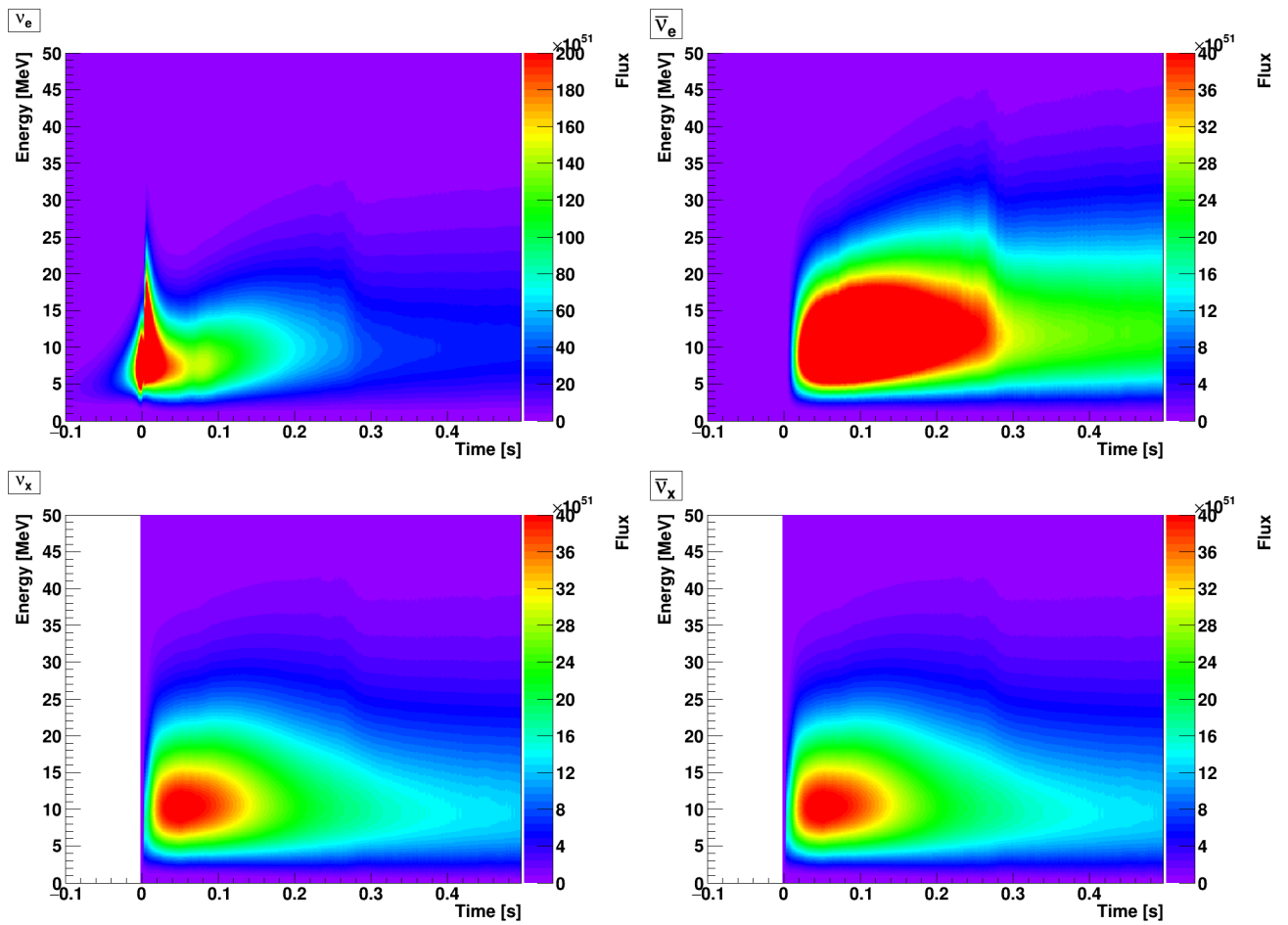
Figure F.41: TEL: SHEN-s20.6 model.
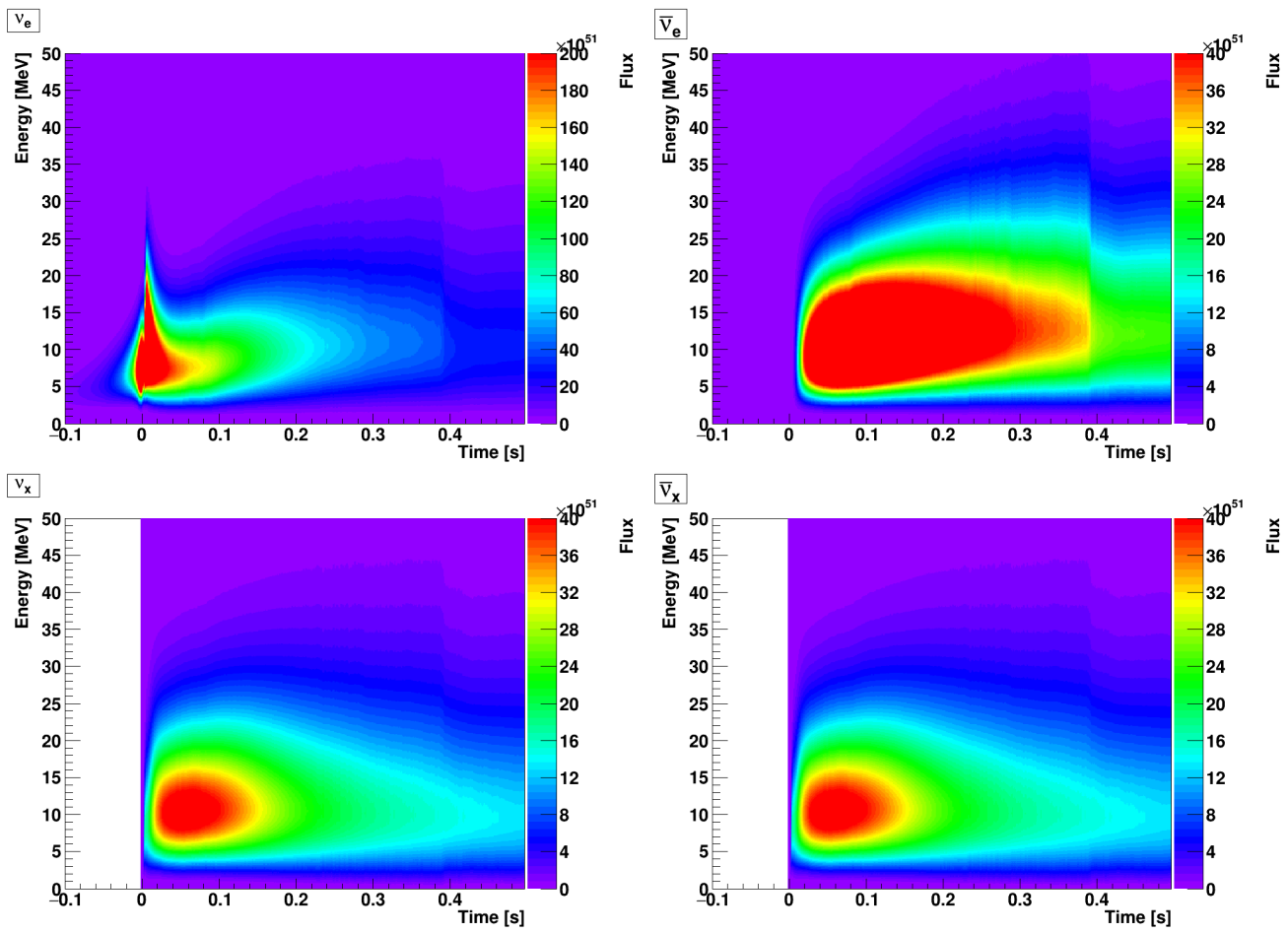
Figure F.42: TEL: SHEN-s25.0 model.
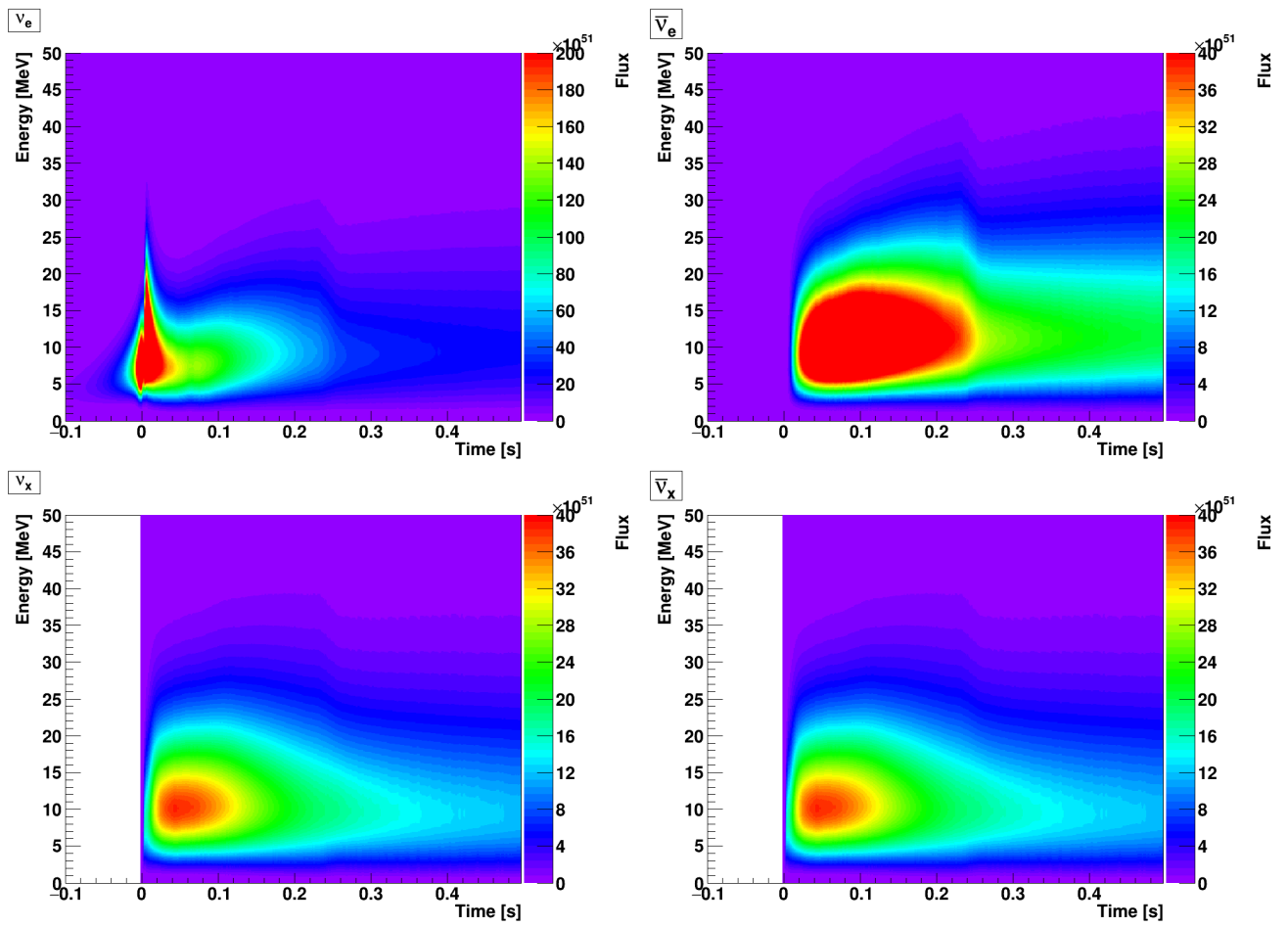
Figure F.43: TEL: SHEN-s27.0 model.
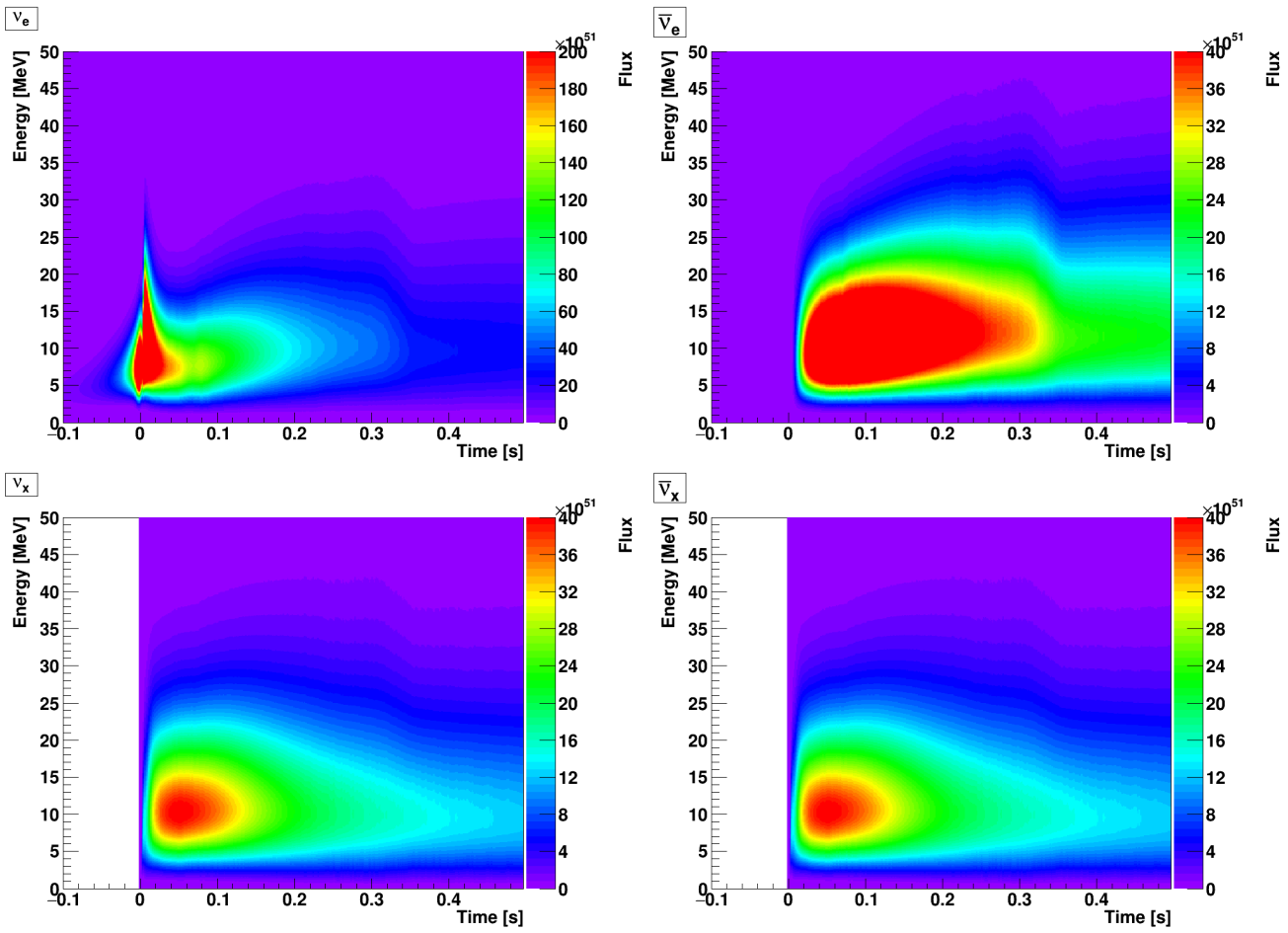
Figure F.44: TEL: SHEN-s40.0 model.

F.2.4 Longer models
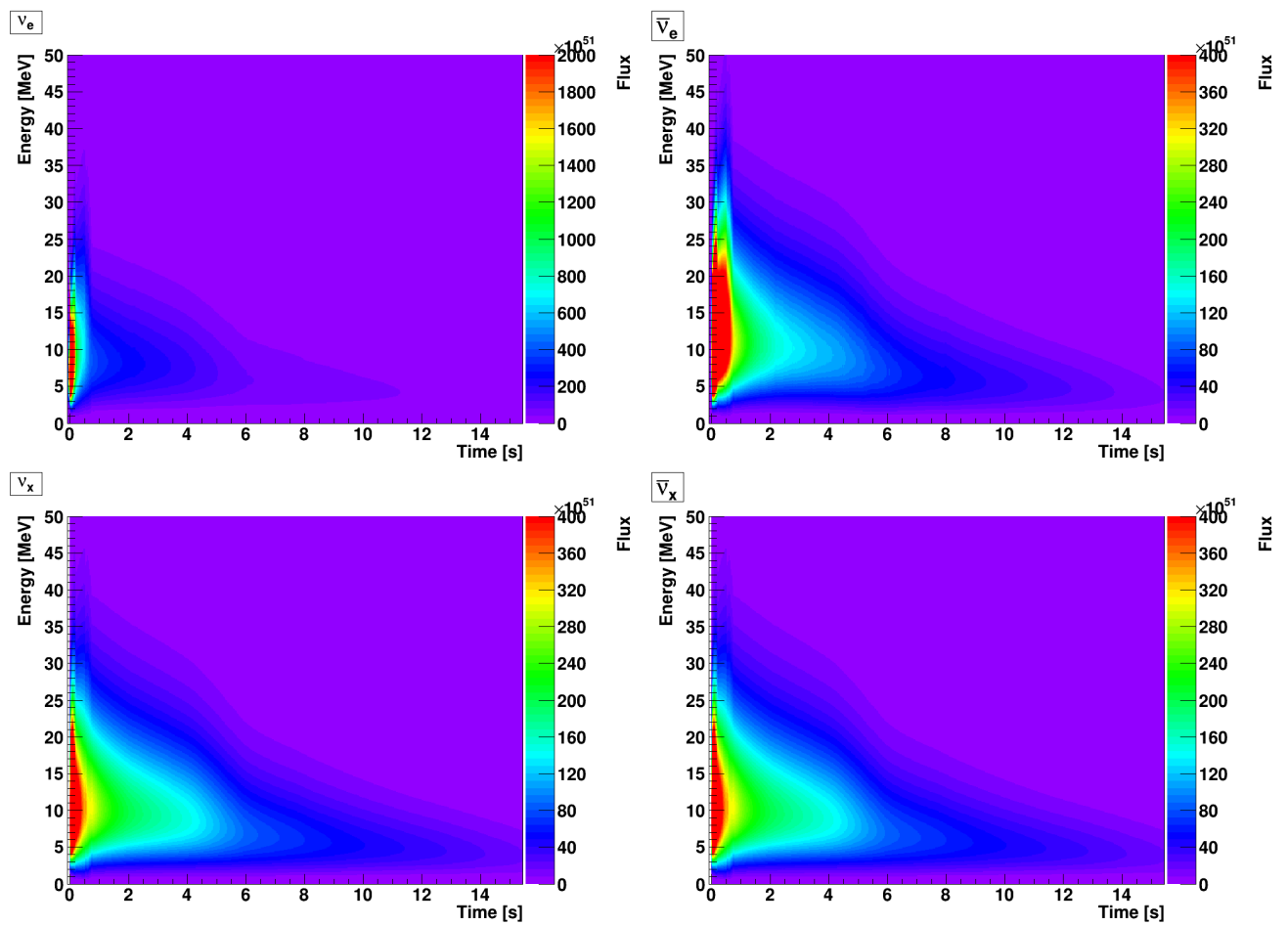
Figure F.45: TEL: LS220-s27.0co model.
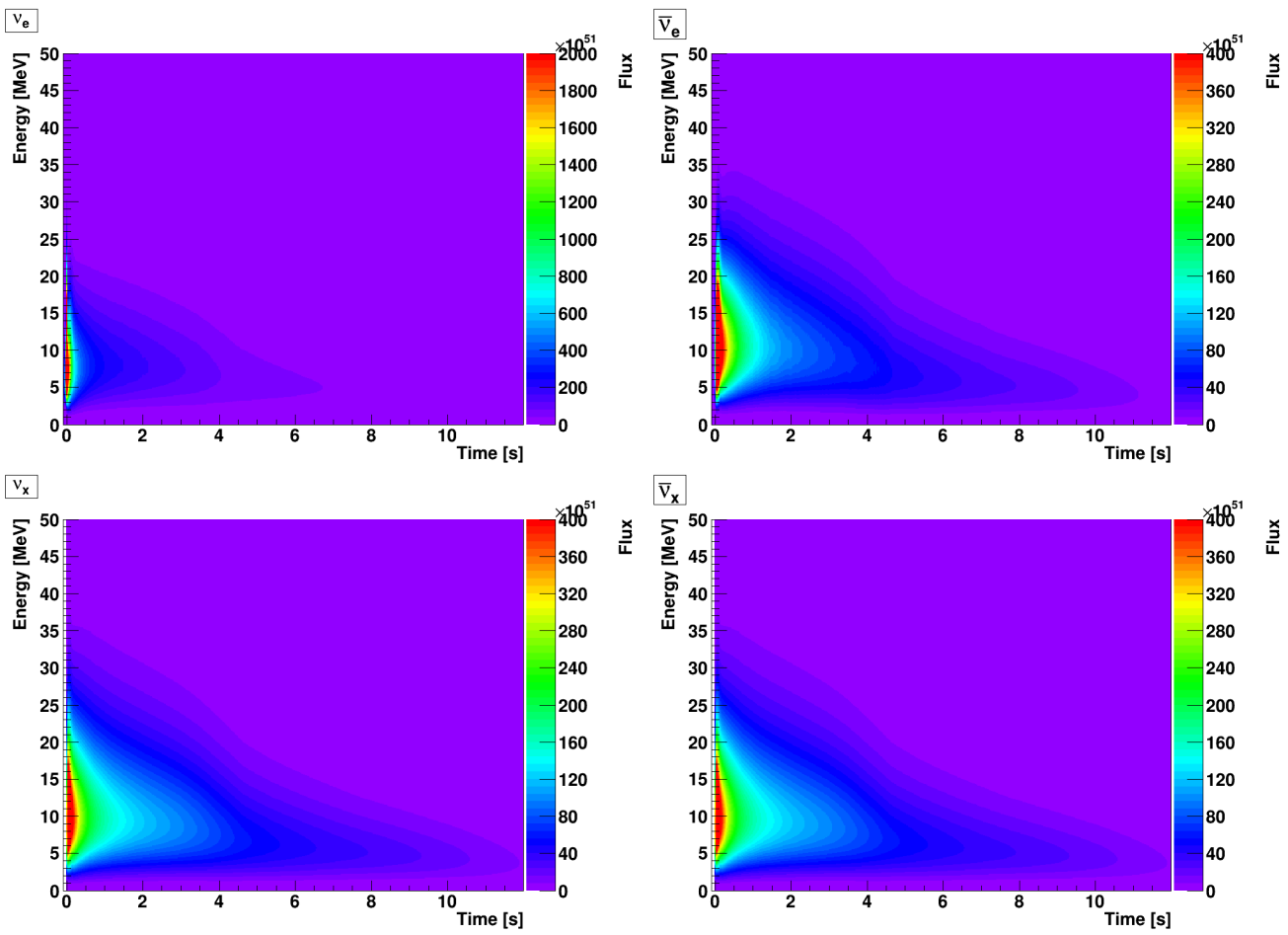
Figure F.46: TEL: LS220-z9.6co model.
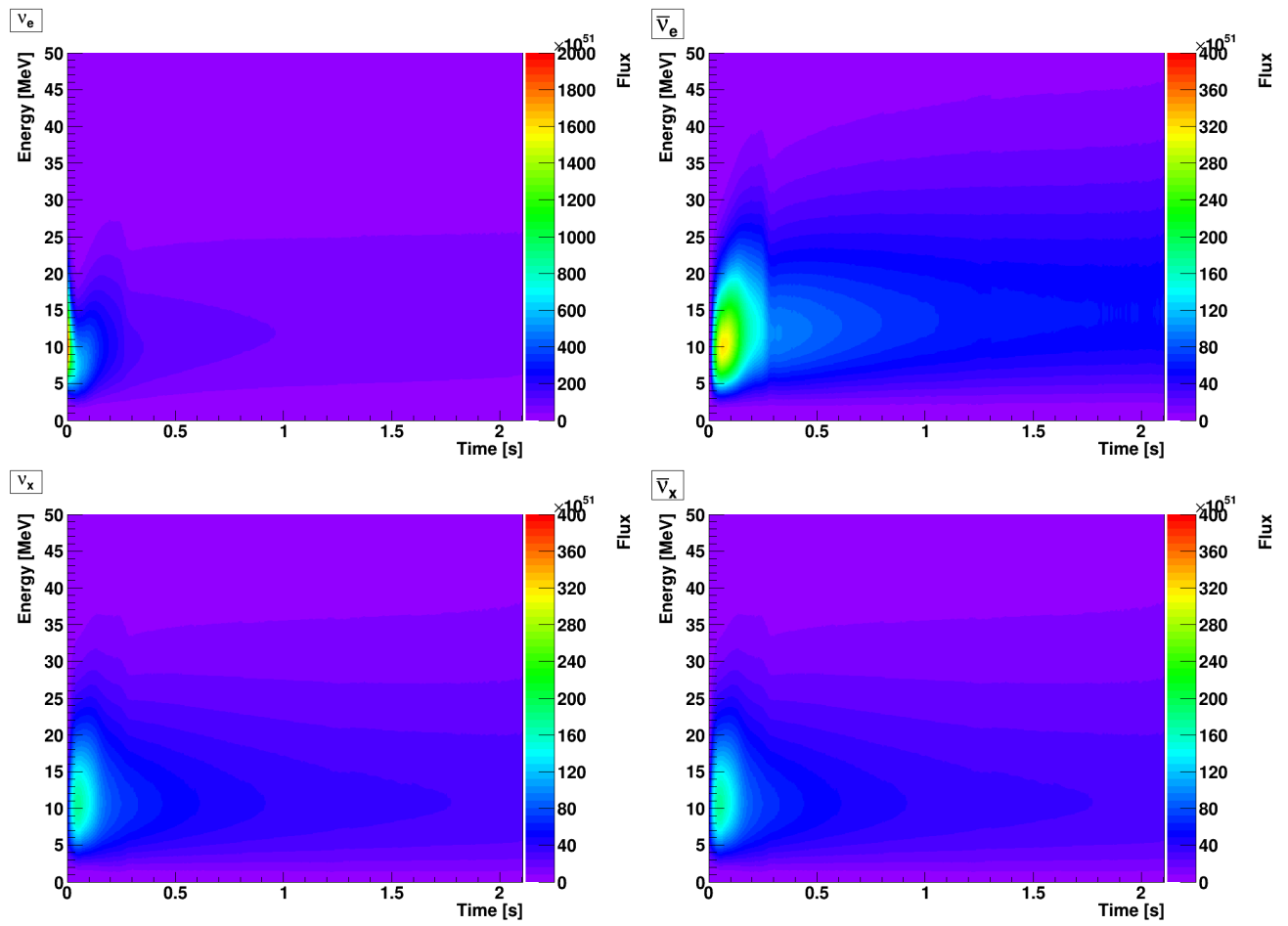
Figure F.47: TEL: LS220-s40.0c-bh model.
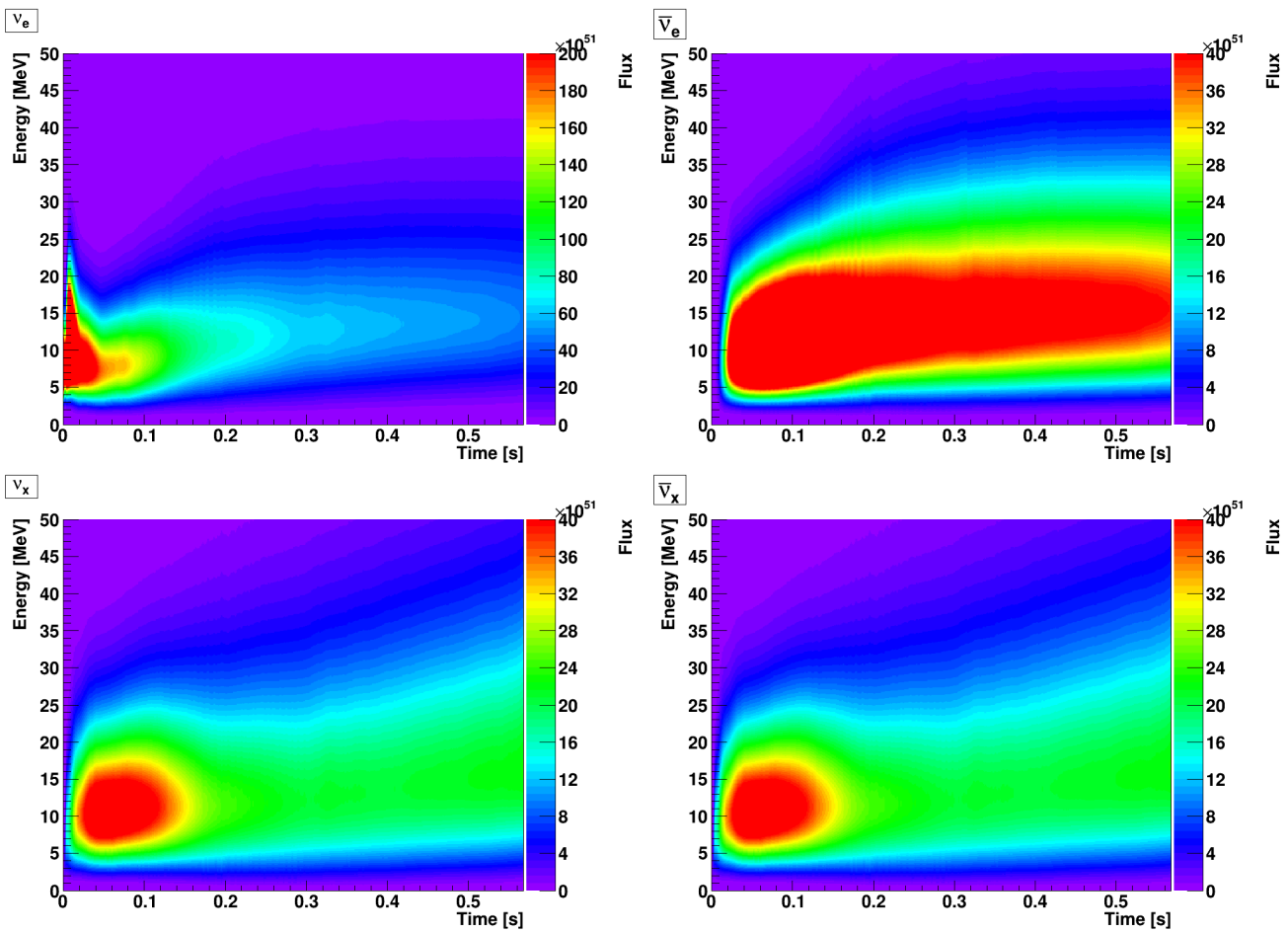
Figure F.48: TEL: LS220-s40s7b2c-bh model.
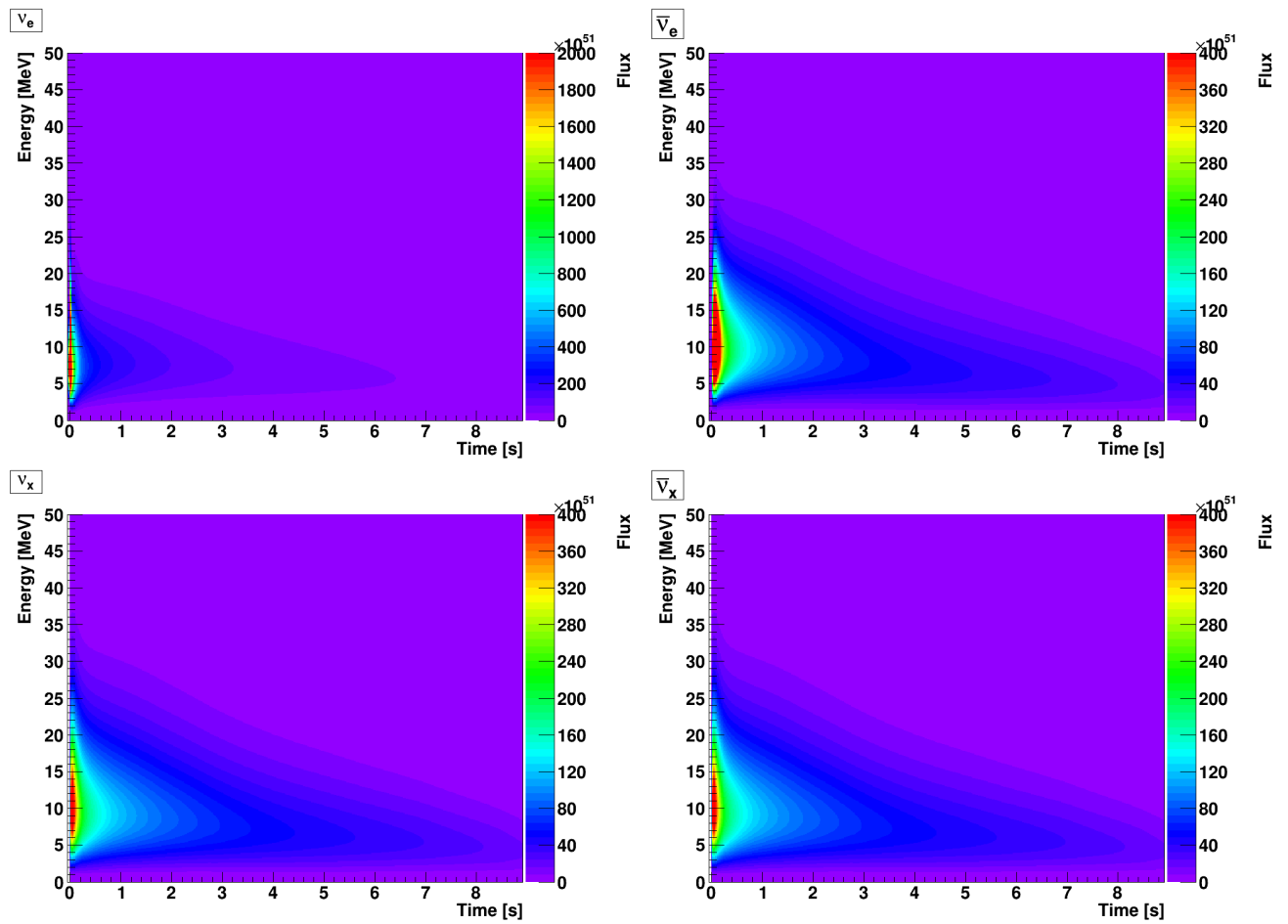
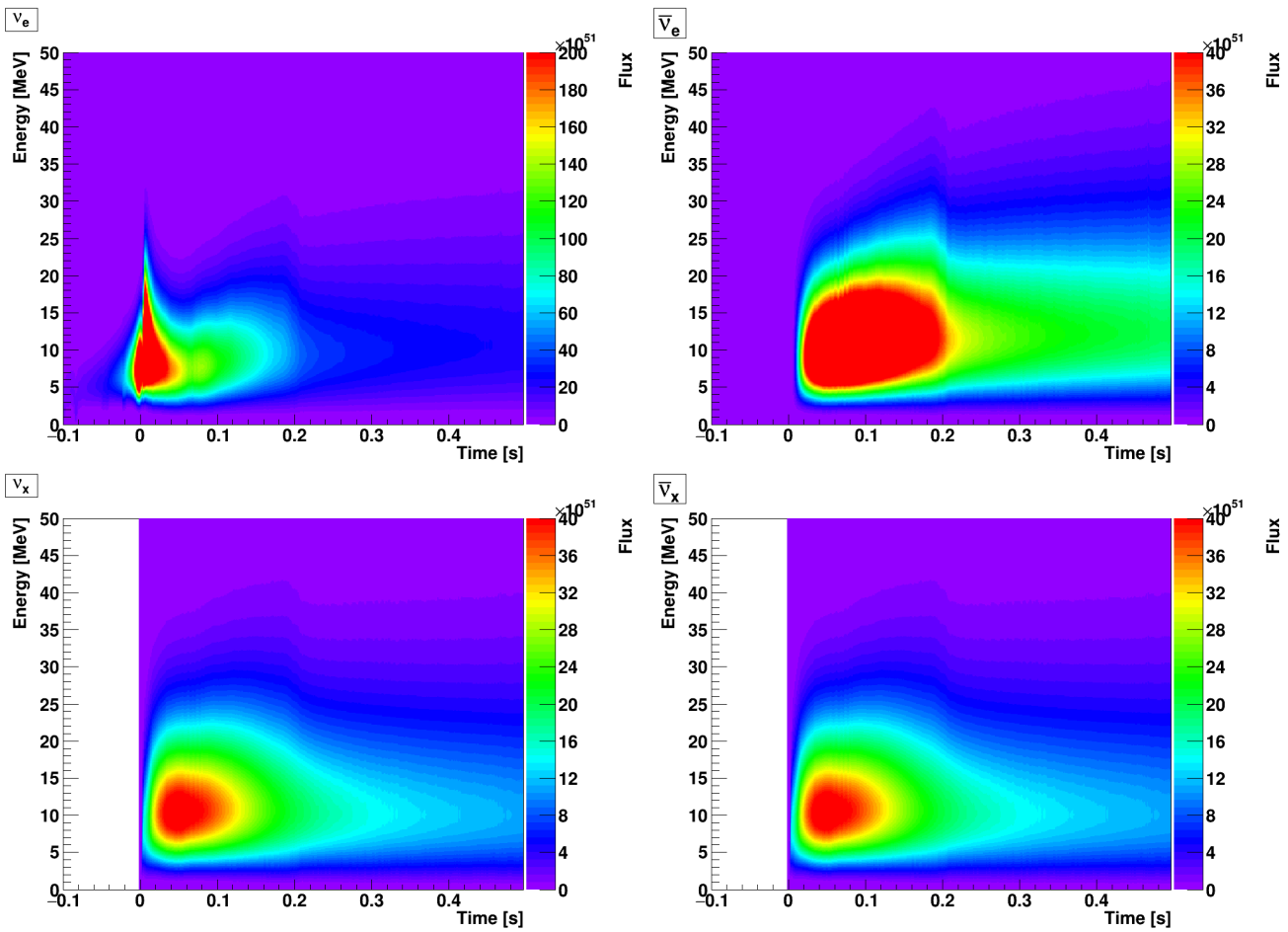**Figure F.49:** TEL: SHEN-s8.8 model.

F.2.5   Hierarchy comparison

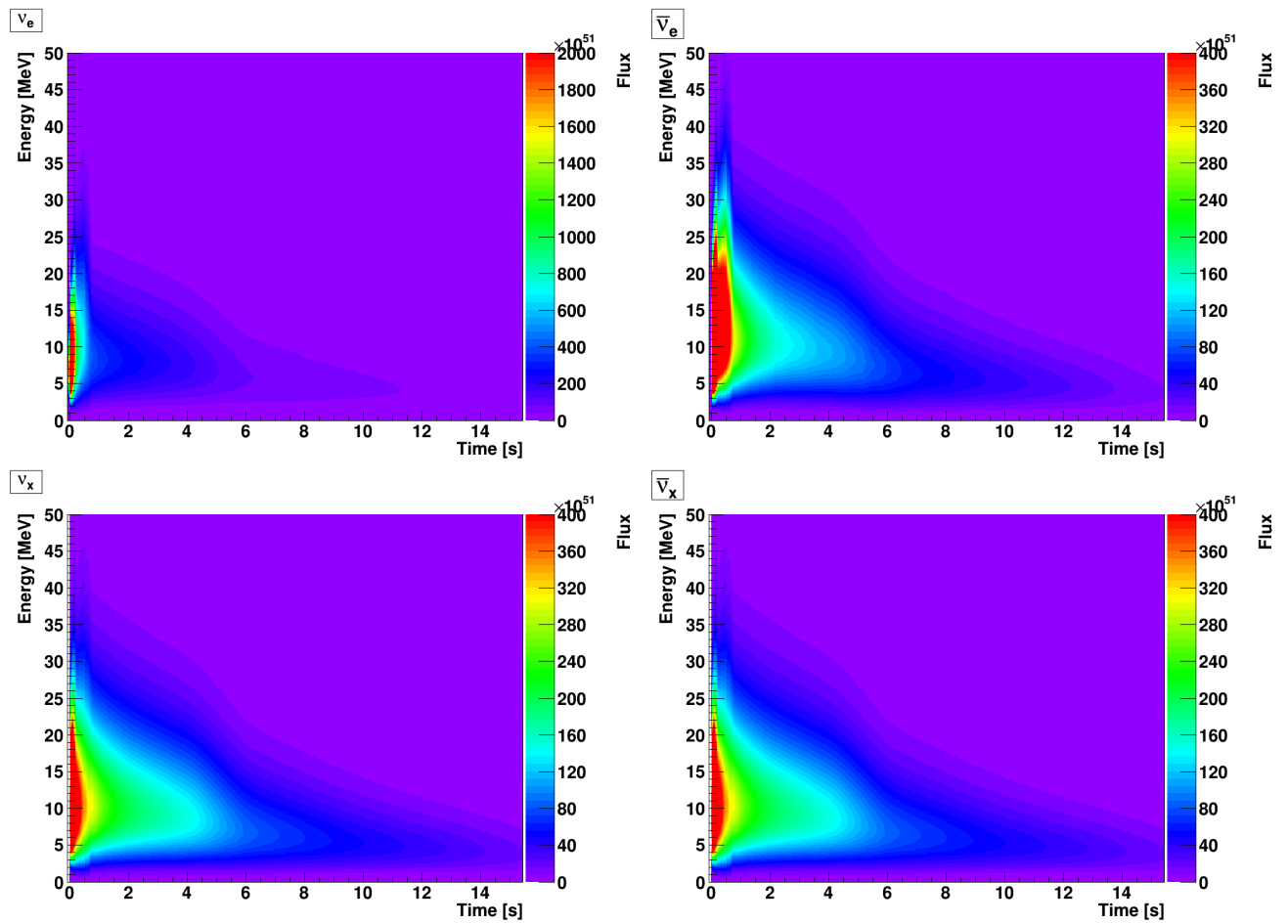**Figure F.50:** TEL: LS220-s27.0 model, inverted hierarchy.

Figure F.51: TEL: LS220-s27.0co model, inverted hierarchy.

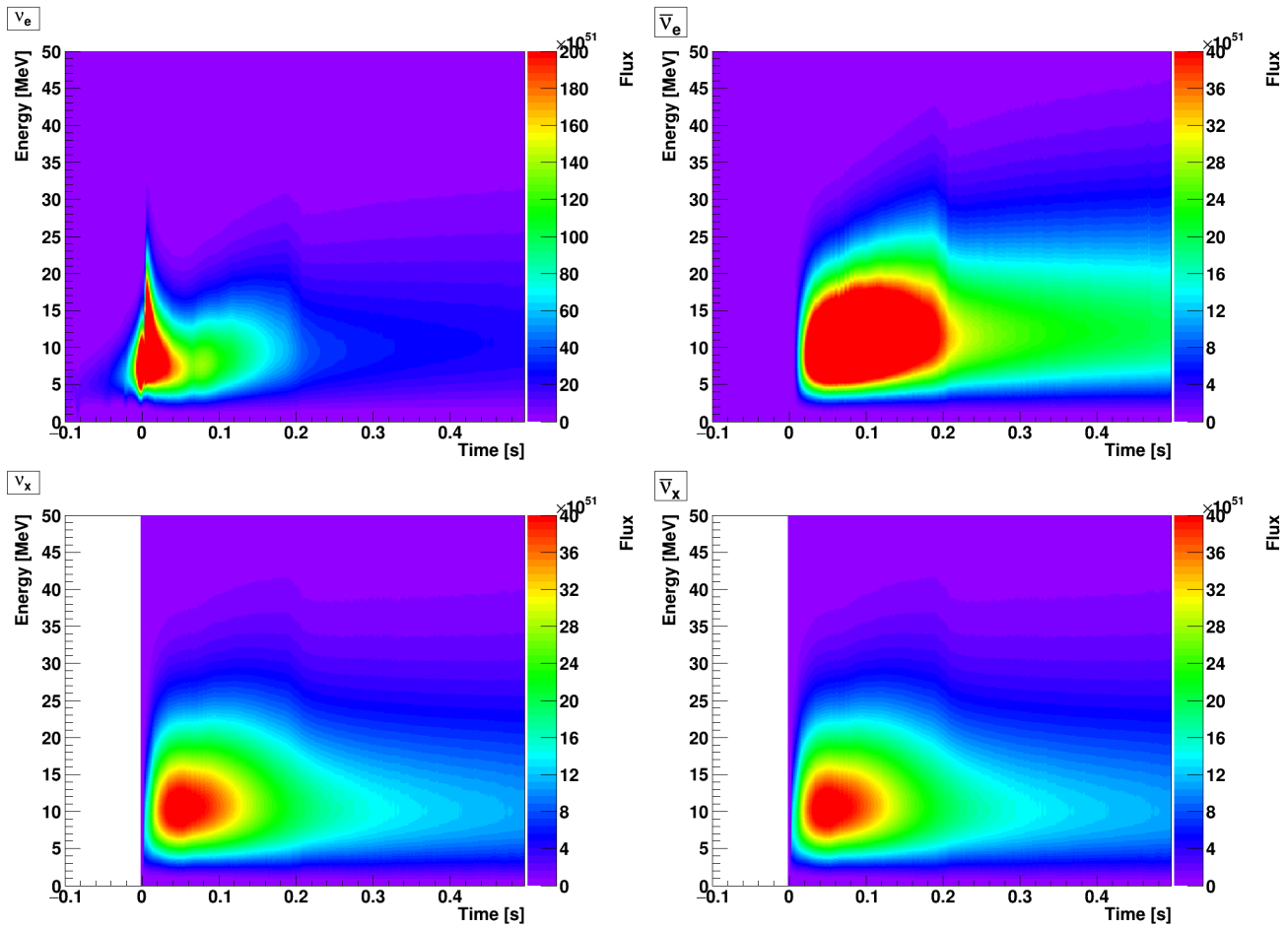## F.2.6   Mikheyev-Smirnow-Wolfenstein effect

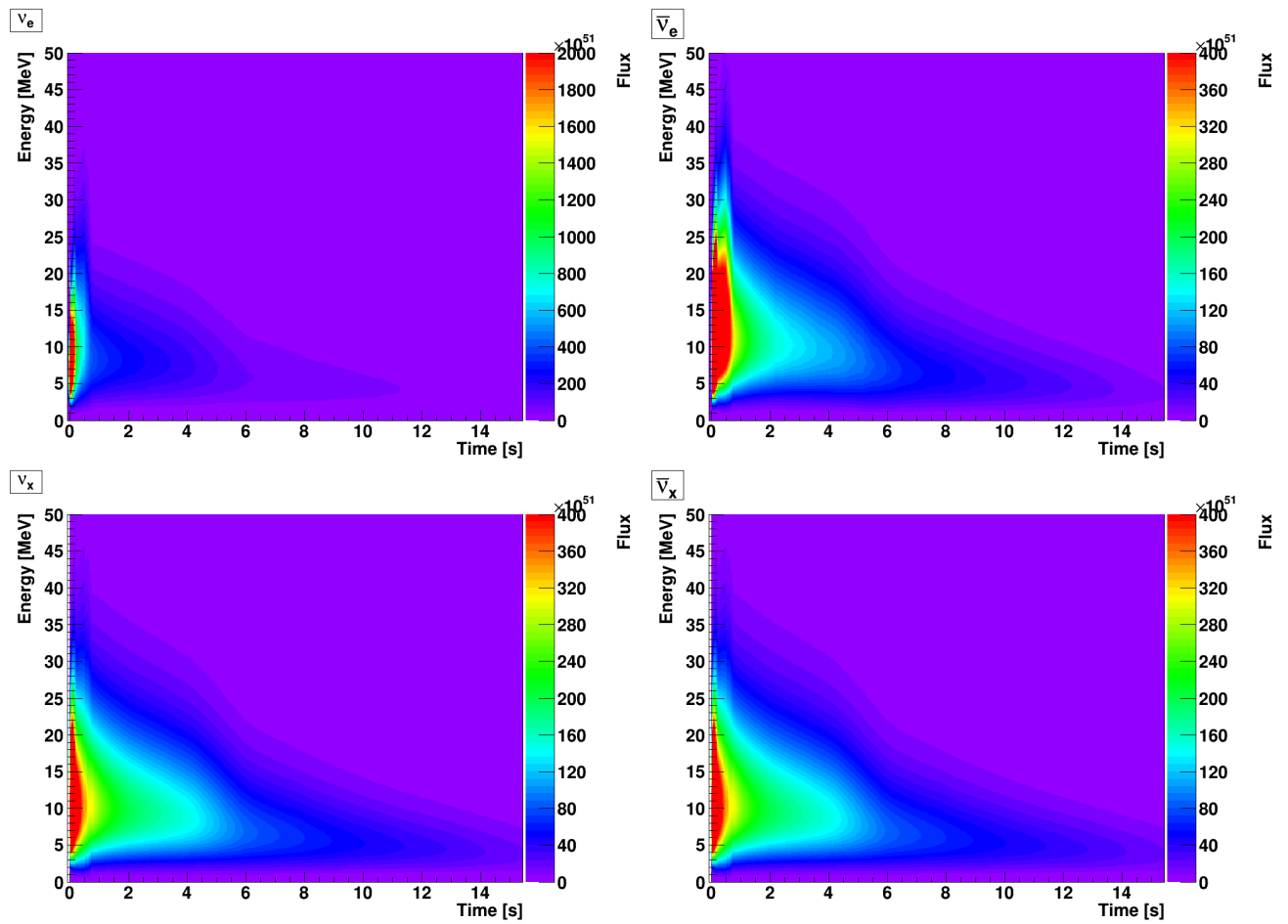**Figure F.52:** TEL: LS220-s27.0 model, assuming MSW effect.

Figure F.53: TEL: LS220-s27.0co model, inverted hierarchy, assuming MSW effect.